Construction of Orogenic Plateaus: Geomorphology and Geodynamics of the Puna Plateau, Central Andes

by

Mitchell McMillan

A thesis submitted in conformity with the requirements
for the degree of Doctor of Philosophy

Department of Earth Sciences
University of Toronto

© Copyright 2022 by Mitchell McMillan

Construction of Orogenic Plateaus: Geomorphology and Geodynamics of the Puna Plateau, Central Andes

Mitchell McMillan
Doctor of Philosophy

Department of Earth Sciences
University of Toronto
2022

Abstract

The Puna Plateau of the Central Andes provides an ideal setting to explore how tectonics and an arid climate interact to shape Earth's surface in orogenic plateaus. This thesis combines geologic mapping, eolian geomorphology, apatite fission track (AFT) thermochronology of the Southern Puna Plateau with numerical modelling to understand the geodynamics of plateau deformation and uplift. Mapping and AFT data of the Antofalla region suggests that the region was initially uplift the Early Eocene (~50 Ma) before being integrated into the Andean orogenic wedge during the Late Oligocene–Miocene (from 29 to 15.5 Ma). Mapping of the Salina del Fraile, a 300 km^2 topographic depression, suggests that its surface was lowered by wind erosion along fold hinges after this latter phase of shortening. Structural cross-sections across the Antofalla region show that Late Miocene and later strata were deposited in a half-graben hanging-wall basin that developed on what had previously been a topographic high when roughly E-W extension reactivated the Antofalla Fault. U-Pb zircon ages from folded strata suggest that the region resumed E-W shortening in the Late Pliocene to Quaternary. The relatively low magnitude of shortening implied by cross-sections suggests that deep-seated geodynamic processes such as lithospheric dripping may be partially responsible for crustal thickening. Lithospheric dripping has been inferred in 26 locations on Earth, but its diverse effects on topography and upper-crustal strain are poorly understood. This thesis develops a lithospheric dripping framework based on relative crustal strength, where a weak crust yields upper-crustal extension and surface uplift, the opposite response of a strong crust. Numerical models presented here suggest that weak-crust dripping can explain the observed kinematics of upper-crustal deformation in Puna Plateau. Among other data, the models explain Oligo–Miocene compression as the result of eclogite production and Mio–Pliocene extension due to lithospheric dripping.

Photographs on previous page (clockwise from top): View south from Sierra de la Quebrada Honda, across Laguna Cajeros toward the Salina del Fraile/Potrerillos anticline; Lindsay Schoenbohm hiking up Vega Chacras canyon, Salina del Fraile; Camp on undated volcanic flow, eastern margin of Salar de Antofalla, looking west toward Antofalla Volcanic Complex; Same camp looking east toward the Sierra de Calalaste.

Acknowledgements

First, I sincerely thank my supervisor Lindsay Schoenbohm for her thoughtful guidance, helpful feedback, and support throughout my Ph.D. Lindsay's mentorship was given freely and kindly, and I would not have been able to conceptualize or complete this research without it. Our weekly meetings were extremely valuable to the research, but they were also intellectually exciting. Throughout these particularly trying times, Lindsay was a truly great mentor, colleague, and friend.

I also thank the members of my committee, Russell Pysklywec and Melissa Anderson, for helping me think through the ins and outs of geodynamic modelling and providing needed institutional guidance. I am greatly appreciative of the folks at the Jack Satterly Geochronology Laboratory at University of Toronto, especially Sandra Kamo and Kim Kwok, for their geochronology expertise. Thanks to Sam Battye for teaching me how to crush and pulverize rocks.

I am deeply thankful to my collaborators around the world. Renjie Zhou (University of Queensland), thanks for lending expertise in zircon dating and thermochronology. Malcolm McMillan (University of Melbourne), thanks for your laboratory skills and deep knowledge of fission track dating. Alexander Tye (University of Toronto, now Dixie State University), thanks for working with me in the field and contributing significantly to my research questions. I also thank Santiago Uriburu, Yanina Rojo, Ignacio Ortiz, and Facundo Zambrano for expert guidance and warm hospitality in Argentina.

Many thanks to Jeremy Rimando, Erin Seagren, Katie Maloney, Evelyn Moorehouse, Monica Giona Bucci, Josh Wolpert, Mauricio Haag, and Scott Jess, who contributed ideas (or shot them down as necessary), honed arguments, and got me through my Ph.D. It was a privilege to work with and hang out with such an interesting and fun group of people. I'm honored to have you as friends and hope to continue working together.

I thank my partner Elizabeth McMillan for always believing in me, even when I didn't. There's no one else I would want to quarantine, isolate, or be snowed in with. Finally, to my family and friends, thanks for always loving and supporting me.

Contents

1 Introduction **1**

1.1 The enigmatic Puna Plateau . . . 2

1.2 Arid plateau landscape evolution . . . 4

1.3 Lithospheric foundering: Delamination and dripping . . . 6

1.4 Structure of this thesis . . . 7

References . . . 9

2 Large-scale Cenozoic wind erosion in the Puna Plateau **18**

2.1 Introduction . . . 19

2.1.1 The Salina del Fraile . . . 20

2.2 Materials and Methods . . . 22

2.3 Results and Discussion . . . 24

2.3.1 Structural interpretation: Against extensional lowering of the depression 24

2.3.2 Little evidence for fluvial incision . . . 27

2.3.3 Evidence in favor of wind erosion . . . 29

2.3.4 Timing and rate of erosion . . . 33

2.3.5 Implications . . . 35

2.4 Conclusions . . . 36

References . . . 38

3 Eocene to Quaternary deformation of the Southern Puna Plateau **43**

3.1 Introduction . . . 44

3.2 Geologic background . . . 46

3.3 Geologic mapping and U-Pb chronostratigraphy . . . 52

3.3.1 Methods . . . 53

3.3.2 Calalaste Range . . . 55

3.3.3 Cerro Campo Negro and Antofalla Fault . . . 60

3.3.4 Salina del Fraile . . . 66

3.3.5 Quebrada Honda Range . . . 70

3.4 Apatite fission track thermochronology . . . 71
3.4.1 Methods . . . 71
3.4.2 Calalaste range . . . 73
3.4.3 Cerro Campo Negro and Antofalla Fault . . . 76
3.4.4 Salina del Fraile . . . 79
3.4.5 Quebrada Honda range . . . 80
3.5 Structural cross-section . . . 81
3.6 Four-phase Cenozoic deformation . . . 83
3.7 Implications for formation and evolution of the Southern Puna Plateau . . . 86
3.7.1 Mesozoic tectonic setting . . . 86
3.7.2 Paleogene tectonic setting . . . 87
3.7.3 Crustal thickness and lithospheric foundering . . . 88
3.8 Conclusions . . . 91
References . . . 92

4 Two styles of lithospheric dripping **101**
4.1 Introduction . . . 102
4.2 Insights from numerical and analogue experiments . . . 104
4.2.1 Temporal scale and time to detachment . . . 105
4.2.2 Spatial scale and the characteristic wavelength . . . 109
4.2.3 Upper crust and topographic response: Two types of dripping . . . 110
4.2.4 Multiple drips during convergent and extensional tectonics . . . 118
4.2.5 Application of modelling studies to lithospheric dripping on Earth . . . 119
4.3 Alternative hypotheses . . . 124
4.3.1 Drips vs. slabs . . . 124
4.3.2 Dripping vs. delamination . . . 125
4.4 Potential dripping events . . . 126
4.4.1 North America . . . 128
4.4.2 South America . . . 139
4.4.3 Eurasia . . . 146
4.4.4 East African Rift and New Zealand . . . 159
4.4.5 Summary of potential dripping events . . . 161
4.5 Discussion . . . 162
4.5.1 Implications of strong-crust and weak-crust drips . . . 163
4.5.2 Directions for future research . . . 169
4.6 Conclusions . . . 175
References . . . 176

5 Geodynamics of continental back-arcs 197
5.1 Introduction . . . 198
5.2 The Southern Puna Plateau: Geologic background and significance . . . 201
5.3 Need for geodynamic models of the Southern Puna Plateau . . . 202
5.4 Geodynamic modelling methods . . . 203
5.4.1 Model geometry . . . 203
5.4.2 Rheological formulation and material properties . . . 204
5.4.3 Initial thermal structure . . . 206
5.4.4 Initial plastic damage . . . 206
5.4.5 Granulite-eclogite transition . . . 207
5.4.6 Velocity boundary conditions . . . 208
5.4.7 Model variation . . . 209
5.5 Results . . . 211
5.5.1 Behavior of the variant models . . . 211
5.5.2 Phase 1: Orogenic shortening . . . 214
5.5.3 Phase 2: Eclogitization . . . 216
5.5.4 Phase 3: Drip growth . . . 217
5.5.5 Phase 4: Detachment . . . 218
5.5.6 Phase 5: Recovery . . . 219
5.5.7 Upper crustal plastic deformation . . . 220
5.6 Discussion . . . 221
5.6.1 Assumptions and limitations . . . 221
5.6.2 Comparison to the Southern Puna Plateau . . . 223
5.6.3 Implications for the Central Andes . . . 227
5.6.4 Alternative hypotheses . . . 229
5.6.5 Implications for crustal deformation and plateau uplift . . . 230
5.7 Conclusions . . . 232
References . . . 232

6 Conclusions 244
6.1 Remaining questions and research opportunities . . . 245
References . . . 247

A Supporting information for Chapter 3 249

B Supporting information for Chapter 4 265

List of Figures

1.1 Tectonic map of the American Cordillera 2
1.2 Topography and morphotectonic regions of the Central Andes 3
1.3 Eolian transport, erosion, and geomorphology 5

2.1 Digital surface model (DSM) of the southern Puna Plateau 20
2.2 Theoretical cross-sections illustrating the two competing hypotheses 22
2.3 Topographic hillshade of the Salina del Fraile 25
2.4 Section A-A' 26
2.5 Section B-B' 26
2.6 Geomorphological evidence of wind erosion across spatial scales 28
2.7 Internal drainage of the Salina del Fraile 30
2.8 Photographs and and aerial imagery of eolian megaripples 32
2.9 Timing of wind erosion and comparison of erosion rates 34
2.10 Eolian landforms in Gale crater, Mars 37

3.1 Apatite fission track ages and crustal thickness of the Puna Plateau 45
3.2 Map of the Antofalla region 47
3.3 Stratigraphic nomenclature 50
3.4 Geologic map and cross-section of the Antofalla basin 54
3.5 Geologic map of the western flank of the Calalaste range 57
3.6 Outcrop photographs of the Lower Member of the Quiñoas Formation 58
3.7 Geologic map of Cerro Campo Negro and the Antofalla Fault System 61
3.8 Photograph looking west from the surface trace of the Antofalla Fault 63
3.9 Measurements of joints in the Quiñoas Formation 64
3.10 Geologic map of the Salina del Fraile and Quebrada Honda Range 67
3.11 Age-elevation plot of the Calalaste range 74
3.12 Thermal history models for the Calalaste range 75
3.13 AFT central ages and the Antofalla fault system 77
3.14 Thermal history models of the Antofalla Fault system 78
3.15 AFT ages for the Quebrada Honda range and Salina del Fraile 79
3.16 Thermal history models for the Potrerillos Anticline 80

3.17 Thermal history models of the Quebrada Honda range 81
3.18 Four phases of tectonic deformation 85
3.19 Illustration of estimation of shortening magnitude 89

4.1 Map of potential lithospheric dripping events 103
4.2 Cartoon depicting phases of Rayleigh–Taylor instability 106
4.3 Illustration of common lithospheric drip model and parameters 107
4.4 Snapshots of laboratory plume experiments 108
4.5 Illustration of strong-crust dripping 111
4.6 Illustration of weak-crust dripping 113
4.7 Drip model results compiled from the literature 115
4.8 Scaled analog model 116
4.9 Snapshots of lithospheric drip models during convergent tectonics 119
4.10 Relations between observable phenomena and drip size 121
4.11 Illustration of characteristic wavelength and width 123
4.12 Comparison of tomography anomalies for various purported drips 128
4.13 Potential dripping events in North America 129
4.14 Topographic features associated with purported dripping events 132
4.15 Comparison of volcanic provinces associated with lithospheric drips 139
4.16 Potential dripping events in South America 141
4.17 Potential dripping events in Europe and the East African Rift 147
4.18 Potential dripping events in Asia 152
4.19 Histograms of detachment age and wavelength 161
4.20 Illustration of idealized scenarios 167

5.1 Map of the Central Andes and Puna Plateau 199
5.2 Numerical model setup 204
5.3 Plot of initial plastic strain 207
5.4 Illustration of the phase transition representing eclogitization 208
5.5 Illustration of the formation and foundering of an eclogite root 212
5.6 Maximum depth of lithologic layers through time 214
5.7 Plot of upper crustal strain rate and eclogitization 215
5.8 Evolution of surface topography through time 216
5.9 Evolution of mid-crustal temperature 217
5.10 Plots of temperature and asthenosphere velocity vectors 219
5.11 Plot of accumulated plastic strain in the crust 221
5.12 Comparing model to observations 224

6.1 Eclogitization in geodynamic models 246

A.1 Large format geologic map 251

A.2 Aerial image of Calalaste Range 253
A.3 Aerial photographs illustrating folds 254
A.4 Photographs showing small faults 255
A.5 Radial plots and track length histograms (Calalaste Range) 257
A.6 Radial plots and track length histograms (Cerro Campo Negro) 258
A.7 Radial plots and track length histograms (Quebrada Honda Range) 259
A.8 Detrital zircon maximum depositional age determination 260

B.1 Drip models demonstrating two types of dripping 266

List of Tables

3.1 Summary of U-Pb zircon depositional age determination 55
3.2 AFT sample description and results 72

4.1 Summary of dripping scenarios predicted by numerical models 110

5.1 Rheology, thickness, and thermal parameters for materials in model. 206
5.2 Description of model variants compared to the base model. 210
5.3 Major results of the variant models 213

A.1 Results of maximum depositional age determination 250
A.2 Structural measurements 250
A.3 Summary of apatite fission track analysis 250
A.4 Detailed AFT age data (single-grain) 250
A.5 HeFTy thermal history modelling parameters 263
A.6 Constraints on stratal thicknesses 264

B.1 Summary of linear stability analyses 267

1 Introduction

Plate tectonics can generate continental mountain belts in two distinct ways: by the collision of two blocks of continental lithosphere, or by the subduction of oceanic lithosphere beneath continental. The Andes of South America are Earth's largest mountain belt formed by oceanic plate subduction. In fact, the entire western backbone of the Americas, from Alaska to Patagonia, consists of a chain of this type of mountain belt, often called a Cordilleran or Andean-type orogen (Figure 1.1). The American Cordillera developed along the western margins of Pangea and Gondwana since the Paleozoic (Dickinson, 2004; Lucassen et al., 2000). Collisional orogens, such as the Alpine-Himalaya chain, also underwent important phases of Cordilleran orogenesis prior to continental collision, which partly controlled the structural and size of the later collisional belt (Kroner & Romer, 2013; von Raumer, 1998; Yin & Harrison, 2000). The Andes are the type example of an active Cordilleran orogen, where ongoing subduction causes not only crustal thickening and mountain building, but earthquakes, landslides, and volcanism.

The Andes span multiple climatic regimes over their 8,000 km length, so the processes and rates of weathering and erosion change along strike. An erosional asymmetry across the orogen (due to latitudinal atmospheric circulation patterns) determines where erosion is able to effectively remove mass from the orogen, which influences the morphology and tectonic structure of the range (Montgomery et al., 2001). The Andes' "formidable topographic barrier", in turn, modifies the local climate, causing strong local variations in precipitation, temperature, wind, and vegetation (Garreaud, 2009). These factors grant the Andes an unrivalled status as a natural laboratory for probing deep questions about how tectonics, climate, and life interact to shape the surface of the Earth over geologic time.

The most striking topographic feature of the Andes is the large, arid region of high topography and volcanism situated in the middle of the mountain belt in Peru, Bolivia, and NW Argentina: the Altiplano-Puna Plateau (Figure 1.2). The Altiplano-Puna Plateau is essentially a welt of hot, thick continental crust buoying up the topography of the region (Isacks, 1988). Similarly large orogenic plateaus existed in the Canadian Cordillera during the Eocene (Bao et al., 2014), the Western U.S. "Nevadaplano" during the Late Cretaceous (Snell et al., 2014), and the Tibetan Plateau prior to India-Asia collision (Kapp & DeCelles, 2019). Orogenic plateaus formed in collisional settings share many of the same properties as Cordilleran plateaus, including crustal thickening and surface uplift, often in arid regions with low erosion rates (the Anatolian and Turkish-Iranian plateaus, Allen et al., 2013; Göğüş & Pysklywec, 2008a). The thickening

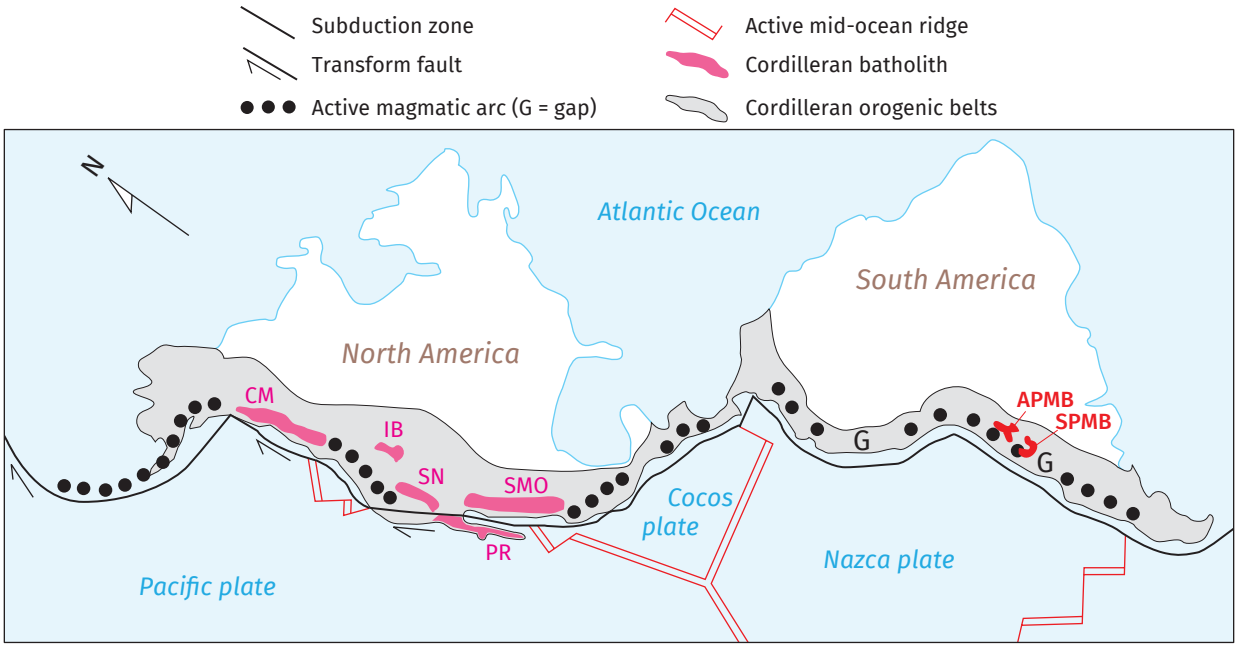

Figure 1.1: Tectonic map of the American Cordillera (after DeCelles et al., 2009; Dickinson, 2004). Exposed batholiths include CM (Coast Mountains), IB (Idaho Batholith), SN (Sierra Nevada), PR (Peninsular Ranges), and SMO (Sierra Madre Occidental). The APMB (Altiplano-Puna Magmatic Body) and SPMB (Southern Puna Magmatic Body) are active mid-crustal batholiths.

and uplift of the Altiplano-Puna Plateau is ultimately due to subduction of the oceanic Nazca Plate, but its extreme crustal thickness of 60 to 70 km is difficult to explain (Kley & Monaldi, 1998). A wide range of models of plateau uplift have been proposed, variously attributing the plateau formation to dominantly climatic (Lamb & Davis, 2003; Sobel et al., 2003) or tectonic processes (Allmendinger & Gubbels, 1996; Strecker et al., 2009). More recently, deep-seated geodynamic processes such as lithospheric delamination have been invoked as an explanation for crustal thickening and plateau uplift (DeCelles et al., 2009; Garzione et al., 2008). The "enigma of continental plateaus formed in the absence of collision" (Allmendinger et al., 1997) is an enduring topic of research and the theme of this thesis.

1.1 The enigmatic Puna Plateau

The Puna Plateau comprises the southern half of the Altiplano-Puna Plateau, and differs from the Altiplano in several key respects (Figure 1.2). First, the 50–65 km crust of the Puna is thinner than the Altiplano (70 km). Its mean elevation is nevertheless ~1 km higher (Allmendinger et al., 1997) because its mantle lithosphere is thin to absent (Beck & Zandt, 2002; Tassara et al., 2006), and its topography is isostatically compensated by the thick felsic crust and hot asthenosphere (Babeyko et al., 2002; Barnes & Ehlers, 2009). This lack of a mantle lid facilitates crustal melting and widespread silicic volcanism on the plateau (de Silva et al., 2006; Ward et al., 2017). The Southern Puna Plateau also hosts a back-arc mafic volcanic province, where monogenetic

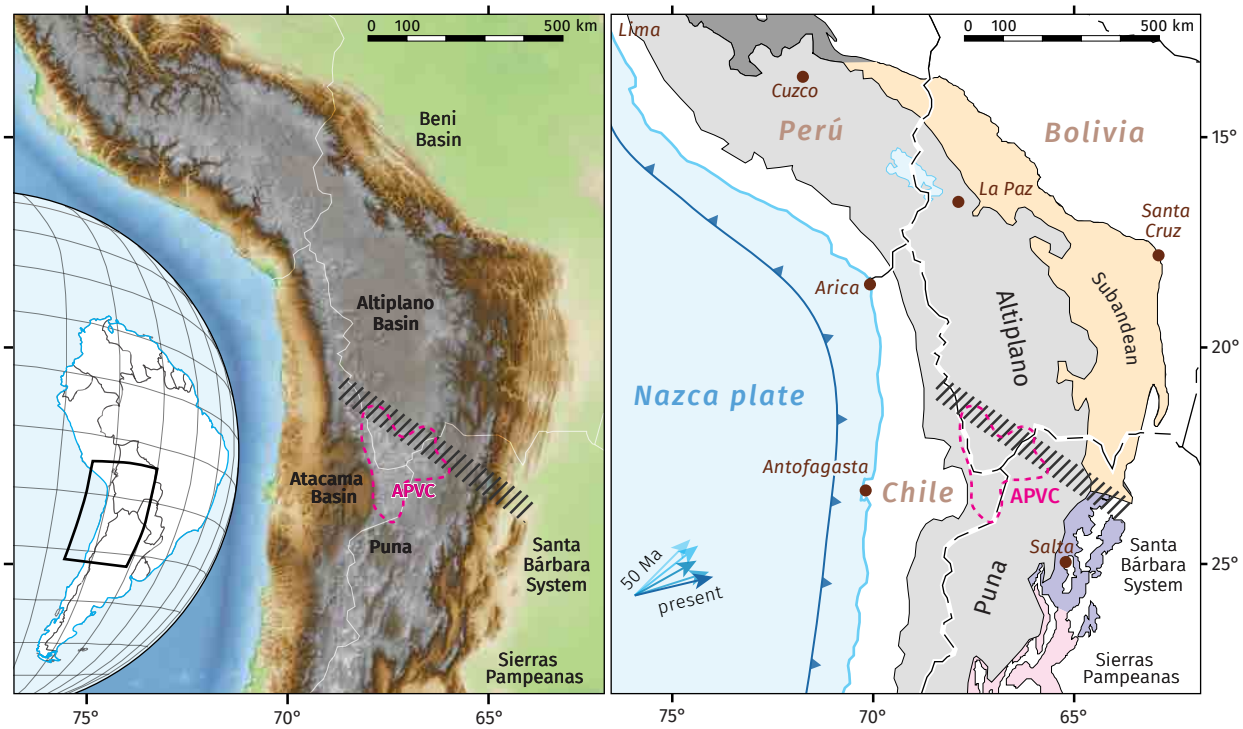

Figure 1.2: Topography (left) and morphotectonic regions (right) of the Central Andes (after Allmendinger et al., 1997). The thick dashed line and APVC (Altiplano-Puna volcanic complex) delineate the structural boundary between the Altiplano/Subandes and Puna Plateau/broken foreland. Nazca plate vectors from Barnes and Ehlers (2009).

flows, cinder cones, and intrusions are products of mantle melting (Kay et al., 1994; Risse et al., 2013). Significantly, the geochemistry of these volcanics is consistent with wet melting of the South American mantle lithosphere, i.e., the mantle lid that is currently missing from beneath the Puna (Ducea et al., 2013; Kay & Kay, 1993).

The plateau's low-relief topography is broken by mountain ranges trending parallel to the orogen, and these ranges are separated by Cenozoic hinterland basins (Strecker et al., 2009). Uplift of the ranges throughout the Cenozoic often deformed and exposed hinterland basin strata, allowing reconstruction of the timing and magnitude of Cenozoic shortening (e.g., McQuarrie & Ehlers, 2018). Shortening budget calculations largely account for the observed thickness of the crust throughout much of the Central Andes (Anderson et al., 2017; McQuarrie, 2002), but at the latitude of the Southern Puna Plateau, there is a large shortening deficit of ~100 km (Coutand et al., 2001; Kley & Monaldi, 1998). Thickening therefore likely involved other processes such as magmatic addition, lower crustal flow (Allmendinger et al., 1997), or crustal megathrust duplexing (McQuarrie, 2002) in order to reach the observed value of 60 km. It is also possible that more shortening was accommodated in the Puna Plateau than is commonly estimated due to a lack of structural data and cross-sections.

In addition to tectonic shortening, deep-seated geodynamic processes are often called upon to explain the uplift and deformation of the Puna Plateau (e.g., Beck & Zandt, 2002; Kay et al.,

1994). Potential processes include delamination (Beck & Zandt, 2002; Krystopowicz & Currie, 2013) and lithospheric dripping (DeCelles et al., 2015a; Göğüş & Pysklywec, 2008b; Schoenbohm & Carrapa, 2015). Several lines of evidence point towards at least two episodes of lithospheric dripping on the Puna Plateau (DeCelles et al., 2015b; Schoenbohm & Carrapa, 2015). The two purported drips were centered on the Arizaro region and the Southern Puna region during the Miocene and Pliocene, respectively. These drips may be imaged by seismic tomography anomalies ~50–100 km in diameter (Beck et al., 2015; Bianchi et al., 2013; Calixto et al., 2013), which roughly matches the size of the associated hinterland basins (Wang et al., 2015). Small-scale dripping, rather than wholesale lithosphere delamination, is capable of explaining the eruption of lithospheric melts, because larger bodies heat more quickly as they descend through the mantle, and are more prone to melting (Murray et al., 2015).

1.2 Arid plateau landscape evolution

This thesis addresses the question of how orogenic plateaus are constructed through the lens of tectonic geomorphology. Tectonic geomorphology involves finding characterizing tectonic deformation by analyzing the landscape, and usually depends on efficient erosional and depositional processes (e.g., fluvial or glacial incision and alluvial fan deposition), interacting with rapidly deforming structures (e.g., normal or reverse faults, folding or tilting) such that evidence of deformation is recorded in the landscape over a range of spatiotemporal scales (Burbank & Anderson, 2012). In this way, landforms such as fault scarps, strath terraces, and longitudinal river profiles can be dated or quantified to infer tectonic activity (Burbank & Anderson, 2012). Orogenic plateaus, however, are often often hyperarid, with limited Quaternary fluvial incision (Kapp et al., 2011) and are usually deformed slowly compared to the more tectonically active regions around their margins (McFarland et al., 2017; Zhou et al., 2015). Large swaths of plateau landscapes are mantled by colluvium or desert pavements, or else covered by recent salt and volcanic deposits. In these ways, these extreme plateau landscapes are more similar to Mars than to humid regions on Earth (Favaro et al., 2020; Xiao et al., 2017). In particular, wind, rather than ice or water, is often the dominant geomorphic agent in such regions (Rohrmann et al., 2013), and the landscapes evolve over much longer timescales as a result (Abell et al., 2020).

Wind can erode the landscape by means of two distinct processes: abrasion and deflation (Laity, 2017). Abrasion involves the sandblasting of bedrock surfaces by windblown particles, sculpting it into streamlined forms such as ventifacts, yardangs, and megayardangs (Figure 1.3). Deflation involves the entrainment and removal of fine-grained particles, which are often produced by salt weathering (Aref et al., 2002), and results in the formation of desert pans, blow-outs, and desert pavements (Goudie & Wells, 1995).

The signatures of both abrasion and deflation are apparent throughout the Southern Puna Plateau. Quaternary ignimbrite deposits are deeply abraded by windblown sand, forming large

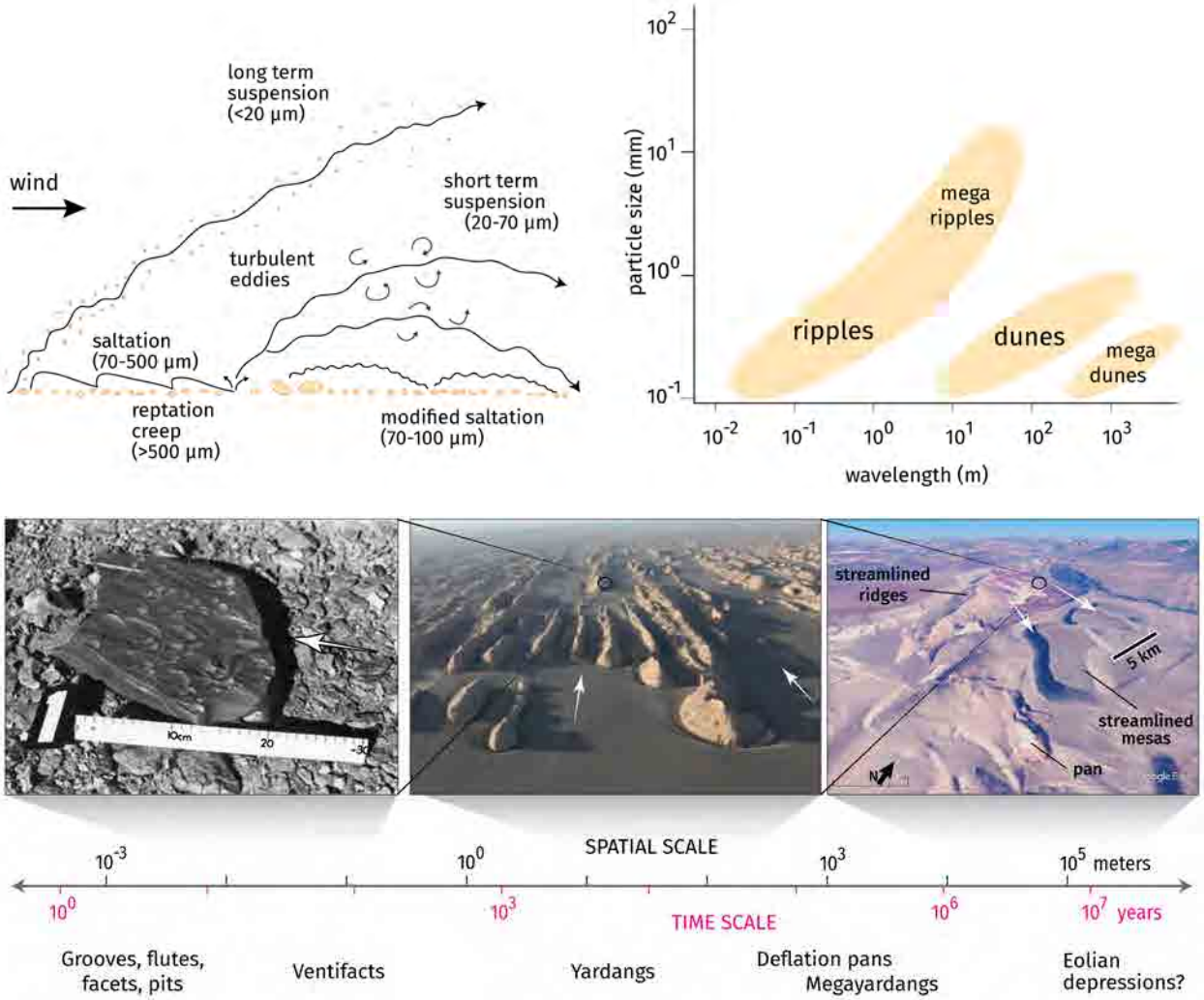

Figure 1.3: Eolian transport, erosion, and geomorphology. (a) Transport process related to particle size (Kok et al., 2012) ultimately sets the spatial scale of depositional bedforms (Milana, 2009; Pelletier, 2009). (b) Wind erosion landforms across a wide range of spatiotemporal scales (Selby, 1971; Wang et al., 2011). Wind direction indicated by white arrows.

fields of yardangs and megaripples (de Silva et al., 2010). Megayardangs occur along the western margin of the Salar de Antofalla (Goudie, 2007). Elsewhere, the landscape is covered with desert pavements and dotted with deflation pans (Goudie & Wells, 1995), and large dust storms have been imaged originating from the Puna Plateau (Milana & Kröhling, 2017), indicating that the region is actively subject to eolian deflation. Measured rates of deflation erosion during the Holocene are geomorphically significant (Milana & Kröhling, 2017). Furthermore, the climate of the Southern Puna region has been arid since at least 15 Ma (Alonso et al., 1991; Strecker et al., 2007), and potentially since 35 Ma (Quade et al., 2015). The extreme wind pattern that characterizes the modern Puna Plateau has been in place for at least 8 Myr, as suggested by sedimentologic studies (Greene, 1995; Ledesma et al., 2022). This evidence of a protracted,

hyperarid climate suggests that even relatively slow erosion driven by eolian deflation and abrasion may have significant effects on the topography of the Puna Plateau.

The potential for extreme wind erosion is especially relevant for interpreting the landscape of the Southern Puna Plateau. Large internally drained depressions (~10–100 km long), such as the Salina del Fraile and Salar de Antofalla, are usually ascribed to tectonic deformation, e.g., as pull-apart basins (Reijs & McClay, 2003; Voss, 2002), but other workers assume such depressions are the result of erosional processes, likely wind ("megapans" in Goudie & Wells, 1995). Whether wind erosion is capable of carving a given topographic depression, or whether the observed geology is better explained by strike-slip or normal faulting along its margins, has important implications for the kinematics of deformation of the Puna Plateau. Because fault exposure is generally poor, addressing these competing hypotheses require detailed geologic and structural mapping, as well as geomorphic mapping of erosional landforms and geomorphic indicators of wind direction.

1.3 Lithospheric foundering: Delamination and dripping

Crustal thickening can lead to prograde metamorphic reactions in the lower crust or mantle lithosphere, producing eclogitic rocks from granulite or gabbro protoliths (Bousquet et al., 1997; Hacker et al., 2003). In continental magmatic arcs, eclogite can also accumulate in the lower crust due as magmatic residues or cumulates due to the fractionation of granitic batholiths (Ducea, 2001; Jull & Kelemen, 2001). These eclogitic phases are predicted to be significantly more dense than mantle peridotite (Bousquet et al., 1997), potentially leading to a gravitational instability in which the dense phase founders and sinks into the mantle (Jull & Kelemen, 2001). Depending on the initial layer geometry and the rheology of the lower crust, the dense material can founder either in the form of delamination, sheets that peel away from the crust largely intact, or as viscous Rayleigh–Taylor instabilities, or drips (Beall et al., 2017; Göğüş & Pysklywec, 2008b; Krystopowicz & Currie, 2013).

Lithospheric dripping or delamination is often considered a viable hypothesis for a wide range of geological and geophysical observations in regions such as the Anatolian Plateau (Göğüş et al., 2017), the SE Carpathians (Göğüş et al., 2016; Lorinczi & Houseman, 2009), the Hindu Kush (Molnar & Bendick, 2019), the Pamir (Chapman et al., 2018), the Tibetan Plateau (Kapp & DeCelles, 2019), the North China Craton (Gao et al., 2004), the Canadian Cordillera (Bao et al., 2014), the Western U.S. (e.g., Levander et al., 2011; West et al., 2009; Zandt et al., 2004), and the Central Andes (e.g., Garzione et al., 2006; Sundell et al., 2019). The buildup and foundering of dense lithospheric roots may be a fundamental process of Cordilleran orogenesis (DeCelles et al., 2009), setting the pace of arc-magmatic flareups (Paterson & Ducea, 2015), propagation of the orogenic front into the foreland, and out-of-sequence deformation in the orogenic hinterland (DeCelles et al., 2015b). Recent research is increasingly leaning on the concept of lithospheric dripping to explain the "antithetical processes" (DeCelles et al., 2015b) observed in the Andean

hinterland, especially the Puna Plateau (e.g., Chen et al., 2020; Morfulis et al., 2020; Tye et al., 2022). However, the effects of lithospheric dripping on upper-crustal strain and topography in convergent settings are not well understood, and these studies often rely on model results that are applicable for locations with relatively strong crusts, where drip growth is accommodated by crustal flexure (Neil & Houseman, 1999). It is not clear if such models are directly applicable to the Puna Plateau, which is is strongly affected by crustal thickening, heating, volcanism, and pre-existing weaknesses.

A dripping event beneath the Arizaro basin in the Northern Puna may explain the coeval accumulation and shortening of lacustrine sediments during the Miocene, followed by silicic volcanism and upper-crustal extension (DeCelles et al., 2015a; Schoenbohm & Carrapa, 2015; Wang et al., 2015). The Arizaro drip seemingly pulled down the crust, causing flexural subsidence, the formation of a saucer-shaped hinterland basin, and the sedimentary burial of the Sierra de Macon; after the drip detached, the basin was uplifted and inverted, and the Sierra de Macon was exhumed (DeCelles et al., 2015a). The geologic record of the Southern Puna is more sparse, and the extent and deformation of Miocene to Pliocene sedimentary strata are not well known. Back-arc volcanism is centered on the Sierra de Calalaste, where the oldest mafic volcanic flows are located (Haag et al., 2019; Schoenbohm & Carrapa, 2015), but most of the sedimentary and structural evidence for dripping, such as contractional growth strata and fault reactivation, was observed in the Pasto Ventura region in the SE margin of the plateau (Schoenbohm & Carrapa, 2015; Zhou & Schoenbohm, 2015). Earlier work in the Antofalla basin, close to the inferred dripping center, suggests a complex history of Cenozoic deformation and sedimentation that could be useful for evaluating hypotheses for the uplift and deformation of the plateau (Adelmann, 2001; Kraemer et al., 1999). These studies, however, mainly consist of stratigraphic and paleoclimate data (Canavan et al., 2014; Kraemer et al., 1999; Quade et al., 2015) that do not tightly constrain the timing and kinematics of deformation. Exhumation data in the Southern Puna is broadly consistent with lithospheric dripping during the Pliocene (Zhou et al., 2017), but do not place additional constraints on the hypothesis because such data is sparse in the key region surrounding the Antofalla basin (Carrapa et al., 2005; Zhou et al., 2017).

1.4 Structure of this thesis

This thesis takes a comprehensive approach to uncover the tectonic history of the Puna Plateau, one that integrates geologic mapping, structural geology, and low-temperature thermochronology with eolian geomorphology and geodynamic modelling. The thesis is composed of four chapters, each of which have been prepared for submission to peer-reviewed journals. Like any research, this work is a result of collaboration with co-authors. For each chapter, I led the conceptualization, field work, sample collection, data interpretation, and writing. I also performed sample processes for apatite and zircon mineral separation. Other laboratory work,

including U-Pb zircon LA-ICP-MS dating and apatite fission track dating was accomplished by collaborators, as described in the relevant chapters. This thesis addresses the following research questions:

Q1. When, where, and how did deformation occur during Andean mountain building?

Q2. What processes are responsible for plateau uplift and topography?

Q3. How is topography modified by climate in hyperarid plateaus?

Chapter 2 explores role of wind erosion as a significant geomorphic agent in the Puna Plateau by focusing on an enigmatic landform, the Salina del Fraile depression. The prevailing interpretation of the Salina del Fraile is that of a pull-apart basin (Reijs & McClay, 2003), implying an episode of strike-slip tectonics in the region. Measurements of bedding collected in the field, combined with existing chronostratigraphic data and sedimentological studies, instead show that the structural setting of the region is compressional, not extensional (question 1). This finding simplifies the known kinematic history of the Southern Puna Plateau, which is relevant for later chapters. The compressional setting also implies that erosion is responsible for creating the large topographic depression (question 3). Observations and mapping of eolian landforms (megaripples, yardangs, and megayardangs), suggest that prevailing NW-SE winds are responsible for carving the depression. Dated alluvial remnants deposited in the floor of the depression are used to infer that most of the erosion began prior to 8.2 Ma, and topographic analyses suggest an average erosion rate of 0.1 to 0.3 mm yr^{-1}, a rate which is similar to wind erosion rates measured in arid Asia. Chapter 2 highlights streamlined landforms mapped in the Salina del Fraile that are similar to ones observed on the surface of Mars, suggesting that over geologic timescales, wind can modify the topography of entire landscapes, sustaining landforms with kilometer-scale topographic relief (question 3).

Chapter 3 uses geologic mapping, structural cross-sections, U-Pb zircon geochronology, and apatite fission track thermochronology to uncover the history of exhumation deformation of the Antofalla region (questions 1 and 2). Thermochronology data reveal a widespread phase of deformation that affected the region between 50 and 35 Ma, uplifting the Calalaste and Quebrada Honda ranges. Dating and mapping of syn-tectonic sediments suggest a second phase of deformation, which propagated westward from the Calalaste range 29–16 Ma, establishing a west-vergent wedge. Structural cross-sections through the region show how Late Miocene and younger strata were deposited in a structural low due to extensional reactivation of a major reverse fault accommodating >1 km of normal slip. These observations suggest that the region was deformed as a broken foreland basin during the Eocene before being incorporated into the orogenic wedge during the Late Oligocene–Miocene. Late Miocene–Pliocene extensional tectonics has implications for lithospheric dripping beneath the plateau.

Chapter 4 explores the concept of lithospheric dripping in a critical review of the relevant literature, especially as it relates to topographic uplift and upper-crustal deformation (question 2). A synthesis of numerical modelling studies suggest that lithospheric dripping

produces two distinct patterns of upper-crustal deformation dependent on the strength of the crust relative to the lithosphere. If the crust is weaker than the mantle lithosphere, dripping produces upper-crustal extension and surface uplift, rather than the commonly assumed upper-crustal contraction and surface subsidence question 2. This study provides a framework for understanding the diverse effects of lithospheric dripping, and includes discussion of emerging research techniques in fields such as volcanic geochemistry, geodynamic modelling, and quantitative geomorphology that show promise for future research into the topic. The concept of weak-crust dripping is relevant for the geodynamics of orogenic plateaus, especially the Southern Puna Plateau (questions 1 and 2).

Chapter 5 explores the lithospheric dripping hypothesis for the Puna Plateau questions 1 and 2. Specifically, numerical models simulate the production and dripping of eclogite beneath a weak, granitic crust resembling the Southern Puna Plateau. The models suggest that lithospheric dripping is a viable explanation for the Late Oligocene–Early Miocene upper-crustal shortening and uplift observed in the Antofalla region , as well as the transient episode of upper-crustal extension during the Late Miocene–Pliocene (Chapter 3). Predictions of upper-crustal deformation largely fit the existing data in the Southern Puna Plateau that indicate the location, timing, and style of deformation. The models also provide an explanation for the current kinematic state of the plateau, characterized by upper-crustal shortening in its interior and orogen-parallel extension along its edges, as due to thermal buoyancy and gravitational collapse following a weak-crust drip.

As of February 2022, Chapter 2 is published in the *Journal of Geophysical Research: Earth Surface*, Chapter 3 is under review in *Tectonics*, Chapter 4 is prepared for submission to *Geochemistry, Geophysics, Geosystems*, and Chapter 5 is prepared for submission to (tentatively) *Geosphere*.

References

Abell, J. T., Pullen, A., Lebo, Z. J., Kapp, P., Gloege, L., Metcalf, A. R., Nie, J., & Winckler, G. (2020). A wind-albedo-wind feedback driven by landscape evolution. *Nature Communications*, *11*(1), 1–9. https://doi.org/10.1038/s41467-019-13661-w

Adelmann, D. (2001). *Känozoische Beckenentwicklung des zentralandinen Puna-Plateaus (NW-Argentinien): Das Gebiet um den Salar de Antofalla und ein Vergleich zur nördlichen Puna* (Doctoral dissertation). Freien Universität Berlin.

Allen, M. B., Saville, C., Blanc, E.-P., Talebian, M., & Nissen, E. (2013). Orogenic plateau growth: Expansion of the Turkish-Iranian Plateau across the Zagros fold-and-thrust belt. *Tectonics*, *32*(2), 171–190. https://doi.org/10.1002/tect.20025

Allmendinger, R. W., & Gubbels, T. (1996). Pure and simple shear plateau uplift, Altiplano-Puna, Argentina and Bolivia. *Tectonophysics*, *259*(1-3), 1–13. https://doi.org/10.1016/0040-1951(96)00024-8

Allmendinger, R. W., Jordan, T. E., Kay, S. M., & Isacks, B. L. (1997). The evolution of the Altiplano-Puna Plateau of the Central Andes. *Annual Review of Earth and Planetary Sciences*, *25*, 139–174. https://doi.org/10.1146/annurev.earth.25.1.139

Alonso, R. N., Jordan, T. E., Tabbutt, K. T., & Vandervoort, D. S. (1991). Giant evaporite belts of the Neogene central Andes. *Geology*, *19*(4), 401–404. https://doi.org/10.1130/0091-7613(1991)019<0401:GEBOTN>2.3.CO;2

Anderson, R. B., Long, S. P., Horton, B. K., Calle, A. Z., & Ramirez, V. (2017). Shortening and structural architecture of the Andean fold-thrust belt of southern Bolivia (21 s): Implications for kinematic development and crustal thickening of the central Andes. *Geosphere*, *13*(2), 538–558. https://doi.org/doi.org/10.1130/GES01433.1

Aref, M. A., El-Khoriby, E., & Hamdan, M. A. (2002). The role of salt weathering in the origin of the Qattara Depression, Western Desert, Egypt. *Geomorphology*, *45*(3-4), 181–195. https://doi.org/10.1016/S0169-555X(01)00152-0

Babeyko, A. Y., Sobolev, S. V., Trumbull, R. B., Oncken, O., & Lavier, L. L. (2002). Numerical models of crustal scale convection and partial melting beneath the Altiplano-Puna plateau. *Earth and Planetary Science Letters*, *199*(3-4), 373–388. https://doi.org/10.1016/S0012-821X(02)00597-6

Bao, X., Eaton, D. W., & Guest, B. (2014). Plateau uplift in western Canada caused by lithospheric delamination along a craton edge. *Nature Geoscience*, *7*(11), 830–833. https://doi.org/10.1038/ngeo2270

Barnes, J. B., & Ehlers, T. A. (2009). End member models for Andean Plateau uplift. *Earth-Science Reviews*, *97*(1-4), 105–132. https://doi.org/10.1016/j.earscirev.2009.08.003

Beall, A. P., Moresi, L., & Stern, T. (2017). Dripping or delamination? A range of mechanisms for removing the lower crust or lithosphere. *Geophysical Journal International*, (September), 671–692. https://doi.org/10.1093/gji/ggx202

Beck, S. L., & Zandt, G. (2002). The nature of orogenic crust in the central Andes. *Journal of Geophysical Research: Solid Earth*, *107*(B10), 2230. https://doi.org/10.1029/2000JB000124

Beck, S. L., Zandt, G., Ward, K. M., & Scire, A. (2015). Multiple styles and scales of lithospheric foundering beneath the Puna Plateau, central Andes. In *Geological Society of America Memoirs* (pp. 43–60). https://doi.org/10.1130/2015.1212(03)

Bianchi, M., Heit, B., Jakovlev, A., Yuan, X., Kay, S. M., Sandvol, E., Alonso, R. N., Coira, B., Brown, L. D., Kind, R., & Comte, D. (2013). Teleseismic tomography of the southern Puna plateau in Argentina and adjacent regions. *Tectonophysics*, *586*, 65–83. https://doi.org/10.1016/j.tecto.2012.11.016

Bousquet, R., Goffé, B., Henry, P., Le Pichon, X., & Chopin, C. (1997). Kinematic, thermal and petrological model of the Central Alps: Lepontine metamorphism in the upper crust and eclogitisation of the lower crust. *Tectonophysics*, *273*(1-2), 105–127. https://doi.org/10.1016/S0040-1951(96)00290-9

Burbank, D. W., & Anderson, R. S. (2012). *Tectonic geomorphology* (2nd ed.). John Wiley & Sons.

Calixto, F. J., Sandvol, E., Kay, S. M., Mulcahy, P., Heit, B., Yuan, X., Coira, B., Comte, D., & Alvarado, P. (2013). Velocity structure beneath the southern Puna plateau: Evidence for delamination. *Geochemistry, Geophysics, Geosystems*, *14*(10), 4292–4305. https://doi.org/10.1002/ggge.20266

Canavan, R. R., Carrapa, B., Clementz, M. T., Quade, J., DeCelles, P. G., & Schoenbohm, L. M. (2014). Early cenozoic uplift of the Puna plateau, central andes, based on stable isotope paleoaltimetry of hydrated volcanic glass. *Geology*, *42*(5), 447–450. https://doi.org/10.1130/G35239.1

Carrapa, B., Adelmann, D., Hilley, G. E., Mortimer, E., Sobel, E. R., & Strecker, M. R. (2005). Oligocene range uplift and development of plateau morphology in the southern central Andes. *Tectonics*, *24*, TC4011. https://doi.org/10.1029/2004TC001762

Chapman, J. B., Scoggin, S. H., Kapp, P., Carrapa, B., Ducea, M. N., Worthington, J., Oimahmadov, I., & Gadoev, M. (2018). Mesozoic to Cenozoic magmatic history of the Pamir. *Earth and Planetary Science Letters*, *482*(November 2017), 181–192. https://doi.org/10.1016/j.epsl.2017.10.041

Chen, J., Kufner, S.-K., Yuan, X., Heit, B., Wu, H., Yang, D., Schurr, B., & Kay, S. (2020). Lithospheric delamination beneath the southern puna plateau resolved by local earthquake tomography. *Journal of Geophysical Research: Solid Earth*, *125*(10), e2019JB019040. https://doi.org/10.1029/2019JB019040

Coutand, I., Cobbold, P. R., De Urreiztieta, M., Gautier, P., Chauvin, A., Gapais, D., Rossello, E. A., & López-Gamundí, O. (2001). Style and history of Andean deformation, Puna plateau, northwestern Argentina. *Tectonics*, *20*(2), 210–234. https://doi.org/10.1029/2000TC900031

DeCelles, P. G., Carrapa, B., Horton, B. K., McNabb, J., Gehrels, G. E., & Boyd, J. (2015a). The Miocene Arizaro Basin, central Andean hinterland: Response to partial lithosphere removal? In *Geological Society of America Memoirs* (pp. 359–386). https://doi.org/10.1130/2015.1212(18)

DeCelles, P. G., Ducea, M. N., Kapp, P., & Zandt, G. (2009). Cyclicity in Cordilleran orogenic systems. *Nature Geoscience*, *2*(4), 251–257. https://doi.org/10.1038/ngeo469

DeCelles, P. G., Zandt, G., Beck, S. L., Currie, C. A., Ducea, M. N., Kapp, P., Gehrels, G. E., Carrapa, B., Quade, J., & Schoenbohm, L. M. (2015b). Cyclical orogenic processes in the Cenozoic central Andes. In *Geological Society of America Memoirs* (pp. 459–490). https://doi.org/10.1130/2015.1212(22)

de Silva, S. L., Bailey, J. E., Mandt, K. E., & Viramonte, J. M. (2010). Yardangs in terrestrial ignimbrites: Synergistic remote and field observations on Earth with applications to Mars. *Planetary and Space Science*, *58*(4), 459–471. https://doi.org/10.1016/j.pss.2009.10.002

de Silva, S. L., Zandt, G., Trumbull, R. B., Viramonte, J. G., Salas, G., & Jiménez, N. (2006). Large ignimbrite eruptions and volcano-tectonic depressions in the Central Andes: a thermomechanical perspective. *Geological Society, London, Special Publications*, *269*(1), 47–63. https://doi.org/10.1144/GSL.SP.2006.269.01.04

Dickinson, W. R. (2004). Evolution of the North American Cordillera. *Annual Review of Earth and Planetary Sciences*, *32*(1), 13–45. https://doi.org/10.1146/annurev.earth.32.101802.120257

Ducea, M. N. (2001). The California arc: Thick granitic batholiths, eclogitic residues, lithospheric-scale thrusting, and magmatic flare-ups. *GSA Today*, *11*(11), 4–10. https://doi.org/10.1130/1052-5173(2001)011<0004:TCATGB>2.0.CO;2

Ducea, M. N., Seclaman, A. C., Murray, K. E., Jianu, D., & Schoenbohm, L. M. (2013). Mantle-drip magmatism beneath the Altiplano-Puna plateau, central Andes. *Geology*, *41*(8), 915–918. https://doi.org/10.1130/G34509.1

Favaro, E. A., Hugenholtz, C. H., Barchyn, T. E., & Gough, T. R. (2020). Wind regime, sediment transport, and landscape dynamics at a Mars analogue site in the Andes Mountains of Northwestern Argentina. *Icarus*, *346*(February), 113765. https://doi.org/10.1016/j.icarus.2020.113765

Gao, S., Rudnick, R., Yuan, H., Liu, X., Liu, Y. S., Xu, W. L., Ling, W. L., Ayers, J., Wang, X. C., & Wang, Q. H. (2004). Recycling lower continental crust in the North China craton. *Nature*, *432*, 892–897.

Garreaud, R. D. (2009). The Andes climate and weather. *Advances in geosciences*, *22*, 3–11. https://doi.org/10.5194/adgeo-22-3-2009

Garzione, C. N., Hoke, G. D., Libarkin, J. C., Withers, S., MacFadden, B., Eiler, J., Ghosh, P., & Mulch, A. (2008). Rise of the Andes. *Science*, *320*(5881), 1304–1307. https://doi.org/10.1126/science.1148615

Garzione, C. N., Molnar, P., Libarkin, J. C., & MacFadden, B. J. (2006). Rapid late Miocene rise of the Bolivian Altiplano: Evidence for removal of mantle lithosphere. *Earth and Planetary Science Letters*, *241*(3-4), 543–556. https://doi.org/10.1016/j.epsl.2005.11.026

Göğüş, O. H., & Pysklywec, R. N. (2008a). Mantle lithosphere delamination driving plateau uplift and synconvergent extension in eastern Anatolia. *Geology*, *36*(9), 723–726. https://doi.org/10.1130/G24982A.1

Göğüş, O. H., & Pysklywec, R. N. (2008b). Near-surface diagnostics of dripping or delaminating lithosphere. *Journal of Geophysical Research: Solid Earth*, *113*(11), 1–11. https://doi.org/10.1029/2007JB005123

Göğüş, O. H., Pysklywec, R. N., & Faccenna, C. (2016). Postcollisional lithospheric evolution of the Southeast Carpathians: Comparison of geodynamical models and observations. *Tectonics*, *35*(5), 1205–1224. https://doi.org/10.1002/2015TC004096

Göğüş, O. H., Pysklywec, R. N., şengör, A. M. C., & Gün, E. (2017). Drip tectonics and the enigmatic uplift of the Central Anatolian Plateau. *Nature Communications*, *8*(1), 1538. https://doi.org/10.1038/s41467-017-01611-3

Goudie, A. S., & Wells, G. L. (1995). The nature, distribution and formation of pans in arid zones. *Earth Science Reviews*, *38*(1), 1–69. https://doi.org/10.1016/0012-8252(94)00066-6

Goudie, A. S. (2007). Mega-yardangs: A global analysis. *Geography Compass*, *1*(1), 65–81. https://doi.org/10.1111/j.1749-8198.2006.00003.x

Greene, L. L. (1995). *Eolian landforms in the Central Andes: implications for the long-term stability of atmospheric circulation* (Doctoral dissertation). Cornell University.

Haag, M. B., Baez, W. A., Sommer, C. A., Arnosio, J. M., & Filipovich, R. E. (2019). Geomorphology and spatial distribution of monogenetic volcanoes in the southern Puna Plateau (NW Argentina). *Geomorphology*, *342*, 196–209. https://doi.org/10.1016/j.geomorph.2019.06.008

Hacker, B. R., Abers, G. A., & Peacock, S. M. (2003). Subduction factory 1. Theoretical mineralogy, densities, seismic wave speeds, and H2O contents. *Journal of Geophysical Research: Solid Earth*, *108*(B1), 1–26. https://doi.org/10.1029/2001jb001127

Isacks, B. L. (1988). Uplift of the central Andean Plateau and bending of the Bolivian Orocline. *Journal of Geophysical Research*, *93*(B4), 3211–3231. https://doi.org/10.1029/JB093iB04p03211

Jull, M., & Kelemen, P. B. (2001). On the conditions for lower crustal convective instability. *Journal of Geophysical Research: Solid Earth*, *106*(B4), 6423–6446. https://doi.org/10.1029/2000JB900357

Kapp, P., & DeCelles, P. G. (2019). Mesozoic–Cenozoic geological evolution of the Himalayan-Tibetan orogen and working tectonic hypotheses. *American Journal of Science*, *319*(3), 159–254. https://doi.org/10.2475/03.2019.01

Kapp, P., Pelletier, J. D., Rohrmann, A., Heermance, R., Russell, J., & Ding, L. (2011). Wind erosion in the Qaidam basin, central Asia: Implications for tectonics, paleoclimate, and the source of the Loess Plateau. *GSA Today*, *21*(4-5), 4–10. https://doi.org/10.1130/GSATG99A.1

Kay, R. W., & Kay, S. M. (1993). Delamination and delamination magmatism. *Tectonophysics*, *219*(1-3), 177–189. https://doi.org/10.1016/0040-1951(93)90295-U

Kay, S. M., Coira, B., & Viramonte, J. (1994). Young mafic back arc volcanic rocks as indicators of continental lithospheric delamination beneath the Argentine Puna Plateau, central Andes. *Journal of Geophysical Research: Solid Earth*, *99*(B12), 24323–24339. https://doi.org/10.1029/94JB00896

Kley, J., & Monaldi, C. R. (1998). Tectonic shortening and crustal thickness in the Central Andes: How good is the correlation-? *Geology*, *26*(8), 723–726. https://doi.org/10.1130/0091-7613(1998)026<0723:TSACTI>2.3.CO;2

Kok, J. F., Parteli, E. J., Michaels, T. I., & Karam, D. B. (2012). The physics of wind-blown sand and dust. *Reports on Progress in Physics*, *75*(10). https://doi.org/10.1088/0034-4885/75/10/106901

Kraemer, B., Adelmann, D., Alten, M., Schnurr, W., Erpenstein, K., Kiefer, E., Van Den Bogaard, P., & Görler, K. (1999). Incorporation of the Paleogene foreland into the Neogene Puna plateau: The Salar de Antofalla area, NW Argentina. *Journal of South American Earth Sciences*, *12*(2), 157–182. https://doi.org/10.1016/S0895-9811(99)00012-7

Kroner, U., & Romer, R. L. (2013). Two plates — Many subduction zones: The Variscan orogeny reconsidered. *Gondwana Research*, *24*(1), 298–329. https://doi.org/10.1016/j.gr.2013.03.001

Krystopowicz, N. J., & Currie, C. A. (2013). Crustal eclogitization and lithosphere delamination in orogens. *Earth and Planetary Science Letters*, *361*, 195–207. https://doi.org/10.1016/j.epsl.2012.09.056

Laity, J. E. (2017). Eolian Erosional Processes and Landforms. *International Encyclopedia of Geography: People, the Earth, Environment and Technology*, 1–7. https://doi.org/10.1002/9781118786352.wbieg0915

Lamb, S., & Davis, P. (2003). Cenozoic climate change as a possible cause for the rise of the Andes. *Nature*, *425*(6960), 792–797. https://doi.org/10.1038/nature02049

Ledesma, J., del Papa, C. E., & Payrola, P. (2022). The late Miocene eolian record at the eastern margin of the Puna Plateau, NW Argentina: Evidence of upper-tropospheric paleocirculation. *Journal of Sedimentary Research*, *92*(1), 32–49. https://doi.org/10.2110/jsr.2021.018

Levander, A., Schmandt, B., Miller, M. S., Liu, K., Karlstrom, K. E., Crow, R. S., Lee, C.-T. A., & Humphreys, E. D. (2011). Continuing Colorado plateau uplift by delamination-style convective lithospheric downwelling. *Nature*, *472*(7344), 461–465. https://doi.org/10.1038/nature10001

Lorinczi, P., & Houseman, G. A. (2009). Lithospheric gravitational instability beneath the Southeast Carpathians. *Tectonophysics*, *474*(1-2), 322–336. https://doi.org/10.1016/j.tecto.2008.05.024

Lucassen, F., Becchio, R., Wilke, H. G., Franz, G., Thirlwall, M. F., Viramonte, J., & Wemmer, K. (2000). *Proterozoic-Paleozoic development of the basement of the Central Andes (18-26° S): A mobile belt of the South American craton* (tech. rep.).

McFarland, P. K., Bennett, R. A., Alvarado, P., & DeCelles, P. G. (2017). Rapid Geodetic Shortening Across the Eastern Cordillera of NW Argentina Observed by the Puna-Andes GPS Array. *Journal of Geophysical Research: Solid Earth*, *122*(10), 8600–8623. https://doi.org/10.1002/2017JB014739

McQuarrie, N. (2002). The kinematic history of the central Andean fold-thrust belt, Bolivia: Implications for building a high plateau. *Bulletin of the Geological Society of America*, *114*(8), 950–963. https://doi.org/10.1130/0016-7606(2002)114<0950:TKHOTC>2.0.CO;2

McQuarrie, N., & Ehlers, T. A. (2018). Techniques for understanding fold-and-thrust belt kinematics and thermal evolution. *Linkages and Feedbacks in Orogenic Systems*, *1213*(02), 25–54. https://doi.org/10.1130/2017.1213(02)

Milana, J. P. (2009). Largest wind ripples on Earth? *Geology*, *37*(4), 343–346. https://doi.org/10.1130/G25382A.1

Milana, J. P., & Kröhling, D. M. (2017). First data on volume and type of deflated sediment from Southern Puna Plateau and its role as source of the Chaco-Pampean loess. *Quaternary International*, *438*(March), 126–140. https://doi.org/10.1016/j.quaint.2017.03.007

Molnar, P., & Bendick, R. (2019). Seismic Moments of Intermediate-Depth Earthquakes Beneath the Hindu Kush: Active Stretching of a Blob of Sinking Thickened Mantle Lithosphere? *Tectonics*, *38*(5), 1651–1665. https://doi.org/10.1029/2018TC005336

Montgomery, D. R., Balco, G., & Willett, S. D. (2001). Climate, tectonics, and the morphology of the Andes. *Geology*, *29*(7), 579–582. https://doi.org/10.1130/0091-7613(2001)029<0579:CTATMO>2.0.CO;2

Morfulis, M., Báez, W., Retamoso, S., Bardelli, L., Filipovich, R., & Sommer, C. A. (2020). Quantitative spatial distribution analysis of mafic monogenic volcanism in the southern Puna, Argentina: Implications for magma production rates and structural control during its ascent. *Journal of South American Earth Sciences*, *104*(September). https://doi.org/10.1016/j.jsames.2020.102852

Murray, K. E., Ducea, M. N., & Schoenbohm, L. M. (2015). Foundering-driven lithospheric melting: The source of central Andean mafic lavas on the Puna Plateau (22°S–27°S). In *Geological Society of America Memoirs* (pp. 139–166). https://doi.org/10.1130/2015.1212(08)

Neil, E. A., & Houseman, G. A. (1999). Rayleigh-Taylor instability of the upper mantle and its role in intraplate orogeny. *Geophysical Journal International*, *138*(1), 89–107. https://doi.org/10.1046/j.1365-246X.1999.00841.x

Paterson, S. R., & Ducea, M. N. (2015). Arc magmatic tempos: Gathering the evidence. *Elements*, *11*(2), 91–98. https://doi.org/10.2113/gselements.11.2.91

Pelletier, J. D. (2009). Controls on the height and spacing of eolian ripples and transverse dunes: A numerical modeling investigation. *Geomorphology*, *105*(3-4), 322–333. https://doi.org/10.1016/j.geomorph.2008.10.010

Quade, J., Dettinger, M. P., Carrapa, B., DeCelles, P. G., Murray, K. E., Huntington, K. W., Cartwright, A., Canavan, R. R., Gehrels, G. E., & Clementz, M. (2015). The growth of the central Andes, 22° S-26° S. In *Geological Society of America Memoirs* (pp. 277–308).

Reijs, J., & McClay, K. (2003). The Salina del Fraile pull-apart basin, northwest Argentina. *Intraplate Strike-Slip Deformation Belts*, *210*, 197–209. https://doi.org/10.1144/Gsl.Sp.2003.210.01.12

Risse, A., Trumbull, R. B., Kay, S. M., Coira, B., & Romer, R. L. (2013). Multi-stage evolution of late Neogene mantle-derived magmas from the Central Andes back-arc in the southern Puna plateau of Argentina. *Journal of Petrology*, *54*(10), 1963–1995. https://doi.org/10.1093/petrology/egt038

Rohrmann, A., Heermance, R., Kapp, P., & Cai, F. (2013). Wind as the primary driver of erosion in the Qaidam Basin, China. *Earth and Planetary Science Letters*, *374*, 1–10. https://doi.org/10.1016/j.epsl.2013.03.011

Schoenbohm, L. M., & Carrapa, B. (2015). Miocene-Pliocene shortening, extension, and mafic magmatism support small-scale lithospheric foundering in the central Andes, NW Argentina. *Geological Society of America Memoirs*, *212*(09), 167–180. https://doi.org/10.1130/2015.1212(09)

Selby, M. J. (1971). Slopes and Their Development in an Ice-Free, Arid Area of Antarctica. *Geografiska Annaler: Series A, Physical Geography*, *53*(3-4), 235–245. https://doi.org/10.1080/04353676.1971.11879849

Snell, K. E., Koch, P. L., Druschke, P., Foreman, B. Z., & Eiler, J. M. (2014). High elevation of the 'Nevadaplano' during the Late Cretaceous. *Earth and Planetary Science Letters*, *386*, 52–63. https://doi.org/10.1016/j.epsl.2013.10.046

Sobel, E. R., Hilley, G. E., & Strecker, M. R. (2003). Formation of internally drained contractional basins by aridity-limited bedrock incision. *Journal of Geophysical Research: Solid Earth*, *108*(B7). https://doi.org/10.1029/2002jb001883

Strecker, M. R., Alonso, R. N., Bookhagen, B., Carrapa, B., Coutand, I., Hain, M. P., Hilley, G. E., Mortimer, E., Schoenbohm, L. M., & Sobel, E. R. (2009). Does the topographic distribution of the central Andean Puna Plateau result from climatic or geodynamic processes? *Geology*, *37*(7), 643–646. https://doi.org/10.1130/G25545A.1

Strecker, M. R., Alonso, R. N., Bookhagen, B., Carrapa, B., Hilley, G., Sobel, E. R., & Trauth, M. (2007). Tectonics and Climate of the Southern Central Andes. *Annual Review of Earth and Planetary Sciences*, *35*(1), 747–787. https://doi.org/10.1146/annurev.earth.35.031306.140158

Sundell, K. E., Saylor, J. E., Lapen, T. J., & Horton, B. K. (2019). Implications of variable late Cenozoic surface uplift across the Peruvian central Andes. *Scientific Reports*, *9*(1), 1–12. https://doi.org/10.1038/s41598-019-41257-3

Tassara, A., Götze, H. J., Schmidt, S., & Hackney, R. (2006). Three-dimensional density model of the Nazca plate and the Andean continental margin. *Journal of Geophysical Research: Solid Earth*, *111*(9), 1–26. https://doi.org/10.1029/2005JB003976

Tye, A. R., McMillan, M., Schoenbohm, L. M., & Zhou, R. (2022). Late Cenozoic extensional formation of the Antofalla depression, southern Puna plateau, Argentina: An effect of lithospheric foundering? *Tectonics*.

von Raumer, J. F. (1998). The Palaeozoic evolution in the Alps: From Gondwana to Pangea. *Geologische Rundschau*, *87*(3), 407–435. https://doi.org/10.1007/s005310050219

Voss, R. (2002). Cenozoic stratigraphy of the southern Salar de Antofalla region, northwestern Argentina. *Andean Geology*, *29*(2), 167189. https://doi.org/10.4067/S0716-02082002000200002

Wang, H., Currie, C. A., & DeCelles, P. G. (2015). Hinterland basin formation and gravitational instabilities in the central Andes: Constraints from gravity data and geodynamic models. In *Geological Society of America Memoirs* (pp. 387–406). https://doi.org/10.1130/2015.1212(19)

Wang, Z. T., Wang, H. T., Niu, Q. H., Dong, Z. B., & Wang, T. (2011). Abrasion of yardangs. *Physical Review E - Statistical, Nonlinear, and Soft Matter Physics*, *84*(3), 1–8. https://doi.org/10.1103/PhysRevE.84.031304

Ward, K. M., Delph, J. R., Zandt, G., Beck, S. L., & Ducea, M. N. (2017). Magmatic evolution of a Cordilleran flare-up and its role in the creation of silicic crust. *Scientific Reports*, *7*(1), 1–8. https://doi.org/10.1038/s41598-017-09015-5

West, J. D., Fouch, M. J., Roth, J. B., & Elkins-Tanton, L. T. (2009). Vertical mantle flow associated with a lithospheric drip beneath the Great Basin. *Nature Geoscience*, *2*(6), 439–444. https://doi.org/10.1038/ngeo526

Xiao, L., Wang, J., Dang, Y., Cheng, Z., Huang, T., Zhao, J., Xu, Y., Huang, J., Xiao, Z., & Komatsu, G. (2017). A new terrestrial analogue site for Mars research: The Qaidam Basin, Tibetan Plateau (NW China). *Earth-Science Reviews*, *164*, 84–101. https://doi.org/10.1016/j.earscirev.2016.11.003

Yin, A., & Harrison, T. M. (2000). Geologic evolution of the Himalayan-Tibetan orogen. *Annual Reviews of Earth and Planetary Sciences*, *28*, 211–280. https://doi.org/10.1080/01947641003598252

Zandt, G., Gilbert, H., Owens, T. J., Ducea, M. N., Saleeby, J. B., & Jones, C. H. (2004). Supporting information for: Active foundering of a continental arc root beneath the southern Sierra Nevada in California. *Nature*, *431*(7004), 41–46. https://doi.org/10.1038/nature02847

Zhou, R., & Schoenbohm, L. M. (2015). Late Miocene upper-crustal deformation within the interior of the southern Puna Plateau, central Andes. *Lithosphere*, *7*(3), 336–352. https://doi.org/10.1130/L396.1

Zhou, R., Schoenbohm, L. M., & Cosca, M. (2015). Recent, slow normal and strike-slip faulting in the Pasto Ventura region of the southern Puna Plateau, NW Argentina. *Tectonics*, *32*(1), 19–33. https://doi.org/10.1029/2012TC003189

Zhou, R., Schoenbohm, L. M., Sobel, E. R., Davis, D. W., & Glodny, J. (2017). New constraints on orogenic models of the southern Central Andean Plateau: Cenozoic basin evolution and bedrock exhumation. *Bulletin of the Geological Society of America*, *129*(1-2), 152–170. https://doi.org/10.1130/B31384.1

2 Large-scale Cenozoic wind erosion in the Puna Plateau

The Salina del Fraile Depression*

Abstract

Wind erosion is integral to the evolution of arid landscapes on Earth and Mars, but the nature of long-term wind erosion of bedrock is poorly understood. Here we describe the Salina del Fraile (SdF) depression in the Puna Plateau of the Central Andes, NW Argentina, as a landform excavated by wind over several million years. New structural cross-sections and a compilation of chronostratigraphic ages rule out the hypothesis that the depression was created by transtensional tectonics. Dated remnant lacustrine and alluvial deposits in the floor of the depression constrain the rate and timing of erosion. Late Oligocene–Miocene compressional folding uplifted friable strata that were preferentially eroded, resulting in the high-relief (900 m) depression. Up to 1.95 km and an average of 1.05 km of strata were eroded during the last 8.2 to 17 Ma, at rates of 0.06 to 0.23 mm/yr. These rates are similar to long-term average wind erosion rates reported in other regions. Coarse-grained eolian megaripples, yardangs, and elongated ridges indicate ongoing eolian abrasion and deflation, aided by salt weathering, of the floor of the depression. Megaripple migration across stony lag surfaces exposes fresh bedrock to continued erosion. The SdF also contains kilometer-scale mesas and ridges that we interpret as erosional remnants. These landforms are similar to megayardangs and erosional topography identified on the lower flanks of Mount Sharp, Gale crater, Mars. In such hyperarid landscapes characterized by lithologic heterogeneities, high relief landforms can be generated and sustained by wind erosion, without significant fluvial or glacial incision. Plain Language Summary We investigated the origin of a large topographic depression in the arid Puna Plateau of the Central Andes, NW Argentina. Previous research interpreted the depression as formed by faulting, but we found that it is likely formed by wind erosion. While rivers and glaciers are usually responsible for erosion on Earth, there is no evidence for river or glacier action in the Salina del Fraile. Rather, much like the surface of Mars, wind was primarily responsible

*This chapter has been published in the *Journal of Geophysical Research: Earth Surface*.
Citation: McMillan, M., & Schoenbohm, L. M. (2020b). Large-scale Cenozoic wind erosion in the Puna Plateau: The Salina del Fraile Depression. *Journal of Geophysical Research: Earth Surface*. https://doi.org/10.1029/2020JF005682.
Supplementary materials are available online (https://doi.org/10.1029/2020JF005682).

for forming the depression and surrounding landscape over several million years. We show that wind was able to excavate the depression because tectonic folding brought fine-grained rocks close to the surface, where they were exposed to strong winds and breakdown by salt weathering. Wind erosion was active for the last 8.2 to 17 million years, and, as evidenced by large dust storms originating from this region, is ongoing today. Wind is lowering the surface at an average rate of 0.06 to 0.23 mm/yr, similar to previous studies. The Salina del Fraile can help researchers understand the long-term effects of wind erosion on Earth and Mars.

2.1 Introduction

The degree to which eolian processes shape the landscape morphology of arid regions is a long-standing point of contention (Brock & Twidale, 2011; Goudie, 2012), albeit one renewed by the exploration of wind-dominated planetary surfaces and their terrestrial analogues (e.g., Xiao et al., 2017). Wind erosion may outpace fluvial incision of bedrock in hyperarid regions, and wind can enhance the erosion of favorably-oriented bedrock canyons (Perkins et al., 2015). On a regional scale, eolian deflation and abrasion can remove hundreds of meters of strata, potentially accelerating tectonic deformation (Kapp et al., 2011). Regional eolian deflation influences Earth's climate through dust emission and often results in the development of widespread desert pavements, which may drive faster surface winds through a wind-albedo-wind feedback (Abell et al., 2020; Pullen et al., 2018). Such research shows how wind erosion, although outpaced by fluvial and other processes in more humid regions, plays an integral role in parts of Earth's arid Cenozoic orogenic belts. On Mars, wind-driven retreat of bedrock scarps is responsible for relatively young surface exposure ages in Gale crater, offering potential locations for sampling well-preserved complex molecules (Farley et al., 2014). Identifying regions of active eolian erosion on Mars is important for exploring geologic units that may preserve signs of ancient life (Chojnacki et al., 2018). Studying the effects of wind erosion is therefore critical for understanding how tectonic processes interact with Earth's climate, and how the surfaces of wind-dominated planets evolve over geologic time scales. Both of these efforts, however, are hampered by a relatively poor understanding of large-magnitude eolian landforms generated over many millions of years on Earth.

Here we show that the Salina del Fraile (SdF), a large, internally-drained depression in the southern Puna Plateau, NW Argentina, is an erosional landform excavated by wind over a time period of at least 8.2 Ma. We present new structural measurements and cross-sections that argue against tectonic lowering of the depression and instead imply up to 2 km of erosion where anticlinal folding exposed a thick package of friable, fine-grained strata. We describe remnants of alluvial surfaces within the depression to argue against significant fluvial incision during this time period. We also document eolian landforms over a wide range of spatial scales, both within and around the depression, to demonstrate the ubiquity of eolian erosion in this

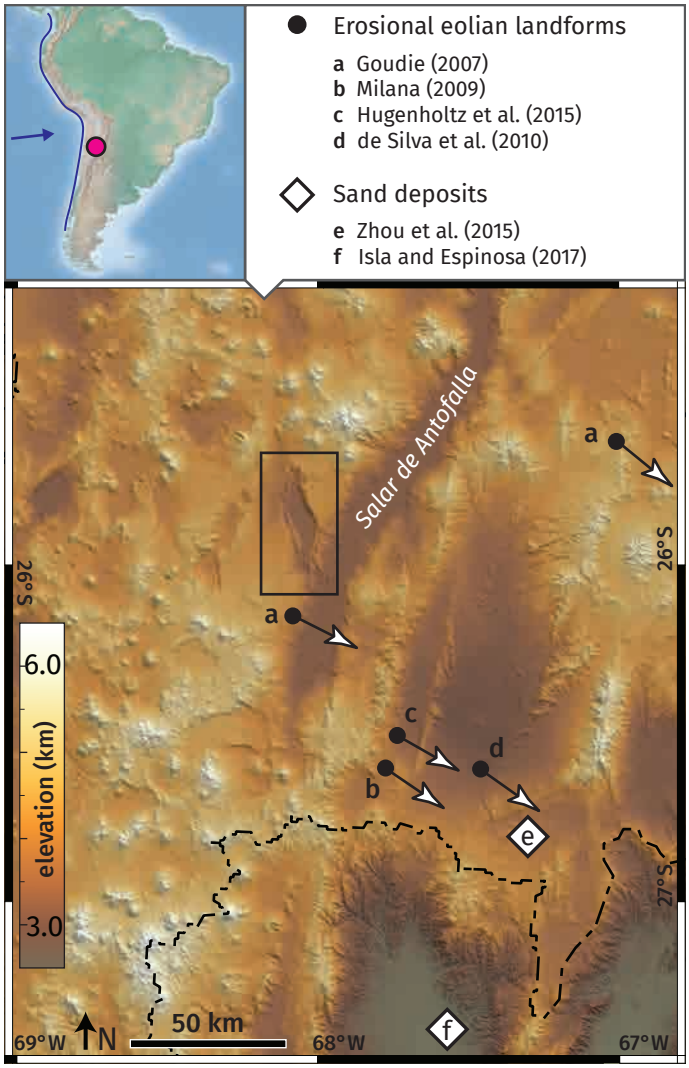

Figure 2.1: Digital surface model (DSM) of the southern Puna Plateau with study area boxed. Letters denote previous studies of eolian erosion (arrows) or deposition (diamonds), with arrows indicating wind direction. Inset shows study location and Nazca plate vector relative to South America. Dashed line shows limit of internally drained plateau. NASA SRTM DEM (1 arc second).

region. Finally, we use existing chronostratigraphic data to estimate the timing and rate of erosion and explore some implications of such long-term, large-scale wind erosion.

2.1.1 The Salina del Fraile

The Salina del Fraile (SdF) is an evaporite basin located to the west of the Salar de Antofalla in the southern Puna Plateau, NW Argentina (Figure 2.1). The present climate of the region is hyperarid, with mean annual rainfall of only ~14 mm (with a range of 0–70 mm) in the vicinity of the SdF (Bookhagen & Strecker, 2008). NASA MERRA reanalysis data indicate that the region experiences a cold desert climate, with summertime daily temperature highs of 20–25 °C and lows of -5–5 °C, and wintertime highs of 0–10 °C and lows of -10 to -15 °C, giving the region a cold

desert climate (Figure S1). Aridity in this region began as early as the Eocene (Quade et al., 2015) and intensified during the Middle to Late Miocene, when the major evaporite playas such as the Salar de Antofalla began forming (Alonso et al., 1991; Strecker et al., 2007). Arid climates, in addition to suppressing fluvial processes, enhance eolian deflation and abrasion due to sediment desiccation, salt weathering, and reduced vegetation cover (e.g., Goudie, 2018). Eolian deflation commonly occurs on the margins of evaporite playas, such as the SdF, because salt accumulation rapidly disintegrates bedrock and alluvial deposits and provides fine-grained particles for removal by wind (Goudie & Day, 1980). Salt accumulation in closed depressions therefore tends to reinforce further eolian excavation in a positive feedback, especially if the host lithology is susceptible to salt weathering, such as would be for porous sandstones or fine-grained siliciclastics (Goudie & Wells, 1995). Eolian deflation aided by salt weathering can lead to the formation of large depressions, as has been suggested for the Qattara Depression in Egypt (Aref et al., 2002). Eolian processes also interact with fluvial and lacustrine deposits in arid playas because precipitation events result in fine-grained sediment being transported and deposited on surfaces prone to deflation (Goudie, 2018). The SdF is situated within a continental-scale NNW–SSE eolian system, in a region characterized by erosional landforms such as yardangs, megayardangs, and periodic bedrock ridges (Figure 2.1 and references therein). Significant eolian sand deposits are rare in the vicinity of the SdF, but occur further downwind in the SE Puna, in the Fiambalá basin (Figure 2.1), and in a belt stretching several hundred kilometers further SE (Isla & Espinosa, 2017). Strong winds in the region are associated with synoptic polar fronts that typically occur during a windy season that lasts from May to October (Milana & Kröhling, 2017). Major dust storms have been imaged originating from evaporite playas on the Puna Plateau, including from the SdF (Goudie & Wells, 1995; Milana & Kröhling, 2017). Although the Puna Plateau is internally drained, sediment is removed from the southern Puna by wind, potentially providing a source of the Chaco-Pampean loess deposits in eastern Argentina (Milana & Kröhling, 2017) and dust in Eastern Antarctic ice cores (e.g., Gaiero, 2007). The SdF-Antofalla region was tectonically deformed as it was incorporated into the Andean orogenic wedge ~30–20 Ma, uplifting and deforming a Paleogene foreland basin system (Carrapa et al., 2005; Kraemer et al., 1999; Zhou et al., 2017). Cenozoic units outcropping in the SdF consist of the Paleogene Quiñoas and Chacras Formations, a coarsening-upward sequence of continental siliciclastics; the Neogene Potrero Grande Formation, a volcaniclastic unit with interbedded ashes and ignimbrites; and later volcanic flows and ignimbrites (Kraemer et al., 1999). The Quiñoas Formation unconformably overlies pre-Cenozoic rocks. In the study area, pre-Cenozoic rocks consist of Permian to Jurassic sedimentary and volcanic strata exposed in the northern part of the SdF depression (Voss, 2002). An angular unconformity separates the Potrero Grande Formation from underlying units, which are tilted to the SE. The SdF is a rhomboidal topographic depression, 300 km^2 in area, with up to 900 m of topographic relief. Goudie and Wells (1995) hypothesized that the SdF (therein termed Potrerillos Depression) is analogous to a giant deflation pan, “the largest Altiplano basin of primarily aeolian origin” (pg.

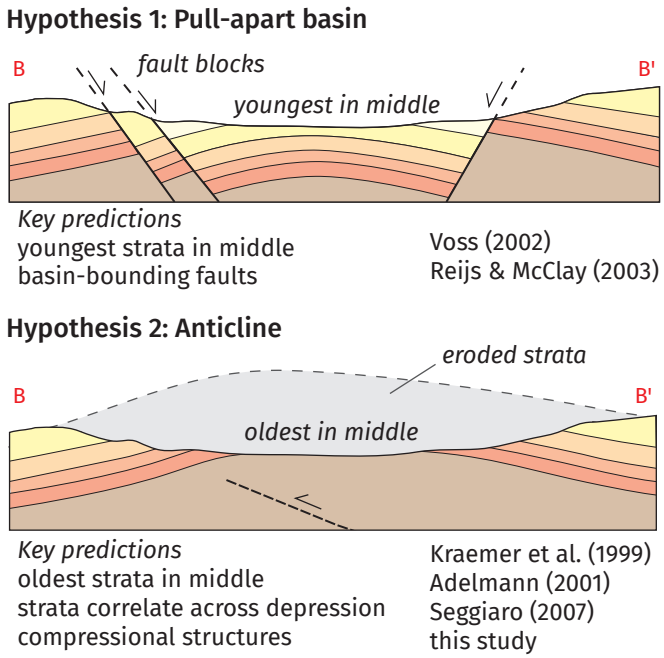

Figure 2.2: Theoretical cross-sections illustrating the two competing hypotheses for the structural setting of the Salina del Fraile depression. Strata are drawn schematically along topographic section B-B' (Figure 2.3).

22), but later research in the region diverged from this interpretation (Figure 2.2). The depression's conspicuous planform shape, rectilinear slopes, and what appeared to be rotated fault blocks along the western edge (labelled "elongated ridges" in Figure 2.3), led some to interpret it as a pull-apart basin, with the basin floor lowered by major normal faults as a result of a left step in an inferred N–S-trending left-lateral fault system (Reijs & McClay, 2003; Voss, 2002). Others mapped the depression as the core of an anticline with only minor faults, an interpretation that also satisfies chronostratigraphic constraints (Adelmann, 2001; Kraemer et al., 1999; Seggiaro et al., 2007). The structural interpretation of the SdF is critical, because a compressional origin requires the erosion of material in order to create a morphologic depression, while a pull-apart basin would not necessitate erosion (Figure 2.2).

2.2 Materials and Methods

We collected measurements of bedding planes in the field using a Brunton Transit ($n = 40$) and mapped the Cenozoic geology along two transects spanning the depression (profiles A and B in Figure 2.3). Transects were oriented perpendicular to major structures, allowing us to test the two hypotheses for the formation of the depression (pull-apart basin or compressional folding). To supplement our structural data, we also digitized strikes and dips from Voss (2002, $n = 52$) and Reijs and McClay (2003, $n = 39$) within the Salina del Fraile by georeferencing their maps in a GIS environment. Our field measurements closely agree with nearby data

from these sources. Cross-sections were constructed using the kink-band method; because a main objective is to estimate the magnitude of erosion, cross-sections were drawn to minimize the amount of eroded material, within realistic geologic constraints. Chronostratigraphic data were compiled from Adelmann (2001, $n = 29$), Canavan et al. (2014, $n = 14$) and Quade et al. (2015, $n = 11$) and mapped when sample locations were given. For ages referenced to a stratigraphic column, we mapped the locations of the samples onto cross-section B-B' using their stratigraphic positions. These data consist of single grain Ar–Ar ($n = 16$; biotite, plagioclase, potassium feldspar), K–Ar ($n = 12$; feldspar, biotite, glass) and U–Pb ($n = 21$, zircon) ages and a K–Ar whole rock age ($n = 1$, andesite). Dated lithologies were largely volcanic tuff ($n = 38$), followed by ignimbrite ($n = 5$), andesite ($n = 2$) and other volcanic lithologies ($n = 5$). The data tabulated by Adelmann (2001, Appendix 1 therein) were published in part by Kraemer et al. (1999, Table 1 therein) and the analytic methods were described by Voss (2002, Table 1 therein). Ar–Ar age determinations were performed by the GEOMAR Forschungszentrum (Kiel, Germany) and K–Ar age determinations by GEOCHRON Laboratories, Krueger Enterprises, Inc. (Cambridge, Massachusetts). U–Pb ages of volcanic zircons were published by Canavan et al. (2014, Tables DR1 and DR2 therein) and Quade et al. (2015, Table 4 therein) and were determined by laser ablation multicollector inductively coupled plasma mass spectrometry (LA-MC-ICPMS) at the University of Arizona LaserChron Center. All ages compiled here are reported with 2σ uncertainty. Structural and chronostratigraphic data used here are available in the University of Toronto Dataverse (McMillan & Schoenbohm, 2020a). Predominant strong wind directions were inferred from landforms mapped using high resolution aerial imagery obtained from Bing Maps (~30 cm/px; Figure S2). Landforms include yardangs, megaripples, dust streaks, and abraded bedrock surfaces. We assume prevailing wind directions are well represented by the long axes of yardangs that taper downwind ($n = 21$); by directions normal to the average crestline orientation of asymmetric megaripples, with more gentle stoss slopes and steeper lee slopes ($n = 5$); and by light-toned dust streaks extending downwind from evaporite or alluvial playas ($n = 4$). Each landform yielded a single measurement of wind direction. Where fields of periodic yardangs or megaripples occur, the wind directions mapped in Figure 2.3 represent an average of all measurements for the field. Although aerial imagery alone did not permit us to unambiguously distinguish the stoss and lee slopes of megaripples, their orientations and associated wind directions were verified in the field. Abraded bedrock surfaces displaying elongated ridges and grooves may also provide information about wind directions; although we are less confident about these measurements ($n = 2$), they parallel other landforms and are therefore shown as dashed arrows in Figure 2.3. Following Perkins et al. (2019), regional wind and temperature data were obtained from the NASA MERRA reanalysis dataset (https://disc.gsfc.nasa.gov/) for a period spanning the windy seasons (May to October) of the years 1982–1992. This decade, the earliest in the dataset, was chosen to minimize any effects of anthropogenic climate change. Hourly wind speeds and downwind directions at a height of 2 m are plotted in the inset of Figure 2.3. Daily statistics for surface temperatures at a height of 2 m

are plotted in Figure S1. We mapped alluvial surfaces and terrace remnants in the depression using the ALOS World 3D (1 arc second) DSM provided by JAXA and verified these interpretations with field observation. The depths of internally drained portions of the landscape were analyzed using TopoToolbox (Schwanghart & Scherler, 2014).

2.3 Results and Discussion

2.3.1 Structural interpretation: Against extensional lowering of the depression

Strata are deformed by a series of roughly N–S-trending folds, with no basin-bounding normal faults (Figure 2.3). The northern portion of the SdF consists of a roughly N–S trending, southward plunging anticline that exhumes Permian and Jurassic strata (Figure 2.4). The fold axial plane dips to the east, and the Potrero Grande thickens rapidly, with dips decreasing up-section on the western limb, consistent with syntectonic sedimentation (Figure 2.4). On the eastern limb of the fold, late Paleogene strata are truncated by the unconformity at the base of the Potrero Grande Formation. Chronostratigraphic data confirm that the flat interior of the depression here is composed of the lower member of the Quiñoas Formation, with K–Ar ages of 37.6 Ma of a volcanic tuff and 36.7 Ma on a reworked pumice clast (Adelmann, 2001). This interpretation is supported by U–Pb zircon ages from Canavan et al. (2014), who dated six volcanic tuffs outcropping in the eastern wall of the depression, 3.5 km north of Section A-A', with ages ranging from 36.1 Ma to 34.4 Ma.

The central portion of the SdF consists of a series of gentle anticlines separated by a doubly inward-plunging syncline (Figure 2.5). Small kink-band folds mapped as monoclines are present on the western limb of the westernmost anticline, where strata are locally overturned. The Vega Chacras canyon on the western limb of this anticline is well-studied, with a chronostratigraphic record comprised of 17 ages in a transect across what had been interpreted as rotated fault blocks (Adelmann, 2001; Canavan et al., 2014; Quade et al., 2015). Stratal ages range from 18.0 Ma at the top of the canyon (K–Ar of volcanic glass) to 38.5 Ma near its base (U–Pb of volcanic zircon). These ages are consistent with uplifted, west-dipping, Cenozoic strata on the western limb of an anticline (Figure 2.5), rather than a late Miocene normal-fault growth sequence Reijs and McClay, 2003. We found no field evidence for repetition of strata in this location, and stratal ages show no offsets across what had been interpreted as normal fault blocks (Figure 2.5).

The relative age of strata in the floor of the depression is a key prediction of both hypotheses (Figure 2.2). Strata outcropping throughout the floor of the depression have been dated by multiple studies. Quade et al. (2015) obtained an age of 38.5 ± 0.7 Ma from an interbedded tuff near the base of Vega Chacras canyon, while Canavan et al. (2014) obtained ages of 35.7 ± 0.9 Ma and 33.9 ± 0.9 Ma from an outcrop in the southern portion of the depression. Adelmann (2001) obtained ages of 37.6 ± 0.3 Ma and 36.7 ± 0.3 Ma from bedrock exposures in the floor of

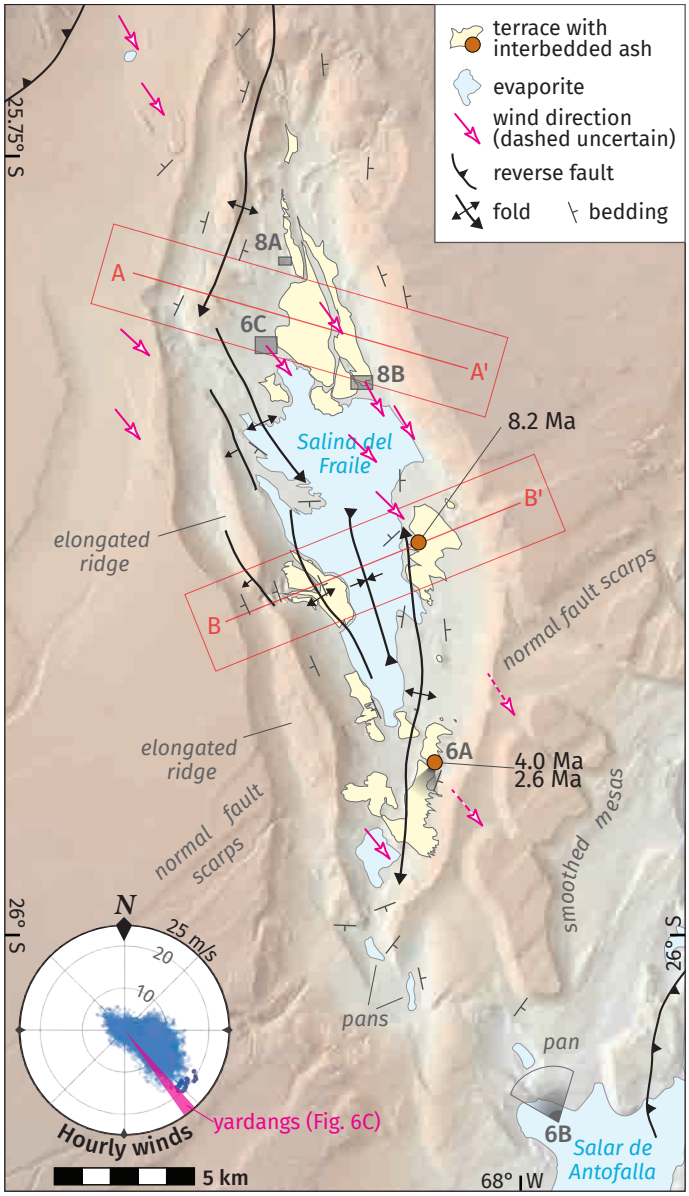

Figure 2.3: Topographic hillshade of the Salina del Fraile. Red boxes denote cross-sections in Figures 4 and 5. Lettered symbols denote images in Figures 6 and 8. Strikes and dips selected from our data, Voss (2002), and Reijs and McClay (2003). Dated ashes and their locations are from Adelmann (2001). Inset plots regional wind speeds and downwind directions from NASA MERRA hourly reanalysis data (https://disc.gsfc.nasa.gov/) during the windy seasons of 1982–1992, with winds >18 m/s shown as bold dots. Pink segment shows orientations of yardangs mapped in Figure 2.8c.

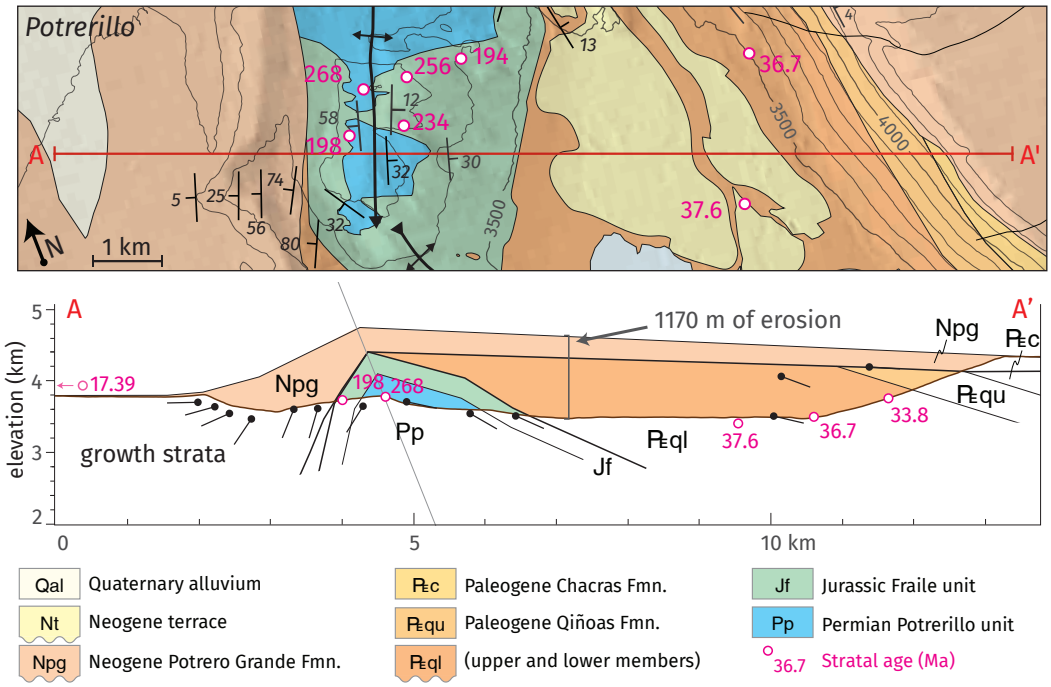

Figure 2.4: Section A-A'. Geologic strip-map and structural cross-section of the northern Salina del Fraile near Potrerillos. Chronostratigraphic ages compiled from Adelmann (2001), Canavan et al. (2014), and Quade et al. (2015). Strikes/dips measured in the field supplemented with those from Voss (2002) and Reijs and McClay (2003) as dark gray symbols.

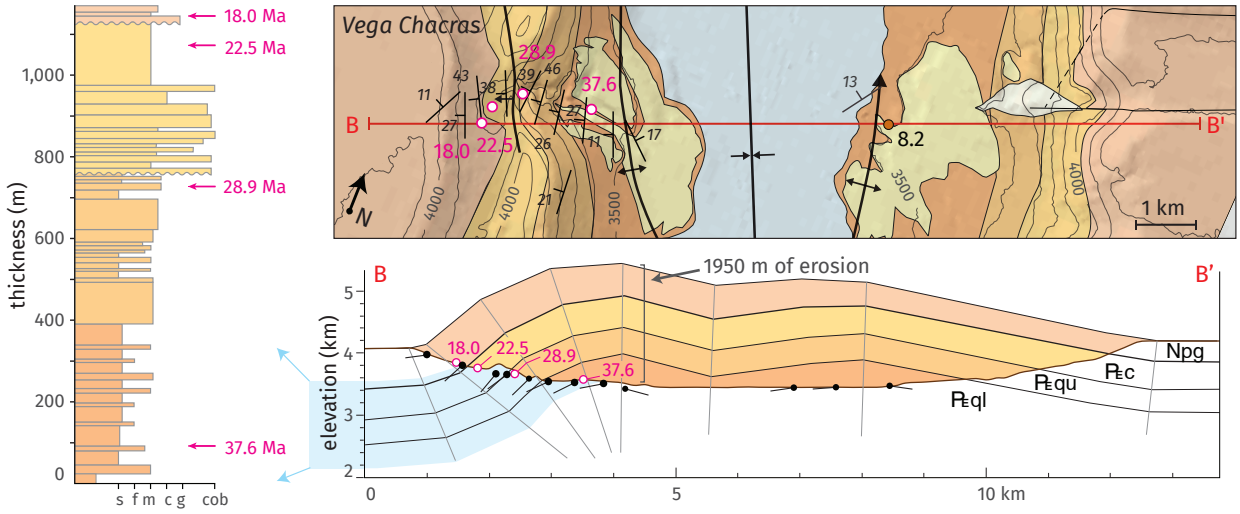

Figure 2.5: Section B-B'. Geologic strip-map and structural cross-section of the central Salina del Fraile near Vega Chacras. Chronostratigraphic ages selected from Adelmann (2001), Canavan et al. (2014), and Quade et al. (2015). Strikes/dips measured in the field supplemented with those from Voss (2002) and Reijs and McClay (2003) as dark gray symbols. Stratigraphic column redrawn from Adelmann (2001). Refer to Figure 2.4 for legend.

the northern part of the depression. These studies indicate that the floor of the depression is composed of relatively old bedrock, the Lower Member of the Quiñoas Formation (late Eocene to early Oligocene). The lithology of this unit consists playa mudstones, evaporites, siltstones, and sandstones (Kraemer et al., 1999) up to 2 km thick in the Salina del Fraile (Figure 2.4). Although the depression does contain thin Neogene terrace deposits (Figures 4 and 5, see below), these deposits rest in angular unconformity on older units and are not consistent with structural lowering of the depression. It is possible that smaller extensional structures are hidden beneath the modern evaporite playa, but exposures of the Quiñoas Formation would necessarily limit any such structures to a small area, and they would not be capable of explaining the origin of the depression. These observations indicate a purely contractional structural setting for the SdF, rather than an extensional or transtensional one (Hypothesis 2, Figure 2.2). The eastern dip of fold axial planes is consistent with fault propagation folding, possibly due to blind, west-vergent thrust faults associated with a major reverse fault system to the east (Adelmann, 2001; Seggiaro et al., 2007; Voss, 2002). The two main N-S trending anticlines in the NW and SE parts of the study area have a wavelength of ~15 km and their geometry mirrors the rhomboidal planform geometry of the depression (Figure 2.3). Compressional folding and subsequent erosion thus provide a compelling explanation for the geometry of the depression.

2.3.2 Little evidence for fluvial incision

If the SdF depression is not formed by structural lowering of the basin floor, then it must have been carved by erosive processes. We rule out the possibility of glacial erosion in this hyper-arid region because no glacial or paleoglacial landforms are present in the Salar de Antofalla region (Haselton et al., 2002). We therefore examine the relative roles of fluvial and wind erosion. There is evidence of minor fluvial reworking within the depression. For example, several terraces cut into tilted Paleogene strata are present within the depression and capped by deposits 10–120 m thick (Figure 2.3). The terrace deposits (lacustrine and alluvial strata with gypsum-rich soil horizons) overlie tilted Paleogene bedrock in angular unconformity (Figure 2.6a) and were deposited in an existing topographic low (Voss, 2002). The terraces have been partially eroded, and their remnants now stand in relief above the SdF floor, often as yardangs (Figure S3b). Interbedded ashes in the terrace deposits dated to 2.6, 4.0, and 8.2 Ma (Adelmann, 2001) imply that significant erosion of the SdF occurred both before 8.2 Ma (to create the initial depression) and since 2.6 Ma (to erode the terraces and further deepen the depression). Erosional episodes were evidently punctuated by periods of net deposition or soil development. The depression is not presently part of an integrated fluvial network. Making the highly conservative assumption that the depression was originally a fluvial valley and that wind erosion is only responsible for the portion of the internally drained topography provides an estimate of the minimum amount of wind erosion. The lowest point on the southern margin of the depression is blocked by an escarpment that extends >212 m above local base level

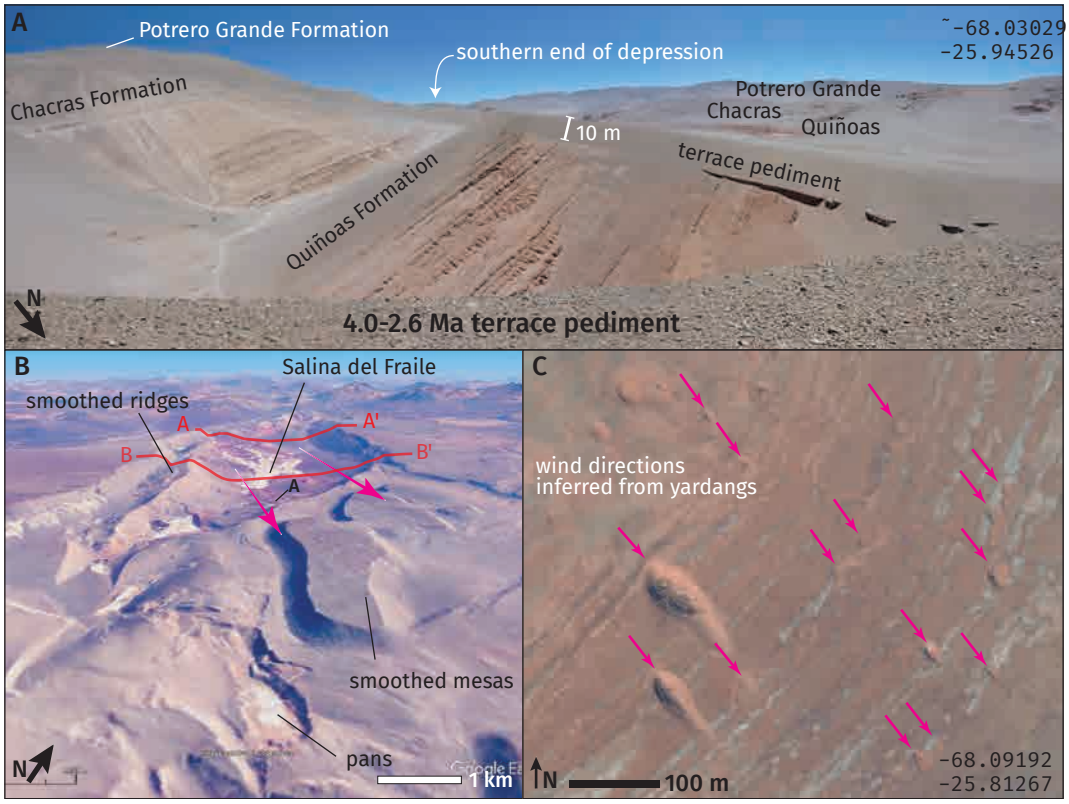

Figure 2.6: Geomorphological evidence of wind erosion across spatial scales. (a) Unconformity between 2.6–4.0 Ma terrace deposit and Cenozoic units, showing erosional streamlining of terrace edge. (b) Upwind view of the Salina del Fraile (Google Earth). Location of Figure 2.6a labelled A. (c) Yardangs carved into the friable Paleogene Quiñoas Formation. Aerial imagery from Bing Maps. Refer to Figure 2.3 for the locations of images.

and does not appear to have been uplifted structurally (Figure 2.7). Wind, which is capable of excavating internally drained depressions, is thus interpreted to be responsible for a minimum of 212 m of erosion (Figure 2.7). However, we find it unlikely that the depression was a fluvial valley in the past and argue for a larger magnitude of wind erosion. If the depression had been externally drained when the internal Neogene terraces were deposited, they would decrease in elevation to the south (i.e., downstream); in contrast, they decrease in elevation to the north, toward the center of the depression. Terrace deposit facies are also indicative of deposition in an internally drained basin in an arid climatic regime similar to the present. Finally, late Miocene–Pliocene units outcropping on the eastern border of the Salar de Antofalla are sourced from, and thicken toward, the Sierra de Calalaste to the east, rather than the Salina del Fraile to the west (Adelmann, 2001). It is therefore unlikely that the SdF was drained fluvially during the last 8.2 Ma (the oldest dated ash in a terrace deposit). While we argue that wind was responsible for excavating the internally drained depression, we do not discount the importance of fluvial processes for redistributing sediment within the SdF. Fluvial canyons and gorges are incised into bedrock along the margins of the SdF, most notably at Vega Chacras, Potrerillo, and Potrero Grande (Figure S2). These channels have headwaters in grassy marshes

and are fed by groundwater seepage and possibly by overland flow during rare precipitation events. The drainage network around Potrero Grande, in particular, is responsible for significant alluvial and fluvial deposits in the NE part of the depression. In the southeastern corner of the depression, small rills and gullies incise gravelly surfaces capping bedrock terraces (Figure S3b). Although fluvial erosion is capable of widening a closed depression, eolian entrainment of the resulting deposits is required to increase its depth, as rivers cannot erode below the base level set by their outlet. Fluvial processes are likely important for detaching sediment and transporting it to the floor of the depression, where clasts are vulnerable to salt weathering and particles can be entrained by wind. Eolian entrainment of fluvial deposits also provides a source of abrasive sand for eroding bedrock surfaces downwind. As is clear from the bedrock terraces described above, deflation of material from the basin has outpaced deposition, resulting in deepening of the depression over time. The lacustrine, alluvial, and fluvial deposits capping terraces indicate that excavation of the SdF was episodic and punctuated by periods of net deposition. These episodes were likely driven by changes in climate, as has been suggested for internal terraces in depression in the Negev Desert, Israel (Plakht et al., 2000).

2.3.3 Evidence in favor of wind erosion

Rather than extensional tectonics or fluvial erosion, we argue that wind is primarily responsible for forming the depression. There is abundant evidence for both eolian abrasion and deflation within and around the SdF (Figure S2; Goudie & Wells, 1995). Yardangs 10–100 m in length with ~1–5 m of relief are carved into lower Quiñoas Formation where it dips gently parallel to the wind direction (Figure 2.6b). Yardangs are streamlined eolian erosional landforms whose size and shape are controlled by the bedding orientation and heterogeneity of host strata (de Silva et al., 2010; Pelletier et al., 2018) as well as lithology. Five kilometers south of the yardangs, the Quiñoas Formation dips perpendicular to wind direction and outcrops as rough, sharp-crested hogbacks and smooth elongated ridges with length/width aspect ratios up to ~13 (Figure S4c). These ridges occur over a larger area than do the yardangs and also indicate the action of eolian abrasion and deflation scouring the basin floor. Eolian megaripples are locally present with wavelengths of 1–3 m and heights of 10–20 cm (Figure 2.8; Figure S4a). The origin of coarse-grained megaripples is debated along with their classification as migrating (Hugenholtz et al., 2015; Milana, 2009) or static bedforms (Bridges et al., 2015; de Silva et al., 2013; de Silva et al., 2010). Observations of the internal structures and morphology of megaripples are broadly consistent with their downwind migration driven by saltation-induced creep (Lämmel et al., 2018). Aerial imagery reveals extensive fields of megaripples that developed on subhorizontal surfaces capped by conglomeratic deposits (Figure 2.8b). The planforms of these megaripples show evidence of migration similar to that observed by Hugenholtz et al. (2015), with orientations indicating NNW wind directions, consistent with other eolian landforms (Figure 2.3). The megaripples observed in the SdF thus give additional evidence of strong winds and the presence of abrasive, saltating particles that drive their downwind migration.

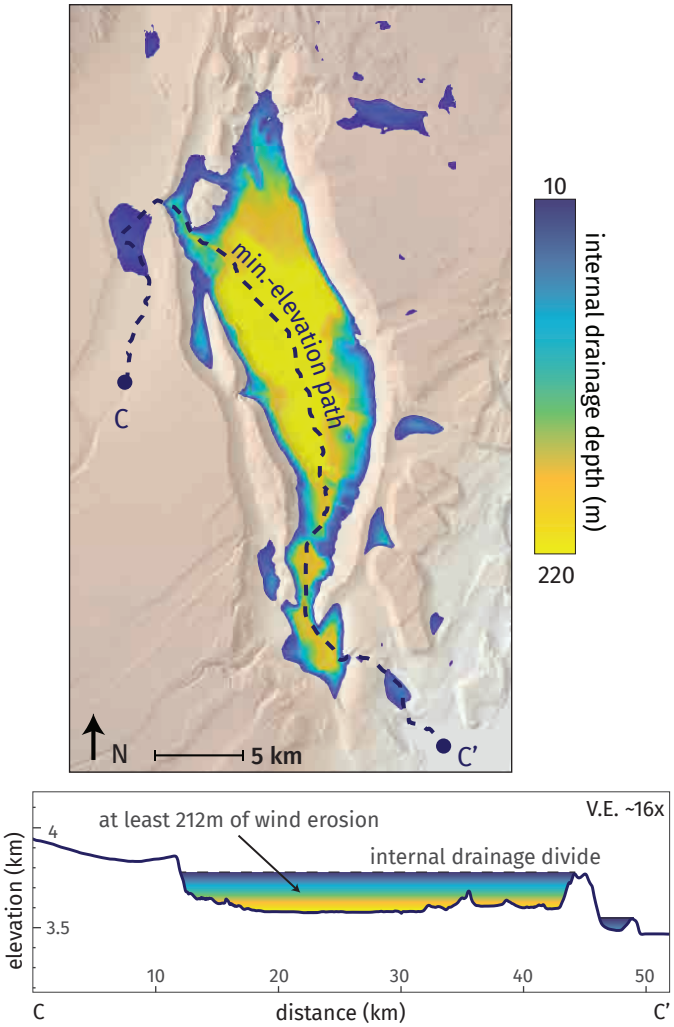

Figure 2.7: Internal drainage of the Salina del Fraile. The internal drainage depth approximates the minimum amount of wind (versus fluvial) erosion required to generate the observed topography. The transect follows the lowest-elevation path to the Salar de Antofalla. Internal drainage depth calculated using "fillsinks" function of TopoToolbox; transect calculated by routing flow using the "carve" pre-processor, which chooses the lowest elevation path across topographic highs (Schwanghart & Scherler, 2014).

Their downwind migration also exposes fresh bedrock (orange surfaces visible in Figure 2.8), providing a means for disrupting stony lag deposits that would otherwise protect bedrock against further erosion (Abell et al., 2020). Stony deposits are also disrupted by small gullies and rills that expose bedrock surfaces in the SE part of the depression (Figure S3b). The sides of the depression are prominent rectilinear bedrock slopes with nearly uniform ~27° angles (Figure S2). The slope angle does not appear to be related to bedrock strength, as no evidence for slope failures is present. The possibility that these slopes are major fault scarps can be ruled out by our structural interpretation. Major erosional rills or gullies in these slopes are rare, occurring only around localized seeps and springs, and the slopes are very smooth overall, but

small linear gullies and associated debris aprons are present (Figure S4b). Most of these slopes have not accumulated talus at the base, where bedrock is often exposed (Figure S4d).Others appear to have shed a thin layer of debris into the depression (contributing the terrace deposits described above). Because the slopes drain into a closed depression, wind erosion is likely required to explain the lack of colluvial and alluvial debris that would accumulate at the base. The rectilinear profile indicates that the slope retreat is weathering-limited, i.e., debris is removed faster than it can accumulate. Given the limited occurrence of major erosional features on the slopes, it is possible that some portions of them retreat mainly by eolian deflation aided by salt weathering, as proposed for rectilinear bedrock slopes in the Dry Valleys of Antarctica (Selby, 1971). Infrequent precipitation events may also be effective at transporting debris down-slope. Zones of active of salt weathering, previously noted by Goudie and Wells (1995), were observed around the the SdF. Salt presently accumulates around the margins of modern pans, and evaporites evidently accumulate on subsurface discontinuities such as unconformities (Figures S5 and S6). Salt crusts are visible in aerial imagery in many locations around the margin of the SdF (Figures S4b, S4c, and S5). We observed tafoni on the windward face of an ignimbrite outcrop located downwind of an evaporite pan NW of the SdF (Figure S7). Given these observations, we infer that salt weathering in the SdF provides a means of breaking down Cenozoic bedrock into particles that can be more easily entrained by wind. Near its western rim, the SdF hosts large, smooth, elongated ridges, 5–10 km in length and up to 600 m tall (Figure 2.3), elsewhere interpreted as fault scarps (Reijs & McClay, 2003). Cross section B (Figure 2.5), however, indicates that these ridges are erosional. They are not parallel to wind directions inferred from smaller-scale landforms, but their long axes generally parallel the strike of underlying strata. The ridges thus reflect the strong influence of bedding orientation and lithology superimposed on erosional processes in the SdF. Their dip slopes correspond to the upper Chacras Formation, a unit of relatively resistant cross-bedded sandstones and conglomerates that contrasts with overlying Potrero Grande volcaniclastics (Adelmann, 2001). We hypothesize that these resistant strata slowed the excavation of the depression, leading to elongated erosional remnants that parallel the strike of bedding planes; these topographic remnants were likely smoothed by weathering, colluvial transport, and eolian deflation.

Five kilometers southeast of the SdF, three ~300 m tall mesas with smooth, linear slopes are present (Figures 3 and 6b). They are 5.5–10.5 km^2 in area with curvilinear planforms 2.5–6 km long that taper slightly to the SE. The tops of the mesas are subhorizontal and characterized by heavily abraded bedrock surfaces (Figure S3d). Although the mesas resemble alluvial terraces in some respects, no evidence of fluvial channels or paleochannels is present. Instead, they correlate with a regional, subhorizontal, Late Miocene–Pliocene surface representing the top of the Potrero Grande Formation and/or Late Miocene volcanic flows in this area (Richards et al., 2006) and are therefore composed of Potrero Grande volcaniclastics. Although it is difficult to imagine how fluvial or tectonic processes could produce these mesas, our wind erosion hypothesis provides a potential explanation. The mesas are larger and smoother than megayardangs

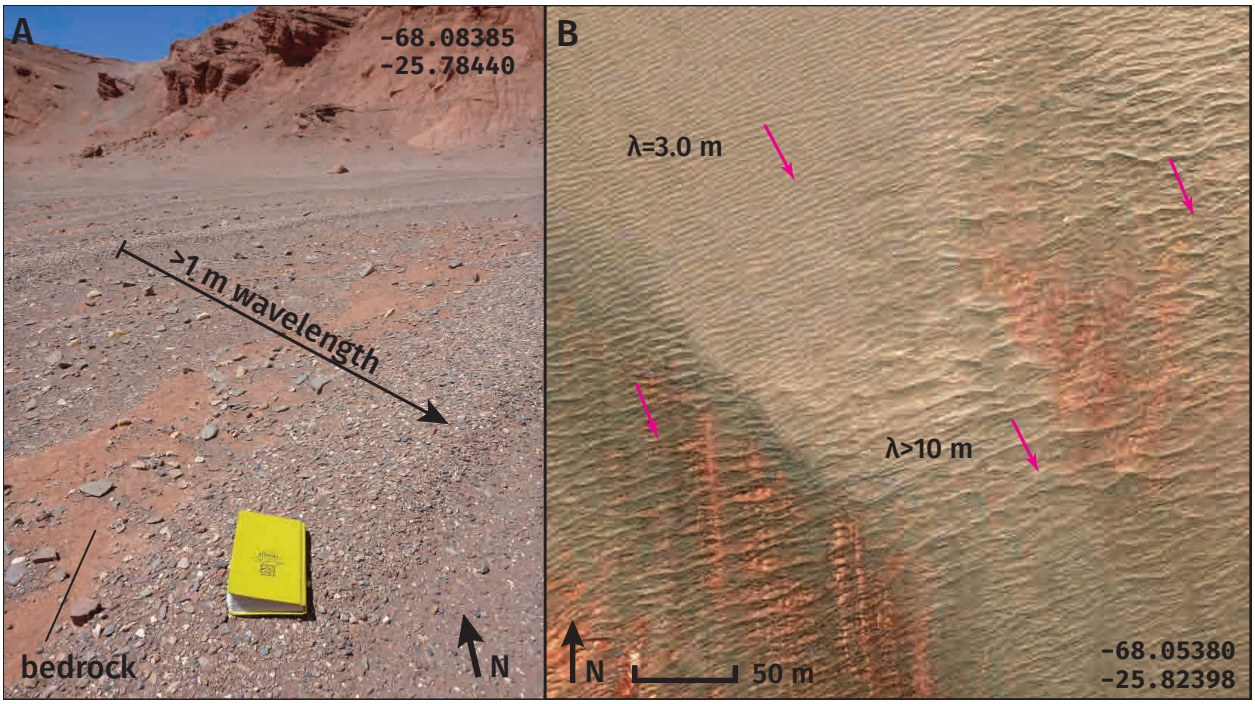

Figure 2.8: (a) Eolian megaripples photographed on a Permian bedrock surface in the Salina del Fraile. (b) Aerial imagery (Bing Maps) of eolian megaripples disrupting a stony lag deposit and exposing orange Quiñoas Formation bedrock. Refer to Figure 2.3 for the locations of images.

described in indurated ignimbrites nearby on the Puna Plateau and in Northern Chile (de Silva et al., 2010), but are similar in planform shape to megayardangs in Crommelin crater, Mars, that developed in canyon networks reworked by wind erosion (Perkins et al., 2015, and Figure 1b therein). As evidenced by the lack of boulder-sized colluvium, the lithologic composition of the smooth mesas is more friable than well-indurated ignimbrite and not capable of supporting the near-vertical slopes characteristic of some megayardangs (de Silva et al., 2010). The volcaniclastic sediments may also be more prone to disintegration by weathering and deflation. Like terrestrial megayardangs, the smooth mesas most likely result from a combination of processes, including colluvial and alluvial diffusion, but their overall forms are indicative of eolian streamlining and deflation. The base of the smooth mesas corresponds to the contact between Potrero Grande Formation volcaniclastics and Chacras Formation conglomerates, an erodibility barrier, while the top of the mesas correlates to a regional subhorizontal surface composed of thin volcanic flows resting on top of the Potrero Grande Formation (Richards et al., 2006; Voss, 2002), which could act as a caprock. Mesa height (~300 m) is roughly equivalent to the thickness of the Potrero Grande Formation. The mesas are separated by smooth troughs elongated in the direction of the dominant wind direction. The troughs are floored by abraded bedrock surfaces, mostly composed of Chacras conglomerates, with meter-scale erosional and fault scarps (Figure S3d). The planform shape of the mesas is elongated and tapers slightly in the downwind direction, and their windward slopes appear to be smoothed

and streamlined. The mesas are morphologically similar to streamlined hills and islands described in megaflood landscapes (e.g., Baker, 2009). Given the lack of evidence for megafloods in the study area, we suggest that the mesas formed by eolian downcutting into an erodible layer (Potrero Grande volcaniclastics) underlying a resistant caprock, a model similar to one proposed for the interior of Gale crater, Mars (Day & Kocurek, 2016). The mesas are deformed by a swarm of penetrative normal faults with 400–800 m spacing that display smaller scarps in the troughs separating the mesas than on their top surfaces (Figure S3d). Twenty kilometers to the southwest, this fault swarm deforms volcanic flows dated to 3.61 Ma (Adelmann, 2001), indicating that a significant portion of the extensional deformation was accommodated by faulting after ~3.6 Ma. This timeframe agrees with the one we infer for wind erosion, suggesting that the smaller scarps observed in the troughs between the mesas is due to preferential erosion of the troughs during active faulting. Predominant wind directions inferred from the long axes of yardangs, megaripple crests, and other landforms match closely with the downwind direction of strong winds obtained from the NASA MERRA reanalysis data (Figure 2.3, inset). Although the hourly MERRA data do not capture extreme wind gusts, which likely exceed 100 m/s in the southern Puna (Milana, 2009), they support the notion that these features result from strong, unidirectional, relatively infrequent winds. The data also suggest that the wind regime in the region has been stable throughout the late Quaternary and similar to the present, with strong winds directed toward the SE.

2.3.4 Timing and rate of erosion

Structural cross-sections, drawn conservatively to minimize the amount of erosion, show that up to 1,170 m and 1,950 m of strata were removed from the northern and central SdF, respectively (Figures 4 and 5). Existing chronostratigraphic ages provide constraints on the timing and rate of this erosion (Figure 2.9a). The initiation of erosion is bracketed by the top unit exposed in the depression, the Potrero Grande Formation, 17.0 Ma (Adelmann, 2001, K–Ar of biotite), and by the oldest volcanic ash deposited within the floor of the depression, 8.2 Ma (Voss, 2002, Ar–Ar of biotite). The depression therefore must have already been partially excavated by 8.2 Ma. Streamlining and erosion of terraces containing 2.6 Ma and 4.0 Ma ashes in the floor of the depression (Voss, 2002, Ar–Ar of plagioclase) also indicates significant erosion since the Pliocene. Yardangs and megaripples, active salt weathering zones, a lack of major sedimentary fill, rectilinear bedrock slopes, and imaged dust storms all indicate that erosion is currently active in the region (Goudie & Wells, 1995; Milana & Kröhling, 2017).

Given that erosion began between 17 and 8.2 Ma and is presently ongoing, we estimate erosion rates using the structural cross-sections presented in Section 2.3. A maximum thickness of eroded material of 1.95 km measured from section B (Figure 2.5), yields maximum erosion rates of 0.11– 0.23 mm/yr in the central part of the depression. An average of 1.05 km of strata have been eroded from cross-sections A and B (Figures 4 and 5). Using this as a spatial average over the area of the basin floor, wind has removed ~315 km^3 of material from the depression

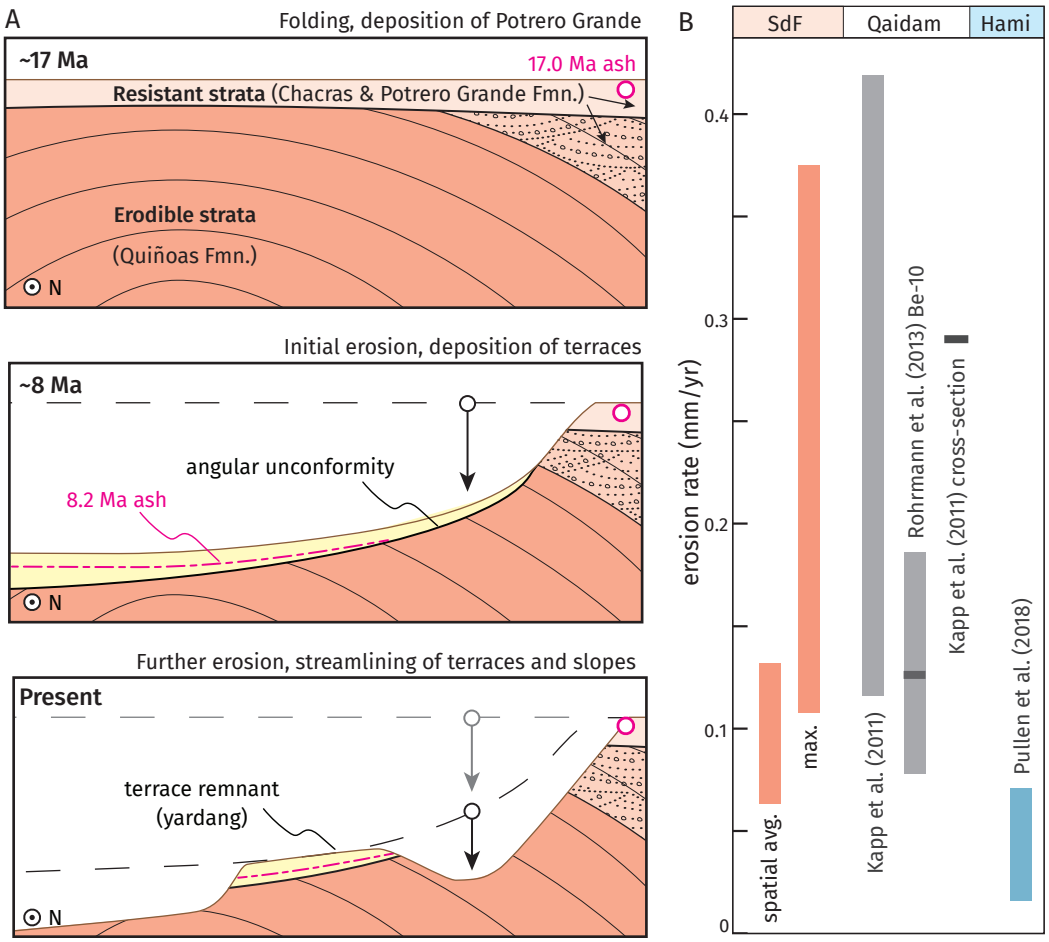

Figure 2.9: (a) Timing of wind erosion of the Salina del Fraile depression inferred from structural and chronostratigraphic data. (b) Comparison of erosion rates to previous studies of wind erosion in the Qaidam Basin, China (Kapp et al., 2011; Rohrmann et al., 2013) and the Hami Basin, China (Pullen et al., 2018).

since 17-8.2 Ma, averaging 0.062–0.13 mm/yr. Fluvial drainage networks (Figure S1) presently cover approximately 10% of the surface in the SdF. These erosion rates may overestimate the contribution of wind erosion of bedrock by up to 10%, but any fluvial sediment ultimately requires wind to be removed from the depression. While these estimates are long-term ($\sim 10^7$ yr), they fall within the range of rates reported elsewhere for wind erosion over time scales of millions of years (Figure 2.9b) and are 2–10 times lower than those calculated from cross-sections in the Qaidam basin, China, involving wind erosion of folded Pliocene strata (Kapp et al., 2011; Rohrmann et al., 2013). The spatially averaged erosion rate of ~0.06 mm/yr estimated here is very similar to the average erosion rate estimated for the Hami depression in northern China (Figure 2.9b), which involved deflation of Neogene strata containing conglomeratic and sandstone layers (Pullen et al., 2018).

2.3.5 Implications

The erosional origin of the Salina del Fraile depression has implications for the late Cenozoic tectonics of the Puna Plateau. Previous researchers suggested a Pliocene phase of orogen-parallel sinistral strike-slip kinematics based on the morphology of the depression, with up to 7.7 km of offset on a purported Salina del Fraile fault system (Reijs & McClay, 2003). Such an interpretation, however, challenges measurements of nearby fault kinematics that imply orogen-parallel dextral deformation during this time (Allmendinger et al., 1989; Kraemer et al., 1999; Zhou & Schoenbohm, 2015). Our inference that the depression is erosional obviates the need to invoke orogen-parallel sinistral tectonics and implies that Pliocene to Recent extensional deformation was accommodated by the normal faults apparent in Figure 2.3, which may be splays off the dextral Acazoque fault system that terminates near the Salar de Antofalla (Kraemer et al., 1999). The initiation of wind erosion between 17 and 8.2 Ma is broadly consistent with a documented phase of aridification on the Puna Plateau partially driven by the uplift of ranges east of the study area (Strecker et al., 2007), such as the Sierra Laguna Blanca (exhumed 15–10 Ma Zhou et al., 2017). Late Miocene aridification is also partially attributed to global cooling forced by a decline in atmospheric CO_2 (Herbert et al., 2016). Global aridification and cooling during the Late Miocene is reflected in ocean temperature proxies and in various moisture and temperature proxies compiled throughout Eurasia (Miao et al., 2012). Large-scale eolian deflation and excavation of topographic depressions, such as the Salina del Fraile and the Hami basin in central Asia (Pullen et al., 2018) may represent a topographic signal of this episode of global climate change. Alternatively, existing data also permit the interpretation that erosion began as soon as the package of friable strata was tectonically deformed and exposed at ~17 Ma. The idea that high-relief topography can be generated and sustained by eolian processes, with magnitudes of deflation up to 2 km, has implications for similar landforms on Earth and other planetary surfaces. The Central Andes hosts several depressions 10–50 km in width that, while little studied, may have been partially formed by wind erosion (Figure 2.1). Previous research indicates that the Purulla Basin (Figure 2.1, location B) may have experienced an average deflation of roughly ~4 m during the Holocene, approximately 0.3 mm/yr (Milana & Kröhling, 2017). Although more work should be done to quantify erosion rates in wind-dominated areas of the Puna, the Salina del Fraile suggests that the magnitude of eolian erosion throughout the Cenozoic may be significant in these internally drained regions lacking major fluvial incision. Many martian landforms are thought to be formed by wind erosion over long timescales. Mounds of sedimentary strata located in the centers of impact craters preserve records of past climates and are important exploration targets (Anderson & Bell, 2010). A substantial amount of wind erosion (up to a few km) is necessary to form the present morphology of many central mounds, whether they are remnants of crater-filling material (Bennett & Bell, 2016; Steele et al., 2018), or they formed in-place (Kite et al., 2013). The lower flank of Mount Sharp, the central mound of Gale crater, consists of erosional buttes, mesas, and

canyons that strongly resemble the smoothed mesas and elongated ridges described above (Figure 2.10).

Mudstones on the floor of Gale crater have exposure ages of only 78 ± 30 Ma, likely due to wind-driven bedrock scarp retreat (Farley et al., 2014). This relatively recent exposure increases the likelihood that complex organic molecules are preserved in near-surface materials. Identifying regions of rapid wind erosion is therefore critical for future missions exploring potentially habitable environments on Mars (Chojnacki et al., 2018). Like Gale and other martian craters including Jezero, the proposed landing site of the Perseverance rover, portions of the interior of the SdF are characterized by ongoing eolian erosion of lacustrine and alluvial strata that once partially filled the depression (Chojnacki et al., 2018; Palucis et al., 2016). The SdF thus represents a terrestrial analogue to martian landforms that are the target of exploratory missions.

2.4 Conclusions

Structural and chronostratigraphic data show that the SdF depression was excavated by erosion of up to 2 km of friable, Paleogene strata exposed in compressional folds. Wind, rather than water or ice, was the dominant agent of erosion during at least the past 8.2 Ma. This inference is based on depositional ages of alluvial and lacustrine deposits contained within the depression, the prevalence of erosional eolian landforms within and around the depression, the lack of integrated fluvial networks, and the regional geomorphic context, which is presently dominated by wind erosion. Inferred erosion rates of 0.06–0.23 mm/yr are typical of arid regions on Earth, but the large magnitude of erosion reflects the long time period (>8.2 Ma) during which eolian deflation took place. The SdF documents a Late Miocene to Quaternary source of eolian sand and dust in the southern Puna Plateau and exhibits some of the largest eolian landforms on Earth. In addition to the SdF depression itself, these include kilometer-scale elongated ridges and smoothed mesas resembling megayardangs and eolian landforms on Mars. Due to lithologic variation and tectonic folding, which produce erodibility contrasts, these high-relief landforms can be sustained without significant fluvial or glacial incision. Although the SdF is relatively well-studied, similar internally drained depressions in the Central Andes and other regions may also have been partially formed by wind erosion. Study of these landforms may yield insights into the evolution of Earth's arid regions on timescales of 10^6–10^7 yr, including how tectonic deformation and climate interact in such landscapes

Acknowledgments

The authors have no conflicts of interest to disclose. Support for this work was provided by an NSERC Discovery Grant and Discovery Accelerator Supplement to L. Schoenbohm. We thank Yanina Rojo and Santiago Uriburu Q. for assistance in the field, and we are grateful to Erin Sea-

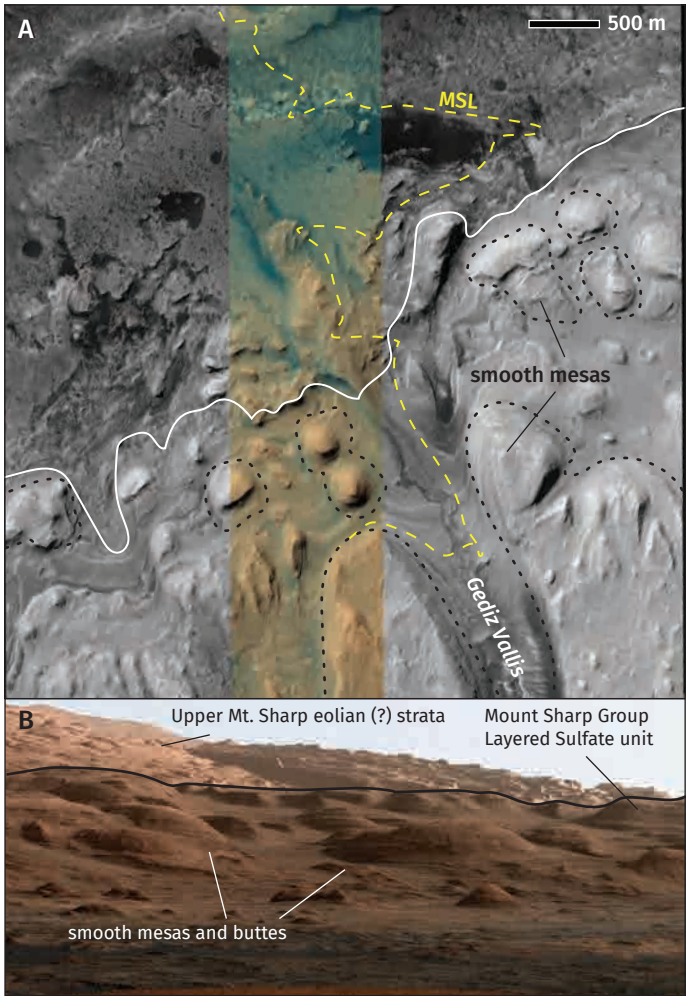

Figure 2.10: Eolian landforms in Gale crater, Mars, analogous to the smooth mesas near Salina del Fraile, Argentina. (a) Strata on the the NW flank of Mt. Sharp are eroded into streamlined mesas and buttes (indicated by black dotted lines) of the Layered Sulfate unit of the Mount Sharp Group (delineated by white line; stratigraphy of Fraeman et al. (2016). Yellow line approximates the planned path of the Mars Science Laboratory Curiosity rover (MSL). Cutout from MRO/HiRISE image ESP_061961_1750_MIRB (NASA/JPL/University of Arizona). The central ~1.2 km wide color band derives from merged infrared, red, and blue-green (IRB) channels, while the grayscale image derives only from the red channel. (b) Portion of white-balanced photomosaic of lower Mt. Sharp showing the profile of these streamlined erosional buttes and mesas. Acquired by Curiosity's Mast Camera (Mastcam) on September 20, 2012 (PIA16768; NASA/JPL-Caltech/MSSS).

gren and Jeremy Rimando for helpful advice and discussions that strengthened the manuscript. We sincerely thank Jon Perkins, Paul Kapp, and an anonymous reviewer for helpful comments. Structural and geochronological data for this research are available in McMillan and Schoenbohm (2020a) and online at https://doi.org/10.5683/SP2/UHDHGY. NASA MERRA data are available online at https://disc.gsfc.nasa.gov/.

References

Abell, J. T., Pullen, A., Lebo, Z. J., Kapp, P., Gloege, L., Metcalf, A. R., Nie, J., & Winckler, G. (2020). A wind-albedo-wind feedback driven by landscape evolution. *Nature Communications*, *11*(1), 1–9. https://doi.org/10.1038/s41467-019-13661-w

Adelmann, D. (2001). *Känozoische Beckenentwicklung des zentralandinen Puna-Plateaus (NW-Argentinien): Das Gebiet um den Salar de Antofalla und ein Vergleich zur nördlichen Puna* (Doctoral dissertation). Freien Universität Berlin.

Allmendinger, R. W., Strecker, M. R., Eremchuk, J. E., & Francis, P. (1989). Neotectonic deformation of the southern Puna Plateau, northwestern Argentina. *Journal of South American Earth Sciences*, *2*(2), 111–130. https://doi.org/10.1016/0895-9811(89)90040-0

Alonso, R. N., Jordan, T. E., Tabbutt, K. T., & Vandervoort, D. S. (1991). Giant evaporite belts of the Neogene central Andes. *Geology*, *19*(4), 401–404. https://doi.org/10.1130/0091-7613(1991)019<0401:GEBOTN>2.3.CO;2

Anderson, R. B., & Bell, J. F. (2010). Geologic mapping and characterization of Gale Crater and implications for its potential as a Mars Science Laboratory landing site. *Mars*, *5*, 76–128. https://doi.org/10.1555/mars.2010.0004

Aref, M. A., El-Khoriby, E., & Hamdan, M. A. (2002). The role of salt weathering in the origin of the Qattara Depression, Western Desert, Egypt. *Geomorphology*, *45*(3-4), 181–195. https://doi.org/10.1016/S0169-555X(01)00152-0

Baker, V. R. (2009). The Channeled Scabland: A Retrospective. *Annual Review of Earth and Planetary Sciences*, *37*(1), 393–411. https://doi.org/10.1146/annurev.earth.061008.134726

Bennett, K. A., & Bell, J. F. (2016). A global survey of martian central mounds: Central mounds as remnants of previously more extensive large-scale sedimentary deposits. *Icarus*, *264*, 331–341. https://doi.org/10.1016/j.icarus.2015.09.041

Bookhagen, B., & Strecker, M. R. (2008). Orographic barriers, high-resolution TRMM rainfall, and relief variations along the eastern Andes. *Geophysical Research Letters*, *35*(6), L06403. https://doi.org/10.1029/2007GL032011

Bridges, N. T., Spagnuolo, M. G., de Silva, S. L., Zimbelman, J. R., & Neely, E. M. (2015). Formation of gravel-mantled megaripples on Earth and Mars: Insights from the Argentinean Puna and wind tunnel experiments. *Aeolian Research*, *17*, 49–60. https://doi.org/10.1016/j.aeolia.2015.01.007

Brock, E. J., & Twidale, C. R. (2011). J.T. Jutson and the Work of the Wind in Shaping the Landscape. *Geographical Research*, *49*(1), 47–58. https://doi.org/10.1111/j.1745-5871.2010.00662.x

Canavan, R. R., Carrapa, B., Clementz, M. T., Quade, J., DeCelles, P. G., & Schoenbohm, L. M. (2014). Early cenozoic uplift of the Puna plateau, central andes, based on stable isotope paleoaltimetry of hydrated volcanic glass. *Geology*, *42*(5), 447–450. https://doi.org/10.1130/G35239.1

Carrapa, B., Adelmann, D., Hilley, G. E., Mortimer, E., Sobel, E. R., & Strecker, M. R. (2005). Oligocene range uplift and development of plateau morphology in the southern central Andes. *Tectonics*, *24*, TC4011. https://doi.org/10.1029/2004TC001762

Chojnacki, M., Banks, M., & Urso, A. (2018). Wind-driven erosion and exposure potential at Mars 2020 rover candidate-landing sites. *Journal of Geophysical Research: Planets*, *123*(2), 468–488. https://doi.org/10.1002/2017JE005460

Day, M., & Kocurek, G. (2016). Observations of an aeolian landscape: From surface to orbit in Gale Crater. *Icarus*, *280*, 37–71. https://doi.org/10.1016/j.icarus.2015.09.042

de Silva, S. L., Spagnuolo, M. G., Bridges, N. T., & Zimbelman, J. R. (2013). Gravel-mantled megaripples of the Argentinean Puna: A model for their origin and growth with implications for Mars. *Bulletin of the Geological Society of America*, *125*(11-12), 1912–1929. https://doi.org/10.1130/B30916.1

de Silva, S. L., Bailey, J. E., Mandt, K. E., & Viramonte, J. M. (2010). Yardangs in terrestrial ignimbrites: Synergistic remote and field observations on Earth with applications to Mars. *Planetary and Space Science*, *58*(4), 459–471. https://doi.org/10.1016/j.pss.2009.10.002

Farley, K. A., Malespin, C., Mahaffy, P., Grotzinger, J. P., Vasconcelos, P. M., Milliken, R. E., Malin, M., Edgett, K. S., Pavlov, A. A., Hurowitz, J. A., Grant, J. A., Miller, H. B., Arvidson, R., Beegle, L., Calef, F., Conrad, P. G., Dietrich, W. E., Eigenbrode, J., Gellert, R., … Moores, J. E. (2014). In situ radiometric and exposure age dating of the Martian surface. *Science*, *343*(6169), 1247166–1247166. https://doi.org/10.1126/science.1247166

Fraeman, A. A., Ehlmann, B. L., Arvidson, R. E., Edwards, C. S., Grotzinger, J. P., Milliken, R. E., Quinn, D. P., & Rice, M. S. (2016). The stratigraphy and evolution of lower Mount Sharp from spectral, morphological, and thermophysical orbital data sets. *Journal of Geophysical Research: Planets*, *121*(9), 1713–1736. https://doi.org/10.1002/2016JE005095

Gaiero, D. M. (2007). Dust provenance in Antarctic ice during glacial periods: From where in southern South America? *Geophysical Research Letters*, *34*(17), 1–6. https://doi.org/10.1029/2007GL030520

Goudie, A. (2018). Dust storms and ephemeral lakes. *Desert*, *23*(1), 153–164. https://doi.org/10.22059/jdesert.2018.66370

Goudie, A. S., & Wells, G. L. (1995). The nature, distribution and formation of pans in arid zones. *Earth Science Reviews*, *38*(1), 1–69. https://doi.org/10.1016/0012-8252(94)00066-6

Goudie, A. S. (2012). Charles Rollin Keyes and extravagant aeolation. *Aeolian Research*, *4*, 51–53. https://doi.org/10.1016/j.aeolia.2012.01.001

Goudie, A. S., & Day, M. J. (1980). Disintegration of fan sediments in Death Valley, California, by salt weathering. *Physical Geography*, *1*(2), 126–137. https://doi.org/10.1080/02723646.1980.10642195

Haselton, K., Hilley, G., & Strecker, M. R. (2002). Average Pleistocene climatic patterns in the southern central Andes: Controls on mountain glaciation and paleoclimate implications. *Journal of Geology*, *110*(2), 211–226. https://doi.org/10.1086/338414

Herbert, T. D., Lawrence, K. T., Tzanova, A., Peterson, L. C., Caballero-Gill, R., & Kelly, C. S. (2016). Late Miocene global cooling and the rise of modern ecosystems. *Nature Geoscience*, *9*(11), 843–847. https://doi.org/10.1038/ngeo2813

Hugenholtz, C. H., Barchyn, T. E., & Favaro, E. A. (2015). Formation of periodic bedrock ridges on Earth. *Aeolian Research*, *18*, 135–144. https://doi.org/10.1016/j.aeolia.2015.07.002

Isla, F., & Espinosa, M. (2017). Upper Quaternary evolution of the dune field of the Bolsón de Fiambalá, Catamarca: Sand dispersal at the Andes piedmonts. *Quaternary International*, *442*, 59–66. https://doi.org/10.1016/j.quaint.2016.07.037

Kapp, P., Pelletier, J. D., Rohrmann, A., Heermance, R., Russell, J., & Ding, L. (2011). Wind erosion in the Qaidam basin, central Asia: Implications for tectonics, paleoclimate, and the source of the Loess Plateau. *GSA Today*, *21*(4-5), 4–10. https://doi.org/10.1130/GSATG99A.1

Kite, E. S., Lewis, K. W., Lamb, M. P., Newman, C. E., & Richardson, M. I. (2013). Growth and form of the mound in Gale Crater, Mars: Slope wind enhanced erosion and transport. *Geology*, *41*(5), 543–546. https://doi.org/10.1130/G33909.1

Kraemer, B., Adelmann, D., Alten, M., Schnurr, W., Erpenstein, K., Kiefer, E., Van Den Bogaard, P., & Görler, K. (1999). Incorporation of the Paleogene foreland into the Neogene Puna plateau: The Salar de Antofalla area, NW Argentina. *Journal of South American Earth Sciences*, *12*(2), 157–182. https://doi.org/10.1016/S0895-9811(99)00012-7

Lämmel, M., Meiwald, A., Yizhaq, H., Tsoar, H., Katra, I., & Kroy, K. (2018). Aeolian sand sorting and megaripple formation. *Nature Physics*, *14*(7), 759–765. https://doi.org/10.1038/s41567-018-0106-z

McMillan, M., & Schoenbohm, L. M. (2020a). *Large-Scale cenozoic wind erosion in the Puna Plateau*. https://doi.org/10.5683/SP2/UHDHGY

McMillan, M., & Schoenbohm, L. M. (2020b). Large-scale Cenozoic wind erosion in the Puna Plateau: The Salina del Fraile Depression. *Journal of Geophysical Research: Earth Surface*. https://doi.org/10.1029/2020JF005682

Miao, Y., Herrmann, M., Wu, F., Yan, X., & Yang, S. (2012). What controlled Mid-Late Miocene long-term aridification in Central Asia?–Global cooling or Tibetan Plateau uplift: A review. *Earth-Science Reviews*, *112*(3-4), 155–172. https://doi.org/10.1016/j.earscirev.2012.02.003

Milana, J. P. (2009). Largest wind ripples on Earth? *Geology*, *37*(4), 343–346. https://doi.org/10.1130/G25382A.1

Milana, J. P., & Kröhling, D. M. (2017). First data on volume and type of deflated sediment from Southern Puna Plateau and its role as source of the Chaco-Pampean loess. *Quaternary International*, *438*(March), 126–140. https://doi.org/10.1016/j.quaint.2017.03.007

Palucis, M. C., Dietrich, W. E., Williams, R. M., Hayes, A. G., Parker, T., Sumner, D. Y., Mangold, N., Lewis, K., & Newsom, H. (2016). Sequence and relative timing of large lakes in Gale crater (Mars) after the formation of Mount Sharp. *Journal of Geophysical Research: Planets*, *121*(3), 472–496. https://doi.org/10.1002/2015JE004905

Pelletier, J. D., Kapp, P., Abell, J. T., Field, J. P., Williams, Z. C., & Dorsey, R. J. (2018). Controls on Yardang Development and Morphology: 1. Field Observations and Measurements at Ocotillo Wells, California. *Journal of Geophysical Research: Earth Surface*, *123*(4), 694–722. https://doi.org/10.1002/2017JF004461

Perkins, J. P., Finnegan, N. J., & De Silva, S. L. (2015). Amplification of bedrock canyon incision by wind. *Nature Geoscience*, *8*(4), 305–310. https://doi.org/10.1038/ngeo2381

Perkins, J. P., Finnegan, N. J., de Silva, S. L., & Willis, M. J. (2019). Controls on Eolian Landscape Evolution in Fractured Bedrock. *Geophysical Research Letters*, *46*(21), 12012–12020. https://doi.org/10.1029/2019GL083955

Plakht, J., Patyk-Kara, N., & Gorellkova, N. (2000). Terrace pediments in Makhtesh Ramon, Central Negev, Israel. *Earth Surface Processes and Landforms*, *25*(1), 29–39. https://doi.org/10.1002/(SICI)1096-9837(200001)25:1<29::AID-ESP44>3.0.CO;2-D

Pullen, A., Kapp, P., & Chen, N. (2018). Development of stratigraphically controlled, eolian-modified unconsolidated gravel surfaces and yardang fields in the wind-eroded Hami Basin, northwestern China. *Bulletin of the Geological Society of America*, *130*(3-4), 630–648. https://doi.org/10.1130/B31734.1

Quade, J., Dettinger, M. P., Carrapa, B., DeCelles, P. G., Murray, K. E., Huntington, K. W., Cartwright, A., Canavan, R. R., Gehrels, G. E., & Clementz, M. (2015). The growth of the central Andes, 22° S-26° S. In *Geological Society of America Memoirs* (pp. 277–308).

Reijs, J., & McClay, K. (2003). The Salina del Fraile pull-apart basin, northwest Argentina. *Intraplate Strike-Slip Deformation Belts*, *210*, 197–209. https://doi.org/10.1144/Gsl.Sp.2003.210.01.12

Richards, J. P., Ullrich, T., & Kerrich, R. (2006). The Late Miocene-Quaternary Antofalla volcanic complex, southern Puna, NW Argentina: Protracted history, diverse petrology, and economic potential. *Journal of Volcanology and Geothermal Research*, *152*(3-4), 197–239. https://doi.org/10.1016/j.jvolgeores.2005.10.006

Rohrmann, A., Heermance, R., Kapp, P., & Cai, F. (2013). Wind as the primary driver of erosion in the Qaidam Basin, China. *Earth and Planetary Science Letters*, *374*, 1–10. https://doi.org/10.1016/j.epsl.2013.03.011

Schwanghart, W., & Scherler, D. (2014). TopoToolbox 2–MATLAB-based software for topographic analysis and modeling in Earth surface sciences. *Earth Surface Dynamics*, *2*(1), 1–7.

Seggiaro, R., Becchio, R., Pereyra, F., & Martínez, L. (2007). *Hoja Geológica 2569-IV, Antofalla*. Servicio Geológico Minero Argentino.

Selby, M. J. (1971). Slopes and Their Development in an Ice-Free, Arid Area of Antarctica. *Geografiska Annaler: Series A, Physical Geography*, *53*(3-4), 235–245. https://doi.org/10.1080/04353676.1971.11879849

Steele, L. J., Kite, E. S., & Michaels, T. I. (2018). Crater Mound Formation by Wind Erosion on Mars. *Journal of Geophysical Research: Planets*, *123*(1), 113–130. https://doi.org/10.1002/2017JE005459

Strecker, M. R., Alonso, R. N., Bookhagen, B., Carrapa, B., Hilley, G., Sobel, E. R., & Trauth, M. (2007). Tectonics and Climate of the Southern Central Andes. *Annual Review of Earth and Planetary Sciences*, *35*(1), 747–787. https://doi.org/10.1146/annurev.earth.35.031306.140158

Voss, R. (2002). Cenozoic stratigraphy of the southern Salar de Antofalla region, northwestern Argentina. *Andean Geology*, *29*(2), 167189. https://doi.org/10.4067/S0716-02082002000200002

Xiao, L., Wang, J., Dang, Y., Cheng, Z., Huang, T., Zhao, J., Xu, Y., Huang, J., Xiao, Z., & Komatsu, G. (2017). A new terrestrial analogue site for Mars research: The Qaidam Basin, Tibetan Plateau (NW China). *Earth-Science Reviews*, *164*, 84–101. https://doi.org/10.1016/j.earscirev.2016.11.003

Zhou, R., & Schoenbohm, L. M. (2015). Late Miocene upper-crustal deformation within the interior of the southern Puna Plateau, central Andes. *Lithosphere*, *7*(3), 336–352. https://doi.org/10.1130/L396.1

Zhou, R., Schoenbohm, L. M., Sobel, E. R., Davis, D. W., & Glodny, J. (2017). New constraints on orogenic models of the southern Central Andean Plateau: Cenozoic basin evolution and bedrock exhumation. *Bulletin of the Geological Society of America*, *129*(1-2), 152–170. https://doi.org/10.1130/B31384.1

3 Eocene to Quaternary deformation of the Southern Puna Plateau

Thermochronology, geochronology, and structural geology of an Andean hinterland basin (NW Argentina)*

Abstract

Cordilleran orogens are complex tectonic systems, strongly influenced by lithospheric deformation and exhumation. However, in the type region of the Central Andes, the timing and mechanisms of deformation and mountain building remain poorly constrained, especially for the high elevation Puna Plateau of NW Argentina. We use geologic mapping, structural cross-sections, low-temperature thermochronology, and U-Pb dating of ash and detrital zircons to elucidate the history and style of orogenic deformation in the Antofalla region of the Puna Plateau. Cooling ages of major reverse fault hanging walls and dated growth strata indicate that crustal shortening activated major reverse faults during the Eocene and continued out-of-sequence through the Early Miocene. This protracted period of shortening, which resulted in the filling of the Antofalla basin, was followed by a transient episode of upper-crustal E–W extension on a major normal fault system during the Late Miocene. Pliocene to Quaternary time saw E–W shortening return to the region. Our structural cross-section permits only a low magnitude of shortening (~15–25%), which stands in contrast to the 60 km thick crust. Triassic to Cretaceous cooling ages from footwall rocks and minor structures indicate that the entire region experienced little exhumation or sedimentation during the Mesozoic, perhaps retaining a crust thickened during multiple episodes of Paleozoic orogenesis. The crust may also reflect lower-crustal thickening due to the growth of a lithospheric drip during the Late Miocene.

*This chapter is under review in *Tectonics*.

Citation: McMillan, M., Tye, A. R., Schoenbohm, L. M., McMillan, M. F., & Zhou, R. (in review). Eocene to Quaternary deformation of the Southern Puna Plateau: Thermochronology, geochronology, and structural geology of an Andean hinterland basin (NW Argentina). *Tectonics*.

Supplementary material is available in Appendix A.

3.1 Introduction

Orogenesis due to tectonic shortening and crustal thickening produces regions of high topography where crustal rocks are exposed, eroded, and transported into sedimentary basins; it is therefore fundamental to the formation and evolution of continental crust and supracrustal geology. As the type-example of a Cordilleran orogen produced by oceanic plate subduction, the Central Andes provides an opportunity to study the orogenic processes operating in a non-collisional setting, including the geodynamics of the lower crust (e.g., Husson & Sempere, 2003) and mantle lithosphere (e.g., DeCelles et al., 2009). High topography in the Andes is mainly due to crustal thickening and lithospheric thinning (Garzione et al., 2017; Isacks, 1988), with the thickest crust occurring in the Central Andean Plateau (Figure 3.1c; Tassara & Echaurren, 2012). The southern part of the Central Andean Plateau, the Puna Plateau, is notable because its ~60 km crust is much thicker than can be accounted for by upper-crustal shortening inferred from structural cross-sections (Kley & Monaldi, 1998), and its ~4.2 km average elevation is partially supported by the nearly complete lack of a significant mantle lithospheric root (Tassara & Echaurren, 2012). The Puna evidently lost its mantle lithosphere during one or more episodes of dripping or delamination during Miocene to Pliocene time (e.g., DeCelles et al., 2015a; Kay et al., 1994; Schoenbohm & Carrapa, 2015).

In order to understand crustal thickening in the Puna Plateau, it is necessary to constrain the history of tectonic deformation, including the timing and magnitude of orogenic shortening in the region. Basement-cored ranges on the plateau provide windows into the tectonic history of the Central Andes through low-temperature thermochronology studies, which document Late Cretaceous through Cenozoic exhumation and shortening on major structures (Figure 3.1a, and see Carrapa et al., 2005; Carrapa & DeCelles, 2015; Stalder et al., 2020). Sedimentary basins on the plateau also record the uplift of source regions (e.g., Zhou et al., 2017), and syn-tectonic sedimentation allows dating of deformation on specific structures (e.g., Schoenbohm & Carrapa, 2015). Structural cross-sections, especially when combined with thermochronologic data and other geologic constraints, allow estimation of the overall magnitude of upper-crustal shortening, as well as assigning deformation to specific structures (e.g., McQuarrie, 2002). In the Puna, such detailed kinematic information may also shed light on the geodynamic processes that led to the loss of the mantle lithospheric root and the uplift of the plateau.

The timing of deformation and plateau surface uplift, however, are still hotly debated for the Southern Puna. Apatite fission track (AFT) ages, although sparse on the Puna Plateau, broadly document Cretaceous to Miocene cooling ages, with Cenozoic ages confined to major ranges, indicating that Andean shortening and exhumation was concentrated on a few major structures (Figure 3.1a). In the central Puna, detrital AFT cooling ages indicate rapid exhumation of proximal source terranes during the late Paleocene to Eocene (Carrapa & DeCelles, 2008; Carrapa et al., 2009), suggesting that significant topography may have developed by late Eocene time. Similarly, paleoelevation proxies from the Southern Puna suggest that topography was already

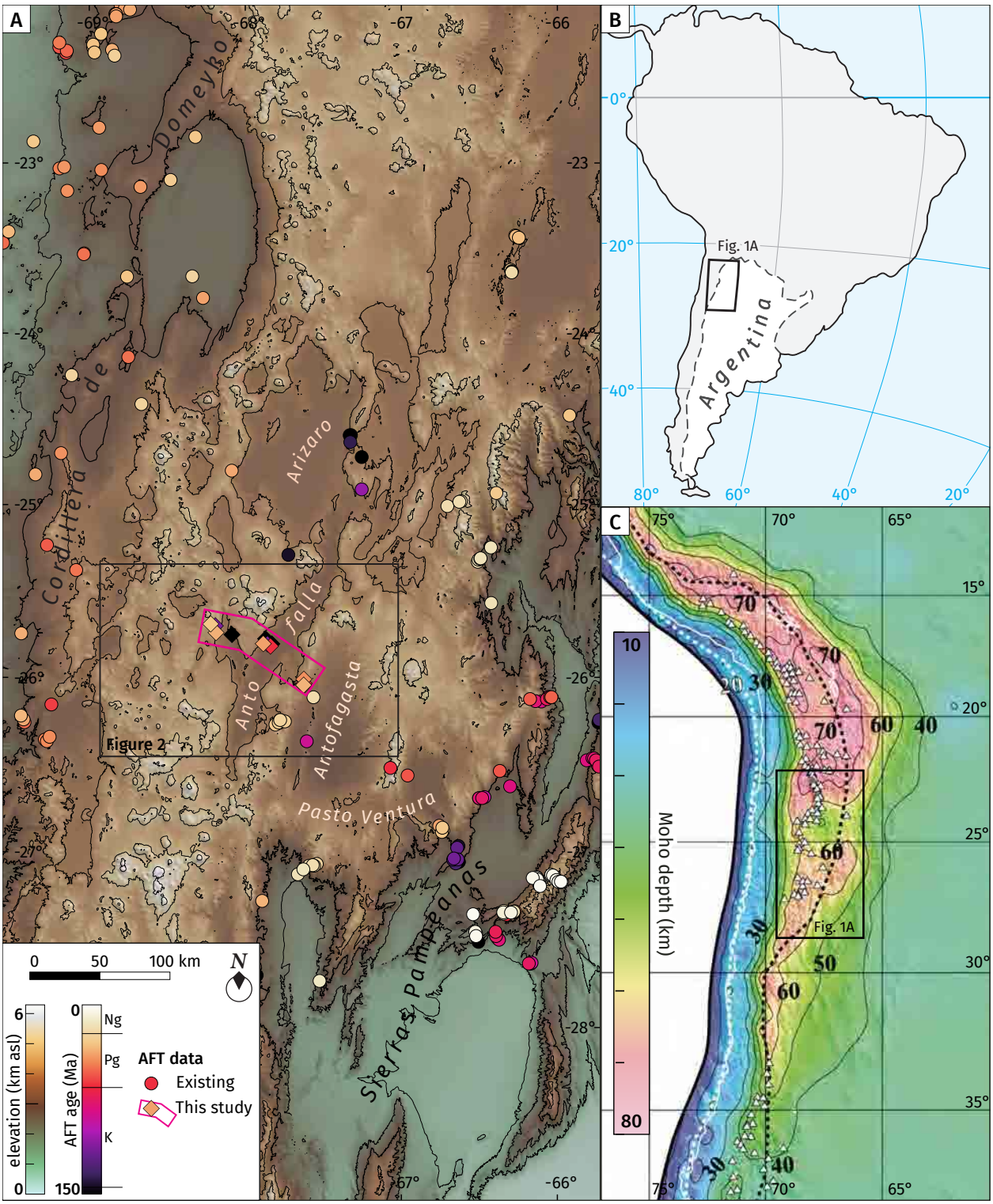

Figure 3.1: (a) Map of apatite fission track (AFT) ages in the Southern Puna Plateau overlaid on elevation (SRTM; 1 km contours; 3 km-contour bolded). Data from this study and from Carrapa et al. (2005), Stalder et al. (2020), Zhou and Schoenbohm (2015), and Zhou et al. (2017). The box denotes location of Figure 3.2. (b) Location within South America. (c) Map of crustal thickness (Moho depth) in the Central Andes from Tassara et al. (2006). Boxes in (b) and (c) give the location of (a).

>3 km by the late Eocene (Canavan et al., 2014; Quade et al., 2015), though more recent analyses have contested this result (Pingel et al., 2020). Evidence for Paleocene–Eocene exhumation has not yet been found in what low-temperature thermochronological data exist in the Southern Puna. As an alternative to a high-elevation plateau during the Paleocene–Eocene, the Southern Puna is sometimes argued to have hosted a foreland basin sitting at relatively low elevations, which was eventually incorporated into the orogenic plateau during the latest Oligocene to early Miocene (Carrapa et al., 2005; Kraemer et al., 1999; Zhou et al., 2017). This interpretation was strengthened by low-temperature thermochronology of the Calalaste range, a major range in the Southern Puna (Figure 3.1a; Carrapa et al., 2005; Zhou et al., 2017). Exhumation of the Calalaste range around 29 to 25 Ma was interpreted to reflect the initial fragmentation of a Paleogene foreland basin and its incorporation into the orogen (Carrapa et al., 2005). The apparent contradictions between the two models of plateau uplift are succinctly captured by the Paleogene Quiñoas Formation, a widespread, 1 to 3 km thick deposit of fluvio-lacustrine strata in the Southern Puna, which has been used to argue for both a high plateau (volcanic glass δD paleoaltimeter; Canavan et al., 2014; Quade et al., 2015) and a foredeep-forebulge setting (sedimentary facies and thickness; Kraemer et al., 1999; Zhou et al., 2016; Zhou et al., 2017) during the late Eocene to early Oligocene.

In this paper, we present new data from the Calalaste range, the Quebrada Honda range, and the Cenozoic Antofalla basin in the Southern Puna to constrain the tectonic history of the region. Quantitative data include AFT analyses and U-Pb dating of volcanic and detrital zircons; we also present new geologic mapping and structural cross-sections that provide the necessary context for interpreting these data. We first present a geologic background with emphasis on lithostratigraphy of the sedimentary deposits that comprise the Cenozoic Antofalla basin (Section 3.2). We then present our geologic mapping, complemented by U-Pb zircon geochronology (Section 3.3). We then turn to the AFT thermochronology data and discuss the results from key locations (Section 3.4). We bring all of our observations together in a structural cross-section, which we present in Section 3.5. Our data constrain the tectonic evolution of the Southern Puna and have implications for the Paleogene tectonic setting, the nature of Neogene deformation within the plateau, and the observed crustal thicknesses. We discuss two possibilities for the thick crust of the modern Puna Plateau which are consistent with our data: antecedent Paleozoic-Mesozoic tectonics and lithospheric foundering during the Miocene.

3.2 Geologic background

The Antofalla region is located in the Southern Puna Plateau and spans ~100 km from the Andean volcanic arc to the Calalaste Range in the central portion of the plateau. Two modern evaporite basins, the Salar de Antofalla and the Salina del Fraile, occur near the central part of the Antofalla basin, and sit at elevations of 3,300 to 3,400 m respectively (Figure 3.2). The study

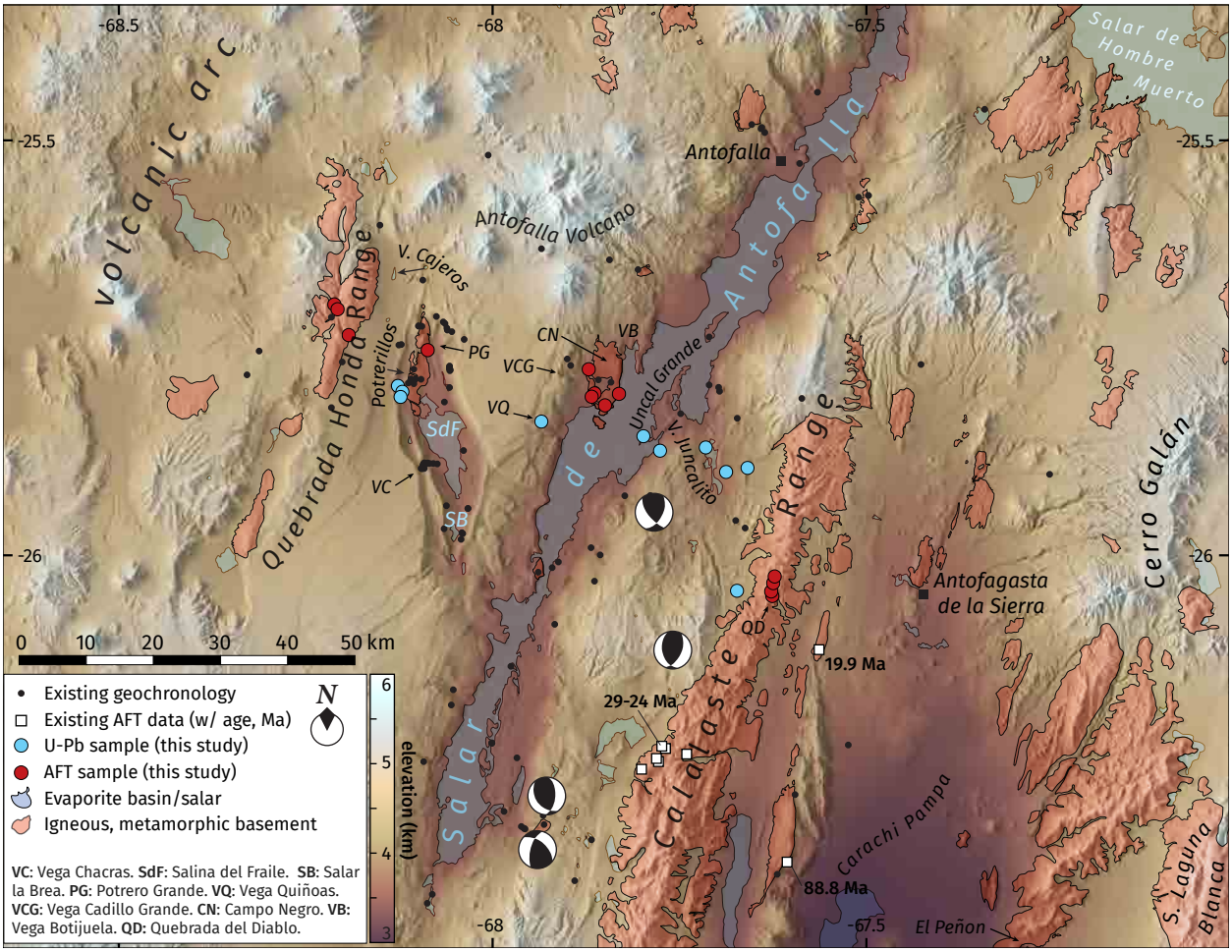

Figure 3.2: Map of the Antofalla region showing basement outcrops and distribution of geochronology and thermochronology samples collected for this study in the context of existing data. Focal mechanisms of crustal earthquakes beneath the Calalaste Range are redrawn from Mulcahy et al. (2014).

area is delimited to the north by the Antofalla volcanic complex, a Miocene to Quaternary edifice of Andean arc volcanism (Richards et al., 2006). The study area is delimited to the south by later volcanic cover, which reduces geologic exposure.

Due to its proximity to the long-lived active margin of western South America, the region records a long history of sedimentation, magmatism, and tectonic deformation, resulting in complex geology (Seggiaro et al., 2007). The oldest crystalline basement in the region is exposed at Cerro Campo Negro, which sits at relatively low elevations of 3320 to 3500 m along the western edge of the Salar de Antofalla (labelled CN in Figure 3.2). Cerro Campo Negro consists of Neoproterozoic to Cambrian metamorphic rocks intruded by the Lower Ordovician Campo Negro Granite (Seggiaro et al., 2007). The metamorphic rocks consist mainly of foliated granitic orthogneiss, quartzite, schist, and phyllite, with minor migmatite (Escayola et al., 2011; Lucassen et al., 2001; Seggiaro et al., 2007; Voss, 2002). Inherited zircon cores are primarily Neoproterozoic and Mesoproterozoic in age (654 to 1881 Ma), with a younger population of 523.0 ± 4.7 Ma (Early

Cambrian) potentially equivalent to the Puncoviscana Formation that outcrops throughout NW Argentina (Escayola et al., 2011; Seggiaro et al., 2007). The intrusive Cerro Negro Granite has been dated to 419 ± 8 Ma and 417 ± 8 Ma (K-Ar on muscovite; Kraemer et al., 1999) and 446 ± 11 Ma (K-Ar on hornblende; Lucassen et al., 2000), indicating emplacement during the Early Ordovician.

The basement also consists of highly deformed Early Paleozoic metasedimentary, metavolcanic, and intrusive rocks, which are exposed in Cerro Campo Negro and make up the cores of the Quebrada Honda and Calalaste Ranges (Kraemer et al., 1999; Seggiaro et al., 2007; Voss, 2002). In the Antofalla region, Early Paleozoic metamorphic rocks are mapped as the Cortaderas Chicas Volcano-Sedimentary Complex (Seggiaro et al., 2007). This lithologically diverse unit consists of a succession of siliciclastic marine turbidites and greywackes with interbedded limestones, lavas, and locally chert (Seggiaro et al., 2007; Voss, 2002). Graptolite assemblages and detrital zircon ages from the Calalaste range and from the Northern Puna suggest deposition during the Early Ordovician (Bahlburg et al., 1990; Seggiaro et al., 2007; Zimmermann et al., 2014). The sedimentary protoliths were derived from a mixture of pre-Ordovician metamorphic basement sources and contemporaneous Early Ordovician volcanic sources (Zimmermann & Bahlburg, 2003). In the Calalaste range, Ordovician strata are placed in tectonic contact with felsic and mafic-ultramafic intrusive igneous bodies that are Ediacaran to Early Cambrian in age (~545 Ma; Zimmermann & Bahlburg, 2003; Zimmermann et al., 2014). Similar Ordovician metasedimentary and metavolcanic strata outcrop along a 400 km-long NNE-trending belt that transects the entire Puna Plateau and represents deformed volcanic, volcaniclastic, and marine strata deposited in the forearc (Niemeyer et al., 2018) of the Famatinian magmatic arc and Puncoviscana orogenic belt (Ducea et al., 2015; Niemeyer et al., 2018; Suzaño et al., 2017; Zimmermann & Bahlburg, 2003). Throughout the Puna, Ordovician-age units display approximately 25–50% shortening that predates the Cenozoic Andean orogeny (Henriquez et al., 2020). Pre-Andean deformation was accomplished by one or more episodes of orogenesis on the Paleozoic western margin of Gondwana (Lucassen et al., 2000), which imparted a steeply east-dipping fabric to the basement in the Antofalla region (Mon & Hongn, 1991).

Igneous and metamorphic basement rocks are locally overlain by unmetamorphosed Upper Paleozoic, Mesozoic, and Cenozoic strata. Permian continental siliciclastic strata outcrop in Cerro Campo Negro and in the core of the Potrerillos Anticline in the northernmost Salina del Fraile (Kraemer et al., 1999; Seggiaro et al., 2007; Voss, 2002). These strata, which are here referred to as the Potrerillo Unit after the latter location (Voss, 2002), have been assigned to the Patquía-de La Cuesta Formation of the Paganzo Group (Seggiaro et al., 2007), and consist of quartz-rich cross-bedded sandstones, quartz-rich conglomerates, siltstones, and eolian sandstones, together interpreted as beach and nearshore deposits (Kraemer et al., 1999). In the Salina del Fraile, Permian strata are intruded by highly altered, mafic to intermediate porphyritic dikes (Seggiaro et al., 2007; Voss, 2002) that have been dated to the Triassic, ~212–234 Ma (Adelmann, 2001; Kraemer et al., 1999). Dikes of similar age throughout Northern Chile

have typical volcanic arc geochemical signatures and trend predominately NE-SW, suggesting intrusion in a Late Triassic continental arc to back-arc setting (González et al., 2018). The largest dikes in the Salina del Fraile trend WNW-ESE and are subvertical with a thickness of 10–20 m and lengths of up to 2 km; a set of smaller dikes trends ENE–WSW and are not well exposed.

The Jurassic Fraile Unit unconformably overlies Permian strata and Triassic intrusive rocks in the Salina del Fraile (Kraemer et al., 1999; Voss, 2002). The Fraile Unit consists of oscillatory rippled sandstones, marls, oolitic limestones, coquina, and basaltic pillow lavas dated to ~194–198 Ma, indicating a shallow marine depositional environment in the Early Jurassic (Kraemer et al., 1999; Seggiaro et al., 2007). The basal contact of the Fraile Unit is characterized by large paleo relief on the order of 100 m, indicating rapid filling of paleotopography (Adelmann, 2001; Seggiaro et al., 2007). Early Jurassic deposits similar to the Fraile Unit are not common in the Southern Puna, but are present in the Cordillera de Domeyko of Chile, where they represent post-rift thermal sag deposits that unconformably onlap syn-rift and pre-rift units, including paleotopographic highs associated with Triassic horsts (Espinoza et al., 2019). The rapid deposition of Jurassic strata in the Salina del Fraile may have been controlled by the location of Triassic or Jurassic structures, possibly normal faults (Seggiaro et al., 2007).

Cretaceous deposits associated with back-arc extension are present in both the Chilean Cordillera de Domeyko (e.g., Amilibia et al., 2008) and the broken foreland region of NW Argentina (e.g., Grier et al., 1991; Marquillas et al., 2005) at 25–26° S latitude. In these regions that flank the Southern Puna on the west and east, respectively, thick packages of folded Cretaceous strata commonly make up the hanging wall blocks of steeply dipping reverse faults. Known deposits of Cretaceous age are absent from the Southern Puna and are mapped only in the Northern Puna where the Salta Rift basin extended westward into the region of the modern plateau (Marquillas et al., 2005). The lack of Cretaceous sedimentation, with Cenozoic strata overlying pre-Cretaceous units in angular unconformity, indicates that the Southern Puna was topographically high during this major episode of back-arc continental extension, and any extensional deformation affecting the region was evidently of minor importance.

In the Antofalla region, the Cenozoic geology consists of approximately 3 km of continental clastic strata representing multiple phases of sedimentation and deformation from the Late Eocene to the Quaternary (Adelmann, 2001; Kraemer et al., 1999; Voss, 2002; Zhou et al., 2017). Three stratigraphic nomenclatures are in use for Cenozoic sedimentary strata in the Antofalla region (Figure 3.3). In this study, we follow the nomenclature described by Adelmann (2001) and Kraemer et al. (1999) based on extensive logging of sedimentary sections throughout the study area.

The base of the Cenozoic section consists of a ~1.5 km package of Late Eocene–Oligocene strata that has been divided based on lithology into the Quiñoas Formation (Upper and Lower Members) and the Chacras Formation (Kraemer et al., 1999). The base of the Quiñoas Formation is exposed at Cerro Campo Negro, where it rests in unconformity on Permian strata (Voss, 2002). The lower part of the Lower Member of the Quiñoas Formation consists of interbedded

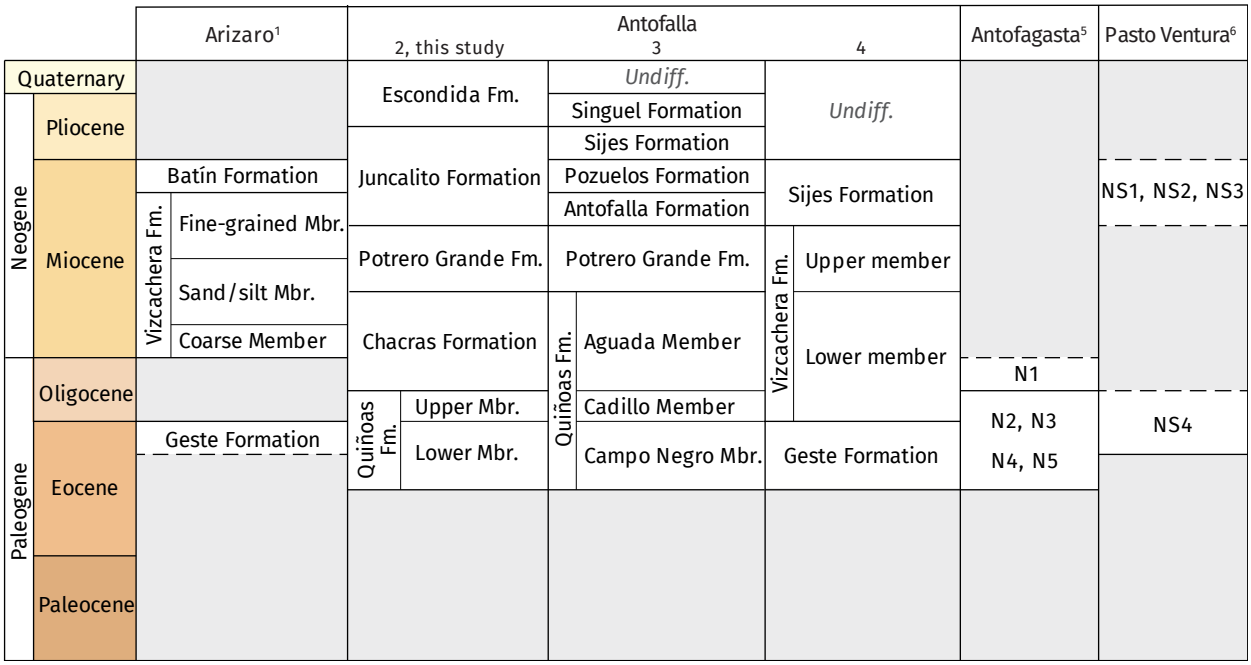

Figure 3.3: Stratigraphic nomenclature for Cenozoic sedimentary strata of the Southern Puna, including the three stratigraphies for the Antofalla region (see Figure 3.1a). 1: DeCelles et al. (2015a) and Schoenbohm and Carrapa (2015). 2: Adelmann (2001) and Kraemer et al. (1999). 3: Voss (2002). 4: Seggiaro et al. (2007). 5: Zhou et al. (2017). 6: Schoenbohm and Carrapa (2015) and Zhou et al. (2016). Dashed lines indicate contacts that are not exposed in a region.

conglomerates and fluvial sandstones indicative of alluvial fan deposition (Adelmann, 2001; Voss, 2002). The thickness and grain size of this unit varies laterally: on the western flank of the Calalaste range, the lowermost Quiñoas reaches a thickness of >500 m and is composed of medium to coarse sandstones interbedded with coarse conglomerate beds indicative of proximal to distal alluvial fan deposition, and paleocurrent indicators suggest transport from a proximal source in the east interpreted as the Proto-Calalaste Range (Adelmann, 2001). At Cerro Campo Negro, the lowermost part of the Quiñoas Formation is 370 m thick and consists of medium to fine sandstones interbedded with meter-scale lenses of pebble conglomerates, indicating distal alluvial fan deposition in braided fluvial channels (Voss, 2002). The top of this unit is capped by a prominent paleosol consisting of greenish-gray and purplish, calcite-cemented conglomerates and sandstones displaying evidence of bioturbation and root traces (Voss, 2002). The Lower Member of the Quiñoas Formation then fines upward into laminated siltstones and mudstones with intercalated evaporites, interpreted as lacustrine, playa, and mudflat environments. This fine-grained unit outcrops throughout the study area and floors the interior of the Salina del Fraile depression (McMillan & Schoenbohm, 2020).

The Upper Member of the Quiñoas Formation coarsens upward from laminated siltstones and mudstones into cross-bedded sandstones, siltstones, and minor conglomeratic layers. On the western flank of the Calalaste, the Upper Member is predominately composed of medium to coarse, cross-bedded sandstones deposited in a fluvial plain (Adelmann, 2001). Further south

along the Calalaste Range, the Lower Member of the Quiñoas Formation is missing, and the Upper Member rests directly on Paleozoic sedimentary strata (Adelmann, 2001). In the Salina del Fraile and Vega Cadillo Grande, the Upper Member of the Quiñoas Formation consists of medium to fine sandstones indicative of fluvial channel and point bar deposits interbedded with minor siltstone and mudstone beds with desiccation cracks and minor gypsum nodules interpreted as playa mudflat deposits (Adelmann, 2001; Voss, 2002). Grain size generally coarsens toward the east in the study area. The uppermost portion of the Upper Member of the Quiñoas Formation consists of interbedded conglomerates and sandstones of distal alluvial fan deposits (Adelmann, 2001; Voss, 2002).

Continental strata of the same Late Eocene–Oligocene age as the Quiñoas Formation outcrop throughout the Southern Puna and have been interpreted as a Paleogene foreland basin system (Carrapa et al., 2005; Kraemer et al., 1999; Zhou et al., 2016; Zhou et al., 2017) ranging from wedge-top deposits in the west (Carrapa & DeCelles, 2008), >3 km thick foredeep deposits east of the Calalaste Range (Zhou et al., 2017), and ~1 km thick forebulge deposits with prevalent paleosols in the SE corner of the plateau (Zhou et al., 2016). However, these deposits also show evidence for deposition in isolated basins, including evaporite-rich lacustrine facies (Canavan et al., 2014; Kraemer et al., 1999; Quade et al., 2015), regional changes in thickness that correlate with inferred paleotopographic highs (Adelmann, 2001), and regionally unique taxa of fossil notoungulates that indicate biogeographic isolation from surrounding basins during the Paleogene (García-López & Babot, 2015). These observations indicate that the Quiñoas Formation may partly result from deposition in isolated basins due to localized tectonic deformation on nearby structures during the Eocene to Oligocene.

The Chacras Formation overlies the Quiñoas Formation and consists of thickly bedded conglomerates and interbedded sandstones locally capped by eolian sandstones (Adelmann, 2001; Kraemer et al., 1999) and has been interpreted as a syn-tectonic alluvial fan and bajada deposit (Adelmann, 2001). The Chacras Formation varies considerably in thickness and grain size, with both increasing near the western margin of the Salar de Antofalla due to the Antofalla High, an inferred Oligocene topographic high now occupied by the Salar de Antofalla (Adelmann, 2001; Voss, 2002). In the Salina del Fraile, at Vega Chacras, alluvial fan conglomerates show fanning dips that have been interpreted as growth strata (Adelmann, 2001; Reijs & McClay, 2003) which overlie the Upper Member of the Quiñoas Formation in angular unconformity (Adelmann, 2001; Kraemer et al., 1999) Further north in the Salina del Fraile, the Chacras Formation pinches beneath a major angular unconformity at the base of the overlying Potrero Grande Formation.

The Miocene Potrero Grande unconformably overlies the Chacras Formation and consists of gray, greenish-gray, tan, and black volcaniclastic sandstones and conglomerates with interbedded ashes dated to ~17 to 19 Ma (Adelmann, 2001; Kraemer et al., 1999; Voss, 2002). Growth strata in the Potrero Grande Formation north of the study area indicate syn-tectonic deposition ~18.5 Ma (Kraemer et al., 1999). Due to its deposition proximal to tectonically active

source regions, the Potrero Grande Formation varies in thickness considerably, from <50 m to >250 m (Kraemer et al., 1999). The Potrero Grande was the final widespread sedimentary unit deposited west of the Salar de Antofalla; Late Miocene to Quaternary units outcrop only on the eastern side of the Salar de Antofalla (on the western flank of the Calalaste Range). The top of the Potrero Grande defines a large, subhorizontal, high-elevation surface between the Salar de Antofalla and the Salina del Fraile. This surface represents a Middle Miocene disconformity and is capped by thin, sporadic Late Miocene to Recent volcanic deposits subjected to intense wind erosion.

After an apparent depositional hiatus between ~16 and 11 Ma, the Late Miocene–Pliocene Juncalito Formation was deposited in a narrow, elongated basin centered on the eastern margin of the Salar de Antofalla (Adelmann, 2001; Kraemer et al., 1999). The lower part of the Juncalito Formation is composed of coarse-grained alluvial fan facies, and the upper part is composed of sandstone, mudstone, and evaporites, including thick layers of halite, indicating a deposition in a restricted basin in an arid environment (Kraemer et al., 1999). Paleocurrent indicators in the conglomeratic unit suggest a proximal source from the east in the Calalaste range (Adelmann, 2001; Kraemer et al., 1999). Deposition of the Juncalito Formation has been used to infer an episode of Late Miocene shortening and uplift of the Calalaste range (Kraemer et al., 1999). Alternatively, its deposition may have been triggered by a transient episode of horizontal extension that reactivated the Antofalla reverse fault system in a normal sense, producing an elongated basin in the hanging wall of a half-graben structure (Tye et al., 2022) and converting the Paleogene Antofalla High into the modern topographic low of the Salar de Antofalla.

The Juncalito Formation is overlain by the Pliocene to Quaternary Escondida Formation, which is confined to the western flank of the Sierra de Calalaste. The Escondida Formation consists of massive, poorly-sorted, coarse conglomerates (Kraemer et al., 1999) and displays evidence of syn-tectonic sedimentation (Adelmann, 2001). The Escondida Formation was previously associated with the onset of horizontal extension in the region (Kraemer et al., 1999), but is alternatively associated with re-establishment of horizontal contraction after an episode of Late Miocene horizontal extension in the Antofalla region (Tye et al., 2022), an idea that we explore below.

3.3 Geologic mapping and U-Pb chronostratigraphy

We completed mapping in the Antofalla region to constrain the deposition and deformation of Cenozoic sedimentary strata, orientations of major structures, and to construct a viable structural cross-section (presented below in Section 3.5). To aid in stratal correlations, we complemented our mapping with U-Pb zircon dating of volcanic and detrital rocks. Figure 3.4 shows a simplified version of the geologic map and cross-section. The full-resolution map and cross-section are available in Figure A.1.

3.3.1 Methods

We measured the orientations of bedding planes, joints, and fault planes using a Brunton Transit and FieldMove application for iPad, with a focus on Late Paleozoic to Cenozoic sedimentary units. Mapping was focused along an approximately 75 km long transect roughly perpendicular to strike, targeting areas with good exposure (Figure 3.4). Despite the low vegetation cover, geologic exposure is commonly poor due to lack of incision on the internally drained plateau and the resulting buildup of volcanic and colluvial cover. Geologic units are well exposed within a few areas of focused erosion, such as canyons, wind-scoured landscapes, and wind gaps. Fault planes are subject to evaporatic soil development and accelerated weathering, and they tend to be poorly exposed. Structural measurements are available in Table A.2.

We supplemented our field mapping with aerial and satellite imagery provided by Maxar (through Bing Maps), and Google to correlate major contacts throughout the study area. The following existing maps and structural data from previous studies also informed our interpretations. Large-scale regional mapping is provided by Schnurr et al. (2006) and Seggiaro et al. (2007). We used the digital geologic map provided by Schnurr et al. (2006) as the starting point for our map. Detailed stratigraphic, geochronologic, and sedimentological data are provided by Adelmann (2001), Canavan et al. (2014), Kraemer et al. (1999), and Voss (2002). Palma et al. (1990) provide detailed lithologic mapping of the Quebrada Honda Range, which still forms the basis of most later mapping (Schnurr et al., 2006; Seggiaro et al., 2007), including ours. We also incorporated into our map portions of the detailed mapping of the Antofalla Volcanic Complex provided by Richards et al. (2006).

To confirm stratigraphic interpretations and constrain the age of syntectonic sedimentation, we collected detrital sandstone and volcanic ash samples (n = 13) for U-Pb zircon dating (Table A.1). Zircon separation and manual picking was performed at the University of Toronto using standard techniques. Approximately 100–150 grains were picked from detrital and volcaniclastic samples and approximately 30 zircon grains from volcanic ash samples. Zircon U-Pb dating was accomplished by laser ablation inductively coupled mass spectrometry (LA-ICPMS) at the University of Brisbane, Queensland, Australia, using the methods described in Zhou et al. (2020). In total, we report the U-Pb ages of 1,463 individual grains. The ^{206}Pb/^{238}U age is more precise for Neoproterozoic and younger zircons, and the ^{206}Pb/^{207}Pb age is more precise for Paleoproterozoic and older zircons, but both systems yield meaningful age information (Vermeesch, 2021). We therefore calculate a hybrid concordia age using methods described by Vermeesch (2021). This concordia age approaches the ^{206}Pb/^{238}U age and ^{206}Pb/^{207}Pb age for very young and very old zircons, respectively, while offering higher precision than either age; it also avoids the need for assuming an arbitrary age cutoff between the two systems.

We primarily use zircons to constrain depositional age. For volcanic ashes, depositional age was estimated as the age of the ash, calculated using the TuffZirc algorithm in the Isoplot spreadsheet (Ludwig, 2003; Ludwig & Mundil, 2002). For detrital samples, a maximum depositional age was estimated using the following algorithms implemented in the “detritalPy”

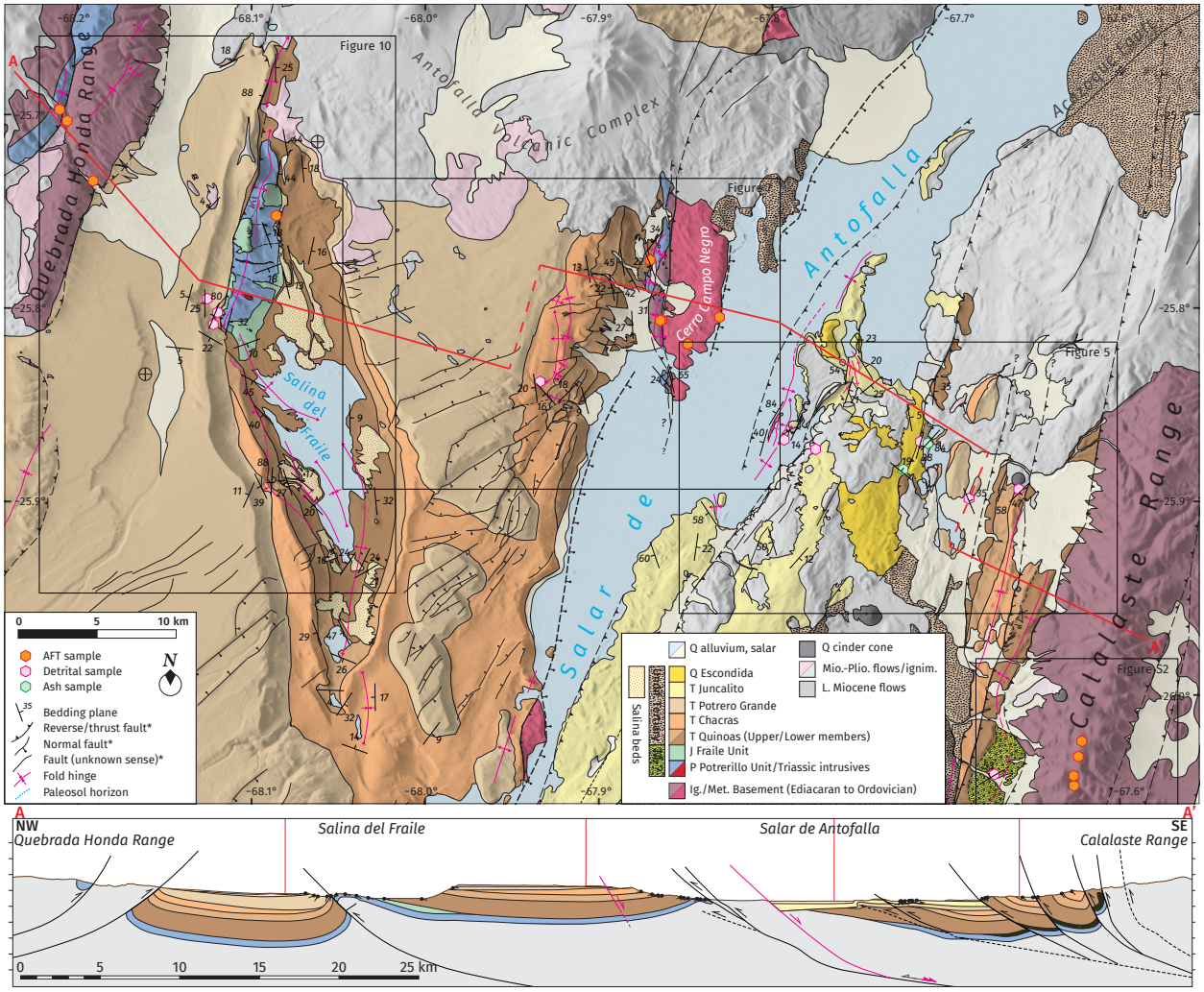

Figure 3.4: Geologic map and cross-section of the Antofalla basin. Boxes give location of small-scale maps discussed in the text (Figures 3.5, 3.7 and 3.10). Refer to Figure 3.3 for ages of Cenozoic strata. The full resolution map is provided by Figure A.1.

software package (Sharman et al., 2018): the youngest single grain age (YSG), the youngest cluster of 2 or more grains whose ages overlap at (YC1σ[2+]), and the youngest cluster of 3 or more grains whose ages overlap at (YC2σ[3+]). When possible, we prefer multiple-grain estimates of maximum depositional age over the YSG age. We applied a discordance filter based on the log ratio distance from the concordia composition ("concordia distance"; Vermeesch, 2021) and excluded discordant analyses before analyzing zircon ages. So as not to exclude too many young zircons, we used a relatively liberal cutoff of -5 to 15 for the concordia distance, which excluded 193 of the 1465 analyzed grains (13.2%). Depositional age determination results are summarized in Table 3.1.

We focus our presentation of geologic data around three key regions as follows, from east to west: the western slope of the Calalaste Range and eastern margin of the Salar de Antofalla (Section 3.3.2); the western margin of the Salar de Antofalla (Section 3.3.3); and the region

Table 3.1: Summary of U-Pb zircon depositional age determination. The first section gives maximum depositional ages of detrital samples. The second section gives ages of interbedded ashes or volcaniclastic strata.

Sample	Lithology	N_c/N_t	Age (Ma)	Uncertainty (Ma)	Metric
AF20T02	sandstone	135/145	34.80	0.40	YC2σ[3+]
AF20T03*	sandstone	—	5.55	0.06	—
AF20T04	sandstone	120/138	12.12	0.17	YC2σ[3+]
AF20T05	sandstone	102/115	16.97	0.18	YC2σ[3+]
AF20T06	sandstone	138/147	21.15	0.50	YSG
AF20T07	sandstone	123/131	250.92	1.25	YC2σ[3+]
AF20T01	sandstone	127/153	15.56	0.19	YC2σ[3+]
AF20T03	pebbly sandstone	165/180	29.66	0.19	YC2σ[3+]
AF20T02*	ash-rich mudstone	—	1.47	0.04	—
AF20T01	volcaniclastic	114/127	35	(+0.2, 0.02)	TuffZirc
AF20T01	volcanic ash	14/49	1.26	(+0.05, -0.04)	TuffZirc
AF20T02	volcanic ash/ignimbrite	37/43	17.54	(+0.34, -0.40)	TuffZirc

N_c/N_t = number of concordant/total grains
YSG = youngest single grain age
YC2σ[3+] = Youngest overlapping age cluster of 3 or more grains (2σ).
*Age reported by Tye et al. (2022).

around the Salina del Fraile depression (Section 3.3.4), which is bounded on the west by the Quebrada Honda Range (Section 3.3.5). These three regions correspond to the three large boxes in Figure 3.4.

3.3.2 Calalaste Range

The core of the Calalaste range along our transect is composed of metamorphosed strata with highly variable lithologies, including fine to coarse quartzite, phyllite, greywackes, and volcanic rocks. While we group these Ordovician rocks under the Cortaderas Chicas Volcano-Sedimentary Complex (CCVSC; Seggiaro et al., 2007), this unit corresponds to the Diablo Formation described by Zimmermann and Bahlburg (2003) in the Quebrada del Diablo (SE corner of Figures 3.4 and A.2). Throughout the Calalaste Range, the CCVSC is highly deformed by upright, nearly isoclinal folds with wavelengths of ~200 to 400 m. We observed poorly outcropping planar surfaces coated with slickenfibres within the CCVSC (Figure A.2). These may represent flexural slip planes and/or cleavage planes formed by pressure dissolution during a pre-Cenozoic episode of shortening, as reported for equivalent rocks in the Northern Puna (Henriquez et al., 2020).

Calalaste Fault. On the western flank of the Calalaste Range, the west-vergent Calalaste Fault carries CCVSC metamorphic rocks in the hanging wall over unmetamorphosed sedimentary strata in the footwall (Figure 3.5). Footwall rocks are folded and cut by two smaller thrust faults (labelled A and B in Figure 3.5), composing two thrust sheets. Although these fault planes are

not exposed, we map them based on the truncation of bedding planes and the prevalence of smaller faults and fractures in hanging wall strata. The structurally lower thrust sheet bounded on the west by Fault B (Figure 3.5) consists of a 300 m thick section of interbedded sandstones and conglomerates overlain by 500 m of mainly medium to coarse sandstones and 300 m of interbedded sandstones and conglomerates (Profile G, Adelmann, 2001). This exposure has been mapped as either proximal facies of the Paleogene Quiñoas and Chacras Formations (Adelmann, 2001; Kraemer et al., 1999; Schnurr et al., 2006) or as Lower Permian (~278–264 Ma) continental clastic strata of the Patquía-de La Cuesta Formation (Seggiaro et al., 2007). Our mapping and detrital zircon ages argue against a Lower Permian age for this unit. The ~1 km thickness of the mapped unit is much greater than that of Permian strata observed in the Potrerillos Anticline or at Cerro Campo Negro (250–300 m), though the base of the Permian unit is not exposed in either location. Zircons from a sandstone bed near the top of the exposure (AF20T06; Figure 3.5 and Table 3.1) include six grains younger than 250 Ma (i.e., Triassic or younger), and four of these have Cretaceous or Cenozoic ages, ruling out deposition during the Permian. Furthermore, the youngest single grain from this sample (21.2 ± 0.50 Ma) is the same age as an interbedded volcanic ash ~8 km to the south along strike, 21.6 ± 2.6 Ma (Ar-Ar on K-feldspar; Adelmann, 2001), supporting our interpretation of these strata as the Quiñoas and Chacras Formations.

The structurally higher thrust sheet bounded on the west by Fault A (Figure 3.5) is composed of 300 m of interbedded coarse conglomerates and coarse sandstones overlain by 800 m of sandstones, shales, mudstones, and rare conglomerate beds (Adelmann, 2001). The basal coarse-grained deposits have been mapped as a proximal facies of the Lower Member of the Quiñoas Formation (or its equivalent), while the finer-grained deposits have been mapped as equivalent to the Upper Member of the Quiñoas Formation (Adelmann, 2001; Kraemer et al., 1999; Schnurr et al., 2006; Seggiaro et al., 2007). However, the outcrop color, topographic relief patterns, and sedimentary facies appear notably different from the Quiñoas Formation in the structurally lower thrust sheet in the footwall of Fault A. To constrain the depositional age of these strata, we collected sample AF20T07 from a coarse sandstone bed within a conglomeratic section (the sample is located approximately 10 km south of the detailed area shown in Figure 3.5, but is visible in the SE corner of Figure 3.4). The sample yielded a young population of Early Triassic zircons indicating a maximum depositional age of ~250 Ma (Table 3.1). Adelmann (2001) reported a K-Ar age of 208 ± 5 Ma (Late Triassic) from a volcanic pebble in the lower part of the section. These data, which only constrain the maximum depositional age, do not rule out the possibility of this entire package of strata belonging to the Paleogene Quiñoas Formation, but they also suggest that an older unit may be exposed at this location. We therefore map the lower part of the section as undifferentiated Mesozoic to Early Tertiary deposits (Figure 3.4), recognizing that more work needs to be done to constrain the depositional age of these strata.

Strata outcropping in a series of hills <1 km to the west of Fault B (Location C in Figure 3.5) help constrain the location and timing of Fault B. The hill-forming strata are composed of

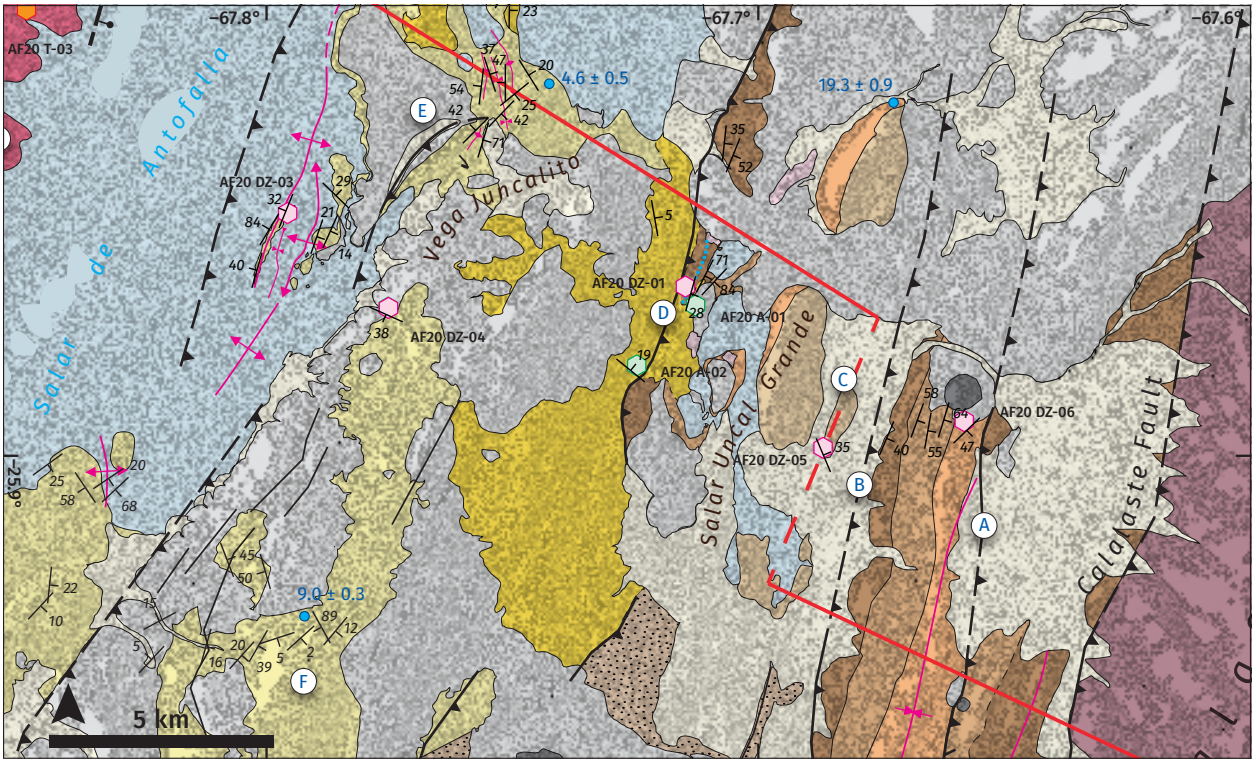

Figure 3.5: Geologic map of the western flank of the Calalaste range and eastern margin of the Salar de Antofalla. See Figure 3.4 or Figure A.1 for legend. Blue circles labelled with blue text give depositional ages (Ma) from Adelmann (2001). Lettered circles denote locations discussed in the text.

a yellowish-tan, cross-bedded, medium sandstone. Estimates of maximum depositional age based on detrital zircons range from 16.6 to 17 Ma (AF20T05; Table 3.1), indicating a late Early Miocene maximum depositional age. This inferred age is ~2.5 Ma younger than a pumice fragment dated to 19.3 ± 0.9 Ma approximately 7 km to the north from a stratigraphically lower exposure that corresponds to the Potrero Grande Formation (Figure 3.5; Adelmann, 2001). Seggiaro et al. (2007) also mapped this outcrop as equivalent to the Potrero Grande Formation (Upper Member of the Vizcachera Formation; Figure 3.3). Because the outcrop is definitively younger than the Paleogene strata in the hanging wall of Fault B, without evidence of significant folding between the two locations, we infer the location of an unexposed reverse or thrust fault (Fault B) that places the Quiñoas Formation on top of the Potrero Grande Formation and is covered by alluvium. The ~17 Ma maximum depositional age of footwall strata implies that Fault B was active after 17 Ma.

Salar Uncal Grande. The lower slopes of the Calalaste Range west of Fault B consist of Paleogene to Quaternary strata, Late Miocene to Pliocene volcanics, and recent evaporite deposits near Salar Uncal Grande (Figure 3.5). At Fault D, strata equivalent to the Quiñoas Formation are thrust over Late Miocene to Pliocene sedimentary strata (Adelmann, 2001; Kraemer et al., 1999; Seggiaro et al., 2007; Voss, 2002) by a west-vergent reverse or thrust fault (Figure 3.5). We

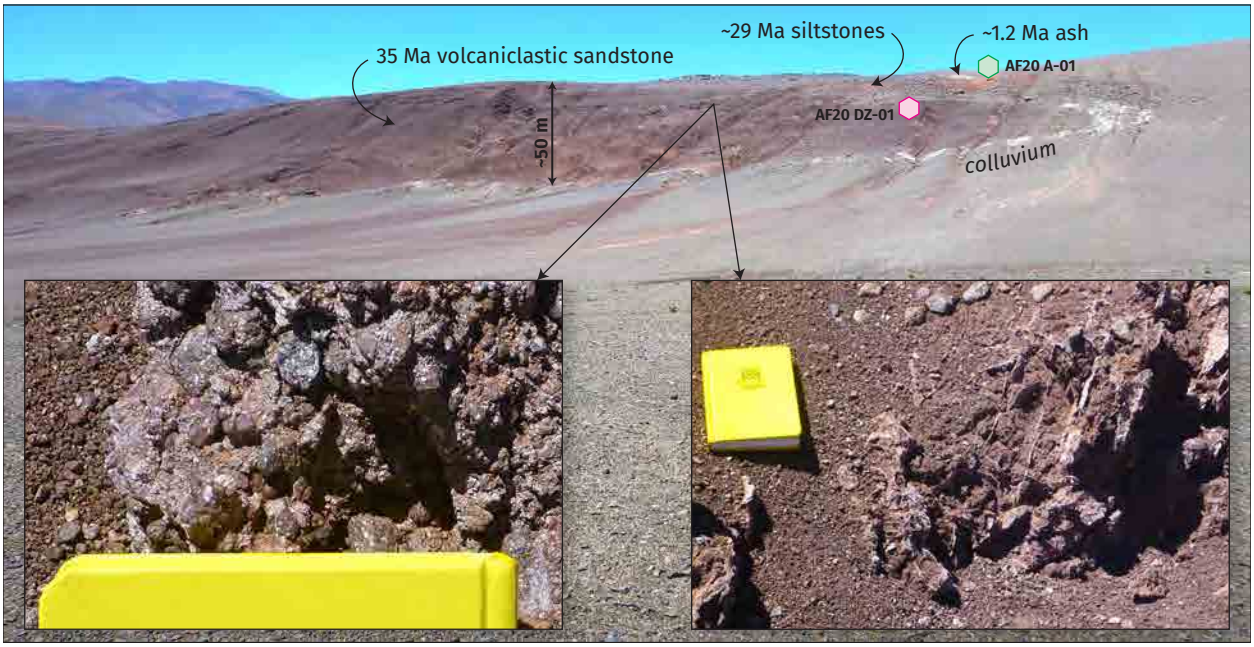

Figure 3.6: Outcrop photographs of the Lower Member of the Quiñoas Formation in the hanging wall of Fault D (Figure 3.5). Inset photos show the portions of a paleosol showing boxwork veins (right) and conglomeratic lag with calcareous nodules (left). The paleosol caps a ~35 Ma volcaniclastic sandstone unit, separating it from overlying ~29 Ma siltstones and Quaternary ash deposits.

correlate this fault to a thrust fault previously observed by Adelmann (2001) 8 km to the north placing Quiñoas Formation on top of volcaniclastic deposits dated to 11.2 ± 0.3 Ma (Ar-Ar on feldspar; Adelmann, 2001). We further constrain the location and timing of Fault D based on our sample of hanging wall strata, AF20T01, and two samples of a younger ash-rich deposit that unconformably overlies both hanging wall and footwall rocks and locally seals the fault, AF20T01 and AF20T02 (Figure 3.5 and Table 3.1). Sample AF20T01 was collected from a purplish-red volcaniclastic unit in the hanging wall of Fault D that consists of siltstones, pebbly sandstones, and pebble conglomerate. The pebbles have clasts ~0.5 to 2 cm in diameter primarily composed of white pumice, with clasts of metamorphic rocks and whitish-tan sandstone also common. The pumice clasts are angular, indicating deposition proximal to a volcanic source. Zircons from AF20T01 are overwhelmingly Late Eocene in age. Due to the prevalence of volcanic clasts and the prominence of young grains in this volcaniclastic unit, we treat the sample as a volcanic ash for the purposes of depositional age determination. The sample yields a TuffZirc age of 35.0 (+0.2, -0.02) Ma (Table 3.1), similar to the sample's youngest single grain (34.1 ± 0.34 Ma) and correlative to the Lower Member of the Quiñoas Formation. We therefore infer that a reverse or thrust fault (Fault D) carries the Lower Quiñoas Formation over folded Late Miocene and Pliocene strata in the footwall.

The volcaniclastic strata of the Quiñoas Formation in the hanging wall of Fault D dip approximately 30 degrees to the east. The 35 Ma volcaniclastic unit is capped by a clast-supported conglomerate. The conglomerate consists of rounded, pebble- to gravel-sized clasts that are

composed of volcaniclastic pebbly sandstone, seemingly derived from underlying beds. The conglomerate layer displays grayish-purple colors, evaporite veins in a boxwork fabric, and nodules of caliche or gypsum (Figure 3.6). We interpret this layer as a conglomeratic lag deposit and paleosol that developed in arid to semiarid environments, representing a subaerial unconformity.

To estimate the time span represented by the subaerial unconformity, we first note that it must be younger than ~35 Ma, the age of the underlying volcaniclastic unit. The unconformity is overlain by reddish-orange to tan, thinly bedded laminated siltstones and medium-bedded medium sandstones with ripple marks and intercalated evaporites, consistent with the fluvial-lacustrine facies of the Lower Member of the Quiñoas Formation (Kraemer et al., 1999). A paleosol separating the same lithologic units is well exposed at Cerro Campo Negro on the western side of the Salar de Antofalla (described below in Section 3.3.3). Voss (2002) reported an age of 28.2 ± 2.4 Ma for an interbedded ash approximately 200 m above the paleosol horizon at Vega Cadillo Grande (Figure 3.7), and Adelmann (2001) obtained an age of 28.9 ± 0.8 from an interbedded ash at Vega Chacras (see Section 3.3.4, below). Both ages correlate to the Upper Member of the Quiñoas Formation and are likely younger than the deposits of the Lower Member of the Quiñoas Formation that directly overlie the subaerial unconformity. We therefore bracket the unconformity to ~35–29 Ma. We cannot rule out that the paleosol and unconformity may be diachronous between Vega Cadillo Grande and Salar Uncal Grande.

East of Fault D, exposure is poor, but mapped outcrops and existing geochronology suggest that the overlying Chacras and Potrero Grande Formations dip eastward approximately 35 degrees and compose an intact thrust sheet bound on the west by Fault D.

A layer of volcanic ash that unconformably overlies hanging wall strata of Fault D yields a depositional age of ~1.2 Ma (AF20T01; Table 3.1) and is tilted eastward. Zircon dating of Quaternary strata in the footwall was reported by Tye et al. (2022) and are summarized as follows in the context of Fault D: a reworked volcanic ash deposit yields 14 zircons younger than 9 Ma, and after applying a nominal common Pb correction yields a maximum depositional age of 1.47 ± 0.04 Ma (AF20T02; Tye et al., 2022, Table 3.1)). Unlike the volcanic ash in the hanging wall of Fault D, the reworked ash in the footwall was subject to intense folding (Tye et al., 2022). The Quaternary volcanic ash-rich unit overlies the Paleogene units in angular unconformity and locally seals Fault D. These relationships indicate that Quaternary strata were deposited after one or more episodes of deformation on Fault D, but before a later episode of deformation that occurred after ~1.2 Ma and resulted in tilting (in the hanging wall of Fault D) and compressional folding (in the footwall of the Fault D) of Quaternary deposits.

Vega Juncalito. On the border between the Salar de Antofalla and the Calalaste Range at Vega Juncalito (Figure 3.5), an en-echelon train of tight, nearly upright folds deforms a sequence of Pliocene limestones, sandstones, and evaporites of the Juncalito Formation. An interbedded ash in this section was previously dated to 4.6 Ma (whole rock K-Ar; Adelmann, 2001, Figure 3.5).

We interpret these as detachment folds that likely detached above a halite or other evaporite layer, which are common in the Juncalito Formation (Adelmann, 2001; Kraemer et al., 1999). The 4.6 Ma depositional age indicates that folding occurred during the Pliocene–Quaternary.

On the western margin of Vega Juncalito, the surface of a Pliocene or Quaternary volcanic flow (undated, but overlying the 4.6 Ma Juncalito Formation) is topographically offset by approximately 80 m over a distance of only 320 m (Location E, Figure 3.5). Brittle faulting is the most likely source of such dramatic deformation of an initially subhorizontal surface. The observed topographic offset is consistent with a west-dipping normal fault or an east-dipping thrust fault. Given the compressional folds just described in the underlying Juncalito Formation strata and the convex-westward geometry of the inferred fault trace (suggesting west-vergence), we favor the simpler interpretation of the fault at Location E as an east-dipping thrust fault associated compressional folding of the Juncalito Formation after 4.6 Ma.

Within the eastern margin of Salar de Antofalla. West of Vega Juncalito within the eastern margin of the Salar de Antofalla, a west-vergent anticline deforms a sequence of halite and interbedded sandstones (Figure 3.5). The sandstones are orange, medium to coarse grained, and occur in tabular beds one to a few decimeters thick interbedded within thicker evaporite bed sets. This sedimentary facies assemblage is typical of the evaporite playa facies of the Juncalito Formation (Adelmann, 2001; Kraemer et al., 1999). Detrital zircon dating of a sandstone bed yielded a maximum depositional age of ~5.5 Ma, consistent with the Juncalito Formation or a younger unit (AF20T03; Table 3.1). Bedding plane measurements collected from this location define a large, asymmetric doubly-plunging anticline with a narrow, subvertical forelimb and a broad, gently dipping backlimb indicative of a fault propagation fold due to a blind west-vergent thrust fault (Figure 3.5). On aerial imagery, such folded sandstone beds can be traced along a distance of at least 14 km along the eastern margin of the salar (Figure A.3), implying the existence of a significant blind thrust fault beneath the eastern margin of the Salar de Antofalla (Figure 3.4).

Folding of Quaternary deposits near Fault D, Juncalito Formation strata at Vega Juncalito, and Juncalito Formation sandstones at Uncal Grande indicate that an episode of horizontal, roughly E–W shortening began to affect the eastern margin of the Salar de Antofalla after ~5.5 Ma and as late as the Quaternary (Tye et al., 2022). In addition, Voss (2002) reported 100 m-scale folds similar to the ones we mapped at Vega Juncalito approximately 10 km SE of our transect (Figure 3.5, Location F), indicating that a similar style of Quaternary compression affected nearly the entire western slope of the Calalaste Range.

3.3.3 Cerro Campo Negro and Antofalla Fault

In contrast to the Calalaste Range on the eastern border of the Salar de Antofalla, the western border of the salar is cut by two east-dipping reverse faults near its base (Figure 3.7), and is dominated by a topographic escarpment ~1 km high that exposes Eocene to Miocene sedimen-

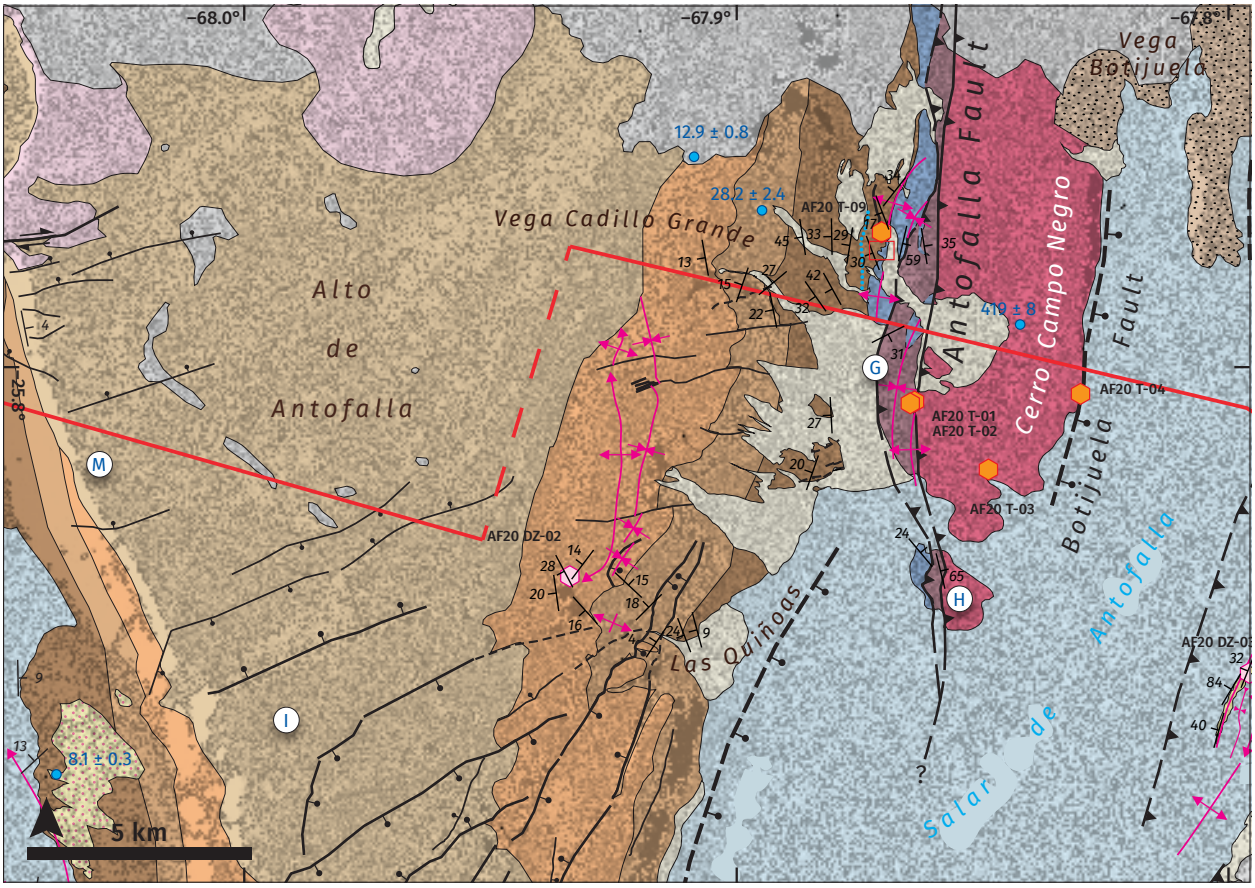

Figure 3.7: Geologic map of Cerro Campo Negro and the Antofalla Fault System, Vega Cadillo Grande, and Vega Quiñoas. The high-elevation, low-relief surface in the center-left portion of the map is a Middle Miocene disconformity discussed in the text. Small red box near sample AF20T09 gives location of Figure 3.8. See Figure 3.4 or Figure A.1 for legend.

tary units (Figure 3.8). The top of this escarpment defines a high-elevation, low-relief surface (Alto de Antofalla, Figure 3.7) that consists of the top of the Miocene Potrero Grande Formation and a thin, sporadic cover of volcanic flows and ignimbrites (Figure 3.7). The escarpment may have formed in the footwall of a major normal fault, here referred as the Botijuela Fault (named after the nearby Vega Botijuela hot springs, Figure 3.7), which we describe last. We first describe Cerro Campo Negro, a low-elevation basement block situated on the western margin of the salar at the base of the topographic escarpment.

Cerro Campo Negro. Cerro Campo Negro consists of a large exposure of igneous and high-grade metamorphic basement rocks mapped as Cerro Negro Granite (Figure 3.7). At the western margin of Cerro Campo Negro, we map two east-dipping reverse faults, the Antofalla Fault and Fault G (Figure 3.7). The Antofalla Fault carries Cerro Negro Granite in the hanging wall over Ordovician metamorphic rocks mapped as the Cortaderas Chicas Volcano-Sedimentary Complex (CCVSC) in the footwall. Although the fault plane is covered by alluvium, we observed that CCVSC rocks in the footwall are increasingly damaged with proximity to the basement

contact (Location H), and the mapped geometry of the contact suggests that the fault dips to the east, implying an east-dipping reverse fault. Geologic exposure of the footwall rocks is poor, but measurements of bedding indicate at least one pair of tight, upright folds in Ordovician metasedimentary rocks, similar to those observed in the Calalaste Range (Section 3.3.2). CCVSC rocks are in turn carried westward over folded Permian and Cenozoic strata by Fault G. Whether the basement was thrust over the CCVSC during the Cenozoic or during a previous tectonic event is not clear from field observations, but as we show below, our AFT data require that significant Cenozoic shortening was accommodated by this structure (samples AF20T01 through 04, Figure 3.7). AFT ages also directly support our interpretation of west-vergent reverse faults at this location and indicate that the Antofalla Fault is a major fault that exhumed rocks from below the apatite partial annealing zone (~120 °C or ~4 km depth), whereas Fault G did not accommodate enough shortening to exhume rocks from such depths (Section 3.4.3). We therefore map Fault G as a splay of the Antofalla Fault (Figure 3.4).

Vega Cadillo Grande and Las Quiñoas. The base of the section exposed west of the Antofalla Fault is composed of the Permian Potrerillo Unit, which here consists of medium to coarse grained, yellowish-tan to white sandstones (Seggiaro et al., 2007). It is overlain in angular unconformity by the Quiñoas Formation, which dips approximately 30 to 40 degrees to the west (Figure 3.7). The base of the Quiñoas consists of medium to coarse sandstones with pebbly conglomeratic lenses, interpreted as distal alluvial fan and fluvial channel deposits (Voss, 2002). These alluvial fan strata correlate with coarse alluvial fan conglomerates in the base of the Quiñoas Formation on the western flank of the Calalaste range ~30 km to the east (Adelmann, 2001). The conglomeratic beds host a set of joints with 15–25 cm spacing clearly exposed throughout an area of about 400×200 m near the contact with the Permian Potrerillo Unit. Measurements taken throughout this area (n = 13) indicate that the joints on average strike 243° and dip vertically; their strikes may rotate to more E–W orientations toward the north (Figure 3.9). We did not observe signs of shear offset across any of these joints, and their vertical orientations are consistent with tension joints. The presence of vertical joints indicates that the region experienced roughly NW-SE tension during the Cenozoic, possibly as a result of Late Miocene extensional tectonics (discussed below in Section 3.6).

A paleosol horizon caps the alluvial fan facies within the Quiñoas Formation (Voss, 2002), outcropping as a ~5 m tall cliff that can be traced over 2 kilometers along strike (Figure 3.8). Voss (2002) dated an ash interbedded within the Quiñoas Formation approximately 200 m above the paleosol horizon to 28.2 ± 2.4 Ma, which correlates to the Upper Member of the Quiñoas Formation. The paleosol is therefore older than ~28 Ma, and if it correlates with the paleosol observed near Salar Uncal Grande, can be bracketed to between 35 and 29 Ma (Section 3.3.2).

Above the paleosol horizon, the Quiñoas Formation consists of thinly bedded mudstones, siltstones, and evaporite layers. This fine-grained sandstone unit is also well-exposed along the western border of the Salar de Antofalla and in the interior of the Salina del Fraile. Along

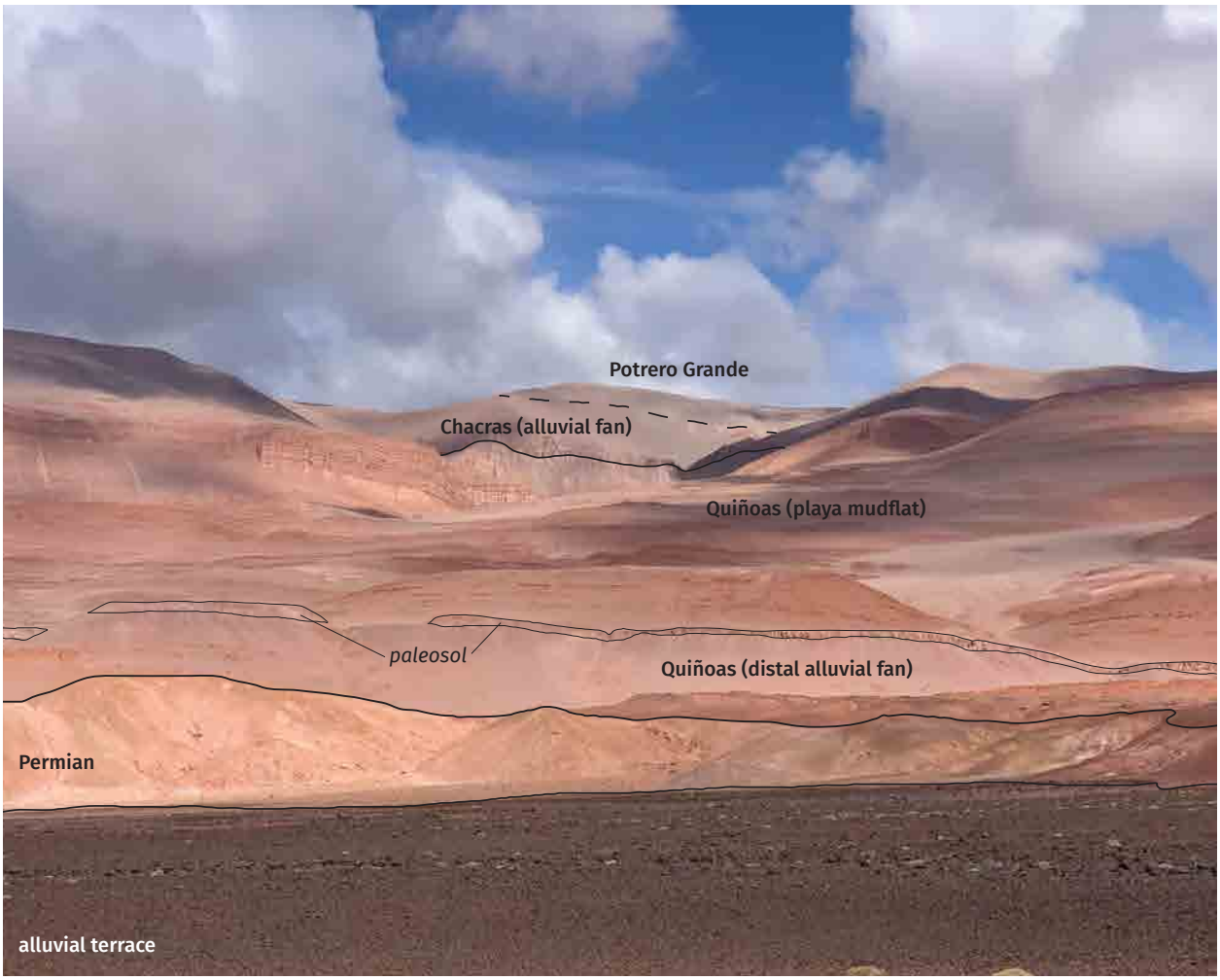

Figure 3.8: Photograph looking west from the surface trace of the Antofalla Fault (not visible in the photograph) at Cerro Campo Negro, showing Permian and Cenozoic sedimentary strata in the footwall. The prominent cliff-forming paleosol horizon within the Lower Member of the Quiñoas Formation is clearly visible.

the western margin of the salar between Vega Quiñoas and Cerro Campo Negro, minor faults are apparent in the Lower Member of the Quiñoas Formation that strike approximately 254° and dip 70° to 80° to the NW or SE, consistent with small strike-slip or oblique faults. Because the faults have small offsets, the lithology does not differ across fault planes, and it is difficult to infer their sense of displacement (Figure A.4). Larger faults with similar orientations are visible on aerial imagery between Vega Quiñoas and Vega Cadillo Grande and display apparent left-lateral displacement of bedding contacts (Figure 3.7). Bedding planes are tilted to the west in this region, so left-lateral offset on NW-striking planes is consistent with either strike-slip or down-to-the-south normal faulting.

Above the fine-grained unit, at Vega Cadillo Grande and Vega Quiñoas, the Quiñoas Formation consists of tabular beds of sandstone interbedded with mudstone and siltstone. The Upper

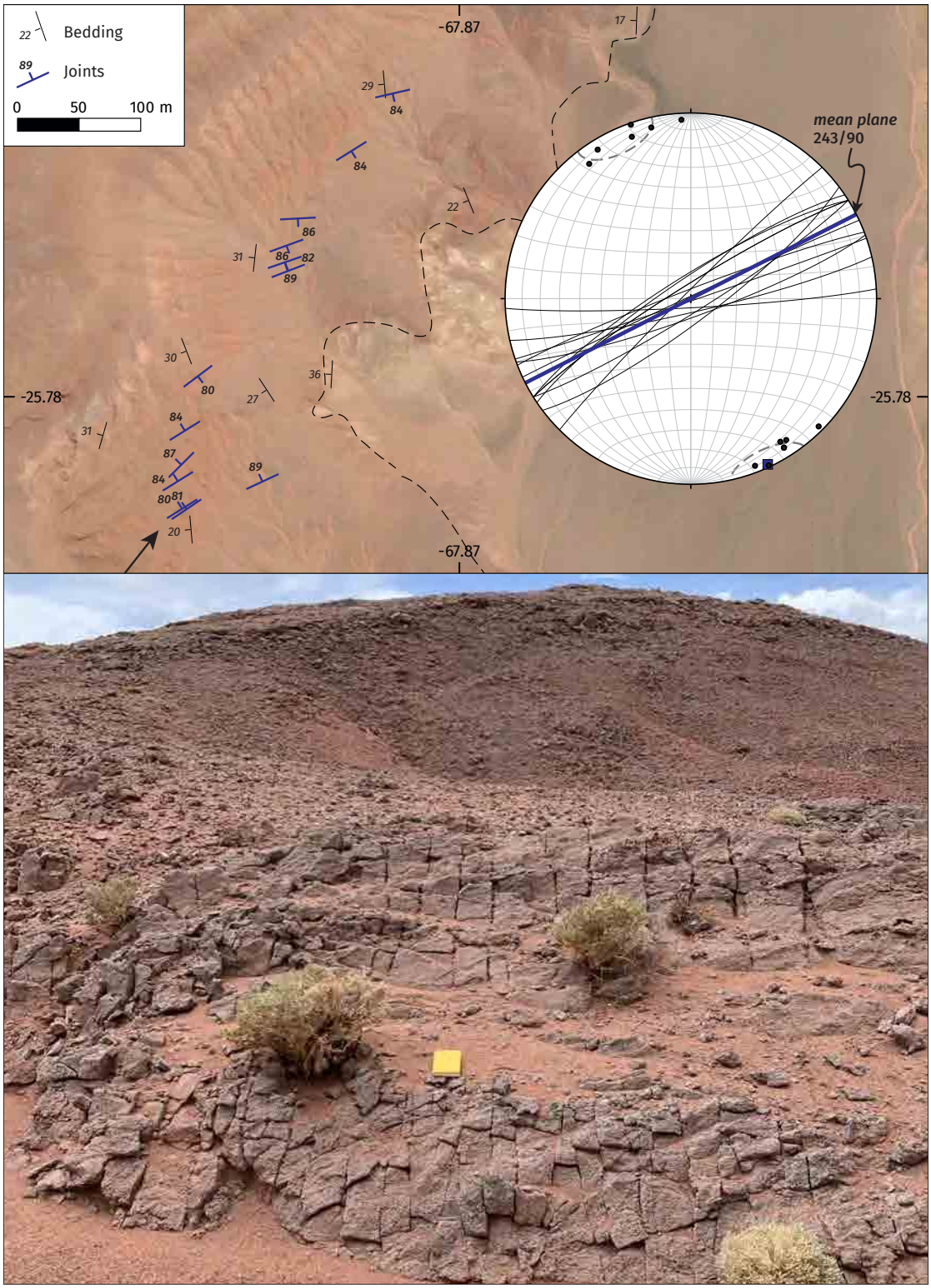

Figure 3.9: Measurements of joints in conglomeratic beds of the Quiñoas Formation, Cerro Campo Negro. Top panel shows an aerial image (provided by Bing) of the area of exposed joints and plots their average orientation (Cardozo & Allmendinger, 2013). The bottom panel shows a photograph of one such conglomeratic bed (field notebook for scale).

Member of the Quiñoas Formation dips 20° to 30° to the west and is unconformably overlain by alluvial fan conglomerates of the Chacras Formation.

At Vega Cadillo Grande, the base of the Chacras Formation consists mainly of sandstones with conglomeratic lenses dipping ~13° WSW. It overlies the Quiñoas Formation in a subtle angular unconformity, where underlying strata dip >15° to the WNW. At Las Quiñoas, the Chacras Formation consists mainly of thickly bedded conglomerates with interbedded sandstones. Conglomeratic Chacras strata have been interpreted as syn-tectonic alluvial fan and bajada deposits that were deposited proximal to an uplifting source region (Adelmann, 2001; Kraemer et al., 1999). Conglomerate clasts are composed of granitic and metamorphic basement rocks and sandstones, and their imbrication suggests that the source region was located to the east (Adelmann, 2001; Kraemer et al., 1999), indicating that uplift on the Antofalla Fault produced a source region for these strata located near the modern Salar de Antofalla ("Antofalla High"; Adelmann, 2001; Voss, 2002). Interbedded volcanic ashes in syn-tectonic alluvial fan deposits of the Chacras Formation have been previously dated to ~24 to 22 Ma (Adelmann, 2001; Canavan, 2012). We collected sample AF20T02 from a sandstone in the Chacras Formation at Vega Quiñoas to constrain its depositional age. The sample contained only 18 Cenozoic zircons and yielded a maximum depositional age of ~34.7 Ma (Table 3.1), which is consistent with Late Oligocene to Early Miocene Chacras Formation but does not tightly constrain its depositional age. Because this sample was collected from well above the contact with the Quiñoas Formation, the maximum depositional age of ~35 Ma, which would correlate to the Lower Member of the Quiñoas Formation, can be ruled out as an estimate of depositional age. Few contemporaneous volcanic zircons were incorporated into the sampled sandstone bed, which may have been deposited during a ~25–20 Ma lull in volcanic activity (Voss, 2002).

Although exposure is poor at Las Quiñoas, we map small folds within the Chacras Formation based on field measurements and satellite imagery (Figure 3.7). The folds consist of an anticline and syncline separated by ~1 km that trend roughly N-S over a distance of ~7 km before they are truncated by the unconformity at the base of the Potrero Grande Formation. This truncation indicates that folding occurred before deposition of the Potrero Grande Formation ~20–18 Ma. The fold axes are offset by small normal or oblique normal faults that formed after deposition of the Potrero Grande Formation. Although we lack direct measurements of the folded strata, the folds appear to be asymmetric with steeper western forelimbs based on aerial imagery. West-vergent folds with similar length, wavelength, and tightness are better exposed in the Salina del Fraile, where they represent west-vergent fault propagation folds, described below (Section 3.3.4).

The Chacras Formation is unconformably overlain by subhorizontal volcaniclastic strata of the Potrero Grande Formation, which is <100 m thick at Vega Cadillo Grande and Las Quiñoas (Figure 3.7). Although the Potrero Grande Formation was deposited syn-tectonically with shortening on the Antofalla Fault ~18.5 Ma approximately 20 km to the north (Adelmann, 2001), in our transect deformation stepped westward into the Salina del Fraile, resulting in syn-tectonic

deposition of the Potrero Grande Formation there. The area between the Salina del Fraile and Cerro Campo Negro accommodated little sedimentation during the late Early Miocene to Middle Miocene, reflected by thinning of the Potrero Grande Formation on the western margin of the modern salar.

The top of the Potrero Grande Formation at this location forms a high-elevation, low-relief topographic surface capped by a thin veneer of volcanic deposits (Alto de Antofalla, Figure 3.7). Chronostratigraphic ages from the Potrero Grande Formation (Adelmann, 2001; Kraemer et al., 1999) and overlying volcanic deposits (Kay et al., 2008; Richards et al., 2006; Risse et al., 2008) indicate that this surface represents a disconformity that began when depositional filling of the Antofalla Basin ceased during the early Middle Miocene. The southern portion of the disconformity surface (Location I, Figure 3.7) is cut by a prominent series of linear escarpments displaying horst-and-graben topography. Escarpments range from 5 to 10 km in length and 20 to 120 m in height. The largest escarpments are associated with normal-sense displacement in bedding contacts, visible in the Salina del Fraile (Tye et al., 2022). We therefore map the horst-and-graben structures as normal faults (Figures 3.4 and 3.7), though it is possible that some or all the faults accommodated a significant component of strike slip. These faults display two distinct trends. In the area east of the Salina del Fraile, they strike ~064° and dip to NW or SE. Moving southward, the orientation of the normal faults rotates counter-clockwise and they strike ~030° near the SE corner of the Salina del Fraile (Figure 3.4) and ~014° further south along the western margin of the Salar de Antofalla.

Botijuela Fault. We map a major normal fault along the western margin of the Salar de Antofalla (Botijuela Fault, Figure 3.7). As described by Tye et al. (2022), the Botijuela Fault was likely formed by extensional reactivation of the Antofalla Fault at depth. The inferred trace of the Botijuela fault implies that extensional deformation to step eastward from the trace of the Antofalla Fault. Tye et al. (2022) reported fault breccia on the eastern margin of Cerro Campo Negro on what appear to be remnant triangular facets, implying that the Botijuela Fault strikes approximately 019° and dips 30–40° to the SE.

3.3.4 Salina del Fraile

The Salina del Fraile is an erosional depression formed by Miocene to Recent wind erosion (McMillan & Schoenbohm, 2020) that exposes Permian strata, Triassic intrusive volcanics, Jurassic strata, and Cenozoic strata (Adelmann, 2001; Voss, 2002).

Potrerillos Anticline and Potrerillos Fault. In the northern part of the Salina del Fraile, the Potrerillos Anticline exhumes Permian to Jurassic strata and Triassic intrusive rocks (Figure 3.10). Permian strata (Potrerillo Unit) consist of reddish, thinly bedded siltstones and sandstones deposited in a playa sandflat capped by reddish-purple, thickly bedded eolian sandstones with high-angle crossbedding. The Potrerillo Unit is intruded by a set of highly weath-

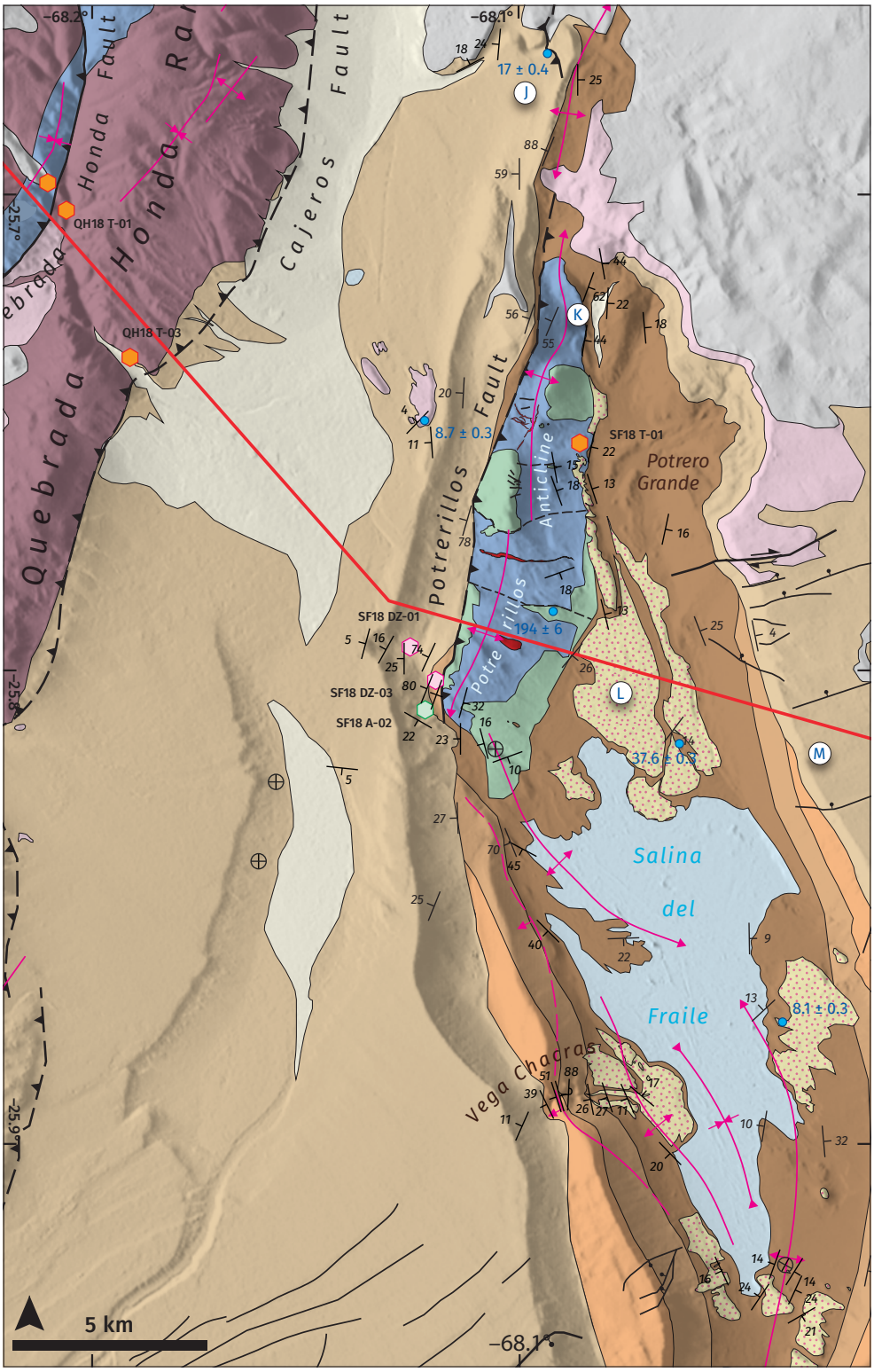

Figure 3.10: Geologic map of the Salina del Fraile and Quebrada Honda Range. See Figure 3.4 or Figure A.1 for legend.

ered mafic-intermediate dikes dated to the Triassic (Adelmann, 2001; Voss, 2002). The largest dikes trend roughly E–W, are 8–12 m thick, and span over 2 km in length. Jurassic strata (the Fraile Unit) consist of marine limestones, marls, and sandstones, and pillow lavas deposited in a shallow marine environment, which are unconformably overlain by the Paleogene Quiñoas Formation (Adelmann, 2001). The axial plane of the Potrerillos Anticline is inferred to dip ~37° to the east, with an interlimb angle of approximately 74°. The asymmetric fold consists of a narrow, subvertical, western forelimb and a broad, gently tilted, eastern backlimb, consistent with fault-propagation folding. The fold hinge trends roughly 015° and plunges to the south and north. To the south, shortening is accommodated by a series of NNW–SSE-trending, west-vergent to upright folds in the Salina del Fraile. To the north, the Potrerillos Anticline dies out and shortening is taken up on a small anticline and east-vergent thrust fault observed in Cenozoic strata (Location J, Figure 3.10). The Paleozoic–Mesozoic rocks in the core of the fold are evidently cut by roughly E–W-trending lineaments. The center of the fold axis, located within the Potrerillo Unit, is seemingly offset in a right-lateral sense by one of these lineaments. This may reflect brittle faulting after Cenozoic folding, or earlier episodes of deformation that preceded Cenozoic folding. The lineaments do not seem to cut overlying Cenozoic strata (thought a small right-lateral fault is evident to the east of the anticline in Figure 3.10), but largely act to juxtapose Jurassic and Permian rocks. The trends of major lineaments do not follow topographic contours and can thus be interpreted as traces of steeply dipping planes that were deformed by later folding. The apparent dip directions combined with the associated younger-over-older stratal juxtaposition would support the interpretation of normal-sense fault offset. Along with this potential fault offset, the abrupt paleorelief between the Jurassic Fraile Unit and Permian Potrerillo Unit causes the former to outcrop sporadically throughout the nucleus of the fold, with highly variable thickness. Because of their E–W trend, offsetting of pre-Cenozoic lithologic contacts, and association with abrupt stratal thickness changes and paleorelief, and we tentatively interpret these lineaments as pre-Cenozoic normal fault traces.

The western forelimb of the Potrerillos Anticline consists of a small exposure of steeply dipping Paleogene strata overlain by a thick section of Middle Miocene to Late Miocene clastics, volcaniclastics, and ignimbrites, whose dips decrease from subvertical at the base to subhorizontal at the top of the section. Detrital zircon ages from steeply dipping strata in the forelimb suggest that the fold is breached by a west-vergent reverse or thrust fault that carries Mesozoic and Paleozoic strata over this thick package of Cenozoic sedimentary strata (the Potrerillos Fault, Figure 3.10). Sample AF20T03 was collected from subvertical, yellowish-tan pebbly sandstone stratigraphically below sample AF20T02 in the forelimb of the fold and in the footwall of the inferred fault (Figure 3.10). The maximum depositional age is 24 to 29 Ma (Table 3.1), and it is stratigraphically below, thus older than, AF20T02 (~17.5 Ma, next paragraph), placing it within the Upper Member of the Quiñoas Formation or the Chacras Formation. Either interpretation would indicate that at least 2 km of the Lower Member of the Quiñoas Formation, which is

present in the backlimb of the fold, is missing from the forelimb (Figure 3.4). We infer that these strata were overthrust by the hanging wall of a west-vergent thrust fault (Figure 3.10).

As just mentioned, the base of the exposed footwall strata consists of steeply dipping to subvertical sandstones of the Chacras or Quiñoas Formations. These strata are overlain by a steeply dipping ignimbrite deposit. Zircon U-Pb dating of the ignimbrite (sample AF20T02; Table 3.1) yields a TuffZirc age of 17.54 (+0.34, -0.40) Ma, indicating deposition in the latest Early Miocene, correlative to the Potrero Grande formation. The ~17.5 Ma age matches the age of an ignimbrite near the base of the Potrero Grande Formation dated in previous studies (17 ± 0.4 Ma from K-Ar on biotite; Adelmann, 2001). The ignimbrite is overlain by matrix-supported conglomerates with subangular to angular clasts 10–40 cm in diameter. Clasts are composed of granite, green quartzite, and dark purple sandstone, and the matrix consists of greenish-gray pebbly coarse sandstone. Strata overlying this coarse conglomerate consist of a fining-upward section of interbedded conglomerates and coarse sandstones. The dip of bedding decreases systematically up-section from subvertical near the base to less than 10 degrees at the top of the section (Figure 3.10). A detrital sample from middle of this section yields a maximum depositional age of 15.62 ± 0.180 Ma (AF20T01; Table 3.1), which we also assign to the Potrero Grande Formation. Potrero Grande strata are conformably overlain by dark gray volcaniclastic sandstones and white-tan ignimbrites previously dated to ~11.5–8.7 Ma (Cajeros ignimbrite Adelmann, 2001; Voss, 2002). In contrast to this >1 km thick package of Potrero Grande strata in the forelimb of the fold, the Potrero Grande is only 100 m thick on the backlimb (Figure 3.10). Although exposure is not good enough to observe unequivocal growth strata, the basal coarse conglomerate, upward decrease in grain size and bedding tilt, and extreme thickness contrast of the Potrero Grande across the fold indicate syn-kinematic deposition during formation of the Potrerillos Anticline. The 8.7 Ma Cajeros ignimbrite is subhorizontal, providing a maximum age for the folding (Figure 3.10). We therefore estimate that folding occurred between 17.5 to 8.7 Ma, and infer from the ~15.6 Ma growth strata that the fold was mainly active around 15 Ma. Our AFT data presented below also shed light on the exhumation of this anticline.

The backlimb of the Potrerillos Anticline consists of a broad panel of Paleogene Quiñoas and Chacras Formations tilted approximately 15 degrees to the SE (Figure 3.10). The base of the Quiñoas Formation, which overlies the Jurassic Fraile unit in angular unconformity, is exposed in the northern portion of the backlimb (Location K, Figure 3.10). The Potrero Grande Formation overlies these units in angular unconformity and is subhorizontal to gently east-dipping and ~100 m thick. The angular unconformity at the base of the Potrero Grande is prominent throughout the eastern wall of the Salina del Fraile depression (Figure 3.10) and is due to tilting, uplift, and erosion of pre-growth strata in the backlimb of the Potrerillos Anticline. The Potrero Grande Formation is overlain by Late Miocene to Pliocene ignimbrites and volcanic flows of the Antofalla Volcanic Complex (Figure 3.10). Within the Salina del Fraile depression, subhorizontal Late Miocene to Pliocene terrace deposits unconformably overlie the Quiñoas Formation (e.g., at Location L, Figure 3.10). Mapped by Voss (2002) as “Salina

beds", these 20 to 100 m thick layers of alluvial sandstones and conglomerates and lacustrine sediments represent remnants of basin-floor deposits that have been eroded by NW-prevailing winds, often into streamlined forms such as yardangs (McMillan & Schoenbohm, 2020).

Vega Chacras. In the southern part of the Saline del Fraile depression, Cenozoic strata are folded into a series of west-vergent, doubly-plunging anticlines, separated by an inward-plunging syncline (Figure 3.4). The southern part of the depression consists mainly of the Lower Member and Upper Member of the Quiñoas Formation, which are tilted SE by a southward plunging anticline (Canavan et al., 2014). In Vega Chacras canyon (Figure 3.10), strata in the forelimb of a west-vergent anticline are exposed. The base of the canyon consists of the Lower Member of the Quiñoas Formation, which dips approximately 26° to the west. Dips increase gradually upsection toward the Upper Member of the Quiñoas Formation, indicative of parallel folding. The Chacras Formation is composed of alluvial fan conglomerates and eolian sandstones dated to ~24–22 Ma; the fanglomerates have been interpreted as syn-tectonic deposits (Adelmann, 2001; Kraemer et al., 1999). The lowermost portion of the Chacras Formation here is subvertical to overturned and east-dipping, and dips decrease up-section to approximately 40° at the top of the Chacras Formation. Such dramatic fanning of dips suggests the presence of growth strata, where overturned beds represent pre-growth deposits incorporated into the forelimb of a fault-propagation fold, and overlying alluvial and eolian deposits of the Chacras Formation represent deposition during fold growth. Reijs and McClay (2003) also interpreted these strata as growth deposits, though their tectonic interpretation invokes normal fault block rotation instead of fold growth. Syn-tectonic alluvial fan deposits of the Chacras Formation also outcrop along the western margin of the Salar de Antofalla (Vega Quiñoas and Vega Cadillo Grande; Figure 3.9) and indicate that deformation during the late Oligocene formed an extensive bajada system due to uplift of the Antofalla High (Adelmann, 2001). This deformation evidently affected the Salina del Fraile area through west-vergent fault-propagation folding. The growth section in the Chacras Formation is overlain by volcaniclastic and volcanic strata of the Potrero Grande Formation, which dips west to northwest at gentler angles of 20° to 11°. As described in the preceding paragraphs, the thick deposit of Potrero Grande strata on the western margin of the Salina del Fraile and its unconformable basal contact (better exposed on the eastern margin of the depression, Location M, Figure 3.10) suggest its deposition during and after uplift of the Potrerillos Anticline and Potrerillos Fault (Figure 3.10).

3.3.5 Quebrada Honda Range

The Quebrada Honda Range is composed of Ordovician metavolcanic and metasedimentary rocks (here mapped as the Cortaderas Chicas Volcano-Sedimentary Complex, CCVSC) and Permian sedimentary strata (here mapped as the Potrerillo Unit; Figure 3.4). The range is cut by two major thrust or reverse faults, the intra-range Quebrada Honda Fault, and the range-bounding Cajeros Fault (Figure 3.10; Palma et al., 1990). Like in the Calalaste Range, the CCVSC

displays a large magnitude of shortening and complex deformation structures, suggesting pre-Cenozoic shortening. Pre-Cenozoic units are unconformably overlain by subhorizontal Late Miocene ignimbrites and volcanic flows (Palma et al., 1990; Seggiaro et al., 2007), but we did not observe places where these flows cross-cut reverse faults; rather, they preferentially filled local topographic lows.

The traces of the two major faults were inferred in the field by their geomorphic expressions. Although the faults are not directly exposed due to weathering and limited landscape incision, existing studies generally agree on their location, orientation, and sense of displacement (Palma et al., 1990; Schnurr et al., 2006; Seggiaro et al., 2007). As we discuss below (section 4.5), our low-temperature thermochronology data from the hanging wall and footwall of the Quebrada Honda Fault support the interpretation of a major east-vergent reverse fault, as apatite fission track (AFT) ages differ drastically over a few hundred meters across the inferred fault trace due to hanging-wall exhumation. Similarly, AFT ages from the hanging wall of the Cajeros Fault support its interpretation as a major, range-bounding, east-vergent fault that was active around the same time as the Quebrada Honda Fault. Both faults exhumed rocks from below the apatite partial-annealing zone (~4 km depth assuming a 30 C°/km geothermal gradient) during the Oligocene to Miocene (section 4.5).

In contrast to the Calalaste Range, we did not observe significant exposures of Cenozoic strata in the Quebrada Honda Range. The Cajeros Fault is sealed by undated subhorizontal Cenozoic deposits at the location of our transect. Approximately 4 km further south, Adelmann (2001) report a depositional age of 17.39 ± 0.08 (Ar-Ar on feldspar of an interbedded ash) for folded strata in the footwall of the Cajeros Fault, indicating that it may have been active ~17 Ma or later.

3.4 Apatite fission track thermochronology

3.4.1 Methods

Thirteen samples were collected for apatite fission track (AFT) analysis (Table 3.2) across the study area, including from all recognized Cenozoic fault systems. Ten of the samples (QH18T01, QH18T03, SF18T01, AF20T02–08) are from the upthrown blocks of major structures (commonly reverse fault hanging walls). Three samples were collected from footwall rocks and are paired with nearby hanging wall samples (QH18T02, AF20T01, AF20T09).

Apatites were separated following conventional heavy liquid separation techniques at the University of Melbourne. Fission track dating is based on the accumulation of tracks from the spontaneous fission of ^{238}U in apatite (e.g., Gleadow et al., 2002). Fission tracks in apatite anneal between temperatures of ~60–120 °C, the partial annealing zone (PAZ; e.g., Gleadow & Duddy, 1981). The length distribution of fission tracks and the apparent fission track age of each sample is therefore dependent on its thermal history. Apatite samples for FT analysis were processed

Table 3.2: AFT sample description and results

Sample	N grains	$P(\chi^2)$ [%]	Central age [Ma ±1σ]	N length	MTL [µm±se]	St.Dev. [µm]	D_{par} [µm±1σ]	^{238}U [ppm ±1σ]
SF18T01	34	57.6	237.6 ± 14.5	101	13.1 ± 0.11	1.07	1.52 ± 0.17	27.6 ± 27.1
QH18T01	28	6.3	29.7 ± 2.7	81	14.0 ± 0.12	1.06	1.47 ± 0.14	11.4 ± 24.2
QH18T02	31	0.0	113.4 ± 14.1	115	11.2 ± 0.18	1.98	1.37 ± 0.15	13.5 ± 15.2
QH18T03	34	97.9	35.0 ± 2.9	102	13.1 ± 0.18	1.86	2.27 ± 0.22	2.0 ± 0.3
AF20T01	26	0.8	118.4 ± 13.3	109	10.8 ± 0.13	1.39	1.22 ± 0.13	10.7 ± 22.4
AF20T02	26	1.2	38.4 ± 2.2	99	13.4 ± 0.17	1.73	1.3 ± 0.12	54.9 ± 27.8
AF20T03	28	83.5	63.9 ± 6.1	98	12.8 ± 0.22	2.18	1.28 ± 0.12	6.6 ± 16.2
AF20T04	29	0.0	183.9 ± 5.9	104	11.3 ± 0.17	1.78	1.47 ± 0.08	67.0 ± 24.8
AF20T05	32	96.8	53.4 ± 5.8	97	13.5 ± 0.16	1.55	1.47 ± 0.19	7.9 ± 4.0
AF20T06	28	5.3	34.2 ± 3.7	98	13.2 ± 0.16	1.62	1.46 ± 0.12	13.2 ± 12.8
AF20T07	35	97.6	63.6 ± 7.5	53	13.3 ± 0.28	2.04	1.83 ± 0.12	3.5 ± 1.4
AF20T08	27	99.0	42.7 ± 6.0	115	12.5 ± 0.20	2.13	1.76 ± 0.31	4.2 ± 1.6
AF20T09*	33	4.6	194.4 ± 6.7	104	11.4 ± 0.15	1.56	1.65 ± 0.43	26.3 ± 22.3

*Detrital sample. MTL: mean track length. D_{par}: long axis of track etch pit.

at the University of Melbourne Thermochronology Lab using Laser Ablation-Inductively Coupled Plasma-Mass Spectrometry (LA-ICP-MS Hasebe et al., 2004) following the procedure in Gleadow et al. (2015). Fission track image sets were captured with TrackWorks using a Zeiss M1m AxioImager microscope. Automatic track counting was conducted by FastTracks using the coincidence mapping technique (Gleadow et al., 2009). Further details on the analytical procedures used in this study are described in Table A.3. Detailed single grain AFT age data and track length measurements are included in Table A.4.

To further constrain the thermal history of basement rocks throughout the study area, we performed inverse thermal history modelling on all AFT samples. We used the HeFTy (Ketcham, 2005) and QTQt (Gallagher, 2012) software packages for thermal modelling, which are based on non-learning and learning Monte Carlo methods, respectively (Gallagher & Ketcham, 2018; Vermeesch & Tian, 2014). Because reheating due to burial overprints prior episodes of cooling, it is useful to place constraints on the possible t-T paths in such models using geologic observations (Gallagher, 2021; Green & Duddy, 2020). We used the presence of major unconformities and the depositional ages of geologic units to infer periods when samples were at near-surface temperatures. For the HeFTy program, which sequentially tests many random, independently chosen t-T paths, constraints can also be used to narrow the field of possible paths, allowing suitable paths to be found more quickly without spending computing time analyzing overtly implausible paths (i.e., “optimizing constraints”; Gallagher & Ketcham, 2018). In addition to these narrowing constraints, broad t-T constraints can also be used to test specific hypotheses that would be more complex than the algorithm would otherwise consider (e.g., to allow for reheating; Gallagher & Ketcham, 2018) without inherently favoring such scenarios over simpler histories. For metasedimentary and igneous lithologies, which represent the majority of our samples, we specify an initial high-temperature constraint (with a minimum bound greater

than the maximum temperature of the AFT PAZ and an age of approximately twice the oldest measured AFT age) representing metamorphism or igneous emplacement, during which AFT were reset. We also impose a constraint at 0 Ma representing mean annual temperatures of ~0–15 °C (McMillan & Schoenbohm, 2020), reflecting the fact that all samples were collected at the surface. We use track-pit diameter, D_{par}, as a proxy for chemical composition annealing behavior. Track lengths were measured as true-dip corrected 3D lengths and projected to the c-axis for modelling. We used the annealing model of Ketcham et al. (2007). For HeFTy (version 1.9.3), we modeled as many t-T paths as necessary until 1,000 good paths ($p > 0.5$) were found (due to computational time, samples QH18T02 and AF20T01 yielded 500 good paths; sample AF20T04 yielded 100). For QTQt (version 5.5.0) we performed 10,000 burn-in and 100,000 post burn-in iterations. The default starting time was based on the oldest AFT age ± the oldest AFT age. Following a model run, the acceptance rates and posterior chain were examined, and parameters changed if necessary (Gallagher, 2012). HeFTy modelling parameters are summarized in Table A.5.

3.4.2 Calalaste range

Four samples (AF20T05 to AF20T08) were collected from Ordovician meta-sandstones in the core of the Calalaste range at Quebrada del Diablo (Figure A.2). Samples were collected along an approximately 2.7 km strike parallel transect that increased in elevation from 4122 m (AF20T05) to 4614 m (AF20T08). These samples yield AFT central ages of approximately 34 to 63 Ma, with relatively long mean track lengths (MTL), indicating that this portion of the Calalaste range cooled relatively rapidly through the PAZ during the Paleocene to Oligocene (Figure 3.11). Track length distributions are negatively skewed and/or bimodal, with a population of short tracks that imply some residence in the PAZ prior to cooling towards near surface temperatures. With increasing elevation along the transect, MTL generally decreases, track length variance increases, and track length histograms become more negatively skewed; at the top of the section, sample AF20T08 preserves a small population of very short tracks (<8 μm). These trends may indicate exhumation from the lower portion of the PAZ, in which the higher-elevation samples (especially AF20T08) were not fully reset prior to exhumation and retained an annealed population of tracks reflecting a previous cooling event. Exhumation of the Calalaste range, therefore, is limited to a maximum of only ~4 km during the Cenozoic (assuming a 30 °C km^{-1} paleogeothermal gradient and a maximum closure temperature of 120 °C).

There is no obvious age-elevation relationship among these four samples (Figure 3.11). Due to the limited topographic relief between these samples (~500 m) it is likely that all four samples passed through the PAZ around the same time, and ideally would record similar AFT ages. Because these samples are from metasandstones, however, the sampled apatite grains can be expected to vary in composition, both within and between samples, which can contribute to dispersion in AFT ages through varying annealing kinematics. All samples pass the χ^2 test, $P(\chi^2) > 0.05$, and samples AF20T05, AF20T07 and AF20T08 have p-values near 100%. However,

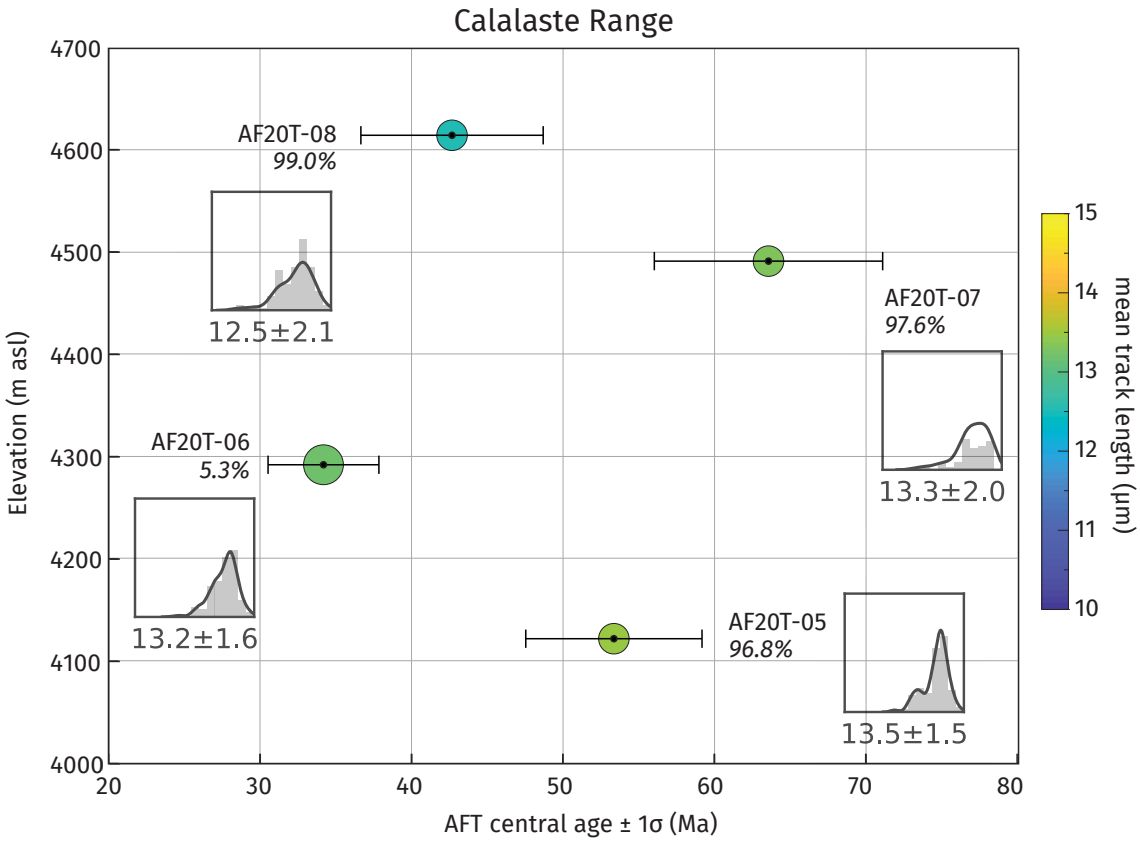

Figure 3.11: Age-elevation plot of apatite fission track data from the Calalaste range. AFT central ages are plotted with 2σ error bars and annotated with sample ID and $P(\chi^2)$, which quantifies apatite homogeneity (see text for discussion). Circle color corresponds to mean track length; circle size is proportional to age dispersion. Histograms show distribution of measured track lengths, annotated with the mean value.

these three samples also have relatively low U concentrations and low track-counts, resulting in less precise single grain ages that may falsely appear as a single homogeneous population in the $P(\chi^2)$ statistic. Sample AF20T06, on the other hand, has grains of both high and low U concentrations that range in precision and appear more dispersed. Moreover, sample AF20T08 has apatites with D_{par} values ranging between 2.8-1.4 μm, with most of the oldest single-grain ages consisting of the longest D_{par} values, indicating considerable heterogeneity that is not evident in the $P(\chi^2)$ statistic. In addition to variance due to apatite heterogeneities, variation in ages may also be caused by spatially non-uniform exhumation due to differences in rock uplift or erosion along strike. The sample locality corresponds to a wind gap in the Calalaste range, which may have been a water gap during range uplift. The resulting paleotopography may have significantly deflected temperature contours beneath the range during exhumation, as well as the amount and timing of exhumation experienced by each sample.

Thermal history models. Thermal history modelling was performed on all samples (Figure 3.12). Like the AFT ages, the results imply variable Cenozoic cooling histories among the

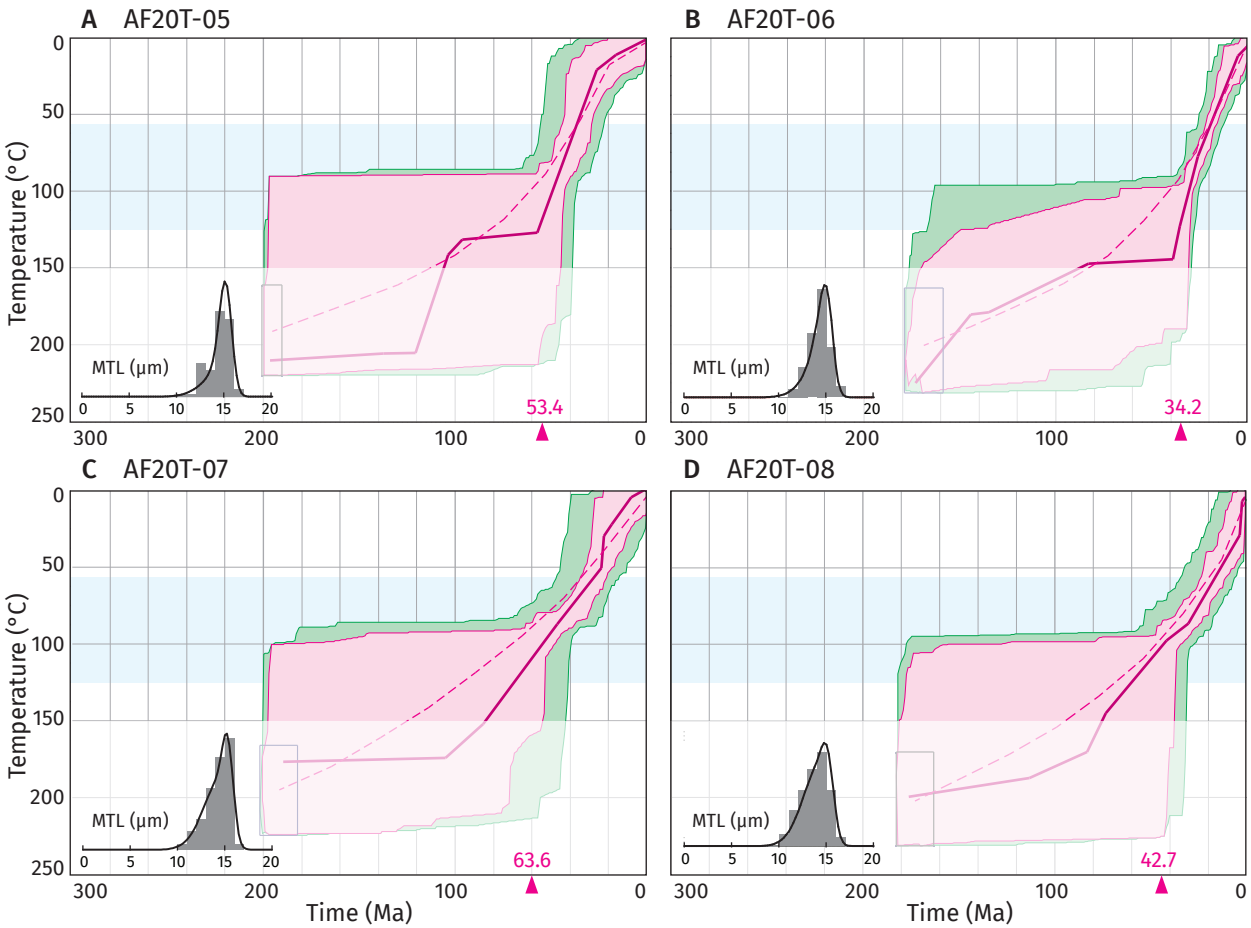

Figure 3.12: HeFTy thermal history models for samples from the Calalaste range. The pink and green regions envelope all good ($p > 0.5$) and acceptable ($p > 0.1$) paths, respectively. The thick magenta line is the single best-fit path, while the dashed magenta line is the mean path. The blue shaded temperature range approximates the AFT partial-annealing zone. Thin black boxes represent geologic constraints, through which all paths must pass. The inset plots a histogram of measured *c*-axis projected track lengths, overlain with a curve showing the distribution predicted by the best-fit path. The pink triangle along the horizontal axis plots the measured AFT pooled age. Cooling histories at temperatures greater than 150 °C are partially shaded because AFT data record no information at these temperatures.

four samples. The "good path" envelopes in HeFTy thermal models broadly indicate cooling between 50 and 30 Ma, though individual samples show cooling episodes with narrower ranges. Temperatures before ~60 Ma are unconstrained by the models. Cooling took place with an average rate of ~2.5 to 3 °C Ma^{-1} (roughly 0.1 to 0.2 km Ma^{-1} assuming a paleogeothermal gradient of 30°C km^{-1}), consistent with exhumation driven by tectonic uplift and erosion. The most likely cooling history for sample AF20T07, which had the oldest central AFT age at 63.6 Ma, suggests that rapid cooling may have begun significantly later than this age, between 45 and 30 Ma. The cooling episodes for the other three samples are more consistent with their central AFT ages. Based on these results, we estimate that Cenozoic uplift of the Calalaste range occurred between 50 and 30 Ma.

3.4.3 Cerro Campo Negro and Antofalla Fault

We collected four samples from the western margin of the Salar de Antofalla straddling the Antofalla Fault: one from Ordovician metasediments in the footwall (AFT20T-01) and three from Cerro Negro Granite in the hanging wall at increasing distance to the east from the fault (AF20T02 to AF20T04) from the Cerro Negro Granite. We also collected a detrital sample from Cenozoic sedimentary rocks in the footwall of Fault G (AF20T09; Figure 3.7). The three hanging wall samples yield central ages of 38.4 ± 2.2Ma, 58.5 ± 7.1 Ma, and 183.9 ± 5.9 Ma, respectively (Figure 3.13). AFT ages systematically increase with distance from the fault plane, while MTL decreases from ~13.4 to ~11.3 µm. This pattern is consistent with exhumation due to west-vergent reverse faulting, which would be greatest near the fault plane due to tilting or folding above a listric fault (García & Davis, 2004). The reset age near the fault plane (AF20T02) implies exhumation of a portion of the crust that was below the AFT partial annealing zone, while partially reset to unreset apatite grains (reflected by shortened MTL measurements) were exhumed in the more distal parts of the hanging wall (Figure 3.13). Track lengths in samples AF20T02 and AF20T03 are negatively skewed, indicating an earlier episode of cooling followed by partial annealing. Sample AF20T04, on the other hand, is positively skewed, with a component of relatively long tracks; this sample is located in the footwall of the Botijuela Fault (Figure 3.7), an inferred Middle Miocene normal fault, slip on which would have exhumed this sample at a date later than the exhumation of samples AF20T02 and AF20T03 (Figure 3.13). The footwall sample (AF20T01) yields an age of 118.4 ± 13.3 Ma and a relatively short MTL of 10.8 ± 0.13 µmwith a generally unimodal track length distribution with slight positive skew, indicating that the sample was exhumed during the Mesozoic and was not buried deeply enough during the Cenozoic to fully reset the AFT system, but spent significant time in the apatite PAZ, resulting in partially annealed tracks.

The detrital sample (AF20T09) was collected from a sandstone bed near the base of the Lower Member of the Quiñoas Formation in the footwall of Fault G. Sample AF20T09 yields AFT ages that are older than the depositional age of the sandstone (~40 Ma) and range from ~124 to 297 Ma, with a central value of 194.4 ± 6.7 Ma (Table 3.2 and Figure A.6e). This indicates that burial following deposition and reverse faulting in the Paleogene did not elevate temperatures sufficiently to reset the AFT system. These detrital AFT ages instead record the exhumation of source regions for the Paleogene Antofalla Basin. Early Triassic to Early Cretaceous ages are broadly consistent with the ~180–140 Ma cooling documented by sample AF20T01 (Figure 3.14a). These data may indicate that regional shortening ~40–35 Ma, which led to the deposition of fluvial-alluvial strata, was imposed on a relict Mesozoic landscape that had experienced little intervening tectonic or erosional exhumation. As we discuss below, Mesozoic exhumation may have been due to an extensional tectonic setting.

Thermal history models. We completed thermal history models for four samples from the Antofalla fault system (AF20T01 through AF20T04). We did not model the unreset detrital sam-

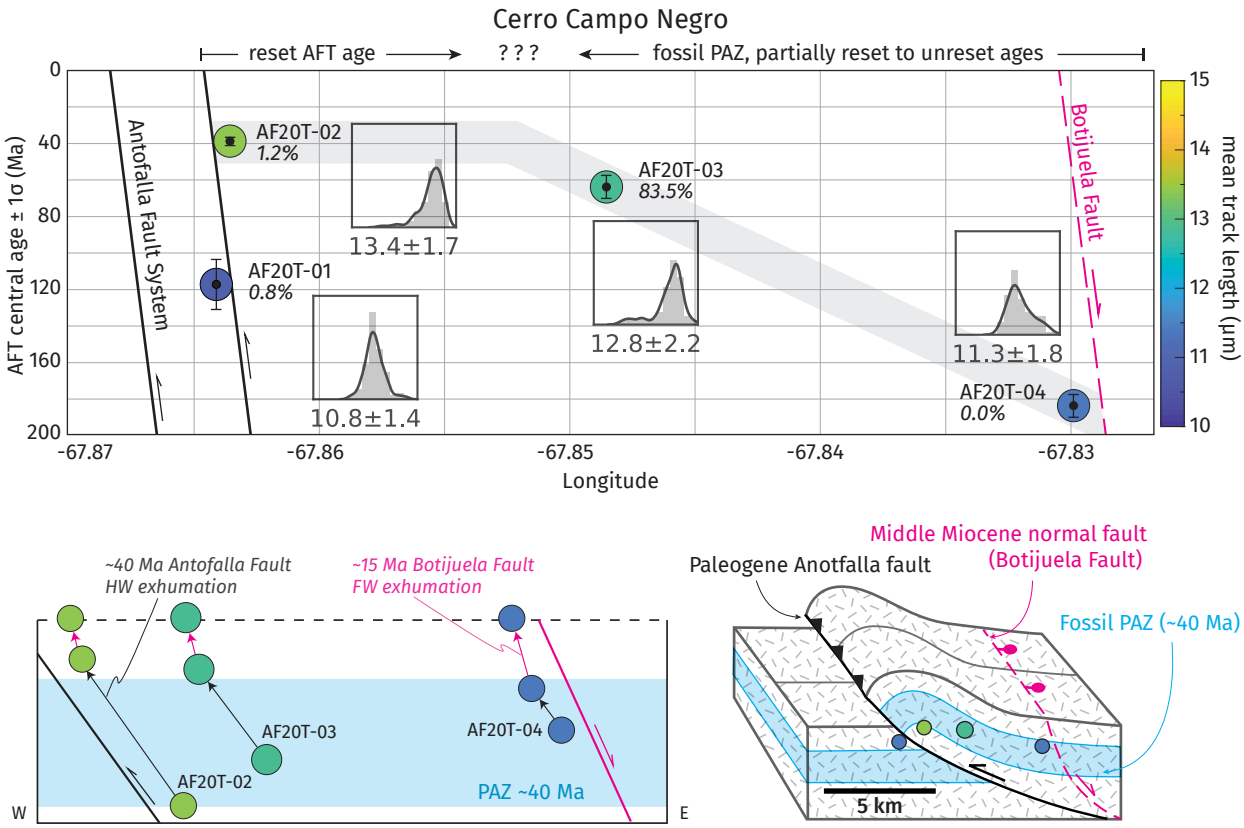

Figure 3.13: Relationship between AFT central ages and distance from the Antofalla fault system. Thick grey line denotes inferred age-distance relationship, with a kink indicating exhumation of a fossil partial annealing zone (PAZ). Refer to Figure 3.11 for further explanation. Bottom panel illustrates the inferred exhumation scenario for hanging-wall samples during two episodes of deformation (Paleogene thrusting, black, and Middle Miocene extension, magenta). Block diagram after García and Davis (2004) illustrates the inferred pre-Middle Miocene reverse fault and fault-propagation fold in granitic basement that resulted in the exhumation of a fossil PAZ. The depth of exhumation varies with distance from the fault because of folding.

ple (AF20T09). Thermal modelling of the footwall sample (AF20T01) suggests that a major episode of cooling occurred during the Jurassic to Early Cretaceous, which brought the sample to near-surface temperatures. The models necessitate some reheating of this sample during the Cretaceous or Cenozoic, followed by later cooling. Although the timing of these later events is not well constrained, the models are consistent with reheating due to reverse faulting and footwall burial during the Paleogene.

The hanging wall sample nearest to the fault plane (AF20T02) requires that cooling began approximately 45 to 38 Ma, while sample AF20T03 shows cooling beginning approximately 65 to 50 Ma. The prior thermal history of AF20T03, which is evident in its bimodal track length distribution (Figure 3.14c), is not resolved by the thermal history models. As a result, the model poorly predicts the measured track length distribution (Table A.5). Both samples AF20T02 and 03 have similar D_{par} dimensions, suggesting similar apatite compositions. However, AF20T03 retains a significant proportion of shorter tracks (5–10 μm), implying that it may contain ap-

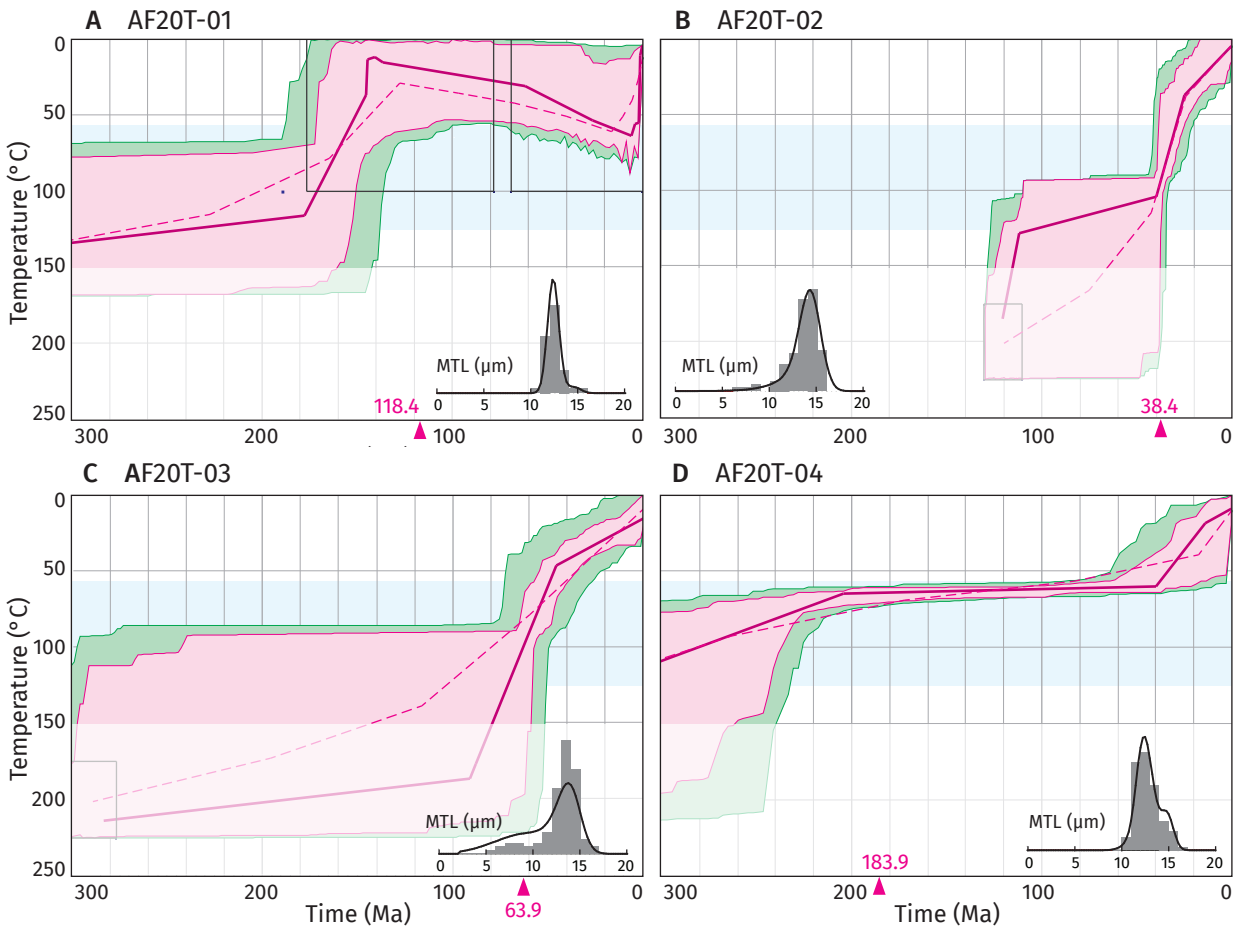

Figure 3.14: HeFTy thermal history models of the Antofalla Fault system. Refer to Figure 3.12 for explanation.

atites with higher track retentivity that is not reconciled by D_{par} as a proxy for composition (e.g., pg. 67 in Donelick et al., 2005). A notable difference between samples AF20T02 and AF20T03 is their respective U concentrations, where AF20T02 has a mean [U] of 54.9 ppm and AF20T03 of 6.6 ppm. In fact, most grains measured for AF20T03 have [U] between 4 and 2 ppm. Low-U apatites measured with LA-ICPMS tend to show older AFT ages than those obtained by the external detector method (Seiler et al., 2013). Furthermore, U and eU (effective U) are often inversely correlated with AFT age in slow cooling basement samples, where compositional variation is not a factor (McDannell et al., 2019). This suggests aspects of fission track annealing that are poorly understood and not well parameterized in thermal history models. The timing of cooling for AF20T03 is likely poorly constrained, and the true AFT age is potentially younger than the measured age due to low [U]. Thus, while it is possible that the Antofalla Fault was active early as ~60 Ma (AF20T03), we consider 45–38 Ma (AF20T02) a more reliable indicator for exhumation of the Antofalla Fault.

The models for sample AF20T04 suggest that the sample was exhumed during the Late Triassic to Early Jurassic and resided in the upper portion of the partial annealing zone until

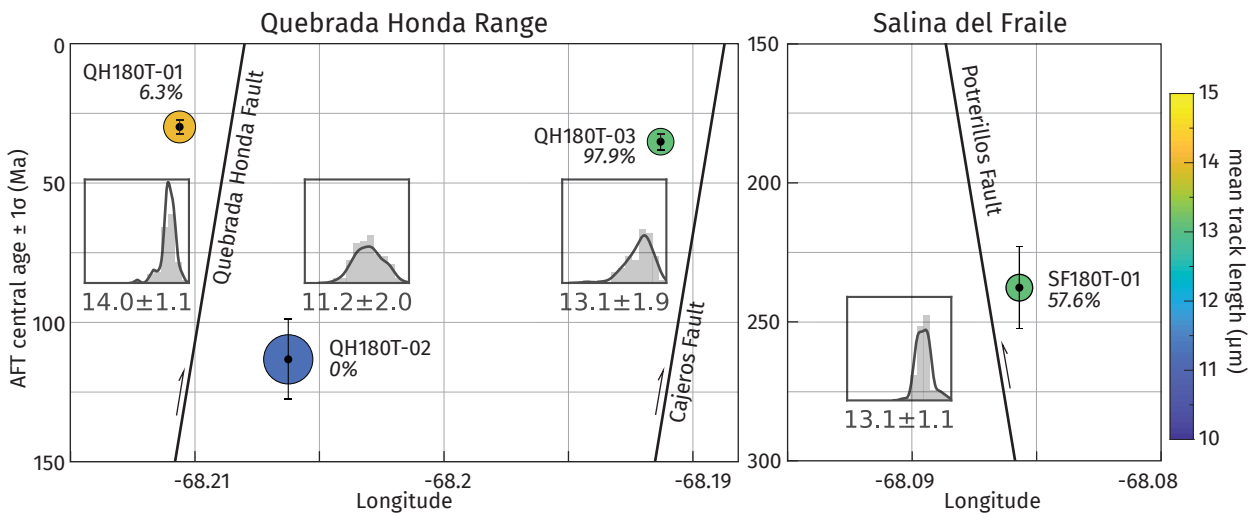

Figure 3.15: Summary of AFT ages and track lengths for the Quebrada Honda range (left panel) and Salina del Fraile (right panel). Note that the vertical scale shifts between for the right panel. Refer to Figure 3.11 for explanation of AFT visualization.

approximately 40 to 10 Ma, at which time the sample cooled to near-surface temperatures. Although not well constrained by the thermal models, this final pulse of cooling is consistent with exhumation due to reverse faulting during the Late Eocene to Oligocene, normal faulting during the Middle Miocene (~15 Ma), or a combination of these two events. Overall, thermal history modelling of hanging wall rocks of the Antofalla Fault suggests that the main pulse of reverse-fault driven exhumation occurred ~40 Ma.

3.4.4 Salina del Fraile

Sample AF20T01 was collected from a mafic-intermediate dike in the Potrerillos Anticline in the northern part of the Salina del Fraile (Figures 3.10 and 3.15). The dike was previously dated to 234 ± 1Ma (Ar-Ar on plagioclase) and 212 ± 5 Ma (whole rock K-Ar; Adelmann, 2001). Sample AF20T01 yields a central AFT age of 237.6 ± 14.5 Ma (Table 3.2) and therefore represents magmatic cooling following initial emplacement of the dike. We infer that the dike was emplaced in the uppermost few km of the crust, above or within the upper part of the PAZ, and was subsequently not buried deeply enough to reset its AFT age during the Mesozoic and Cenozoic. The mean track length of 13.1 ± 0.11 µmindicates that some annealing has occurred since emplacement, likely due to some residence in the shallowest portion of the PAZ, either due to emplacement of the dike at such depths or to shallow burial by Jurassic and Cenozoic sediments.

Thermal history models. The thermal history models for sample AF20T01 demonstrates that the major episode of cooling corresponds to magmatic cooling of the igneous sample after its intrusion into the shallow crust during the Triassic (Figure 3.16). After this initial

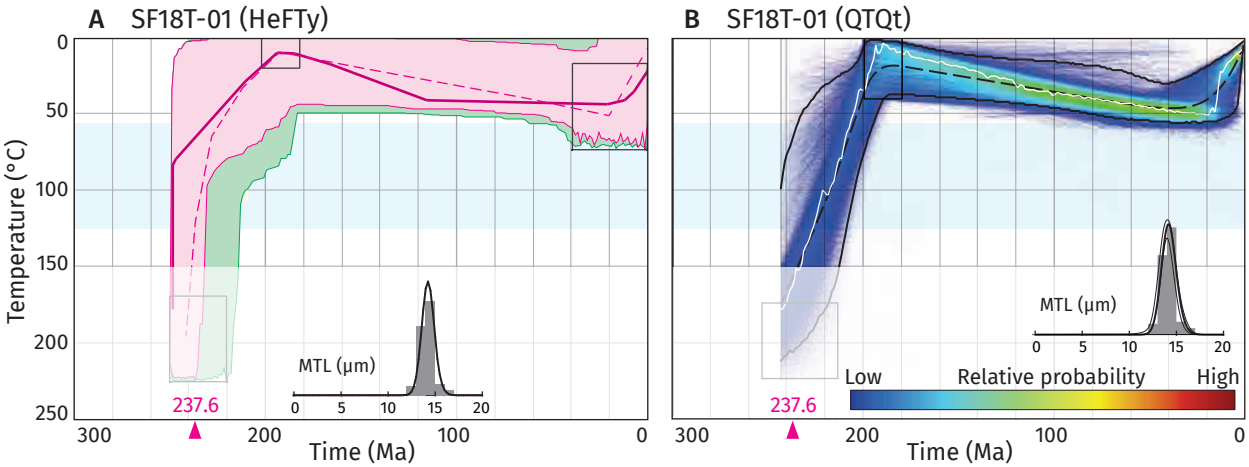

Figure 3.16: Thermal history models for the Potrerillos Anticline in the Salina del Fraile using (a) HeFTy and (b) QTQt. For explanation of (a), refer to Figure 3.12. QTQt models (b) depict the relative probability of time-temperature paths. The dashed line represents the expected model (weighted by probability), the white line passes through regions with the largest number of paths, and the 95% credible interval is given by solid lines. These models corroborate an inferred cooling pulse around 15 Ma.

cooling episode, the sample resided at temperatures corresponding to the uppermost crust, and the models suggest it may have been shallowly buried, reaching temperatures of ~60 °C. The HeFTy models suggest that the sample ultimately cooled to near-surface temperatures approximately 40 to 0 Ma (Figure 3.16a), while the QTQt models constrain this minor cooling episode to between 20 and 10 Ma (Figure 3.16b). This final cooling pulse is likely predicted by the models due to the minor proportion of very long (>15 µm) tracks. Both modeling results are consistent with growth strata dated to 15.6 Ma in the footwall of this structure, indicating the hanging wall was uplifted during this time.

3.4.5 Quebrada Honda range

Samples AF20T01 and AF20T02 were collected from Ordovician metasandstones in the hanging wall and footwall, respectively, of the Quebrada Honda Fault, an intra-range reverse fault within the Quebrada Honda range (Figure 3.15). Sample AF20T01 yields a central AFT age of 29.7 ± 2.7 Ma and long MTL (~14 µm) (Table 3.2) with a generally unimodal distribution (Figure 3.17), indicating rapid cooling of hanging-wall rocks from depths below the PAZ, consistent with reverse fault-driven exhumation during the Early Oligocene. The paired footwall sample QH18T02 yields a central age of 113.4 ± 14.1, with annealed MTL (~11.2 µm). The track lengths show a weakly bi-modal, broad distribution.

Sample AF20T03 was collected from Ordovician metasandstone in the hanging wall of the range-bounding Cajeros Fault and yields a central AFT age of 35.0 ± 2.9 Ma, indicating cooling during the Middle to Late Eocene. The mean track length, 13.1 ± 0.18 µm, is shorter than that of AF20T01, and the track length distribution is negatively skewed, with a significant component

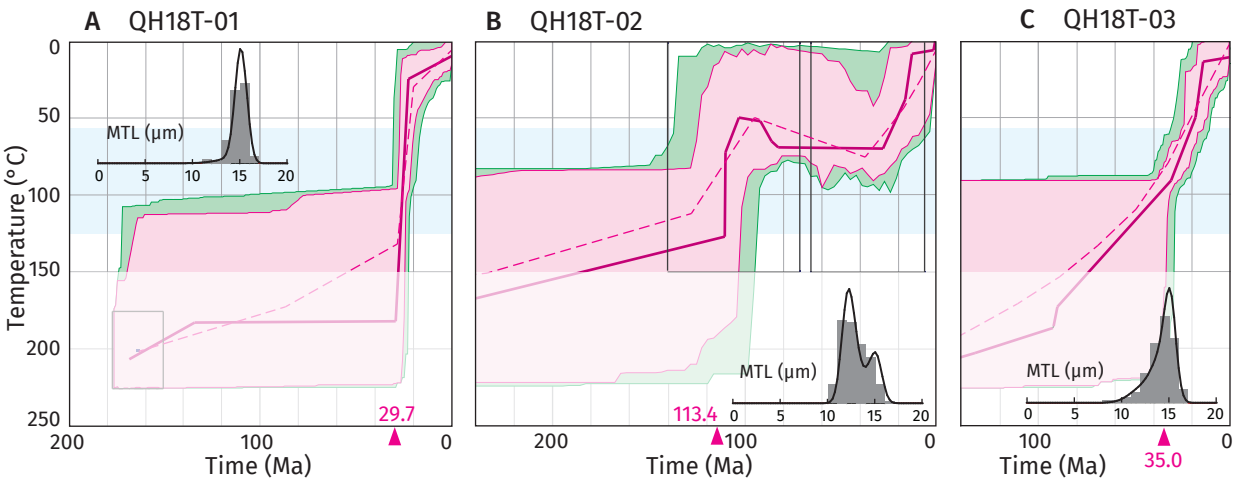

Figure 3.17: HeFTy thermal history models of samples from the Quebrada Honda range. Refer to Figure 3.12 for explanation.

of 9–12 µmtracks, indicating that the sample likely experienced prolonged monotonic cooling through the PAZ .

AFT data from the Quebrada Honda range are consistent with the uplift and exhumation of reverse fault hanging wall rocks around 30 to 35 Ma. The footwall sample was exhumed during the Cretaceous and may have been subsequently reburied, but not enough to reset its AFT age.

Thermal history models. Thermal history modelling of the two hanging wall samples (AF20T01 and AF20T03) implies cooling initiating ~35–30 Ma (Figure 3.17). Sample AF20T01 shows evidence for rapid cooling to near-surface temperatures at ~30 Ma, possibly followed by an episode of slower cooling from 20 Ma to the present. AF20T03 displays relatively uniform cooling from ~35 Ma to the present with a more protracted history within the PAZ compared to AF20T01. The footwall sample (AF20T02) displays a more complex thermal history, due to the slightly bi-modal track length distribution, that involves exhumation during the Cretaceous (~140–110 Ma), reheating between 60 Ma and 30 Ma, and a final pulse of cooling from ~30 Ma to the present (Figure 3.17). Although the timing of these events is not well constrained by sample AF20T02, this reheating is broadly consistent with burial by the hanging wall (and any syntectonic sediments) of the reverse fault. The initial cooling during the Cretaceous may reflect footwall exhumation in an extensional tectonic setting, as suggested for the Quebrada Honda Range by Seggiaro et al. (2007).

3.5 Structural cross-section

Based on our bedding plane measurements, mapped contacts, and thermochronology results, we constructed a viable structural cross-section through the Antofalla region (Figure 3.4). Given

the ~75 km length of the section, the thickness of units was allowed to vary along the section according to measured thicknesses (Table A.6). In general, fault planes are not exposed, and we therefore lack information on fault dips and kinematics. The presence, location, and sense of displacement of faults are inferred from lithologic contacts. The cross-section represents a synthesis of our geologic mapping, geochronology, and thermochronology results with existing studies on the stratigraphy of the Antofalla region. Our structural interpretation is in broad agreement with previous studies (Adelmann, 2001; Kraemer et al., 1999; Schurr et al., 2006; Seggiaro et al., 2007; Voss, 2002), though in some cases our dataset conflicts with previous interpretations of the number, location, and sense of displacement of major faults.

The transect is dominated by three east-dipping basement-involved faults, the Calalaste Fault, the Antofalla Fault, and the Potrerillos Fault, spaced at approximately 20 km. Secondary compressional structures developed between these three major faults, most often as imbricate thrusts that stepped into the footwall.

The western flank of the Calalaste range consists of fault-bounded packages of folded Cenozoic strata, composing eight thrust sheets (Section 3.3.2). The leading thrust fault tips out beneath the eastern margin of the Salar de Antofalla (Section 3.3.2). AFT and sedimentological data suggest that these faults were active during multiple episodes of shortening. The major basement-involved reverse faults near the crest of the range, such as the Calalaste Fault (Figure 3.5), were likely responsible for uplift of the range ~50–30 Ma, because this time period is older than the depositional age of all or most of the folded and faulted strata further west along the transect. Smaller thrust faults generally young to the west and were active at various times during the Miocene (Section 3.3.2) and Pliocene – Quaternary (Sections 3.3.2 to 3.3.2). Although we lack direct observation of fault dips, the eastward increase in tilting of folded rocks is consistent with deformation of older faults and folds by progressively younger structures in a west-vergent imbricate thrust system.

At Cerro Campo Negro, crystalline basement was carried over Ordovician metamorphic rocks and Permian and Cenozoic sedimentary strata by a steeply-dipping, west-vergent reverse fault (Antofalla Fault) and a relatively minor splay (Section 3.3.3). We also infer a blind reverse fault, assumed to be a splay of the Antofalla Fault, based on observed folding in Permian and Cenozoic strata.

We infer that the Antofalla Fault was reactivated as a fault that accommodated normal-sense displacement during the late Early Miocene to Middle Miocene (Tye et al., 2022). It is worth noting that Voss (2002) also mapped a normal fault bounding the western margin of the Salar de Antofalla, but without presenting concrete evidence or justification for it. Extensional reactivation of the Antofalla Fault with a normal slip throw of >1 km is the best explanation for the lowering of the Antofalla High from an elevation of at least 4300 m (the elevation of the Alto de Antofalla surface) to ~3320 m, the elevation of the Salar de Antofalla. Additional evidence for extensional deformation related to the Botijuela Fault includes the deposition of

Late Miocene–Pliocene Juncalito Formation at elevations up to 1 km lower than Early–Middle Miocene strata on the western margin of the Salar de Antofalla (Figure 3.4).

In the Salina del Fraile, contractional deformation produced a series of west-vergent fault-propagation folds, most significantly the Potrerillos Anticline in the northern end of the topographic depression. As described in Section 3.3.4, the west-vergent reverse Potrerillos Fault was responsible for uplift of the Potrerillos Anticline and deposition of syntectonic sediments in the Potrero Grande Formation in the footwall (Figure 3.10).

The geology of the Quebrada Honda range is still relatively poorly known. Although it difficult to determine the nature of Cenozoic deformation of the Quebrada Honda based on surface geology, our AFT ages and thermal models suggest that the range was uplifted and exhumed ~35–30 Ma. The contrast in AFT ages and thermal histories between samples from reverse fault hanging walls (AF20T01 and AF20T03) and footwalls (AF20T02) confirms the location of two major west-dipping faults mapped by previous studies (Adelmann, 2001; Kraemer et al., 1999; Palma et al., 1990; Schnurr et al., 2006; Seggiaro et al., 2007). The ~35 Ma uplift of the Quebrada Honda range agrees with previous studies inferring it as a source for the Eocene-Oligocene Quiñoas Formation (Kraemer et al., 1999; Zhou et al., 2017).

3.6 Four-phase Cenozoic deformation

Based on AFT data and geologic observations, we find evidence for four major episodes of Cenozoic deformation in the Antofalla region (Figure 3.18). Our four-phase sequence of deformation is similar to the prevailing conception proposed by Kraemer et al. (1999) and adds additional evidence for how Andean shortening was accommodated in the Antofalla region.

The initial episode Eocene to Early Oligocene shortening is documented mainly by AFT data. AFT ages ~50 to 30 Ma from the Calalaste range, ~40 Ma from Cerro Campo Negro, and ~35 to 30 Ma in the Quebrada Honda range reflect this period of deformation. Uplift of the Quebrada Honda range ~35–30 Ma agrees with the previous studies inferring it as a source for the Quiñoas Formation (Zhou et al., 2017). However, we show that other major ranges were also uplifting during this time. Coarse conglomerates near the base of the Lower Member of the Quiñoas Formation, interpreted as proximal alluvial fan deposits, were deposited on the western flank of the Calalaste range and can be correlated with more distal alluvial and fluvial conglomeratic sandstones at Cerro Campo Negro (e.g., Figure 3.9). Uplift of the Calalaste range may also be recorded by a package of coarse conglomeratic strata with a maximum depositional age of ~250 Ma that we map as unknown Mesozoic to Early Paleogene deposits (alternatively, these strata may have been deposited during the Mesozoic). A paleosol and subaerial unconformity observed at the top these deposits (Figure 3.5, Location D; Figure 3.8) and bracketed to ~35–29 Ma reflects a period of reduced sedimentation following this episode of regional shortening and uplift (Section 3.3.2). As discussed below, these observations point

toward the existence of a Paleogene broken foreland basin system, perhaps analogous to the modern Santa Barbara System and Northern Sierras Pampeanas in NW Argentina.

The second phase of deformation involved out-of-sequence shortening within the Andean orogen. This phase is documented by alluvial fan deposits, growth strata, and AFT data throughout the transect (Figure 3.18). AFT thermal history models suggest that significant cooling of the Calalaste Range, Antofalla Fault, Salina del Fraile, and Quebrada Honda range occurred during the 29 to 15 Ma period (Figure 3.18). While our AFT ages from the Calalaste range reflect the first phase of exhumation, thermal history models suggest that cooling occurred throughout the Cenozoic; models for sample AF20T05 suggest that major cooling of the Calalaste occurred prior to ~20 Ma (Figure 3.12). Carrapa et al. (2005) and Zhou et al. (2017) reported 29 to 20 Ma AFT ages from different portions of the Calalaste range (Figure 3.2), which we interpret to reflect this phase of deformation. Adelmann (2001) and Kraemer et al. (1999) inferred an episode of uplift that led to deposition of alluvial fan conglomerates in the Chacras Formation in the Calalaste Range (the upper portion of which we date to ~22 Ma using sample AF20T06, Table 3.1). Folding and faulting of these deposits may reflect this phase of deformation or a later one.

During ~24 to 15 Ma, shortening propagated westward from the Calalaste Range by exploiting east-dipping faults, including the series of faults on the western flank of the Calalaste Range, the Antofalla Fault, and the Potrerillos Fault. Westward propagation of shortening is mainly indicated by growth strata and syntectonic sediments, which provide evidence of deformation on individual structures. Alluvial fan deposits of the Chacras Formation in Vega Quiñoas and Vega Chacras indicate uplift of the Antofalla Fault ~24–22 Ma (Sections 3.3.3 and 3.3.4). Growth strata in the Potrero Grande Formation indicate deformation within the Salina del Fraile ~17–15 Ma (Section 3.3.4 and Figure 3.16). This westward propagation of deformation on east-dipping structures suggests the construction of a west-vergent wedge during the Late Oligocene to Early Miocene, which further fragmented the Antofalla Basin. Uplift on the Antofalla Fault produced a paleotopographic high, the Antofalla High, west of which the basin was filled with volcaniclastics of the Middle Miocene Potrero Grande Formation and later volcanic cover. In previous studies, this phase of deformation was interpreted as reflecting the incorporation of a Paleogene foreland basin system into the Puna Plateau (Carrapa et al., 2005; Kraemer et al., 1999). We return to this topic in .

The third phase of deformation involved extensional reactivation of the Antofalla Fault, creating a hanging-wall basin into which Late Miocene to Pliocene sediments of the Juncalito Formation were deposited (Figure 3.18). Additional arguments for this episode of transient extension are described by Tye et al. (2022), but our mapping and cross-sections support the formation of a half-graben structure as the best explanation for why the Juncalito Formation and later units were deposited at lower elevations than older units immediately to the west (Figures 3.4 and A.1). Existing volcanic ash geochronology for the Juncalito Formation constrains the initiation of half-graben extension to ~16–11 Ma (Adelmann, 2001; Kraemer et al.,

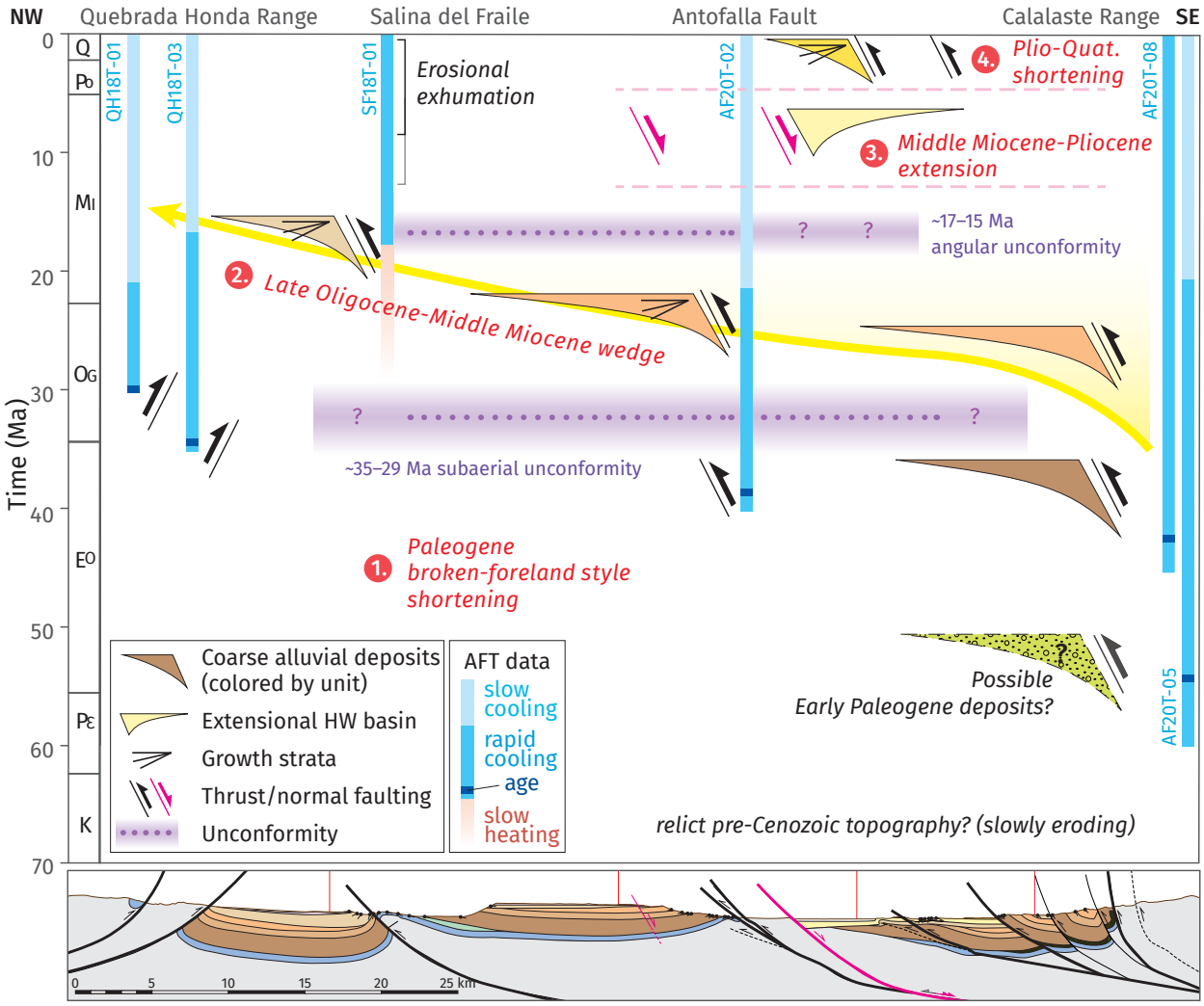

Figure 3.18: Summary of thermochronologic and geologic evidence for 4 phases of tectonic deformation in the Antofalla region along our transect. Blue bars summarize apatite fission track cooling histories of hanging wall rocks. Geologic evidence includes proximal alluvial deposition, growth strata, and unconformities. See Figure 3.4 for location and geologic legend.

1999). Extensional structures do not cut young volcanic flows along our transect; however, the same series of normal faults offsets the 3.6 Ma Vallecito ignimbrite sheet 50 km to the south, indicating that extension was active after that time (Adelmann, 2001; Kraemer et al., 1999). The inference that the Calalaste Range underwent ~E–W contraction during Quaternary to recent times (Section 3.3.2) implies that horizontal extension ceased in the region between 3.6 Ma and the present. Middle to Late Miocene extensional reactivation of the major Antofalla Fault provides a means of converting the Antofalla High, an inferred paleotopographic high and source region of the Oligo-Miocene Chacras Formation (Adelmann, 2001), into the topographic low occupied by the modern salt flat. Previous studies, which assumed that extension occurred only during the Quaternary (Adelmann, 2001; Kraemer et al., 1999), are unable to explain the conversion of the Antofalla High into the modern topographic low of Juncalito lacustrine basin, and ultimately the modern Salar de Antofalla.

The fourth phase of deformation involves a return to roughly E–W horizontal shortening within the Calalaste Range during the Pliocene to Quaternary (Figure 3.18). Contractional deformation is indicated by fault-propagation folds and detachment folds along the entire eastern margin of the Salar de Antofalla (Figure 3.5), which involve sediments dated to <5 Ma, and ashes as young as ~1 Ma (Tye et al., 2022). Shortening also resulted in deposition of coarse alluvial fan deposits of the Late Pliocene to Quaternary Escondida Formation. The spatial extent of these folds and sediments suggests that shortening is limited to the fault system comprising the western flank of the Calalaste range (Figure 3.4; Adelmann, 2001; Kraemer et al., 1999). That the Calalaste is currently undergoing shortening is supported by earthquake focal mechanisms, which show oblique thrust fault plane solutions (Figure 3.2; Mulcahy et al., 2014). Given that Oligocene to Miocene shortening established a west-vergent tectonic wedge in the study area, this most recent phase of shortening may reflect the re-establishment of taper in a smaller wedge after a drastic reduction in taper due to Miocene–Pliocene extension. Shortening uplifted and inverted the eastern portion of the extensional basin, producing the elongated sublinear geometry of the modern Salar de Antofalla (e.g., Figure 3.2).

3.7 Implications for formation and evolution of the Southern Puna Plateau

3.7.1 Mesozoic tectonic setting

The Mesozoic tectonic setting of the Southern Puna is somewhat enigmatic due a lack of geologic deposits. Our AFT data, however, do place some constraints on the exhumation of the landscape during this time. AFT ages and thermal history models of footwall rocks suggest that, outside of major structures, the landscape was exhumed approximately 150 to 100 Ma (Figures 3.14a and 3.17b). Detrital AFT ages from sample AF20T09 fall within the 250 to 150 Ma time period (Figure A.6e), reflecting Paleogene source terranes that were exhumed during

the Late Triassic to Early Cretaceous. Combined with the sparse sedimentary cover during Mesozoic extensional episodes, the Southern Puna may have been characterized as a region of relict topography following Paleozoic orogenesis. This idea is consistent with the Southern Puna's location on the uplifted shoulders of the continental Salta Rift system (the "Transpampean Arch"; DeCelles et al., 2011; Salfity & Marquillas, 1994) and the Triassic Domeyko Rift basin (Espinoza et al., 2019). While Cretaceous and Triassic AFT ages may reflect exhumation of the flanks of these rifts, we infer that the Southern Puna avoided significant extension and crustal thinning during the Mesozoic. We return to this idea in Section 3.7.3 in the context of crustal thickness.

3.7.2 Paleogene tectonic setting

Key questions remain concerning the development of high topography in the Central Andes and how tectonic shortening was accommodated within the Puna Plateau. One model for plateau formation invokes the development of an orogenic wedge and flexural foreland basin system (DeCelles et al., 2011; DeCelles et al., 2015b). Recent studies argue that the wedge deformation front was located in the Cordillera de Domeyko (west of the modern volcanic arc) in the late Cretaceous, propagated eastward in a series of jumps punctuated by periods of internal deformation (Carrapa & DeCelles, 2015; DeCelles et al., 2015b; Quade et al., 2015), and currently encompasses the Santa Barbara system and northern Sierras Pampeanas of the broken foreland region in NW Argentina (McFarland et al., 2017). A second model argues that plateau deformation was accomplished by unsteady shortening on widely-spaced reverse faults that accommodate pure shear deformation of the lithosphere (Allmendinger & Gubbels, 1996) by exploiting pre-existing structures such as Cretaceous normal faults or earlier compressional faults (e.g., Kley et al., 2005), perhaps aided by episodes of flat-slab subduction (Gianni et al., 2020). This style of shortening results in intermontane basins that become fragmented into isolated depocenters as intra-foreland ranges are uplifted (Iaffa et al., 2013; Mortimer et al., 2007). The geodynamics of a crustal-scale wedge, however, would produce a regional foreland basin system accommodated by lithospheric flexure (DeCelles & Giles, 1996). These two models are not necessarily mutually exclusive, as shortening within a heterogeneous orogenic wedge would presumably involve activation of existing structures and planes of weakness, including those in the basement.

DeCelles et al. (2011) argued that the growth of an orogenic wedge incorporating thick-skinned structures would involve the in-sequence uplift of basement-cored ranges within an established foreland basin system, producing wedge-top depocenters that become incorporated into a widening Puna Plateau. Under this model, deformation in the modern broken foreland region of NW Argentina represents a subcritical wedge and wedge-top basins (McFarland et al., 2017). Zhou et al. (2017) applied a similar concept to the Tertiary Southern Puna Plateau, suggesting that the region was incorporated into a thick-skinned wedge wherein deformation propagated west-to-east during the Late Oligocene to Middle Miocene. Eastward

propagation was evidenced by AFT exhumation ages of major ranges in the Southern Puna, from the Calalaste range in the west (~25 Ma) to the Laguna Blanca range in the east (~15 Ma). The wedge seemingly propagated into and incorporated a contiguous foreland basin system represented by the Eocene Geste Formation, Quiñoas Formation, and lateral equivalents, which would have been deposited as a result of the flexure generated by the wedge's orogenic load.

However, as we show in this paper, the basement of the Antofalla region, including the Quebrada Honda and Calalaste ranges and the Antofalla Uplift, was already being exhumed throughout the Eocene and Oligocene (~50 to 30 Ma), prior to and during the deposition of the Quiñoas Formation. Furthermore, the exhumation of these ranges did not propagate from west to east in the Antofalla Region (Figure 3.18). In fact, this period of Paleogene exhumation is similar to AFT ages from the Chango Real range on the SE margin of the plateau (Coutand et al., 2001), underscoring the conclusion that deformation occurred within a ~250 km wide region during the Paleogene. Paleoelevation proxies and paleoclimate indicators from the Quiñoas Formation have been used to argue that the Southern Puna was high and dry by the Late Eocene as a result of its incorporation into the orogenic wedge (Canavan et al., 2014; Quade et al., 2015). While our data support the interpretation of an intermontane or wedge-top depositional setting for the Quiñoas Formation, the paleoelevation data remain in dispute (Pingel et al., 2020). Our data could indicate either of the following: (1) the deformation front of a subcritical wedge was located at the Chango Real Range during the Eo-Oligocene, with widespread exhumation in the Antofalla region due to internal wedge deformation, or (2) the region is better characterized as a Paleogene broken foreland, where deformation and sedimentation were largely controlled by uplift on pre-existing weaknesses.

In broken foreland settings, sedimentation is controlled by the uplift and growth of basin-bounding ranges, leading to progressive fragmentation and isolation of the intermontane basins and the deposition of coarse alluvial and syntectonic sediments (Iaffa et al., 2013; Mortimer et al., 2007; Schoenbohm & Carrapa, 2015; Seagren et al., 2022). The Eocene to Middle Miocene Antofalla basin seems to reflect these same processes, especially when viewed in light of exhumation ages, dated growth strata, and syntectonic deposits that show that sedimentation occurred in a basin progressively fragmented by uplifting source regions (Figure 3.18). While we see evidence for a broken foreland-type setting for the Southern Puna during the Eocene to Middle Miocene, the two models for plateau deformation exist on a continuum defined by the relative influence of the orogenic wedge vs. pre-existing weaknesses in controlling uplift and sedimentation. More detailed sedimentological studies of the Quiñoas Formation (and lateral equivalents) are necessary to determine these influences.

3.7.3 Crustal thickness and lithospheric foundering

It has long been argued that additional factors besides Cenozoic upper-crustal shortening are necessary to explain the high elevation and thick crust of the Southern Puna (Allmendinger et al., 1997; Kley & Monaldi, 1998). Although the lack of information on fault dips and poor geologic

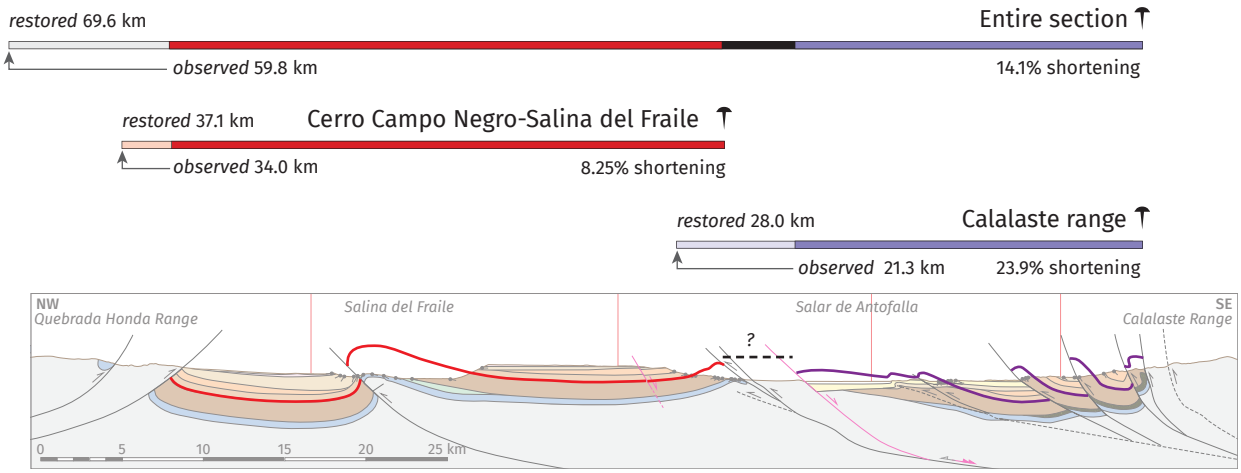

Figure 3.19: Illustration of estimation of shortening magnitude for our cross-section by restoring the upper contact of the Lower Member of the Quiñoas Formation. Purple lines represent shortening related to the Calalaste Range. Red represents shortening on structures west of Cerro Campo Negro. The deformed length of the contact (59.8 km) restores to a length of 69.9 km (14.1% contraction).

exposure throughout much of the study area makes estimating shortening magnitudes difficult, we conservatively estimate that the Antofalla region was shortened by approximately 14% (~10 km) during the Cenozoic, concentrated on the western flank of the Calalaste range (~24% shortening, Figure 3.19). This estimate of shortening is based on the observed deformation of the top of the Lower Member of the Quiñoas Formation (the earliest Cenozoic depositional unit) and assumes zero shortening where this contact is not exposed at Cerro Campo Negro. Although this is a minimum estimate, restoring even 15–25% contraction to the width of the modern Puna Plateau would imply only 50–90 km of Cenozoic shortening, much less than the 150–170 km (~40% contraction) expected from crustal thickness (Figure 3.1; Kley & Monaldi, 1998)).

There are several possible mechanisms that may have thickened the crust of the Southern Puna in the absence of sufficient upper-crustal shortening. Crustal duplexing or underthrusting beneath the plateau can increase crustal thickness without affecting upper-crustal strain (e.g., McQuarrie, 2002), as can magmatic addition (Perkins et al., 2016) and flow of lower crust from overthickened regions (Husson & Sempere, 2003). Another potential source of crustal thickness is provided by the inference, discussed above, that the Southern Puna did not experience significant extension during two episodes of major continental rifting in the Mesozoic. The Southern Puna was involved in multiple orogenic episodes during the Paleozoic, most likely leading to substantial crustal shortening and thickening (Ducea et al., 2015; Escayola et al., 2011; Lucassen et al., 2000; Lucassen et al., 2001). A portion of this pre-Cenozoic crustal shortening is preserved in Ordovician metamorphic rocks (e.g., the Cortaderas Chicas Volcano-Sedimentary Complex), which exhibit ~25–50% shortening (Henriquez et al., 2020). The Southern Puna, having escaped major crustal extension during the Mesozoic, may have retained a larger portion of its Paleozoic crustal thickness than surrounding regions. Combined with the magmatic ad-

dition reflected by the Southern Puna Magmatic Body (Bianchi et al., 2013; Ward et al., 2017), only a relatively low amount of Cenozoic shortening (such as the estimated 15–25%) may have been required to thicken the crust to ~60 km. In the absence of lithospheric strength or density gradients, shortening tends to concentrate along the margins of thickened crust in order to reduce gravitational potential energy contrasts (e.g., Molnar et al., 1998). This scenario, in which Cenozoic shortening increased the thickness of an already thickened crust, may therefore imply that the Puna's crust was significantly weaker than surrounding regions, perhaps due to its long-lived position in the Andean arc to back-arc and episodes flat-slab subduction (e.g., Allmendinger et al., 1997; Coira et al., 1993; Kay & Coira, 2009).

Crustal thickness changes have been tracked in volcanic arcs using trace element volcanic geochemistry, based on an observed relationship between Sr/Y and La/Yb with Moho depth (e.g., Chapman et al., 2015; Lieu & Stern, 2019). For example, Profeta et al. (2016) estimated that the crust in the Altiplano region was 40–55 km thick by 50 Ma. These or similar techniques could in theory be applied to the Southern Puna to test the hypothesis that the crust was >40 km thick at the end of the Mesozoic, but a dearth of volcanic rocks from the critical Paleocene-Paleogene time period would make this task difficult.

Lithospheric foundering may provide another source of crustal thickening. Foundering of the Southern Puna mantle lithosphere has been linked to horizontal extension and mafic back-arc volcanism (Kay & Kay, 1993; Kay et al., 1994; Schoenbohm & Carrapa, 2015; Zhou & Schoenbohm, 2015). Numerical models suggest that if lithospheric foundering occurs where the crust is relatively weak—as the Southern Puna crust seems to be, both compositionally (Lucassen et al., 2001) and thermally (Heit et al., 2014)—upper-crustal horizontal extension can occur at the same time as the lower crust is being thickened and dragged toward the downgoing lithosphere (Molnar, 2015; Neil & Houseman, 1999). Moreover, divergence of the upper crust above the center of the foundering lithosphere is accommodated by upper-crustal compression in the surrounding regions (Molnar, 2015). This pattern roughly matches the inferred kinematics of deformation in the Southern Puna during the Late Miocene (Tye et al., 2022), when the Antofalla region was undergoing horizontal extension, but surrounding regions such as Pasto Ventura were being shortened (Schoenbohm & Carrapa, 2015; Zhou & Schoenbohm, 2015). If lithospheric foundering occurred in the Southern Puna, therefore, it likely involved overall thickening of the weak, buoyant crust, even though the upper crust was in extension.

DeCelles et al. (2015b) incorporated both lithospheric foundering and wedge dynamics into the hypothesis that Andean orogenesis is driven by the buildup of dense lithospheric roots formed as a result of crustal shortening and magmatism, the removal of which increases gravitational potential energy and allows deformation to rapidly propagate eastward. If the Southern Puna lost its mantle lithosphere through gravitational foundering (e.g., Kay & Kay, 1993; Kay et al., 1994; Schoenbohm & Carrapa, 2015), we hypothesize that the out-of-sequence, west-vergent shortening that occurred during the Late Oligocene to Early Miocene (Figure 3.18),

may reflect the build-up of a dense lithospheric root beneath the Antofalla region. The localized Middle Miocene ~E–W extension in the Antofalla region may reflect the foundering of this root as a lithospheric drip. Further geodynamic modelling is necessary to explore this hypothesis for the Southern Puna Plateau.

3.8 Conclusions

We present geologic mapping, structural cross-sections, low-temperature temperature thermochronology results, and U-Pb dating of ash and detrital zircons to elucidate the history and style of orogenic deformation in the Antofalla region in the SW Puna Plateau. Cooling ages of major reverse fault hanging walls and dated growth strata indicate that crustal shortening began during the Early Eocene and continued through the Early Miocene. We argue that Eocene to Early Oligocene shortening was accommodated by deformation on widely-spaced reverse faults in a tectonic setting analogous to the broken foreland region of NW Argentina, while Oligocene to Middle Miocene shortening involved the construction of a west-vergent wedge within the Andean orogen. Oligocene to Middle Miocene shortening in this region largely propagated westward from the Calalaste range, potentially by exploiting steeply dipping heterogeneities in the basement, and constitutes a significant phase of out-of-sequence deformation. This protracted period of horizontal shortening, which resulted in the syn-tectonic filling of the Antofalla Basin, was followed by a transient episode of upper-crustal E–W extension on a major normal fault system. Pliocene to Quaternary time was characterized by a return to E–W shortening and coarse sedimentation proximal to the Calalaste range.

Our structural cross-section permits only a low magnitude of shortening (~15–25%), which stands in contrast to the ~60 km thick crust. Triassic to Cretaceous cooling ages from rocks that were not exhumed during Cenozoic shortening indicate that the entire region experienced little exhumation or sedimentation during the Mesozoic, perhaps retaining a crust thickened during multiple episodes of Paleozoic orogenesis. We speculate that lithospheric foundering and orogenic wedge propagation driven by gravitational potential energy gradients may have triggered the switch from horizontal compression to extension during the Middle to Late Miocene.

Acknowledgments, Samples, and Data

Support for this work was provided by an NSERC Discovery Grant and Discovery Accelerator Supplement to L. Schoenbohm. Structural measurements, zircon geochronology, and apatite-fission track analysis data are available in the supporting information (Tables A.1 to A.4) and accessible through the Scholars Portal Dataverse (https://doi.org/10.5683/SP3/XTFUJP).

References

Adelmann, D. (2001). *Känozoische Beckenentwicklung des zentralandinen Puna-Plateaus (NW-Argentinien): Das Gebiet um den Salar de Antofalla und ein Vergleich zur nördlichen Puna* (Doctoral dissertation). Freien Universität Berlin.

Allmendinger, R. W., & Gubbels, T. (1996). Pure and simple shear plateau uplift, Altiplano-Puna, Argentina and Bolivia. *Tectonophysics*, *259*(1-3), 1–13. https://doi.org/10.1016/0040-1951(96)00024-8

Allmendinger, R. W., Jordan, T. E., Kay, S. M., & Isacks, B. L. (1997). The evolution of the Altiplano-Puna Plateau of the Central Andes. *Annual Review of Earth and Planetary Sciences*, *25*, 139–174. https://doi.org/10.1146/annurev.earth.25.1.139

Amilibia, A., Sàbat, F., McClay, K. R., Muñoz, J. A., Roca, E., & Chong, G. (2008). The role of inherited tectono-sedimentary architecture in the development of the central Andean mountain belt: Insights from the Cordillera de Domeyko. *Journal of Structural Geology*, *30*(12), 1520–1539. https://doi.org/10.1016/j.jsg.2008.08.005

Bahlburg, H., Breitkreuz, C., Maletz, J., Moya, M. C., & Salfity, J. A. (1990). The Ordovician sedimentary rocks in the northern Puna of Argentina and Chile: New stratigraphical data based on graptolites. *Newsletters on Stratigraphy*, *23*(2), 69–89. https://doi.org/10.1127/nos/23/1990/69

Bianchi, M., Heit, B., Jakovlev, A., Yuan, X., Kay, S. M., Sandvol, E., Alonso, R. N., Coira, B., Brown, L. D., Kind, R., & Comte, D. (2013). Teleseismic tomography of the southern Puna plateau in Argentina and adjacent regions. *Tectonophysics*, *586*, 65–83. https://doi.org/10.1016/j.tecto.2012.11.016

Canavan, R. (2012). *Cenozoic paleoelevation reconstructions of the Puna Plateau, NW Argentina* (Doctoral dissertation). University of Wyoming.

Canavan, R. R., Carrapa, B., Clementz, M. T., Quade, J., DeCelles, P. G., & Schoenbohm, L. M. (2014). Early cenozoic uplift of the Puna plateau, central andes, based on stable isotope paleoaltimetry of hydrated volcanic glass. *Geology*, *42*(5), 447–450. https://doi.org/10.1130/G35239.1

Cardozo, N., & Allmendinger, R. W. (2013). Spherical projections with OSXStereonet. *Computers & Geosciences*, *51*, 193–205. https://doi.org/10.1016/j.cageo.2012.07.021

Carrapa, B., Adelmann, D., Hilley, G. E., Mortimer, E., Sobel, E. R., & Strecker, M. R. (2005). Oligocene range uplift and development of plateau morphology in the southern central Andes. *Tectonics*, *24*, TC4011. https://doi.org/10.1029/2004TC001762

Carrapa, B., & DeCelles, P. G. (2008). Eocene exhumation and basin development in the Puna of northwestern Argentina. *Tectonics*, *27*(1). https://doi.org/10.1029/2007TC002127

Carrapa, B., & DeCelles, P. G. (2015). Regional exhumation and kinematic history of the central Andes in response to cyclical orogenic processes. *Memoir of the Geological Society of America*, *212*, 201–213. https://doi.org/10.1130/2015.1212(11)

Carrapa, B., DeCelles, P. G., Reiners, P. W., Gehrels, G. E., & Sudo, M. (2009). Apatite triple dating and white mica40Ar/39Ar thermochronology of syntectonic detritus in the Central Andes: A multiphase tectonothermal history. *Geology*, *37*(5), 407–410. https://doi.org/10.1130/G25698A.1

Chapman, J. B., Ducea, M. N., DeCelles, P. G., & Profeta, L. (2015). Tracking changes in crustal thickness during orogenic evolution with Sr/Y: An example from the North American Cordillera. *Geology*, *43*(10), 919–922. https://doi.org/10.1130/G36996.1

Coira, B., Kay, S. M., & Viramonte, J. (1993). Upper Cenozoic magmatic evolution of the Argentine Puna–A model for changing subduction geometry. *International Geology Review*, *35*(8), 677–720. https://doi.org/10.1080/00206819309465552

Coutand, I., Cobbold, P. R., De Urreiztieta, M., Gautier, P., Chauvin, A., Gapais, D., Rossello, E. A., & López-Gamundí, O. (2001). Style and history of Andean deformation, Puna plateau, northwestern Argentina. *Tectonics*, *20*(2), 210–234. https://doi.org/10.1029/2000TC900031

DeCelles, P. G., Carrapa, B., Horton, B. K., & Gehrels, G. E. (2011). Cenozoic foreland basin system in the central Andes of northwestern Argentina: Implications for Andean geodynamics and modes of deformation. *Tectonics*, *30*, TC6013. https://doi.org/10.1029/2011TC002948

DeCelles, P. G., Carrapa, B., Horton, B. K., McNabb, J., Gehrels, G. E., & Boyd, J. (2015a). The Miocene Arizaro Basin, central Andean hinterland: Response to partial lithosphere removal? In *Geological Society of America Memoirs* (pp. 359–386). https://doi.org/10.1130/2015.1212(18)

DeCelles, P. G., Ducea, M. N., Kapp, P., & Zandt, G. (2009). Cyclicity in Cordilleran orogenic systems. *Nature Geoscience*, *2*(4), 251–257. https://doi.org/10.1038/ngeo469

DeCelles, P. G., & Giles, K. A. (1996). Foreland basin systems. *Basin Research*, *8*(2), 105–123. https://doi.org/10.1046/j.1365-2117.1996.01491.x

DeCelles, P. G., Zandt, G., Beck, S. L., Currie, C. A., Ducea, M. N., Kapp, P., Gehrels, G. E., Carrapa, B., Quade, J., & Schoenbohm, L. M. (2015b). Cyclical orogenic processes in the Cenozoic central Andes. In *Geological Society of America Memoirs* (pp. 459–490). https://doi.org/10.1130/2015.1212(22)

Donelick, R. A., O'Sullivan, P. B., & Ketcham, R. A. (2005). Apatite fission-track analysis. *Reviews in Mineralogy and Geochemistry*, *58*, 49–94. https://doi.org/10.2138/rmg.2005.58.3

Ducea, M. N., Otamendi, J. E., Bergantz, G. W., Jianu, D., & Petrescu, L. (2015). The origin and petrologic evolution of the Ordovician Famatinian-Puna arc. *Memoir of the Geological Society of America*, *212*(07), 125–138. https://doi.org/10.1130/2015.1212(07)

Escayola, M. P., van Staal, C. R., & Davis, W. J. (2011). The age and tectonic setting of the Puncoviscana Formation in northwestern Argentina: An accretionary complex related to Early Cambrian closure of the Puncoviscana Ocean and accretion of the Arequipa-Antofalla block. *Journal of South American Earth Sciences*, *32*(4), 438–459. https://doi.org/10.1016/j.jsames.2011.04.013

Espinoza, M., Montecino, D., Oliveros, V., Astudillo, N., Vásquez, P., Reyes, R., Celis, C., González, R., Contreras, J., Creixell, C., & Martínez, A. (2019). The synrift phase of the early Domeyko Basin (Triassic, northern Chile): Sedimentary, volcanic, and tectonic interplay in the evolution of an ancient subduction-related rift basin. *Basin Research*, *31*(1), 4–32. https://doi.org/10.1111/bre.12305

Gallagher, K. (2012). Transdimensional inverse thermal history modeling for quantitative thermochronology. *Journal of Geophysical Research: Solid Earth*, *117*(2), 1–16. https://doi.org/10.1029/2011JB008825

Gallagher, K. (2021). Comment on "Discussion: Extracting thermal history from low temperature thermochronology/A comment on the recent exchanges between Vermeesch and Tian and Gallagher and Ketcham", by Paul Green and Ian Duddy, Earth Science Reviews, https://doi.org/10.1016/j. *Earth-Science Reviews*, (40). https://doi.org/10.1016/j.earscirev.2021.103549

Gallagher, K., & Ketcham, R. A. (2018). Comment on "Thermal history modelling: HeFTy vs. QTQt" by Vermeesch and Tian, Earth-Science Reviews (2014), 139, 279–290. *Earth-Science Reviews*, *176*(March 2017), 387–394. https://doi.org/10.1016/j.earscirev.2017.11.001

García, P. E., & Davis, G. H. (2004). Evidence and mechanisms for folding of granite, Sierra de Hualfín basement-cored uplift, Northwest Argentina. *AAPG Bulletin*, *88*(9), 1255–1276. https://doi.org/10.1306/04290403092

García-López, D. A., & Babot, M. J. (2015). Notoungulate faunas of north-western Argentina: New findings of early-diverging forms from the Eocene Geste Formation. *Journal of Systematic Palaeontology*, *13*(7), 557–579. https://doi.org/10.1080/14772019.2014.930527

Garzione, C. N., McQuarrie, N., Perez, N. D., Ehlers, T. A., Beck, S. L., Kar, N., Eichelberger, N., Chapman, A. D., Ward, K. M., Ducea, M. N., Lease, R. O., Poulsen, C. J., Wagner, L. S., Saylor, J. E., Zandt, G., & Horton, B. K. (2017). Tectonic evolution of the Central Andean Plateau and implications for the growth of plateaus. *Annual Review of Earth and Planetary Sciences*, *45*, 529–559. https://doi.org/10.1146/annurev-earth-063016-020612

Gianni, G. M., García, H. P., Pesce, A., Lupari, M., González, M., & Giambiagi, L. (2020). Oligocene to present shallow subduction beneath the southern Puna plateau. *Tectonophysics*, *780*, 228402. https://doi.org/10.1016/j.tecto.2020.228402

Gleadow, A. J., & Duddy, I. R. (1981). A natural long-term track annealing experiment for apatite. *Nuclear Tracks*, *5*(1-2), 169–174. https://doi.org/10.1016/0191-278X(81)90039-1

Gleadow, A., Harrison, M., Kohn, B., Lugo-Zazueta, R., & Phillips, D. (2015). The Fish Canyon Tuff: A new look at an old low-temperature thermochronology standard. *Earth and Planetary Science Letters*, *424*, 95–108. https://doi.org/10.1016/j.epsl.2015.05.003

Gleadow, A. J., Belton, D. X., Kohn, B. P., & Brown, R. W. (2002). Fission track dating of phosphate minerals and the thermochronology of apatite. *Reviews in Mineralogy and Geochemistry*, *48*(1), 579–630. https://doi.org/10.2138/rmg.2002.48.16

Gleadow, A. J., Gleadow, S. J., Belton, D. X., Kohn, B. P., Krochmal, M. S., & Brown, R. W. (2009). Coincidence mapping - A key strategy for the automatic counting of fission tracks in natural minerals. *Geological Society Special Publication*, *324*(2005), 25–36. https://doi.org/10.1144/SP324.2

González, J., Oliveros, V., Creixell, C., Velásquez, R., Vásquez, P., & Lucassen, F. (2018). The Triassic magmatism and its relation with the Pre-Andean tectonic evolution: Geochemical and petrographic constrains from the High Andes of north central Chile (29°30' – 30°S). *Journal of South American Earth Sciences*, *87*, 95–112. https://doi.org/10.1016/j.jsames.2017.12.009

Green, P., & Duddy, I. (2020). Discussion: Extracting thermal history from low temperature thermochronology. A comment on recent exchanges between Vermeesch and Tian and Gallagher and Ketcham. *Earth-Science Reviews*, (September 2019), 103197. https://doi.org/10.1016/j.earscirev.2020.103197

Grier, M. E., Salfity, J. A., & Allmendinger, R. W. (1991). Andean reactivation of the Cretaceous Salta rift, northwestern Argentina. *Journal of South American Earth Sciences*, *4*(4), 351–372.

Hasebe, N., Barbarand, J., Jarvis, K., Carter, A., & Hurford, A. J. (2004). Apatite fission-track chronometry using laser ablation ICP-MS. *Chemical Geology*, *207*(3-4), 135–145. https://doi.org/10.1016/j.chemgeo.2004.01.007

Heit, B., Bianchi, M., Yuan, X., Kay, S. M., Sandvol, E., Kumar, P., Kind, R., Alonso, R. N., Brown, L. D., & Comte, D. (2014). Structure of the crust and the lithosphere beneath the southern Puna plateau from teleseismic receiver functions. *Earth and Planetary Science Letters*, *385*, 1–11. https://doi.org/10.1016/j.epsl.2013.10.017

Henriquez, S., DeCelles, P. G., Carrapa, B., Hughes, A., Davis, G. H., & Alvarado, P. (2020). Deformation history of the Puna plateau, Central Andes of northwestern Argentina. *Journal of Structural Geology*, 104133. https://doi.org/10.1016/j.jsg.2020.104133

Husson, L., & Sempere, T. (2003). Thickening the Altiplano crust by gravity-driven crustal channel flow. *Geophysical Research Letters*, *30*(5), 1–4. https://doi.org/10.1029/2002gl016877

Iaffa, D. N., Sàbat, F., Muñoz, J. A., & Carrera, N. (2013). Basin fragmentation controlled by tectonic inversion and basement uplift in Sierras Pampeanas and Santa Bérbara system, northwest Argentina. *Geological Society Special Publication*, *377*(1), 101–117. https://doi.org/10.1144/SP377.13

Isacks, B. L. (1988). Uplift of the central Andean Plateau and bending of the Bolivian Orocline. *Journal of Geophysical Research*, *93*(B4), 3211–3231. https://doi.org/10.1029/JB093iB04p03211

Kay, R. W., & Kay, S. M. (1993). Delamination and delamination magmatism. *Tectonophysics*, *219*(1-3), 177–189. https://doi.org/10.1016/0040-1951(93)90295-U

Kay, S. M., & Coira, B. L. (2009). Shallowing and steepening subduction zones, continental lithospheric loss, magmatism, and crustal fl ow under the Central Andean Altiplano-

Puna Plateau. *Geological Society of America Memoir*, *204*, 229–259. https://doi.org/10.1130/2009.1204(11)

Kay, S. M., Coira, B., & Mpodozis, C. (2008). Field trip guide: Neogene evolution of the central Andean Puna plateau and southern Central Volcanic Zone. *GSA Field Guides*, *13*(September 2015), 117–181. https://doi.org/10.1130/2008.0013(05)

Kay, S. M., Coira, B., & Viramonte, J. (1994). Young mafic back arc volcanic rocks as indicators of continental lithospheric delamination beneath the Argentine Puna Plateau, central Andes. *Journal of Geophysical Research: Solid Earth*, *99*(B12), 24323–24339. https://doi.org/10.1029/94JB00896

Ketcham, R. A. (2005). Forward and inverse modeling of low-temperature thermochronometry data. *Reviews in Mineralogy and Geochemistry*, *58*, 275–314. https://doi.org/10.2138/rmg.2005.58.11

Ketcham, R. A., Carter, A., Donelick, R. A., Barbarand, J., & Hurford, A. J. (2007). Improved modeling of fission-track annealing in apatite. *American Mineralogist*, *92*(5-6), 799–810. https://doi.org/10.2138/am.2007.2281

Kley, J., & Monaldi, C. R. (1998). Tectonic shortening and crustal thickness in the Central Andes: How good is the correlation-? *Geology*, *26*(8), 723–726. https://doi.org/10.1130/0091-7613(1998)026<0723:TSACTI>2.3.CO;2

Kley, J., Rossello, E. A., Monaldi, C. R., & Habighorst, B. (2005). Seismic and field evidence for selective inversion of Cretaceous normal faults, Salta rift, northwest Argentina. *Tectonophysics*, *399*(1-4 SPEC. ISS.), 155–172. https://doi.org/10.1016/j.tecto.2004.12.020

Kraemer, B., Adelmann, D., Alten, M., Schnurr, W., Erpenstein, K., Kiefer, E., Van Den Bogaard, P., & Görler, K. (1999). Incorporation of the Paleogene foreland into the Neogene Puna plateau: The Salar de Antofalla area, NW Argentina. *Journal of South American Earth Sciences*, *12*(2), 157–182. https://doi.org/10.1016/S0895-9811(99)00012-7

Lieu, W. K., & Stern, R. J. (2019). The robustness of Sr/Y and La/Yb as proxies for crust thickness in modern arcs. *Geosphere*, *15*(3), 621–641. https://doi.org/10.1130/GES01667.1

Lucassen, F., Becchio, R., Wilke, H. G., Franz, G., Thirlwall, M. F., Viramonte, J., & Wemmer, K. (2000). *Proterozoic-Paleozoic development of the basement of the Central Andes (18-26° S): A mobile belt of the South American craton* (tech. rep.).

Lucassen, F., Becchio, R., Harmon, R., Kasemann, S., Franz, G., Trumbull, R., Wilke, H. G., Romer, R. L., & Dulski, P. (2001). Composition and density model of the continental crust at an active continental margin - The Central Andes between 21° and 27°S. *Tectonophysics*, *341*(1-4), 195–223. https://doi.org/10.1016/S0040-1951(01)00188-3

Ludwig, K. (2003). User's manual for isoplot 3.00, a geochronlogical toolkit for Microsoft Excel. *Berkeley Geochronology Center Special Publication*, *4*.

Ludwig, K., & Mundil, R. (2002). Extracting reliable U-Pb ages and errors from complex populations of zircons from Phanerozoic tuffs. *Goldschmidt Conference Abstracts*, A463.

Marquillas, R. A., del Papa, C., & Sabino, I. F. (2005). Sedimentary aspects and paleoenvironmental evolution of a rift basin: Salta Group (Cretaceous-Paleogene), northwestern Argentina. *International Journal of Earth Sciences*, *94*(1), 94–113. https://doi.org/10.1007/s00531-004-0443-2

McDannell, K. T., Issler, D. R., & O'Sullivan, P. B. (2019). Radiation-enhanced fission track annealing revisited and consequences for apatite thermochronometry. *Geochimica et Cosmochimica Acta*, *252*, 213–239. https://doi.org/10.1016/j.gca.2019.03.006

McFarland, P. K., Bennett, R. A., Alvarado, P., & DeCelles, P. G. (2017). Rapid Geodetic Shortening Across the Eastern Cordillera of NW Argentina Observed by the Puna-Andes GPS Array. *Journal of Geophysical Research: Solid Earth*, *122*(10), 8600–8623. https://doi.org/10.1002/2017JB014739

McMillan, M., Tye, A. R., Schoenbohm, L. M., McMillan, M. F., & Zhou, R. (in review). Eocene to Quaternary deformation of the Southern Puna Plateau: Thermochronology, geochronology, and structural geology of an Andean hinterland basin (NW Argentina). *Tectonics*.

McMillan, M., & Schoenbohm, L. M. (2020). Large-scale Cenozoic wind erosion in the Puna Plateau: The Salina del Fraile Depression. *Journal of Geophysical Research: Earth Surface*. https://doi.org/10.1029/2020JF005682

McQuarrie, N. (2002). The kinematic history of the central Andean fold-thrust belt, Bolivia: Implications for building a high plateau. *Bulletin of the Geological Society of America*, *114*(8), 950–963. https://doi.org/10.1130/0016-7606(2002)114<0950:TKHOTC>2.0.CO;2

Molnar, P. (2015). Gravitational instability of mantle lithosphere and core complexes. *Tectonics*, *34*(3), 478–487. https://doi.org/10.1002/2014TC003808

Molnar, P., Houseman, G. A., & Conrad, C. P. (1998). Rayleigh-Taylor instability and convective thinning of mechanically thickened lithosphere: Effects of non-linear viscosity decreasing exponentially with depth and of horizontal shortening of the layer. *Geophysical Journal International*, *133*, 568–584.

Mon, R., & Hongn, F. (1991). The structure of the Precambrian and Lower Paleozoic basement of the Central Andes between 22° and 32° S. Lat. *Geologische Rundschau*, *80*(3), 745–758. https://doi.org/10.1007/BF01803699

Mortimer, E., Carrapa, B., Coutand, I., Schoenbohm, L. M., Sobel, E. R., Gomez, J. S., & Strecker, M. R. (2007). Fragmentation of a foreland basin in response to out-of-sequence basement uplifts and structural reactivation: El Cajón - Campo del Arenal basin, NW Argentina. *Bulletin of the Geological Society of America*, *119*(5-6), 637–653. https://doi.org/10.1130/B25884.1

Mulcahy, P., Chen, C., Kay, S. M., Brown, L. D., Isacks, B. L., Sandvol, E., Heit, B., Yuan, X., & Coira, B. L. (2014). Central Andean mantle and crustal seismicity beneath the Southern Puna plateau and the northern margin of the Chilean-Pampean flat slab. *Tectonics*, *33*(8), 1636–1658. https://doi.org/10.1002/2013TC003393

Neil, E. A., & Houseman, G. A. (1999). Rayleigh-Taylor instability of the upper mantle and its role in intraplate orogeny. *Geophysical Journal International*, *138*(1), 89–107. https://doi.org/10.1046/j.1365-246X.1999.00841.x

Niemeyer, H., Götze, J., Sanhueza, M., & Portilla, C. (2018). The Ordovician magmatic arc in the northern Chile-Argentina Andes between 21° and 26° south latitude. *Journal of South American Earth Sciences*, *81*, 202–214. https://doi.org/10.1016/j.jsames.2017.11.016

Palma, M. A., Brisson, I., & Vujovich, G. (1990). Geológia del bloque de la Quebrada Honda , Puna Cartamarqueña. *Asociacion Geologica Aregentina, Revista*, *45*(1-2), 145–158.

Perkins, J. P., Ward, K. M., De Silva, S. L., Zandt, G., Beck, S. L., & Finnegan, N. J. (2016). Surface uplift in the Central Andes driven by growth of the Altiplano Puna Magma Body. *Nature Communications*, *7*, 1–10. https://doi.org/10.1038/ncomms13185

Pingel, H., Strecker, M. R., Mulch, A., Alonso, R. N., Cottle, J., & Rohrmann, A. (2020). Late Cenozoic topographic evolution of the Eastern Cordillera and Puna Plateau margin in the southern Central Andes (NW Argentina). *Earth and Planetary Science Letters*, *535*, 116112. https://doi.org/10.1016/j.epsl.2020.116112

Profeta, L., Ducea, M. N., Chapman, J. B., Paterson, S. R., Gonzales, S. M. H., Kirsch, M., Petrescu, L., & DeCelles, P. G. (2016). Quantifying crustal thickness over time in magmatic arcs. *Scientific reports*, *5*, 17786. https://doi.org/10.1038/srep17786

Quade, J., Dettinger, M. P., Carrapa, B., DeCelles, P. G., Murray, K. E., Huntington, K. W., Cartwright, A., Canavan, R. R., Gehrels, G. E., & Clementz, M. (2015). The growth of the central Andes, 22° S-26° S. In *Geological Society of America Memoirs* (pp. 277–308).

Reijs, J., & McClay, K. (2003). The Salina del Fraile pull-apart basin, northwest Argentina. *Intraplate Strike-Slip Deformation Belts*, *210*, 197–209. https://doi.org/10.1144/Gsl.Sp.2003.210.01.12

Richards, J. P., Ullrich, T., & Kerrich, R. (2006). The Late Miocene-Quaternary Antofalla volcanic complex, southern Puna, NW Argentina: Protracted history, diverse petrology, and economic potential. *Journal of Volcanology and Geothermal Research*, *152*(3-4), 197–239. https://doi.org/10.1016/j.jvolgeores.2005.10.006

Risse, A., Trumbull, R. B., Coira, B., Kay, S. M., & van den Bogaard, P. (2008). 40Ar/39Ar geochronology of mafic volcanism in the back-arc region of the southern Puna plateau, Argentina. *Journal of South American Earth Sciences*, *26*(1), 1–15. https://doi.org/10.1016/j.jsames.2008.03.002

Salfity, J. A., & Marquillas, R. A. (1994). Tectonic and sedimentary evolution of the Cretaceous-Eocene Salta Group Basin, Argentina. In *Cretaceous tectonics of the andes* (pp. 266–315).

Schnurr, W. B. W., Risse, A., Trumbull, R. B., & Munier, K. (2006). Digital Geological Map of the Southern and Central Puna Plateau, NW Argentina. In *The andes* (pp. 563–564). https://doi.org/10.1007/978-3-540-48684-8_29

Schoenbohm, L. M., & Carrapa, B. (2015). Miocene-Pliocene shortening, extension, and mafic magmatism support small-scale lithospheric foundering in the central Andes, NW Argentina. *Geological Society of America Memoirs*, *212*(09), 167–180. https://doi.org/10.1130/2015.1212(09)

Schurr, B., Rietbrock, A., Asch, G., Kind, R., & Oncken, O. (2006). Evidence for lithospheric detachment in the central Andes from local earthquake tomography. *Tectonophysics*, *415*(1-4), 203–223. https://doi.org/10.1016/j.tecto.2005.12.007

Seagren, E. G., McMillan, M., & Schoenbohm, L. M. (2022). Tectonic control on drainage evolution in broken forelands: Examples from NW Argentina. *Tectonics*, *41*(1), e2020TC006536. https://doi.org/https://doi.org/10.1029/2020TC006536

Seggiaro, R., Becchio, R., Pereyra, F., & Martínez, L. (2007). *Hoja Geológica 2569-IV, Antofalla*. Servicio Geológico Minero Argentino.

Seiler, C., Gleadow, A. J., & Kohn, B. P. (2013). Apatite fission track dating by LA-ICP-MS and External Detector Method: How do they stack up? *American Geophysical Union, Fall Meeting 2013*, abstract #T42C–07.

Sharman, G. R., Sharman, J. P., & Sylvester, Z. (2018). detritalPy: A Python-based toolset for visualizing and analysing detrital geo-thermochronologic data. *The Depositional Record*, *4*(2), 202–215. https://doi.org/10.1002/dep2.45

Stalder, N. F., Herman, F., Fellin, M. G., Coutand, I., Aguilar, G., Reiners, P. W., & Fox, M. (2020). The relationships between tectonics, climate and exhumation in the Central Andes (18–36°S): Evidence from low-temperature thermochronology. *Earth-Science Reviews*, *210*(October 2019), 103276. https://doi.org/10.1016/j.earscirev.2020.103276

Suzaño, N. O., Sola, A. M., Palacios, J. E., Becchio, R. A., Ortiz, A., Nieves, A. A., & Quiroga, M. F. (2017). Magmatismo plutónico del Paleozoico Inferior de Salta y Jujuy. *Relatorio XX Congreso Geológico Argentino*, 323–351.

Tassara, A., & Echaurren, A. (2012). Anatomy of the Andean subduction zone: Three-dimensional density model upgraded and compared against global-scale models. *Geophysical Journal International*, *189*(1), 161–168. https://doi.org/10.1111/j.1365-246X.2012.05397.x

Tassara, A., Götze, H. J., Schmidt, S., & Hackney, R. (2006). Three-dimensional density model of the Nazca plate and the Andean continental margin. *Journal of Geophysical Research: Solid Earth*, *111*(9), 1–26. https://doi.org/10.1029/2005JB003976

Tye, A. R., McMillan, M., Schoenbohm, L. M., & Zhou, R. (2022). Late Cenozoic extensional formation of the Antofalla depression, southern Puna plateau, Argentina: An effect of lithospheric foundering? *Tectonics*.

Vermeesch, P. (2021). On the treatment of discordant detrital zircon U-Pb data. *Geochronology Discussions*, 1–19.

Vermeesch, P., & Tian, Y. (2014). Thermal history modelling: HeFTy vs. QTQt. *Earth-Science Reviews*, *139*, 279–290. https://doi.org/10.1016/j.earscirev.2014.09.010

Voss, R. (2002). Cenozoic stratigraphy of the southern Salar de Antofalla region, northwestern Argentina. *Andean Geology*, *29*(2), 167189. https://doi.org/10.4067/S0716-02082002000200002

Ward, K. M., Delph, J. R., Zandt, G., Beck, S. L., & Ducea, M. N. (2017). Magmatic evolution of a Cordilleran flare-up and its role in the creation of silicic crust. *Scientific Reports*, *7*(1), 1–8. https://doi.org/10.1038/s41598-017-09015-5

Zhou, R., Aitchison, J. C., Lokho, K., Sobel, E. R., Feng, Y., & Zhao, J.-x. (2020). Unroofing the Ladakh Batholith: constraints from autochthonous molasse of the Indus Basin, NW Himalaya. *Journal of the Geological Society*, *177*, 818–825. https://doi.org/10.1144/jgs2019-188

Zhou, R., & Schoenbohm, L. M. (2015). Late Miocene upper-crustal deformation within the interior of the southern Puna Plateau, central Andes. *Lithosphere*, *7*(3), 336–352. https://doi.org/10.1130/L396.1

Zhou, R., Schoenbohm, L. M., Sobel, E. R., Carrapa, B., & Davis, D. W. (2016). Sedimentary record of regional deformation and dynamics of the thick-skinned southern Puna Plateau, central Andes (26-27°S). *Earth and Planetary Science Letters*, *433*, 317–325. https://doi.org/10.1016/j.epsl.2015.11.012

Zhou, R., Schoenbohm, L. M., Sobel, E. R., Davis, D. W., & Glodny, J. (2017). New constraints on orogenic models of the southern Central Andean Plateau: Cenozoic basin evolution and bedrock exhumation. *Bulletin of the Geological Society of America*, *129*(1-2), 152–170. https://doi.org/10.1130/B31384.1

Zimmermann, U., & Bahlburg, H. (2003). Provenance analysis and tectonic setting of the Ordovician clastic deposits in the southern Puna Basin, NW Argentina. *Sedimentology*, *50*(6), 1079–1104. https://doi.org/10.1046/j.1365-3091.2003.00595.x

Zimmermann, U., Bahlburg, H., Mezger, K., Berndt, J., & Kay, S. M. (2014). Origin and age of ultramafic rocks and gabbros in the southern Puna of Argentina: An alleged Ordovician suture revisited. *International Journal of Earth Sciences*, *103*(4), 1023–1036. https://doi.org/10.1007/s00531-014-1020-y

4 Two styles of lithospheric dripping

Synthesizing gravitational instability models, continental tectonics, and geologic observations*

Abstract

Density instabilities in the lithosphere gravitationally founder in the form of Rayleigh–Taylor instabilities, or lithospheric drips, a concept that has been invoked across the globe to explain anomalous or conspicuous geological observations. In recent years, as geophysical data have increased in quality and quantity, the number of proposed drips has grown concomitantly. The ubiquity and inferred consequences of these drips, if confirmed, would demand a shift in our understanding of continental tectonics from a paradigm dominated by oceanic plate subduction to one in which the continental lithosphere plays a significant role in crustal deformation. The increasing availability of relevant geophysical datasets, numerical modelling studies, and geologic observations over the last few decades provides an opportunity for a comprehensive, up-to-date synthesis of our current understanding of where, how, and in what form lithospheric drips occur. Here we present a review and analysis of all lithospheric dripping events proposed in the literature to date, to the best of our knowledge. We first synthesize a broad range of mathematical, numerical, and scaled analogue model experiments to show that the crustal and topographic deformation resulting from drips displays two distinct styles. We describe these styles and how their occurrence largely depends on the strength and buoyancy of the crust relative to the mantle lithosphere. In light of this result, we then analyze the evidence for each dripping event proposed in existing literature, including drip size, drip depth, timing of detachment, and any associated volcanism, upper crustal deformation, and topographic deflection. We find 26 events for which lithospheric dripping is a key hypothesis, including 9 with clear evidence for strong-crust dripping, and 3 with clear evidence of weak-crust dripping. We next synthesize these data to compare and contrast the proposed dripping events in terms of tectonic setting, timing, size, and the main lines of evidence associated with each event. Finally, we identify emerging research methods with potential for identifying drips

*This chapter has been prepared for submission to *Geochemistry, Geophysics, Geosystems*.
Citation: McMillan, M., & Schoenbohm, L. M. (in prep.). Two styles of lithospheric dripping: Synthesizing gravitational instability models, continental tectonics, and geologic observations. *Geochemistry, Geophysics, Geosystems*.
Supplementary material is available in Appendix B.

in the geologic and geophysical record, and we consider implications for future research on this topic.

4.1 Introduction

Lithospheric dripping is a gravitational instability that results in the piecemeal removal of the mantle lithosphere and possibly lower crust. Lithospheric dripping has been proposed as an explanation for patterns of crustal strain, volcanism, and sedimentation in many locations (Figure 4.1) and may profoundly influence the evolution of Earth's continents (e.g., DeCelles et al., 2009; Jull & Kelemen, 2001). In continental arcs, extensional regions, or regions affected by plumes, removal of the ultramafic layer generated during the evolution of silicic magmas from basaltic melts may explain the bulk composition of the crust as well as the sharp Moho often observed in seismic data, which indicates a lithologic break between mafic lower crust and ultramafic mantle (Jull & Kelemen, 2001). In Cordilleran orogens, the buildup and removal of dense mantle lithosphere and lower crust is associated with magmatic flareups and cyclical propagation of orogenic shortening into the foreland (DeCelles et al., 2009; Paterson & Ducea, 2015). The lithospheric dripping hypothesis has also been invoked to explain the formation and inversion of sedimentary basins located in orogenic hinterlands in the Andes (DeCelles et al., 2015b), Tibet (Kapp & DeCelles, 2019), and the western U.S. (Smith et al., 2017), as well as the eruption of some continental flood basalts (Furman et al., 2016; Hales et al., 2005; Mori et al., 2009).

Lithosphere may be actively foundering today beneath the southern Sierra Nevada range (e.g., Zandt et al., 2004), the Colorado Plateau (Levander et al., 2011), the SE Carpathians (Lorinczi & Houseman, 2009), and the Hindu Kush (Molnar & Bendick, 2019). The latter two locations experience active seismicity in the mantle that may be a direct result of lithospheric dripping. The Vrancea seismic zone beneath the SE Carpathians is capable of generating destructive earthquakes, including the 1940, 7.7 M_w, event near Bucharest and an 1802 event (estimated 7.5–7.9 M_w) that destroyed nearby cities and damaged structures as far away as Moscow (Constantin et al., 2011). In addition to potentially operating during the present, lithospheric dripping may have played a role in the formation of early Archean cratons (e.g., Gorczyk et al., 2013; Rapp & Watson, 1995; Wiemer et al., 2018). The concept of lithospheric dripping is not limited to Earth and has been hypothesized for Venus, where some circular tectonic provinces known as Coronae may have formed as a result of lithospheric dripping (Elkins-Tanton, 2007; Hoogenboom & Houseman, 2006; Piskorz et al., 2014). Identifying and characterizing lithospheric drips, including ones that may be currently active, is therefore key to understanding Earth's continental tectonics throughout geologic time.

The strongest cases for dripping can be made when geophysical observations of the subsurface such as seismic tomography are combined with geologic constraints, such as sedimentation and volcanism. Both lines of inquiry, however, often prove to be equivocal in interpretation.

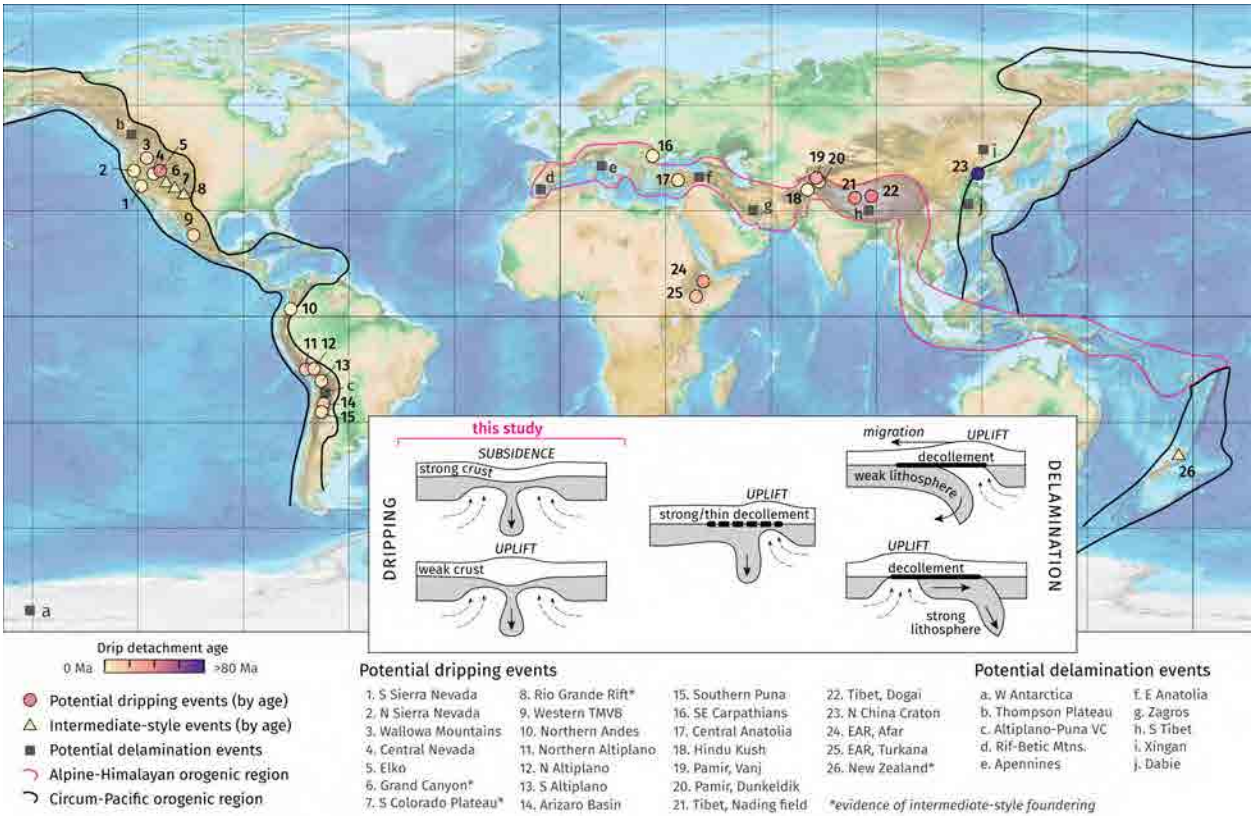

Figure 4.1: Map of the 26 potential lithospheric dripping events discussed in this paper, 10 potential delamination events (a–j), and major orogenic regions from Dickinson (2004). Inset: Range of foundering mechanisms, including dripping and delamination end-members (after DeCelles et al., 2015b) and intermediate styles (Beall et al., 2017). Basemap modified from ETOPO1 global relief model (https://doi.org/10.7289/V5C8276M).

Some aspects of seismic tomographic imaging noted by Foulger et al. (2013) are especially relevant to investigating the dripping hypothesis. For example, approximately equal portions of negative and positive anomalies can be expected when the mean anomaly is constrained to be zero, and "depth leakage" can cause anomalies to be smeared vertically (Foulger et al., 2013). Weak anomalies, such as may be expected for smaller drips, could be misidentified as or mistaken for anisotropies in the upper mantle (Foulger et al., 2013). Nevertheless, tomographic anomalies in the upper mantle are often interpreted as lithospheric drips. Geologic observations that may shed light on lithospheric dripping include continental volcanism (often potassic or adikitic in composition), surface uplift and subsidence patterns, and sedimentary basin development. Of course, such phenomena are commonly caused by processes other than lithospheric drips, and the factors that distinguish one cause from another may be subtle at best. Lithospheric dripping is often invoked as a geodynamic hypothesis only when observations cannot be readily explained by more ordinary tectonic processes such as orogenic wedge dynamics (e.g. during the Late Cenozoic in the Puna Plateau; Schoenbohm & Carrapa, 2015), or

when multiple lines of inquiry provide independent support to the dripping hypothesis (e.g., mantle xenoliths, volcanism, and tomographic anomalies; Dygert et al., 2019).

Numerical and analogue modelling experiments of lithospheric dripping provide a powerful method for formulating and refining hypotheses related to lithospheric dripping, especially when combined with geologic and geophysical observations. Even though these studies consistently show that lithospheric drips can have widely differing, but predictable, effects on upper-crustal strain, surface topography, and volcanism (e.g., Neil & Houseman, 1999; Wang & Currie, 2015, 2017; Wang et al., 2015), this result remains underutilized by the broader community.

Despite the importance of lithospheric dripping as a geologic concept, the community lacks a framework for comparing the evidence for lithospheric dripping events in different parts of the world. In this paper, we develop such a framework and apply it to each location for which lithospheric dripping has been proposed. To do this, we first review the understanding of lithospheric dripping in terms of the Rayleigh Taylor (R–T) instability, including its expected temporal scale (Section 4.2.1) and characteristic spatial scale (Section 4.2.2). We then synthesize models of lithospheric dripping to suggest that two distinct types of lithospheric dripping may occur (Section 4.2.3). These types largely depend on the relative strength of the crust and mantle lithosphere and result in differing patterns of crustal deformation and surface uplift/-subsidence. The occurrence of one type of dripping or the other can provide information on the rheology of the continental lithosphere over 1-30 Myr timescales. We briefly consider how convergent or extensional tectonics may interact with Rayleigh–Taylor drips, making their near-surface expression more complex, but still amenable to this framework (Section 4.2.4). We then explore how this new understanding of lithospheric dripping can be used to analyze geologic and geophysical observations (Section 4.2.5). To evaluate the applicability of this framework to the real world, we first discuss alternative hypotheses that complicate the interpretation of lithospheric drips (Section 4.3). Then we synthesize the evidence for each lithospheric dripping event, including size (both drip width and wavelength), depth, age, and any supporting geologic observations, such as near-surface deformation, sedimentation, and volcanism (Section 4.4). Although the available evidence is sometimes sparse, inferred dripping events broadly fit the framework we develop, indicating that it can be used to guide research into regions that may have experienced lithospheric dripping. Finally, we discuss the implications of this synthesis for future studies, including methods with potential for identifying drips in the geologic and geophysical record (Section 4.5).

4.2 Insights from numerical and analogue experiments

Lithospheric dripping can be readily analyzed in terms of the Rayleigh–Taylor (R–T) instability, a fluid-dynamic instability that occurs when perturbations to an interface between two layers induces a pressure gradient that drives further growth of those perturbations (Chandrasekhar,

1961). The R–T instability is applicable to a wide range of physical phenomena (Sharp, 1984) and geologic processes including rising mantle plumes (e.g., Whitehead Jr & Luther, 1975), convection in magma chambers (Jellinek et al., 1999) and salt tectonics (Turcotte & Schubert, 2002). In continental lithosphere, the gravitational instability occurs when the lower crust and/or mantle lithosphere attains negative buoyancy due to (1) mechanical thickening, which pushes relatively cold lithosphere into warmer mantle (Conrad & Molnar, 1997; Houseman et al., 1981), possibly with prograde metamorphism forming dense eclogitic phases in the lower crust or lithosphere (Kay & Kay, 1993); or (2) magmatic residues and cumulates that form in the lower crust as the result of crustal melting and fractional crystallization, producing a dense ultramafic root (Ducea & Saleeby, 1998; Rapp & Watson, 1995).

In the following sections, we discuss the temporal and spatial scales of dripping predicted from R–T instability analyses. We then synthesize geodynamic modelling results, focusing on those that include crustal deformation and surface deflection (uplift and subsidence). This synthesis shows that drips can be categorized into two types. One occurs when crust is strong relative to the mantle lithosphere, and dripping pulls down the topographic surface, resulting in upper-crustal horizontal shortening. The other occurs when crust is relatively weak, and dripping thickens the lower crust and uplifts the surface, resulting in upper-crustal horizontal extension. These types of dripping exist in a continuum defined by relative crustal strength, buoyancy, and density, but their outcomes are distinct. We denote them as “strong-crust” and “weak-crust” drips, respectively. Although analytical models have long predicted these two tendencies of dripping, we show here that more complex numerical models and physical analogue models also support the existence of two types of drips. These models further suggest that both types of drips would be expected on Earth, given realistic variations in crustal composition, geothermal gradient, and degrees of mantle hydration. In short, the framework we introduce below provides a realistic means for understanding lithospheric dripping on Earth.

Before introducing the framework that categorizes drips into two distinct types, we review the predictions for temporal and spatial scales of dripping. Understanding these basic predictions of linear stability analysis is essential for identifying potential drips in the geologic or geophysical record.

4.2.1 Temporal scale and time to detachment

An R–T instability is usually described in terms of four temporal stages (Sharp, 1984, Figure 4.2, Phases 1 to 4), followed by a 5th relaxation and recovery stage (Figure 4.2, Phase 5). The first stage involves small perturbations to the interface, with magnitudes on the order of 10% of their wavelength, or 0.1λ (Figure 4.2, Phase 1). During this phase, the perturbation is amenable to linear stability analysis, which predicts that a single, least-stable wavelength will quickly dominate and grow exponentially, giving the system a characteristic wavelength, λ_c. The second phase occurs as perturbations grow larger ($\sim 1\lambda$) and linear analysis breaks down; the interface is characterized by “spikes” of heavy fluid that accelerate downward separated by

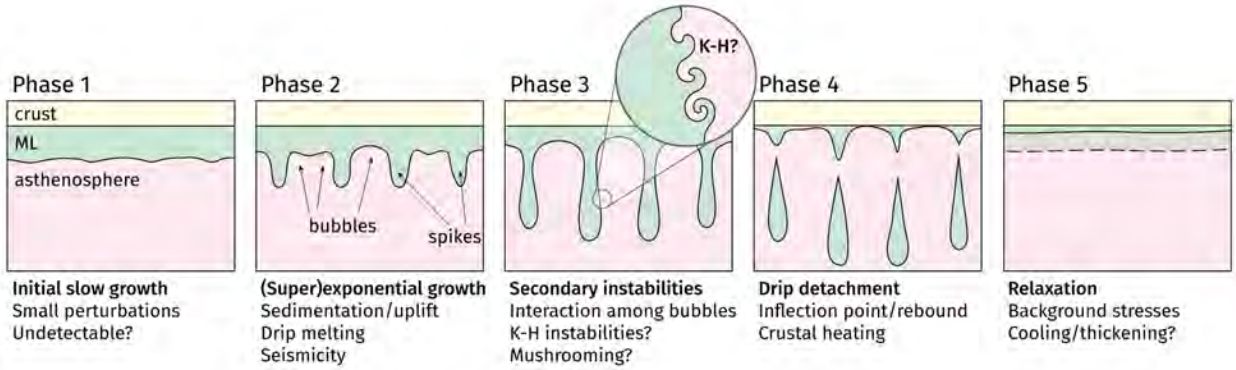

Figure 4.2: Cartoon depicting phases of Rayleigh–Taylor instability as applied to the mantle lithosphere (ML). Panels 1 through 4 correspond to the traditional phases 1 through 4 Sharp1984, while panel 5 represents post-detachment relaxation and recovery. "Bubbles" and "spikes" are the traditional names for the ascending and descending fluid interfaces, respectively (Sharp, 1984); spikes correspond to lithosphere drips. Phase 3 depicts the development of Kelvin-Helmholtz (K-H) instabilities, which are not expected for dripping lithosphere due to its large viscosity.

"bubbles" of light fluid that rise at approximately constant velocity (He et al., 1999; Sharp, 1984, Figure 4.2, Phase 2). During the second phase, the density ratio or Atwood number (At) of the interface heavily influences the behavior of the instability (Sharp, 1984, see Figure 4.3 for an explanation of parameters). For At slightly larger than zero, which is applicable to the lithosphere-asthenosphere boundary (LAB), the second phase is characterized by two sets of interpenetrating three-dimensional bubbles (Sharp, 1984), the morphology of which is sensitive to the viscosity contrast between the layers (Jellinek et al., 1999; Prakash et al., 2017). If the heavy layer is much more viscous than the light layer, as would be the case for mantle lithosphere and asthenosphere, the descending spikes take on elongated finger-like, rather than spherical, morphologies. In three dimensions, the spikes may be organized into curtains, or may be largely separated (Figure 4.4). The third stage is characterized by the development of secondary turbulent structures, such as Kelvin-Helmholtz instabilities, and by interaction between bubbles (Sharp, 1984, Figure 4.2, Phase 3). The very large viscosity of the lithosphere would impede the development of secondary structures, and geodynamic models do not depict such instabilities forming on lithospheric drips. The fourth and final stage of the R–T instability involves the breakup of the spikes, the possible penetration of the bubbles through a layer of finite thickness, and mixing between the two fluids (Sharp, 1984, Figure 4.2, Phase 4). The large viscosity contrast between the lithosphere and asthenosphere likely suppresses mixing between the two materials (Jellinek et al., 1999; Prakash et al., 2017), so lithospheric dripping most likely results in the descent of relatively intact pieces of lithosphere through the convecting mantle (Figure 4.2, Phase 4). After drip detachment, dynamic stresses related to the instability are removed, and the remaining lithosphere deforms to adjust to its new rheological, density, and thermal structure, eventually becoming dominated by background tectonic stresses (Figure 4.2, Phase 5).

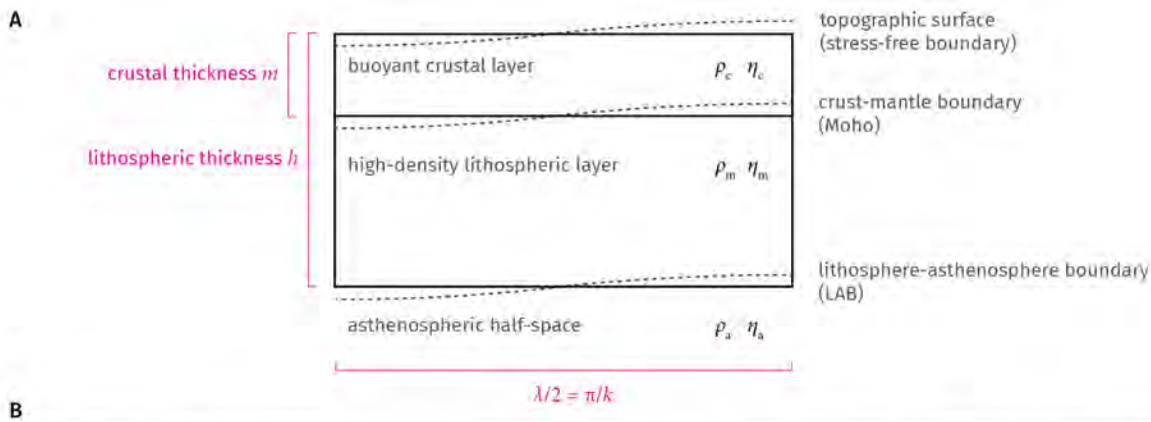

B

Relevant parameter		Importance	Application to lithosphere	Range of values
Atwood number	$A = (\rho_m - \rho_a) / (\rho_m + \rho_a)$	interface stability	nominally stable when $A<0$	−0.01 to 0.01
Kinematic viscosity contrast	$U = (\eta_a/\eta_m)(\rho_m/\rho_a)$	drip morphology	Elongated (vs. spherical) when $U<1$	<0.01
Relative crustal strength	$\eta' = \eta_c / \eta_m$	crustal response, timescale	weak-crust vs. strong-crust drip	<0.01 to >100
Dimensionless wavenumber	$k' = kh = 2\pi h/\lambda$	wavelength, timescale	size of drip & affected region	2.0 to 3.5
Crustal thickness ratio	$m' = m/h$	crustal response	large values dampen	0.2 to 0.5
Crustal density contrast ratio	$\rho' = (\rho_c - \rho_a) / (\rho_m - \rho_a)$	surface topography magnitude	maximum uplift at −20	−5 to −25 (often −16.7)

Figure 4.3: (a) Illustration of a common lithospheric drip model with uniform layer density and viscosity (ρ and η, respectively) in a periodic domain of one-half wavelength ($\lambda/2$). Small initial perturbations to the interfaces (dashed lines) trigger the instability (modified from Neil & Houseman, 1999). (b) Parameters derived from Rayleigh–Taylor instability analysis relevant to lithospheric dripping. The final column denotes ranges of values expected for Earth (Gorczyk et al., 2013; Jellinek et al., 1999; Molnar, 2015; Molnar & Houseman, 2013; Neil & Houseman, 1999; Prakash et al., 2017).

The initial phase of drip growth (Figure 4.5, Phase 1) is difficult to observe in the geologic record because it is slow (Houseman & Molnar, 1997), the perturbations are small, and the dynamic stresses may not be significant in the upper crust (Neil & Houseman, 1999). Exponential growth (Figure 4.5, Phase 2) and detachment (Figure 4.5, Phase 4) are easier to define in the geologic record. If basin sedimentation is associated with the drip, the depositional ages of the earliest sediments can be used to estimate the beginning of exponential growth (e.g., DeCelles et al., 2015a; Saleeby & Foster, 2004; Smith et al., 2017). Xenoliths have been used to constrain the presence or absence of a dense root (Ducea & Saleeby, 1998), and records of surface uplift and tilting (e.g., Unruh, 1991) may be used to infer the timing of exponential growth and detachment (Molnar & Jones, 2004).

Differing definitions for lithospheric drip detachment have been used in the literature, including the time at which the instability transitions to superexponential growth (Figure 4.5, Phase 2) and the asymptotic time at which the displacement of the instability tends to infinity, or “blow-up” time (e.g., Molnar et al., 1998; Neil & Houseman, 1999). Both depend on lithosphere viscosity and the size of the initial perturbation (Molnar et al., 1998; Neil & Houseman, 1999), which in turn are dependent on composition, temperature, and strain rate, and could vary by

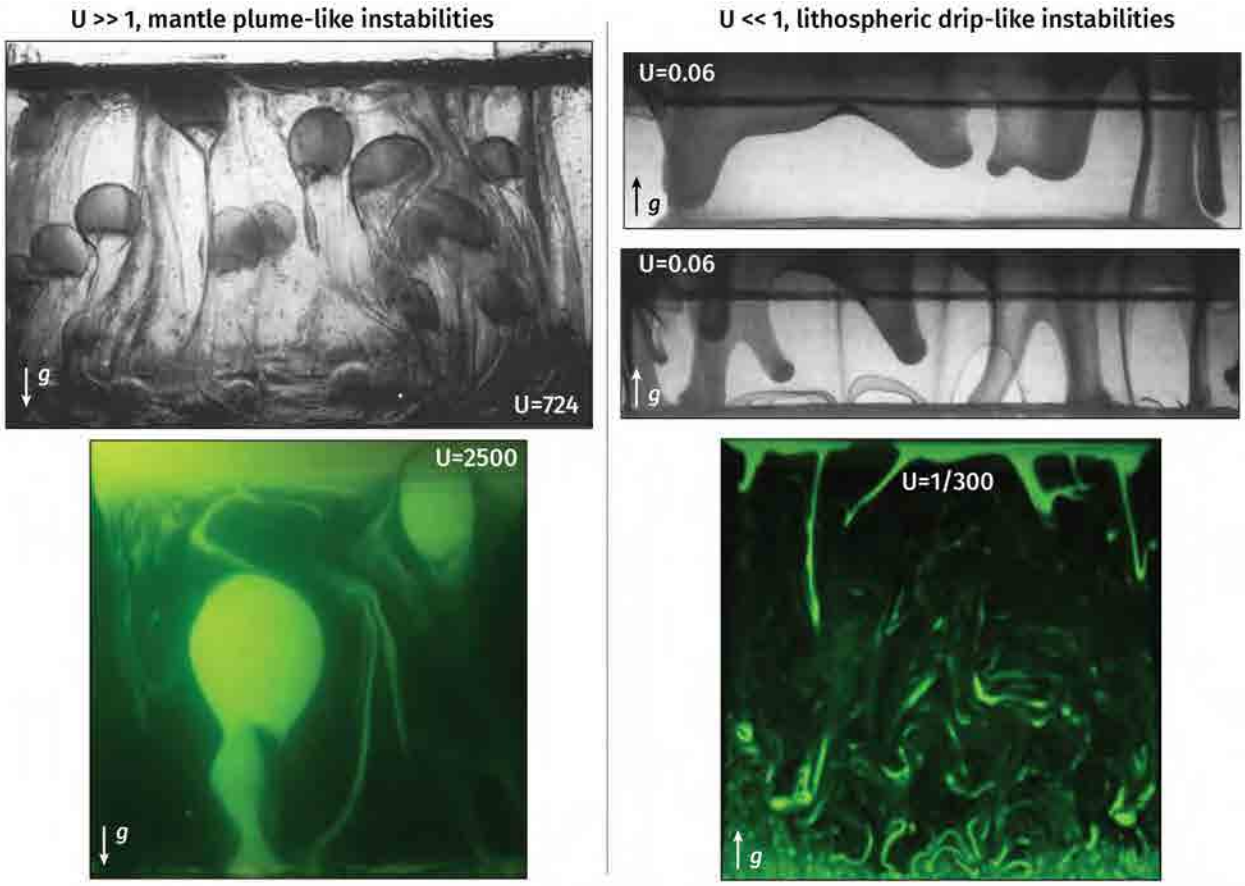

Figure 4.4: Snapshots of laboratory plume experiments demonstrating dependence of morphology on the viscosity contrast, U. In the left column, large values of U (unstable material less viscous than background material) produce spherical instabilities applicable to hot mantle plumes. In the right column, small values of U (unstable material more viscous than background) produce sheets and finger-like instabilities applicable to lithospheric dripping. Images in right column rotated 180° (denoted by arrow indicating gravity, *g*) to emphasize applicability to dripping. Top row from Jellinek et al. (1999, ~30 cm wide); bottom row from Prakash et al. (2017, 15.5 cm wide).

3 to 4 orders of magnitude. For a plausible range of densities and viscosities, drip detachment could occur after as little as 10^5 years or as long as 10^8 years or greater (Jull & Kelemen, 2001; Molnar et al., 1998). For time spans longer than ~30 Ma, however, thermal diffusion is likely to outpace growth of the instability and erase the density contrast (Neil & Houseman, 1999). These definitions of the timing of drip detachment, while well-defined mathematically, are difficult to use in practice because they cannot be directly observed, and because estimating the viscosity of the lithosphere involves large uncertainties, even when the growth and detachment of a drip are well-constrained (e.g., Molnar & Jones, 2004).

In this paper, we consider drip detachment as the moment when the drip mechanically decouples from overlying lithosphere (Wang & Currie, 2017), corresponding to Phase 4 of the R–T instability (Figure 4.5; Sharp, 1984). This decoupling is often accompanied by a marked increase in the downward velocity of the drip in geodynamic models (Beall et al., 2017; Wang &

Currie, 2017) and an inflection point in surface uplift or subsidence rates (DeCelles et al., 2015a; Molnar, 2015; Wang & Currie, 2017; Wang et al., 2015). Drip detachment also coincides with major crustal heating associated with asthenospheric upwelling (Göğüş & Pysklywec, 2008). Thus, the primary observables of drip detachment are a change in surface uplift/subsidence rates, basin inversion or extensional collapse, and an increase in heat flow and volcanism.

4.2.2 Spatial scale and the characteristic wavelength

The spatial scale of dripping is best analyzed by the characteristic wavelength, rather than by the size of the descending drip. The dimensions of the descending drip can only be roughly estimated by geophysical observations and they are affected by independent factors such as mantle flow, vertical stretching, and asthenosphere viscosity. The characteristic wavelength, on the other hand, is directly related to the region of thinned lithosphere after the drip detaches, and it is thus recognizable in the sedimentary, magmatic, and surface uplift records. In addition, the wavelength derives from fundamental properties of the instability, such as thickness of the unstable layer and the instability timescale, providing useful data about the lithospheric rheology and structure of a region that undergoes dripping.

Table B.1 summarizes models of the R–T instability of a lithospheric layer under different scenarios. If the lithosphere has a uniform viscosity, the characteristic wavelength depends mainly on lithospheric thickness, h. For a rigid top boundary (representing the Moho in the simple two-layer case), the characteristic wavelength is approximately $2.5h$ to $3h$, i.e., approximately 100–250 km for mantle lithosphere 40–80 km thick (Conrad & Molnar, 1997; Turcotte & Schubert, 2002). Scenarios that include exponential decrease of viscosity with depth, linear decrease of density with depth, and thermal diffusion of small perturbations, produce wavelengths in the range of 100–200 km (Conrad & Molnar, 1997). Prescribing a stress-free boundary at the top of the mantle lithosphere, representing decoupling from overlying crust (which is not included in these two-layer models), can increase the wavelength to $12h$ or greater, depending on the viscosity decay length L and viscosity exponent n (Harig et al., 2008). Harig et al. (2008) estimated a range for h/L of 5 to 9 for the Sierra Nevada to suggest a wavelength of 500 km for an initial layer thickness of 200 km, or $\lambda_c = 2.5h$. Models incorporating a third layer representing a buoyant crust and allowing for a stress-free top boundary show that the characteristic wavelength also depends on relative crustal thickness (see Figure 4.3a for illustration; Neil & Houseman, 1999). Very thin crusts (on the order of 10% of the total lithospheric thickness) favor larger wavelengths, while crusts comprising 1/2 to 1/3 of the lithosphere again result in wavelengths of $2h$ to $2.5h$.

Such analyses suggest that lithospheric dripping will often occur with wavelengths of $2h$ to $3h$, or 100–500 km depending on lithospheric thickness, viscosity structure, and crustal thickness. While we discuss below how other factors, including the size of the drip itself, are related to this wavelength, the ultimate result of a lithospheric drip should be a large region of thinned

Table 4.1: Summary of dripping scenarios predicted by numerical models

Type	Syn-drip topography	Syn-drip upper crustal strain	Model Scenarios	Controlling factors
Strong-crust	Permanent depression	Moderate compression	$\eta' \gg 10$	Topographic surface coupled to Moho
Strong-crust	Transient basin	Strong compression	$\eta' > 10$ with weaker lower crust	Middle–lower crustal thickening
Weak-crust	Major uplift	Moderate extension	$\eta' \sim 1$ or large wavelength	Major crustal thickening
Weak-crust	Minor uplift	Strong extension	$\eta' \ll 1$ or weak crustal channels	Crustal flow, surface decoupled from Moho

Note: $\eta' = \eta_c/\eta_m$ denotes the viscosity of the crust η_c scaled to that of the mantle lithosphere η_m.

lithosphere approximately equal in diameter to the characteristic wavelength, 2 to 3 times as wide as the thickness of the unstable portion of the lithosphere.

4.2.3 Upper crust and topographic response: Two types of dripping

A broad range of numerical and analogue modelling studies suggest how variations in the viscosity structure of the crust and mantle lithosphere during dripping can lead to two distinct responses in the upper crust and topographic surface: uplift and extension vs. subsidence and compression (Figure 4.1, inset). We denote these two tendencies as weak-crust and strong-crust drips, respectively, and also identify variations within these tendencies, such as permanent topographic depressions vs. transient basins, and uplift-dominated vs. extension-dominated crusts (Table 4.1). Given realistic ranges of parameters, these models suggest that the average viscosity of the crust relative to that of the mantle lithosphere, $\eta' = \eta_c/\eta_m$, where η_c and η_m are the effective viscosities of the crust and mantle lithosphere, respectively, largely determines the behavior of the crust and topographic surface during dripping(e.g., Molnar, 2015; Neil & Houseman, 1999).

Strong-crust drips. Models suggest that values of η' greater than 10–13 (i.e., when the average crustal viscosity is at least an order of magnitude greater than that of the mantle lithosphere) give rise to a type of dripping we denote as “strong-crust” (Neil & Houseman, 1999).

Strong crusts behave like an elastic plate that flexes down during drip growth and rebounds after detachment (DeCelles et al., 2015a; Göğüş et al., 2017; Wang et al., 2015). As a result, the topographic surface is pulled down above the center of the drip and flexural uplift occurs on peripheral bulges (Figure 4.5). Because the strong crust couples the topographic surface to the descending boundary with the mantle lithosphere, the amount of surface subsidence increases with increasing relative crustal strength, at least up to a factor of $\eta' \sim 100$ (Neil & Houseman, 1999). As η' increases beyond a few hundred, the crust behaves as a rigid layer with little deformation or subsidence, and the problem approximates a single layer with a rigid

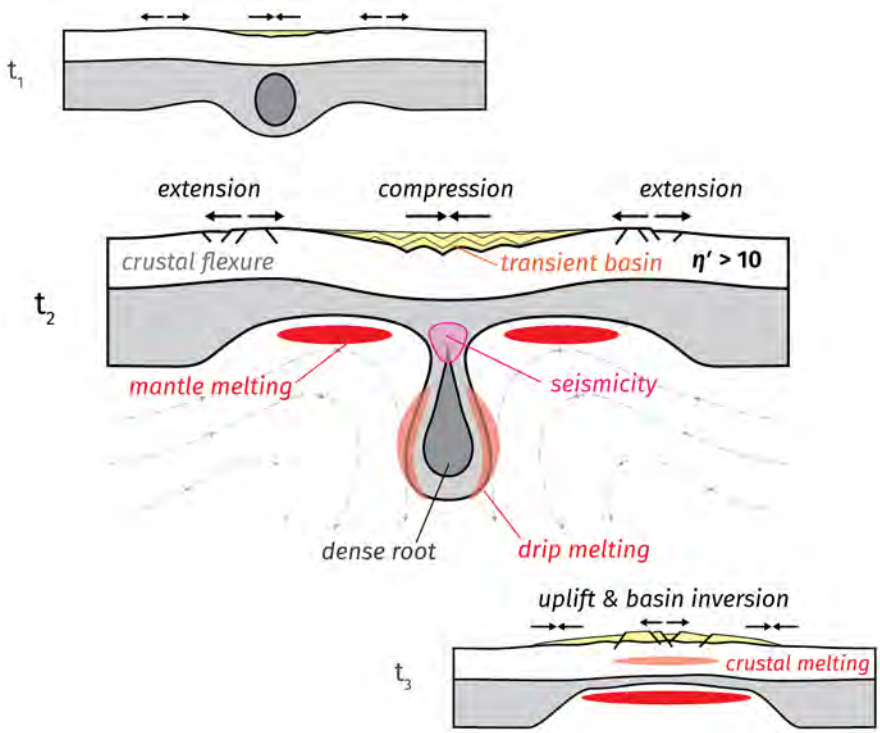

Figure 4.5: Illustration of strong-crust dripping, which occurs when relative crustal viscosity $\eta' > 10$. The strong crust deforms flexurally, producing a central depression and peripheral bulges. The drip pulls down the topographic surface as it grows (t_1) leading to the formation of a transient basin (t_2). Basin deposits experience syn- to post-depositional compression, while the peripheral bulge experiences flexural extension. Basin deposits are uplifted and inverted after detachment (t_3). Upwelling of hot asthenosphere induced by the drip can lead to partial melting of remaining crust, mantle lithosphere, or decompression melting of the asthenosphere.

upper boundary (at the Moho), such as those listed in Table B.1 (Neil & Houseman, 1999). The amount of subsidence also depends on relative layer thicknesses and densities (Figure 4.3b). Models with reasonable choices for these parameters predict magnitudes of surface subsidence ranging from 0.5 km to 1.5 km (Göğüş & Pysklywec, 2008; Göğüş et al., 2017; Wang et al., 2015).

The topographic depression generated by strong-crust dripping rebounds flexurally and isostatically after drip detachment (Göğüş & Pysklywec, 2008; Wang et al., 2015). Rebound is negligible (<50 m) for the strongest crusts ($\eta' > 100$, Elkins-Tanton, 2007) but is significant for crusts with more moderate strengths ($\eta' \sim 10$, Wang et al., 2015). Post-drip rebound is increased in models that include a weaker middle–lower crust, which allows for some lower-crustal thickening during drip growth (Göğüş & Pysklywec, 2008; Göğüş et al., 2017; Kaus & Becker, 2007; Wang & Currie, 2017; Wang et al., 2015, e.g.,). The thickened low-density crust increases isostatic rebound after drip removal, in some cases completely inverting the topographic depression (Figures 4.5 and B.1; Elkins-Tanton, 2007; Göğüş et al., 2017; Wang et al., 2015). For the models in Göğüş and Pysklywec (2008), surface rebound due after drip detachment results in ~1 km of increased elevation above the center of the drip.

Flexural bending stresses control the distribution of crustal strain. During the growth of the drip, the upper crust experiences contraction caused by compressive bending stresses. Sediments deposited in the transient basin may therefore record evidence of syn-contractional deposition, such as growth strata or folding that decreases in amplitude up-section (DeCelles et al., 2015a; DeCelles et al., 2015b; Kapp & DeCelles, 2019). The uplifted peripheral bulges circumscribing the drip experience extensional bending stresses (DeCelles et al., 2015a; DeCelles et al., 2015b; Kaus & Becker, 2007). After drip detachment, the pattern of upper-crustal stresses is inverted. The central region experiences horizontal extension due to unbending, updoming by upwelling asthenosphere, and gravitational potential energy contrasts generated by the elevated topography (Göğüş et al., 2017).

A strong-crust drip therefore leads to the formation of a transient basin, where sediment accommodation space is generated during growth of the drip and sediments may be deposited syn-contractionally. Accommodation space is eliminated by drip detachment, and the basin is inverted and undergoes horizontal extension (Figure 4.5). Even though the lower crust may thicken somewhat during strong-crust dripping, the primary characteristics that distinguish strong-crust drips from weak-crust drips are syn-drip upper-crustal shortening, syn-drip surface subsidence.

Weak-crust drips. Models with $\eta' < 10$ predict that lower crustal stresses imposed by the growing lithospheric drip are compensated by flow within the crust (Figure 4.7a; Molnar, 2015). We denote this style of dripping "weak-crust" (Figure 4.6). Models predict that the upper-crustal expression of weak-crust dripping is distinct from that of strong-crust dripping. Specifically, syn-drip surface uplift and extension occur in the upper crust rather than subsidence and contraction (Figures 4.6 and B.1; Neil & Houseman, 1999).

Syn-drip surface uplift during weak-crust dripping is caused by overall thickening of the relatively weak crust. Upper-crustal extension occurs when thickening of the lower crust is significant enough to cause the middle crust to flow upward. Upward flow of the middle and upper crust, and uplift of the topography, are resisted by gravity, causing vertical compression and horizontal extension in the upper crust (Molnar, 2015). Weak-crust drips therefore yield a pattern of upper-crustal extension and thinning at the same as the lower crust is being shortened and thickened due to the growing drip.

The behavior of weak-crust drips is sensitive to variation in the relative viscosity structure of the crust and mantle lithosphere (Figures 4.7a to 4.7c and 4.7e), the instability wavelength (Figure 4.7b), and crustal thickness and density (Figures 4.7c and 4.7d). Crustal thickening and surface uplift are greatest when the viscosity contrast between the crust and the negatively buoyant lithosphere is negligible, i.e., when $\eta' = 1$ (Figure 4.7d; Neil & Houseman, 1999). In such models, the crust can thicken by a factor of up to 1.4 (Neil & Houseman, 1999). As η' decreases below 1, surface uplift diminishes and horizonal extension rates increase, until the magnitude of surface uplift is negligible (Figure 4.7d; Molnar & Houseman, 2013). Low viscosity lower crust

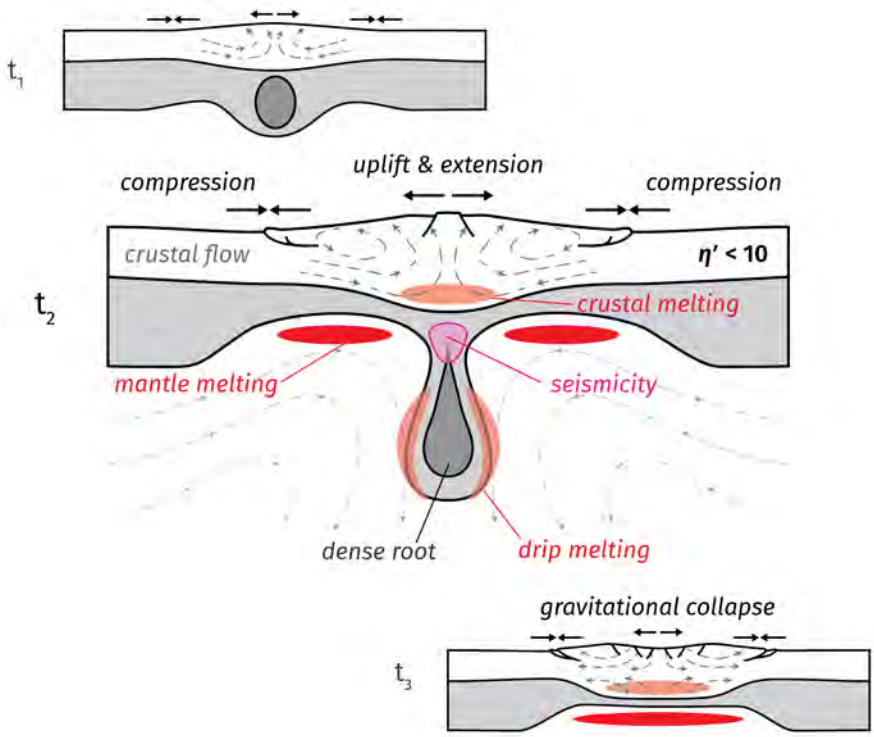

Figure 4.6: Illustration of weak-crust dripping, which occurs when relative crustal viscosity $\eta' < 10$. The weak crust flows in response to drip-imposed stresses, producing a thickened crustal welt. The crust thickens as the drip grows (t_1), leading to syn-drip uplift and horizontal extension in the upper crust (t_2). The thickened crust is prone to partial melting and may collapse gravitationally after detachment (t_3). Upwelling of hot asthenosphere induced by the drip can also lead to partial melting of remaining crust, mantle lithosphere, or decompression melting of the asthenosphere.

(represented by a viscosity decay factor) tends to decouple surface deformation from mantle flow and thus suppress the near-surface expression of dripping. Crustal thickening and near-surface extension are reduced by approximately 50% for moderate values of a viscosity decay factor (e.g., decay by a factor of 10 throughout the crust), and become negligible at larger values of the decay factor (e.g., decay by a factor of 1000; Figure 4.7e; Molnar, 2015). For more realistic decay factors (10–100), e.g., due to a temperature-dependent rheology, syn-drip extension of the upper crust is reduced but still significant (Figure 4.7e; Molnar, 2015).

The instability wavelength (relative to lithosphere thickness) exerts a strong control on the upper crust during dripping (Molnar, 2015). In general, longer wavelengths induce a stronger surface uplift response than smaller instabilities (Figure 4.7b). Very large instabilities (e.g., those with wavelengths on the order of 1000 km) can overwhelm crustal strength and lead to thickening and surface uplift of even very strong crusts (Figure 4.7b; Neil & Houseman, 1999; Pysklywec & Shahnas, 2003). The critical η' value that separates drips that cause surface uplift from those that cause subsidence increases for large instabilities (Figure 4.7b; Neil & Houseman, 1999). For wavelengths of lithospheric instabilities realistic for continental regions

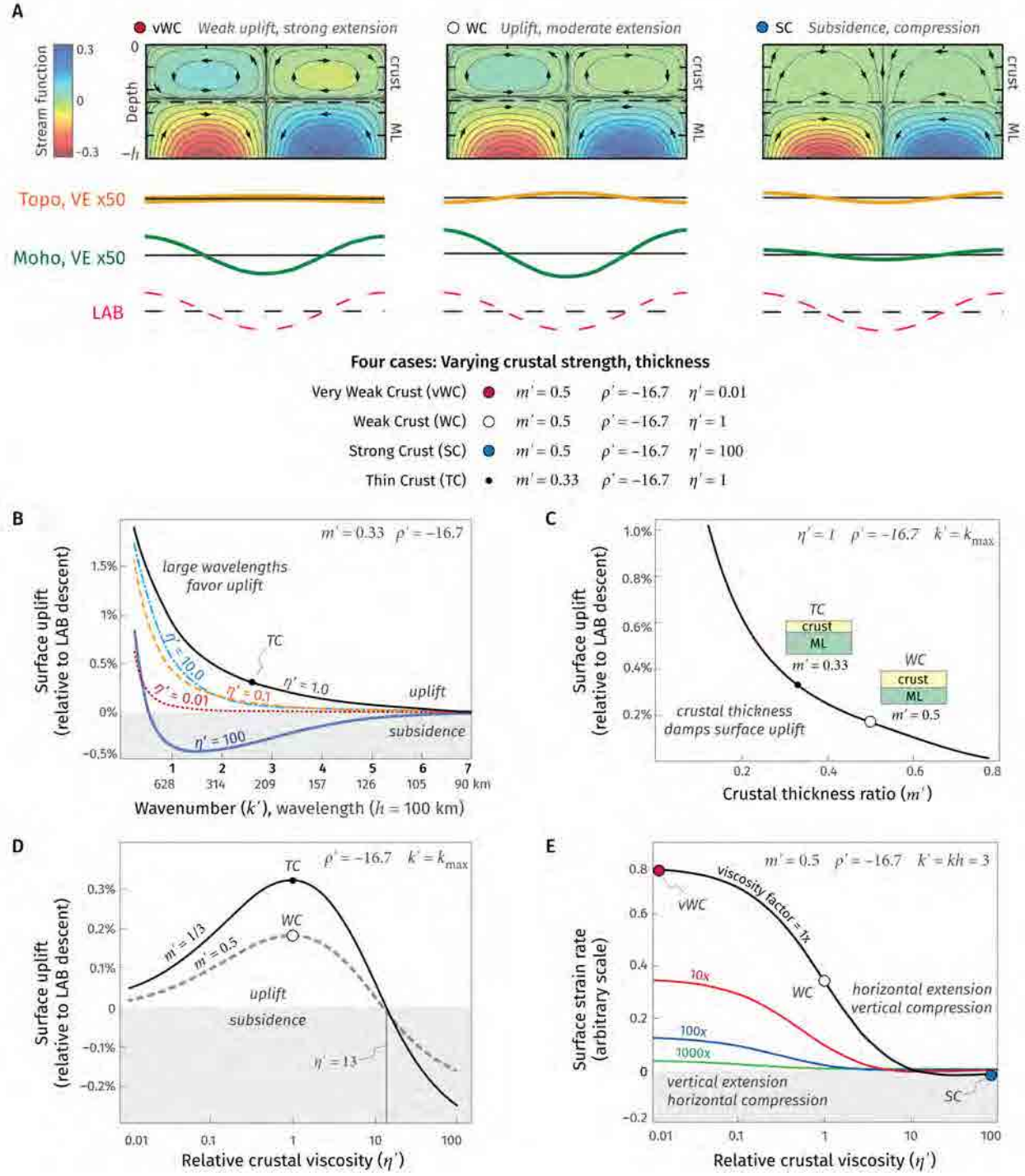

Figure 4.7: *Caption on next page.*

Figure 4.7 (previous page): Drip model results compiled from Molnar (2015), Molnar and Houseman (2013), and Neil and Houseman (1999), illustrating the conditions that favor strong-crust vs. weak-crust dripping. (a) Three models illustrate the weak-crust and strong-crust scenarios with flow streamlines and interface deflections. Four cases which can be tracked through the following panels are described (refer to Figure 4.3 for symbols). (b) Surface uplift as a function of wavenumber (or wavelength, assuming $h = 100$ km) and crustal strength (η'). Strong crusts $\eta' > 10$ cause subsidence; weaker crusts favor uplift, maximum when $\eta' = 1$. Extremely small wavenumbers (large wavelengths) also favor uplift. (c) Surface uplift as a function of crustal thickness for $\eta' = 1$. Thick crusts dampen the surface uplift response. (d) Surface uplift as a function of crustal viscosity η' and crustal thickness, showing how the largest surface uplift occurs around $\eta' = 1$ and subsidence occurs when $\eta' > 10$ to 13. (e) Relative surface strain rates (positive indicates horizontal extension) as a function of η' and crustal viscosity exponential decay factor (ratio of the viscosity at the top of the crust to that at the base; a value of 1 indicates uniform viscosity). Horizontal extension increases with decreasing η' and for more uniform viscosity profiles.

on Earth (100–500 km), the surface switches from uplift to subsidence between $\eta' = 10$ and $\eta' = 100$, often around $\eta' = 13$ (Figures 4.7a, 4.7b and 4.7d).

Increasing crustal thickness relative to the lithosphere damps the surface uplift response, both because the thinner mantle lithosphere results in smaller drips that impart smaller stresses to the base of the crust, and because the increased crustal buoyancy works against the downward deflection of the Moho that drives crustal thickening and internal flow (Figures 4.7c and 4.7d; Neil & Houseman, 1999). Decreasing the density of the crust therefore increases the contribution of crustal thickening to surface uplift but reduces the magnitude of crustal thickening, so that the magnitude of surface uplift tends to peak at moderate crustal density contrast ratios, ρ', around −20, where $\rho' = (\rho_c - \rho_a)/(\rho_m - \rho_a)$, and c, a, and m denote the crust, asthenosphere, and mantle lithosphere, respectively (Neil & Houseman, 1999). Because crust with an average density of 2,800 kg m^{-3} would yield a density contrast ratio of –16.7 for $\rho_m = 3330$ kg m^{-3}, $\rho_a = 3300$ kg m^{-3} (Neil & Houseman, 1999), realistic variations in crustal or lithospheric densities would have notable effects on surface uplift magnitude (Figure 4.7).

Numerical models that include temperature- and strain rate-dependent viscous rheologies (e.g., dislocation creep) suggest that surface uplift may be limited to a few hundred meters at most (Wang et al., 2015). If the middle or lower crust is rheologically weak, surface uplift results from lower crustal thickening due Poiseuille flow driven by the descending drip (Wang & Currie, 2017). Although we expect that more realistic geodynamic models that include various deformation mechanisms such as dislocation creep, Peierls creep, and elasticity will yield weak-crust drips, the style of dripping is likely to be highly dependent on crustal temperature, tectonic strain rate, and the chosen rheological parameters. We discuss the implications for future studies of lithospheric dripping below (Section 4.5.2).

Summary of strong-crust and weak-crust drips. In summary, models suggest that the response of the upper crust and topographic surface during dripping is determined by fundamental properties of the crust and mantle and can be generalized into two distinct behaviors

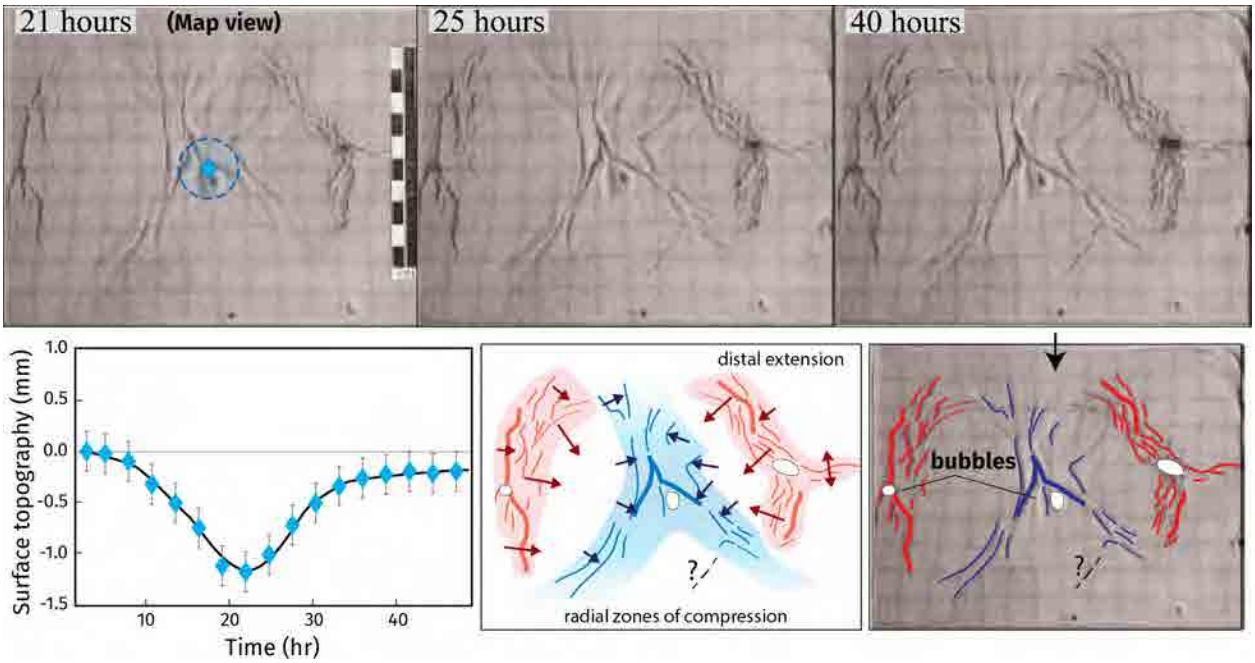

Figure 4.8: Scaled analogue model (Pysklywec & Cruden, 2004) of a strong-crust drip, showing central syn-drip contraction and distal extension and topography characterized as a transient basin. The top row shows map-view photographs of the experiment at three time-steps with the initial density anomaly annotated as a blue circle. Blue diamond represents the location of the topography plotted in the bottom-left panel (modified from Pysklywec & Cruden, 2004). The bottom-right panels show our interpretation of compression (blue) and extension (red). Gray blobs represent air bubbles.

(Table 4.1). The first behavior, strong-crust dripping, is characterized by syn-drip subsidence and syn-drip upper-crustal shortening (Figure 4.7). For instability wavelengths realistic for continental lithosphere, it occurs when $\eta' > 10$ (Figures 4.7a, 4.7c and 4.7e). The syn-drip topographic depression rebounds flexurally during drip detachment, and the lithosphere rebounds isostatically following removal of the negatively buoyant drip. If viscosity decays within an overall strong crust, thickening of the lower crust also produces isostatic rebound. After detachment, the crust above the drip undergoes horizontal extension. In contrast, the second behavior, weak-crust dripping, is characterized by syn-drip uplift, syn-drip upper crustal horizontal extension, and crustal thickening. Weak-crust drips occur when the crust is similar in viscosity to the mantle lithosphere, $\eta' \sim 1$, especially when the crust is thin to moderately thick (Figure 4.7b) and are sensitive to variation in crustal thickness (Figure 4.7b), viscosity decay factor (Figure 4.7d), and the buoyancy of the crust (Neil & Houseman, 1999). For very weak crusts, $\eta' \ll 1$, topographic uplift is reduced but horizontal extension rates increase as the upper crust becomes decoupled from the mantle (Figures 4.7d and 4.7e).

Although these differing effects on crustal strain have long been predicted by simplified models, more recent numerical experiments based on laboratory-derived rheologies also support the existence of two distinct types of drips. In the models of Wang et al. (2015), scenarios that have a relatively weak crust display syn-drip uplift on the order of 100–300 m, while

stronger crusts produce syn-drip subsidence (Figure B.1). In these models, weak-crust dripping is due to a pressure-dependent plastic yield criterion (Drucker & Prager, 1952), radiogenic heat production within crustal materials, and a strong mantle rheology characterized by dry olivine. Crust was also preferentially weakened by frictional-plastic strain softening, which further limited the effective viscosity of mid to upper crustal materials, where plastic deformation is common (Figure B.1). These models also illustrate how a strong upper crust that would initially result in strong-crust dripping may be weakened through deformation, radiogenic heating, or hydration to result in weak-crust dripping (Figure B.1). Similarly, the occurrence of weak channels within an overall strong crust can influence the type of lithospheric drip, with mid-crustal channels tending to result in surface subsidence, while lower-crust channels lead to syn-drip uplift (Wang & Currie, 2015).

Wang et al. (2015) presented a classification of lithospheric drips similar to the one we present here. Specifically, two styles of crustal and topographic deformation related to dripping were recognized: surface subsidence on the order of >500 m followed by rebound, and uplift of a few hundred meters followed by topographic collapse. These two styles generally map onto the strong-crust and weak-crust drips we present here.

It is possible that three-dimensional models of lithospheric dripping would lead to quantitatively different outcomes, but the same qualitative behaviors are expected. An analogue model experiment found that instability of a linear density anomaly (analogous to a 2.5-D numerical model) and of a cylindrical "point" anomaly (analogous to a 3-D numerical model) shared similar maximum growth rates (Pysklywec & Cruden, 2004). Multiple drips developed along the length of the linear anomaly, presumably because its length was greater than the characteristic wavelength of instability. The experiments with a cylindrical "point" anomaly show the potential for spatial heterogeneity when dripping occurs in three dimensions (Figure 4.8). In experiments with a brittle layer approximating the upper crust, a network of radial contractional structures developed over the center of the drip, while the distal regions developed extensional structures (Figure 4.8). These upper crustal features were evidently influenced by heterogeneities in the materials (e.g., air bubbles) but demonstrate how dripping in three dimensions is likely to be significantly more complex than 2-D and 2.5-D numerical models predict. Furthermore, two crustal strengths were investigated by Pysklywec and Cruden (2004): one similar in viscosity to the mantle lithosphere ($\eta' = 0.88$), and one that was stronger ($\eta' = 2.1$). The crust with $\eta' = 2.1$ behaved as a classic strong-crust drip, resulting in a topographic depression that rebounded after detachment (Figure 4.8). The weaker crust initially developed a topographic depression created by isostatic subsidence, but it quickly (<10 hr.) transitioned to uplift as the fluid dynamic stresses thickened the crust; after the drip detached, the crustal welt slowly relaxed and the topography decreased (Pysklywec & Cruden, 2004).

4.2.4 Multiple drips during convergent and extensional tectonics

Geodynamic models suggest that concurrent lithospheric drips can be triggered by convergent tectonics, where convergent thickening triggers a gravitational instability beneath the zone of convergence if the lithosphere is negatively buoyant (Houseman et al., 2000). Depending on crustal strength and buoyancy, the lithosphere founders either in the form of a single central drip or as paired marginal drips on the edges of the zone of convergence (Figure 4.9; Houseman et al., 2000; Molnar & Houseman, 2004). In the latter case, crustal buoyancy resists the downward deflection of the Moho that would accompany crustal thickening, and the lower crust circulates outward from the convergent zone as upper crust continues to converge. This outward flow of lower crust shifts the local maxima of lithosphere descent outward, causing drips to seed on the margins of the convergent zone. If on the other hand the crust in the convergent zone is less buoyant and is able to thicken sufficiently, a single drip is seeded in the center of the convergent zone (Figure 4.9; Houseman et al., 2000; Molnar & Houseman, 2004).

Paired marginal drip instabilities can also occur during the collapse of overthickened crust, where crustal thinning and asthenospheric upwelling in the center of the collapsing region are accommodated by downwelling on its edges (Gemmer & Houseman, 2007). Gemmer and Houseman (2007) investigated the collapse of thick crust overlying mantle lithosphere, each with similar viscosities ($\eta' \sim 1$) and found that a wave of extension-driven topographic subsidence propagated outward from the center, but as marginal drips developed, the overlying crust thickened, causing localized uplift. The width of the region undergoing extension corresponded to the characteristic wavelength of the instability (Gemmer & Houseman, 2007). Hoogenboom and Houseman (2006) investigated a related mode of instability, termed "central upwelling", wherein a perturbation to a dense layer was seeded as an initial thinning, and compared it to the traditional "central downwelling" case (i.e., an instability initiated via lithospheric thickening). In both cases, topography above downwelling regions was dominated by uplift when the crust was relatively weak, $\eta' = 1$, and by subsidence when the crust was strong, $\eta' = 25$, as predicted by the strong-crust vs. weak-crust framework laid out above.

The occurrence of single vs. paired drips cannot be mapped directly onto strong-crust vs. weak-crust styles (Section 4.2.3) despite a similar dependence on relative crustal strength. Molnar and Houseman (2004) depict cases where $\eta' < 1$ yields either a single drip or paired marginal drips depending on crustal thickness and density. In general, both single and paired drips are possible when the crust is weak (Figure 4.9), but for strong crusts with $\eta' > 10$, paired marginal drips may require unrealistically large values of crustal thickness and/or viscosity. Therefore, strong-crust drips likely only develop as single downwellings.

These studies show that multiple drip instabilities, though they result in more complex crustal and surface deformation, can be analyzed using the same framework as the more traditional single Rayleigh–Taylor instability. In particular, drips triggered by lithospheric thickening, thinning, convergence, or crustal collapse all involve crustal thickening and uplift when

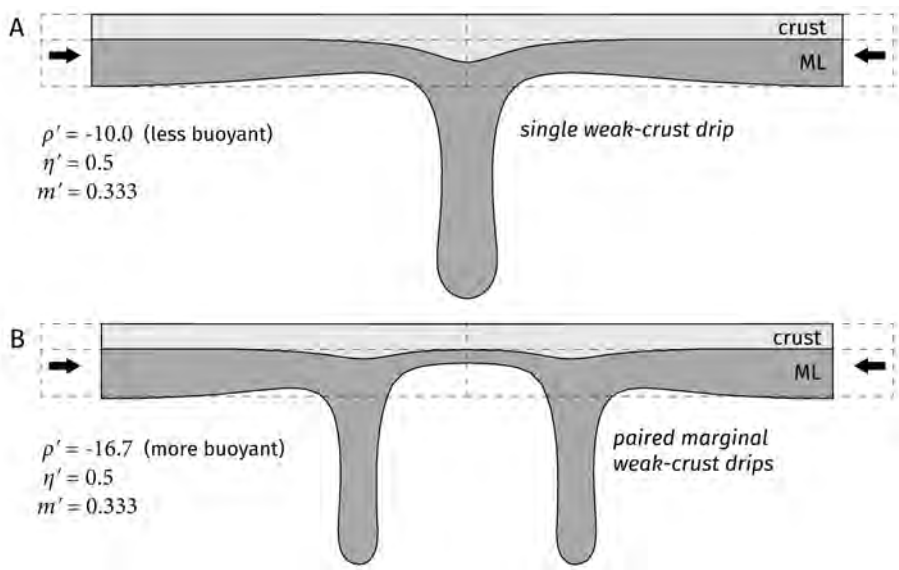

Figure 4.9: Snapshots of lithospheric drip models during convergent tectonics. (a) Single drip that develops when the crust is less buoyant. (b) the paired marginal drips that develop when the crust is buoyant enough to resist convergent thickening. Both cases involve weak-crust dripping due to the relatively low crustal viscosity ($\eta' = 0.5$). Modified from Molnar and Houseman (2004). Initial model geometry is shown as dashed lines. See Figure 4.3b for explanation of mathematical symbols.

the crust has a viscosity similar to the mantle lithosphere (weak-crust drips) and surface subsidence contraction when the mantle lithosphere is significantly stronger (strong-crust drips).

4.2.5 Application of modelling studies to lithospheric dripping on Earth

The numerical and analogue model experiments discussed above provide a powerful framework for understanding the temporal and spatial scales of lithospheric dripping, as well as the two types of upper-crustal deformation that result from varying crustal strength. In this section, we summarize the observable evidence for lithospheric dripping, especially the spatial dimension of geophysical and geologic observations, and how it relates to these properties. Identifying dripping events involves comparing the spatial scale and timing inferred from the geologic record with those predicted by R–T instability analysis and other models of dripping.

Relationship of drip width to wavelength. During the early stage of instability, the width, d, of the drip is approximately $\lambda/2$, because the downgoing lithospheric material is compensated by lithospheric thinning (Figure 4.11). As the R–T instability continues to evolve, the drip is not likely to remain in a compact, spherical shape. The morphology of the sinking drip depends on the density ratio between it and the surrounding asthenosphere or the Atwood number (Figure 4.3b; He et al., 1999), and on the viscosity contrast between the lithosphere and asthenosphere (Figure 4.4; Jellinek et al., 1999; Prakash et al., 2017). The boundary between mantle lithosphere and asthenosphere typically has a low Atwood number (<0.01), but because the viscosity of mantle asthenosphere is much less than the viscosity of the dripping lithosphere,

the drip undergoes vertical stretching (Lorinczi & Houseman, 2009; Molnar & Bendick, 2019) and takes on an elongated, rather than spherical, morphology (Jellinek et al., 1999; Prakash et al., 2017). Laboratory experiments indicate that spherical lithospheric drips would only be possible if the lithosphere were much lower in viscosity than the asthenosphere (Figure 4.4).

As a result of this dependence of drip morphology on viscosity contrast, realistic numerical models of lithospheric dripping consistently produce drips that are less than $\lambda/2$ in width (e.g., Beall et al., 2017; Wang & Currie, 2015; Wang et al., 2015); in fact, drip widths are often $\lambda < /4$ in such models (Figure 4.11). Therefore, given a drip's width d, a conservative estimate of its wavelength λ is $2d$ to $4d$. This implies that a drip imaged by seismic data to be 100 km in width would affect a broader region (e.g., through lithospheric thinning, subsidence, and volcanism), corresponding to the instability wavelength, as large as ~400 km in diameter. These studies also suggest that the morphologies of individual drips are likely to be highly variable, dependent upon local conditions in the upper mantle.

Geophysical techniques could also systematically under- or over-estimate the size of a drip, depending on the resolution of the data and the method of delimiting the downwelling material. Mantle seismic zones associated with dripping are most likely focused in the actively necking and vertically stretching portion of the drip (Lorinczi & Houseman, 2009; Molnar & Bendick, 2019) and are often clustered in a relatively narrow zone situated above a much larger seismic anomaly (Figure 4.12; Koulakov, 2011; Lorinczi & Houseman, 2009). Mantle seismic zones are therefore likely significantly smaller than the drip itself and permit a minimum estimate of its width and of the instability wavelength (Figure 4.10).

In the case where gravitational instability is triggered by the foundering of a dense magmatic root, the instability wavelength may be constrained by the width of the negatively buoyant root. If the width of the root is not much greater than λ, the foregoing discussion indicates that the entire magmatic root should founder as a single drip (e.g., Currie et al., 2015; Valera et al., 2014; Wang & Currie, 2017; Wang et al., 2015). If the width of the magmatic root is greater than λ, or if it is elongated along strike, multiple drips can develop along the root as proposed by Harig et al. (2008) for the Sierra Nevada Batholith. To illustrate this point, two-dimensional numerical models with magmatic roots ~200 km in width resulted in the formation of multiple drips depending on the thickness and rheology of the dense root (Wang & Currie, 2015), and a three-dimensional analogue model with an elongated anomaly also resulted in multiple drips forming along strike (Pysklywec & Cruden, 2004).

In light of the foregoing discussion, we hypothesize that the most reliable indicators of the wavelength of instability λ are the widths of regional surface deflection (subsidence or uplift) and volcanism, as these are directly related to the lithospheric thickening or thinning caused by the instability. Surface deflection can produce sedimentary deposits that also approximate the drip wavelength, especially for strong-crust drips that result in syn-drip surface subsidence (Figure 4.10). For hypothesized drips lacking this data, tomographic images most commonly provide a rough estimate of the size of the drip itself, which is likely between $\lambda/4$ and $\lambda/2$

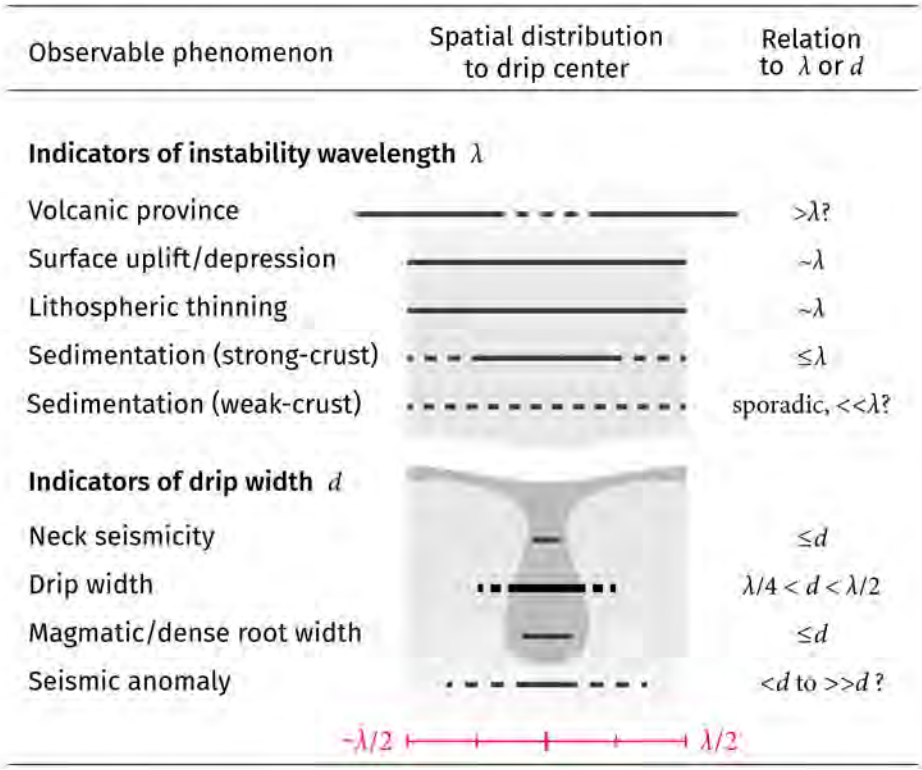

Figure 4.10: Relations between observable phenomena and measurements of drip size (wavelength and drip width). Scale bar (bottom) shows the length of a single wavelength, while other bars and values in the final column denote the expected widths of observable phenomena. Dashed bars indicate uncertain or likely ranges of spatial distributions. Image inset into the background illustrates a lithospheric drip for reference.

in width. Mantle seismic zones, in turn, are likely to occur in a necking region significantly smaller than the width of the drip itself (Figure 4.10).

Estimating drip width. Assuming that a given seismic anomaly corresponds to a dense piece of foundering lithosphere, estimating the size of the drip from the anomaly is not straightforward. Ideally, a relative wavespeed threshold (e.g., 1% or 3.5% faster than average) could be identified to delineate the foundering lithosphere from surrounding asthenosphere, but because the composition and absolute temperature of the upper mantle are poorly constrained, the expected relative wavespeed of any lithospheric drip in a given tomographic model is unknown. It is therefore not clear what the threshold should be (e.g., Calixto et al., 2013; Jones et al., 2014), and the chosen value is largely arbitrary. As an alternative, researchers often report drip sizes as a low-precision measurement of the horizontal width of the strongest part of the anomaly. This crude method allows some information to be gleaned from the tomographic anomaly, but it is affected by the resolution and sensitivity of the tomographic model; some models will show a large, strong anomaly where others show a small, weak one. For example, in the P-wave tomography model of Roth et al. (2008), the “Nevada cylinder” anomaly has a

fast relative wavespeed that is similar to the wavespeed of the Juan de Fuca plate and has an inferred width of ~150 km. In the model of Schmandt and Humphreys (2010), however, the Nevada cylinder appears as a broader (~225 km wide), more muted anomaly, much weaker than the Juan de Fuca Plate and weaker than other anomalies in the western U.S. that have been associated with lithospheric drips. As noted by Jones et al. (2014), a compact high-velocity anomaly in the upper mantle will commonly be smeared and appear as a larger, lower amplitude anomaly in a tomographic model. Seismic anomalies can therefore only provide a rough estimate of the width of dripping lithosphere and are most useful for ruling out hypotheses that call for drastically larger or smaller drip sizes. For example, if linear stability analysis of a 50 km thick layer predicts instability wavelengths of approximately 125–150 km and thus drip widths on the order of 50–75 km (Figure 4.10), the existence of a high-amplitude, 200 km-wide P-wave anomaly would not strongly support this particular hypothesis.

Measuring the size of anomalies in this way is also prone to confirmation bias: if a researcher expects a drip of a certain size based on estimates of layer thicknesses and rheology, unless the anomaly is of a drastically different scale, it is usually easy enough to delineate the anomaly in a way that confirms this size. Such difficulties significantly challenge the utility of seismic anomaly width as the preferred measure of a lithospheric drip's size. In general, the presence or absence of a high-wavespeed anomaly in tomographic models may often be more useful than the estimated width of the anomaly for constraining the lithospheric dripping hypothesis in a given location.

Importance of the instability wavelength. For a periodic instability, the instability wavelength λ is the average horizontal distance between neighboring drips, i.e., the distance between locations of maximum descent of either the LAB or the Moho (locations of maximum lithospheric thickening), or equivalently, between locations of maximum uplift of the LAB (locations of maximum lithospheric thinning; Figure 4.11). In the R–T instability framework, the characteristic wavelength is a consequence of the thickness, density contrast, and rheology of the negatively buoyant layer. The size and shape of the foundering drip, on the other hand, depend on other factors (Section 4.2.5) and are difficult to measure consistently (Section 4.2.5) and thus are less useful as an indicator of the spatial scale of the drip (Figure 4.11).

Instead, we suggest that wavelength can be estimated from surface deflections and volcanism for regions where dripping has been hypothesized. When descent of the Moho and lithospheric thickening also pulls down the topographic surface (i.e., a strong-crust drip), lithospheric thinning around the flanks of the drip produces an annulus of surface uplift (Neil & Houseman, 1999) or a "peripheral bulge" (Kapp & DeCelles, 2019), visible in numerical models of periodic and single drips (Figure 4.11). Therefore, the simplest interpretation of the topographic depression pulled down by the drip is that its width approximates the instability wavelength (Figures 4.5 and 4.11). If sediment accumulates in this depression, the width of sedimentary basin fill will also approximate the characteristic wavelength, but the width of the sedimen-

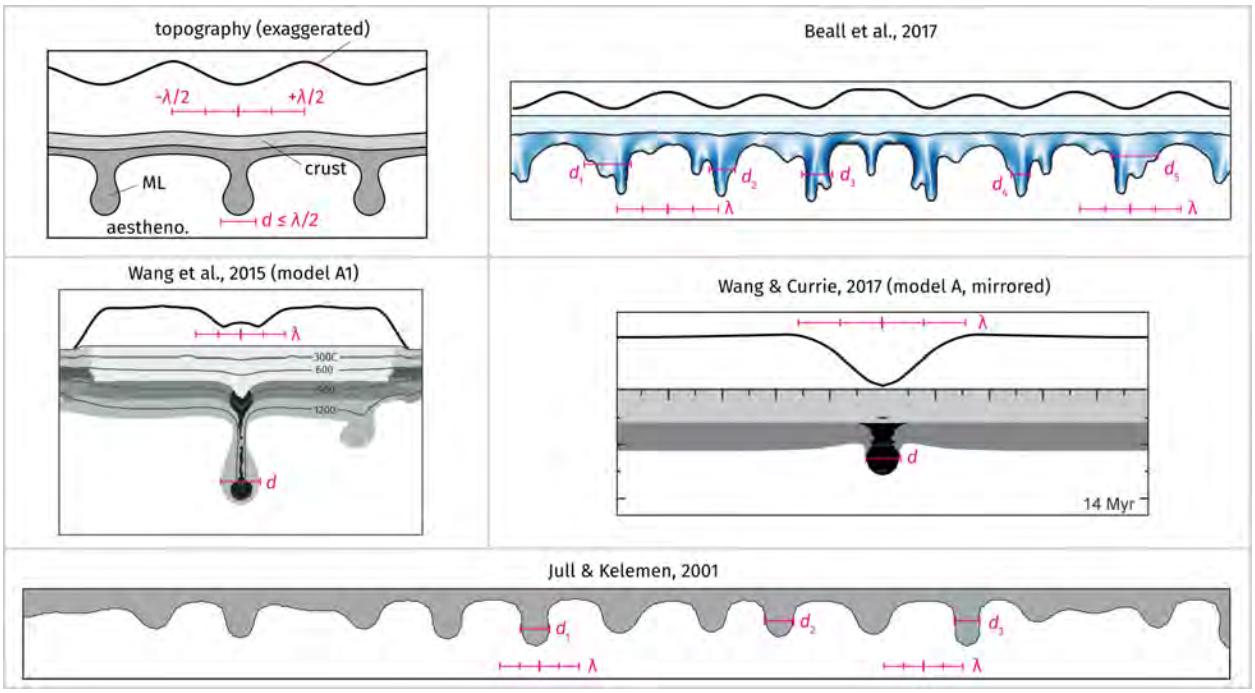

Figure 4.11: Illustration of characteristic wavelength (λ) and how it relates to the width of isolated drips (d_i). The first panel illustrates an idealized scenario, and the others are numerical modelling results. Drip widths are consistently less than one-half drip wavelength. For single drips, the wavelength corresponds to the width of the topographic depression. For multiple drips, even though the wavelength or drip spacing is relatively consistent, drip widths vary between $\lambda/2$ and $\lambda/4$, depending in part on where the measurement is taken. Together, these results illustrate the variable nature of drip morphology, even for a consistent drip wavelength.

tary basin may underestimate the wavelength if the depression is underfilled (Figure 4.10). Weak-crust drips should likewise produce regions of topographic uplift approximating the characteristic wavelength, though surface uplift of a few hundred meters may be difficult to detect in practice. Weak-crust drips should also produce thickened crustal welts that may be distinguished by an increase in Moho depth over a region of a size corresponding to the characteristic wavelength (Figure 4.6).

For either type of drip, upper-crustal deformation (horizontal compression and extension) may extend beyond the bounds of the drip wavelength, as central extension is accommodated by distal compression weak-crust drip (and vice-versa for a strong-crust drip, as illustrated by Figure 4.8). If the style of drip can be inferred, the patterns of surface deformation can provide information on the characteristic wavelength, but existing data do not often provide the level of detail necessary. For example, a contractional region overlying the center of the drip may switch to from contraction to extension after drip detachment while a peripheral region switches from extension to contraction; due to structural overprinting and the relatively low magnitude of deformation involved (e.g., DeCelles et al., 2015a), it may not be possible to determine the sequence of deformation in a given location. Drip-related deformation may also take advantage of pre-existing weaknesses in the upper crust, and the real-world expression

of upper crustal deformation associated with dripping may be more complex than numerical models predict.

Locations where the lithosphere thins are also prone to magmatism and high temperature metamorphism after drip detachment (Molnar & Houseman, 2004); middle to lower crust thickened by the growing drip is prone to partial melting and silicic magmatism (Kay & Kay, 1993). In the context of lithospheric dripping, heating and partial melting of the crust and upper mantle are a direct result of lithospheric thinning and upwelling of the asthenosphere during drip growth and detachment (Wang & Currie, 2015). Melts can also be generated by partial melting of the drip itself as it descends through the upper mantle (Ducea et al., 2013; Elkins-Tanton, 2007; Mori et al., 2009; Murray et al., 2015; Wang & Currie, 2015). Magmatism should therefore concentrate where the lithosphere is thinned, i.e., within a radius of $\lambda/2$ from the dripping center (Figure 4.11), but its ultimate occurrence at the surface as volcanic products may be more complex. Considering the variable preservation of volcanic rocks depending on the action of erosional surface processes, as well as the influence of crustal stresses and pre-existing faults and lineaments on the magma's path to the surface (e.g., Haag et al., 2019; Marrett & Emerman, 1992), the extent of volcanic regions may provide useful constraints on the instability wavelength but may not be able to directly confirm it.

4.3 Alternative hypotheses

4.3.1 Drips vs. slabs

In Cordilleran orogenic systems, subduction of oceanic plates at shallow angles produces flat slab events that can transport oceanic lithosphere many hundreds of kilometers inboard of subduction zones, providing another potential explanation for seismic anomalies in the upper mantle. Many of the seismic anomalies interpreted by some researchers as lithospheric drips have been interpreted by others as previously subducted oceanic lithosphere, whether sinking or stalled in the upper mantle (slabs and slab fragments; van der Meer et al., 2018), or still attached to a tectonic plate (fossil slabs; Dougherty et al., 2020; Pikser et al., 2012). In North America, for example, fragmentation and foundering of the Farallon slab has been hypothesized to explain many of the anomalies in the upper mantle (e.g., Burkett & Gurnis, 2013; Porritt, 2013; van der Meer et al., 2018), while the Isabella Anomaly in southern California has been interpreted both as a lithospheric drip (Section 4.4.1) and as a fossil slab still attached to the Monterey microplate (Cox et al., 2016; Pikser et al., 2012; Wang et al., 2013). In addition to tomographic anomalies, other geophysical data have proven to be equivocal in interpretation. For example, shear-wave splitting patterns interpreted by West et al. (2009) as evidence of vertical mantle flow induced by a lithospheric dripping event have also be interpreted to reflect toroidal flow around the edge of the Juan de Fuca plate (Zandt & Humphreys, 2008),

and the associated P-wave anomaly has been interpreted both as a drip (West et al., 2009) and as a fragment of the Farallon slab (Pavlis et al., 2012; Porritt, 2013).

The near-surface effects of lithospheric dripping, such as subsidence followed by uplift (e.g., Göğüş & Pysklywec, 2008) and volcanism (e.g., Kay & Kay, 1993; Kay et al., 1994; Wang & Currie, 2015) are qualitatively similar to the expected effects of low-angle subduction followed by slab rollback (e.g., Ramos & Folguera, 2009), or to oceanic slab break-off (e.g., Şengül-Uluocak et al., 2019). A Miocene flat slab event has been proposed for the Puna Plateau based on a reconstruction of the Juan Fernandez ridge (a volcanic hotspot track in the subducting Nazca plate; Yáñez et al., 2001), as well as geologic evidence such as upper crustal deformation and volcanism (e.g., Kay & Mpodozis, 2002; Ramos & Folguera, 2009). Many of the same geologic observations have also been interpreted to support two or more lithospheric drips beneath the Puna Plateau during the Middle to Late Miocene (e.g., DeCelles et al., 2015b; Schoenbohm & Carrapa, 2015). However, the existence of lithospheric drips and episodes of flat slab subduction are not mutually exclusive. It is possible that they may even be causally related (Kusky et al., 2014), and that dripping may have been triggered by the rollback of such slabs in some cases (e.g., Smith et al., 2017).

A related slab-vs.-drip problem exists in collisional settings, such as the SE Carpathians, the Hindu Kush, and the Pamir, where the closing of ocean basins and continental suturing leads to slab breakoff (e.g., Davies & von Blanckenburg, 1995; Garzanti et al., 2018) or wholesale delamination of the mantle lithosphere (e.g., G öğüş & Ueda, 2018). Two hypothesized drips with active mantle seismicity in the SE Carpathians and in the Hindu Kush have been alternatively interpreted as post-collisional oceanic slabs (McKenzie et al., 2019; Şengül-Uluocak et al., 2019) or delaminating mantle lithosphere (Göğüş et al., 2016). Adakitic melts are often thought to originate from partial melting of young oceanic slabs (e.g., Defant & Drummond, 1990), but may also reflect melting of basaltic lower crust following foundering continental lithosphere in drips or delamination events, or even melting of the drips themselves (e.g., Chapman et al., 2018; Ducea et al., 2013; Elkins-Tanton, 2007; Kay & Kay, 1993; Kay et al., 1994; Kay & Mpodozis, 2002). While there is often ambiguity between lithospheric dripping and slab-related dynamics, our goal here is to synthesize the evidence for the dripping hypothesis specifically. As we discuss below, progress in this area may come by directly testing these competing hypotheses against each other using geodynamic models or new analytical approaches.

4.3.2 Dripping vs. delamination

Many proposed drips have also been interpreted as delamination events (Figure 4.1 inset), including the Southern Sierra Nevada (e.g., Liang et al., 2014). Although both delamination and dripping involve gravitational foundering of dense mantle lithosphere (e.g., Krystopowicz & Currie, 2013), delamination requires a weak decollement layer that decouples the mantle lithosphere from overlying crust (Beall et al., 2017), and it produces an asymmetric, migrating upper-crustal response distinct from dripping (Göğüş & Pysklywec, 2008). Dripping and

delamination can be viewed as end-members in a spectrum of mechanisms for lithospheric foundering defined by the strength and thickness of the decollement layer (Figure 4.1 inset Beall et al., 2017). Delamination is susceptible to stalling if thermal diffusion cools and strengthens the decollement layer, which can force the instability to continue growing by internal deformation rather than by peeling away, resulting in styles of foundering intermediate to dripping and delamination (Beall et al., 2017). Delamination and intermediate styles of foundering can be triggered by step-changes in lithospheric thickness (Beall et al., 2017), which may be applicable to continental rifting and transform zones such as the Rio Grande Rift (e.g., Agrawal et al., 2019) and the North Island of New Zealand (Stern et al., 2013).

Although dripping and delamination share broadly similar outcomes, including thinned lithosphere, volcanism, and changes in surface uplift and subsidence, delamination is characterized by a spatially asymmetric response as the foundering lithosphere migrates in a preferred direction (Göğüş & Pysklywec, 2008). As described above, analysis of the Rayleigh–Taylor instability provides additional constraints for lithospheric drips that distinguish them from delamination, most notably the relationship between layer thickness and characteristic wavelength (and thus lithospheric thinning), and the rate of instability growth, which may be an order of magnitude higher for delamination than for dripping (Beall et al., 2017). Given the range of intermediate styles between dripping and delamination, the two end-members may be difficult to distinguish in practice, and this difficulty is reflected in many studies of lithospheric foundering. For the southern Sierra Nevada Batholith, for example, researchers have argued that foundering is characterized as dripping (e.g., Saleeby & Foster, 2004; Zandt, 2003), delamination (Le Pourhiet et al., 2006), or an intermediate style (Beall et al., 2017).

4.4 Potential dripping events

In the following sections, we synthesize the evidence for lithospheric dripping events reported in the literature. We recognize that each observation is likely to have multiple competing interpretations, and in most cases, lithospheric dripping is only one hypothesis among many under active investigation. Some locations have little evidence in support of a lithospheric dripping event, while others have more; this could be due to a larger volume of work done in a particular area, or it could be that the dripping hypothesis is only supported by a few observations in these locations. It is beyond the scope of our work to attempt to confirm or refute the dripping hypothesis for any particular location. Rather we synthesize, to the best of our ability, the evidence for all events around the globe for which any researchers have proposed a drip origin, regardless of the amount of evidence or the existence of competing hypotheses.

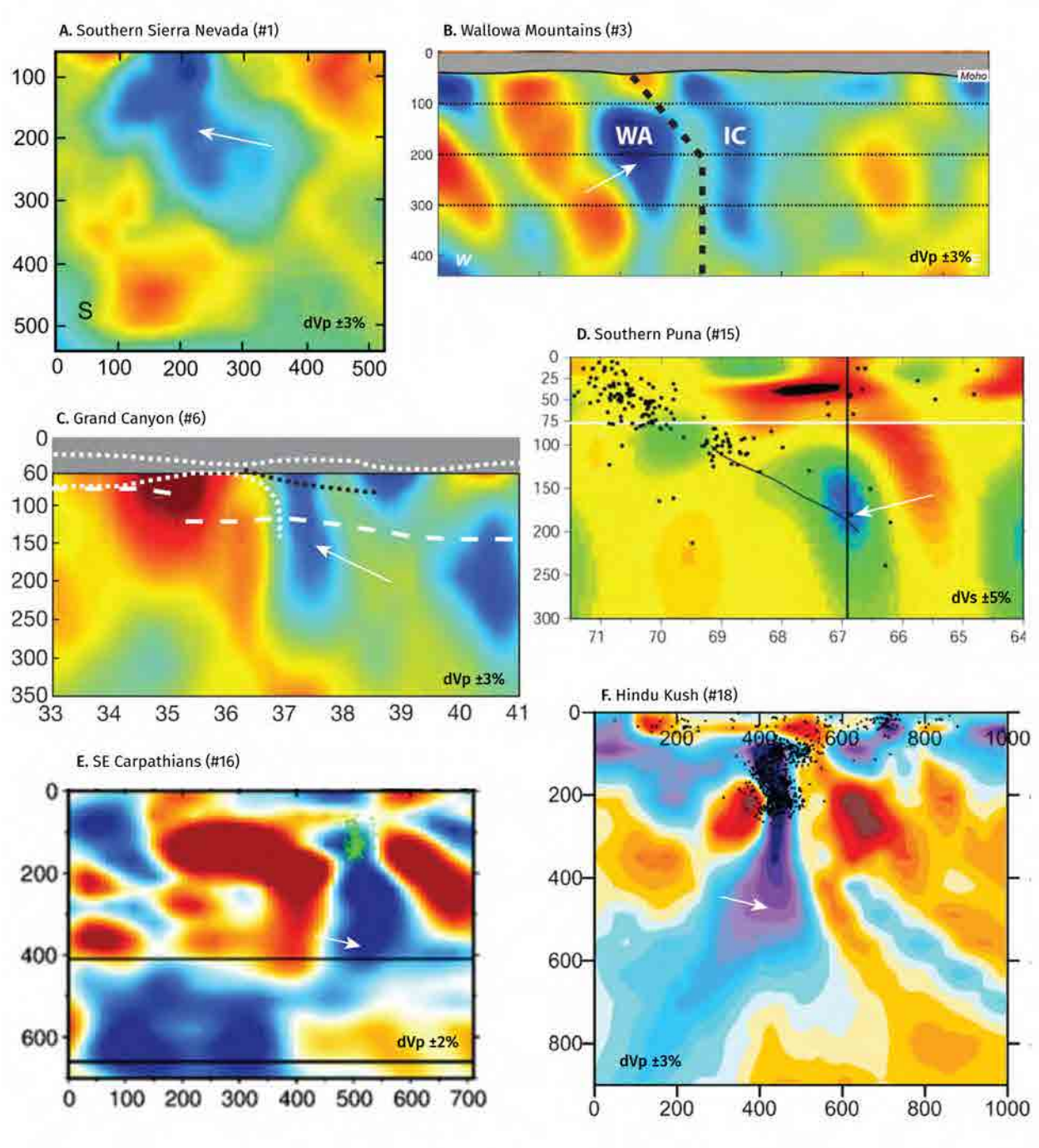

Figure 4.12: *Caption on next page.*

Figure 4.12 (previous page): Comparison of tomography anomalies for various purported drips. All panels show vertical slices through P-wave anomaly (dVp) models (except for the Southern Puna S-wave anomaly model, dVs). White arrows point to inferred lithospheric drips. Southern Sierra Nevada (Schmandt & Humphreys, 2010), Wallowa Mountains (Hales et al., 2005), Grand Canyon (Levander et al., 2011), Southern Puna (Calixto et al., 2013), SE Carpathians (Ren et al., 2012) and Hindu Kush (Koulakov, 2011). The latter three also display earthquake locations(dots).

4.4.1 North America

Studies of lithospheric dripping events in North America are concentrated in the tectonically active portion of the western U.S. (Figure 4.1). Lithospheric instabilities have long been proposed in western North America, including early studies of the Transverse Ranges (Humphreys & Hager, 1990) and Colorado Plateau (Bird, 1979). Much work has focused on the southern Sierra Nevada, where a prominent high-wavespeed anomaly (Figure 4.12a) coincides with patterns of uplift, subsidence, volcanism, and other indicators of lithosphere removal (e.g., Zandt & Carrigan, 1993, and see below). The advent of the EarthScope USArray project allowed the generation of many high-resolution tomographic models of the upper mantle beneath the U.S. that generally agree on the location of major 100–200 km scale anomalies (Becker, 2012), many of which have been interpreted as lithospheric drips (e.g., Schmandt & Humphreys, 2010). Nevertheless, the interpretation of these anomalies is not unequivocal, and alternate lines of research propose that they represent fragments of the Farallon slab (e.g., Pavlis et al., 2012; Porritt, 2013; Wang et al., 2013). In this section, we synthesize the literature on lithospheric dripping in North America (Figure 4.13).

Southern Sierra Nevada (#1) and Northern Sierra Nevada (#2). Two dripping events have been proposed for the Sierra Nevada Batholith (Figures 4.1 and 4.13). Early seismic tomography studies in the Sierra Nevada imaged a 4–5% fast anomaly extending up to 200 km depth beneath the Central Valley, termed the Isabella Anomaly (Figure 4.12a), originally interpreted as sinking lithospheric material (Jones et al., 1994). A positive P-wave anomaly was also identified beneath the northern Sierra Nevada, termed the Redding Anomaly (Benz & Zandt, 1993). Both anomalies extend to depths of 300–400 km and may be connected by a N–S-trending, shallower high wavespeed anomaly that could represent residual material that was entrained by the two larger anomalies (Jones et al., 2014). The southern Sierra Nevada topography is supported by low density upper mantle and lacks a thick crustal root, suggesting that eclogitic lower crust and underlying mantle lithosphere have been removed, replaced by hot asthenosphere (Wernicke et al., 1996). Xenoliths that were erupted before 8 Ma are composed of eclogite and garnet pyroxenite, while those that were erupted after 1 Ma are composed of spinel peridotite (Ducea & Saleeby, 1998), suggesting that removal was underway by ~10 Ma and was complete by 1 Ma, if not earlier. Potassic basalts from 3.5 Ma lack garnet-bearing xenoliths and may reflect

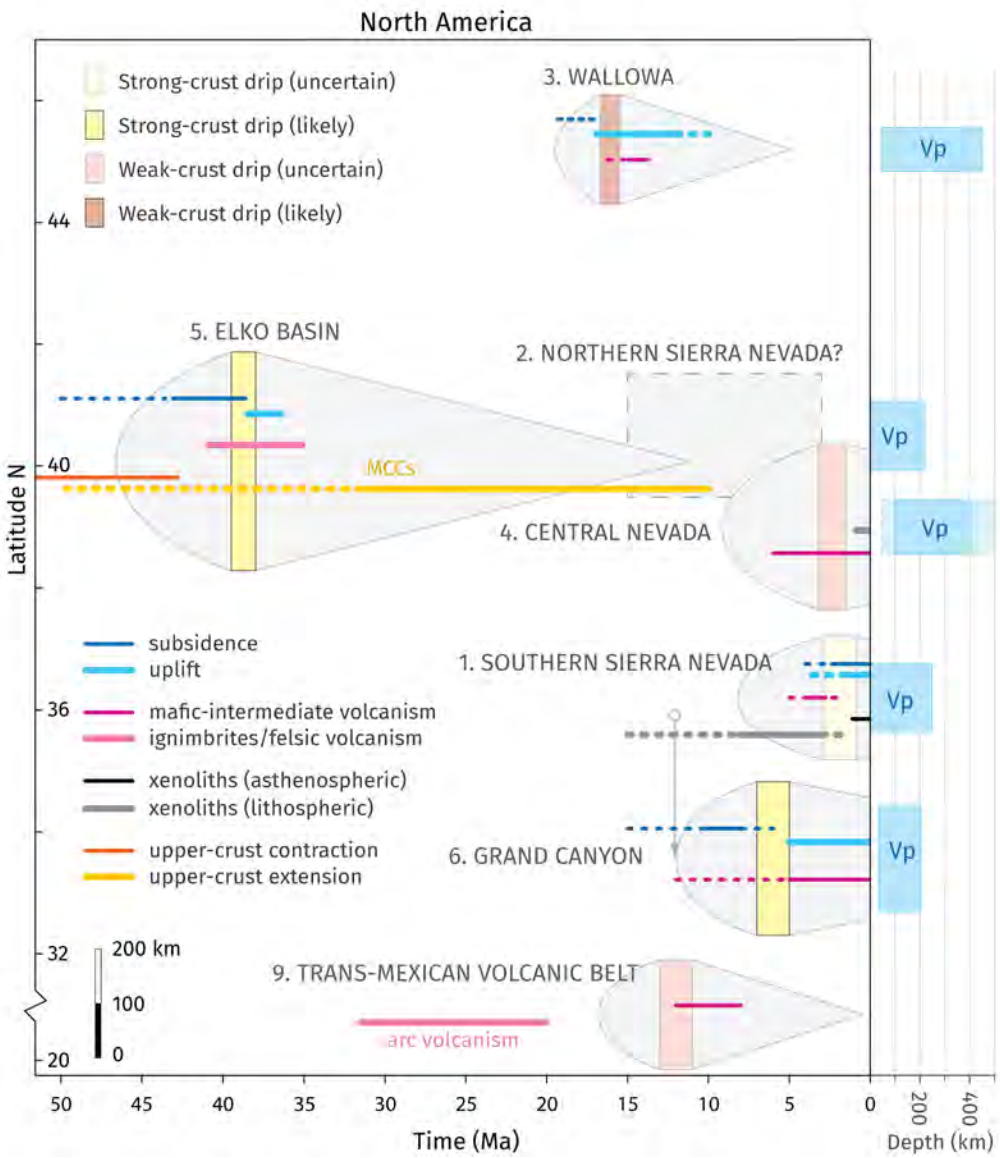

Figure 4.13: Potential dripping events in North America. Lines of varying colors plot the temporal range of various geological observations. Grey shapes represent our inferred periods of drip growth (parabolic heads), detachment (vertical bars), and lithospheric rebound/relaxation (tapering tails). Drips are labelled and numbered according to Figure 4.1. Dripping events are scaled according to their inferred wavelengths (see text for discussion). The axis on the right side plots the approximate widths and depths of seismic anomalies associated with each drip (blue for P-wave, purple for S-wave models). The arrow pointing to the Grand Canyon drip denotes a shift along the vertical axis of the plot to avoid overlap with the Southern Sierra Nevada drip. The Northern Sierra Nevada drip, which lacks extensive evidence, is depicted schematically. MCCs: metamorphic core complexes.

the final stage of the removal event, i.e., drip detachment (Figure 4.2), at approximately 3 Ma (Farmer et al., 2002; Molnar & Jones, 2004).

Zandt (2003) and Boyd et al. (2004) hypothesized actively foundering eclogitic material originating from the Sierra Nevada batholith as the source Isabella anomaly beneath the southern Great Valley. Zandt (2003) also related a cluster of Miocene volcanic provinces in the eastern Sierra to the removal event. The idea that lower crust is foundering as an R–T instability that drifted from east to west was elaborated by Zandt et al. (2004), who imaged a thickened crustal welt and lower crustal seismic anisotropies interpreted as shear zones associated with westward migration of a drip. Active removal of the lithosphere is also supported by the topography of the region, which is depressed in western Sierran foothills and Tulare lake basin of the Central Valley, but is elevated in the eastern part of the Sierra Nevada (Figure 4.14a; Saleeby & Foster, 2004). Jones et al. (2004) hypothesized removal of eclogitic lower crust around 3.5 Ma from the entire length of the Sierra Nevada batholith to explain a pulse of ~1 km uplift between 8 and 3 Ma that would have increased gravitational potential energy and influenced the migration of extension near the eastern side of the Sierra and compression into the California Coast Ranges. These authors identified the Redding and Isabella anomalies as evidence of this process. Molnar and Jones (2004), Harig et al. (2008), and Jones et al. (2014) applied the concept of multiple drips to explain both the Isabella anomaly beneath the Southern Sierra Nevada and Redding anomaly beneath the Northern Sierra Nevada. Cecil et al. (2012), on the other hand, posited that the Northern Sierra Nevada batholith had developed a dense root by Cretaceous time, and hypothesized gravitational foundering to explain why the root is not clearly imaged in some seismic data.

The removal timescale can be inferred from volcanism, seismic tomography, and topographic subsidence. Molnar and Jones (2004) estimated that drip growth (Figure 4.2, Phases 1 to 2) began ~10 Ma and that detachment (Figure 4.2, Phase 4) was largely complete by 3 Ma. Subsidence in the Tulare basin began ~2.2 Ma, however, consistent with westward migration of syn-drip subsidence after 3 Ma (Saleeby & Foster, 2004), and if the Isabella and Redding anomalies correspond to actively foundering material, they imply that material has sunk to a depth of 300–400 km but not yet detached (Molnar & Jones, 2004). Geologic evidence in the form of volcanism and topographic deflection is less apparent for the Northern Sierra Nevada dripping event, and its timing is poorly constrained (Cecil et al., 2012). Cecil et al. (2012) hypothesize that the more dispersed arc magmatism in the northern portion of the batholith may have resulted in multiple smaller dripping events over time, or that the root was destabilized during a ~15 Ma flareup of the proto-Cascade arc and was removed ~10.4 Ma. On the other hand, a low-amplitude, linear anomaly connecting the northern “Redding anomaly” with the Isabella anomaly in the south would place the removal around 3 Ma (Jones et al., 2014). Due to the relative lack of evidence for the northern dripping event, we depict it as a dashed box in Figure 4.13 and focus on the Southern Sierra Nevada event.

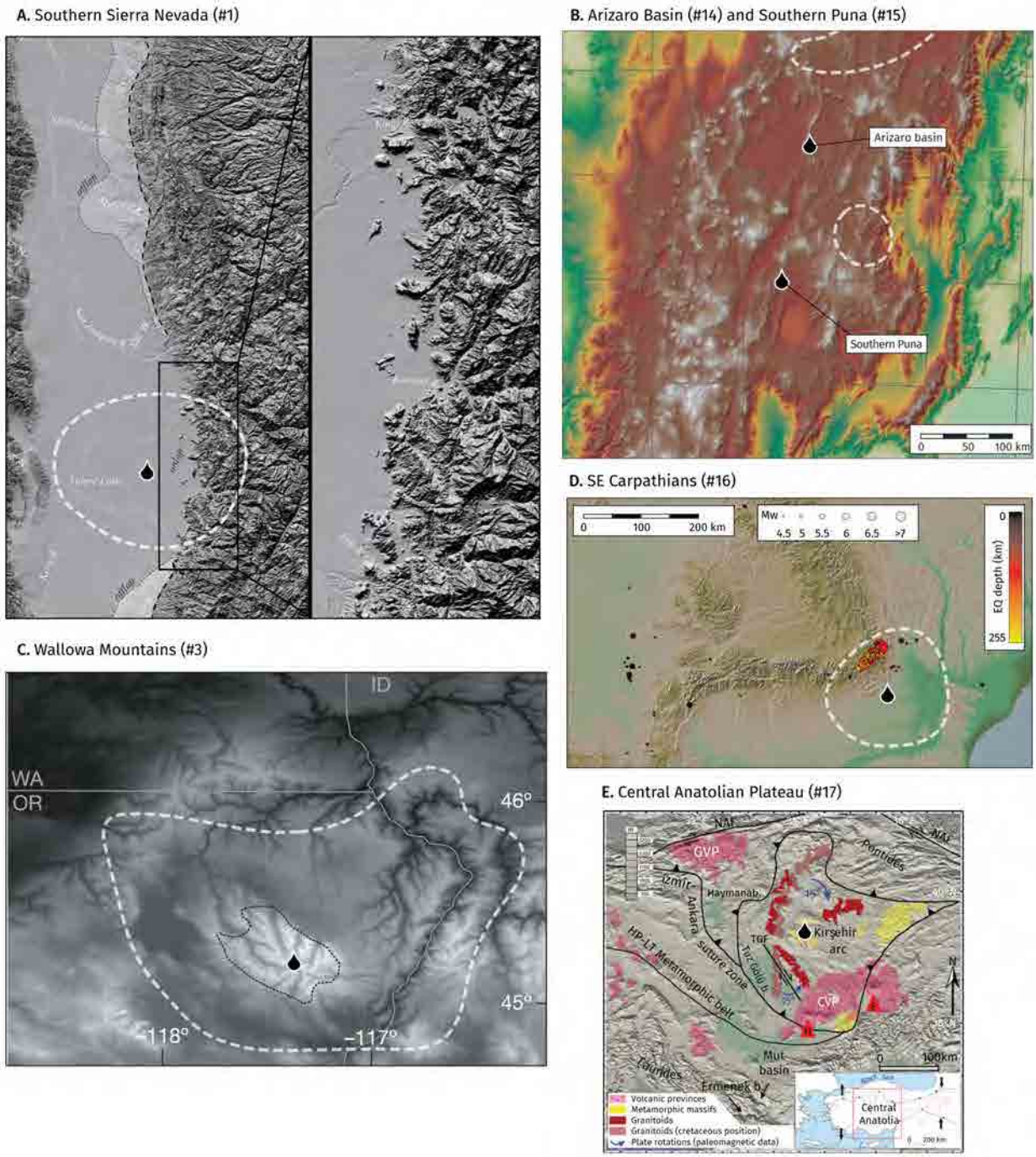

Figure 4.14: *Caption on next page.*

Figure 4.14 (previous page): Topographic features associated with purported dripping events. (a) Onlapping of Cenozoic deposits (shaded area) onto eroded basement (Saleeby & Foster, 2004). (b) Subdued topography interrupted by compressional faults and folds in the Arizaro region (DeCelles et al., 2015a), with more rugged topography interrupted by major ranges and extensional faults in the Southern Puna (modified from Schoenbohm & Carrapa, 2015). (c) Uplift and subsidence in a bullseye pattern centered on the Wallowa pluton (black dotted line; modified from Hales et al., 2005). (d) Range uplift and subsidence of the Focşani depression associated with mantle earthquakes (after Ren et al., 2012). (e) ~2 km of enigmatic uplift flanked by volcanism (from Göğüş et al., 2017). White dashed lines trace upper mantle seismic anomalies.

The characteristic wavelength of the Southern Sierra Nevada event can be approximated by the width of the associated topographic response and by the extent of volcanism related to removal. The Miocene volcanism associated with removal occurs in a circular region ~200 km in diameter (Zandt, 2003). The distance from the center of the Tulare basin to the center of high Sierran topography (which should represent one-half wavelength of the instability) is approximately 125 km (Saleeby & Foster, 2004). Insofar as the foundering of the lower crustal root and/or mantle lithosphere is characterized as R–T instability, these data indicate a wavelength of 200–250 km. As expected for R–T instability (see above), this wavelength is substantially larger than the width of the Isabella anomaly itself (~150 km). We therefore depict a dripping event 225 km in wavelength and the associated seismic anomaly in Figure 4.13.

The inferred syn-drip subsidence and post-drip rebound are consistent with the strong-crust style of dripping, indicating that the crust is relatively strong compared to the lithosphere. The “strong-crust” response is also consistent with the relatively low surface heat flux in the region, 20–40 mW $^{-}$2 (Wisian et al., 1999), which indicates that the middle to upper crust may be relatively cool and therefore rheologically strong.

Wallowa Mountains (#3). The Wallowa Mountains (NE Oregon, U.S.) are composed of Late Jurassic plutonic rocks that intruded the Permian to Triassic Wallowa island-arc terrane (Schwartz et al., 2010). Hales et al. (2005) imaged a high velocity anomaly ~80 km in width in the upper mantle, interpreting it as a sinking magmatic root of the Wallowa pluton (Figure 4.12b). A circular anomaly imaged by Schmandt and Humphreys (2010) has a width of ~125 km and extends from 90 to ~350 km depth. Darold and Humphreys (2013) later imaged a curtain-shaped high velocity anomaly and interpreted it as a foundering remnant of Farallon slab lithosphere, hypothesizing that the slab remnant was destabilized by the Yellowstone hotspot and then delaminated from south to north, triggering the Columbia River flood basalt eruptions. More recently, Stanciu and Humphreys (2020) argued that the Wallowa anomaly is separated from overlying lithosphere and distinguished it from other nearby “curtain” anomalies, from which it is also separated by the 87Sr/86Sr 0.706 isopleth representing the Precambrian margin of North America. Stanciu and Humphreys (2020) favored the interpretation that the Wallowa anomaly represents a piece of the Farallon slab that is largely detached from the overlying lithosphere.

The hypothesis that the Wallowa anomaly represents a lithospheric drip is due to Hales et al. (2005), who related lithospheric dripping to the eruption of the Columbia River flood basalts ca. 16 Ma and to an episode of rapid uplift totaling ~2 km over a 4 Myr period that was partially synchronous with volcanism. The region of flood basalt volcanism associated with dripping is approximately 150–200 km in width, as is the zone of surface uplift identified by Hales et al. (2005). These data, along with the anomaly width of ~80 km (Hales et al., 2005) suggest a characteristic wavelength of ~200 km (Figure 4.14b). The crust above the anomaly is substantially thickened (Darold & Humphreys, 2013), suggesting that, if the lithospheric dripping hypothesis is correct, the crust was relatively weak in the region and foundering occurred as a weak-crust drip. Weak-crust dripping is also consistent with the inference that rapid surface uplift occurred in the same region centered above the anomaly, with only minor subsidence of a few hundred meters occurring before the eruption of flood basalts (Hales et al., 2005). A weak crust is also consistent with the high surface heat flux, >100 mW $^{-}$2 (Wisian et al., 1999), extensive volcanism, and proximity to the Yellowstone hotspot track, all of which point to an elevated geothermal gradient. Flood basalt units thin over the center of uplift, indicating that a large portion of basalts were erupted during a phase of surface uplift ca. 16–15 Ma (Hales et al., 2005). We take 15 Ma as the most likely date for the detachment of the drip. We therefore infer that the Wallowa anomaly represents a weak-crust drip that began growing prior to 16 Ma and detached around 15 Ma.

Central Nevada (#4). West et al. (2009) proposed the existence of a drip beneath the Great Basin (Central Nevada, U.S.) to explain the presence of a positive tomographic anomaly (the "Nevada cylinder"; Roth et al., 2008) and mantle shear-wave splitting patterns. As defined by the 1.5% P wave contour, the anomaly is roughly 100 km in diameter and extends from depths of 50–100 km to 300 km (Roth et al., 2008), 500 km (West et al., 2009), or possibly up to 800 km or deeper in some images (West et al., 2009). The anomaly dips to the NE (Roth et al., 2008; West et al., 2009). Mantle peridotite xenoliths recovered from a young flow of the ~6 Ma–35 ka Lunar Crater Volcanic Field (LCVF) may be sourced from melts generated by the sinking drip (Dygert et al., 2019). Olivine recrystallization temperatures and grain sizes in myolinitc dunite xenoliths suggest ~50 MPa of differential stress at temperatures of 1,200–1,300 °C, implying low effective viscosities on the order of 10^{13} – –10^{16} Pa s, perhaps due to high strain rates in the neck of a vertically stretching drip (Dygert et al., 2019). The magmatic source of the LCVF became progressively deeper and lower in volume and percentage melting through time (Yogodzinski et al., 1996). Assuming that the Great Basin drip is related to eruption of the LCVF, Dygert et al. (2019) bracketed its growth to have begun before 6 Ma, while the highly strained xenoliths from a ~35 ka flow suggest that the drip began detaching before this time, and detachment may be presently ongoing. The apparent separation between the top of the tomographic anomaly and overlying lithosphere in some images (West et al., 2009) would imply that detachment of the drip was recently completed.

There is no unequivocal topographic signal associated with the drip (West et al., 2009), but smoothed topography in a ~300 km-wide region above the anomaly is ~100 m higher on average than the surrounding Great Basin (Dygert et al., 2019). This heightened topography is evidently not supported by thickening of the crust (Porter et al., 2014), which is actually 10–20 km thinner than the regional average (Dygert et al., 2019). Therefore, the topographic surface was evidently decoupled from the mantle lithosphere during dripping (West et al., 2009), suggesting either a very strong crust able to withstand stresses imposed from the mantle lithosphere with little to no deformation, or a very weak crust that flowed in response to dripping, without significant thickening. Given the location of the purported drip in an extensional tectonic province with elevated tectonic strain rates and regional heat flow exceeding 100 mW $^{-}$2 (Wisian et al., 1999), it is more likely that the crust was very weak compared to the mantle lithosphere. It is also possible that the pre-drip lithosphere was relatively thin and therefore imparted relatively small stresses to the crust when it foundered (West et al., 2009).

Based on the geometry of tomographic anomaly, a drip 100 km in diameter (West et al., 2009) would be expected to affect a region 200–400 km wide corresponding to the instability wavelength. The topographically elevated region ~300 km in diameter supports a drip of ~300 km wavelength. A 300 km wavelength of instability is consistent with dripping of a 100–120 km thick column of lithosphere, suggesting that the drip did not significantly deform the upper crust because of decoupling from the lithosphere, not because of a small size. We therefore estimate that the Central Nevada drip is best characterized as a weak-crust drip, with a characteristic wavelength of approximately 300 km (Figure 4.13).

subsubsectionElko, Nevada (#5)

Prior to the mid-Cenozoic, northeastern Nevada was located in the hinterland of the North American Cordillera between the Central Nevada thrust belt to the west and the Sevier fold-and-thrust belt to the east (e.g., DeCelles, 2004). Smith et al. (2017) hypothesized that lithospheric dripping occurred in the context of a Paleogene hinterland plateau during the NE to SW roll-back of the subhorizontal Farallon slab. Lake basins began forming in the Elko, Nevada, region ~48.7 Ma and lacustrine deposits grew in extent until between 43.4 and 40.8 Ma, onlapping local fluvial deposits and Paleozoic strata, and becoming hydrologically closed during the latter interval (Smith et al., 2017). Lacustrine conditions continued during deposition of increasingly proximal volcanic deposits (ash and ignimbrite beds), which are separated from overlying Oligocene units by a ~20 Myr unconformity. Smith et al. (2017) relate the overall SW-ward younging of lake deposits to reflect dynamic subsidence and uplift related to eclogitization and sinking of the Farallon plate but invoke R–T instabilities to explain the symmetrical bullseye-like subsidence patterns of the 100–200 km diameter basins. The Eocene-Oligocene unconformity would reflect increased crustal buoyancy following drip removal, which may have driven uplift and initiated metamorphic core complex extension (Smith et al., 2017).

Eocene sedimentary deposits near Elko occur within an ellipsoidal, 240×150 km region and the contemporaneous volcanic fields span a 160 km region. Taking this as an approximation

of the drip's characteristic wavelength gives an estimate of ~200 km. Although the Elko basin was the focus of their study, Smith et al. (2017) suggest that other Eocene lake basins may reflect this same process, including the Challis volcanic field (Idaho and Montana), Copper Basin (Nevada), the White Sage Basin (Utah), and lake deposits near Ely, Nevada. These basins were active depocenters during a ~12 Myr period and were activated in a SW-ward trending fashion. Distances of 220–250 km separate sequential depocenters. This spacing is consistent with a characteristic wavelength of ~200–250 km. Such a wavelength corresponds to dripping of a 60–100 km thick layer, supporting the notion that the entire mantle lithosphere may not have been removed as a result of these drips (Smith et al., 2017).

The occurrence of transient basins above lithospheric drips is consistent with strong-crust dripping, where the topographic surface is coupled to the descending Moho by a relatively strong crust. This type of dripping also predicts upper-crustal contraction during basin development, with extension occurring after drip detachment. Smith et al. (2017) describe two likely scenarios for the timing of extension (reflected in the Ruby Mountains core complex) in relation to basin deposition, one in which extension is synchronous with lacustrine deposition, and one in which extension begins after lacustrine deposition, during the Oligocene. The latter scenario is consistent with strong-crust dripping and is depicted in the schematic cross-sections by (Smith et al., 2017, fig. 6 therein). Volcanic deposits are intercalated with lacustrine deposits and are sourced from nearby calderas, indicating they may reflect partial melting of the lower crust, likely as a consequence of slab rollback and asthenospheric upwelling. The accumulation of dense magmatic residues may have promoted the formation of drips (Smith et al., 2017).

Grand Canyon (#6) and S Colorado Plateau (#7). Bird (1979) originally proposed that uplift of the relatively undeformed Colorado Plateau (western U.S.) was driven by delamination of the mantle lithosphere along a lower crustal weak channel. van Wijk et al. (2010) reported multiple, small (~100 km in width) fast shear-wave anomalies beneath the edges of the Colorado Plateau at depths of 100–200 km in the upper mantle. The same anomalies appear in the joint-inversion model of Obrebski et al. (2011) but are larger (~200 km in width) and reach depths of ~400 km. Schmandt and Humphreys (2010) imaged a vertical high wavespeed anomaly extending to 200 km in depth beneath the western Colorado Plateau, which Levander et al. (2011) combined with receiver functions to interpret as a sinking piece of upper mantle and lower crust (Figure 4.12c). Levander et al. (2011) used Grand Canyon incision rates and nearby volcanism to constrain the initiation of foundering to ~6 Ma. Xenoliths from the southern Colorado Plateau crystallized as arc-magmatic cumulates around 60 Ma, coincident with flat subduction and the Laramide orogeny, indicating that the seismically fast material imaged beneath the Colorado Plateau may in part represent foundering of a magmatic root (Erdman et al., 2016). The seismic anomalies seem to correlate with volcanism that migrated toward the center of the plateau, increased in volume, and became more mafic during the last 15 Ma (van Wijk et al., 2010). The locations of

the anomalies also correspond to residual peaks in Cenozoic uplift rates inferred by Roy et al. (2009) (Obrebski et al., 2011).

The gravitational instability beneath the western Colorado Plateau and Grand Canyon has characteristics of dripping, such as a vertically-extending, vertically oriented fast anomaly, as well as characteristics more commonly associated with delamination, such as an asymmetric thinning of the lithosphere concentrated on the eastern side of the anomaly, and a wave of surface uplift that propagated northeast to southwest (Levander et al., 2011). The width of the seismic anomaly, 200 km (Levander et al., 2011), is large compared with the width of the region affected by crustal thinning and surface uplift, 280 km. While it is possible that seismic images overestimate the size of foundering material, a 200 km-wide drip would be expected to affect a region at least 400 km wide with lithospheric thinning and uplift, corresponding to the instability wavelength. Furthermore, Levander et al. (2011) identify a gently-dipping interface extending from the lower crust that defines the top of the anomaly. The foregoing evidence favors a mode of foundering intermediate between the dripping and delamination end-members (Figure 4.1 inset) similar to the "triggered dripping" case analyzed by Beall et al. (2017), in which foundering begins as delamination along a weak zone but stalls out and evolves as a vertically stretching drip.

van Wijk et al. (2010) hypothesize that small-scale dripping along the southern edge of the Colorado Plateau explains the shear wave anomalies, volcanism, and ~400 m of anomalous topography at the edges of the plateau relative to the center. In the models of van Wijk et al. (2010), tectonic extension of the lithosphere surrounding the plateau results in the formation of a step-change in lithospheric thickness that becomes gravitationally unstable, generating elongated drips that are ~75 km wide and spaced ~275 km apart, in agreement with the shear wave anomalies. This spacing corresponds to the characteristic wavelength of instability of 275 km if the anomalies are lithospheric drips.

Volcanism flared up ~2.1–1.4 Ma around the edges of the fast S-wave anomaly, indicating that dripping may have begun ~3 Ma (van Wijk et al., 2010). The occurrence of high topography and volcanism around the edge of the drip with slightly lower elevations in the center indicates a strong-crust drip that has yet to detach. Strong-crust dripping is supported by the fact that the Colorado Plateau crust is inferred to be relatively strong from fast seismic velocities, local seismicity that extends deep into the crust, and low heat flow (Obrebski et al., 2011).

Alternatively, the migration of volcanism toward the center of the plateau may suggest that the entire southwestern edge of the Colorado Plateau lithosphere may be foundering in a piecemeal style intermediate to the delamination and dripping end-members (Beall et al., 2017). Foundering triggered by a step-change in lithospheric thickness at the edge of the plateau (van Wijk et al., 2010), rather than by small-scale perturbations to a negatively-buoyant layer would favor this intermediate style (Beall et al., 2017). For the purposes of this paper, we consider the foundering of the edge of the Colorado Plateau lithosphere to be intermediate

to delamination and dripping and therefore do not include it in our synthesis (Figure 4.13), though future research may provide additional constraints that change this conclusion.

Rio Grande Rift (#8). Song and Helmberger (2007) imaged a fast S-wave anomaly beneath the eastern flank of the Southern Rio Grande rift on the LA RISTRA seismic transect in New Mexico (U.S.) and interpreted it as a foundering portion of Archean cratonic lithosphere. On the 2-D seismic transect, the anomaly appears as a steeply E-dipping, fast S-wave region, approximately 100–125 km in width, and extending to at least 550 km depth. Schmandt and Humphreys (2010) imaged the anomaly in 3-D as a fast P-wave anomaly elongated along the NNW–SSE-trending axis of the rift. Seismic discontinuities or gaps in both the Moho and LAB occur above the anomaly, and surface topography above the LAB gap is consistently elevated (Agrawal et al., 2019).

While Agrawal et al. (2019) argued for progressive eastward delamination driven by a step in lithospheric thickness due to rifting (Stern et al., 2013), van Wijk et al. (2008) proposed that the lithospheric step seeded small-scale convective instabilities approximately 100 km in width, consistent with the size of the seismic anomalies. Removal of a portion of cratonic lithosphere could yield up to 500 m of isostatic uplift over a ~150–200 km wide region (van Wijk et al., 2010). Lithospheric dripping is favored by Byerly and Lassiter (2012) to explain xenoliths sourced from both the asthenosphere and cratonic lithosphere that equilibrated at only 45 km depth, because it would not require the wholesale removal of the cratonic lithosphere. Byerly and Lassiter (2012) hypothesized that “convective erosion” of the cratonic lithosphere could have been triggered by the mid-Tertiary rollback of the Farallon slab. Schmandt and Humphreys (2010) and Ricketts et al. (2016), on the other hand, suggested that the seismic anomaly associated with the Rio Grande Rift is a fragment of the Farallon slab.

Although the timing and style (strong-crust vs. weak-crust) of removal are not well constrained, the ~100 km width of seismic anomalies matches an approximately 100 km-wide gap in the LAB inferred from receiver function images (Agrawal et al., 2019), both of which support an instability wavelength of 200 km or greater. Similar to the foundering beneath the southern Colorado Plateau (#7) discussed above, a likely scenario for lithosphere removal beneath the Rio Grande Rift is that it was triggered by a step-change in lithospheric thickness (van Wijk et al., 2008). Depending on the presence of a weak decollement layer separating the crust from the mantle lithosphere, this style of foundering can proceed by peeling back the lithosphere, or by an asymmetric, migrating sinking of part of the lithosphere, with a high magnitude of shear strain, resembling a drip (Beall et al., 2017). We therefore omit this event in Figure 4.13.

Trans-Mexican Volcanic Belt (#9). Mori et al. (2009) hypothesized a drip to explain Miocene volcanic patterns in the Trans-Mexican Volcanic Belt (TMVB), which was preceded by the Oligocene development of the Sierra Madre Occidental volcanic arc and large silicic province (Ferrari et al., 2002). The eastern TMVB became active 22–11 Ma, while a volcanic gap existed in

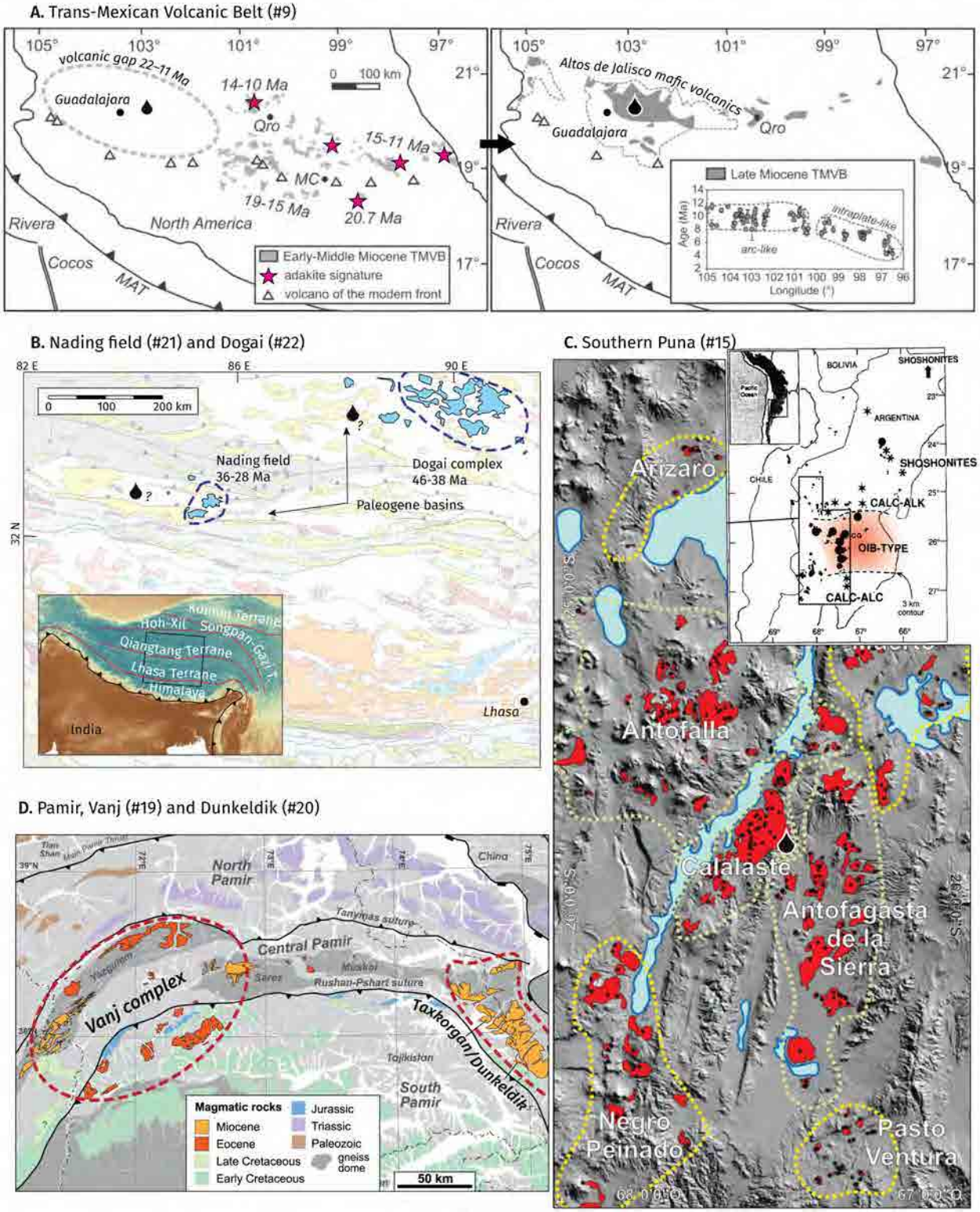

Figure 4.15: *Caption on next page.*

Figure 4.15 (previous page): Comparison of volcanic provinces associated with lithospheric drips. (a) Volcanic gap in the Early-Middle Miocene followed by flood basalts in the Late Miocene (modified from Mori et al., 2009). (b) Undeformed Eocene volcanic flows flank Paleogene basins with folded strata (modified from Kapp & DeCelles, 2019; Su et al., 2019). (c) Eocene and Miocene igneous complexes (outlined in orange) with geochemical evidence for lithospheric melting (modified from Chapman et al., 2018). (d) Region of OIB-type mafic volcanism flanked by calc-alkaline volcanics (inset; modified from Kay et al., 1994). Mafic back-arc volcanism is concentrated above the inferred dripping center (from Morfulis et al., 2020).

the western TMVB, in the southern portion of the Sierra Madre Occidental (Figure 4.15a). Mori et al. (2009) hypothesize that the volcanic gap resulted from the preceding buildup of a thick, dense mafic root beneath the Sierra Madre Occidental arc. The volcanic gap was followed by a pulse of Late Miocene flood basalt volcanism consisting of tholeiitic magmas sourced from spinel peridotites and a high-K suite with garnet signatures, indicating melting of the lithosphere (Mori et al., 2009). Basaltic volcanism occupied a roughly 200×200 km area in the Altos de Jalisco region during 11–8 Ma and was interpreted by Mori et al. (2009) to reflect drip detachment and sinking (Figure 4.15a). Assuming that the volcanic gap represented the earliest stages of R–T instability, dripping can be bracketed between 22–8 Ma, with detachment most likely ~12 Ma.

Ferrari et al. (2012) interpreted the Miocene volcanic gap and flood basalt eruptions as slab flattening followed by a slab tear and point out that no topographic signal is associated with the purported drip. The lack of an obvious topographic signal would also be expected if the mantle lithosphere is strongly decoupled from the upper crust during dripping. Urrutia-Fucugauchi and Flores-Ruiz (1996) estimated a crustal thickness of ~40 km throughout TMVB with only minor variations, indicating that little thickening or thinning of the crust can be ascribed to a drip. The surface heat flow of the region is extremely high, >200 mW $^{-}$2 (Prol-Ledesma & Morán-Zenteno, 2019), which would weaken the lithosphere and lower crust, decoupling the topographic surface from dynamic stresses originating in the upper mantle. Elevated lithospheric temperatures during the 8–11 Ma flareup are supported by the extensive eruption of flood basalts. The lack of a significant topographic response, therefore, may also be consistent with weak-crust dripping in the tectonic setting of the western TMVB. We estimate the wavelength of dripping as ~200 km based on the inferred size of volcanic gap and the average diameter of the Altos de Jalisco flood basalt province (Figure 4.15a). Given a wavelength of 200 km, we expect a drip 50–100 km in width (Figure 4.13).

4.4.2 South America

Lithospheric foundering has been inferred for many sections of the Andes, with much of the work concentrated in the high-elevation Central Andean Plateau in southern Peru, Bolivia, and NW Argentina (Figure 4.1). Many geophysical studies show that the Central Andes has a heterogeneous upper mantle characterized by seismic anomalies with a horizontal spatial

scale of 50–200 km beneath the Altiplano (e.g., Beck & Zandt, 2002; Beck et al., 2015; Myers et al., 1998; Scire et al., 2015) and Puna Plateaus (e.g., Bianchi et al., 2013; Calixto et al., 2013). The Central Andes also is characterized by a very thin mantle lithosphere, but with crust in excess of 60 km thick (Tassara & Echaurren, 2012) and with low shear wave velocities correlated to major silicic volcanic centers (Ward et al., 2013). Such geophysical datasets along with sedimentary records (e.g., DeCelles et al., 2015a; Schoenbohm & Carrapa, 2015), volcanism (Ducea et al., 2013; Kay & Kay, 1993; Kay et al., 1994; Murray et al., 2015), and paleoelevation proxy data (Garzione et al., 2006; Sundell et al., 2019) have been interpreted to reflect several episodes lithospheric foundering (Figure 4.16). Current evidence suggests that the southern Altiplano may have experienced rapid surface uplift in the late Miocene as a result of wholesale delamination of large swaths of the lithosphere (e.g., Garzione et al., 2008; Hoke & Garzione, 2008) or a large lithospheric drip (Molnar & Garzione, 2007), while mantle lithosphere and eclogitic lower crust may have been removed in piecemeal fashion, consistent with smaller lithospheric drips, from the Northern Altiplano (Sundell et al., 2019) and the Puna Plateau (DeCelles et al., 2015b; Schoenbohm & Carrapa, 2015). Research into potential lithospheric dripping events in other portions of the orogen is emerging, particularly in the Northern Andes of Ecuador and Colombia (Bloch et al., 2017), though these events are not as well characterized as those further south (Figure 4.16).

Northern Andes (#10). Within the Northern Volcanic Zone of the Andes (1°S to 5°N), Bloch et al. (2017) identify lower-crustal and upper mantle xenoliths that equilibrated at depths of 60–80 km and are negatively buoyant by ~2–10% with respect to underlying mantle. Bloch et al. (2017) infer from the relatively low elevations and high crustal thickness estimated for the region that the xenoliths are sourced from a gravitationally unstable root that is still attached to overlying crust, but that has been foundering in small-scale, piecemeal events due to thermal weakening and partial melting, similar to a process inferred by numerical models (Jull & Kelemen, 2001). Given the relative lack of data for this potential dripping event, and extremely early stage of instability, we are unable to infer the timing, size, or style of dripping for this region and have not included it in our synthesis in Figure 4.16.

Northern Altiplano (#11 and #12). Using a large dataset of hydrated volcanic glass paleoelevation proxies, Sundell et al. (2019) found evidence for one or two lithosphere removal events in the vicinity of the Northern Altiplano (14°S to 16°S). Elevations in the Western Cordillera volcanic arc at ~15°S increased from ~1.5 km to ~4.5 km between 21 and 17.5 Ma, consistent with dripping of magmatic residues or cumulates and mantle lithosphere. The elevation of the of the Altiplano at this latitude increased from ~1 km to ~4 km significantly later, between 15 Ma and 10 Ma. These high surface uplift rates (>0.5 km Ma^{-1}) are consistent with lithospheric foundering, though there are other explanations for the isotopic trends used to infer changes in paleoelevation (Sundell et al., 2019). Flexural modeling of a balanced cross-section of the

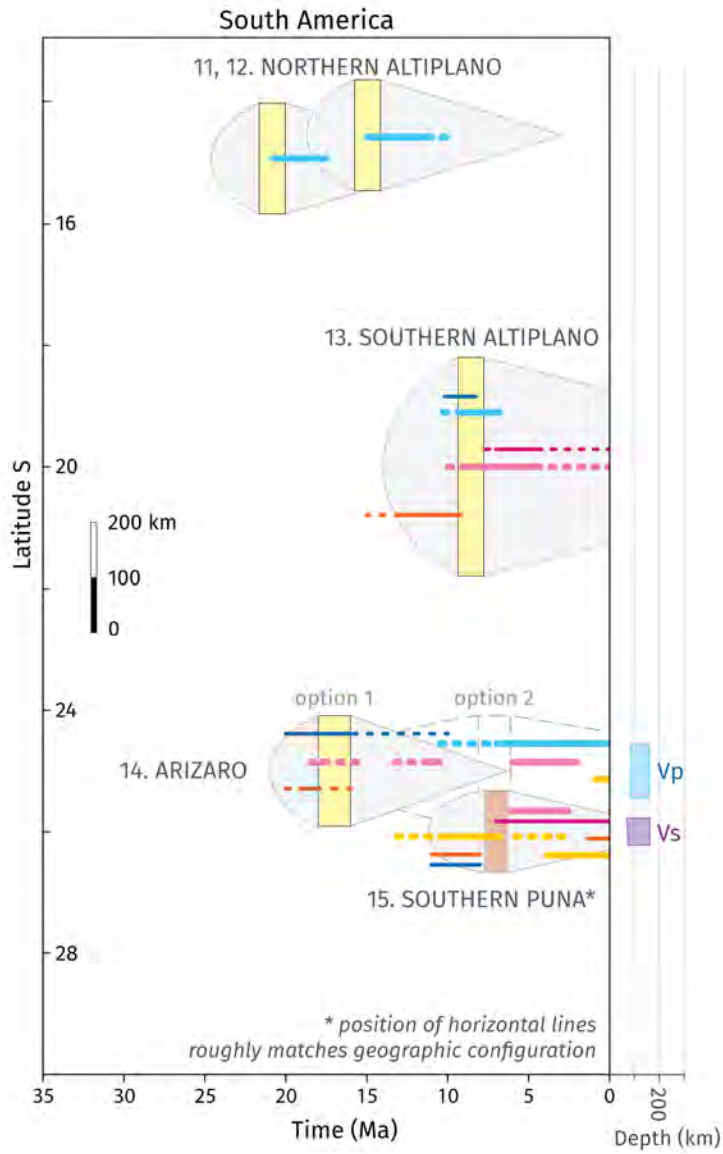

Figure 4.16: Potential dripping events in South America. Drips are labelled and numbered according to Figure 4.1. See Figure 4.13 for explanation of symbols. For the Arizaro drip, two different timings have been inferred in the literature, represented by option 1 vs. option 2.

Andes at this latitude requires imposing a long-wavelength uplift signal in addition to observed crustal shortening to match the elevation of the Altiplano, which indicates that a dynamic process such as lithospheric foundering is partly responsible for its ~4 km elevation (Buford Parks & McQuarrie, 2019). Alternatively, surface uplift of the Altiplano that immediately followed that of the Western Cordillera may be due to crustal flow (Sundell et al., 2019).

Assuming that lithospheric dripping is responsible for the inferred surface uplift in the northern Altiplano, we use the extensive dataset of Sundell et al. (2019) to estimate the characteristic wavelength. The centers of rapid surface uplift are separated by a distance of approximately ~185 km; additionally, each pulse of uplift affected a region of ~200 km in width,

suggesting that the characteristic wavelength is ~200 km. Sundell et al. (2019) infer that surface uplift was decoupled from crustal shortening but potentially associated with the detachment of R–T instabilities. We therefore estimate that dripping in the northern Altiplano is characterized as the strong-crust type, and that the period of surface uplift is associated with the detachment, rather than the growth, of each drip.

Southern Altiplano (#13). Intact mantle lithosphere is imaged to depths of 125–150 km beneath the Altiplano at 20° S, while it is largely absent beneath the western part of the Eastern Cordillera at the same latitude (Beck & Zandt, 2002; Myers et al., 1998), and a thick crustal welt directly beneath the Los Frailes volcanic field may reflect crustal thickening and volcanism after removal of mantle lithosphere (Beck & Zandt, 2002; Ryan et al., 2016). Garzione et al. (2006) linked removal of mantle lithosphere between ~10.3 Ma and 6.8 Ma to a rapid increase of 2.5–3.5 km in surface elevation inferred from oxygen isotopes of carbonates. This late Miocene time frame also corresponds to incision of low-relief paleosurfaces, accelerated exhumation of the Eastern Cordillera, and eruption of mafic lavas that began ~7.5 Ma (Garzione et al., 2006, and references therein). The large magnitude of surface uplift is consistent with removal of a thick layer of mantle lithosphere and eclogitized lower crust after the crust in the Central Andes had already attained thicknesses of ~70 km (Molnar & Garzione, 2007).

Inferred removal of Altiplano lithosphere was accompanied by the eastward propagation of the Andean thrust-front by ca. 11–8 Ma after a ~6 Myr period during which the thrust fault was stalled, possibly reflecting orogenic wedge propagation driven by increased taper following lithosphere removal (Anderson et al., 2018). Crustal mass balance calculations assuming an initial 40 km crust indicate that ~10 km of crust may have also been removed along with the lithosphere (McQuarrie, 2002). The composition of late-Cenozoic basalts on the Altiplano is consistent with partial melting of lithospheric material containing pyroxene, and individual volcanic fields show progressively higher temperature melts, consistent with melting of the descending drips (Ducea et al., 2013). These data, however, were interpreted as reflecting smaller, more recent dripping events (Ducea et al., 2013) than the large event inferred to have caused uplift of the Altiplano during the late Miocene.

Garzione et al. (2008) argue that lithosphere removal is partially responsible for the post-10 Ma uplift of a region encompassing most of the Western Cordillera, Altiplano, and Eastern Cordillera, a region >400 km in width. If this region corresponds to the ultimate extent of lithospheric thinning and removal, it suggests that the characteristic wavelength of the drip was also >400 km, corresponding to a negatively-buoyant layer 130–160 km thick. This process would yield a lithospheric drip approximately 200-100 km in diameter.

Molnar and Garzione (2007) argue that the mantle lithosphere was characterized by low viscosity during removal, consistent with a relatively cool Moho that had not yet equilibrated to increased heat flow due to extreme crustal thickening, and that the drip grew relatively quickly and detached over only a ~3 Ma period. Such weak mantle lithosphere is consistent

with the inference that the dripping began soon after tectonic thickening of the Altiplano crust and lithosphere, and with the inferred rapid surface uplift following drip detachment. The small magnitude of syn-drip crustal thickening, a relatively weak mantle lithosphere, and post-drip surface uplift all correspond to strong-crust dripping in our framework. We therefore estimate that the southern Altiplano experienced a large (~400 km wavelength) strong-crust drip that detached around 10 Ma (Figure 4.16).

Arizaro Basin (#14). The Arizaro Basin is a Miocene depocenter located in the central Puna Plateau between two major Cenozoic silicic volcanic centers: the Altiplano-Puna Volcanic Complex to the north (e.g., de Silva et al., 2006) and the more dispersed ignimbrite centers in the southern Puna (e.g., Beck et al., 2015; Kay et al., 2010; Ward et al., 2017). Low-temperature thermochronology and chronostratigraphic dating suggest that the Arizaro region was incorporated into the high elevation Puna Plateau by the mid to late Eocene and remained an erosional surface in the Andean hinterland until subsidence began in the Miocene (Carrapa et al., 2009; DeCelles et al., 2015a). DeCelles et al. (2015a) suggested that a growing lithospheric drip was responsible for the Miocene subsidence (~21–9 Ma) of the entire Arizaro Basin. On the western margin of the basin, out-of-sequence thrusting on a reverse fault and syn-tectonic sedimentation ~20–17 Ma followed by eruption of ignimbrites ~17 Ma supports the inferred lithospheric dripping event (Schoenbohm & Carrapa, 2015). The thrust fault was reactivated as a normal fault in the Pliocene–Quaternary, indicating post-drip extension (Schoenbohm & Carrapa, 2015). DeCelles et al. (2015a) also interpreted the low-temperature thermochronology of the basement-cored Sierra de Macon Range in the center of the basin to suggest a mid-Miocene heating event coeval with rapid sedimentation in the Arizaro Basin, and contractional folds in fine-grained sediments suggest that the basin fill was shortened during or soon after deposition around 10 Ma (DeCelles et al., 2015a).

The sediment accumulation curve, thermochronology, and ~100–150 km diameter of the Arizaro Basin (Figure 4.14b) are consistent with convective removal of a small (~50–75 km diameter) drip, perhaps reflecting removal of eclogitic lower crust. In the models of Wang et al. (2015), dripping eclogitic lower crust yields a drip of approximately 75 km in width, and subsidence affects a 200–250 km wide region at the surface. This width of surface subsidence corresponds to the instability wavelength and is larger than known outcrops of sedimentary fill, but the eastern limit of the basin is not exposed (DeCelles et al., 2015a). A drip width of 50–75 km also matches the size of a tomographic anomaly located in the upper mantle northeast of Arizaro (Bianchi et al., 2013; Calixto et al., 2013; Schurr et al., 2006). We thus estimate the characteristic wavelength of the Arizaro drip as ~200 km. The occurrence of syn-drip topographic subsidence and contraction, sedimentation above the center of the drip, and post-drip flexural rebound is consistent with strong-crust dripping.

The timing of the Arizaro drip is constrained by multiple lines of evidence but remains somewhat equivocal. Sedimentation in both the western margin (Quebrada del Agua For-

mation; Schoenbohm & Carrapa, 2015) and central parts of the basin (Vizcachera Formation; DeCelles et al., 2015a) suggests that the drip began forming ~20 Ma, with the most rapid accumulation occurring 18–16 Ma in the central part of the basin (DeCelles et al., 2015a). Syndepositional contraction is indicated by 17 Ma growth strata on the western margin of the basin (Schoenbohm & Carrapa, 2015) and folded fine-grained sediments dated to ~10 Ma toward the center of the basin (DeCelles et al., 2015a). The center of the basin was inverted and uplifted after the deposition of the Upper Miocene Batín Formation (~8.4 Ma), leading DeCelles et al. (2015a) to suggest drip detachment by ~7 Ma. In the models of Wang et al. (2015), topographic rebound occurs a few Myr before the drip fully separates from the overlying crust, largely due to lower crustal thickening, also pointing to detachment around 7 Ma. On the other hand, Schoenbohm and Carrapa (2015) suggested that detachment was signaled by the eruption of the Aguas Calientes ignimbrites (17.2 and 10.5 Ma) to the NE of the Arizaro Basin, and thus indicated detachment of the Arizaro drip as early as 17 Ma. Although the Aguas Calientes region did yield a silicic eruption around 17 Ma (Petrinovic et al., 2010), the largest ignimbrites in the region cluster temporally around 10.5–10 Ma (Kay et al., 2010), closer to the timing of detachment inferred from sedimentary evidence. Lithospheric thinning around the edges of the growing drip may have allowed asthenospheric upwelling and crustal heating before the drip had fully detached. More complex geodynamic models are likely required to distinguish these competing hypotheses; we depict the two main scenarios for the detachment of the Arizaro drip (17 Ma vs. 7 Ma; Figure 4.16).

Southern Puna (#15). Kay and Kay (1993) and Kay et al. (1994) proposed lithosphere removal beneath the southern Puna Plateau as an explanation for the spatiotemporal cluster of back-arc volcanism in the late Miocene–Pliocene located above a seismic gap in the subducting Nazca slab. Back-arc volcanism in this region yielded mafic, OIB-type volcanic fields west of major silicic calderas, such as Cerro Galán (Figure 4.15c). Ignimbrites from these silicic volcanic centers may represent crustal melting by upwelling asthenosphere following lithospheric removal (Kay & Kay, 1993; Kay et al., 1994). The southern Puna experienced an ignimbrite flareup ca. 7.5–0.2 Ma that saw the eruptions of the Cerro Galán and Cerro Blanco calderas, as well as three smaller ignimbrite complexes (Kay et al., 2010), suggesting that lithosphere removal was well underway if not completed by around 8–7 Ma.

Geochemical studies of mafic back-arc volcanics support the occurrence of multiple drips rather than wholesale lithospheric delamination. Back-arc mafic lavas show evidence for progressively higher equilibration temperatures that increase 100–250 °C over 1–5 Myr within a volcanic field (Ducea et al., 2013). Whole-rock Fe/Zn ratios suggest partial melting of descending, pyroxenite-rich lithospheric material (Murray et al., 2015). Back-arc basalts are concentrated around the Sierra de Calalaste range in the center of the southern Puna (Figure 4.15c; Kay et al., 1994; Risse et al., 2008), and the volcanic region expanded over time, with older flows >7 Ma mainly concentrated in the center (Haag et al., 2019; Schoenbohm & Carrapa, 2015).

Ward et al. (2013) and Ward et al. (2017) imaged multiple low shear-wave velocity zones in the southern Puna crust circumscribing the Calalaste Range, correlated to Pliocene–Quaternary silicic volcanic centers (Kay et al., 2010). The zone of back-arc volcanism in the southern Puna coincides with a region of very thin mantle lithosphere and the thickest crust in the Puna (e.g., Tassara & Echaurren, 2012), consistent with a dripping event that removed most of the lithosphere and thickened the remaining crust.

Back-arc volcanism was also roughly contemporaneous with a shift in the stress regime of the southern Puna Plateau, from E-W compression to E-W extension and strike-slip faulting (Allmendinger et al., 1989; Kay & Kay, 1993). Studies of sedimentary basins and upper-crustal strain in the southern Puna support the drip hypothesis. The Paleogene to Quaternary Antofalla basin, situated immediately to the west of the Sierra de Calalaste and approximately above the center of the purported drip (Figure 4.14b), experienced a phase of transient extension that began ~11 Ma and lasted until the Late Pliocene–Quaternary (Tye et al., 2022). This extensional episode represents the earliest evidence for major extension in the region and syn-extensional strata are overlain by the earliest dated back-arc basaltic volcanics in the Southern Puna Plateau (Tye et al., 2022). Approximately 200 km to the SE of Antofalla, Schoenbohm and Carrapa (2015) reported a pulse of sedimentation in the Pasto Ventura basin accompanied by syn-sedimentary contraction around 10.5–7.8 Ma, the later phases of which are contemporaneous with the beginning of mafic volcanism (8.7 Ma) in the Sierra de Calalaste and predate the eruption of ignimbrites from Cerro Galán by a 2 to 3 Myr. Extensional deformation in the Pasto Ventura region began as early as 6 Ma by reactivating pre-existing contractional faults (Schoenbohm & Carrapa, 2015; Zhou & Schoenbohm, 2015). This evidence points toward a drip that began growing by ~11 Ma and detached ca. 6 Ma, with the region still experiencing post-drip volcanism (Schoenbohm & Carrapa, 2015).

Geophysical studies are supportive of the drip hypothesis. Lithospheric drips would initially be sheared to the west by subduction-driven corner flow and then transported eastward along the top of the Nazca slab (Currie et al., 2015). High-velocity anomalies in the upper mantle beneath the eastern margin of the Puna are interpreted as pieces of sinking lithosphere (Figure 4.12; Bianchi et al., 2013; Calixto et al., 2013). Models indicate that westward asthenospheric flow would induce lithospheric thinning and crustal heating mainly on the eastern margin of a drip (Wang et al., 2021). Liang et al. (2014) imaged a crustal low-Q region beneath the Cerro Galán caldera (90 km east of Antofalla), and a high-Q anomaly at 50–150 km depth immediately east of the crustal anomaly, together interpreted as evidence of lithosphere removal. DeCelles et al. (2015b) summarized available geophysical studies to suggest a crustal zone of low shear velocity beneath Cerro Galán and a high P-wave anomaly immediately to the east above the subducting Nazca slab as evidence of lithospheric foundering.

In contrast to the strong-crust drip inferred for the Arizaro Basin (Section 4.4.2), several lines of evidence point to weak-crust dripping beneath the Southern Puna. The co occurrence of 60 km thick crust (Beck et al., 2015; Tassara & Echaurren, 2012) structures accommodating

Pliocene to Quaternary horizontal extension and strike-slip (e.g., Allmendinger et al., 1989) is consistent with weak-crust dripping, which involves lower crustal thickening and upper-crustal extension. The weak rheological behavior of the southern Puna crust is corroborated by its low elastic thickness (<10 km; Tassara et al., 2007), and is consistent with crustal low-velocity zones, elevated volcanism, and the back-arc setting of the region (Babeyko et al., 2002). The pattern of syn-drip upper-crustal extension centered on the Antofalla region accompanied by syn-drip contraction in peripheral regions such as Pasto Ventura also supports the interpretation of a weak-crust drip (Figure 4.6).

The size of the Southern Puna drip is less well-constrained than for the Arizaro drip due to the fact that dripping did not produce a contiguous hinterland basin deposit. However, available evidence points toward a slightly smaller drip beneath the Southern Puna. The area of concentrated late-Cenozoic extension covers a roughly circular region ~165 km in diameter (Schoenbohm & Carrapa, 2015). This region is delimited on its western edge by a concentration of mafic volcanism, and on its NE side by the Cerro Galan silicic caldera (see fig. 1 in Schoenbohm & Carrapa, 2015). Assuming that the region of strongest extension and volcanism corresponds to the characteristic wavelength of the drip, it can be estimated as at least 165 km, approximately 20% smaller than the Arizaro drip. The upper mantle seismic anomaly that has been associated with the Southern Puna drip is roughly half the size of the one associated with the Arizaro drip. A distance of 150–200 km separates the center of the Arizaro Basin from the inferred dripping center in the Southern Puna, which, assuming both locations experienced Rayleigh–Taylor-like instabilities, points to a characteristic wavelength of <200 km (Figure 4.14b). Spatiotemporal patterns of upper-crustal strain in the southern Puna also provide an estimate of the instability wavelength. While extension associated with the growth of the drip was underway near Antofalla around ~11 Ma, Pasto Ventura and other flanking regions were experiencing contraction (Tye et al., 2022), as would be expected at a distance of approximately one-half wavelength from the center of a weak-crust drip (e.g., Molnar, 2015). These regions lie ~75–100 km from the purported dripping center beneath the Salar de Antofalla and Sierra de Calalaste. We therefore estimate that the drip in the Southern Puna had a characteristic wavelength of ~160 km.

4.4.3 Eurasia

Researchers have invoked the lithospheric dripping hypothesis throughout the Alpine-Himalaya collisional orogen (Figure 4.1). Distinguishing lithospheric drips from remnant oceanic slabs is a key challenge in exploring the lithospheric dripping hypothesis in these collisional settings. A purported drip beneath the SE Carpathians is the most well-studied in the region, with evidence including mantle seismicity, tomographic images, volcanism, sedimentation, and patterns of surface uplift and subsidence (e.g., Lorinczi & Houseman, 2009, and see below). The mantle seismicity beneath the SE Carpathians indicates that cold lithosphere is actively vertically stretching (Lorinczi & Houseman, 2009). A similar pattern exists beneath both the

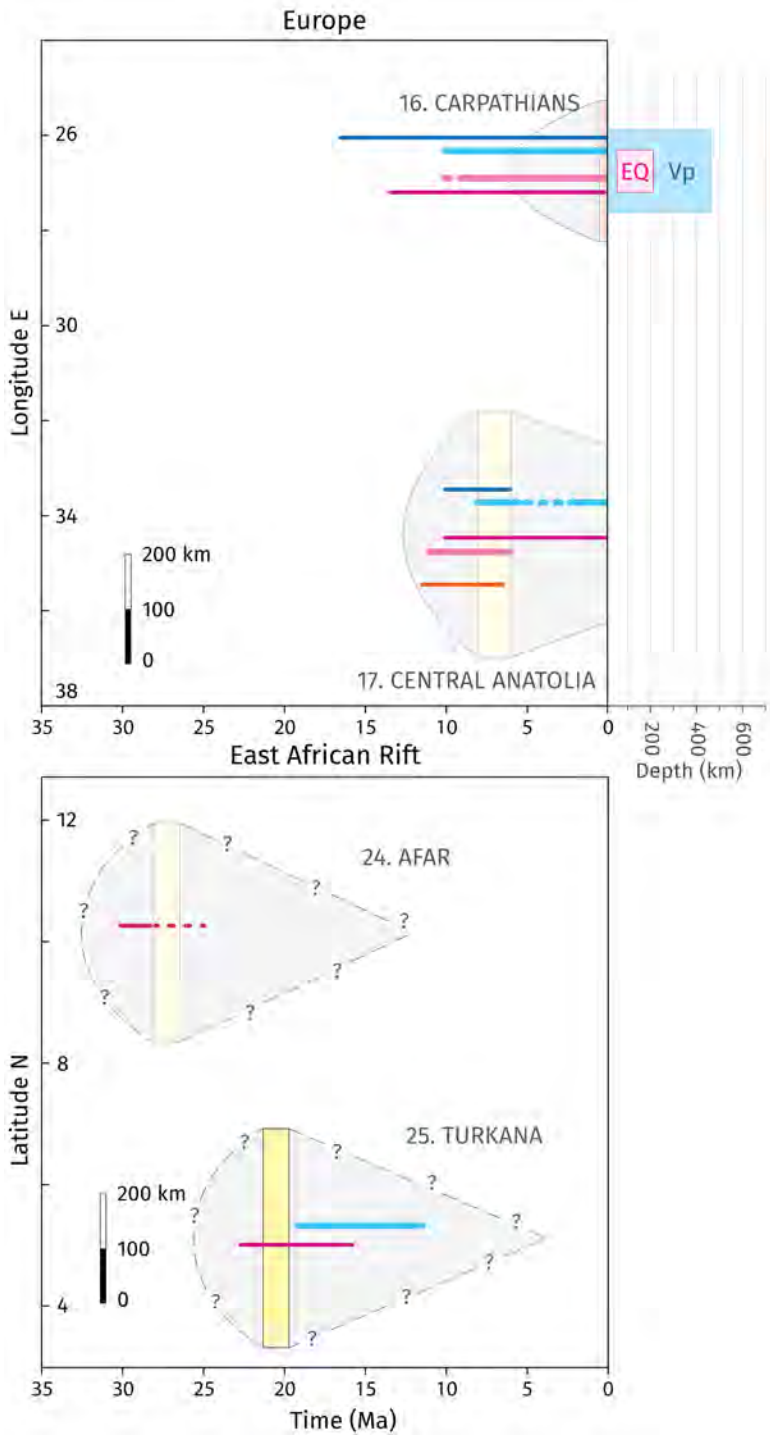

Figure 4.17: Potential dripping events in Europe and the East African Rift. Note the change in vertical axis units between the top and bottom panels. Drips are labelled and numbered according to Figure 4.1. See Figure 4.13 for explanation of symbols. Regions of active mantle seismicity shown as magenta boxes (EQ).

Hindu Kush and Pamir mountain ranges, though the dipping interface of mantle seismicity beneath the latter region appears to outline the remnant of an oceanic slab (Molnar & Bendick, 2019). An older episode of dripping beneath the Pamir, however, is hypothesized based on the geochemistry of Paleogene magmatic rocks (Chapman et al., 2018). Similar Cenozoic magmatic and volcanic rocks are also distributed throughout the Tibetan Plateau and have been interpreted as partial melts of descending drips (Kapp & DeCelles, 2019).

SE Carpathians (#16). The Carpathian Mountains result from Miocene crustal shortening and thickening (e.g., Knapp et al., 2005) concomitant with horizontal extension of continental crust in the Pannonian Basin (e.g., Royden et al., 1983). The SE Carpathians (Vrancea, Romania) are underlain by a seismogenic zone in the upper mantle extending to depths of 200 km (Figure 4.12e; Roman, 1970). In the foreland of the SE Carpathians, the Focşani basin developed during the Middle Miocene, but the foredeep migrated away from the Carpathian orogenic load around 8–5 Ma, and a pulse of >4 km of sedimentation occurred during the Pliocene–Quaternary during a period of extensional faulting (Tărăpoancă et al., 2003).

Early work tied mantle earthquakes to volcanism and gravity anomalies to hypothesize sinking lithosphere beneath the SE Carpathians (Roman, 1970) which became the dominant interpretation of the region (Horváth, 1993; Wortel & Spakman, 2000). The topographic and volcanic phenomena are often attributed to slab rollback (e.g., Horváth, 1993), or slab breakoff following subduction-closure of a narrow ocean basin (Mason et al., 1998), while Knapp et al. (2005) proposed that delamination of the continental lithosphere followed collision. The latter interpretation was supported by Fillerup et al. (2010) with seismic data showing high topography underlain by thin crust and a shallow Moho. Martin and Wenzel (2006) imaged a vertical, positive tomographic anomaly extending to depths of ~300 km beneath the SE Carpathians, as well as a slow anomaly beneath a region of Neogene volcanism in the Transylvania Basin. Ren et al. (2012) imaged a cylindrical anomaly ~125–150 km in width reaching depths of ~450 km (Figure 4.12e) and interpreted the pattern of positive and negative anomalies in the region as evidence of lithospheric foundering, either as delamination or R–T instability.

Lorinczi and Houseman (2009) proposed the R–T instability and lithospheric dripping as an explanation for mantle seismicity at depths of 60-200 km in the Vrancea region of the SE Carpathians. Rates of vertical extension for the seismogenic region in the mantle would require a slab that ceased subducting at 10 Ma to be ~200 km deep (Lorinczi & Houseman, 2009). Lorinczi and Houseman (2009) showed vertical extensional strain would be concentrated in the neck of an active R–T drip, with the deeper parts of the drip experiencing little strain. The 3-D geodynamic models of Lorinczi and Houseman (2009) include a crust and mantle lithosphere with similar viscosity that would explain the crustal thickening observed in the Vrancea region and lithospheric thinning in the Transylvanian basin. Harangi et al. (2013) supported the drip hypothesis by analyzing alkali basalts of the Perşani volcanic field, which derived from decompression melts of the asthenosphere at depths of 60–90 km.

If the SE Carpathians is undergoing lithospheric dripping, the seismogenic zone, which covers a horizontal area of ~30 by 80 km, represents a region of high strain in the actively necking portion of the drip (Lorinczi & Houseman, 2009). Tomographic images resolve a high-velocity body 150 km in width (Figure 4.12e), meaning we can expect a characteristic wavelength of dripping on the order of 300 km or greater. Assuming an initial lithospheric thickness of 100 km including a 37.5 km crust (Lorinczi & Houseman, 2009) results in an instability with characteristic wavelength ~300–350 km (Neil & Houseman, 1999). If the high topography of the SE Carpathians flanked by the Focşani and Transylvanian basins results from a drip of the weak-crust type, as the models suggest, its wavelength can be approximated by the width of the welt of elevated topography. Although the actual topography of the SE Carpathians region is more complex than that predicted by these simple drip models, the width of the topographic welt roughly matches the predicted 350 km wavelength (Figure 4.14d). This wavelength also matches the distance between flanking low-velocity regions in tomographic images, approximately 300 km (Ren et al., 2012).

Central Anatolian Plateau (#17). Göğüş et al. (2017) proposed lithospheric dripping in Central Anatolia to explain patterns of surface uplift and a V-shaped lithosphere-asthenosphere boundary in tomographic images, hypothesizing that tectonic shortening and oroclinal folding of the late Cretaceous Kırşehir arc during a late Paleocene–early Eocene collisional event triggered negative buoyancy and an R–T instability (Figure 4.14e). Dripping of the arc root may have resulted in ~1 km of regional uplift and the eruption of both the Cappadocia and Galatia volcanic provinces. As summarized by Meijers et al. (2018) and references therein, Central Anatolia switched from shortening to extension ~6 Ma and has been dominated by extension since then. Meijers et al. (2018) used paleoelevation proxies to constrain the surface uplift history of the region and invoked the drip hypothesis to account for rapid Late Miocene (~11 Ma) surface uplift, further noting that uplift was coincident with upper crustal shortening and ignimbrite volcanism and was followed by regional extension.

Göğüş et al. (2017) estimate the beginning of dripping at ~10 Ma based on the ages of Cappadocian and Galatian volcanism. The timing of drip detachment can be estimated by the age of rapid surface uplift and the initiation of regional extension. Schildgen et al. (2012) inferred a phase of uplift on the southern margin of the Central Anatolian plateau from ~8–5.45 Ma, and the plateau underwent extensional deformation beginning ~6 Ma. We thus estimate that drip detachment occurred ~8–6 Ma.

The models of Göğüş et al. (2017) predict moderate crustal thickening and the topographic development of a transient basin that becomes inverted after drip detachment. In these models, the dripping of a 280 km-wide root entrains surrounding lithosphere and produces a broader region of thinned lithosphere approximately 400 km in diameter, as well as a crustal welt approximately 500 km in diameter before extension. These models thus imply an instability wavelength of approximately 400–500 km, while the Cappadocia and Galatia volcanic provinces,

which are thought to result from asthenospheric upwelling following removal, are approximately 420 km apart (Göğüş et al., 2017). We therefore estimate a characteristic wavelength of approximately 450 km for the Central Anatolian drip. This wavelength is near the upper end of what is considered realistic for dripping of mantle lithosphere on Earth (Harig et al., 2008) and indicates that early Cenozoic shortening may have contributed to increasing the size of the instability, as hypothesized by Göğüş et al. (2017).

Given that shortening was followed by extension in Central Anatolia, we infer a strong-crust drip. The numerical models of Göğüş et al. (2017) also depict a strong-crust drip characterized by syn-drip subsidence and upper-crustal horizontal compression, followed by a period of post-drip extension. The models also suggest that, despite a relatively strong crust, the lower crust was able to thicken by ~5 km during drip growth, leading to post-drip surface rebound and higher average elevations after drip detachment. Permanently elevated topography due to dripping is necessary to match the uplift history inferred from marine sediments and fluvial terraces (Schildgen et al., 2012).

Hindu Kush (#18). The upper mantle beneath the Hindu Kush, like beneath the SE Carpathians, hosts a narrow, subvertical seismogenic zone reaching depths of 250 km (Figure 4.12f; Sippl et al., 2013). Vertical extension rates across the seismic zone are $> 10^{-14}$ s^{-1}, and the downward velocity obtained from summing the vertical extension averages 40 mm/yr (Molnar & Bendick, 2019). Koulakov (2011) hypothesized that a high wavespeed anomaly extending to depths of 400-500 km below the seismic zone is a lithospheric drip (framed therein as continental delamination but described as an "isometric drop"). Under the dripping hypothesis, the seismic zone would represent a region of concentrated strain in the actively necking portion of a drip (Koulakov, 2011; Lorinczi & Houseman, 2009; Molnar & Bendick, 2019). Given that oceanic subduction beneath the Hindu Kush likely ceased before 40 Ma at the latest (Tapponnier et al., 1981), these rates of vertical extension and sinking support the notion that downgoing material is continental lithosphere rather than a remnant of an oceanic slab (Koulakov, 2011; Molnar & Bendick, 2019).

Molnar and Bendick (2019) point out that tomographic images indicate significant portions of crust descending with the downgoing material, consistent with both the crust and lithosphere being relatively warm and weak (Molnar & Bendick, 2019). Low overall viscosity, weak crust, and a large wavelength instability are all favorable toward the generation of a crustal welt and high topography during dripping (Neil & Houseman, 1999). Strain in the Hindu Kush region is characterized by contraction along its southern and northern edges due to India-Asia convergence, but low east–west extensional strain in the interior of the range (Ischuk et al., 2013). The Hindu Kush are growing laterally by crustal shortening and transport of material into surrounding regions such as the Tajik depression (Ischuk et al., 2013; Molnar & Bendick, 2019). The Hindu Kush is thus a laterally-spreading crustal welt characterized upper-crustal

extension in the interior and contraction around the edges, which is consistent with a large weak-crust drip (Molnar, 2015).

The high wavespeed region in the upper mantle extends to depths of 600 km in the Hindu Kush (Figure 4.12f), indicating that more material is entrained in the drip here than in the SE Carpathians (Molnar & Bendick, 2019). We thus expect the characteristic wavelength to be larger than the 300–350 km estimated for the SE Carpathians. The wavespeed anomaly imaged by Koulakov (2011) varies from ~100 km in width in the shallower portion coincident with mantle seismicity, and up to 250 km in the deeper portion resembling an isometric drop. We expect the characteristic wavelength associated to such a drip to be 500 km in width or more. If the topographic expression of the Hindu Kush is partly a result of syn-drip thickening, the range's ~450–500 km width may give a clue to the characteristic wavelength. A wavelength of 500 km is near the upper range of what is expected for the R–T instability under Earth-like conditions (Harig et al., 2008); it may have been increased by tectonic shortening driven by India-Asia convergence, which could trigger foundering of a large region of tectonically thickened lithosphere. More research is needed investigating the possible expressions of such a drip in the Hindu Kush, and it is unlikely that dripping is responsible for all of the >2 km topography of the range. An estimate of 500 km for its characteristic wavelength, however, is consistent with the size of the tomographic anomaly and compares favorably to the better-constrained SE Carpathian drip.

Although removal is evidently ongoing, the timing of initiation of the Hindu Kush drip is uncertain. The early phases of R–T instability and crustal thickening were likely dominated by tectonic shortening due to India-Asia convergence. Modeling of the seismogenic expression of R–T instabilities, similar to that done for the SE Carpathian drip (Lorinczi & Houseman, 2009), may provide constraints on the start of dripping beneath the Hindu Kush.

Pamir, Vanj (#19). Lithospheric dripping during the Eocene in the Central and South Pamir is hypothesized based on the geochemistry of the Vanj magmatic complex (Chapman et al., 2018). The Vanj magmas show intermediate, high-K calc-alkaline to shoshonitic compositions, and high La/Yb with small or absent negative Eu anomalies (Chapman et al., 2018). Chapman et al. (2018) interpret the magmas, which were emplaced within an ellipsoidal region ~250×150 km during 42–36 Ma (Figure 4.15d), as high-pressure partial melts of foundering continental lithosphere.

We estimate that this drip beneath the Pamir had a characteristic wavelength of ~200 km based on the average diameter of the magmatic region. This estimate assumes that drip-related magmatism corresponds to a region of thinned lithosphere that would have been present immediately after dripping. A characteristic wavelength of 200 km predicts a drip 50–100 km in diameter. This relatively small size supports the notion that partial melting of the drip was a magmatic source, as conductive heating of larger drips would be less efficient and would produce melt less rapidly (Ducea et al., 2013).

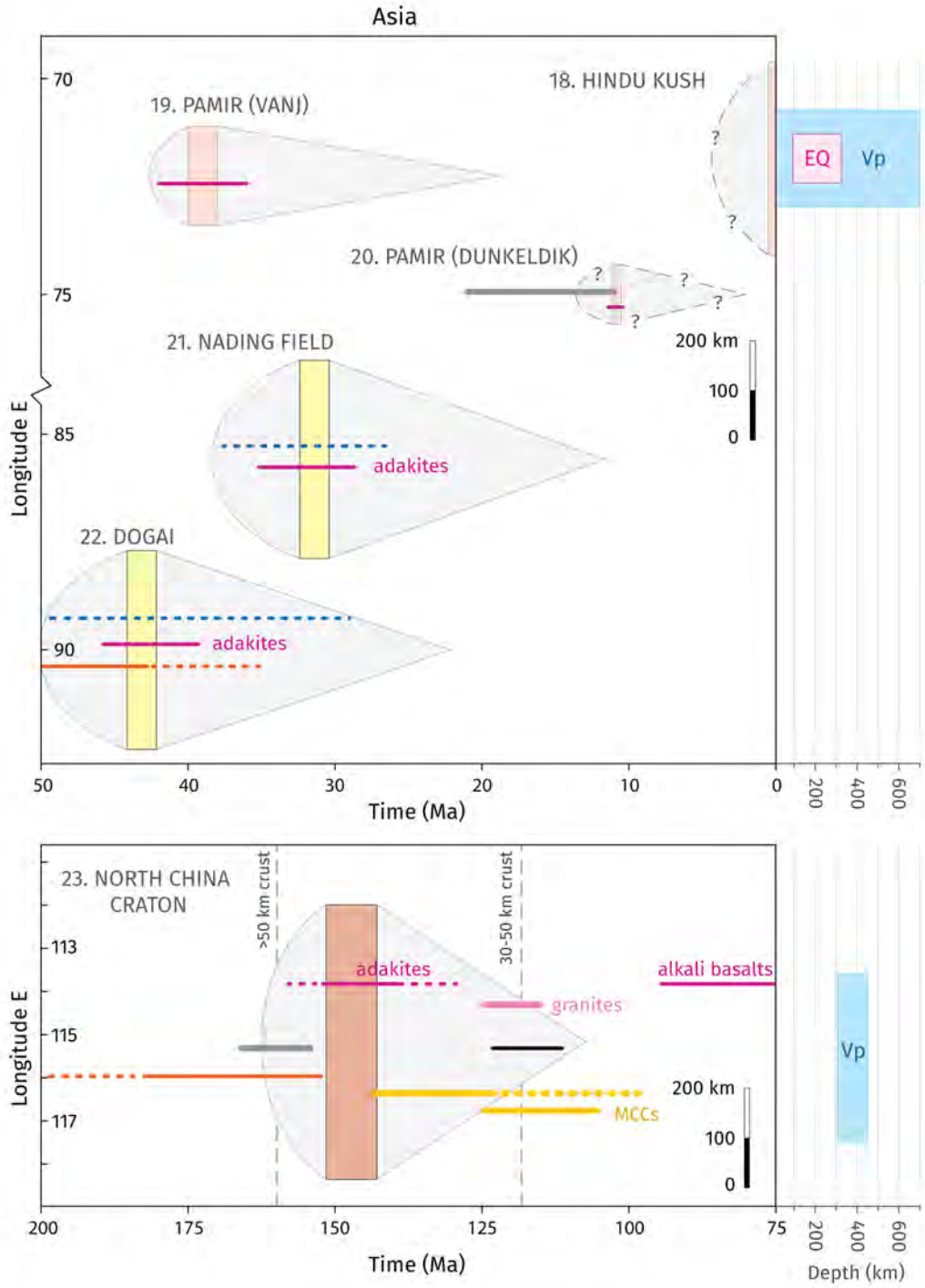

Figure 4.18: Potential dripping events in Asia. Drips are labelled and numbered according to Figure 4.1. See Figure 4.13 for explanation of symbols. Regions of active mantle seismicity shown as magenta boxes (EQ). Note the change of temporal scale between the top and bottom panels. MCCs: metamorphic core complexes.

At present, the timing of the Pamir drip is only constrained by the emplacement of the Vanj magmas. Drip-derived magmatism likely represents the late stages of drip growth and the early stages of drip detachment and sinking through the uppermost mantle (Ducea et al., 2013; Kay & Kay, 1993; Murray et al., 2015). Given that the ultimate emplacement of drip-derived magmas in the upper crust may lag their generation in the upper mantle, we estimate an age of 39 Ma for the detachment of the Pamir drip.

Due to a lack of data on the evolution of surface topography and upper-crustal strain during the Eocene, we are unable to infer the type of drip (weak-crust vs. strong-crust), though Chapman et al. (2018) hypothesize that foundering was triggered as a result of India-Asia convergence that focused crustal thickening onto the rheologically weak Karakul-Mazar terrane; such a situation would favor the formation of weak-crust drips.

Pamir, Dunkeldik (#20). Shaffer et al. (2017) and Chapman et al. (2018) interpreted the Dunkeldik/-Taxkorgan igneous rocks in the SE Pamir, Tajikistan, in the context of lithospheric foundering (Figure 4.15d). Xenoliths from the shoshonitic Dunkeldik Volcanic Field are derived from crustal material metamorphosed at temperatures >1000 °C and pressures indicative of >90 km depth (Shaffer et al., 2017, and references therein). Combined with $^{40}Ar/^{39}Ar$and U-Pb dating, the pressure-temperature paths of xenoliths suggest that they are derived from lower crustal material that experienced modest heating due to crustal thickening ~20–15 Ma and descended to depths of nearly 100 km during 14–11 Ma before being erupted at 11 Ma (Ducea et al., 2003; Shaffer et al., 2017).

These data indicate that the lower crust and mantle lithosphere beneath the SE Pamir may have foundered in the form of a drip that began growing as early as 20 Ma, with accelerated foundering beginning by 14 Ma and detachment at 11 Ma (Shaffer et al., 2017). Unlike the Vanj complex, the Taxkorgan magmas do not comprise an ellipsoidal region indicative of drip size but outcrop as an elongated belt approximately 110 km long by 30 km wide (Figure 4.15d; Chapman et al., 2018). In addition, foundering is thought to have been triggered by renewed indentation of Indian lithosphere into Asia following slab breakoff ~25–20 Ma (Chapman et al., 2018; Shaffer et al., 2017); Shaffer et al. (2017) hypothesize that magma was injected along the closing gap between Indian and Asian cratonic blocks and note that, given the shortening magnitude of this region, and assuming a pre-Cenozoic crustal thickness of 35–40 km, at least 40 km of crust has been lost to lateral extrusion or foundering. Dripping of 40 km-thick layer of lower crust would produce a wavelength of approximately 120 km, though this does not account for the involvement of underlying mantle lithosphere, which could increase the wavelength. The instability wavelength may also be increased by tectonic convergence and crustal shortening. We therefore tentatively estimate a minimum wavelength of 120 km. Given that both the size of the potential instability beneath the Dunkeldik/Taxkorgan complex and its effects on surface topography and upper crustal strain are poorly constrained, we are unable to infer the type of drip from currently available data. Like the drip associated with the Vanj complex in the Cen-

tral Pamir (#19), foundering may have been triggered by tectonic compression and thickening of a rheologically weak, accreted "Gondwana terrane" sandwiched between stronger cratonic lithospheric blocks (Shaffer et al., 2017). This situation would favor weak-crust dripping.

Tibet, Nading field (#21) and Dogai (#22). The Himalayan-Tibetan orogen formed as the result of a diverse set of tectonic processes since the early Paleozoic, culminating in the ~70–50 Ma to present collision of the Indian and Eurasian continents (Yin & Harrison, 2000). In Tibet, tectonic contraction related to oceanic subduction, terrane accretion, and finally continental collision produced crust of extreme thickness, and upper crustal deformation is presently characterized by gravitational spreading and orogen-parallel extension (Molnar & Tapponnier, 1978; Yin & Harrison, 2000). A full summary of the tectonic assembly and uplift of Tibet is beyond the scope of this paper, but the Lhasa and Qiangtang terranes that make up the central portion of the modern Tibetan Plateau figure prominently into the lithospheric dripping hypothesis (Kapp & DeCelles, 2019; Lu et al., 2018). These terranes are fragments of Gondwana that rifted from India during the Early to Late Paleozoic and accreted onto the South China block along with the Songpan-Gazi-Hoh Xil terrane, a flysch complex representing a remnant ocean basin (Yin & Harrison, 2000). After these terranes accreted during the Late Jurassic to Early Cretaceous, the southern margin of Eurasia was a Cordilleran-type continental arc comprised of the Cretaceous Gangdese batholith and Xigaze forearc basin in the southern Lhasa terrane (Yin & Harrison, 2000). Behind the Gangdese arc, the northern Lhasa terrane was deformed by a retro-arc thrust belt and distributed thrusting due to Cretaceous suturing with the Qiangtang terrane (Kapp & DeCelles, 2019). Late Paleocene-Early Eocene volcanic rocks in the Lhasa terrane are flat-lying, indicating the absence of major tectonic compression during the Cenozoic (Yin & Harrison, 2000), while the Qiangtang terrane was a relative topographic high, deformed by a series of north-vergent thrust belts (Kapp & DeCelles, 2019).

Convective removal of the Tibetan lithosphere and lower crust has been given a significant role in many geodynamic hypotheses for the formation and evolution of the Tibetan Plateau (Hatzfeld & Molnar, 2010, e.g.,), but the precise timing, location, and style of removal events is a topic of ongoing research. Early studies recognized that the removal of strong, dense mantle lithosphere in general may have contributed to the onset of orogen-parallel extension in Tibet during the Miocene (England & Houseman, 1989). Turner et al. (1996) interpreted the widespread potassic volcanism in the Lhasa and Qiangtang terranes, with high-temperature source magmas, as the result of lithospheric mantle melting beginning ~16–20 Ma. Houseman and Molnar (2001) argued that the low wavespeed upper mantle and recent ~10 Ma basaltic volcanism in northern Tibet indicate convective removal of the lithosphere by 8 Ma, possibly in the form of multiple Rayleigh–Taylor drips. Working in southern Tibet, Chung et al. (2003) interpreted ~26–10 Ma adakites in the Lhasa terrane to reflect lower crustal heating following wholesale delamination of mantle lithosphere. Kapp and DeCelles (2019) note that this magmatism swept southward across the Lhasa terrane at a rate similar to India-Asia convergence at

the time and infer delamination of the lithosphere driven by anchoring of the Indian slab in the mantle transition zone.

Lithospheric dripping has been invoked based on the presence of potassic-ultrapotassic and adakitic volcanic rocks that outcrop throughout the Qiangtang and Lhasa terranes (Kapp & DeCelles, 2019; Lu et al., 2018), as well as Paleogene sedimentary deposits in the Qiangtang terrane (Kapp & DeCelles, 2019). Tomographic studies image a large high-wavespeed anomaly at 350–600 km depth centered beneath the central Lhasa terrane, inferred to represent lithosphere that foundered during the Oligocene (Chen et al., 2017). The anomaly consists of two zones of high P-wave velocities: a 750-km wide zone sitting at approximately 350 km depth, and a weaker ~200 km wide zone sitting at ~600 km depth (Chen et al., 2017). In eastern Tibet, Bao and Shen (2020) interpreted shallower anomalies in the upper mantle as evidence of actively foundering lithosphere, potentially involving the Indian slab. Temperature and P-wave models indicate a high-temperature asthenosphere and thin lithosphere beneath the Qiangtang terrane as compared to the relatively cool, thick Lhasa terrane (Tunini et al., 2016). Although the large spatial extent and long tectonic history of Tibet would permit multiple episodes of lithospheric dripping at various times and locations in the orogen (Kapp & DeCelles, 2019), we focus on the Oligocene to Miocene events in the central portion of the Tibetan plateau, where multiple lines of evidence point toward two lithospheric dripping events during the Paleogene.

Two episodes of lithospheric dripping in the Paleogene were hypothesized by Kapp and DeCelles (2019), who argue that potassic-adakitic magmatism in the Qiangtang Terrane resulted from foundering of Tibetan lithosphere shortly before or coeval with the region attaining elevations >4 km (Kapp & DeCelles, 2019). This volcanism occurred as a series of discrete pulses, each limited to ~100×100 km areas and lasting <10 Ma, younging to the south and west across central Tibet. The earliest pulse of Cenozoic volcanism, the 46–38 Ma Dogai volcanic complex near the Tanggula Mountains, is exposed in an elliptical area averaging 150 km in diameter with a potassic-adakitic composition (Figure 4.15b); its strata are subhorizontal and undeformed, overlying deformed Mesozoic strata (Kapp & DeCelles, 2019, and references therein). Studying the same volcanic rocks, Zeng et al. (2020) found evidence that the melts are derived from eclogitized lower crust, which would have begun foundering shortly after the end of crustal shortening in the region. To the west of the Dogai volcanics, Paleogene sediments were deposited within a 150×150 km region showing evidence of syn-contractional deposition in an arid high-elevation environment between ~51 and ~28 Ma (Kapp & DeCelles, 2019).

A later pulse of volcanism in the Nading volcanic field (~36 to 28 Ma) in the southern Qiangtang terrane (Figure 4.15b) is also spatially associated with folded Paleogene lacustrine strata dated to 35 Ma (Kapp & DeCelles, 2019). Qi et al. (2021) estimated based on geochemical evidence that the Nading field volcanics were derived from melting of mantle lithosphere at approximately 70 km depth and ~1400 °C and inferred that the magmas were generated due to asthenospheric upwelling after foundering of a portion of the mantle lithosphere, estimated to have occurred ~38 Ma.

Syn-contractional deposition of hinterland basin strata immediately adjacent to relatively undeformed, roughly coeval volcanic rocks is consistent with occurrence of two strong-crust drips during the Paleogene (Figure 4.15b). In strong-crust dripping scenarios, sedimentation occurs above the actively shortening center of the drip, while volcanic regions correspond to more distal regions of lithospheric thinning, or "basin-bounding topographic bulges" (Figure 4.5; Kapp & DeCelles, 2019). Strong-crust dripping may have been favored by metasomatism and weakening of the Tibetan mantle lithosphere (Kapp & DeCelles, 2019), a hypothesis also inferred by Zeng et al. (2020) in considering an apparent lack of a surface uplift following lithospheric removal. It is notable that Zeng et al. (2020) refer to a weak crust in central Tibet, but only in reference the lower portion of the crust that would have been eclogitized during crustal thickening and foundered along with underlying mantle lithosphere; the overlying crust can behave in rheologically strong fashion in such a scenario, yielding strong-crust drips. Other interpretations of the paleoaltimetry record infer ~1.5 to 3 km of surface uplift during the Oligocene to Early Miocene (Lu et al., 2018), which would also be consistent with strong-crust dripping, where post-drip uplift occurs due to flexural and isostatic rebound.

The sedimentary basins roughly 100 km in diameter flanked by 100–150 km wide volcanic regions (Kapp & DeCelles, 2019) together suggest a characteristic wavelength of 350–400 km, which also approximately corresponds to the distance between Paleogene sedimentary depocenters in Tibet (~400 km). A wavelength of 400 km indicates of removal of a ~120–150 km thick layer of mantle lithosphere, consistent with thermal and tomographic models (Lu et al., 2018).

The dated sedimentary section near the Dogai volcanic complex allows bracketing of the main phase of growth (Figure 4.2, Phases 1 to 2) of the Dogai drip to between 51 and 28 Ma (Kapp & DeCelles, 2019). More precise chronostratigraphic dating of these deposits would more tightly constrain the growth of the purported drip. We assume that drip-related melting and volcanism could have accompanied drip growth (e.g., Furman et al., 2016) and continued after its detachment. We therefore use the median age of volcanism as a best estimate of drip detachment and estimate ~42 Ma based on the age of peripheral volcanism (46–38 Ma). If volcanism instead largely post-dated drip detachment, that would place detachment around 46 Ma.

The purported Paleogene drip associated with the Nading volcanic field is represented by 36–28 Ma volcanic flows and fluviolacustrine strata with a 35 Ma interbedded tuff that were deposited syn-tectonically during a phase of horizontal shortening. We thus infer that drip growth would have been well underway by 35 Ma, generating accommodation space for lacustrine sedimentation. Detachment thus occurred no earlier than 35 Ma. Similarly to the Dogai drip, we estimate detachment ca. 32 Ma based on the median age of peripheral volcanism.

Lu et al. (2018) also interpreted the Oligocene to Miocene tectonics of Tibet in the context of lithospheric dripping. Potassic-ultrapotassic volcanic rocks were erupted in the Lhasa terrane

~26–25 Ma, potentially during ~1.5–3 km of surface uplift of the Qiangtang and Songpan-Gazi terranes; meanwhile, the convergence rate between India and Asia slowed and shortening propagated to the edges of the plateau, perhaps due to increased gravitational potential energy of the interior of the plateau (Lu et al., 2018). Lu et al. (2018) infer that a 120 km thick column of lithosphere has been lost mainly beneath the Qiangtang terrane, which would correspond to Rayleigh–Taylor instabilities with a 300–360 km wavelengths, similar to the wavelength inferred for the Dogai and Nading drips described by Kapp and DeCelles (2019). Lu et al. (2018) estimate a date of 26 Ma for drip detachment based on the age of volcanic rocks in the Lhasa terrane, though, based on the foregoing discussion, these rocks occur on the peripheral margin of the inferred dripping center and could have been emplaced after the detachment of a drip, during the phase of flexural-isostatic rebound in the Qiangtang terrane.

Compared to the ~26 Ma potassic volcanics in the Lhasa terrane (Lu et al., 2018), the Eocene–Oligocene strata in the Qiangtang terrane and volcanics are 10 to 16 Myr older and are situated directly above the zone of thinned lithosphere. Given that the lithosphere beneath the Lhasa terrane seemingly retains much of its thickness, we hypothesize that the Lhasa volcanics are related not to a third dripping event, but to mantle upwelling following the detachment of the Dogai and Nading field drips. Alternatively, they may reflect lithospheric delamination or roll-back of the Indian slab (Kapp & DeCelles, 2019).

North China Craton (#23). Cratonic lithosphere, although nominally much stronger than that of the orogenic regions discussed in the foregoing sections, is vulnerable to gravitational instabilities in regions of convergence or extension (Gorczyk et al., 2013) or where subducting slabs provide fluids to the base of the lithosphere (Kusky et al., 2014; Liu & Li, 2018). The North China Craton (NCC) initially formed during the Archean to Proterozoic (2.7–1.9 Ga) but has since lost much of its thick, buoyant cratonic lithosphere beneath its eastern block (Gao et al., 2002). Loss of the lithosphere evidently occurred during the Late Jurassic to Early Cretaceous and involved melting and foundering of a dense lower crustal root (Gao et al., 2002; Gao et al., 2004; Sun et al., 2017; Zhang et al., 2014). Geochemistry of Mesozoic intermediate to felsic volcanic rocks indicates a shift from a >50 km-thick crust to a 30–50 km crust between 165 and 122 Ma (Sun et al., 2017). Lithospheric thinning during this period was contemporaneous with intrusive magmatism (132–117 Ma) that was partially a result of dehydration melting of a thickened lower crust of eclogitic composition ~123 Ma (Zhang et al., 2014). Presently, the western block of the craton retains a >215 km thick lithospheric keel, but in the east, the lithosphere is only 70–100 km in thickness, and the crust thins from 40–50 km in the west to 30 km in the east (Zhu et al., 2012). Seismic images of the upper mantle beneath the NCC show high P-Wave anomalies at ~410 km depth interpreted as delaminated lithospheric blocks (Xu & Zhao, 2009).

Although the traditional view holds that the lithosphere beneath the NCC was lost to delamination, the mechanisms leading to destruction of the cratonic lithosphere, and the role of oceanic plate subduction throughout the Phanerozoic, remain a topic of ongoing research

(Kusky et al., 2014; Liu & Li, 2018; Zhu et al., 2012). Zhang (2012) hypothesized that the lithosphere foundered through Rayleigh–Taylor drips induced by lithospheric folding and interprets the NNE–SSW-trending mountain ranges and Mesozoic basins (Ordos and Zhongyuan-Bohai) as anticlines and synclines, respectively, that reflect folding of the entire lithosphere caused by collision of the Yangzi craton during the Triassic to Middle Jurassic. Zhang (2012) argues that this folding decreased the strength of the lithosphere, especially along the hinge zones of the folds, allowed magmatic intrusion and the accumulation of dense magmatic residues, and possibly eclogitized portions of the lithosphere, making it negatively buoyant; lithospheric dripping then occurred in the eastern block of the craton, where folding was greatest in amplitude (Zhang, 2012). Major sediment accumulation began in the Triassic and continued into the Late Jurassic, concomitant with shortening along the Tanlu fault zone (Zhang, 2012). During the Early Cretaceous, crustal horizontal extension occurred on either side of the Tanlu fault and accommodated displacement of the lower plate ESE-ward away from the stable NCC, forming metamorphic core complexes (Liu et al., 2005). Early Cretaceous extension also involved the formation of extensional–transtensional basins and mafic volcanism derived from asthenospheric melting (Zhang, 2012). Liu et al. (2005) date the development of core complexes to 130–110 Ma, while asthenosphere-derived volcanism evidently began ~100 Ma.

The spacing between Triassic-Jurassic basins is approximately 550 km (Zhang, 2012) and gives an estimate of the characteristic wavelength of dripping. This wavelength is significantly larger than other drips we discuss in this study and would be consistent with R–T instability of a 180–200 km thick portion of the lithosphere (assuming λ/h of 2.5 to 3). Evidently, the lithosphere beneath the eastern block was thinned by only ~100 km (Zhu et al., 2012). The large wavelength of dripping could be due to seeding on the compressional lithospheric folds inferred by Zhang (2012), or the lithosphere could have been removed by multiple smaller drips with 200–300 km wavelengths. Due to the elongated geometry of the inferred folds, which extend ~1000 km along strike, it is likely that R–T instabilities would develop multiple drips along strike in either case.

If drips were seeded by lithospheric folding, it follows that they were centered beneath the synclinal hinges and associated basins, where the Moho and LAB would have descended, but dynamic stress during dripping may have led to upper crustal divergence and uplift of these basins. Zhang (2012) report a shift from contractional basins to extensional basins as the purported drips developed, suggesting that dripping may have driven upper crustal extension above the center of the drip (i.e., in an example weak-crust dripping). As discussed in Section 4.2.3, syn-drip extension is also consistent with instability of a thick, strong mantle lithosphere relative to the crust. Although we lack data on syn-drip surface uplift, Zhang et al. (2014) infer two episodes of lower-crustal thickening; the first (155–180 Ma) is concomitant with collision, while the second (132–117 Ma) overlaps in time with upper crustal extension. Zhang (2012) infer a moderately thickened crust (50–60 km) prior to removal. Moderate lower-crustal thickening and significant upper-crustal extension agrees with drip models with a crust that

is moderately to significantly weaker than the mantle lithosphere and the occurrence of a weak-crust drip.

4.4.4 East African Rift and New Zealand

Afar (#24) and Turkana (#25). The East African Rift is comprised of distinct tectonic provinces from the Malawi Rift in the south to the Ethiopian Rift in the north, which forms a triple junction with the Red Sea and the Gulf of Aden within the central Afar depression (e.g., Corti, 2009). Surface uplift and volcanism associated with rifting and the Afar Plume created the Ethiopian and Kenyan domes, two circular topographic plateaus roughly 900–1300 km in diameter. Furman et al. (2016) suggested that lithospheric dripping is also required to explain the surface uplift, volcanic patterns, volcanic geochemistry, and lithospheric thinning associated with the Ethiopian Rift and Afar depression (Figure 4.17).

Oligocene (~30 Ma) flood basalts in the Afar region of Ethiopia record Zn/Fe ratios indicating the presence of pyroxene or garnet during melting (Le Roux et al., 2010), consistent with melting of lithospheric drips (Ducea et al., 2013). These basalts are in turn encircled by a suite of volcanics sourced from asthenospheric melts, and all volcanic suites have geochemical signatures reflecting metasomatism by the Afar plume (Furman et al., 2016). Furman et al. (2016) inferred that the detachment of a lithospheric drip played a major role in the initiation of the Main Ethiopian Rift and the eruption of the Ethiopian flood basalt province. Lavas erupted during the Miocene to Quaternary in the Afar region do not display signatures of drip melting, bracketing the age of the drip to the time of Oligocene magmatism. The Oligocene basalts were emplaced during a ~1–2 Myr time period that was preceded by 1–2 km of rock uplift (Furman et al., 2016).

Evidence for drip magmatism is also expressed in Early Miocene lavas from the Turkana depression and in Quaternary lavas throughout the rift system (Furman et al., 2016). Furman et al. (2016) interpreted the episodic uplift of the Ethiopian dome since the Oligocene as reflecting the combined influence of plume heating and lithospheric dripping, with a phase of rapid uplift in the southern portion of the Ethiopian dome near the Turkana depression ~19–12 Ma correlated to an episode of mafic volcanism and inferred lithospheric dripping event (Furman et al., 2016).

Furman et al. (2016) inferred that the “characteristic radius” of the Turkana drip is 50 km, from which we estimate a drip diameter of 100 km and a characteristic wavelength of approximately 200–400 km. A distance of 500 km separates the center of 30 Ma drip-related volcanism in Afar from the portion of the southern Ethiopian dome that was rapidly uplifted ca. 19 Ma near Turkana; if these two locations reflect the foundering of two neighboring lithospheric drips, this distance suggests a wavelength of 500 km, though this measurement does not account for extensional deformation since the Oligocene–Miocene. The volcanic fields reported by Furman et al. (2016) occur within a region approximately 500 km in diameter (this measurement also includes post-Oligocene extension). Cratonic lithosphere was evidently thinned by

70–130 km beneath the rift, which would correspond to a characteristic wavelength of ~175–400 km. Thus, while the spatial scale of the purported drips beneath the East African rift remain poorly constrained, we estimate a characteristic wavelength of ~400 km based on the drip size inferred by Furman et al. (2016), the distance between inferred dripping centers, and the extent of volcanics possibly associated with drip melting.

It is difficult to assess with available data whether crustal thickening and uplift occurred during the growth of the inferred drips (reflecting weak-crust drips), or after their detachment (reflecting strong-crust drips). Based on available studies, we cannot currently distinguish surface uplift associated with the Afar Plume from the uplift associated with the purported dripping events, which were likely triggered by plume upwelling and would only be responsible for a fraction of the uplift (Furman et al., 2016). This would be especially true for the Afar region in the Oligocene, where volcanism occurred after 1–2 km of uplift and was followed by an additional 1 km of uplift. The inference that the southern portion of the Ethiopian dome experienced a period of uplift 19–12 Ma, which overlapped with and post-dated volcanism interpreted as drip melting 23–16 Ma, indicates that surface uplift most likely occurred after the detachment of a lithospheric drip, consistent with strong-crust dripping. We therefore tentatively categorize the two purported drips in the East African Rift as strong-crust drips, but additional studies may change this conclusion in the future.

New Zealand (#26). Stern et al. (2010) interpreted the seismic properties of the lower crust and upper mantle beneath the North Island, New Zealand, to reflect lithospheric foundering during the Miocene. Stern et al. (2013) modeled the instability as the foundering of a lithospheric step that was created in the Middle to Late Miocene due to dextral offset along a plate boundary (e.g., Lamb, 2011). The step-change in lithospheric thickness results in both viscous foundering and lateral migration (Stern et al., 2013) in a style intermediate to the dripping and delamination end-members (Beall et al., 2017). Miocene–Quaternary sedimentary deposits suggest that the step migrated approximately 300 km southward over the last 12 Ma, likely facilitated by a weak lower-crustal layer (Stern et al., 2013). Foundering of a laterally migrating instability with such a strong asymmetry in near-surface stress is closer to the delamination end-member in our view, and Dimech et al. (2017) interpreted the geophysical and geologic evidence in the context of nearly wholesale delamination of the mantle lithosphere. In particular, the strongly asymmetric and laterally migrating nature of the instability precludes determining a characteristic wavelength, and we do not therefore include it in our synthesis. The numerical models of Stern et al. (2013) were able fit the observed sedimentary deposits best with $\eta' = 5$ for the upper crust, and $\eta' = 0.1$ for the lower crust and produced up to 900 m of surface uplift above the migrating hinge, all consistent with a rheologically weak crust similar to that of weak-crust dripping.

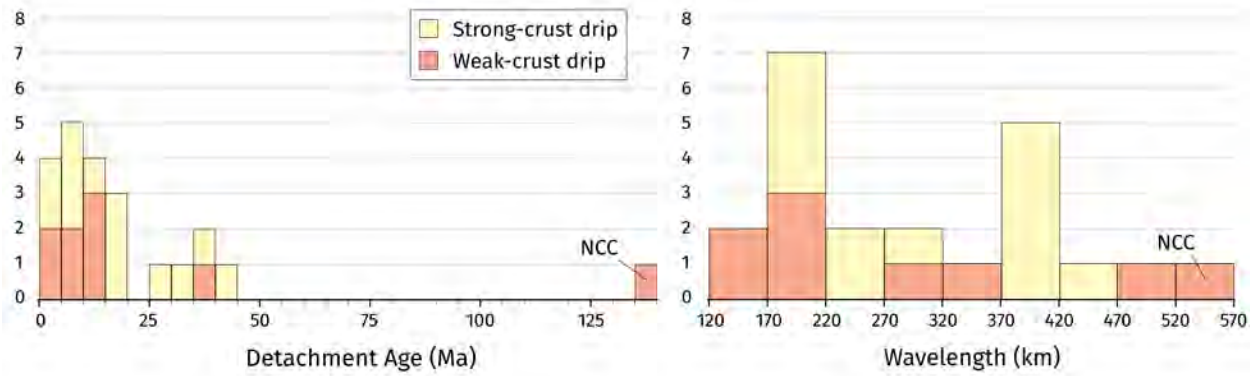

Figure 4.19: Histograms of detachment age (5-Myr bins) and wavelength (50-km bins) for reported dripping events. The North China Craton drip (NCC) is labelled. Dripping events cluster in the Middle and Late Cenozoic, likely due to measurement bias. Drip wavelengths cluster around ~200 km and ~400 km wavelengths, which may reflect original lithospheric thickness, the influence of background tectonic deformation, or both.

4.4.5 Summary of potential dripping events

In Sections 4.4.1 to 4.4.5, we identified and described 26 locations where lithospheric dripping has been proposed based on geologic, topographic, or geophysical evidence, or a combination thereof (Figure 4.1). All but one of the proposed drips are located in tectonically active continental regions—the North and South American Cordilleran orogenic belts, the Circum-Pacific subduction/collision zones, the Eurasian collision zone, and the East-African Rift. Dripping is evidently not limited to either cratonic regions or orogenic belts, as both types of continental lithosphere may have experienced dripping. Although nominally located in a cratonic region, the purported drip beneath the North China Craton also involves tectonic deformation (oceanic plate subduction and terrane accretion) throughout the Mesozoic that preceded the development of the purported drip. It therefore seems that tectonic deformation of the lithosphere plays an important role in seeding or triggering lithospheric instabilities, whether through the accumulation of dense magmatic residues, juxtaposition of lithospheric blocks with different thicknesses, weakening the lithosphere through hydration or strain softening, or lithospheric folding during cratonic collisions.

The estimated ages of drip detachment range from Jurassic (North China Craton) to the present (many locations; Figure 4.1), with a large cluster of ages in the middle–late Cenozoic (Figure 4.19). The evidence for dripping events tends to be erased over time as the detached lithosphere warms and sinks deeper into the mantle and becomes more difficult to detect seismically, and drip-related volcanism, uplift, subsidence, and sedimentation are overprinted or erased by later tectonic events. The cluster of dripping events in the Late Cenozoic therefore most likely reflects a lack of data for earlier events, rather than an increase in the frequency of dripping during the Late Cenozoic; evidence for drips deeper in time may continue to be uncovered.

We find that many drips have a similar ~200 km wavelength, indicative of an unstable lithospheric column ~60–100 km thick, although with notable exceptions (Figure 4.20). Another peak around ~400 km wavelength may reflect the influence of background tectonic stresses increasing the size of the most unstable wavelength during dripping, but as we discuss below, the wavelengths of many of these larger events are less well constrained, and future work may uncover evidence for a larger number of smaller dripping events in these locations. The relatively large drip sizes associated with collisional orogenic regions is nevertheless consistent with the idea that tectonically-driven lithospheric thickening can trigger Rayleigh–Taylor instabilities larger than otherwise predicted. The largest wavelength we infer is the ~550 km drip beneath the eastern region of the North China Craton. This wavelength reflects the large initial thickness of cratonic lithosphere, potentially combined with long wavelength lithospheric folding that provided the initial perturbation to the lithosphere-asthenosphere boundary. On the other end of the spectrum of drip wavelengths, regions subjected to back-arc volcanism, elevated mantle heat flux, and hydration from subducting slabs, such as the modern Central Andes and Mesozoic North America, display smaller drip sizes (~150 to 200 km in wavelength). The small drip sizes associated with active Cordilleran orogens is consistent with modelling studies that infer smaller drips for sections of lithosphere with steeper temperature and viscosity gradients, or for lithosphere that has been previously thinned by metasomatism or thermal erosion in continental arc settings.

4.5 Discussion

The foregoing sections provide a framework for understanding lithospheric dripping events on Earth that categorizes events into either strong-crust or weak-crust styles. Studies of lithospheric dripping encompass a wide range of geologic phenomena, including syn-drip sedimentary deposits; drip-related upper-crustal and topographic deformation; volcanism produced by drip melting, upwelling asthenosphere, and crustal melts; and geophysical observations such as tomographic anomalies and mantle seismic zones. Analytical and numerical models of dripping predict that two distinct styles of dripping are possible, depending largely on the rheological strength, and to a lesser degree on the buoyancy and thickness, of the crust relative to the mantle lithosphere. One style occurs when the crust is strong and is characterized by upper-crustal contraction and topographic subsidence above the drip. The other style occurs when the crust is weak and is characterized by upper-crustal extension and topographic uplift above the drip. Numerical models that explore the conditions that favor one style of drip over the other suggest that the weak-crust style may be prevalent in regions with high radiogenic heat production in the crust, elevated mantle heat flux, weak (felsic and/or hydrated) lower-crustal materials, crustal strain softening, or a combination of these factors. Conversely, strong-crust drips are expected in regions with low crustal heat production, low mantle heat flux, and strong (dry and/or mafic) crustal materials. Other rheological properties such as par-

tial melt and elasticity may also affect dripping style, though these are less well constrained by numerical models.

To test this classification framework, we synthesized observations for proposed lithospheric dripping events on Earth, including the inferred size, timing, and geophysical and geological observations associated with each drip. Although the data for some of the proposed lithospheric dripping events is sparse, and alternative explanations are available, we found evidence to support this categorization. Of the 26 proposed dripping events reviewed in the sections above, we found that 12 displayed some evidence for the strong-crust style, while 9 displayed some evidence for the weak-crust style. The remaining 5 events either did not have sufficient evidence for categorization (Southern Sierra Nevada (#1) and Northern Sierra Nevada (#2) and Northern Andes (#10)) or the evidence favored a process closer to the delamination style of foundering (Grand Canyon (#6) and S Colorado Plateau (#7), Rio Grande Rift (#8)), and New Zealand (#26))). Of the 9 inferred weak-crust drips, only three were categorized with any degree of confidence, because they display tell-tale signatures of weak-crust dripping such as significant crustal thickening (Wallowa Mountains (#3) and North China Craton (#23)) and syn-drip upper crustal extension (Southern Puna (#15) and North China Craton (#23)). Of the 12 inferred strong-crust drips, we were relatively confident in categorizing 9 of these, largely due to the occurrence of syn-drip basin deposits (Elko, Nevada (#5); Arizaro Basin (#14); Tibet, Dogai (#21) and Nading field (#22)) or a pulse of rapid surface uplift that evidently post-dates drip detachment (Grand Canyon (#6) and S Colorado Plateau (#7); Northern Altiplano (#11 and #12); Southern Puna (#15); East African Rift, Afar (#24) and Turkana (#25); and Arizaro Basin (#14)). In the following paragraphs, we discuss the implications for the occurrence of both styles of lithospheric dripping, with emphasis on the locations for which multiple lines of supporting evidence are available.

4.5.1 Implications of strong-crust and weak-crust drips

Because the rheology of Earth's continental lithosphere is not well-constrained, the style of lithospheric dripping at a particular location can give insight into the relative strengths of the crust and mantle lithosphere there. The strength profile of the lithosphere is a longstanding topic of research in geodynamics (for a review, see Burov, 2011). Lithospheric strength is often depicted as a yield-strength envelope, which plots the brittle yield stress of a lithospheric column against depth and/or temperature. More relevant for continental lithosphere is the ductile strength, which is characterized by constitutive relationships between stress and various deformation mechanisms in the form of rheological models and varies depending on the age of the lithospheric column and its intrinsic properties (Burov, 2011). As we discuss in this paper, the occurrence of strong-crust or weak-crust dripping is mainly sensitive to the effective viscosity of the crust relative to the mantle lithosphere, especially for values of this ratio around 0.1 to 100, and realistic changes in crustal and mantle material properties can favor one style of dripping over the other. Therefore, the style of lithospheric drip in a given location contains critical information on the strength profile of continental lithosphere. The period of

time involved in the deformation of a lithospheric drip (~1 to 30 Myr) and its spatial extent (>100 km) provide large spatiotemporal scales not probed by other geodynamic processes such as post-seismic deformation (1–10 yr; e.g., Hines & Hetland, 2016) and glacial isostatic rebound (10–20 kyr; e.g., Lambeck et al., 1998), but similar to the growth of orogenic or volcanic loads (Watts et al., 2013). Where lithospheric dripping can be recognized in the geologic record, it can yield information on lithospheric strength back into the geologic past, perhaps to periods where the thermomechanical configuration of the lithosphere was different from the present (e.g., the orogenic setting during the Oligocene in western North America prior to widespread extension). Furthermore, if the timing of drip initiation and detachment are well-constrained, Rayleigh–Taylor instability analysis yields an estimate of the average long-term viscosity of the lithosphere (Molnar & Garzione, 2007; Molnar & Jones, 2004). Applying Rayleigh–Taylor instability scaling laws to such locations indicates that the viscosity of the mantle lithosphere matches rheological models derived from laboratory experiments on olivine and eclogite (Molnar & Garzione, 2007; Molnar & Jones, 2004).

Strong-crust drips are more common in our data set than weak-crust drips. This may be because their greater preservation potential in the geologic record, as they produce surface subsidence that can lead to the accumulation of sedimentary and volcanic strata that record the growth of the drip. The drips associated with transient basins in orogenic hinterlands (Elko, Nevada (#5); Arizaro Basin (#14); and Tibet, Dogai (#21) and Nading field (#22)) are perhaps the most typical examples of strong-crust drips.

The prevalence of strong-crust drips may also reflect more typical lithospheric conditions. Crustal materials such as granite and quartzite are weaker than mantle olivine at equivalent temperatures, but they are significantly stronger at the cooler temperatures representative of upper continental crust (e.g., Beaumont et al., 2006; Brace & Kohlstedt, 1980; Bürgmann & Dresen, 2008, and see Figure B.1). Strong-crust drips would therefore be expected in regions with low crustal heat production and compositionally strong crustal lithologies (e.g., diorite, dry feldspar, or diabase Bürgmann & Dresen, 2008; Burov, 2011). Alternatively or coincidentally, strong-crust drips may develop when the mantle is weakened relative to the crust due to melting or metasomatism (Beaumont et al., 2006; Hirth & Kohlstedt, 2003). In addition, frictional-plastic yielding at high stresses tends to weaken the overall strength of the crust relative to the mantle lithosphere (Burov, 2011), such that the crustal average η' is closer to the critical value of ~10 that separates strong-crust and weak-crust drips. If the upper crust is weakened due to frictional-plastic yielding, brittle faulting, radiogenic heating, or composition, a strong lower crustal layer and/or a weakened mantle lithosphere may be required to sustain strong-crust drips (e.g., Wang et al., 2015).

While strong-crust drips may be more common due to the inherently strong nature of cold crustal lithologies, weak-crust drips may occur in regions of high heat flow (Wang & Currie, 2017), regions weakened by prior events of tectonism (Wang et al., 2015), or regions of high regional strain rates (Molnar, 2015). Important examples of inferred weak-crust dripping occur in

collisional orogens (SE Carpathians, Pamir, Hindu Kush), where tectonic shortening may have weakened the crust and seeded larger lithospheric instabilities than would have otherwise occurred. Very large weak-crust drips capable of generating orogenic plateaus may not be represented on Earth (Molnar & Houseman, 2013; Neil & Houseman, 1999), but the most diagnostic feature of a weak-crust drip may be the crustal welt produced by syn-drip crustal thickening that coincides with upper-crustal extension. Numerical models predict moderate amounts of crustal thickening and surface uplift on the order of a few hundred meters, combined with moderate amounts of syn-drip extensional strain (Wang & Currie, 2017; Wang et al., 2015).

Interestingly, in at least one case, we find neighboring drips with strongly contrasting styles. The evidence associated with Southern Puna (#15) (Section 4.4.2) is one of the most typical weak-crust drips that we identify here, but it is separated by less than 200 km from the strong-crust Arizaro Basin (#14) (Section 4.4.2). If both locations experienced lithospheric dripping as described above, the differing style of dripping points to a heterogeneous crust and/or mantle lithosphere beneath the Puna Plateau. Basement outcrops in both locations are composed of Cambrian to Ordovician granitoids (e.g., DeCelles et al., 2015a; Seggiaro et al., 2007) and there is no documented terrane boundary between the two locations. While the crust in the Southern Puna is evidently thicker, with more volcanism than in the Arizaro region, it is not clear if this is a cause of weak-crust dripping or an effect of it. One clear difference between the two regions that may account for varying crustal strengths is a series of NW-SE trending, continental-scale lineaments that are prominent in the Southern Puna but are absent from the Arizaro region. These lineaments may represent Triassic extensional structures, some of which may be currently reactivated as strike-slip faults (Amilibia et al., 2008). In the Puna, the lineaments coincide with eastward protrusions of the Andean volcanic arc and with clusters of late-Cenozoic mafic volcanism (Trumbull et al., 2006). The Southern Puna crust is likely more greatly intruded by melts and metasomatizing fluids than the crust beneath Arizaro. It is therefore possible that the pre-existing structure of the Puna crust conditioned the region for differing styles of dripping, but this hypothesis needs to be further investigated. Finally, we point out that the 7 Ma age of detachment inferred by DeCelles et al. (2015a) for the Arizaro dip is roughly the same as the inferred age of detachment for the Southern Puna drip (Figure 4.16), and syn-depositional shortening of Arizaro basin fill around 10 Ma also coincides with shortening of the Pasto Ventura region on the southern margin of the Puna (Schoenbohm & Carrapa, 2015). Therefore, a final possibility is that the Puna is more readily characterized by a single dripping event centered in the Southern Puna that detached ~7 Ma, and the Arizaro and Pasto Ventura regions represent peripheral basins that developed around a central topographic bulge associated with a weak-crust drip.

The oldest and possibly largest proposed drip identified by our synthesis occurred in the eastern portion of the North China Craton (#23, Section 4.4.3), where dripping is inferred to result from folding of the lithosphere during the collision of the Yangzi craton (Zhang, 2012). Long-wavelength folding of the lithosphere produced the synclinal Ordos and Zhongyuan-

Bohai basins, as well as intervening anticlinal mountain ranges, and may have led to eclogitization of the lower crust and/or mantle lithosphere, producing one or more gravitational instabilities. The Mesozoic basins were initially deformed compressionally, but deformation switched to extension (Zhang, 2012), possibly reflecting the influence of weak-crust dripping. Upper-crustal deformation after the inferred detachment of the drip is characterized by major horizontal extension and the development of metamorphic core complexes (Liu et al., 2005). Assuming that drips would seed on the synclinal hinges of the folds yields an estimate of ~550 km for the dripping wavelength, which is substantially larger than the ~200–300 km wavelength that would be predicted by the 100 km of estimated lithospheric thinning (Zhu et al., 2012). It is therefore possible that dripping would occur in the form of multiple smaller drips spaced ~250 km along the strike of fold hinges. Future work in this tectonically complex region should seek to test the dripping hypothesis by refining the timing and kinematics of upper-crustal deformation and volcanism in relation to inferred dripping centers along synclinal fold hinges. Geodynamic models could be constructed to yield specific predictions on the distribution of crustal strain under the inferred scenario of folding-induced weak-crust dripping.

By reference to the plots synthesizing each dripping event (Figures 4.13 and 4.16 to 4.18) it is apparent that the evidence for each dripping event varies in quantity and quality. Figure 4.20 illustrates idealized scenarios for weak-crust and strong-crust dripping using the same visualization as described in Figure 4.13. Only a few of the inferred dripping events match the idealized scenarios to some degree. Some events present complications that question the validity of the dripping hypothesis or would require modifications to the simple scenario involving a pure Rayleigh–Taylor instability. A larger number of events have been inferred using 1 or 2 lines of evidence (often volcanic or magmatic geochemistry) and lack other types of supporting data. In this section, we weigh the strength of evidence for inferred dripping events.

The Southern Altiplano drip (#13, Section 4.4.2; Figure 4.16) matches the strong-crust scenario well. Evidence such as surface subsidence followed by rapid uplift, volcanism, and upper-crustal compression support the dripping hypothesis. In a similar manner, the Arizaro Basin drip (#14, Section 4.4.2; Figure 4.16) matches the strong-crust dripping hypothesis, but its detachment was not associated with a pulse of large-scale surface uplift and so the timing of detachment remains somewhat unclear. In North America, the Elko, Nevada drip (#5, Section 4.4.1) best matches the strong-crust scenario, though it occurred also in the context of flat-slab subduction and widely distributed continental extension. The Dogai and Nading Field drips in Tibet (#21, #22, Section 4.4.3; Figure 4.18) display key evidence of strong-crust dripping, such as syn-drip surface subsidence and contraction, but currently lack additional supporting observations that would be expected such as post-drip surface uplift and post-drip extension.

Weak-crust drips are best represented by the Southern Puna drip (#15, Section 4.4.2; Figure 4.16) which only lacks xenolith evidence. As detailed in Section 4.4.2, geologic observations throughout the Southern Puna constrain the location and timing of upper-crustal strain, sedimentation, and volcanism not only above the center of the purported drip, but around its

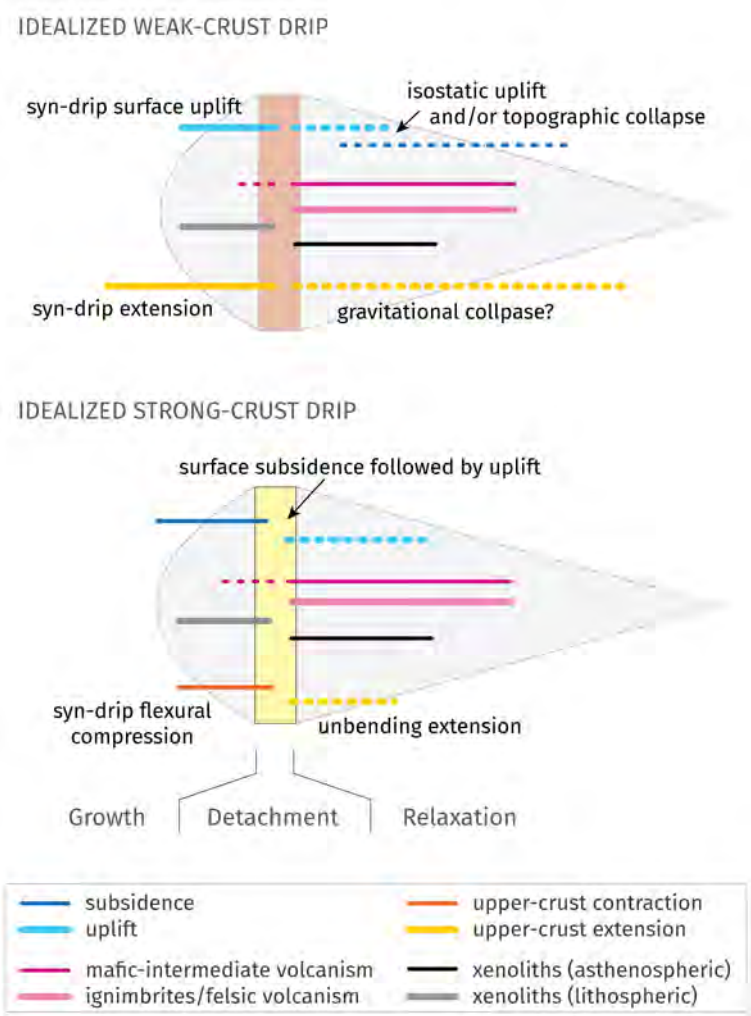

Figure 4.20: Illustration of idealized scenarios depicting (top) weak-crust dripping and (bottom) strong-crust dripping. The key observations that distinguish one type of drip from the other are labelled.

edges as well. In North America, the Wallowa Mountains drip (#3, Section 4.4.1; Figure 4.13) is the best example of weak-crust dripping, largely inferred from the thickened crust directly above the Wallowa anomaly. Unlike for the Southern Puna drip, the protracted pulse of surface uplift after the inferred detachment of the Wallowa drip most likely indicates significant isostatic rebound. Syn-drip upper-crustal extension, a critical piece of evidence for weak-crust dripping, has currently not been associated with the Wallowa Mountains drip. Other candidates for weak-crust drips include the Hindu Kush drip (#18, Section 4.4.3) and the two Pamir drips (Vanj, #19, Section 4.4.3; Dunkeldik, #20, Section 4.4.3), which may have seeded on crustal thickening due to continental collision.

In our synthesis of reported dripping events, we identified four locations where the available evidence suggests that, if lithospheric foundering is entailed, it is more likely to be as delamination or a style intermediate between dripping and delamination (Beall et al., 2017). These locations include the Grand Canyon (#6, Section 4.4.1), Southern Colorado Plateau (#7,

Section 4.4.1), Rio Grande Rift (#8, Section 4.4.1), and New Zealand (#26, Section 4.4.5). A few other locations also warrant discussion in this regard because they have been interpreted as delamination events elsewhere. The Southern Sierra Nevada (Southern Sierra Nevada (#1) and Northern Sierra Nevada (#2), Section 4.4.1) is often described as a lithospheric drip but is evidently characterized by a westward migration of topographic subsidence that could indicate delamination of the lithosphere. Westward delamination could have been triggered by continental extension in the Great Basin and Death Valley immediately to the east of the Sierra Nevada Batholith (Le Pourhiet et al., 2006). Saleeby et al. (2012) hypothesized that the opening of a slab window ~10 Ma combined with tectonic extension destabilized the eclogitic root of the batholith and triggered its westward delamination. However, because other mechanisms such as tectonic strain (Gemmer & Houseman, 2007) or background mantle flow fields (Currie et al., 2015; Zandt, 2003) can cause a Rayleigh–Taylor instability to shift laterally, we included the event in our analysis of lithospheric dripping. As an alternative to the lateral migration hypothesis, the instability may have initiated in its current position to the west of the Sierra Nevada as a result of a more dominantly mafic composition of the batholith there (Saleeby & Foster, 2004). In the SE Carpathians, a similar asymmetry of topographic, volcanic, and crustal strain patterns requires modification of the initial conditions of Rayleigh–Taylor instability model to match observations (Lorinczi & Houseman, 2009); alternatively, these observations may be due to delamination of the continental lithosphere (Göğüş et al., 2016), or the influence of a post-collisional remnant of an oceanic slab (Vrancea slab; Şengül-Uluocak et al., 2019).

The most significant controversies surrounding the identification of lithospheric dripping seem to occur in regions that have been studied most intensely, e.g., using seismic tomography. In the Western U.S., for example, tomographic models closely agree on the locations, but not the precise sizes and relative magnitudes, of major anomalies in the upper mantle (e.g., Becker, 2012). The ongoing debate about the origin of the Isabella Anomaly and purported Southern Sierra Nevada drip (e.g., Yu et al., 2020) suggests that even as tomographic models improve, interpreting the anomalies will nevertheless remain difficult. Another prominent anomaly in the Western U.S., the Wallowa Anomaly, has been interpreted as dripping lithosphere (Wallowa Mountains (#3), Section 4.4.1), and as fragment of the oceanic Farallon plate (Darold & Humphreys, 2013). In fact, Porritt (2013) interpreted all of the major high wavespeed anomalies beneath the western U.S. as fragments of the Farallon slab, and van der Meer et al. (2018) traced the Nevada Anomaly and Wallowa Anomaly back to the Farallon slab (therein identified as the Great Basin and Bitterroot anomalies, respectively).

The competing explanations of such anomalies as foundered pieces of continental lithosphere on the one hand, or remnants of subducted slabs of oceanic lithosphere on the other, is a common pattern globally. Tomographic anomalies below active seismic zones in the mantle beneath the SE Carpathians and the Hindu Kush have also been interpreted as both lithospheric drips and remnant slabs, igniting a debate on the long-term strength of continental lithosphere, the fate of fossil slabs during continental suturing, and the origin of intracontinen-

tal mantle seismic zones (McKenzie et al., 2019; Şengör & Dewey, 2020). In the Central Andean Plateau, however, tomographic anomalies do not correspond to the subducting Nazca slab, nor have they been interpreted as remnants of previously subducted slabs. The interpretation of tomographic anomalies in the Central Andes is therefore slightly less equivocal than in the regions discussed above. However, the sedimentation and volcanism associated with lithospheric dripping in the Puna Plateau have also been interpreted to result from an inferred episode of Miocene low-angle subduction analogous to the modern Pampean flat slab (e.g., Ramos & Folguera, 2009). Though the evidence for a Miocene flat slab event and its potential effects on upper-crustal strain and volcanism are still hotly debated (see pp. 481–2 in DeCelles et al., 2015b), the hypothesis provides an alternative explanation involving more traditional plate tectonic processes. In our view, the drip-vs.-slab debate represents an opportunity for geodynamic models to provide detailed predictions for each scenario and identify specific observations that may be able to falsify one hypothesis or the other in a given location. In the following section, we discuss the role of geodynamic models and other lines of investigation in improving our understanding of lithospheric drips.

4.5.2 Directions for future research

Future advances will come from combining independent lines of investigation such as geodynamic modelling, geomorphological analyses, geochemistry, and thermochronology, as well as from utilizing existing methods in new ways to test competing hypotheses against one another. In this section, we discuss how our synthesis suggests potential avenues for further understanding and testing the lithospheric dripping hypothesis.

Geodynamic modelling. Geodynamic models are the source of most insight into lithospheric dripping, including the framework laid out in this paper. The approach taken by geodynamic models generally defines a spectrum between complex models that aim to reproduce real-world conditions and simple models that parameterize or neglect real-world complexities in favor of isolating specific processes (e.g., van Zelst et al., 2021). Relatedly, the philosophy of geodynamic modelling can be either generic or specific (e.g., Tackley et al., 2005). Applied to lithospheric dripping, the goal of generic modelling is to investigate the fundamental dynamics of the instability process to uncover scaling relationships, different regimes or styles of behavior (such as strong-crust vs. weak-crust drips), and the expected observational phenomena (Tackley et al., 2005). Conversely, specific models are tailored to certain times and locations and attempt to match specific observations (Tackley et al., 2005). Both approaches are useful for developing explanations for the geologic and tectonic history of a region.

Generic lithospheric dripping models are critical to our understanding of the behaviors of strong-crust and weak-crust drips (Section 4.2.3), but the full range of outcomes expected from dripping remains underexplored. In our presentation of the weak-crust dripping concept (Section 4.2.3), we noted that complex geodynamic models that include a range of deformation

mechanisms (e.g., viscous diffusion, dislocation, and Peierls creep; elastic and plastic deformation) are likely to produce more complex patterns of crustal strain, deformation, and magmatism during lithospheric foundering. Future studies would benefit from further exploring the range of expected outcomes of lithospheric dripping in such models. As an example of one potential direction for lithospheric dripping modelling, consider the possibility of background tectonic strain on a region experiencing a lithospheric instability. Superimposing regional compression or extension onto a lithospheric drip is applicable to most, if not all, lithospheric drips discussed above, especially those in extensional (e.g., Central Nevada (#4), Section 4.4.1) or convergent orogenic regions (e.g., Southern Puna (#15), Section 4.4.2). Such studies do net yet exist for lithospheric drips, but Burov and Gerya (2014) found that extensional stress imposed on stresses generated from impingement of a mantle plume on the base of the lithosphere significantly affected the patterns upper-crustal strain and surface topography. Rather than the simple, radially symmetric patterns often exhibited by plume models, extensional stress produced complex linear features such as narrow rifts and half-grabens, which can only be resolved in high-resolution 3-D models (Burov & Gerya, 2014). This consideration points toward another avenue for progress in lithospheric drip modelling, the addition of the third spatial dimension, which we discuss below.

The specific modelling approach is well suited to providing falsifiable predictions of observable phenomena (Tackley et al., 2005). Lithospheric dripping models whose initial and boundary conditions match geologic and geophysical data, which are not sensitive to small changes in parameters, and which generate testable predictions (e.g., the existence, size, and location of a tomographic anomaly; volcanism of a certain affinity at a certain time and location) are eminently useful as geodynamic hypotheses. As an example of this approach, Le Le Pourhiet et al. (2006) modelled the westward-migrating foundering of the Southern Sierra Nevada batholith root (Southern Sierra Nevada (#1) and Northern Sierra Nevada (#2), Section 4.4.1) as the result of normal faulting in Death Valley and found that such a model can explain the location and age of basaltic volcanism, the location of the Isabella Anomaly to the west of the Sierra Nevada range, and a ~3.5 Ma pulse of uplift of the Sierra Nevada range. A highly specified modelling approach was also pursued by Wang et al. (2015) in their models of the Arizaro Basin drip (Arizaro Basin (#14), Section 4.4.2), which predict that a strong crust, including a lower crust with a mafic composition, is responsible for the strong-crust style of dripping proposed for this location. Geophysical studies point to the Puna crust being hot and felsic, with major zones of partial melt (e.g., Ward et al., 2017). Such observations challenge, but do not necessarily contradict, the idea that the crust was rheologically strong relative to the mantle lithosphere ca. 20 Ma. In particular, multiple drips may have been required to fully remove the mafic lower crust from the Puna Plateau.

No matter how well the lithospheric dripping hypothesis is specified, alternative hypotheses will often predict broadly similar consequences. We outline a few important alternative hypotheses, those involving subducted slabs and delamination, above (Section 4.3). Earth sci-

entists often face this problem of underdetermination, when the observed effects of some causal process are insufficient to choose one explanation over another (Kleinhans et al., 2005). One well-worn strategy for dealing with underdetermination is that of "multiple working hypotheses", which allows for multiple distinct explanations to be developed and tested against each other based on their predictions of observable consequences; by inference to the best explanation, one hypothesis can be tentatively favored over others (Kleinhans et al., 2005). Inferring the best explanation out of a set of competing hypotheses involves accumulating observations at many locations using a range of techniques. To that end, future modeling efforts should thoroughly explore the consequences of a range of processes in order to provide more detailed, falsifiable predictions for specific locations. Experiments that compare and contrast the effects of both dripping and delamination are examples of such modelling studies (Beall et al., 2017; Göğüş & Pysklywec, 2008; Krystopowicz & Currie, 2013; Wang & Currie, 2015). Based on our discussion in Section 4.3.1, similar efforts in the future should include flat slab subduction, slab breakoff, or other processes that directly compete against the lithospheric dripping hypothesis in a given location.

The differing topographic response to strong-crust and weak-crust drips provides another target for modelling efforts. Utilizing coupled geodynamic and landscape evolution models (e.g., Underworld2 and pyBadlands; Beucher et al., 2019) may be useful for refining hypotheses based on recognizing patterns in surface uplift/subsidence and erosion/deposition related to lithospheric dripping. A key challenge of such models is the requirement that the topographic surface respond freely and accurately to geodynamic stresses (Kaus et al., 2010). Three-dimensional geodynamic models incorporating a free surface are notoriously unwieldy due to numerical instabilities that introduce inaccuracies to the surface topography and require small computational time steps, drastically increasing the computational expense of these models (Crameri et al., 2012; Kaus et al., 2010). As discussed in this paper, however, simplified R–T instability models incorporating two or more viscous layers (representing layers of crust and mantle lithosphere), overlying a third viscous layer or inviscid half-space (asthenosphere), with a stress-free top boundary, reproduce many of the characteristics of more complex models with greater computational requirements. Improving the numerical performance of realistic, laboratory-derived rheological formulations is a topic of current work (e.g., Duretz et al., 2020; Spiegelman et al., 2016), as is finding more efficient solution algorithms for nonlinear systems (e.g., Fraters et al., 2019). One way to make progress may be to simplify the rheological structure of the lithosphere in three-dimensional models in order to model the surface-topographic response more precisely in a computationally efficient manner, keeping in mind that strain-localization phenomena such as shear zones brittle faulting will be poorly reproduced in such models. Our current understanding of the three-dimensional effects of lithospheric dripping, especially on surface topography, is so rudimentary that such models may yet offer valuable insight.

The foregoing discussion indicates that models are useful, among other reasons, because they predict near-surface observables that may distinguish lithospheric dripping from other processes such as delamination or slab dynamics. In the following sections, we discuss the main observable phenomena that have been used to investigate lithospheric dripping.

Near-surface evidence of dripping. According to our synthesis of lithospheric dripping evidence (Section 4.4), the primary geologic evidence for lithospheric dripping includes surface uplift, surface subsidence, basaltic volcanism, silicic volcanism, mantle xenoliths, and upper-crustal deformation (Figure 4.20). This full suite of evidence, however, is rarely reported in support of a purported dripping event, and even the most well-constrained drips lack key lines of evidence. The Arizaro and Southern Puna drips, for example, currently lack a mantle xenolith record (Figure 4.16), an important line of evidence for some North American drips (Figure 4.13). Additionally, some studies may rely on only one or two types of data (e.g. volcanic geochemistry) without addressing the other phenomena that a given drip would be expected to effect. We suggest that future studies collect and report on the full range of drip-related observations, especially those that distinguish weak-crust from strong-crust dripping (Figure 4.20), and those that may support or refute alternate hypotheses (Section 4.3). In the event that such evidence is absent from a region, studies should address this absence whether due to lack of data, preservation issues such as erosion or tectonism, or because a particular drip may not have produced the expected outcomes. In addition to the observations compiled in this paper, it is likely that new forms of evidence will be uncovered by applying existing techniques in new ways. Below, we discuss a few techniques with the potential to provide further insight into lithospheric dripping events.

Geomorphology. Geomorphological analysis techniques are well suited to study the effects that lithospheric dripping is predicted to have on surface topography (Section 4.2.3). Quantitative techniques such as river profile analysis, terrace dating, and mountain range morphometric analysis shed light on the geodynamic processes operating at late-Cenozoic time scales and could be utilized in locations where active or recent dripping is hypothesized. Because river incision is often driven by tectonic processes that produce surface uplift, the spatial pattern of incision rates sheds light on mantle dynamic processes. For example, the spatiotemporal pattern of Colorado River incision in the Grand Canyon (western U.S.) inferred by Karlstrom et al. (2008) provides further evidence for a northward propagating lithospheric instability, agreeing with the sequence of events inferred from seismic anomalies (Section 4.4.1; Levander et al., 2011). In the Colorado River system more broadly, knickzones and reaches with rapid incision rates often correspond to seismic anomalies and other geologic data indicative of dynamic upper mantle processes (Karlstrom et al., 2012). At a regional scale, Roberts et al. (2012) lend support to the general idea of “gradual convective removal of the lithosphere” beneath the western U.S. by inverting the profiles of major continental drainage systems.

In the case of the Southern Sierra Nevada (drip #1, Section 4.4.1), a circular region of "drowned topography" (basement topography covered by onlapping of Quaternary sediments) is indicative of surface subsidence above the Isabella Anomaly, while offlap of Quaternary sediments to the north and south indicates surface uplift (Saleeby & Foster, 2004). In the nearby Kern River watershed, Krugh and Foreshee (2018) analyzed stream profiles and relict low-relief landscapes to support the notion of surface uplift driven by lithospheric foundering. For the Central Anatolian Plateau (drip #17, Section 4.4.3), Göğüş et al. (2017) used the history of surface uplift rates inferred from river incision rates and uplifted marine deposits (Schildgen et al., 2012) to discriminate among different parameterizations of numerical models of dripping.In the Central Andes, rapid surface uplift rates over large areas have been presented as evidence of lithospheric foundering (dripping or delamination; Garzione et al., 2014; Garzione et al., 2006; Hoke & Garzione, 2008; Sundell et al., 2019).

These studies suggest that information on lithospheric dripping may be encoded in familiar geomorphic features such as river profiles and incision rates. One characteristic of dripping that remains relatively unexplored in modelling studies and real-world applications is the spatial heterogeneity in the surface response to dripping (uplift vs. subsidence). As described above (Section 4.2.3), the central region of surface subsidence due to a strong-crust drip should be surrounded by a region of flexural uplift ("peripheral bulge"), while the central region of uplift due to a weak-crust drip may be surrounded by a region of surface subsidence. The widths and geometries of these regions would provide information on the drip's characteristic wavelength, while the temporal sequence of uplift and subsidence would provide information on the type of drip, and therefore the relative strength of the crust.

Thermochronology. The interactions among crustal thickening, upper crustal burial or exhumation, and heat flux from the mantle creates a complex thermal setting during a lithospheric drip. In some cases, low-temperature thermochronology may provide an independent test of the dripping hypothesis. DeCelles et al. (2015a), for example, combined existing low-temperature thermochronology data (Carrapa & DeCelles, 2015) with sediment back-stripping analysis to argue that the Sierra de Macon range had been buried and exhumed due to the growth and detachment of the Arizaro Basin drip (#14, Section 4.4.2). For the Southern Sierra Nevada (#1, Section 4.4.1), McPhillips and Brandon (2010) argued that surface uplift and tilting induced by lithospheric foundering is able to explain detrital apatite (U-Th)/He (AHe) cooling ages that imply highly nonuniform changes in relief during the late Cenozoic. Similarly, Cecil et al. (2014) inferred that a ~6 Ma pulse of heating resolved by thermal modelling of detrital AHe data reflects dynamic subsidence, sediment burial, and finally exhumation due to lithosphere removal.

Heat in the lithosphere is a result of thermal conduction, melt intrusion, and heat producing elements concentrated in the upper crust (e.g., Mareschal & Jaupart, 2013). Thickening of the mantle lithosphere followed by its removal in a strong-crust drip may therefore result in signif-

icant crustal cooling followed by heating (Kay & Kay, 1993). On the other hand, syn-drip crustal thickening, such as during a weak-crust drip, would yield an increase in crustal thickness and therefore in radiogenic heating (e.g., Huerta et al., 1998). What is not clear are the conditions under which these thermal events would be recorded by various thermochronometers. High-temperature thermochronometers record thermal perturbations to the lower crust (Blackburn et al., 2011), and have been used to infer heating due to a mantle plume and lithosphere removal in the 1.1 Ga Midcontinent Rift System of North America (U-Pb in rutile and apatite; Edwards & Blackburn, 2018). Similar techniques may be able to investigate the occurrence of lithospheric dripping in the geologic past if crustal rocks are exposed by later volcanism or exhumation. For thermochronology to be truly useful for investigating lithospheric dripping, modelling studies are needed that would elucidate the timing and magnitude of crustal heating and cooling events produced by various styles of lithospheric foundering. By tracking the temperature of discrete particles, models can also provide hypothetical time-temperature histories that can be confirmed or falsified by reverse thermal modelling of thermochronological data (e.g., Ketcham, 2005).

Igneous geochemistry. Recent studies have focused on identifying geochemical fingerprints of mineralogies indicative of lithosphere in magma sources. Adakitic magmas, usually thought to result from the partial melting of young oceanic slabs (e.g., Defant & Drummond, 1990), may also result from melting of the lower crust during a lithospheric dripping event (Kay & Kay, 1993; Kay et al., 1994). When combined with estimates of equilibration temperatures and crystallization ages, a strong case can be made for the melting of progressively descending lithosphere (Ducea et al., 2013; Murray et al., 2015). Given the rapid descent of drips through the upper mantle, these authors argue for the melting of small drips (a few kilometers in width) based on the inference that conductive heating of smaller objects occurs more rapidly. However, as noted in our framework for growth of the Rayleigh Taylor instability (Figure 4.2), it may be possible that small secondary instabilities form on the edges of the drip, producing smaller pieces of lithosphere that can more easily be melted by the surrounding asthenosphere.

An emerging technique is described by Dygert et al. (2019), who use laboratory relationships between differential stress and the grain size of recrystallized olivine (Van der Wal et al., 1993), which, when combined with geothermometry and olivine flow laws (Hirth & Kohlstedt, 2003) yield estimates of the viscosity and strain rate of rapidly deforming lithosphere. Such techniques allow investigation of lithospheric drips deeper in time, as volcanic and especially magmatic rocks may be preserved in the geologic record. Based largely on igneous geochemical data, lithospheric dripping has been hypothesized during in the Miocene (Furman et al., 2016), Oligocene (Kapp & DeCelles, 2019), Eocene (Chapman et al., 2018), and Cretaceous (Zhang et al., 2014). The study of older volcanic and magmatic rocks may therefore extend the record of lithospheric dripping Earth further back into geologic time, providing new insights into the evolution and rheology of Earth's continental lithosphere.

4.6 Conclusions

In this paper, we synthesize the literature related to lithospheric dripping to develop a framework for understanding such events on Earth. We suggest that, in the upper crust and near-surface environment where most geologic observations are available, the process of lithospheric dripping displays two distinct tendencies, summarized as strong-crust and weak-crust drips. Whether a lithospheric dripping event results in syn-drip upper-crustal compression and subsidence (strong-crust) or syn-drip crustal thickening and surface uplift accompanied by upper-crustal extension (weak-crust) mainly depends on the strength of the crust relative to the mantle lithosphere: crusts at least an order of magnitude stronger than the lithosphere yield strong-crust drips, while crusts weaker than this yield weak-crust drips. Uplift is greatest when the strengths of the crust and mantle lithosphere are similar, and extremely weak crusts yield higher rates of horizontal extension, but little surface uplift, above the drip. While additional modelling work is necessary to fully understand the range of possible outcomes due to lithospheric dripping, complex numerical models and 3-D analog models suggest that strong-crust and weak-crust drips can both occur in Earth's continental lithosphere, depending on the thermal, compositional, and mechanical structure of a particular region.

We also present evidence for all the proposed lithospheric dripping events on Earth identified to date, to the best of our knowledge, to infer wavelength, age of detachment, and associated geologic effects of each. Where possible, we also categorize each drip according to our framework. A majority of dripping events have sufficient evidence associated with them to categorize them as either strong-crust or weak-crust drips, and this inference is often supported by independent observations such as surface heat flux and tectonic setting. Of the 26 proposed dripping events, we find that 12 display some evidence for the strong-crust style, while 9 display some evidence for the weak-crust style. Strong-crust drips may result in the formation of transient sedimentary basins in orogenic hinterlands, while weak-crust drips may result in significant surface uplift and extension. Other evidence such as volcanic and magmatic products, mantle xenoliths, and tomographic anomalies are associated with both types of drip. The identification of differing styles of lithospheric dripping in Earth's continental regions can provide insight into the long term (~10 Myr) rheology of the continents, pinpointed to specific times and locations, and may thus be used to infer thermal or compositional states of the lithosphere. However, evidence for many of the purported dripping events is sparse, especially concerning the timing of drip growth and detachment. Given the available evidence, we are relatively confident in categorizing 9 of the strong-crust drips and three of the weak-crust drips. We discuss the full suite of evidence that could be marshalled to test the lithospheric dripping hypothesis and suggest that applying existing techniques, such as quantitative geomorphology, thermochronology, and igneous geochemistry in novel ways may provide additional insights into and constraints on purported lithospheric drips. This work represents the first comprehensive synthesis of inferred lithospheric dripping events

for Earth's continents and provides a framework for understanding lithospheric dripping that can be used to guide further research on the topic.

Acknowledgements

We thank many colleagues including Claire Currie, Erin Seagren, Jeremy Rimando, Alexander Tye, and Oğuz Gogus for thoughtful discussion of ideas contained in this manuscript. This work was supported by an NSERC Discovery Grant to L. Schoenbohm.

References

Agrawal, M., Pulliam, J., Sen, M. K., & Grand, S. P. (2019). Lithospheric removal beneath the eastern flank of the Rio Grande Rift from receiver function velocity analysis. *Geochemistry, Geophysics, Geosystems*, 1–18. https://doi.org/10.1029/2018gc007911

Allmendinger, R. W., Strecker, M. R., Eremchuk, J. E., & Francis, P. (1989). Neotectonic deformation of the southern Puna Plateau, northwestern Argentina. *Journal of South American Earth Sciences*, *2*(2), 111–130. https://doi.org/10.1016/0895-9811(89)90040-0

Amilibia, A., Sàbat, F., McClay, K. R., Muñoz, J. A., Roca, E., & Chong, G. (2008). The role of inherited tectono-sedimentary architecture in the development of the central Andean mountain belt: Insights from the Cordillera de Domeyko. *Journal of Structural Geology*, *30*(12), 1520–1539. https://doi.org/10.1016/j.jsg.2008.08.005

Anderson, R. B., Long, S. P., Horton, B. K., Thomson, S. N., Calle, A. Z., & Stockli, D. F. (2018). Orogenic wedge evolution of the central Andes, Bolivia (21°S): Implications for Cordilleran cyclicity. *Tectonics*. https://doi.org/10.1029/2018TC005132

Babeyko, A. Y., Sobolev, S. V., Trumbull, R. B., Oncken, O., & Lavier, L. L. (2002). Numerical models of crustal scale convection and partial melting beneath the Altiplano-Puna plateau. *Earth and Planetary Science Letters*, *199*(3-4), 373–388. https://doi.org/10.1016/S0012-821X(02)00597-6

Bao, X., & Shen, Y. (2020). Early-stage lithospheric foundering beneath the Eastern Tibetan Plateau revealed by full-wave Pn tomography. *Geophysical Research Letters*, *47*(8), 1–9. https://doi.org/10.1029/2019gl086469

Beall, A. P., Moresi, L., & Stern, T. (2017). Dripping or delamination? A range of mechanisms for removing the lower crust or lithosphere. *Geophysical Journal International*, (September), 671–692. https://doi.org/10.1093/gji/ggx202

Beaumont, C., Nguyen, M. H., Jamieson, R. A., & Ellis, S. (2006). Crustal flow modes in large hot orogens. *Geological Society Special Publication*, *268*, 91–145. https://doi.org/10.1144/GSL.SP.2006.268.01.05

Beck, S. L., & Zandt, G. (2002). The nature of orogenic crust in the central Andes. *Journal of Geophysical Research: Solid Earth*, *107*(B10), 2230. https://doi.org/10.1029/2000JB000124

Beck, S. L., Zandt, G., Ward, K. M., & Scire, A. (2015). Multiple styles and scales of lithospheric foundering beneath the Puna Plateau, central Andes. In *Geological Society of America Memoirs* (pp. 43–60). https://doi.org/10.1130/2015.1212(03)

Becker, T. W. (2012). On recent seismic tomography for the western United States. *Geochemistry, Geophysics, Geosystems*, *13*(1), 1–11. https://doi.org/10.1029/2011GC003977

Benz, H., & Zandt, G. (1993). Lithospheric structure of the San Adreas Fault system in northern and central California. In *Teleseismic tomography* (pp. 440–465).

Beucher, R., Moresi, L., Giordani, J., Mansour, J., Sandiford, D., Farrington, R., Mondy, L., Mallard, C., Rey, P., Duclaux, G., Kaluza, O., Laik, A., & Morón, S. (2019). UWGeodynamics: A teaching and research tool for numerical geodynamic modelling. *Journal of Open Source Software*, *4*(36), 1136. https://doi.org/10.21105/joss.01136

Bianchi, M., Heit, B., Jakovlev, A., Yuan, X., Kay, S. M., Sandvol, E., Alonso, R. N., Coira, B., Brown, L. D., Kind, R., & Comte, D. (2013). Teleseismic tomography of the southern Puna plateau in Argentina and adjacent regions. *Tectonophysics*, *586*, 65–83. https://doi.org/10.1016/j.tecto.2012.11.016

Bird, P. (1979). Continental delamination and the Colorado Plateau. *Journal of Geophysical Research: Solid Earth*, *84*(B13), 7561–7571. https://doi.org/10.1029/JB084iB13p07561

Blackburn, T., Bowring, S. A., Schoene, B., Mahan, K., & Dudas, F. (2011). U-Pb thermochronology: Creating a temporal record of lithosphere thermal evolution. *Contributions to Mineralogy and Petrology*, *162*(3), 479–500. https://doi.org/10.1007/s00410-011-0607-6

Bloch, E., Ibañez-Mejia, M., Murray, K. E., Vervoort, J., & Müntener, O. (2017). Recent crustal foundering in the Northern Volcanic Zone of the Andean arc: Petrological insights from the roots of a modern subduction zone. *Earth and Planetary Science Letters*, *476*, 47–58. https://doi.org/10.1016/j.epsl.2017.07.041

Boyd, O. S., Jones, C. H., & Sheehan, A. F. (2004). Foundering lithosphere imaged beneath the Southern Sierra Nevada, California, USA. *Science*, *305*(5684), 660–662. https://doi.org/10.1126/science.1099181

Brace, W. F., & Kohlstedt, D. L. (1980). Limits on lithospheric stress imposed by laboratory experiments. *Journal of Geophysical Research: Solid Earth*, *85*(B11), 6248–6252. https://doi.org/10.1029/jb085ib11p06248

Buford Parks, V. M., & McQuarrie, N. (2019). Kinematic, flexural, and thermal modelling in the Central Andes: Unravelling age and signal of deformation, exhumation, and uplift. *Tectonophysics*, *766*(June), 302–325. https://doi.org/10.1016/j.tecto.2019.06.008

Bürgmann, R., & Dresen, G. (2008). Rheology of the lower crust and upper mantle: Evidence from rock mechanics, geodesy, and field observations. *Annual Review of Earth and Planetary Sciences*, *36*(1), 531–567. https://doi.org/10.1146/annurev.earth.36.031207.124326

Burkett, E., & Gurnis, M. (2013). Stalled slab dynamics. *Lithosphere*, *5*(1), 92–97. https://doi.org/10.1130/L249.1

Burov, E. B. (2011). Rheology and strength of the lithosphere. *Marine and Petroleum Geology*, *28*(8), 1402–1443. https://doi.org/10.1016/j.marpetgeo.2011.05.008

Burov, E., & Gerya, T. (2014). Asymmetric three-dimensional topography over mantle plumes. *Nature*, *513*(7516), 85–89. https://doi.org/10.1038/nature13703

Byerly, B. L., & Lassiter, J. C. (2012). Evidence from mantle xenoliths for lithosphere removal beneath the central Rio Grande Rift. *Earth and Planetary Science Letters*, *355-356*, 82–93. https://doi.org/10.1016/j.epsl.2012.08.034

Calixto, F. J., Sandvol, E., Kay, S. M., Mulcahy, P., Heit, B., Yuan, X., Coira, B., Comte, D., & Alvarado, P. (2013). Velocity structure beneath the southern Puna plateau: Evidence for delamination. *Geochemistry, Geophysics, Geosystems*, *14*(10), 4292–4305. https://doi.org/10.1002/ggge.20266

Carrapa, B., & DeCelles, P. G. (2015). Regional exhumation and kinematic history of the central Andes in response to cyclical orogenic processes. *Memoir of the Geological Society of America*, *212*, 201–213. https://doi.org/10.1130/2015.1212(11)

Carrapa, B., DeCelles, P. G., Reiners, P. W., Gehrels, G. E., & Sudo, M. (2009). Apatite triple dating and white mica40Ar/39Ar thermochronology of syntectonic detritus in the Central Andes: A multiphase tectonothermal history. *Geology*, *37*(5), 407–410. https://doi.org/10.1130/G25698A.1

Cecil, M. R., Saleeby, Z., Saleeby, J., & Farley, K. A. (2014). Pliocene-Quaternary subsidence and exhumation of the southeastern San Joaquin Basin, California, in response to mantle lithosphere removal. *Geosphere*, *10*(1), 129–147. https://doi.org/10.1130/GES00882.1

Cecil, M., Rotberg, G., Ducea, M. N., Saleeby, J. B., & Gehrels, G. E. (2012). Magmatic growth and batholithic root development in the northern Sierra Nevada, California. *Geosphere*, *8*(3), 592. https://doi.org/10.1130/GES00729.1

Chandrasekhar, S. (1961). *Hyrdodynamic and Hydromagnetic Stability*. Dover Publications, Inc.

Chapman, J. B., Scoggin, S. H., Kapp, P., Carrapa, B., Ducea, M. N., Worthington, J., Oimahmadov, I., & Gadoev, M. (2018). Mesozoic to Cenozoic magmatic history of the Pamir. *Earth and Planetary Science Letters*, *482*(November 2017), 181–192. https://doi.org/10.1016/j.epsl.2017.10.041

Chen, S. S., Fan, W. M., Shi, R. D., Gong, X. H., & Wu, K. (2017). Removal of deep lithosphere in ancient continental collisional orogens: A case study from central Tibet, China. *Geochemistry, Geophysics, Geosystems*, *18*(3), 1225–1243. https://doi.org/10.1002/2016GC006678

Chung, S. L., Liu, D., Ji, J., Chu, M. F., Lee, H. Y., Wen, D. J., Lo, C. H., Lee, T. Y., Qian, Q., & Zhang, Q. (2003). Adakites from continental collision zones: Melting of thickened lower crust beneath southern Tibet. *Geology*, *31*(11), 1021–1024. https://doi.org/10.1130/G19796.1

Conrad, C. P., & Molnar, P. (1997). The growth of Rayleigh-Taylor-type instabilities in the lithosphere for various rheological and density structures. *Geophysical Journal International*, *129*(1), 95–112. https://doi.org/10.1111/j.1365-246X.1997.tb00939.x

Constantin, A. P., Pantea, A., & Stoica, R. (2011). Vrancea (Romania) subcrustal earthquakes: Historical sources and macroseismic intensity assessment. *Romanian Reports of Physics*, *56*(5-6), 813–826.

Corti, G. (2009). Continental rift evolution: From rift initiation to incipient break-up in the Main Ethiopian Rift, East Africa. *Earth-Science Reviews*, *96*(1-2), 1–53. https://doi.org/10.1016/j.earscirev.2009.06.005

Cox, P., Stubailo, I., & Davis, P. (2016). Receiver function and geometric tomography along the monterey microplate to test slab delamination or lithospheric drip models of the Isabella Anomaly, California. *Bulletin of the Seismological Society of America*, *106*(1), 267–280. https://doi.org/10.1785/0120140339

Crameri, F., Schmeling, H., Golabek, G. J., Duretz, T., Orendt, R., Buiter, S. J., May, D. A., Kaus, B. J., Gerya, T. V., & Tackley, P. J. (2012). A comparison of numerical surface topography calculations in geodynamic modelling: An evaluation of the 'sticky air' method. *Geophysical Journal International*, *189*(1), 38–54. https://doi.org/10.1111/j.1365-246X.2012.05388.x

Currie, C. A., Ducea, M. N., DeCelles, P. G., & Beaumont, C. (2015). Geodynamic models of Cordilleran orogens: Gravitational instability of magmatic arc roots. In *Geological Society of America Memoirs* (pp. 1–22). https://doi.org/10.1130/2015.1212(01)

Darold, A., & Humphreys, E. D. (2013). Upper mantle seismic structure beneath the Pacific Northwest: A plume-triggered delamination origin for the Columbia River flood basalt eruptions. *Earth and Planetary Science Letters*, *365*(December 2010), 232–242. https://doi.org/10.1016/j.epsl.2013.01.024

Davies, J. H., & von Blanckenburg, F. (1995). Slab breakoff: A model of lithosphere detachment and its test in the magmatism and deformation of collisional orogens. *Earth and Planetary Science Letters*, *129*(1-4), 85–102. https://doi.org/10.1016/0012-821X(94)00237-S

DeCelles, P. G. (2004). Late Jurassic to Eocene evolution of the Cordilleran thrust belt and foreland basin system, western U.S.A. *American Journal of Science*, *304*(2), 105–168. https://doi.org/10.2475/ajs.304.2.105

DeCelles, P. G., Carrapa, B., Horton, B. K., McNabb, J., Gehrels, G. E., & Boyd, J. (2015a). The Miocene Arizaro Basin, central Andean hinterland: Response to partial lithosphere removal? In *Geological Society of America Memoirs* (pp. 359–386). https://doi.org/10.1130/2015.1212(18)

DeCelles, P. G., Ducea, M. N., Kapp, P., & Zandt, G. (2009). Cyclicity in Cordilleran orogenic systems. *Nature Geoscience*, *2*(4), 251–257. https://doi.org/10.1038/ngeo469

DeCelles, P. G., Zandt, G., Beck, S. L., Currie, C. A., Ducea, M. N., Kapp, P., Gehrels, G. E., Carrapa, B., Quade, J., & Schoenbohm, L. M. (2015b). Cyclical orogenic processes in the Cenozoic central Andes. In *Geological Society of America Memoirs* (pp. 459–490). https://doi.org/10.1130/2015.1212(22)

Defant, M., & Drummond, M. (1990). Derivation of some modern arc magmas by melting of young subducted lithosphere. *Nature*, *347*, 662–665.

de Silva, S. L., Zandt, G., Trumbull, R. B., Viramonte, J. G., Salas, G., & Jiménez, N. (2006). Large ignimbrite eruptions and volcano-tectonic depressions in the Central Andes: a thermomechanical perspective. *Geological Society, London, Special Publications*, *269*(1), 47–63. https://doi.org/10.1144/GSL.SP.2006.269.01.04

Dickinson, W. R. (2004). Evolution of the North American Cordillera. *Annual Review of Earth and Planetary Sciences*, *32*(1), 13–45. https://doi.org/10.1146/annurev.earth.32.101802.120257

Dimech, J.-L., Stern, T., & Lamb, S. (2017). Mantle earthquakes, crustal structure, and gravitational instability beneath western North Island, New Zealand. *Geology*, *45*(2), 155–158. https://doi.org/10.1130/G38476.1

Dougherty, S. L., Jiang, C., Clayton, R. W., Schmandt, B., & Hansen, S. M. (2020). Seismic evidence for a fossil slab origin for the Isabella anomaly. *Geophysical Journal International*, *224*(2), 1188–1196. https://doi.org/10.1093/gji/ggaa472

Drucker, D., & Prager, W. (1952). Soil mechanics and plastic analysis or limit design. *Quarterly of Applied Mathematics*, *10*(2), 157–165.

Ducea, M. N., Lutkov, V., Minaev, V. T., Hacker, B., Ratschbacher, L., Luffi, P., Schwab, M., Gehrels, G. E., McWilliams, M., Vervoort, J., & Metcalf, J. (2003). Building the Pamirs: The view from the underside. *Geology*, *31*(10), 849–852. https://doi.org/10.1130/G19707.1

Ducea, M. N., & Saleeby, J. B. (1998). A case for delamination of the deep batholithic crust beneath the Sierra Nevada, California. *International Geology Review*, *40*(1), 78–93. https://doi.org/10.1080/00206819809465199

Ducea, M. N., Seclaman, A. C., Murray, K. E., Jianu, D., & Schoenbohm, L. M. (2013). Mantle-drip magmatism beneath the Altiplano-Puna plateau, central Andes. *Geology*, *41*(8), 915–918. https://doi.org/10.1130/G34509.1

Duretz, T., de Borst, R., Yamato, P., & Le Pourhiet, L. (2020). Toward robust and predictive geodynamic modeling: The way forward in frictional plasticity. *Geophysical Research Letters*, *47*(5), e2019GL086027. https://doi.org/10.1029/2019GL086027

Dygert, N., Bernard, R. E., & Behr, W. M. (2019). Great Basin Mantle Xenoliths Record Active Lithospheric Downwelling Beneath Central Nevada. *Geochemistry, Geophysics, Geosystems*, *20*(2), 751–772. https://doi.org/10.1029/2018GC007834

Edwards, G. H., & Blackburn, T. (2018). Detecting the extent of ca. 1.1 Ga Midcontinent Rift plume heating using U-Pb thermochronology of the lower crust. *Geology*, *46*(10), 911–914. https://doi.org/10.1130/G45150.1

Elkins-Tanton, L. T. (2007). Continental magmatism, volatile recycling, and a heterogeneous mantle caused by lithospheric gravitational instabilities. *Journal of Geophysical Research: Solid Earth*, *112*(3), 1–13. https://doi.org/10.1029/2005JB004072

England, P., & Houseman, G. A. (1989). Extension during continental convergence, with application to the Tibetan Plateau. *Journal of Geophysical Research*, *94*(B12), 17561. https://doi.org/10.1029/JB094iB12p17561

Erdman, M. E., Lee, C. T. A., Levander, A., & Jiang, H. (2016). Role of arc magmatism and lower crustal foundering in controlling elevation history of the Nevadaplano and Colorado Plateau: A case study of pyroxenitic lower crust from central Arizona, USA. *Earth and Planetary Science Letters*, *439*(February), 48–57. https://doi.org/10.1016/j.epsl.2016.01.032

Farmer, G. L., Glazner, A. F., & Manley, C. R. (2002). Did lithospheric delamination trigger late Cenozoic potassic volcanism in the southern Sierra Nevada, California? *Bulletin of the Geological Society of America*, *114*(6), 754–768. https://doi.org/10.1130/0016-7606(2002)114<0754:DLDTLC>2.0.CO;2

Ferrari, L., López-Martínez, M., & Rosas-Elguera, J. (2002). Ignimbrite flare-up and deformation in the southern Sierra Madre Occidental, western Mexico: Implications for the late subduction history of the Farallon plate. *Tectonics*, *21*(4), 17–1–17–24. https://doi.org/10.1029/2001tc001302

Ferrari, L., Orozco-Esquivel, T., Manea, V., & Manea, M. (2012). The dynamic history of the Trans-Mexican Volcanic Belt and the Mexico subduction zone. *Tectonophysics*, *522-523*, 122–149. https://doi.org/10.1016/j.tecto.2011.09.018

Fillerup, M. A., Knapp, J. H., Knapp, C. C., & Rasoazanamparany, C. (2010). Mantle earthquakes in the absence of subduction? Continental delamination in the Romanian Carpathians. *Lithosphere*, *2*(5), 333–340. https://doi.org/10.1130/L102.1

Foulger, G. R., Panza, G. F., Artemieva, I. M., Bastow, I. D., Cammarano, F., Evans, J. R., Hamilton, W. B., Julian, B. R., Lustrino, M., Thybo, H., & Yanovskaya, T. B. (2013). Caveats on tomographic images. *Terra Nova*, *25*(4), 259–281. https://doi.org/10.1111/ter.12041

Fraters, M. R. T., Bangerth, W., Thieulot, C., Glerum, A. C., & Spakman, W. (2019). Efficient and practical Newton solvers for non-linear Stokes systems in geodynamic problems. *Geophysical Journal International*, *218*(2), 873–894. https://doi.org/10.1093/gji/ggz183

Furman, T., Nelson, W. R., & Elkins-Tanton, L. T. (2016). Evolution of the East African rift: Drip magmatism, lithospheric thinning and mafic volcanism. *Geochimica et Cosmochimica Acta*, *185*, 418–434. https://doi.org/10.1016/j.gca.2016.03.024

G öğüş, O. H., & Ueda, K. (2018). Peeling back the lithosphere: Controlling parameters, surface expressions and the future directions in delamination modeling. *Journal of Geodynamics*, *117*(March), 21–40. https://doi.org/10.1016/j.jog.2018.03.003

Gao, S., Rudnick, R. L., Carlson, R. W., McDonough, W. F., & Liu, Y. S. (2002). Re-Os evidence for replacement of ancient mantle lithosphere beneath the North China craton. *Earth and Planetary Science Letters*, *198*(3-4), 307–322. https://doi.org/10.1016/S0012-821X(02)00489-2

Gao, S., Rudnick, R., Yuan, H., Liu, X., Liu, Y. S., Xu, W. L., Ling, W. L., Ayers, J., Wang, X. C., & Wang, Q. H. (2004). Recycling lower continental crust in the North China craton. *Nature*, *432*, 892–897.

Garzanti, E., Radeff, G., & Malusà, M. G. (2018). Slab breakoff: A critical appraisal of a geological theory as applied in space and time. *Earth-Science Reviews*, *177*(November 2017), 303–319. https://doi.org/10.1016/j.earscirev.2017.11.012

Garzione, C. N., Auerbach, D. J., Jin-Sook Smith, J., Rosario, J. J., Passey, B. H., Jordan, T. E., & Eiler, M. M. (2014). Clumped isotope evidence for diachronous surface cooling of the Altiplano and pulsed surface uplift of the Central Andes. *Earth and Planetary Science Letters*, *393*, 173–181. https://doi.org/10.1016/j.epsl.2014.02.029

Garzione, C. N., Hoke, G. D., Libarkin, J. C., Withers, S., MacFadden, B., Eiler, J., Ghosh, P., & Mulch, A. (2008). Rise of the Andes. *Science*, *320*(5881), 1304–1307. https://doi.org/10.1126/science.1148615

Garzione, C. N., Molnar, P., Libarkin, J. C., & MacFadden, B. J. (2006). Rapid late Miocene rise of the Bolivian Altiplano: Evidence for removal of mantle lithosphere. *Earth and Planetary Science Letters*, *241*(3-4), 543–556. https://doi.org/10.1016/j.epsl.2005.11.026

Gemmer, L., & Houseman, G. A. (2007). Convergence and extension driven by lithospheric gravitational instability: Evolution of the Alpine-Carpathian-Pannonian system. *Geophysical Journal International*, *168*(3), 1276–1290. https://doi.org/10.1111/j.1365-246X.2006.03327.x

Göğüş, O. H., & Pysklywec, R. N. (2008). Near-surface diagnostics of dripping or delaminating lithosphere. *Journal of Geophysical Research: Solid Earth*, *113*(11), 1–11. https://doi.org/10.1029/2007JB005123

Göğüş, O. H., Pysklywec, R. N., & Faccenna, C. (2016). Postcollisional lithospheric evolution of the Southeast Carpathians: Comparison of geodynamical models and observations. *Tectonics*, *35*(5), 1205–1224. https://doi.org/10.1002/2015TC004096

Göğüş, O. H., Pysklywec, R. N., şengör, A. M. C., & Gün, E. (2017). Drip tectonics and the enigmatic uplift of the Central Anatolian Plateau. *Nature Communications*, *8*(1), 1538. https://doi.org/10.1038/s41467-017-01611-3

Gorczyk, W., Hobbs, B., Gessner, K., & Gerya, T. (2013). Intracratonic geodynamics. *Gondwana Research*, *24*(3-4), 838–848. https://doi.org/10.1016/j.gr.2013.01.006

Haag, M. B., Baez, W. A., Sommer, C. A., Arnosio, J. M., & Filipovich, R. E. (2019). Geomorphology and spatial distribution of monogenetic volcanoes in the southern Puna Plateau (NW Argentina). *Geomorphology*, *342*, 196–209. https://doi.org/10.1016/j.geomorph.2019.06.008

Hales, T. C., Abt, D. L., Humphreys, E. D., & Roering, J. J. (2005). A lithospheric instability origin for Columbia River flood basalts and Wallowa Mountains uplift in northeast Oregon. *Nature*, *438*(7069), 842–845. https://doi.org/10.1038/nature04313

Harangi, S., Sági, T., Seghedi, I., & Ntaflos, T. (2013). Origin of basaltic magmas of Perşani volcanic field, Romania: A combined whole rock and mineral scale investigation. *Lithos*, *180-181*, 43–57. https://doi.org/10.1016/j.lithos.2013.08.025

Harig, C., Molnar, P., & Houseman, G. A. (2008). Rayleigh-Taylor instability under a shear stress free top boundary condition and its relevance to removal of mantle lithosphere from beneath the Sierra Nevada. *Tectonics*, *27*(6), 1–15. https://doi.org/10.1029/2007TC002241

Hatzfeld, D., & Molnar, P. (2010). Comparisons of the kinematics and deep structures of the Zagros and Himalaya and of the Iranian and Tibetan plateaus and geodynamic implications. *Reviews of Geophysics*, *48*(2), 1–48. https://doi.org/10.1029/2009RG000304

He, X., Zhang, R., Chen, S., & Doolen, G. D. (1999). On the three-dimensional Rayleigh–Taylor instability. *Physics of Fluids*, *11*(5), 1143–1152. https://doi.org/10.1063/1.869984

Hines, T. T., & Hetland, E. A. (2016). Rapid and simultaneous estimation of fault slip and heterogeneous lithospheric viscosity from post-seismic deformation. *Geophysical Journal International*, *204*(1), 569–582. https://doi.org/10.1093/gji/ggv477

Hirth, G., & Kohlstedt, D. (2003). Rheology of the upper mantle and the mantle wedge: A view from the experimentalists. In *Geophysical monograph series* (pp. 83–105). https://doi.org/10.1029/138GM06

Hoke, G. D., & Garzione, C. N. (2008). Paleosurfaces, paleoelevation, and the mechanisms for the late Miocene topographic development of the Altiplano plateau. *Earth and Planetary Science Letters*, *271*(1-4), 192–201. https://doi.org/10.1016/j.epsl.2008.04.008

Hoogenboom, T., & Houseman, G. A. (2006). Rayleigh-Taylor instability as a mechanism for corona formation on Venus. *Icarus*, *180*(2), 292–307. https://doi.org/10.1016/j.icarus.2005.11.001

Horváth, F. (1993). Towards a mechanical model for the formation of the Pannonian basin. *Tectonophysics*, *226*, 333–357. https://doi.org/10.1016/0040-1951(93)90126-5

Houseman, G. A., McKenzie, D. P., & Molnar, P. (1981). Convective instability of a thickened boundary layer and its relevance for the thermal evolution of continental convergent belts. *Journal of Geophysical Research*, *86*(B7), 6115–6132. https://doi.org/10.1029/JB086iB07p06115

Houseman, G. A., & Molnar, P. (1997). Gravitational (Rayleigh-Taylor) instability of a layer with non-linear viscosity and convective thinning of continental lithosphere. *Geophysical Journal International*, *128*(1), 125–150. https://doi.org/10.1111/j.1365-246X.1997.tb04075.x

Houseman, G. A., & Molnar, P. (2001). Mechanisms of lithospheric rejuvenation associated with continental orogeny. *Geological Society, London, Special Publications*, *184*(1), 13–38. https://doi.org/10.1144/GSL.SP.2001.184.01.02

Houseman, G. A., Neil, E. A., & Kohler, M. D. (2000). Lithospheric instability beneath the Transverse Ranges of California. *Journal of Geophysical Research: Solid Earth*, *105*(B7), 16237–16250. https://doi.org/10.1029/2000jb900118

Huerta, A. D., Royden, L. H., & Hodges, K. V. (1998). The thermal structure of collisional orogens as a response to accretion, erosion, and radiogenic heating. *Journal of Geophysical Research: Solid Earth*, *103*, 15287–15302. https://doi.org/10.1029/98JB00593

Humphreys, E. D., & Hager, B. H. (1990). A Kinematic Model for the Late Cenozoic Development of Southern California Crust and Upper Mantle. *Journal of Geophysical Research-Solid Earth and Planets*, *95*(B12), 19747–19762.

Ischuk, A., Bendick, R., Rybin, A., Molnar, P., Khan, S. F., Kuzikov, S., Mohadjer, S., Saydullaev, U., Ilyasova, Z., Schelochkov, G., & Zubovich, A. V. (2013). Kinematics of the Pamir and Hindu Kush regions from GPS geodesy. *Journal of Geophysical Research: Solid Earth*, *118*(5), 2408–2416. https://doi.org/10.1002/jgrb.50185

Jellinek, A. M., Kerr, R. C., & Griffiths, R. W. (1999). Mixing and compositional stratification produced by natural convection 1. Experiments and their application to Earth's core and mantle. *Journal of Geophysical Research: Solid Earth*, *104*(B4), 7183–7201. https://doi.org/10.1029/1998jb900116

Jones, C. H., Farmer, G. L., & Unruh, J. (2004). Tectonics of Pliocene removal of lithosphere of the Sierra Nevada, California. *Bulletin of the Geological Society of America*, *116*(11-12), 1408–1422. https://doi.org/10.1130/B25397.1

Jones, C. H., Kanamori, H., & Roecker, S. W. (1994). Missing roots and mantle "drips": regional Pn and teleseismic arrival times in the southern Sierra Nevada and vicinity, California. *Journal of Geophysical Research*, *99*(B3), 4567–4601. https://doi.org/10.1029/93JB01232

Jones, C. H., Regard, V., Zandt, G., Gilbert, H., Owens, T. J., & Stachnik, J. (2014). P-wave tomography of potential convective downwellings and their source regions, Sierra Nevada, California. *Geosphere*, *10*(3), 505–533. https://doi.org/10.1130/GES00961.1

Jull, M., & Kelemen, P. B. (2001). On the conditions for lower crustal convective instability. *Journal of Geophysical Research: Solid Earth*, *106*(B4), 6423–6446. https://doi.org/10.1029/2000JB900357

Kapp, P., & DeCelles, P. G. (2019). Mesozoic–Cenozoic geological evolution of the Himalayan-Tibetan orogen and working tectonic hypotheses. *American Journal of Science*, *319*(3), 159–254. https://doi.org/10.2475/03.2019.01

Karlstrom, K. E., Coblentz, D., Dueker, K., Ouimet, W., Kirby, E., VanWijk, J., Schmandt, B., Kelley, S., Lazear, G., Crossey, L. J., Crow, R., Aslan, A., Darling, A., Aster, R., MacCarthy, J., Hansen, S. M., Stachnik, J., Stockli, D. F., Garcia, R. V., … Donahue, M. S. (2012). Mantle-driven dynamic uplift of the Rocky Mountains and Colorado Plateau and its surface response: Toward a unified hypothesis. *Lithosphere*, *4*(1), 3–22. https://doi.org/10.1130/L150.1

Karlstrom, K. E., Crow, R., Crossey, L. J., Coblentz, D., & Van Wijk, J. W. (2008). Model for tectonically driven incision of the younger than 6 Ma Grand Canyon. *Geology*, *36*(11), 835–838. https://doi.org/10.1130/G25032A.1

Kaus, B. J., & Becker, T. W. (2007). Effects of elasticity on the Rayleigh–Taylor instability: Implications for large-scale geodynamics. *Geophysical Journal International*, *168*(2), 843–862. https://doi.org/10.1111/j.1365-246X.2006.03201.x

Kaus, B. J., Mühlhaus, H., & May, D. A. (2010). A stabilization algorithm for geodynamic numerical simulations with a free surface. *Physics of the Earth and Planetary Interiors*, *181*(1-2), 12–20. https://doi.org/10.1016/j.pepi.2010.04.007

Kay, R. W., & Kay, S. M. (1993). Delamination and delamination magmatism. *Tectonophysics*, *219*(1-3), 177–189. https://doi.org/10.1016/0040-1951(93)90295-U

Kay, S. M., Coira, B., & Viramonte, J. (1994). Young mafic back arc volcanic rocks as indicators of continental lithospheric delamination beneath the Argentine Puna Plateau, central

Andes. *Journal of Geophysical Research: Solid Earth*, *99*(B12), 24323–24339. https://doi.org/10.1029/94JB00896

Kay, S. M., Coira, B. L., Caffe, P. J., & Chen, C. H. (2010). Regional chemical diversity, crustal and mantle sources and evolution of central Andean Puna plateau ignimbrites. *Journal of Volcanology and Geothermal Research*, *198*(1-2), 81–111. https://doi.org/10.1016/j.jvolgeores.2010.08.013

Kay, S. M., & Mpodozis, C. (2002). Magmatism as a probe to the Neogene shallowing of the Nazca plate beneath the modern Chilean flat-slabs. *Journal of South American Earth Sciences*, *15*(1), 39–57. https://doi.org/10.1016/S0895-9811(02)00005-6

Ketcham, R. A. (2005). Forward and inverse modeling of low-temperature thermochronometry data. *Reviews in Mineralogy and Geochemistry*, *58*, 275–314. https://doi.org/10.2138/rmg.2005.58.11

Kleinhans, M. G., Buskes, C. J., & De Regt, H. W. (2005). Terra incognita: Explanation and reduction in earth science. *International Studies in the Philosophy of Science*, *19*(3), 289–317. https://doi.org/10.1080/02698590500462356

Knapp, J. H., Knapp, C. C., Raileanu, V., Matenco, L., Mocanu, V., & Dinu, C. (2005). Crustal constraints on the origin of mantle seismicity in the Vrancea Zone, Romania: The case for active continental lithospheric delamination. *Tectonophysics*, *410*(1-4), 311–323. https://doi.org/10.1016/j.tecto.2005.02.020

Koulakov, I. (2011). High-frequency P and S velocity anomalies in the upper mantle beneath Asia from inversion of worldwide traveltime data. *Journal of Geophysical Research: Solid Earth*, *116*(4), 1–22. https://doi.org/10.1029/2010JB007938

Krugh, W. C., & Foreshee, B. C. (2018). Geomorphic constraints on the incision history of the lower Kern River, southern Sierra Nevada, California. *Geosphere*, *14*(3), 1101–1118. https://doi.org/10.1130/GES01603.1

Krystopowicz, N. J., & Currie, C. A. (2013). Crustal eclogitization and lithosphere delamination in orogens. *Earth and Planetary Science Letters*, *361*, 195–207. https://doi.org/10.1016/j.epsl.2012.09.056

Kusky, T. M., Windley, B. F., Wang, L., Wang, Z., Li, X., & Zhu, P. (2014). Flat slab subduction, trench suction, and craton destruction: Comparison of the North China, Wyoming, and Brazilian cratons. *Tectonophysics*, *630*(100), 208–221. https://doi.org/10.1016/j.tecto.2014.05.028

Lamb, S. (2011). Cenozoic tectonic evolution of the New Zealand plate-boundary zone: A paleomagnetic perspective. *Tectonophysics*, *509*(3-4), 135–164. https://doi.org/10.1016/j.tecto.2011.06.005

Lambeck, K., Smither, C., & Johnston, P. (1998). Sea-level change, glacial rebound and mantle viscosity for northern Europe. *Geophysical Journal International*, *134*(1), 102–144. https://doi.org/10.1046/j.1365-246X.1998.00541.x

Le Pourhiet, L., Gurnis, M., & Saleeby, J. B. (2006). Mantle instability beneath the Sierra Nevada Mountains in California and Death Valley extension. *Earth and Planetary Science Letters*, *251*(1-2), 104–119. https://doi.org/10.1016/j.epsl.2006.08.028

Le Roux, V., Lee, C. T., & Turner, S. J. (2010). Zn/Fe systematics in mafic and ultramafic systems: Implications for detecting major element heterogeneities in the Earth's mantle. *Geochimica et Cosmochimica Acta*, *74*(9), 2779–2796. https://doi.org/10.1016/j.gca.2010.02.004

Levander, A., Schmandt, B., Miller, M. S., Liu, K., Karlstrom, K. E., Crow, R. S., Lee, C.-T. A., & Humphreys, E. D. (2011). Continuing Colorado plateau uplift by delamination-style convective lithospheric downwelling. *Nature*, *472*(7344), 461–465. https://doi.org/10.1038/nature10001

Liang, X., Sandvol, E., Kay, S. M., Heit, B., Yuan, X., Mulcahy, P., Chen, C., Brown, L. D., Comte, D., & Alvarado, P. (2014). Delamination of southern Puna lithosphere revealed by body wave attenuation tomography. *Journal of Geophysical Research: Solid Earth*, *119*(1), 549–566. https://doi.org/10.1002/2013JB010309

Liu, J., Davis, G. A., Lin, Z., & Wu, F. (2005). The Liaonan metamorphic core complex, Southeastern Liaoning Province, North China: A likely contributor to Cretaceous rotation of Eastern Liaoning, Korea and contiguous areas. *Tectonophysics*, *407*(1-2), 65–80. https://doi.org/10.1016/j.tecto.2005.07.001

Liu, M., & Li, Z. (2018). Dynamics of thinning and destruction of the continental cratonic lithosphere: Numerical modeling. *Science China Earth Sciences*. https://doi.org/10.1007/s11430-017-9184-x

Lorinczi, P., & Houseman, G. A. (2009). Lithospheric gravitational instability beneath the Southeast Carpathians. *Tectonophysics*, *474*(1-2), 322–336. https://doi.org/10.1016/j.tecto.2008.05.024

Lu, H., Tian, X., Yun, K., & Li, H. (2018). Convective removal of the Tibetan Plateau mantle lithosphere by ̃26 ma. *Tectonophysics*, *731-732*(March), 17–34. https://doi.org/10.1016/j.tecto.2018.03.006

Mareschal, J. C., & Jaupart, C. (2013). Radiogenic heat production, thermal regime and evolution of continental crust. *Tectonophysics*, *609*, 524–534. https://doi.org/10.1016/j.tecto.2012.12.001

Marrett, R., & Emerman, S. H. (1992). The relations between faulting and mafic magmatism in the Altiplano-Puna plateau (central Andes). *Earth and Planetary Science Letters*, *112*(1-4), 53–59. https://doi.org/10.1016/0012-821X(92)90006-H

Martin, M., & Wenzel, F. (2006). High-resolution teleseismic body wave tomography beneath SE-Romania - II. Imaging of a slab detachment scenario. *Geophysical Journal International*, *164*(3), 579–595. https://doi.org/10.1111/j.1365-246X.2006.02884.x

Mason, P. R., Seghedi, I., Szákacs, A., & Downes, H. (1998). Magmatic constraints on geodynamic models of subduction in the East Carpathians, Romania. *Tectonophysics*, *297*(1-4), 157–176. https://doi.org/10.1016/S0040-1951(98)00167-X

McKenzie, D., Jackson, J., & Priestley, K. (2019). Continental collisions and the origin of subcrustal continental earthquakes. *Canadian Journal of Earth Sciences*, *56*(11), 1101–1118. https://doi.org/10.1139/cjes-2018-0289

McMillan, M., & Schoenbohm, L. M. (in prep.). Two styles of lithospheric dripping: Synthesizing gravitational instability models, continental tectonics, and geologic observations. *Geochemistry, Geophysics, Geosystems*.

McPhillips, D., & Brandon, M. T. (2010). Using tracer thermochronology to measure modern relief change in the Sierra Nevada, California. *Earth and Planetary Science Letters*, *296*(3-4), 373–383. https://doi.org/10.1016/j.epsl.2010.05.022

McQuarrie, N. (2002). The kinematic history of the central Andean fold-thrust belt, Bolivia: Implications for building a high plateau. *Bulletin of the Geological Society of America*, *114*(8), 950–963. https://doi.org/10.1130/0016-7606(2002)114<0950:TKHOTC>2.0.CO;2

Meijers, M. J., Brocard, G. Y., Cosca, M. A., Lüdecke, T., Teyssier, C., Whitney, D. L., & Mulch, A. (2018). Rapid late Miocene surface uplift of the Central Anatolian Plateau margin. *Earth and Planetary Science Letters*, *497*, 29–41. https://doi.org/10.1016/j.epsl.2018.05.040

Molnar, P. (2015). Gravitational instability of mantle lithosphere and core complexes. *Tectonics*, *34*(3), 478–487. https://doi.org/10.1002/2014TC003808

Molnar, P., & Bendick, R. (2019). Seismic Moments of Intermediate-Depth Earthquakes Beneath the Hindu Kush: Active Stretching of a Blob of Sinking Thickened Mantle Lithosphere? *Tectonics*, *38*(5), 1651–1665. https://doi.org/10.1029/2018TC005336

Molnar, P., & Garzione, C. N. (2007). Bounds on the viscosity coefficient of continental lithosphere from removal of mantle lithosphere beneath the Altiplano and Eastern Cordillera. *Tectonics*, *26*(2). https://doi.org/10.1029/2006TC001964

Molnar, P., & Houseman, G. A. (2004). The effects of buoyant crust on the gravitational instability of thickened mantle lithosphere at zones of intracontinental convergence. *Geophysical Journal International*, *158*(3), 1134–1150. https://doi.org/10.1111/j.1365-246X.2004.02312.x

Molnar, P., & Houseman, G. A. (2013). Rayleigh-Taylor instability, lithospheric dynamics, surface topography at convergent mountain belts, and gravity anomalies. *Journal of Geophysical Research: Solid Earth*, *118*(5), 2544–2557. https://doi.org/10.1002/jgrb.50203

Molnar, P., Houseman, G. A., & Conrad, C. P. (1998). Rayleigh-Taylor instability and convective thinning of mechanically thickened lithosphere: Effects of non-linear viscosity decreasing exponentially with depth and of horizontal shortening of the layer. *Geophysical Journal International*, *133*, 568–584.

Molnar, P., & Jones, C. H. (2004). A test of laboratory based rheological parameters of olivine from an analysis of late Cenozoic convective removal of mantle lithosphere beneath

the Sierra Nevada, California, USA. *Geophysical Journal International*, *156*(3), 555–564. https://doi.org/10.1111/j.1365-246X.2004.02138.x

Molnar, P., & Tapponnier, P. (1978). Active tectonics of Tibet. *Journal of Geophysical Research*, *83*, 5361–5375. https://doi.org/10.1029/JB083iB11p05361

Morfulis, M., Báez, W., Retamoso, S., Bardelli, L., Filipovich, R., & Sommer, C. A. (2020). Quantitative spatial distribution analysis of mafic monogenic volcanism in the southern Puna, Argentina: Implications for magma production rates and structural control during its ascent. *Journal of South American Earth Sciences*, *104*(September). https://doi.org/10.1016/j.jsames.2020.102852

Mori, L., Gómez-Tuena, A., Schaaf, P., Goldstein, S. L., Pérez-Arvizu, O., & Solís-Pichardo, G. (2009). Lithospheric removal as a trigger for flood basalt magmatism in the Trans-Mexican Volcanic Belt. *Journal of Petrology*, *50*(11), 2157–2186. https://doi.org/10.1093/petrology/egp072

Murray, K. E., Ducea, M. N., & Schoenbohm, L. M. (2015). Foundering-driven lithospheric melting: The source of central Andean mafic lavas on the Puna Plateau (22°S–27°S). In *Geological Society of America Memoirs* (pp. 139–166). https://doi.org/10.1130/2015.1212(08)

Myers, S. C., Beck, S. L., Zandt, G., & Wallace, T. (1998). Lithospheric-scale structure across the Bolivian Andes from tomographic images of velocity and attenuation for P and S waves. *Journal of Geophysical Research: Solid Earth*, *103*(B9), 21233–21252. https://doi.org/10.1029/98JB00956

Neil, E. A., & Houseman, G. A. (1999). Rayleigh-Taylor instability of the upper mantle and its role in intraplate orogeny. *Geophysical Journal International*, *138*(1), 89–107. https://doi.org/10.1046/j.1365-246X.1999.00841.x

Obrebski, M., Allen, R. M., Pollitz, F., & Hung, S. H. (2011). Lithosphere-asthenosphere interaction beneath the western United States from the joint inversion of body-wave traveltimes and surface-wave phase velocities. *Geophysical Journal International*, *185*(2), 1003–1021. https://doi.org/10.1111/j.1365-246X.2011.04990.x

Paterson, S. R., & Ducea, M. N. (2015). Arc magmatic tempos: Gathering the evidence. *Elements*, *11*(2), 91–98. https://doi.org/10.2113/gselements.11.2.91

Pavlis, G. L., Sigloch, K., Burdick, S., Fouch, M. J., & Vernon, F. L. (2012). Unraveling the geometry of the Farallon plate: Synthesis of three-dimensional imaging results from USArray. *Tectonophysics*, *532-535*, 82–102. https://doi.org/10.1016/j.tecto.2012.02.008

Petrinovic, I. A., Martí, J., Aguirre-Díaz, G. J., Guzmán, S., Geyer, A., & Paz, N. S. (2010). The Cerro Aguas Calientes caldera, NW Argentina: An example of a tectonically controlled, polygenetic collapse caldera, and its regional significance. *Journal of Volcanology and Geothermal Research*, *194*(1-3), 15–26. https://doi.org/10.1016/j.jvolgeores.2010.04.012

Pikser, J. E., Forsyth, D. W., & Hirth, G. (2012). Along-strike translation of a fossil slab. *Earth and Planetary Science Letters*, *331-332*, 315–321. https://doi.org/10.1016/j.epsl.2012.03.027

Piskorz, D., Elkins-Tanton, L. T., & Smrekar, S. E. (2014). Coronae formation on Venus via extension and lithospheric instability. *Journal of Geophysical Research: Planets*, *119*(12), 2568–2582. https://doi.org/10.1002/2014JE004636

Porritt, R. W. (2013). *Tracing the Farallon plate through seismic imaging with USArray* (Doctoral dissertation). University of California, Berkeley.

Porter, R. C., Fouch, M. J., & Schmerr, N. C. (2014). Dynamic lithosphere within the Great Basin. *Geochemistry, Geophysics, Geosystems*, *15*(4), 1128–1146. https://doi.org/10.1002/2013GC005151

Prakash, V. N., Sreenivas, K. R., & Arakeri, J. H. (2017). The role of viscosity contrast on plume structure in laboratory modeling of mantle convection. *Chemical Engineering Science*, *158*(October 2016), 245–256. https://doi.org/10.1016/j.ces.2016.10.012

Prol-Ledesma, R. M., & Morán-Zenteno, D. J. (2019). Heat flow and geothermal provinces in Mexico. *Geothermics*, *78*(December 2018), 183–200. https://doi.org/10.1016/j.geothermics.2018.12.009

Pysklywec, R. N., & Cruden, A. R. (2004). Coupled crust-mantle dynamics and intraplate tectonics: Two-dimensional numerical and three-dimensional analogue modeling. *Geochemistry, Geophysics, Geosystems*, *5*, Q10003. https://doi.org/10.1029/2004GC000748

Pysklywec, R. N., & Shahnas, M. H. (2003). Time-dependent surface topography in a coupled crust-mantle convection model. *Geophysical Journal International*, *154*(2), 268–278. https://doi.org/10.1046/j.1365-246X.2003.01987.x

Qi, Y., Wang, Q., Wei, G.-j., Zhang, X.-Z., Dan, W., Hao, L.-L., & Yang, Y.-N. (2021). Late Eocene post-collisional magmatic rocks from the southern Qiangtang terrane record the melting of pre-collisional enriched lithospheric mantle. *GSA Bulletin*, 1–13. https://doi.org/10.1130/b35864.1

Ramos, V. A., & Folguera, A. (2009). Andean flat-slab subduction through time. *Geological Society, London, Special Publications*, *327*(1), 31–54. https://doi.org/10.1144/SP327.3

Rapp, R. P., & Watson, E. B. (1995). Dehydration melting of metabasalt at 8-32 kbar: Implications for continental growth and crust-mantle recycling. *Journal of Petrology*, *36*(4), 891–931. https://doi.org/10.1093/petrology/36.4.891

Ren, Y., Stuart, G. W., Houseman, G. A., Dando, B., Ionescu, C., Hegedüs, E., Radovanović, S., & Shen, Y. (2012). Upper mantle structures beneath the Carpathian-Pannonian region: Implications for the geodynamics of continental collision. *Earth and Planetary Science Letters*, *349-350*(December 2018), 139–152. https://doi.org/10.1016/j.epsl.2012.06.037

Ricketts, J. W., Kelley, S. A., Karlstrom, K. E., Schmandt, B., Donahue, M. S., & van Wijk, J. (2016). Synchronous opening of the Rio Grande rift along its entire length at 25-10 Ma supported by apatite (U-Th)/He and fission-track thermochronology, and evaluation of possible driving mechanisms. *Bulletin of the Geological Society of America*, *128*(3-4), 397–424. https://doi.org/10.1130/B31223.1

Risse, A., Trumbull, R. B., Coira, B., Kay, S. M., & van den Bogaard, P. (2008). 40Ar/39Ar geochronology of mafic volcanism in the back-arc region of the southern Puna plateau, Argentina. *Journal of South American Earth Sciences*, *26*(1), 1–15. https://doi.org/10.1016/j.jsames.2008.03.002

Roberts, G. G., White, N. J., Martin-Brandis, G. L., & Crosby, A. G. (2012). An uplift history of the Colorado Plateau and its surroundings from inverse modeling of longitudinal river profiles. *Tectonics*, *31*(4), 1–25. https://doi.org/10.1029/2012TC003107

Roman, C. (1970). Seismicity in Romania - Evidence for the sinking lithosphere. *Nature*, *228*(5277), 1176–1178. https://doi.org/10.1038/2281176a0

Roth, J. B., Fouch, M. J., James, D. E., & Carlson, R. W. (2008). Three-dimensional seismic velocity structure of the northwestern United States. *Geophysical Research Letters*, *35*(15). https://doi.org/10.1029/2008GL034669

Roy, M., Jordan, T. H., & Pederson, J. (2009). Colorado Plateau magmatism and uplift by warming of heterogeneous lithosphere. *Nature*, *459*(7249), 978–982. https://doi.org/10.1038/nature08052

Royden, L., Horváth, F., & Rumpler, J. (1983). Evolution of the Pannonian Basin System: 1. Tectonics. *Tectonics*, *2*(1), 63–90. https://doi.org/10.1029/TC002i001p00063

Ryan, J., Beck, S. L., Zandt, G., Wagner, L., Minaya, E., & Tavera, H. (2016). Central Andean crustal structure from receiver function analysis. *Tectonophysics*, *682*, 120–133. https://doi.org/10.1016/j.tecto.2016.04.048

Saleeby, J. B., & Foster, Z. (2004). Topographic response to mantle lithosphere removal in the southern Sierra Nevada region, California. *Geology*, *32*(3), 245–248. https://doi.org/10.1130/G19958.1

Saleeby, J. B., Le Pourhiet, L., Saleeby, Z., & Gurnis, M. (2012). Epeirogenic transients related to mantle lithosphere removal in the southern Sierra Nevada region, California, part I: Implications of thermomechanical modeling. *Geosphere*, *8*(6), 1286–1309. https://doi.org/10.1130/GES00746.1

Schildgen, T. F., Cosentino, D., Bookhagen, B., Niedermann, S., Yildirim, C., Echtler, H., Wittmann, H., & Strecker, M. R. (2012). Multi-phased uplift of the southern margin of the Central Anatolian plateau, Turkey: A record of tectonic and upper mantle processes. *Earth and Planetary Science Letters*, *317-318*, 85–95. https://doi.org/10.1016/j.epsl.2011.12.003

Schmandt, B., & Humphreys, E. D. (2010). Complex subduction and small-scale convection revealed by body-wave tomography of the western United States upper mantle. *Earth and Planetary Science Letters*, *297*(3-4), 435–445. https://doi.org/10.1016/j.epsl.2010.06.047

Schoenbohm, L. M., & Carrapa, B. (2015). Miocene-Pliocene shortening, extension, and mafic magmatism support small-scale lithospheric foundering in the central Andes, NW Argentina. *Geological Society of America Memoirs*, *212*(09), 167–180. https://doi.org/10.1130/2015.1212(09)

Schurr, B., Rietbrock, A., Asch, G., Kind, R., & Oncken, O. (2006). Evidence for lithospheric detachment in the central Andes from local earthquake tomography. *Tectonophysics*, *415*(1-4), 203–223. https://doi.org/10.1016/j.tecto.2005.12.007

Schwartz, J. J., Snoke, A. W., Frost, C. D., Barnes, C. G., Gromet, L. P., & Johnson, K. (2010). Analysis of the Wallowa-Baker terrane boundary: Implications for tectonic accretion in the Blue Mountains province, northeastern Oregon. *Bulletin of the Geological Society of America*, *122*(3-4), 517–536. https://doi.org/10.1130/B26493.1

Scire, A., Biryol, C. B., Zandt, G., & Beck, S. L. (2015). Imaging the Nazca slab and surrounding mantle to 700 km depth beneath the central Andes (18°S to 28°S). *Memoir of the Geological Society of America*, *212*(02), 23–41. https://doi.org/10.1130/2015.1212(02)

Seggiaro, R., Becchio, R., Pereyra, F., & Martínez, L. (2007). *Hoja Geológica 2569-IV, Antofalla*. Servicio Geológico Minero Argentino.

Şengör, A. M., & Dewey, J. F. (2020). A discussion of "hidden subduction" in orogenic belts. *Canadian Journal of Earth Sciences*, *57*(3), 418–425. https://doi.org/10.1139/cjes-2019-0199

Şengül-Uluocak, E., Pysklywec, R. N., Göğüş, O. H., & Ulugergerli, E. U. (2019). Multidimensional Geodynamic Modeling in the Southeast Carpathians: Upper Mantle Flow-Induced Surface Topography Anomalies. *Geochemistry, Geophysics, Geosystems*, *20*(7), 3134–3149. https://doi.org/10.1029/2019GC008277

Shaffer, M., Hacker, B. R., Ratschbacher, L., & Kylander-Clark, A. R. (2017). Foundering triggered by the collision of India and Asia captured in xenoliths. *Tectonics*, *36*(10), 1913–1933. https://doi.org/10.1002/2017TC004704

Sharp, D. H. (1984). An overview of Rayleigh-Taylor instability. *Physica D: Nonlinear Phenomena*, *12*(1-3), 3–18. https://doi.org/10.1016/0167-2789(84)90510-4

Sippl, C., Schurr, B., Yuan, X., Mechie, J., Schneider, F. M., Gadoev, M., Orunbaev, S., Oimahmadov, I., Haberland, C., Abdybachaev, U., Minaev, V., Negmatullaev, S., & Radjabov, N. (2013). Geometry of the Pamir-Hindu Kush intermediate-depth earthquake zone from local seismic data. *Journal of Geophysical Research: Solid Earth*, *118*(4), 1438–1457. https://doi.org/10.1002/jgrb.50128

Smith, M. E., Cassel, E. J., Jicha, B. R., Singer, B. S., & Canada, A. S. (2017). Hinterland drainage closure and lake formation in response to middle Eocene Farallon slab removal, Nevada, U.S.A. *Earth and Planetary Science Letters*, *479*, 156–169. https://doi.org/10.1016/j.epsl.2017.09.023

Song, T. R. A., & Helmberger, D. V. (2007). A depleted, destabilized continental lithosphere near the Rio Grande rift. *Earth and Planetary Science Letters*, *262*(1-2), 175–184. https://doi.org/10.1016/j.epsl.2007.07.052

Spiegelman, M., May, D. A., & Wilson, C. R. (2016). On the solvability of incompressible Stokes with viscoplastic rheologies in geodynamics. *Geochemistry, Geophysics, Geosystems*, *17*(6), 2213–2238. https://doi.org/10.1002/2015GC006228

Stanciu, A. C., & Humphreys, E. D. (2020). Upper mantle tomography beneath the Pacific Northwest interior. *Earth and Planetary Science Letters*, *539*, 116214. https://doi.org/10.1016/j.epsl.2020.116214

Stern, T., Stratford, W., Seward, A., Henderson, M., Savage, M., Smith, E., Benson, A., Greve, S., & Salmon, M. (2010). Crust-mantle structure of the central North Island, New Zealand, based on seismological observations. *Journal of Volcanology and Geothermal Research*, *190*(1-2), 58–74. https://doi.org/10.1016/j.jvolgeores.2009.11.017

Stern, T., Houseman, G. A., Salmon, M., & Evans, L. (2013). Instability of a lithospheric step beneath western North Island, New Zealand. *Geology*, *41*(4), 423–426. https://doi.org/10.1130/G34028.1

Su, T., Farnsworth, A., Spicer, R. A., Huang, J., Wu, F. X., Liu, J., Li, S. F., Xing, Y. W., Huang, Y. J., Deng, W. Y., Tang, H., Xu, C. L., Zhao, F., Srivastava, G., Valdes, P. J., Deng, T., & Zhou, Z. K. (2019). No high Tibetan Plateau until the Neogene. *Science Advances*, *5*(3), 1–9. https://doi.org/10.1126/sciadv.aav2189

Sun, J., Liu, Z., Zhang, S., Li, X., & Qi, J. (2017). Large-scale removal of lithosphere underneath the North China Craton in the Early Cretaceous: Geochemical constraints from volcanic lavas in the Bohai Bay Basin. *Lithos*, *292-293*(September), 69–80. https://doi.org/10.1016/j.lithos.2017.09.004

Sundell, K. E., Saylor, J. E., Lapen, T. J., & Horton, B. K. (2019). Implications of variable late Cenozoic surface uplift across the Peruvian central Andes. *Scientific Reports*, *9*(1), 1–12. https://doi.org/10.1038/s41598-019-41257-3

Tackley, P. J., Xie, S., Nakagawa, T., & Hernlund, J. W. (2005). Numerical and laboratory studies of mantle convection: Philosophy, accomplishments, and thermochemical structure and evolution. In *Earth's deep mantle: Structure, composition, and evolution* (pp. 83–99). https://doi.org/https://doi.org/10.1029/160GM07

Tapponnier, P., Mattauer, M., Proust, F., & Cassaigneau, C. (1981). Mesozoic ophiolites, sutures, and arge-scale tectonic movements in Afghanistan. *Earth and Planetary Science Letters*, *52*(2), 355–371. https://doi.org/10.1016/0012-821X(81)90189-8

Tărăpoancă, M., Bertotti, G., Matenco, L., Dinu, C., & Cloetingh, S. A. P. L. (2003). Architecture of the focşani depression: A 13 km deep basin in the carpathians bend zone (romania). *Tectonics*, *22*(6), 1–7. https://doi.org/10.1029/2002TC001486

Tassara, A., & Echaurren, A. (2012). Anatomy of the Andean subduction zone: Three-dimensional density model upgraded and compared against global-scale models. *Geophysical Journal International*, *189*(1), 161–168. https://doi.org/10.1111/j.1365-246X.2012.05397.x

Tassara, A., Swain, C., Hackney, R., & Kirby, J. (2007). Elastic thickness structure of South America estimated using wavelets and satellite-derived gravity data. *Earth and Planetary Science Letters*, *253*(1-2), 17–36. https://doi.org/10.1016/j.epsl.2006.10.008

Trumbull, R. B., Riller, U., Oncken, O., Scheuber, E., Munier, K., & Hongn, F. D. (2006). The time-space distribution of Cenozoic volcanism in the South-Central Andes: A new data compi-

lation and some tectonic implications. In *The andes* (pp. 29–43). https://doi.org/10.1023/A:1020794814975

Tunini, L., Jiménez-Munt, I., Fernandez, M., Vergés, J., Villaseñor, A., Melchiorre, M., & Afonso, J. C. (2016). Geophysical-petrological model of the crust and upper mantle in the India-Eurasia collision zone. *Tectonics*, *35*(7), 1642–1669. https://doi.org/10.1002/2016TC004161

Turcotte, D. L., & Schubert, G. (2002). Geodynamics, 472 pp. https://doi.org/10.1017/CBO9780511807442

Turner, S., Arnaud, N., Liu, J., Rogers, N., Hawkesworth, C., Harris, N., Kelley, S., Van Calsteren, P., & Deng, W. (1996). Post-collision, shoshonitic volcanism on the Tibetan plateau: Implications for convective thinning of the lithosphere and the source of ocean island basalts. *Journal of Petrology*, *37*(1), 45–71. https://doi.org/10.1093/petrology/37.1.45

Tye, A. R., McMillan, M., Schoenbohm, L. M., & Zhou, R. (2022). Late Cenozoic extensional formation of the Antofalla depression, southern Puna plateau, Argentina: An effect of lithospheric foundering? *Tectonics*.

Unruh, J. R. (1991). The uplift of the Sierra Nevada and implications for late Cenozoic epeirogeny in the western Cordillera. *Geological Society of America Bulletin*, *103*(11), 1395–1404. https://doi.org/10.1130/0016-7606(1991)103<1395

Urrutia-Fucugauchi, J., & Flores-Ruiz, J. H. (1996). Bouguer gravity anomalies and regional crustal structure in central mexico. *International Geology Review*, *38*(2), 176–194. https://doi.org/10.1080/00206819709465330

Valera, J., Negredo, A., Billen, M., & Jiménez-Munt, I. (2014). Lateral migration of a foundering high-density root: Insights from numerical modeling applied to the southern Sierra Nevada. *Lithos*, *189*, 77–88. https://doi.org/10.1016/j.lithos.2013.08.021

Van der Wal, D., Chopra, P., Drury, M., & Gerald, J. F. (1993). Relationships between dynamically recrystallized grain size and deformation conditions in experimentally deformed olivine rocks. *Geophysical Research Letters*, *20*(14), 1479–1482. https://doi.org/10.1029/93GL01382

van der Meer, D. G., van Hinsbergen, D. J., & Spakman, W. (2018). Atlas of the underworld: Slab remnants in the mantle, their sinking history, and a new outlook on lower mantle viscosity. *Tectonophysics*, *723*(June 2017), 309–448. https://doi.org/10.1016/j.tecto.2017.10.004

van Wijk, J. W., Baldridge, W. S., van Hunen, J., Goes, S., Aster, R., Coblentz, D. D., Grand, S. P., & Ni, J. (2010). Small-scale convection at the edge of the Colorado Plateau: Implications for topography, magmatism, and evolution of Proterozoic lithosphere. *Geology*, *38*(7), 611–614. https://doi.org/10.1130/G31031.1

van Wijk, J., van Hunen, J., & Goes, S. (2008). Small-scale convection during continental rifting: Evidence from the Rio Grande rift. *Geology*, *36*(7), 575–578. https://doi.org/10.1130/G24691A.1

van Zelst, I., Crameri, F., Pusok, A. E., Glerum, A., Dannberg, J., & Thieulot, C. (2021). 101 geodynamic modelling: How to design, carry out, and interpret numerical studies. *Solid Earth Discussions*, 1–80. https://doi.org/10.5194/se-2021-14

Wang, H., & Currie, C. A. (2015). Magmatic expressions of continental lithosphere removal. *Journal of Geophysical Research B: Solid Earth*, *120*(10), 7239–7260. https://doi.org/10.1002/2015JB012112

Wang, H., & Currie, C. A. (2017). Crustal deformation induced by mantle dynamics: Insights from models of gravitational lithosphere removal. *Geophysical Journal International*, *210*(2), 1070–1091. https://doi.org/10.1093/gji/ggx209

Wang, H., Currie, C. A., & DeCelles, P. G. (2015). Hinterland basin formation and gravitational instabilities in the central Andes: Constraints from gravity data and geodynamic models. In *Geological Society of America Memoirs* (pp. 387–406). https://doi.org/10.1130/2015.1212(19)

Wang, H., Currie, C. A., & DeCelles, P. G. (2021). Coupling between lithosphere removal and mantle flow in the central Andes. *Geophysical Research Letters*, (Figure 1), 1–11. https://doi.org/10.1029/2021gl095075

Wang, Y., Forsyth, D. W., Rau, C. J., Carriero, N., Schmandt, B., Gaherty, J. B., & Savage, B. (2013). Fossil slabs attached to unsubducted fragments of the Farallon plate. *Proceedings of the National Academy of Sciences*, *110*(14), 5342–5346. https://doi.org/10.1073/pnas.1214880110

Ward, K. M., Delph, J. R., Zandt, G., Beck, S. L., & Ducea, M. N. (2017). Magmatic evolution of a Cordilleran flare-up and its role in the creation of silicic crust. *Scientific Reports*, *7*(1), 1–8. https://doi.org/10.1038/s41598-017-09015-5

Ward, K. M., Porter, R. C., Zandt, G., Beck, S. L., Wagner, L. S., Minaya, E., & Tavera, H. (2013). Ambient noise tomography across the Central Andes. *Geophysical Journal International*, *194*(3), 1559–1573. https://doi.org/10.1093/gji/ggt166

Watts, A. B., Zhong, S. J., & Hunter, J. (2013). The behavior of the lithosphere on seismic to geologic timescales. *Annual Review of Earth and Planetary Sciences*, *41*, 443–468. https://doi.org/10.1146/annurev-earth-042711-105457

Wernicke, B., Clayton, R., Ducea, M. N., Jones, C. H., Park, S., Ruppert, S., Saleeby, J. B., Snow, J. K., Squires, L., Fliedner, M., Jiracek, G., Keller, R., Klemperer, S., Luetgert, J., Malin, P., Miller, K., Mooney, W., Oliver, H., & Phinney, R. (1996). Origin of high mountains in the continents: The southern Sierra Nevada. *Science*, *271*(5246), 190–193. https://doi.org/10.2307/2889536

West, J. D., Fouch, M. J., Roth, J. B., & Elkins-Tanton, L. T. (2009). Vertical mantle flow associated with a lithospheric drip beneath the Great Basin. *Nature Geoscience*, *2*(6), 439–444. https://doi.org/10.1038/ngeo526

Whitehead Jr, J. A., & Luther, D. S. (1975). Dynamics of laboratory diapir and plume models. *Journal of Geophysical Research*, *80*(5), 705–717. https://doi.org/10.1029/JB080i005p00705

Wiemer, D., Schrank, C. E., Murphy, D. T., Wenham, L., & Allen, C. M. (2018). Earth's oldest stable crust in the Pilbara Craton formed by cyclic gravitational overturns. *Nature Geoscience*, *11*, 357–361. https://doi.org/10.1038/s41561-018-0105-9

Wisian, K. W., Blackwell, D. D., & Richards, M. (1999). Heat flow in the Western United States and extensional geothermal systems. *Twenty-Fourth Workshop on Geothermal Reservoir Engineering*, 8.

Wortel, M. J., & Spakman, W. (2000). Subduction and slab detachment in the Mediterranean-Carpathian region. *Science*, *290*(5498), 1910–1917. https://doi.org/10.1126/science.290.5498.1910

Xu, P., & Zhao, D. (2009). Upper-mantle velocity structure beneath the North China Craton: Implications for lithospheric thinning. *Geophysical Journal International*, *177*(3), 1279–1283. https://doi.org/10.1111/j.1365-246X.2009.04120.x

Yáñez, G. A., Rasoazanamparany, C., Von Huene, R., & Díaz, J. (2001). Magnetic anomaly interpretation across the southern central Andes (32°-34°S): The role of the Juan Fernández Ridge in the late Tertiary evolution of the margin. *Journal of Geophysical Research: Solid Earth*, *106*(B4), 6325–6345. https://doi.org/10.1029/2000jb900337

Yin, A., & Harrison, T. M. (2000). Geologic evolution of the Himalayan-Tibetan orogen. *Annual Reviews of Earth and Planetary Sciences*, *28*, 211–280. https://doi.org/10.1080/01947641003598252

Yogodzinski, G. M., Naumann, T. R., Smith, E. I., Bradshaw, T. K., & Walker, J. D. (1996). Evolution of a mafic volcanic field in the central Great Basin, south central Nevada. *Journal of Geophysical Research: Solid Earth*, *101*(B8), 17425–17445. https://doi.org/10.1029/96jb00816

Yu, Y., Gao, S. S., Liu, K. H., & Zhao, D. (2020). Foundered lithospheric segments dropped into the mantle transition zone beneath southern California, USA. *Geology*, *48*(2), 200–204. https://doi.org/10.1130/G46889.1

Zandt, G. (2003). The southern Sierra Nevada drip and the mantle wind direction beneath the southwestern United States. *International Geology Review*, *45*(3), 213–224. https://doi.org/10.2747/0020-6814.45.3.213

Zandt, G., & Carrigan, C. R. (1993). Small-scale convective instability and upper mantle viscosity under California. *Science*, *261*(5120), 460–463.

Zandt, G., Gilbert, H., Owens, T. J., Ducea, M. N., Saleeby, J. B., & Jones, C. H. (2004). Supporting information for: Active foundering of a continental arc root beneath the southern Sierra Nevada in California. *Nature*, *431*(7004), 41–46. https://doi.org/10.1038/nature02847

Zandt, G., & Humphreys, E. D. (2008). Toroidal mantle flow through the western U.S. slab window. *Geology*, *36*(4), 295–298. https://doi.org/10.1130/G24611A.1

Zeng, Y., Ducea, M. N., Xu, J., Chen, J., & Dong, Y.-H. (2020). Negligible surface uplift following foundering of thickened central Tibetan lower crust. *Geology*, *48*. https://doi.org/10.1130/g48142.1

Zhang, J. B., Ling, W. L., Liu, Y. S., Duan, R. C., Gao, S., Wu, Y. B., Yang, H. M., Qiu, X. F., & Zhang, Y. Q. (2014). Episodic Mesozoic thickening and reworking of the North China Archean lower crust correlated to the fast-spreading Pacific plate. *Journal of Asian Earth Sciences*, *80*, 63–74. https://doi.org/10.1016/j.jseaes.2013.10.031

Zhang, K. J. (2012). Destruction of the North China Craton: Lithosphere folding-induced removal of lithospheric mantle? *Journal of Geodynamics*, *53*(1), 8–17. https://doi.org/10.1016/j.jog.2011.07.005

Zhou, R., & Schoenbohm, L. M. (2015). Late Miocene upper-crustal deformation within the interior of the southern Puna Plateau, central Andes. *Lithosphere*, *7*(3), 336–352. https://doi.org/10.1130/L396.1

Zhu, R. X., Xu, Y. G., Zhu, G., Zhang, H. F., Xia, Q. K., & Zheng, T. Y. (2012). Destruction of the North China Craton. *Science China Earth Sciences*, *55*(10), 1565–1587. https://doi.org/10.1007/s11430-012-4516-y

5 Geodynamics of continental back-arcs

Lithospheric foundering under a weak crust in the Central Andes*

Abstract

Lithospheric foundering has been hypothesized to affect many of Earth's orogenic regions, including the Puna Plateau in the Central Andes. In the Southern Puna Plateau, crustal thickening, mantle-lithospheric thinning, back-arc volcanism, upper-crustal strain, and Late Cenozoic syn-tectonic sedimentation have all been ascribed to deep-seated geodynamic processes. Here, we develop the hypothesis that lithospheric foundering occurred in this region during the Late Miocene to Early Pliocene in the form of a Rayleigh–Taylor drip involving a relatively weak granitic crust. We explore this hypothesis using 2-dimensional numerical models of a pre-strained lithosphere undergoing tectonic shortening. In the models, foundering occurs due to a phase transition from granulite to high-density eclogite in the lower crust. Drip growth drives upper-crustal horizontal extension and above the center of the drip, which is accommodated by horizontal compression in the peripheral regions. Instead of flexural subsidence and the formation of a long-wavelength basin, the models predict long-wavelength surface uplift, with local subsidence due to the formation extensional structures such as normal faults. Existing geologic data, such as the ages of range exhumation and syntectonic sedimentation, can be explained by this model of lithospheric dripping. We identify the Late Miocene to present Antofalla depression as an epi-drip extensional basin, and the Late Miocene Pasto Ventura basin as a peri-drip compressional basin. The hypothesis of a weak-crust drip for the Southern Puna solves many geological complexities and problems encountered when trying to explain the tectonics of the Central Andean Plateau. This interpretation does not necessarily conflict with the strong-crust drip previously inferred for the Arizaro basin ~150 km to the north, but it implies that lithosphere rheology differs between the two regions. This work highlights the diverse nature of lithospheric foundering and its varying effects on upper crustal strain and surface topography.

*This chapter has been prepared for submission to *Geosphere*.
Citation: McMillan, M., Tye, A. R., & Schoenbohm, L. M. (in prep.). Geodynamics of continental back-arcs: Lithospheric foundering under a weak crust in the Central Andes. *Geosphere*.

5.1 Introduction

Gravitational instabilities of the lithosphere, including Rayleigh–Taylor drips (e.g., Conrad & Molnar, 1997), have been invoked as explanations for a wide range of geological phenomena such as upper-crustal deformation and sedimentation (e.g., DeCelles et al., 2015a; Schoenbohm & Carrapa, 2015; Smith et al., 2017), lithospheric magmatic signatures (e.g., Chapman et al., 2018; Ducea et al., 2013; Furman et al., 2016), topographic and gravity anomalies (e.g., Göğüş et al., 2017; Lorinczi & Houseman, 2009; Molnar & Houseman, 2013; Saleeby & Foster, 2004; Wang et al., 2015), and geophysical observations such as tomographic anomalies (e.g., Beck & Zandt, 2002; Bianchi et al., 2013; Levander et al., 2011; West et al., 2009; Zandt et al., 2004) and mantle seismicity (Lorinczi & Houseman, 2009; Molnar & Bendick, 2019). The gravitational instability that gives rise to lithospheric dripping may be generated by prograde metamorphism of the lower crust (e.g., Jull & Kelemen, 2001; Krystopowicz & Currie, 2013) or the accumulation of ultramafic magmatic residues in the crust or mantle lithosphere (e.g., Ducea, 2001; Paterson & Ducea, 2015; Zandt et al., 2004). Gravitational foundering removes the density anomaly, along with underlying lithosphere, and induces a wide range of effects on crustal structure, temperature, and the topographic surface as the remaining lithosphere deforms in response to this removal (e.g., Göğüş & Pysklywec, 2008; Krystopowicz & Currie, 2013; Molnar, 2015; Wang & Currie, 2017). Although the concept is applicable to many tectonic settings (e.g., Furman et al., 2016; West et al., 2009), lithospheric dripping may play a major role in the deformation and uplift of orogenic plateaus such as the Anatolian Plateau (Göğüş et al., 2017), the Hindu Kush (Molnar & Bendick, 2019), the Tibetan Plateau prior to India-Asia collision (Kapp & DeCelles, 2019), the Western U.S. prior to extensional collapse (Smith et al., 2017), and the Central Andean Plateau (DeCelles et al., 2009; DeCelles et al., 2015b). Lithospheric dripping is therefore a powerful explanation capable of informing our understanding of how continental lithosphere deforms and evolves through geologic time.

In the Puna Plateau of the Central Andes, lithospheric drips are associated with the development of hinterland basins and silicic volcanism (DeCelles et al., 2015a; Schoenbohm & Carrapa, 2015; Wang et al., 2021). Two inferred dripping centers are located in the Arizaro region and in the Southern Puna Plateau, respectively (Figure 5.1). In the Arizaro region, subsidence is attributed crustal flexure in response to the growth of the drip (Wang et al., 2015), creating accommodation space that was filled by fluvio-lacustrine strata deposited syntectonically during the Miocene (DeCelles et al., 2015a). Deposition was accompanied by horizontal contraction due to inner-arc bending stresses in the downward-flexed panel of upper crust (DeCelles et al., 2015a). After the drip detached, the basin was structurally and topographically inverted, and the upper crust underwent horizontal extension (Schoenbohm & Carrapa, 2015). Because of this vertical oscillation in surface topography driven by dynamic stresses, the term “bobber basin” has been used to summarize this upper-crustal response to lithospheric dripping (DeCelles et al., 2009). This response is expected if the effective strength of the crust is greater than that of

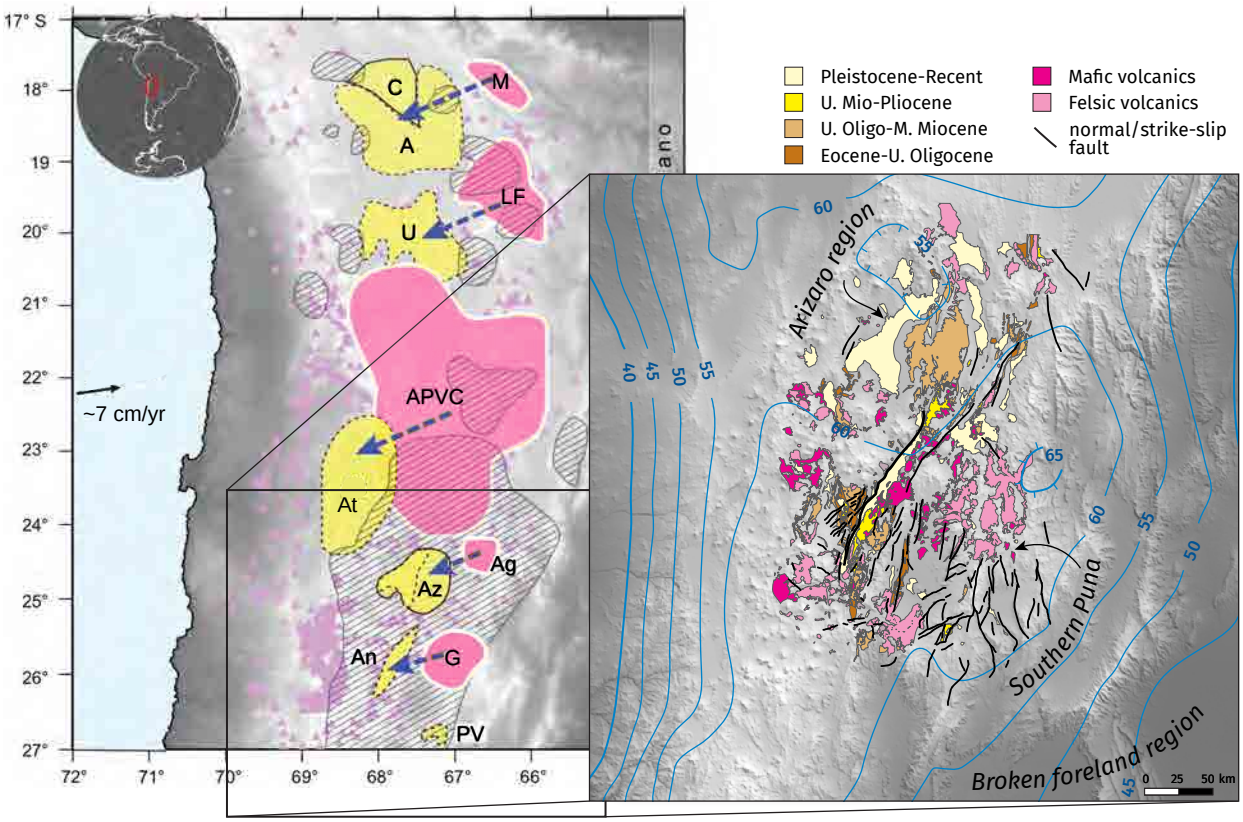

Figure 5.1: Left: Map of the Central Andes showing silicic volcanic centers (pink) and hinterland basins (yellow) associated with potential lithospheric foundering events, after Wang et al. (2021). (M: Morococala, C: Corque, A: Altiplano, LF: Los Frailes, U: Uyuni, APVC: Altiplano-Puna Volcanic Complex, At: Atacama, Ag: Aguas Calientes, Az: Arizaro, G: Galán, An: Antofalla, PV: Pasto Ventura). Right: Map of Southern Puna Cenozoic geology and extensional faults, after Schoenbohm and Carrapa (2015). Geologic data from Schnurr et al. (2006) supplemented with faults from Schoenbohm and Carrapa (2015). Moho contours from Schoenbohm and Carrapa (2015) (Tassara et al., 2006).

the mantle lithosphere during dripping, with a necessary strength factor of > 10 suggested by most modelling studies (Conrad & Molnar, 1997; Elkins-Tanton, 2007; Göğüş & Pysklywec, 2008; Houseman & Molnar, 1997). We therefore designate the hypothesized lithospheric drip associated with the Arizaro Basin as a “strong-crust” drip. Drips displaying this type of upper-crustal response have been identified around the world, e.g., in the Oligocene Tibetan Plateau (Kapp & DeCelles, 2019), the Oligocene Nevadaplano hinterland plateau in Western North America (Smith et al., 2017).

Lithospheric foundering was originally proposed for this region based on the geochemistry of back-arc magmatism in the Southern Puna Plateau (Kay & Kay, 1993; Kay et al., 1994). However, the spatiotemporal pattern of sedimentation, upper-crustal strain, and volcanism in the Southern Puna differ markedly from that in the Arizaro region (Figure 5.1). Instead of a broad, roughly circular hinterland depocenter, Miocene to Pliocene sedimentation in the Southern Puna is closely associated with proximal structures (Kraemer et al., 1999; Zhou & Schoenbohm,

2015; Zhou et al., 2016), especially extensional faults (Schoenbohm & Carrapa, 2015). Upper-crustal extension and associated structures are much more significant in the Southern Puna than in the Arizaro Region (Figure 5.1). The Southern Puna region is more strongly affected by silicic volcanism (Figure 5.1) and crustal melting (the Southern Puna Magmatic Body, Bianchi et al., 2013) and also hosts a prominent zone of Pliocene-Quaternary mafic volcanic fields (e.g., Haag et al., 2019; Kay et al., 1994; Risse et al., 2008). Finally, the crust beneath the southern Puna is ~10 km thicker than beneath the Arizaro region (Figure 5.1).

Numerical models of the Rayleigh–Taylor instability suggest that if the crust is similar in strength to or weaker than the dripping lithosphere, the growing drip is capable of entraining mid- to lower-crustal material, leading to significant syn-drip crustal thickening (Conrad & Molnar, 1997; Molnar, 2015; Molnar & Houseman, 2004; Wang & Currie, 2017). This thickening produces syn-drip surface uplift and upper-crustal extension (Molnar, 2015; Molnar & Houseman, 2013). The response of a weak crust during lithospheric dripping is therefore distinct from that of a strong crust described above. We denote this as "weak-crust" dripping and hypothesize that such a lithospheric drip can explain many of the geologic observations in the Southern Puna.

While the weak-crust dripping concept predicts different upper-crustal strain kinematics and sedimentation from the traditional strong-crust hypothesis, such behavior has largely been inferred from analyses of the Rayleigh–Taylor instability (Conrad & Molnar, 1997; Houseman & Molnar, 1997; Molnar & Houseman, 2004, 2013), relatively simple mathematical models without the complexities inherent to natural tectonic settings. Only a few studies have applied the concept to geologic scenarios (e.g., core complexes, Molnar, 2015) or regions (e.g., Wallowa Mountains, Wang & Currie, 2017). Such studies point toward the importance of crustal thickness, overall crustal strength, and of viscosity decay within the crust due to temperature-dependent rheology, in determining the outcome of weak-crust dripping. However, models that incorporate frictional-plastic yielding, tectonic convergence, and laboratory-derived rheologies have not yet explored the consequences of weak-crust dripping (e.g., Wang et al., 2015). The possibility of two distinct crustal responses to lithospheric dripping leads to the following related questions. What are the tectonic conditions in which the weak-crust response may prevail? More specifically, what is the evidence, if any, for the weak-crust response in the geologic record?

In this paper, we address this gap in our understanding of the realistic range of effects of lithospheric dripping using numerical modelling experiments. Because we are interested in modelling scenarios that can be applied to Earth, we base our models on the current understanding of the lithospheric structure of the Puna Plateau. To do this, we first discuss how the tectonic history of the Southern Puna Plateau, as currently understood, leaves open the possibility of weak-crust dripping. We then describe the first-order features of the Southern Puna, including lithospheric composition, density, layer thicknesses, temperature, and tectonic history, which we incorporate into our geodynamic models. After describing our modelling ap-

proach, initial conditions, and boundary conditions, we present a suite of lithospheric dripping models. Because we are interested in simulating topographic uplift during the growth of a drip, we present a relatively new type of dripping model, one that involves the gradual formation of dense eclogite within a portion of the lower crust as a response to crustal shortening and thickening according to a Clapeyron slope relationship. Our models suggest that weak-crust dripping is indeed applicable to the Southern Puna and is the expected outcome of tectonic shortening if our parameterizations describing lithospheric composition, structure, and eclogitization are appropriate. Finally, we discuss how variations in initial conditions, boundary conditions, and model parameters influence the outcomes of these models, and make specific predictions for the history of the Puna Plateau based on the weak-crust dripping hypothesis.

5.2 The Southern Puna Plateau: Geologic background and significance

The Central Andes is the type of example of an orogen generated by crustal shortening, thickening, and magmatism due to oceanic plate subduction (e.g., Allmendinger et al., 1997; Isacks, 1988). Orogenic thickening of the crust reaches a maximum in the Central Andean Plateau, which includes the Altiplano Plateau in Bolivia and the Puna Plateau in NW Argentina. Multiple lithospheric drips beneath the Central Andes have been inferred based on geological and geophysical data (Bloch et al., 2017; DeCelles et al., 2015b; Kay & Kay, 1993; Sundell et al., 2019). Here we describe the geologic background and tectonic setting of the Puna Plateau as they relate to our geodynamic models and the lithospheric dripping hypothesis.

The Puna has been located in a continental arc to back-arc setting since the Early Paleozoic (Niemeyer et al., 2018), and the crust has been deformed by multiple Phanerozoic tectonic events (e.g., Lucassen et al., 2000). Ordovician metasedimentary rocks were shortened by a much greater magnitude than overlying Paleozoic to Cenozoic strata, indicating a episode of Early Paleozoic shortening (Henriquez et al., 2020). These metasedimentary rocks are overlain by 1 to 3 km of sedimentary strata, mainly Cenozoic continental sandstones and conglomerates (Kraemer et al., 1999; Schnurr et al., 2006; Seggiaro et al., 2007; Zhou et al., 2017).

The upper crust was shortened by high-angle reverse faults (Allmendinger & Gubbels, 1996) resulting in the uplift of basement-cored mountain ranges that trend roughly N-S throughout the plateau (Schnurr et al., 2006; Seggiaro et al., 2007). Low-temperature thermochronology studies indicate that major shortening on these structures took place ~80 to 20 Ma (Carrapa & DeCelles, 2015). The Puna Plateau hosts a 55 to 65 km-thick crust, but seismic and gravimetric evidence suggests that the mantle lithosphere is only 5 to 10 km thick (Beck & Zandt, 2002; Tassara et al., 2006). The composition of the crust is relatively uniform and dominantly andesitic to dacitic, based on the composition of lower crustal xenoliths, exposures of lower crust, and the composition of Paleozoic sediments (Babeyko et al., 2002; Lucassen et al., 2001; Lucassen et al., 1999). High crustal temperatures are indicated by the prevalence of back-arc volcanism and by low crustal shear-wave velocities (Ward et al., 2013). All of these factors (felsic crustal

composition, tectonic strain, crustal heating, and major pre-existing structures) may have contributed to a crust that was rheologically weak compared to the underlying lithosphere by Miocene time.

The Southern Puna Plateau is broadly deformed by strike-slip, oblique, and extensional faults that accommodate roughly N-S horizontal extension and vertical shortening (Allmendinger et al., 1989; Daxberger & Riller, 2015; Marrett et al., 1994). Most studies indicate that the Southern Puna underwent a transition from thrust kinematics to extension and strike-slip during the Pliocene to Quaternary (Allmendinger et al., 1989; Marrett et al., 1994). The onset of mafic volcanism seems to coincide with a non-thrust kinematic regime in the Southern Puna (Marrett & Emerman, 1992; Schoenbohm & Carrapa, 2015), and both volcanism and extensional kinematics appear to have initiated in the Sierra de Calalaste and Antofalla region (the central sector of the Southern Puna) and migrated outward toward the edges during the Pliocene (Schoenbohm & Carrapa, 2015). Extension may have affected the edges of the plateau as early as 6 Ma (Schoenbohm & Strecker, 2009).

5.3 Need for geodynamic models of the Southern Puna Plateau

Several recent studies have focused on modelling the consequences of lithospheric foundering beneath the Puna Plateau, especially in the Arizaro region (Currie et al., 2015; Wang et al., 2015, 2021). However, explaining the geologic observations in the Southern Puna Plateau requires a different approach from existing models for two key reasons. First, existing models incorporate rheologies that assume that the crust was significantly stronger than the mantle lithosphere during foundering. As a result of this assumption, drips occur as the strong-crust type, which results in syn-drip surface subsidence, contraction, and the development of a ~100 km-wide hinterland basin, in contrast to the sedimentation in the Southern Puna described above. Existing models ensure a strong crust by incorporating a strong mafic rheology such as dry Maryland diabase into the lower crust (e.g., Wang et al., 2015). But seismic wavespeeds in many regions, including the Central Andes, are consistent with a lower crust that is andesitic to dacitic, not mafic, in composition (Hacker et al., 2015).

Second, modelling of weak crust drips requires a new approach for how dripping is triggered in geodynamic models. Models commonly assume that lithospheric foundering occurs as a result of the production of negatively buoyant eclogite, either as a magmatic cumulate or through a high-pressure phase change in the lower crust (e.g., Currie et al., 2015; Krystopowicz & Currie, 2013; Wang et al., 2015, 2021). Increasing the density of a relatively small region of the lower crust or mantle lithosphere is one way to trigger a single lithospheric drip (Currie et al., 2015; Wang et al., 2015, 2021). However, this densification has the side-effect of producing isostatic surface subsidence, which is especially significant in the first ~3 Myr of drip growth (Wang et al., 2015). This subsidence is detrimental to modelling weak-crust dripping, because under this hypothesis, drip growth is accompanied by surface uplift.

To address these issues, we consider that the Puna crust, including the lower crust, is dominantly felsic in composition, and use rheological formulations for felsic lithologies in the crust and mafic lithologies in the mantle. The thermal structure of the model includes significant radiogenic heating in crustal layers, reflecting their felsic compositions. The rheological formulations also incorporate plastic yielding and strain softening, further weakening the crust during tectonic deformation. The model incorporates convergent velocity boundary conditions to allow crustal thickening and the uplift of an orogenic plateau in a pure shear style as inferred for the Southern Puna (Allmendinger & Gubbels, 1996). To facilitate this, we incorporate a broad region of pre-damaged upper crust and high-damage shear zones in the initial condition of the model. We incorporate eclogite production by means of a phase transition in the lower crust. The phase transition incorporates a Clapeyron slope defining a pressure- and temperature-dependent transition from felsic granulite to garnet pyroxenite (Bousquet et al., 1997). Eclogite thus forms dynamically as a result of crustal thickening, allowing the lithosphere to realistically adjust to the isostatic load. The net effect of these choices is that a weak-crust drip is triggered beneath the center of an orogenic plateau. These modelling parameters are described in the following sections.

5.4 Geodynamic modelling methods

5.4.1 Model geometry

We simulate tectonic thickening, eclogitization, and eclogite dripping of continental lithosphere using two-dimensional numerical models. The model consists of a domain that is 800 km wide by 400 km deep, representing a cross-section through an orogenic plateau parallel to convergence direction. The model includes layers representing continental lithosphere and underlying asthenosphere. The lithosphere is initially 100 km thick and composed of four layers representing sedimentary strata (3 km), upper crust (22 km), lower crust (25 km), and mantle lithosphere (50 km). Given that the primary focus of the model is gravitational instability, an initially thick crust of 50 km was chosen to allow eclogitization and dripping within a reasonable computational time. The initial thickness of the crust of the Central Andes at the beginning of Andean orogenesis is a longstanding topic of research (Allmendinger et al., 1997), and volcanic geochemistry indicates that at least part of the Southern Puna Plateau may have been already attained a 50 km thick crust by 25 Ma (Allmendinger et al., 1997; Kay et al., 1994).

A stress-free boundary condition is imposed on the top surface of the model, allowing topographic deformation (Rose et al., 2017). To simulate tectonic shortening, the upper 100 km of the left boundary is prescribed an inflow horizontal velocity (6 mm/yr in the base model), and the upper 100 km of the right boundary is prescribed a fixed boundary condition. The lower 300 km of both side boundaries are prescribed small outflow horizontal velocities to

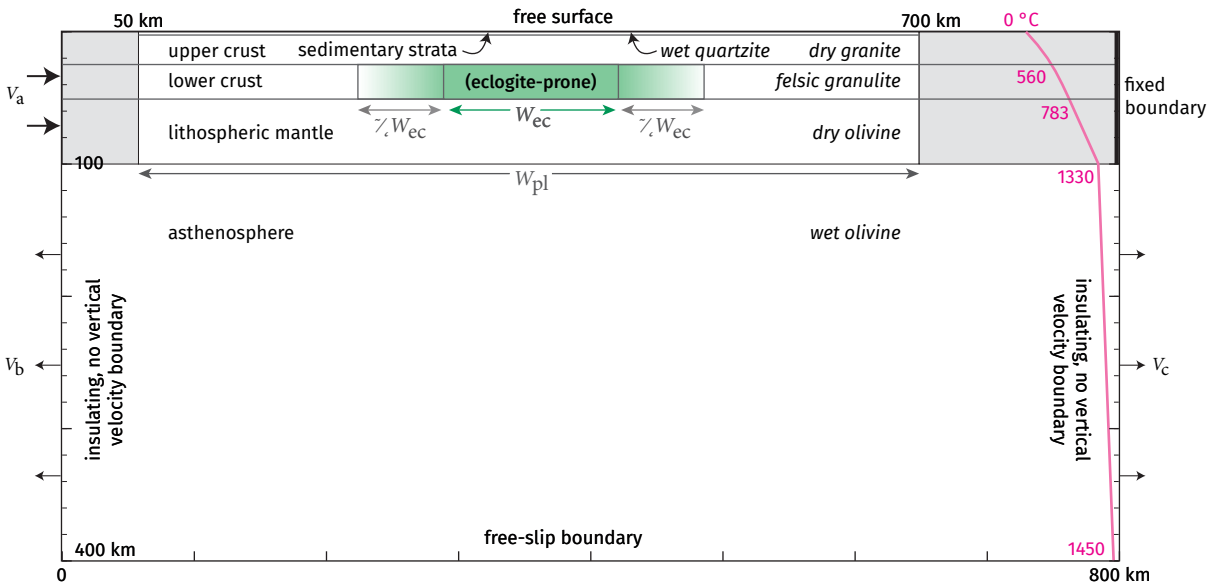

Figure 5.2: Numerical model setup. The shaded regions denote blocks of strong lithosphere that force tectonic convergence between them in a region denoted as the plateau. V_a, V_b, and V_c denote velocities prescribed to the left boundary lithosphere, left boundary asthenosphere, and right boundary asthenosphere, respectively. In the base model, convergence is imposed by setting $V_a = 0.6$ cm/yr and assigning V_b and V_c small outflux velocities to conserve mass. W_{ec} and W_{pl} denote the width of eclogite-prone lower crust and the width of the plateau, respectively. Material properties are given in Table 5.1.

compensate for the inflowing lithosphere. The vertical velocity component on the side surfaces is fixed to zero. The bottom surface is a free-slip boundary.

Computations were done using the ASPECT code version 2.4.0-pre (08b6a15) (Gassmöller et al., 2018; Heister et al., 2017; Kronbichler et al., 2012; Rose et al., 2017). Model simulations are carried out on a nonuniform finite-element mesh with a cell size of 2 km in upper 60 km of the domain, 4 km between 60 and 120 km depth, and 8 km below depths of 120 km. The mesh contains 19,400 cells and approximately 2 million degrees of freedom. To preserve sharper boundaries between materials, we use the discontinuous Galerkin method for discretization implemented by He et al. (2017).

5.4.2 Rheological formulation and material properties

Deformation of all materials is simulated using an incompressible viscoplastic rheology. The rheological formulation for viscous deformation incorporates diffusion and dislocation creep, with each mechanism given a viscosity ν defined as

$$\nu = \frac{1}{2} f A^{\frac{-1}{n}} d^{\frac{m}{n}} \dot{\epsilon}_{ii} \exp\left(\frac{E + PV}{nRT}\right)$$

where f is a strength factor, A is the viscosity prefactor, n is the stress exponent, $\dot{\epsilon}_{ii}$ is the square root of second invariant of the deviatoric strain rate tensor, d is grain diameter, m is the grain

size exponent, E is activation energy, V is activation volume, P is pressure, R is the gas constant, and T is temperature. Diffusion creep corresponds to $n = 1$ and $m \neq 0$ and dislocation creep to $n > 1$ and $m = 0$.

Viscosity is limited by a Drucker-Prager yield stress σ_y given by

$$\sigma_y = c\cos(\phi) + P\sin(\phi)$$

where c is cohesion and ϕ is the angle of internal friction. Crustal materials are assigned cohesions of 2 MPa, while mantle lithosphere, sublithospheric mantle, and eclogite are assigned cohesions of zero. All materials undergo strain softening, whereby ϕ is linearly reduced from 15° to 2° as plastic strain increases from 0.5 to 1.5.

We choose material rheologies based on laboratory studies (Table 5.1), using the material definitions of Gouiza and Naliboff (2021) as a starting point, and modifying these based on studies of the Puna Plateau. For crustal density and composition, we use the values for the Altiplano-Puna from Ibarra et al. (2019), which are based on exposures of basement rocks, gravity data, and P-wave velocity models for the Central Andes. Supracrustal sedimentary strata and metamorphic rocks are composed of wet quartzite (Rutter & Brodie, 2004). The upper crust is composed of dry Westerly granite (Ranalli & Murphy, 1987) and the lower crust of felsic granulite (Wilks & Carter, 1990) or garnet pyroxenite (Jull & Kelemen, 2001). The mantle lithosphere and asthenosphere are composed of dry olivine and wet olivine, respectively (Hirth & Kohlstedt, 2003). This felsic crustal composition is also consistent with comprehensive studies that suggest that a large fraction of Earth's continental crust is predominately felsic (Hacker et al., 2015).

The strength factor f is often used as a scaling parameter explore variation or uncertainty in rock strength, allowing effective viscosity to vary over a few orders of magnitude under the same ambient conditions (e.g., Beaumont et al., 2006; Wang et al., 2015). Here, we generally set $f = 1$ with the exception of the asthenosphere, where we set $f = 0.1$. Combined with the wet olivine rheology for mantle asthenosphere, this choice reflects the observation that, on average, the asthenosphere is around 50 to 500 times less viscous than the lithosphere (Steinberger & Calderwood, 2006). As described below, we also explore models with $f = 1$ and $f = 0.5$ for the asthenosphere.

All materials are assigned a temperature-dependent density, radiogenic heat production values, specific heat capacities, and thermal conductivities (Table 5.1). We follow Ibarra et al. (2019) in assigning radiogenic heat production values that are relatively high, reflecting the granitic composition of the crust. However, we set the heat production of the upper crust to 1.5 $\mu\mathrm{W\,m^{-3}}$ based on the assumption that the modern thermal state of the crust is affected heating due to lithospheric thinning, which would not be present at the beginning of the model run. As described below, we also run variants with crustal heating values of 1.9 and 1.0 $\mu\mathrm{W\,m^{-3}}$.

Table 5.1: Rheology, thickness, and thermal parameters for materials in model.

Layer	Initial thickness	Flow law	Type	c	ϕ_0	f	Q	ρ_0	C
Sedimentary strata	3 km	Wet quartzite[1]	Dislocation	2.0	15	1.0	0.9	2450	750
Upper crust	22 km	Westerly granite[2]	Dislocation	2.0	15	1.0	1.5	2700	750
Lower crust	25 km	Felsic granulite[3]	Dislocation	2.0	15	1.0	0.5	3000	750
Mantle lithosphere	50 km	Dry olivine[5]	Dislocation/ Diffusion	0.0	15	1.0	0.02	3300	1250
Asthenosphere	300 km	Wet olivine[5]	Dislocation/ Diffusion	0.0	15	0.5	0.0	3300	1250
Eclogite	—	Garnet pyroxenite[4]	Dislocation	0.0	15	1.0	0.5	3370	750

All materials have thermal conductivity $k = 3.0\ \mathrm{W\,m^{-1}\,K^{-1}}$.
c: Plastic cohesion (MPa). ϕ_0: undamaged friction angle (degrees). f: strength coefficient.
Q: volumetric heat production rate ($\mu\mathrm{W\,m^{-3}}$). ρ_0: reference density ($\mathrm{kg\,m^{-3}}$). C: heat capacity ($\mathrm{J\,K^{-1}}$).
1: Rutter and Brodie (2004). 2: Ranalli and Murphy (1987). 3: Wilks and Carter (1990).
4: Jull and Kelemen (2001). 5: Hirth and Kohlstedt (2003).

5.4.3 Initial thermal structure

The initial temperature field of the model assumes a surface temperature of 0 °C, temperature at the base of the lithosphere of 1330 °C, and an adiabatic temperature gradient of 0.4 °C $\mathrm{km^{-1}}$ in the asthenosphere (Katsura et al., 2010), giving a temperature of 1450 °C at the base of the model (400 km depth). The initial temperature profile, plotted in Figure 5.2, is calculated according to the equation

$$T(z) = T_t + \frac{q_t}{k}z - \frac{Az^2}{2k}q_t = q_b + Q\Delta z$$

where T is temperature, z is depth, T_t is the temperature at the top of the layer, q_t is the heat flow at the top of the layer, q_b is heat flow at the base of the layer, Q is heat production of the layer, k is the thermal conductivity of the layer, and Δz is thickness of the layer (Table 5.1). The resulting thermal field yields a temperature of 783 °C at the Moho (Figure 5.2).

5.4.4 Initial plastic damage

To allow the formation of an elevated plateau due to tectonic shortening, a central 650 km-wide portion of the domain (W_{pl}) is initialized such that the upper crust takes on random values of plastic strain between 0.5 and 1.5 (Figure 5.3) following Gouiza and Naliboff (2021), and the rest of the domain begins with plastic damage values of zero. The width of $W_{\mathrm{pl}} = 650$ km was chosen (Figure 5.2) so that, after ~45 Myr of shortening, the width of the elevated region is similar to the modern 250 km width of the Southern Puna Plateau. We also impose narrow

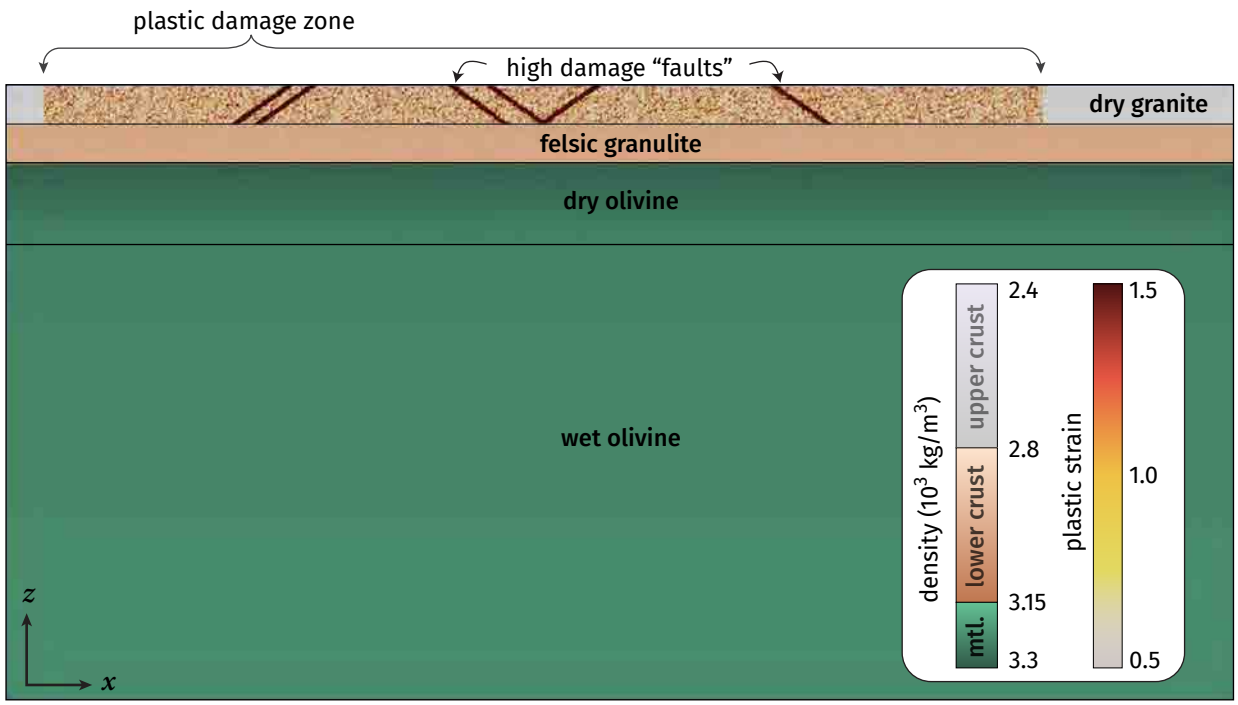

Figure 5.3: Plot of initial plastic strain in the upper crust, illustrating the 650 km-wide damage zone corresponding to the plateau, and narrow high-damage bands corresponding to pre-existing faults.

bands of high plastic strain (with a value of 1.5) in the upper crust to represent pre-existing weaknesses (e.g., reverse faults). These weaknesses are initialized with a vertical thickness of 4 km and dips of 35°, which approximates the expected shear band angle for shear bands formed during compression (Glerum et al., 2018), facilitating activation of these structures during shortening. These widely-spaced, pre-imposed weaknesses allow strain localization in positions that roughly correspond to major basement-cored mountain ranges on the Southern Puna Plateau and mainly serve to facilitate comparison of the patterns of deformation between the model and the Southern Puna Plateau. The dip direction of band weakness corresponds to the inferred vergence of these ranges (west- or east-vergent). Variants of the models without the initial plastic damage zone, faults, or both, are described below.

5.4.5 Granulite-eclogite transition

The lower crust includes a region with the potential for transitioning to a dense eclogite phase ("eclogite-prone region", Figure 5.2). Eclogitization occurs in the models when crustal thickening moves the lower crust into a region of pressure-temperature space that favors the formation of high-pressure granulite and eclogites Figure 5.4. In our numerical models, the reference density of eclogite is 3370 kg m^{-3} (Bousquet et al., 1997), 70 kg m^{-3} denser than the reference density of underlying mantle lithosphere.

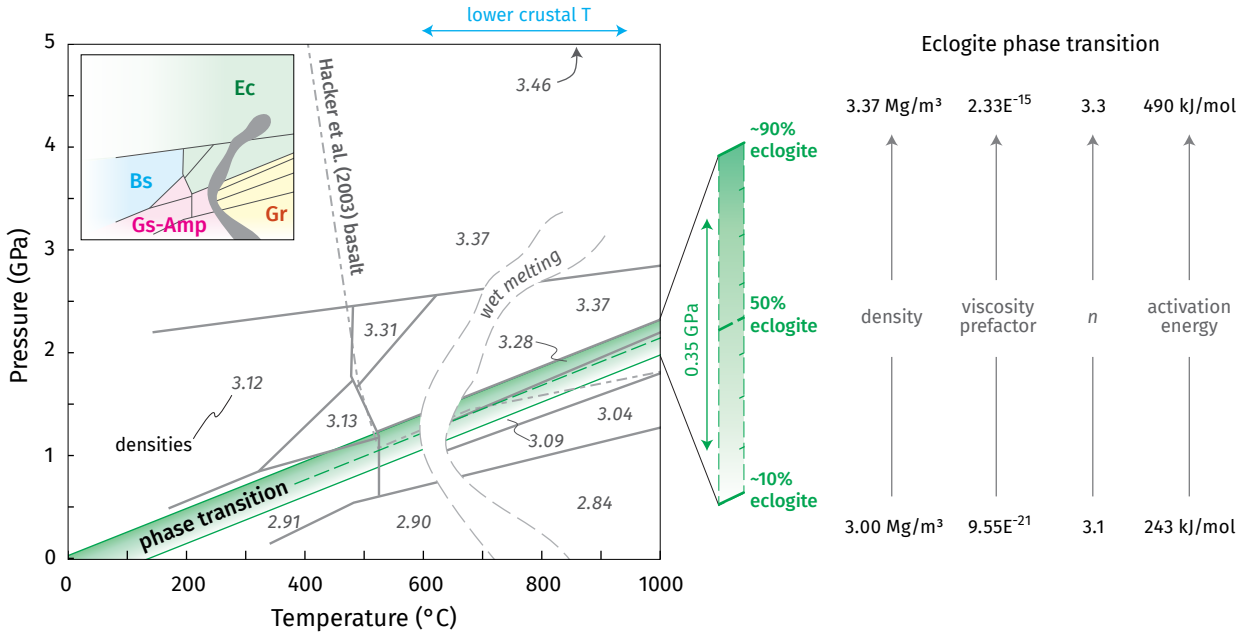

Figure 5.4: Illustration of the phase transition representing eclogitization of lower crustal granulite in the models. Phase diagram annotated with densities computed for felsic mineralogies (Bousquet et al., 1997). The dashed line shows the eclogite transition of basalt (Hacker et al., 2003). The phase transition implemented in the models is overlaid in green, with a Clapeyron slope and pressure width chosen to fit the underlying phase diagram. Model parameters that vary described on right.

The proportion of eclogite $Ec \in [0, 1]$ at a given pressure P_0 and temperature T_0 is given by

$$Ec = \frac{1}{2} + \frac{1}{2} \tanh \left(\frac{(P_0 - P_t) - C(T_0 - T_t)}{\Delta P} \right)$$

where P_t and T_t are a phase transition pressure and temperature, respectively, C is the Clapeyron slope, and ΔP is a pressure width. We chose values of phase transition pressure, temperature, Clapeyron slope, and pressure width to closely fit the experimental phase diagrams of Bousquet et al. (1997).

This approach is similar to previous numerical modelling studies of continental back-arcs (Krystopowicz & Currie, 2013), except that we limit the width of the region that is prone to eclogitization, W_{ec}, to promote dripping instead of delamination. In the base model, $W_{\text{ec}} = 150$ km such that the drip that forms is similar in size to the 50–75 km tomographic anomaly interpreted as foundered lithosphere (Beck et al., 2015; Scire et al., 2015). We explore variants where W_{ec} ranges from 75 km to 650 km (the entire plateau).

5.4.6 Velocity boundary conditions

Strong lithosphere is introduced at the left side of the model domain at a rate of $v_a = 6$ mm yr^{-1}, while the strong lithospheric block on the right side of the domain is kept fixed. The rate of 6

mm yr^{-1} approximately matches the shortening rate accommodated within modern Andean deformation front (McFarland et al., 2017), and the model assumes that the same rate was responsible for uplifting the Puna Plateau during the Cenozoic.

After 38 Myr (the approximate time of drip detachment) convergence rate can be modulated to explore various hypotheses. In the base model (v0), the rate is reduced to 2 mm yr^{-}1, which roughly matches the shortening rate accommodated within the modern Puna Plateau inferred from GPS velocities (McFarland et al., 2017). The base model therefore assumes that drip detachment coincides with a reduction in crustal shortening rate on the plateau, e.g., due to the propagation of the strain front into the Eastern Cordillera and broken foreland region (e.g., DeCelles et al., 2009), a process which is not explicitly included in the model.

Because horizontal extension is an important aspect of this study and could be sensitive to the imposed convergence rate, we also explore a models (v8) in which shortening rate is reduced to zero (v8.1), 1 mm yr^{-1} (v8.2), or remains unchanged at 6 mm yr^{-1} (v8.3). Model v8.3 is conceptually useful because it isolates the crustal deformation patterns due to dripping, and represents a worst-case scenario for the idea that dripping is associated with upper-crustal extension (as we show below, dripping still yields upper-crustal extension even in the background of this relatively high shortening rate). Model v8.3 is also simpler because it does not assume a change in convergence rate, but this also yields unrealistically high topography by ~50 Myr.

The asthenosphere boundaries on the left and right sides are prescribed a horizontal outflow value of v_o to balance the inflowing lithosphere. In this case $v_b = -v_o = -v_c$ (Figure 5.2), where the minus sign denotes flow toward the left-hand side of the model. Some models also prescribe lateral flow $-v_l$ through the asthenosphere boundaries such that $v_b = -v_o - v_l$ and $v_c = v_o - v_l$ (Figure 5.2). Lateral mantle flow crudely approximates corner flow in the mantle wedge above a subduction zone. The base model sets $v_l = 0$, i.e., no explicit lateral mantle flow.

5.4.7 Model variation

We conducted a number of experiments that varied a number of parameters in the base model (Table 5.2). The goal of these variant models is to investigate the factors that control the formation and evolution of lithospheric dripping in an orogenic plateau. We are especially interested in the potential range of upper-crustal and topographic deformation that may be induced by a drip. As such, we mainly varied parameters related to convergence rate, rheologies, and plastic damage. The base model is labelled v0, and the variant models are labelled v1.1, v1.2, etc., where the number on the left-hand side of the decimal encodes which parameter is varied (e.g., 1 corresponds to asthenosphere viscosity factor f) and the number to the right of the decimal encodes specific values for this parameter. Although we focus on the base model, v0, we briefly explore the behavior of the variant models below.

Table 5.2: Description of model variants compared to the base model.

Model	Parameter	Relevant behavior
Asthenosphere strength factor, f		Affects asthenosphere interaction with drip
0	0.1	Weakly interacts
1.1	0.5	Interacts more strongly
1.2	1.0	Strongly influences the drip
Initial plastic damage		Controls strain distribution
0	Damage zone + faults	Realistic for Puna Plateau
2.1	Damage zone only	All faults to form dynamically
2.2	Faults only	Concentrates strain onto pre-imposed faults
2.3	No damage zone or faults	Initially homogeneous, no damage
Crust strength factor, f		Controls the viscous strength of the crust
0	1.0	Westerly granite flow law
3.1	0.1	Weakens the granitic crust
3.2	10	Strengthens the granitic crust
3.3	100	Very strong granitic crust
Lateral mantle flow (cm yr^{-1})		Approximates mantle corner flow
0	0	Flows only relative to overriding plate
4.1	4	Upper range of uncertainty
4.2	2	Follows Wang et al. (2015)
4.3	1	Lower range of uncertainty
Upper crust heating Q (μW m^{-3})		Affects upper-crustal strength
0	1.5	Realistic for granitoids
5.1	1.0	Follows Wang et al. (2015), Arizaro
5.2	1.9	Follows Ibarra et al. (2019)
Eclogite-prone width (km)		Controls size of drip and affected region
0	150	Yields realistic drip size
6.1	75	Lower range of uncertainty
6.2	250	Upper range of uncertainty
6.3	650	Entire plateau
6.4	0	No eclogite-prone region
Crustal rheology flow law		Controls crustal strength
0	DG upper, FG lower	Follows Ibarra et al. (2019) for the Puna Plateau
7.1	WQ upper, DMD lower	Follows Wang et al. (2015), Arizaro
7.2	DG upper, DMD lower	Assumes a mafic lower crust
7.3	WQ upper, FG lower	Arizaro with felsic lower crust
Post-38 Myr convergence (mm yr^{-1})		Parameterizes strain migration into foreland
0	2	Modern GPS rate across Puna (McFarland et al., 2017)
8.1	0	Follows Wang et al. (2015), Arizaro
8.2	1	Half the modern GPS rate across Puna
8.3	6	No change from pre-38 Myr rate
Crustal cohesion, c (MPa)		Controls plastic strength of mid-upper crust
0	2	Wang et al. (2015), weak crust
9.1	0	No cohesive strength
9.2	10	Stronger crust
9.3	20	Common value for intact crust (e.g., Gouiza & Naliboff, 2021)

DG = dry granite. FG = felsic granulite. WQ = wet quartzite. DMD = dry Maryland diabase.

5.5 Results

Horizontal shortening and crustal thickening lead to the formation of an eclogitic root in the lower crust, followed by its gravitational foundering in the form of a Rayleigh–Taylor drip (Figure 5.5).

We propose a 5 phase framework for understanding lithospheric foundering as modeled in this study (Figure 5.6). Although the framework applies to all of our lithospheric dripping models, we here focus on the base model (v0). Phase 1 corresponds to crustal thickening prior to the production of eclogite. The base of the crust gradually descends during this phase solely due to thickening. Phase 2 corresponds to the production of negatively buoyant eclogite. The base of the crust descends more rapidly during phase 2 due to a positive feedback between eclogite formation and subsidence discussed below. Phase 3 corresponds to growth of the drip, which is seeded on the perturbation to the crust-mantle boundary created by the eclogitic root. The displacement of the crust is strongly nonlinear during this phase, increasing exponentially and then super-exponentially as the drip begins to detach. Phase 4 corresponds to drip detachment, which we view as the mechanical decoupling of the descending drip from overlying lithosphere. In our models, drip detachment occurs over a period of ~200 kyr and has marked effects on crustal deformation and temperature. Phase 5 corresponds to the recovery and relaxation of the lithosphere after drip detachment.

We consider eclogitization (Phase 2) to be distinct from dripping (Phases 3 and 4) for the following reasons. First, eclogite subsidence is driven by an isostatic response to densification of the lower crust, not a dynamical interface instability such as dripping. This isostatic adjustment could occur even in the absence of a drip if eclogite obtained a density greater than lower crust but less underlying mantle lithosphere. Eclogite subsidence could also occur without dripping if the lithosphere were sufficiently rigid to prevent the growth of a drip during the relevant timescale (Jull & Kelemen, 2001). Eclogitization may also, under different layer configurations and crustal strengths, drive delamination instead of dripping (Beall et al., 2017; Krystopowicz & Currie, 2013). While eclogite subsidence provokes Poiseuille flow and thickening of the middle crust (Castellanos et al., 2022; Wang & Currie, 2017), Rayleigh–Taylor dripping results in more complex flow patterns in weak crusts (Molnar, 2015). As a result, eclogite subsidence during Phase 2 produces effects on crustal strain and temperature distinct from those produced by dripping during Phase 3.

5.5.1 Behavior of the variant models

The variant models largely reproduce the weak-crust dripping behavior summarized here. Because eclogitization depends on the crust attaining a critical thickness, differences in the viscous or plastic strength of the crust often change the timing of drip formation and detachment. Variation in the post-drip convergence rate quantitatively changes the rates of shortening and extension on the plateau after drip detachment, but the patterns of deformation are qualita-

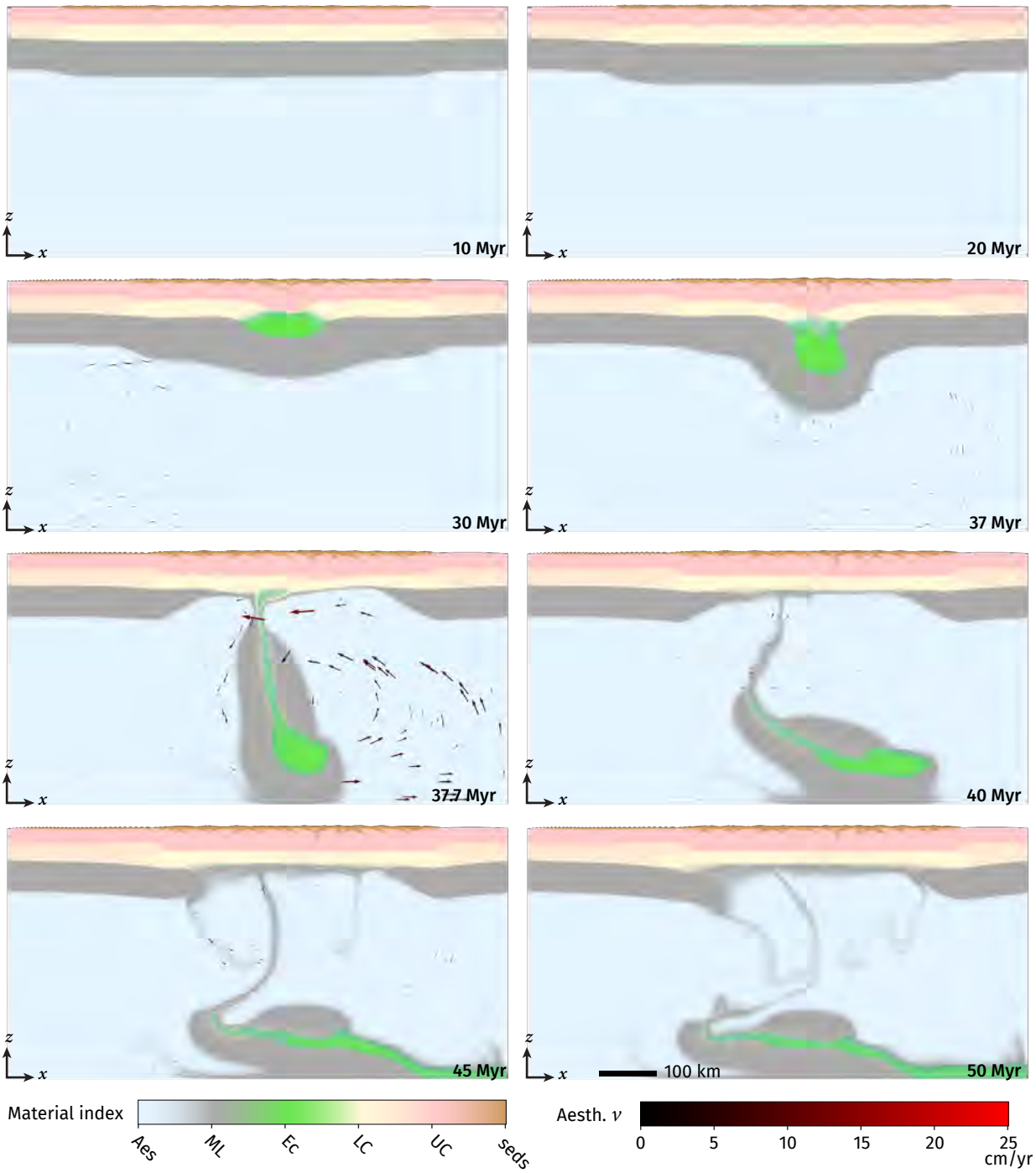

Figure 5.5: Illustration of the formation and foundering of an eclogite root in the numerical model.

Table 5.3: Major results of the variant models. See Table 5.2 for explanation.

Model	Value	Syn-drip extension?	Detachment (Ma)	Notes
Asthenosphere strength factor, f (0.1)				
1.1	0.5	Y	42	Extension shifts to west side of drip
1.2	1.0	Y	46	Extension only on west side of drip
Initial plastic damage (damage zone + faults)				
2.1	damage zone	Y	38	Faults form with closer spacing
2.2	faults	Y	38	Almost no strain between faults
2.3	none	N	38	No strain localization, no syn-drip extension
Crustal strength factor, f (1.0)				
3.1	0.1	Y	31	Edges of plateau experience extension during eclogitization; topography reduced
3.2	10	Y	42	Syn- and post-drip extension reduced
3.3	100	N	38	Strong-crust behavior (syn-drip contraction)
Lateral mantle flow (0 $cm\,yr^{-1}$)				
4.1	4	Y	39	Phase 5 crustal heating offset ~100 km to the east
4.2	2	Y	39	Phase 5 crustal heating offset ~50 km to the east
4.3	1	Y	38	Crustal heating enhanced and roughly symmetric
Upper crust heating, Q (1.5 $\mu W\,m^{-3}$)				
5.1	1.0	Y	37	Extensional strain enhanced and more protracted
5.2	1.9	N	42	Extension is briefer; enhanced crustal cooling due to thickening
Eclogite-prone width (150 km)				
6.1	75	Y	38	Syn-drip extension diminished
6.2	250	Y	42	Dripping and extension focused on western half
6.3	650	Y	45	Dripping initiates on western edge of plateau
6.4	0	—	—	No lithospheric dripping
Crustal flow law (DG upper/FG lower)				
7.1	WQ upper	Y	38	Minor syn- and post-drip extension
7.2	DMD lower	N	38	No syn-drip extension; major post-drip extension & uplift
7.3	WQ/DMD	Y	38	Minor syn-drip extension; major post-drip extension & uplift
Post-38 Myr convergence (2 $mm\,yr^{-1}$)				
8.1	0	Y	38	Post-drip extension greatly enhanced
8.2	1	Y	38	Post-drip extension enhanced
8.3	6	Y	38	Post-drip extension reduced; unrealistic plateau elevation
Crustal cohesion c (2 MPa)				
9.1	0	Y	38	Post-drip extension enhanced
9.2	10	Y	38	Post-drip extension slightly diminished
9.3	20	Y	38	Syn- and post-drip extension diminished

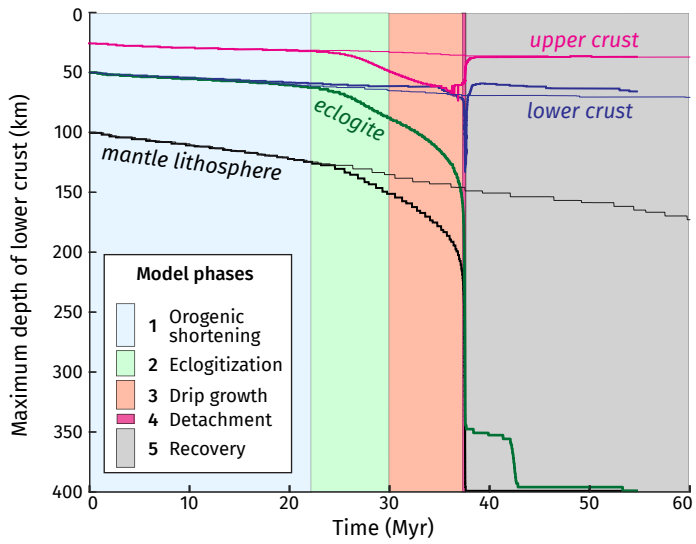

Figure 5.6: Maximum depth of lithologic layers through time, illustrating the 5 phases discussed in the text. Thick lines correspond to the base model (v0); thin lines correspond to a model where eclogite does not form (v6.4).

tively similar. Syn-drip upper-crustal extension was not reproduced in models with no initial plastic damage, with crustal strength factor of 100, or with dry Maryland diabase lower crust due to the increased crustal strength. Syn-drip upper-crustal extension was also not reproduced in the model with crustal heating increased to 1.9 $\mu W\,m^{-3}$, because the middle crust was hot and weak enough to fully decouple upper-crustal deformation from from lower-crustal flow. The major behaviors of the variant models are summarized below in Table 5.3. Insights offered by key variant models are discussed in the following sections.

5.5.2 Phase 1: Orogenic shortening

The first phase is characterized by tectonic shortening and crustal thickening from 0 to 22 Myr. Positive topography develops due to shortening on distinct structures in the uppermost crust and through viscous shortening and thickening of the middle to lower crust and mantle lithosphere. Shortening is mainly confined to the zone of pre-weakened crust, creating a broad region of high mean elevation, which we refer to as the plateau. Within the plateau, rugged topography develops that reflects shortening and surface uplift on individual structures (Figure 5.7 15 Myr). The shortest wavelength topography is dominated by an oscillatory numerical instability, which mainly affects the left side of the model domain during the first 30 Myr (Figure 5.7, 15 Myr). At the end of Phase 1, the plateau has a compressional basin-and-range topography with a mean elevation of ~2.5 km and topographic relief of ~2 km (Figure 5.8a). The temperature field is characterized by gradual cooling of the lithosphere due to thickening (Figure 5.9). Cooling of the middle crust is limited to the region beneath the plateau.

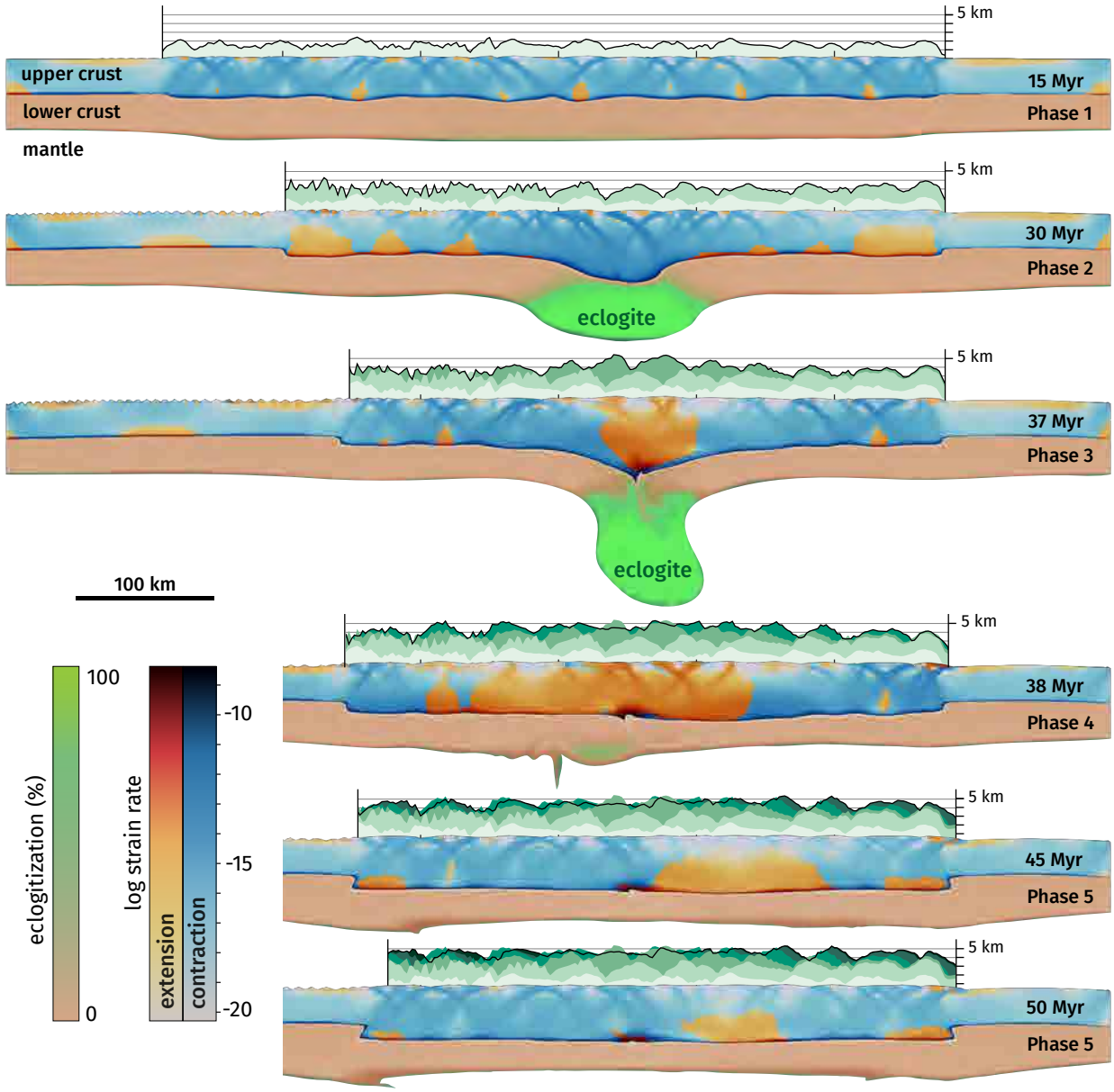

Figure 5.7: Plot of upper crustal strain rate (colored by compression vs. extension) and eclogitization at six time steps. Vertically-exaggerated topographic profiles are plotted above each time step. The plots illustrate the crustal and topographic response to eclogitization and dripping.

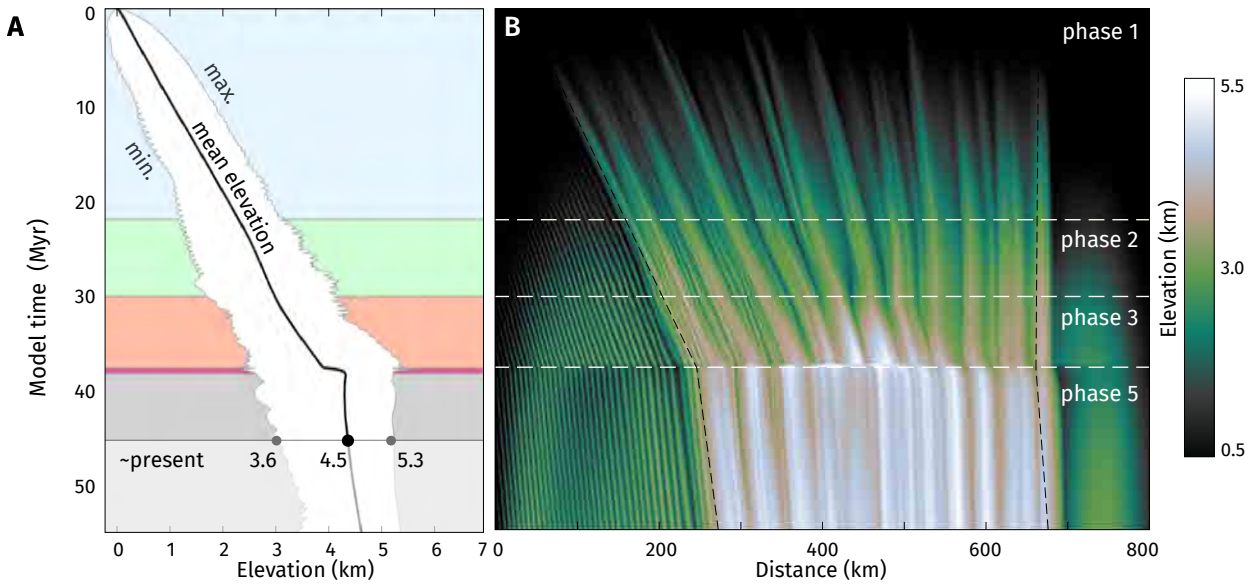

Figure 5.8: Evolution of surface topography through time. (a) Plot of mean, maximum, and minimum elevation of the plateau through time. Elevation increases along the horizontal axis. Background colors correspond to the five model phases (Figure 5.6) (b) Carpet plot of elevations, with horizontal distance along the horizontal axis and time increasing from top to bottom. The vertical dashed lines delimit the region plotted in (a).

5.5.3 Phase 2: Eclogitization

The second phase is characterized by the formation of an eclogitic root in the lower crust. Pressure-temperature conditions favorable to eclogitization are reached at 22 Myr, and eclogitization continues until ~30 Myr. The negatively buoyant eclogite sinks isostatically, dragging lower crust into the high pressure regions favorable for further eclogitization in a positive feedback loop. Root subsidence results in buckling of the lower crust and mantle lithosphere, which necessitates horizontal shortening of the middle to upper crust overlying the eclogite. This shortening is accommodated by convergent Poiseuille flow in the middle to upper crust, which thickens significantly as a result (Figure 5.7, 30 Myr). Due to the fixed velocity boundary conditions, shortening above the root is compensated by a reduction in shortening rate in the peripheral regions of the plateau. The net effect is that crustal strain rate increases above the root (in the center of the plateau), and decreases toward the peripheral regions of the plateau (Figure 5.7, 30 Myr). In model variants that include a significantly weaker crust (v3.1), eclogite subsidence and associated crustal shortening are accommodated by horizontal extension in the peripheral regions. The formation of the eclogitic root therefore reconfigures the distribution of deformation on the plateau, concentrating it directly above the root for approximately 8 Myr, at which time the root begins to founder (Phase 3).

Long wavelength topography is elevated above the root as a result of both lower-crustal viscous thickening and accelerated upper-crustal shortening (Figure 5.7, 30 Myr). Plateau elevations continue increasing during this phase (Figure 5.8). Long-wavelength topography is

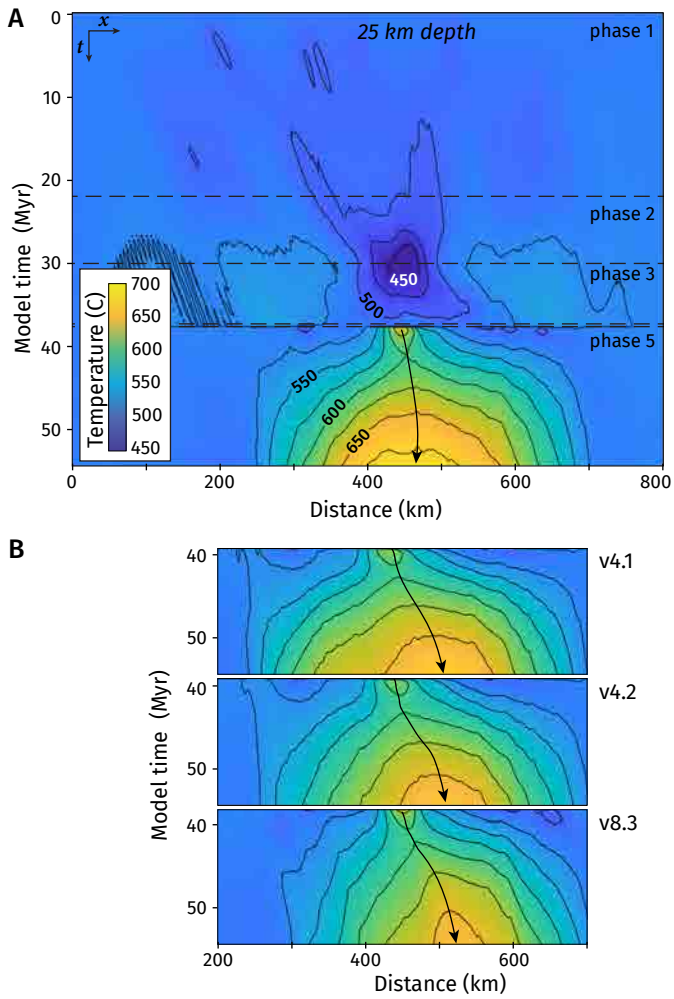

Figure 5.9: (a) Evolution of mid-crustal temperature (25 km depth) through time. Dashed lines delimit the 5 phases discussed in the text (phase 4, detachment, is too brief to label). Arrow tracks the post-drip temperature maximum. (b) Model variants that illustrate the eastward shift of the mid-crustal heating due to westward mantle flow (v4.1 and v4.2) or increased convergence rate (v8.3) causing asymmetric foundering.

subdued directly above the root (Figure 5.7, 30 Myr). The crustal temperature field is characterized by significant localized cooling due to the crustal thickening driven by the sinking eclogitic root, and the middle crust reaches its minimum temperature at the end of Phase 2 (Figure 5.9).

5.5.4 Phase 3: Drip growth

The third phase is characterized by the growth of a large Rayleigh–Taylor instability of the eclogitic root from approximately 30 to 37.7 Myr. The growth of the drip entrains surrounding lithosphere and induces further crustal thickening and flow within the crust (Figure 5.7, 37 Myr). As a result of this flow, the upper crust switches from contraction to extension directly above the drip (Figure 5.7, 37 Myr). Extension is limited to a 50–75 km wide region centered on

the drip in which crustal flow yields divergent velocities in the upper crust. Syn-drip upper-crustal extension is stronger on the left side of the drip than the right (Figure 5.7, 37 Myr). Extension reactivates pre-existing contractional structures (reverse faults that were either pre-imposed or generated during earlier phases) in a net-extensional sense. Horizontal shortening propagates outward to the edges of the plateau, where it had previously been reduced during Phase 2 (Figure 5.7, 37 Myr). Dripping again reconfigures the kinematics upper crustal deformation on the plateau, producing a narrow region of horizontal extension in the center of the plateau, flanked by regions of strong horizontal contraction.

Plateau elevations generally increase during Phase 3. Crustal thickening due to drip growth increases elevations above the drip; this effect, like horizontal extension, is stronger on the left side of the drip. Elevations also increase on the shoulders of the drip, due to the acceleration of horizontal shortening and uplift of compressional structures.

The temperature field in Phase 3 is characterized by slow heating of the mid-crust, raising the temperature of the localized chilled zone that had formed as a result of eclogitization (Figure 5.9a). The shoulders of the drip experience mid-crustal heating on the order of 40 °C by the end of Phase 3 and are approximately 55 °C warmer than the central portion of the drip prior to detachment (Figure 5.9a). This heating is due to lower crustal thinning and asthenosphere upwelling. The temperature gradient of the upper crust is relatively unperturbed by the growth of the drip.

5.5.5 Phase 4: Detachment

The fourth phase is characterized by the mechanical decoupling, i.e. detachment, of the drip from overlying lithosphere. Detachment is a rapid process that lasts only ~200 kyr (from 37.6 to 37.8 Myr). The removal of the dynamic load associated with the negatively buoyant root has strong effects on the remaining lithosphere. The crustal welt that was generated by eclogite subsidence and drip growth collapses gravitationally (Figure 5.7, 38 Myr). The gravitational collapse yields a transient pulse of horizontal extension that rapidly grows outward from the central plateau. As in phase 3, extension re-activates previously compressional structures in the upper crust (Figure 5.7, 38 Myr). Horizontal shortening is confined to the extreme edges of the plateau, where new structures form to accommodate this contraction (Figure 5.7, 38 Myr). Due to the brief timescale of detachment, topography is not significantly changed from Phase 3 (Figure 5.7, 38 Myr).

The temperature field during the final stages of drip growth and detachment is characterized by steep temperature gradients corresponding to areas where lithosphere is removed (Figure 5.10). Dripping drives the upwelling of hot asthenosphere, which comes directly into contact with relatively cool lower crust (Figure 5.10a). Because the lithosphere converges from left side of the model, the drip migrates to the left while detaching relative to the overriding lithosphere (Figure 5.10b). The right side of the asthenosphere experiences drastically larger flow velocities during dripping (Figure 5.10c). Lower crustal heating is also asymmetric with

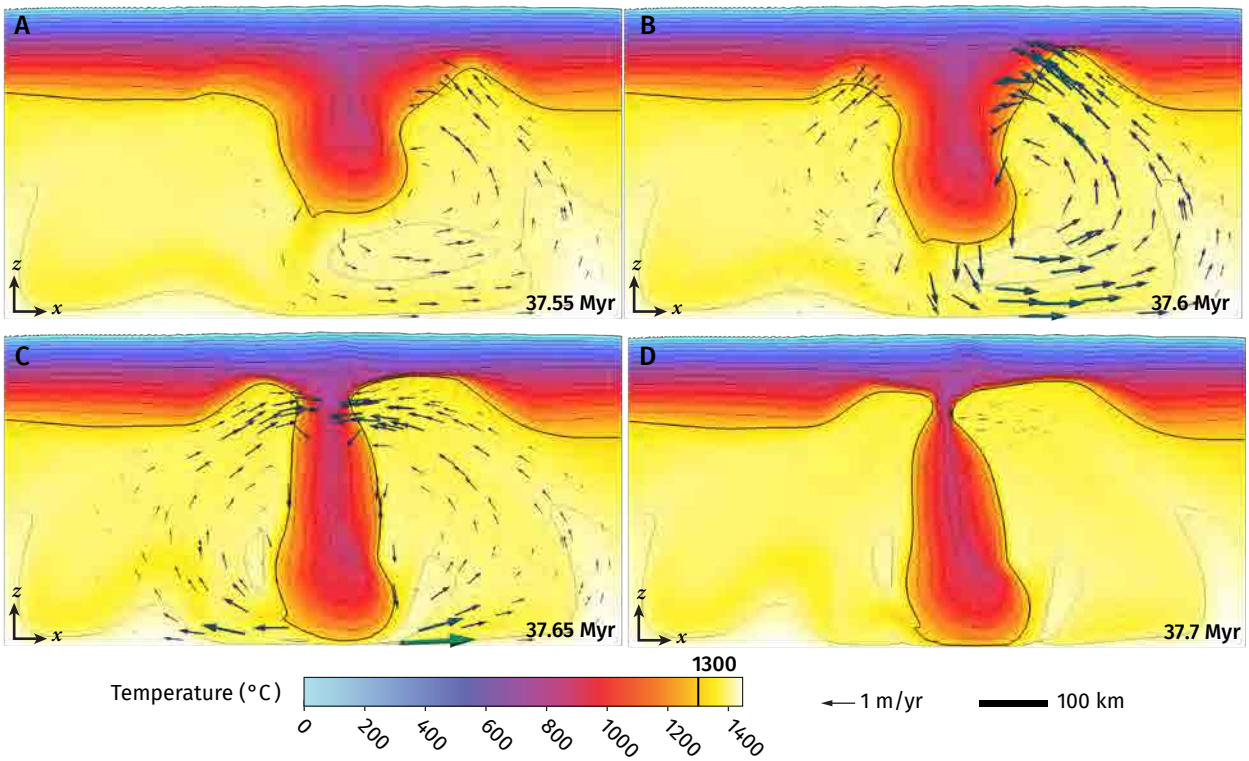

Figure 5.10: Plots of temperature and asthenosphere velocity vectors during the detachment of the drip. The plots highlight asymmetric lithospheric thinning due to tectonic convergence on the left-hand side of the lithosphere.

respect to the drip, with the right flank experiencing larger temperature contrasts than the left side (Figure 5.10c). In addition, the removal of the relatively cool drip allows heating of the middle crust in the central plateau, producing steepened thermal gradients in the upper crust in a small (~20 km) region (Figure 5.10d).

5.5.6 Phase 5: Recovery

The fifth phase is characterized by recovery of the lithosphere after detachment of the drip, and the eventual resumption of tectonic shortening throughout the model domain. Phase 5 occurs from ~38 Ma until the end of the model run. At the beginning of the recovery phase, the crust is still overthickened in the central portion of the plateau where the drip detached (Figure 5.7, 38 Myr). Heterogeneities in crustal thickness and temperature produce contrasts in gravitational potential energy (GPE), which ultimately controls how the crust deforms during Phase 5. The overthickened welt rapidly collapses, and a large portion of the center of the plateau experiences significant crustal spreading and upper-crustal extension (Figure 5.7, 38 Myr). Similarly, elevations and topographic relief rapidly decrease in the center of the plateau (Figure 5.8b and Figure 5.7, 38 Myr). Meanwhile, mountain range elevations and topographic relief increase in the eastern sector of the plateau (Figure 5.7, 45 Myr). This rapid kinematic reorganization lasts

for ~4 Myr in the model and results in nearly homogeneous crustal thicknesses throughout the plateau (Figure 5.7, 45 Myr).

Diffusive heating due to lithospheric thinning and asthenosphere upwelling continues heating the mid-crust until the end of the model run (Figure 5.9a). Due to the asymmetric nature of drip detachment described in Phase 4, crustal heating is greatest on the east side of the plateau, producing a thermal maximum that is offset from the drip center (Figure 5.9b). The amount of offset depends on lithospheric convergence rate and the lateral flow velocity of the mantle. For the base model (v0) with a post-drip convergence rate of 2 mm yr^{-1} and no lateral mantle flow, the mid-crustal temperature maximum is offset only ~20 km to the east of the dripping center. For the model in which convergence rate is kept constant at 6 mm yr^{-1} (v8.3), the temperature maximum is offset ~50 km to the east. Models that include lateral mantle flow to the left (v4) show a positive correlation between flow velocity and temperature offset. In the model with the largest mantle velocity of 4 cm yr^{-1} (v4.1), the mid-crustal temperature maximum is offset ~100 km to the east.

The hot, buoyant crust in the eastern sector resists shortening and instead is placed into extensional to neutral conditions (Figure 5.7, 40 Myr). This extensional to neutral region in the central to eastern section of the plateau shrinks in width as crustal thickness and temperature gradients are neutralized. Shortening initially resumes in the western half of the plateau, where crustal thickening and heating were minimal and the lithosphere is less buoyant (Figure 5.7, 38 Myr). The time at which the western sector of the model returns to horizontal contraction is dictated by the imposed shortening rate. Models that impose a reduced post-38 Myr convergence rate (v0, v8.1, v8.2) result in a ~4–5 Myr period of horizontal extension in the western sector, while in the model that retains a 6 mm yr^{-1} convergence rate (v8.3), horizontal shortening obtains in the western sector ~2 Myr after detachment. The eastern sector also recovers from horizontal extension and gravitational collapse more slowly in models that reduce the post-drip convergence rate. In the base model, the entire lithosphere experiences horizontal shortening qualitatively resembling Phase 1 by ~50 Myr (Figure 5.7, 50 Myr). During the entirety of Phase 5, shortening is prominent along the edges of the plateau due to the GPE contrast with the relatively undeformed blocks of lithosphere on the edges of the model.

5.5.7 Upper crustal plastic deformation

Within the plateau, upper-crustal deformation is concentrated on narrow shear bands which we interpret as approximating thick-skinned reverse and normal faults. During the first 5 Myr, shortening is almost entirely accommodated by the widely-spaced faults imposed in the initial conditions of the model. Additional faults develop between these faults and by 22 Myr are accommodating a similar proportion of strain as the pre-imposed faults (Figure 5.11). During Phases 2 and 3, faults in the center of the plateau are preferentially activated due to their location above the negatively buoyant eclogitic root and drip. These centrally located faults therefore obtain higher finite strains than more peripheral faults (Figure 5.11, 25–35 Myr). The

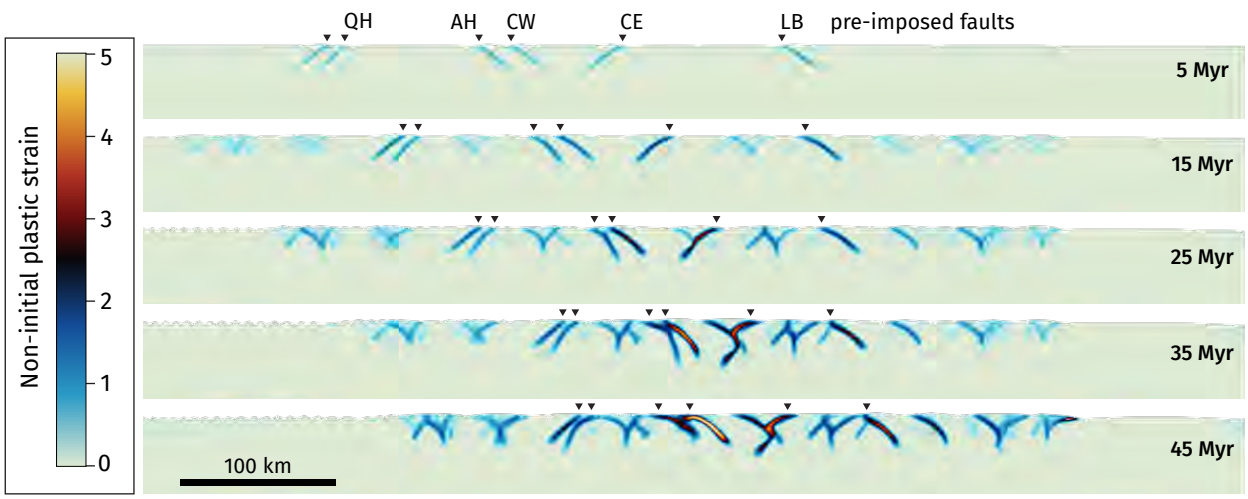

Figure 5.11: Plot of accumulated plastic strain in the crust showing that structures near the center of the plateau where eclogitization and dripping occur accommodate a larger proportion of strain than more peripheral structures.

most centrally-located faults are also re-activated as normal faults during the phase of upper-crustal extension driven by drip growth during Phase 3. A larger swath of faults are re-activated in a normal sense during extensional collapse of the thickened crust following drip detachment, but the relatively brief time period involved means that these faults accommodate a relatively low amount of extensional strain. As a result, the faults that accommodate the most strain, both contractional and extensional, are located in the central portion of the plateau above the eclogitic root (Figure 5.11).

5.6 Discussion

5.6.1 Assumptions and limitations

Important assumptions are built into the model that limit its applicability in the case that they are not supported by observation. The model assumes that the plateau deforms by pure shear (Allmendinger & Gubbels, 1996). Although the interpretation of the major mountain ranges on the plateau as reverse fault-bounded and basement-cored tends to support this assumption, an alternate model of an eastward-propagating orogenic wedge that incorporated the plateau during the Cenozoic remains a topic of research (e.g., McFarland et al., 2017; Zhou et al., 2017). While pure shear-style deformation is still capable of producing crust of significant thickness and eclogitization of the lower crust, the patterns of upper crustal strain associated with this style of shortening would be different from those observed in our models.

The applicability of the model is limited by its two-dimensional domain. Three-dimensional lithospheric drips may evolve on temporal and spatial scales quantitatively different from 2-D drips. The upper-crustal strain kinematics due to a 3-D drip is also likely to be complex, po-

tentially consisting of regions of shortening and extension-related structures to accommodate the heterogeneous stress field (Pysklywec & Cruden, 2004). It is also possible, however, that a uniform stress field due to tectonic convergence would yield strongly 2-D results, even in a 3-D model. For example, in the 3-D models of mantle plumes impinging on the lithosphere, a small amount of background extensional strain was sufficient to produce linear arrays of faults and horst-and-graben topography in the upper crust, rather than axisymmetric patterns of uplift and subsidence (Burov & Gerya, 2014; Koptev et al., 2018).

Similarly, our 2-D experiments are unable to model out-of-plane deformation, and strain is confined to occur as pure thrusting or pure extension. This limits the applicability of the model to the Southern Puna Plateau, where significant strike-slip and oblique strain has occurred throughout the Cenozoic (Kraemer et al., 1999), most notably the Pliocene to Quaternary strike-slip and extension (e.g., Schoenbohm & Strecker, 2009). However, the first-order tectonic features on the plateau (basement cored ranges) are linear and oriented roughly parallel to the orogen, and are thus amenable to modelling of an orogen-perpendicular transect, as represented by our 2-D models. We hypothesize that regions in the model that experience little to no strain would be prone to out-of-plane deformation (i.e., strike-slip and orogen-parallel extension) in a 3-D setting. This assumption has implications for the application of Phase 5 to the Southern Puna Plateau.

The model omits processes related to melting and magmatism. By neglecting melting, the thermal evolution of the model reflects the effects of lithospheric foundering, but this limits the capability of the model to predict patterns of volcanism. As the models of Wang et al. (2021) show, lithospheric foundering may be able to explain the distribution of back-arc volcanism in the Southern Puna Plateau, including mafic volcanism in the interior of the plateau, and mid-crustal melting and silicic volcanism in its eastern sector. Arc volcanism is another key process the models lack. Magmatism and crustal heating due to arc volcanism may significantly alter the rheology and buoyancy of the crust during dripping. As such, we expect that the western sector of the Puna Plateau, which abuts the volcanic arc, is modeled less accurately than the central and eastern sectors.

The production of eclogite in the models, like previous lithospheric-scale models, is still ad-hoc and simplified. Although we employ a phase diagram to parameterize the transition from granulite to eclogite (Bousquet et al., 1997; Krystopowicz & Currie, 2013), the models do not include fluid migration and hydration. Fluids are critical for eclogitization, because phase transition reaction is limited by water availability (Austrheim, 1987). As a result, eclogitization often occurs in fluid-rich settings such as major shear zones, where water can migrate along fractures, and metastable granulite occurs outside of these zones (Austrheim, 1990). Rather than the coherent block of eclogite often found in numerical modelling studies, natural exposures of eclogite are more complex and anastomosing at the kilometer scale (Austrheim, 1990). Future models should incorporate more realistic prograde metamorphic reactions that include fluid migration and latent heating.

5.6.2 Comparison to the Southern Puna Plateau

In this section we evaluate the ability of the models to explain key characteristics of the Southern Puna Plateau (SPP). The SPP experienced a long history of upper-crustal deformation since the Eocene, which largely exploited basement-cored reverse faults associated with mountain ranges on the plateau (e.g., Carrapa et al., 2005; Kraemer et al., 1999; Zhou et al., 2017). Figure 5.12a plots the upper-crustal strain rate of the model through time, allowing major faults to be traced from top (0 Myr) to bottom (55 Myr). Numerous studies inferred detachment of the Southern Puna drip ~7 Ma based on basaltic volcanism (Kay & Kay, 1993; Kay et al., 1994; Morfulis et al., 2020; Schoenbohm & Carrapa, 2015). We therefore assume that 38 Myr in the model corresponds to 7 Ma on the geologic timescale for the SPP, allowing us to compare model results (Figure 5.12a) directly to geologic observations (Figures 5.12b to 5.12d).

We compare our models to a transect oriented parallel to plate convergence direction across the modern SPP (Figure 5.12). From west to east, the transect includes the following mountain ranges and major faults: the Quebrada Honda range (QH) (Palma et al., 1990); the Salina del Fraile anticline (SdF) (McMillan & Schoenbohm, 2020); the Antofalla High (AH) (Adelmann, 2001; Voss, 2002); the Calalaste range, western side (CW) (Carrapa et al., 2005; Kraemer et al., 1999); the Calalaste range, eastern flank (CE) (Zhou et al., 2017); the Laguna Blanca range (LB) (Zhou et al., 2016); and the Chango Real range (Coutand et al., 2001).

Phases 1 and 2 of the model involves widespread shortening on individual structures from 0 to 22 Myr and accelerated shortening on structures in the central portion of the plateau between 22 and 30 Myr (Figure 5.12a). Phases 1 and 2 of the model correspond to times earlier than ~19 Ma on the SPP timescale (Figure 5.12b). The SPP experienced widespread deformation on widely-spaced structures prior to the Late Oligocene–Early Miocene. Faults on the margin of the SPP were activated during the Late Cretaceous (Figure 5.12b) as extensional structures on the shoulder of a continental rift (e.g., Carrapa et al., 2014). Andean shortening began affecting the SPP region as early as the Eocene (Canavan et al., 2014; Quade et al., 2015), uplifting the Quebrada Honda (~35 Ma, sediment provenance Zhou et al., 2017), Chango Real, (~29–38 Ma, AFT Coutand et al., 2001), and potentially the Western Calalaste ranges (40 Ma?, sedimentary provenance, Adelmann, 2001). Major arc-related volcanic centers in the SPP such as Antofalla Volcanic Complex were not yet active during this time (Kraemer et al., 1999; Richards et al., 2006).

Phase 2 of the models involves the concentration of shortening into the central sector of the plateau due to the formation of an eclogitic root (Figure 5.12a). In the central SPP, the Calalaste range was exhumed from ~29–24 Ma (Carrapa et al., 2005) to ~20 Ma (Zhou et al., 2017). The Antofalla High was also likely uplifted during this time (~22 Ma, Adelmann, 2001; Voss, 2002). This pattern of range exhumation and compressional deformation are consistent with an increased shortening rate in the central sector of the SPP during the Late Oligocene to Early Miocene (Figure 5.12a). It is notable that no exhumation has been documented for both the western sector (Quebrada Honda range) or eastern sector (Laguna Blanca and Chango Real

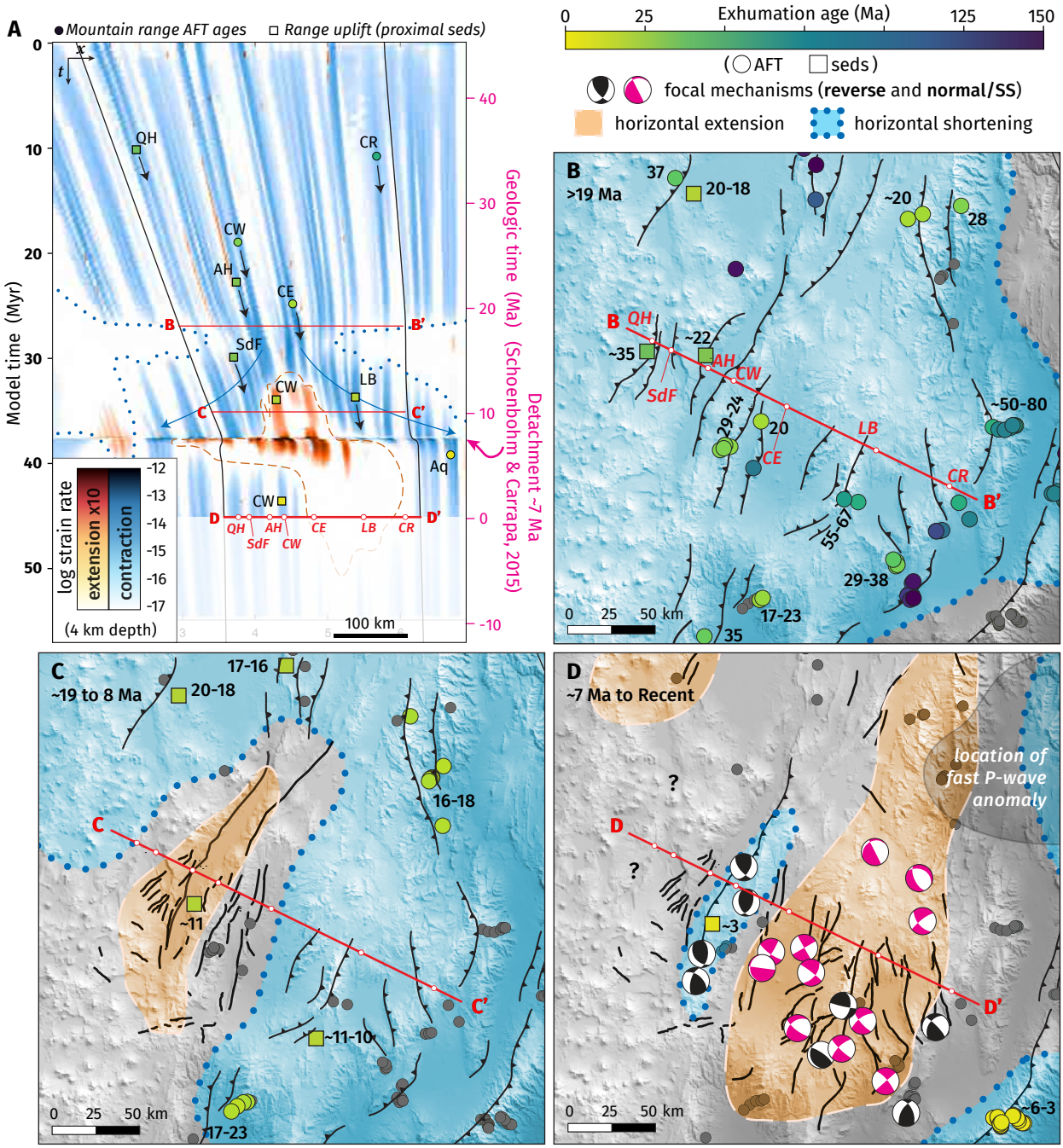

Figure 5.12: Comparing model to observations. (a) Evolution of model strain rate at 4 km depth, correlated to major structures (see text). Dotted/dashed regions show reduced shortening/upper-crustal extension. (b) Widespread exhumation data prior to the Middle Miocene. (c) Exhumation and extension during the Middle to Late Miocene. (d) Exhumation and earthquake kinematics during the Pliocene to Quaternary. Blue and orange regions: inferred regions of upper-crustal shortening and extension, respectively (after Tye et al., 2022). Data include major thrust faults (Schnurr et al., 2006) and normal/strike-slip faults (Schoenbohm & Carrapa, 2015; Tye et al., 2022) drawn according to inferred shortening or extension; earthquake focal mechanisms (Mulcahy et al., 2014); P-wave anomaly from <100 to ~200 km depth (Beck et al., 2015); AFT ages (Carrapa et al., 2005; Stalder et al., 2020); and sedimentology (Adelmann, 2001; DeCelles et al., 2015a; Schoenbohm & Carrapa, 2015; Zhou & Schoenbohm, 2015).

ranges) of the transect during the ~20–10 Ma time period, which is consistent with the decrease in upper-crustal shortening rate in these sectors predicted by the model.

Late Miocene–Quaternary back-arc basaltic lavas that erupted on the SPP during the Late Miocene to Quaternary have geochemical signatures consistent with lithosphere melts (Kay & Kay, 1993) and the presence of a garnet-pyroxenite source material (Ducea et al., 2013; Murray et al., 2015). Such magmas have been associated with the melting of an eclogitic drip following its detachment (Schoenbohm & Carrapa, 2015) and would therefore significantly post-date the formation of the garnet-pyroxenite root (DeCelles et al., 2015b). The region of Late Miocene back-arc volcanism is centered on the Calalaste range, where the earliest dated flows also occur (Haag et al., 2019; Kay et al., 1994; Schoenbohm & Carrapa, 2015), and where Early Miocene shortening was concentrated. It is therefore possible that an eclogitic root formed beneath the Calalaste range prior to ~7 Ma (specifically during the Early Miocene) and was the source of this volcanism.

Phase 3 of the models involves horizontal extension in the central sector of the plateau due to growth of the drip, while horizontal shortening propagates outward from the center to the edges of the plateau over an 8 Myr period (Figure 5.12a). Phase 3 corresponds to ~19 to 8 Ma on the SPP timescale (Figure 5.12c). The earliest evidence for horizontal extension in the SPP is located in the Antofalla region west of the Calalaste Range and likely reactivated a major reverse fault (the Antofalla Fault) as a normal or oblique normal fault (Tye et al., 2022). Sedimentary strata deposited in the hanging wall of this fault have been dated to 11 Ma (Adelmann, 2001; Kraemer et al., 1999), while the youngest strata in the footwall block are approximately 16 Ma (Adelmann, 2001; Kraemer et al., 1999). Half-graben extension therefore began after 16 Ma and had produced a significant hanging wall basin by 11 Ma. This timeframe is consistent with the model results, which predict significant upper-crustal extension beginning at 29 Myr, or ~14 Ma on the SPP timescale (Figure 5.12a). During this time period, the Antofalla High, a paleotopographic high and sediment source, was converted into the topographic low now occupied by the Salar de Antofalla basin (Kraemer et al., 1999; Voss, 2002).

During the period when the Antofalla region and Calalaste range were undergoing extension, the surrounding regions of the SPP were undergoing horizontal shortening (Figure 5.12c). Thrusting ~50 km west of the Calalaste range ~16–11 Ma (northern Salina del Fraile, McMillan & Schoenbohm, 2020) the exhumation of the Laguna Blanca range ~100 km to the east of the Calalaste range ~15–10 Ma (Zhou & Schoenbohm, 2015), and the deposition of syn-contractional strata in the Pasto Ventura region ~11 Ma (Schoenbohm & Carrapa, 2015) are explained by the outward propagation of shortening related to the growth of the drip in the model.

Phase 4 of the models involves the detachment of the drip at ~38 Myr. Detachment in our model involves significant, widespread upper-crustal extension (Figure 5.12a) as well as crustal heating (Figure 5.9), which agrees with existing studies throughout the SPP that hypothesize that upper-crustal extension, strike-slip, and volcanism are associated with the detachment foundering lithosphere (Kay & Kay, 1993; Kay et al., 1994; Kraemer et al., 1999). The volcanic

geochemistry, ages, and spatial pattern of back-arc volcanics in the Antofalla and Calalaste regions indicate significant mantle upwelling and crustal heating beginning ~8–7 Ma. Based mafic volcanics, silicic volcanism, and the beginning of extension in the SE corner of the SPP, Schoenbohm and Carrapa (2015) estimated an age of 7 Ma for drip detachment. Due to the short time scale of detachment in our model (~200 kyr), we do not show it as a time slice in Figure 5.12.

During phase 5 of the models, the remaining lithosphere recovers from the detachment of the drip. First, a pulse of extension due to gravitational collapse of the thickened crust propagates outward from the central plateau. Afterward, the western sector of the plateau experiences a return to horizontal shortening, while the eastern sector is characterized by a slow rate of horizontal extension. Phase 5 corresponds to ~7 Ma to Recent on the SPP timescale (Figure 5.12d).

For the central region of the SPP, it is not clear when the Calalaste range returned to horizontal shortening. Adelmann (2001) document thrusting of ~2–3 Ma Quaternary alluvial deposits over Paleozoic strata. Ignimbrites and flows dated to 3.6 Ma around the southwest margin of the Salar de Antofalla are deformed by horst-and-graben structures (Adelmann, 2001). These observations indicate that compressional kinematics resumed in the region between 3.6 and 2 Ma. Upper-crustal earthquake focal mechanisms from the SPP (Mulcahy et al., 2014) indicate that the Calalaste range is currently undergoing horizontal shortening; the eastern sector of the plateau, however, experiences significant horizontal extension (Figure 5.12d).

Pliocene to recent horizontal extension is well documented in the SE margin of the SPP (e.g., Allmendinger et al., 1989; Marrett et al., 1994; Schoenbohm & Strecker, 2009). Extensional stress is oriented roughly perpendicular to the margins of the plateau (Allmendinger et al., 1989; Schoenbohm & Strecker, 2009) in a manner consistent with gravitational spreading (Daxberger & Riller, 2015). The general pattern of ~N-S extension and ~E-W shortening of the margins of the plateau combined with ~E-W shortening and vertical extension in the interior of the plateau is consistent with the model results (Figure 5.12a). The latter is driven by tectonic compression transmitted from the boundary of the model, while the former is a result of contrasts in gravitational potential energy, which ultimately derive from patterns of crustal heating and thickening that were produced during the growth and detachment of the drip. Specifically, the westward migration of the drip relative to the overriding lithosphere produces asymmetric lithospheric thinning, which would have preferentially heated the eastern sector of the plateau and increased its buoyancy. High crustal temperatures in the SPP are documented by crustal shear velocity studies (Ward et al., 2013). These studies indicate that hot regions of partial melt surround the Calalaste range, which itself is relatively cool.

Crustal melting produced silicic volcanic centers, the largest of which, Cerro Galán, was active 6–2 Ma (Figure 5.1) (Cas et al., 2011; Folkes et al., 2011). As suggested by Wang et al. (2021), the patterns of crustal melting and silicic volcanism on the Southern Puna are broadly consistent with the thermal effects resulting from a lithospheric dripping event that migrated to the west

during its descent. In the models of Wang et al. (2021), westward migration of the drip is due to the influence of a subducting slab, which generates mantle corner flow. The slab also interacts with the descending drip, advecting it back eastward at depth. The net result of corner flow and subduction in Wang et al. (2021) is that the drip migrates approximately 100 km to the west of the eclogitic root, while maximum lithospheric thinning occurs approximately 50 km to the east of the root (Wang et al., 2021, and Figure 2 therein). In our models, westward migration is due to east-directed convergence in the lithosphere, causing the lithosphere to override the descending drip. In our models, the drip migrates approximately 50 km to the west, while maximum lithospheric occurs 50 km to the east of the eclogitic root. We therefore argue that our base model captures the first-order effects of drip migration and asymmetric lithospheric thinning that would be expected in models with a subducting plate. Although our models lack magmatism and melting, the broad zone of crustal heating on the eastern half of the plateau during Phase 5 (Figure 5.9b) is consistent with crustal melting and silicic volcanism beginning ~6 Ma.

5.6.3 Implications for the Central Andes

Dripping under a weak crust is capable of explaining the timing, location, and kinematics of upper crustal deformation of the Southern Puna Plateau during the Cenozoic. First, our numerical model explains out-of-sequence shortening in the interior of the Puna Plateau during the Late Oligocene to Miocene (Carrapa et al., 2005; Kraemer et al., 1999; Zhou et al., 2017) as due to the formation and subsidence of a negatively buoyant crustal root. Our model also suggests that foundering of this root generated upper-crustal horizontal extension in the interior plateau during the Middle to Late Miocene, as argued by (Tye et al., 2022). Finally, gravitational collapse of the thickened crustal welt following drip detachment may influence the Pliocene to Recent stress field of the Southern Puna Plateau, which is characterized by extension in the eastern sector (Schoenbohm & Strecker, 2009) and compression in the central sector (Mulcahy et al., 2014; Tye et al., 2022).

Our model also provides testable predictions of the timing and location of Cenozoic upper-crustal shortening (Figure 5.7). The model predicts that the periphery of the drip experienced uplift and exhumation during the Middle to Late Miocene (~16 to 8 Ma), which would have propagated outward from the center to the margins of the plateau until drip detachment ~7 Ma (Figure 5.7). Structures such as the Salina del Fraile anticline, Quebrada Honda range, Laguna Blanca range, and Chango Real range are predicted to have been exhumed by this outward-propagating episode of horizontal shortening. Existing sedimentary data for the Salina del Fraile (McMillan & Schoenbohm, 2020) and Laguna Blanca range (Zhou & Schoenbohm, 2015) indicate that horizontal shortening was indeed active during this time period, resulting in the deposition of syn-tectonic strata. Given that AFT ages in the region were largely reset during the Cretaceous to Early Cenozoic (Figure 5.12b), these predictions could be tested against a thermochronometry system with lower closure temperatures, such as apatite (U-Th)/He (AHe).

Although AHe data do not exist for most of the locations involved in this shortening episode, thermal modelling of AFT and AHe data from the Laguna Blanca range shows evidence of a cooling episode ~11 Ma (Zhou, 2015), which matches syn-contractional strata deposited in the nearby Pasto Ventura region (Carrapa & DeCelles, 2015; Zhou & Schoenbohm, 2015). This ~11 Ma episode of exhumation and sedimentation matches model predictions of shortening for the Laguna Blanca and Pasto Ventura regions.

Lithospheric dripping may also partially explain the ~60 km thickness of the Puna's crust and observed variation in Moho topography throughout the plateau (Beck & Zandt, 2002; Tassara & Echaurren, 2012). Balanced cross-sections of deformed Cenozoic strata are unable to account for the observed ~60 km thickness of the Puna crust (Kley & Monaldi, 1998). Besides upper-crustal shortening, other sources of crustal thickness that need to be taken into account include initial crustal thickness, flow of lower crust from adjacent regions, and magmatic addition (Allmendinger et al., 1997). Although lithospheric dripping would influence many of these considerations, its role in crustal thickening and shortening has been underappreciated, because most existing models deal with a strong crust that tends to resist deformation. Our model shows that lithospheric dripping under a weak crust can cause substantial crustal thickening, both in the form of upper-crustal shortening and lower crustal flow. Although our 2-D models are incapable of investigating differences in crustal strength along strike, previous modelling studies suggest that the hypothesized Arizaro drip involved a relatively strong crust, and would thus be incapable of thickening the crust by the same magnitude as observed in our models (Wang et al., 2015). Such a difference could contribute to the comparatively shallow Moho beneath the Arizaro region, even though the crust in both locations is thick in absolute terms (Figure 5.1).

This difference in crustal response between the Arizaro region and the Southern Puna would imply heterogeneous crustal or mantle strength between the two locations. In models for the Arizaro basin (Wang et al., 2015), strong crustal rheology is due to a strong mafic lower crustal composition and a relatively weak mantle lithosphere characterized by a wet olivine rheology, and our model with a strong lower crust yields a similar behavior (v7.2, Table 5.3). Given that there are no documented sutures or major tectonic boundaries between these two regions, we consider it unlikely that lithosphere composition differs drastically between them, so other sources of heterogeneity need to be considered. One clear difference between the two regions is the inherited tectonic features that would have affected crustal rheology since the beginning of the Cenozoic. First, a series of continental-scale, NW–SE-trending lineaments cuts through the Puna Plateau, but are more concentrated in the Southern Puna. As noted by DeCelles et al. (2015a), the Arizaro basin is cradled between two such lineaments. The Southern Puna region, on the other hand, is transected by several of these lineaments (Chernicoff et al., 2002). Although the tectonic setting and origin of the lineaments is not well known, they may represent Triassic rifting structures such as major normal faults, which were reactivated during Cenozoic shortening (Amilibia et al., 2008). As evidenced by the alignment of major

volcanic centers along these lineaments, they likely provided conduits for melting and metasomatism during the Cenozoic, which may have preferentially weakened the crust beneath the Southern Puna. Crustal shear velocity maxima (Bianchi et al., 2013; Ward et al., 2013) and the prevalence of back-arc volcanism discussed above may reflect a crust that is more thermally weakened than beneath the Arizaro region. This inference is supported by compilations of volcanic activity showing more prevalent volcanism in the Southern Puna region since 30 Ma (Trumbull et al., 2006). Other factors such as changes in slab dip during the Cenozoic, though less well-known, may have differently affected the crust and lithosphere of the two regions (Gianni et al., 2020; Kay & Coira, 2009). Finally, underthrusting of cold, strong lithosphere was more likely beneath the Arizaro region, due to the simple shear mode of orogenic deformation expressed at that latitude (DeCelles et al., 2011), while the Southern Puna Plateau may have accommodated a pure shear mode of deformation that does not require underthrusting of lithosphere from the east.

5.6.4 Alternative hypotheses

Although our models focus on lithospheric dripping, other geodynamic hypotheses are also viable for explaining the Cenozoic tectonics of the Puna Plateau. Lithospheric foundering in the form of delamination has long been proposed for the Puna Plateau (Beck et al., 2015; Kay et al., 1994). Although conceptually related to dripping, delamination models predict that observable effects such as surface uplift, deformation, heating, and volcanism, migrate laterally above a retreating lithospheric hinge zone (Beall et al., 2017; Göğüş & Pysklywec, 2008). Entrainment of lower crust above the hinge zone can yield crustal thickening and upper-crustal shortening (Krystopowicz & Currie, 2013), providing an alternate explanation for the Middle to Late Miocene exhumation of the eastern sector of the Southern Puna Plateau. The dripping hypothesis, on the other hand, predicts that a similar outward-migrating episode of shortening and exhumation would also occur in the western sector of the plateau, which is supported by uplift of the Antofalla High ~22 Ma (Adelmann, 2001; Voss, 2002) and northern Salina del Fraile ~16 Ma (McMillan & Schoenbohm, 2020) (Figure 5.12).

Neogene upper-crustal deformation and volcanism may also be explained by Middle to Late Miocene flat-slab subduction beneath the Puna Plateau (Ramos & Folguera, 2009) due to the subduction of the Juan Fernandez Ridge (JFR) hotspot track (Bello-González et al., 2018). Slab shallowing may have deformed the interior of the plateau during the Late Oligocene–Early Miocene (Gianni et al., 2020), producing a magmatic lull and slab steepening and rollback may have caused horizontal extension and volcanism to sweep through the plateau during the Late Miocene (Kay & Coira, 2009; Kay & Mpodozis, 2002). Flat-slab subduction may also result in the thinning of the mantle lithosphere (Axen et al., 2018; Kusky et al., 2014). It is currently unclear, however, how slab steepening could explain the outward growth of mafic volcanism from the Antofalla region in the Late Miocene (Haag et al., 2019; Schoenbohm & Carrapa, 2015) or the early onset of extension in the Antofalla region compared to the eastern sector of the Southern

Puna Plateau (Tye et al., 2022). Furthermore, the magmatic lull and deformation ascribed to flat-slab subduction in the Puna Plateau are minor in comparison to those in the modern flat-slab regions of the Andes (DeCelles et al., 2015b). Although shallow subduction may or may not be able to fully explain the geologic observations, we speculate that it may play a role in the production of eclogite in the lower crust or mantle lithosphere: shallow subduction results in significant cooling (Collo et al., 2017) and hydration (Porter et al., 2012) of the upper plate (Collo et al., 2017), which could drive the formation of eclogite in a thick crust or mantle lithosphere (Figure 5.4).

The Pliocene to Quaternary kinematics of deformation of the Southern Puna Plateau are often ascribed to orogen-parallel stretching (Allmendinger et al., 1989; Marrett et al., 1994; Riller & Oncken, 2003) or gravitational collapse or spreading (Daxberger & Riller, 2015; Schoenbohm & Strecker, 2009). Similarly, changes in relative plate motion (Pardo-Casas & Molnar, 1987) and plate coupling (Horton, 2018) may have played a role in the tectonic evolution Puna Plateau, especially the occurrence of horizontal extension during the Miocene, which could be due to a decrease in plate-boundary stresses. While these processes may explain the normal and strike-slip faulting in parts of the Puna Plateau, they do not explain the deformation history of the Antofalla region, namely Late Oligocene–Early Miocene shortening, Middle–Late Miocene horizontal extension, and Pliocene–Quaternary horizontal shortening (Tye et al., 2022). Gravitational collapse is also predicted by our numerical models of lithospheric dripping as a direct result of crustal thickening and mantle lithosphere (Figure 5.7). These factors point toward a need for more realistic models that include subduction (Currie et al., 2015; Wang et al., 2021), unsteady plate convergence rate, and changes in subduction angle through time.

5.6.5 Implications for crustal deformation and plateau uplift

Our models suggest that lithospheric dripping under a weak crust is capable of generating a high-elevation, low-relief plateau in a tectonic setting characterized by overall crustal shortening and thickening. Lower crustal thickening due to eclogitization and dripping increases the elevation of the overlying region and reduces its topographic relief. Relief is also reduced by the reactivation of contractional structures as extensional ones during the growth of the drip. Thinning of the mantle lithosphere and lower crust after drip detachment (Figure 5.6) contributes to isostatic uplift of the plateau. Based on these results, we suggest that lithospheric dripping may play a role in setting the topographic differences between the Puna Plateau and the broken foreland region immediately to the east and southeast (Figure 5.1). The Puna Plateau and broken foreland are interrupted by major mountain ranges and share a similar short-wavelength topography, but the plateau is more elevated and has lower relief at longer wavelengths (Strecker et al., 2009). If both regions were initially broken foreland settings during the early Cenozoic, lithospheric dripping beneath the Antofalla region could have converted that region into an orogenic plateau.

Our model sheds light on the geodynamic evolution of orogenic plateaus, especially those for which lithospheric foundering is hypothesized. In the Central Andes, multiple episodes of lithospheric foundering have been inferred beneath Altiplano Plateau (e.g., Garzione et al., 2006; Molnar & Garzione, 2007; Sundell et al., 2019). Paleoelevation studies throughout the Altiplano and Eastern Cordillera suggest that lithosphere removal resulted in a rapid increase in elevations (Garzione et al., 2014; Sundell et al., 2019). In Tibet, Oligocene hinterland basins may be due to lithospheric dripping in a manner analogous to the Arizaro basin, with sediments deposited syn-tectonically in a compressional basin (Kapp & DeCelles, 2019). Sedimentology studies in the Great Basin region of the Western U.S. documented evidence for hinterland basin development and volcanism related to lithospheric dripping beneath the Oligocene hinterland plateau, or Nevadaplano (Smith et al., 2017). In all of these cases, surface uplift is usually attributed to isostatic and flexural rebound following detachment of the lithosphere (e.g., Garzione et al., 2008). This pattern is distinct from the behavior observed in our models, in which plateau uplift is mainly accomplished due to eclogitization and the growth of a drip, not by its detachment. The relationship between surface uplift and drip detachment is key, because it places constraints on the relative strength of the continental crust. Numerical modelling studies predict that the crust must be significantly stronger than the foundering lithosphere, on the order of 10 to 100 times (Conrad & Molnar, 1997), in order for downward flexure and rebound to occur during dripping. If the crust was indeed strong during the uplift of the Altiplano, Nevadaplano, and pre-collisional Tibet, our results suggest that the weak crust inferred for the Southern Puna may be an outlier. Similar studies in the future should also consider the possibility that elevation gain is accomplished during the growth of the drip, rather than after its detachment. Our models also suggest that the surface uplift response to dripping may be highly variable depending on location relative to the center of the drip and proximity to major faults.

More relevant to the weak-crust dripping behavior we model here are instances where significant crustal thickening and/or extension have been ascribed to a Rayleigh–Taylor instability. For example, the Wallowa Mountains are hypothesized to have been uplifted due to lithosphere removal, with a circular region of uplifted topography flanked by a broad region of topographic subsidence (Hales et al., 2005). In Central Nevada, a seismic anomaly interpreted as a lithospheric drip by West et al. (2009) is associated with a broad, subdued topographic welt without evidence of crustal thickening (Dygert et al., 2019). Our models generally support the inference that these locations experienced dripping beneath a weak crust, but more numerical modelling is needed to address the specific tectonic settings of these locations, which are broadly extensional rather than compressional.

5.7 Conclusions

Lithospheric dripping under a weak crust results in predictable patterns of upper-crustal deformation. The formation of a negatively buoyant root beneath the center of an orogenic plateau significantly thickens the crust and accelerates upper-crustal shortening. Dripping of the root causes crustal flow, producing upper-crustal extension above the drip and upper-crustal shortening in the peripheral regions of the plateau. Growth of the drip also decreases topographic relief in the center of the plateau. After the drip detaches, the overthickened crust collapses gravitationally, sending a wave of extension through the plateau. As the crust deforms to reduce contrasts in gravitational potential energy, this zone of extension reduces in extent over time until the plateau is again under tectonic contraction. This sequence of events compares favorably with existing low-temperature thermochronology data, sedimentology studies, and the crustal thickness data from the Southern Puna Plateau. Our models suggest that dripping under a weak crust may be responsible for the relatively low relief, thick crust, and patterns of Cenozoic extension and shortening on the Puna Plateau. This result contrasts with previous studies of the Arizaro region of the Puna Plateau, where models suggest that dripping involved a strong crust that responded by downward flexure and upper-crustal shortening, rather than crustal flow and extension. Studies that infer lithospheric dripping beneath other regions, such as the Altiplano and Tibet, should consider the possibility that dripping involved a relatively weak crust. The weak-crust response to dripping may apply to regions such as the Wallowa Mountains (Hales et al., 2005) and central Nevada (Dygert et al., 2019; West et al., 2009), where crustal thickening and/or extension are observed.

Acknowledgments

This work was funded by an NSERC Discovery Grant and Accelerator Supplement to L. Schoenbohm. We thank the Computational Infrastructure for Geodynamics (geodynamics.org) which is funded by the National Science Foundation under award EAR-0949446 and EAR-1550901 for supporting the development of ASPECT.

References

Adelmann, D. (2001). *Känozoische Beckenentwicklung des zentralandinen Puna-Plateaus (NW-Argentinien): Das Gebiet um den Salar de Antofalla und ein Vergleich zur nördlichen Puna* (Doctoral dissertation). Freien Universität Berlin.

Allmendinger, R. W., & Gubbels, T. (1996). Pure and simple shear plateau uplift, Altiplano-Puna, Argentina and Bolivia. *Tectonophysics*, *259*(1-3), 1–13. https://doi.org/10.1016/0040-1951(96)00024-8

Allmendinger, R. W., Jordan, T. E., Kay, S. M., & Isacks, B. L. (1997). The evolution of the Altiplano-Puna Plateau of the Central Andes. *Annual Review of Earth and Planetary Sciences*, *25*, 139–174. https://doi.org/10.1146/annurev.earth.25.1.139

Allmendinger, R. W., Strecker, M. R., Eremchuk, J. E., & Francis, P. (1989). Neotectonic deformation of the southern Puna Plateau, northwestern Argentina. *Journal of South American Earth Sciences*, *2*(2), 111–130. https://doi.org/10.1016/0895-9811(89)90040-0

Amilibia, A., Sàbat, F., McClay, K. R., Muñoz, J. A., Roca, E., & Chong, G. (2008). The role of inherited tectono-sedimentary architecture in the development of the central Andean mountain belt: Insights from the Cordillera de Domeyko. *Journal of Structural Geology*, *30*(12), 1520–1539. https://doi.org/10.1016/j.jsg.2008.08.005

Austrheim, H. (1987). Eclogitization of lower crustal granulites by fluid migration through shear zones. *Earth and Planetary Science Letters*, 221–232.

Austrheim, H. (1990). The granulite-eclogite facies transition: A comparison of experimental work and a natural occurrence in the Bergen Arcs, western Norway. *Lithos*, *25*(1-3), 163–169. https://doi.org/10.1016/0024-4937(90)90012-P

Axen, G. J., van Wijk, J. W., & Currie, C. A. (2018). Basal continental mantle lithosphere displaced by flat-slab subduction. *Nature Geoscience*, *11*(12), 961–964. https://doi.org/10.1038/s41561-018-0263-9

Babeyko, A. Y., Sobolev, S. V., Trumbull, R. B., Oncken, O., & Lavier, L. L. (2002). Numerical models of crustal scale convection and partial melting beneath the Altiplano-Puna plateau. *Earth and Planetary Science Letters*, *199*(3-4), 373–388. https://doi.org/10.1016/S0012-821X(02)00597-6

Beall, A. P., Moresi, L., & Stern, T. (2017). Dripping or delamination? A range of mechanisms for removing the lower crust or lithosphere. *Geophysical Journal International*, (September), 671–692. https://doi.org/10.1093/gji/ggx202

Beaumont, C., Nguyen, M. H., Jamieson, R. A., & Ellis, S. (2006). Crustal flow modes in large hot orogens. *Geological Society Special Publication*, *268*, 91–145. https://doi.org/10.1144/GSL.SP.2006.268.01.05

Beck, S. L., & Zandt, G. (2002). The nature of orogenic crust in the central Andes. *Journal of Geophysical Research: Solid Earth*, *107*(B10), 2230. https://doi.org/10.1029/2000JB000124

Beck, S. L., Zandt, G., Ward, K. M., & Scire, A. (2015). Multiple styles and scales of lithospheric foundering beneath the Puna Plateau, central Andes. In *Geological Society of America Memoirs* (pp. 43–60). https://doi.org/10.1130/2015.1212(03)

Bello-González, J. P., Contreras-Reyes, E., & Arriagada, C. (2018). Predicted path for hotspot tracks off South America since Paleocene times: Tectonic implications of ridge-trench collision along the Andean margin. *Gondwana Research*, *64*, 216–234. https://doi.org/10.1016/j.gr.2018.07.008

Bianchi, M., Heit, B., Jakovlev, A., Yuan, X., Kay, S. M., Sandvol, E., Alonso, R. N., Coira, B., Brown, L. D., Kind, R., & Comte, D. (2013). Teleseismic tomography of the southern Puna plateau

in Argentina and adjacent regions. *Tectonophysics*, *586*, 65–83. https://doi.org/10.1016/j.tecto.2012.11.016

Bloch, E., Ibañez-Mejia, M., Murray, K. E., Vervoort, J., & Müntener, O. (2017). Recent crustal foundering in the Northern Volcanic Zone of the Andean arc: Petrological insights from the roots of a modern subduction zone. *Earth and Planetary Science Letters*, *476*, 47–58. https://doi.org/10.1016/j.epsl.2017.07.041

Bousquet, R., Goffé, B., Henry, P., Le Pichon, X., & Chopin, C. (1997). Kinematic, thermal and petrological model of the Central Alps: Lepontine metamorphism in the upper crust and eclogitisation of the lower crust. *Tectonophysics*, *273*(1-2), 105–127. https://doi.org/10.1016/S0040-1951(96)00290-9

Burov, E., & Gerya, T. (2014). Asymmetric three-dimensional topography over mantle plumes. *Nature*, *513*(7516), 85–89. https://doi.org/10.1038/nature13703

Canavan, R. R., Carrapa, B., Clementz, M. T., Quade, J., DeCelles, P. G., & Schoenbohm, L. M. (2014). Early cenozoic uplift of the Puna plateau, central andes, based on stable isotope paleoaltimetry of hydrated volcanic glass. *Geology*, *42*(5), 447–450. https://doi.org/10.1130/G35239.1

Carrapa, B., Adelmann, D., Hilley, G. E., Mortimer, E., Sobel, E. R., & Strecker, M. R. (2005). Oligocene range uplift and development of plateau morphology in the southern central Andes. *Tectonics*, *24*, TC4011. https://doi.org/10.1029/2004TC001762

Carrapa, B., & DeCelles, P. G. (2015). Regional exhumation and kinematic history of the central Andes in response to cyclical orogenic processes. *Memoir of the Geological Society of America*, *212*, 201–213. https://doi.org/10.1130/2015.1212(11)

Carrapa, B., Reyes-Bywater, S., Safipour, R., Sobel, E. R., Schoenbohm, L. M., DeCelles, P. G., Reiners, P. W., & Stockli, D. (2014). The effect of inherited paleotopography on exhumation of the central andes of NW Argentina. *Bulletin of the Geological Society of America*, *126*(1-2), 66–77. https://doi.org/10.1130/B30844.1

Cas, R. A., Wright, H. M., Folkes, C. B., Lesti, C., Porreca, M., Giordano, G., & Viramonte, J. G. (2011). The flow dynamics of an extremely large volume pyroclastic flow, the 2.08-Ma Cerro Galán Ignimbrite, NW Argentina, and comparison with other flow types. *Bulletin of Volcanology*, *73*(10), 1583–1609. https://doi.org/10.1007/s00445-011-0564-y

Castellanos, J. C., Humphreys, E., & Clayton, R. W. (2022). Evidence of mantle-based deformation across the western US. *Geophysical Research Letters*, e2021GL094854. https://doi.org/10.1029/2021GL094854

Chapman, J. B., Scoggin, S. H., Kapp, P., Carrapa, B., Ducea, M. N., Worthington, J., Oimahmadov, I., & Gadoev, M. (2018). Mesozoic to Cenozoic magmatic history of the Pamir. *Earth and Planetary Science Letters*, *482*(November 2017), 181–192. https://doi.org/10.1016/j.epsl.2017.10.041

Chernicoff, C. J., Richards, J. P., & Zappettini, E. O. (2002). Crustal lineament control on magmatism and mineralization in northwestern Argentina: Geological, geophysical, and

remote sensing evidence. *Ore Geology Reviews*, *21*(3-4), 127–155. https://doi.org/10.1016/S0169-1368(02)00087-2

Collo, G., Dávila, F. M., Teixeira, W., Nóbile, J. C., Sant' Anna, L. G., & Carter, A. (2017). Isotopic and thermochronologic evidence of extremely cold lithosphere associated with a slab flattening in the Central Andes of Argentina. *Basin Research*, *29*(1), 16–40. https://doi.org/10.1111/bre.12163

Conrad, C. P., & Molnar, P. (1997). The growth of Rayleigh-Taylor-type instabilities in the lithosphere for various rheological and density structures. *Geophysical Journal International*, *129*(1), 95–112. https://doi.org/10.1111/j.1365-246X.1997.tb00939.x

Coutand, I., Cobbold, P. R., De Urreiztieta, M., Gautier, P., Chauvin, A., Gapais, D., Rossello, E. A., & López-Gamundí, O. (2001). Style and history of Andean deformation, Puna plateau, northwestern Argentina. *Tectonics*, *20*(2), 210–234. https://doi.org/10.1029/2000TC900031

Currie, C. A., Ducea, M. N., DeCelles, P. G., & Beaumont, C. (2015). Geodynamic models of Cordilleran orogens: Gravitational instability of magmatic arc roots. In *Geological Society of America Memoirs* (pp. 1–22). https://doi.org/10.1130/2015.1212(01)

Daxberger, H., & Riller, U. (2015). Kinematics of Neogene to Recent upper-crustal deformation in the southern Central Andes (23°-28°S) inferred from fault-slip analysis: Evidence for gravitational spreading of the Puna Plateau. *Tectonophysics*, *642*(1), 16–28. https://doi.org/10.1016/j.tecto.2014.12.003

DeCelles, P. G., Carrapa, B., Horton, B. K., & Gehrels, G. E. (2011). Cenozoic foreland basin system in the central Andes of northwestern Argentina: Implications for Andean geodynamics and modes of deformation. *Tectonics*, *30*, TC6013. https://doi.org/10.1029/2011TC002948

DeCelles, P. G., Carrapa, B., Horton, B. K., McNabb, J., Gehrels, G. E., & Boyd, J. (2015a). The Miocene Arizaro Basin, central Andean hinterland: Response to partial lithosphere removal? In *Geological Society of America Memoirs* (pp. 359–386). https://doi.org/10.1130/2015.1212(18)

DeCelles, P. G., Ducea, M. N., Kapp, P., & Zandt, G. (2009). Cyclicity in Cordilleran orogenic systems. *Nature Geoscience*, *2*(4), 251–257. https://doi.org/10.1038/ngeo469

DeCelles, P. G., Zandt, G., Beck, S. L., Currie, C. A., Ducea, M. N., Kapp, P., Gehrels, G. E., Carrapa, B., Quade, J., & Schoenbohm, L. M. (2015b). Cyclical orogenic processes in the Cenozoic central Andes. In *Geological Society of America Memoirs* (pp. 459–490). https://doi.org/10.1130/2015.1212(22)

Ducea, M. N. (2001). The California arc: Thick granitic batholiths, eclogitic residues, lithospheric-scale thrusting, and magmatic flare-ups. *GSA Today*, *11*(11), 4–10. https://doi.org/10.1130/1052-5173(2001)011<0004:TCATGB>2.0.CO;2

Ducea, M. N., Seclaman, A. C., Murray, K. E., Jianu, D., & Schoenbohm, L. M. (2013). Mantle-drip magmatism beneath the Altiplano-Puna plateau, central Andes. *Geology*, *41*(8), 915–918. https://doi.org/10.1130/G34509.1

Dygert, N., Bernard, R. E., & Behr, W. M. (2019). Great Basin Mantle Xenoliths Record Active Lithospheric Downwelling Beneath Central Nevada. *Geochemistry, Geophysics, Geosystems*, *20*(2), 751–772. https://doi.org/10.1029/2018GC007834

Elkins-Tanton, L. T. (2007). Continental magmatism, volatile recycling, and a heterogeneous mantle caused by lithospheric gravitational instabilities. *Journal of Geophysical Research: Solid Earth*, *112*(3), 1–13. https://doi.org/10.1029/2005JB004072

Folkes, C. B., Wright, H. M., Cas, R. A., de Silva, S. L., Lesti, C., & Viramonte, J. G. (2011). A reappraisal of the stratigraphy and volcanology of the Cerro Galán volcanic system, NW Argentina. *Bulletin of Volcanology*, *73*(10), 1427–1454. https://doi.org/10.1007/s00445-011-0459-y

Furman, T., Nelson, W. R., & Elkins-Tanton, L. T. (2016). Evolution of the East African rift: Drip magmatism, lithospheric thinning and mafic volcanism. *Geochimica et Cosmochimica Acta*, *185*, 418–434. https://doi.org/10.1016/j.gca.2016.03.024

Garzione, C. N., Auerbach, D. J., Jin-Sook Smith, J., Rosario, J. J., Passey, B. H., Jordan, T. E., & Eiler, M. M. (2014). Clumped isotope evidence for diachronous surface cooling of the Altiplano and pulsed surface uplift of the Central Andes. *Earth and Planetary Science Letters*, *393*, 173–181. https://doi.org/10.1016/j.epsl.2014.02.029

Garzione, C. N., Hoke, G. D., Libarkin, J. C., Withers, S., MacFadden, B., Eiler, J., Ghosh, P., & Mulch, A. (2008). Rise of the Andes. *Science*, *320*(5881), 1304–1307. https://doi.org/10.1126/science.1148615

Garzione, C. N., Molnar, P., Libarkin, J. C., & MacFadden, B. J. (2006). Rapid late Miocene rise of the Bolivian Altiplano: Evidence for removal of mantle lithosphere. *Earth and Planetary Science Letters*, *241*(3-4), 543–556. https://doi.org/10.1016/j.epsl.2005.11.026

Gassmöller, R., Lokavarapu, H., Heien, E., Puckett, E. G., & Bangerth, W. (2018). Flexible and Scalable Particle-in-Cell Methods With Adaptive Mesh Refinement for Geodynamic Computations. *Geochemistry, Geophysics, Geosystems*, *19*(9), 3596–3604. https://doi.org/10.1029/2018GC007508

Gianni, G. M., García, H. P., Pesce, A., Lupari, M., González, M., & Giambiagi, L. (2020). Oligocene to present shallow subduction beneath the southern Puna plateau. *Tectonophysics*, *780*, 228402. https://doi.org/10.1016/j.tecto.2020.228402

Glerum, A., Thieulot, C., Fraters, M., Blom, C., & Spakman, W. (2018). Nonlinear viscoplasticity in ASPECT: Benchmarking and applications to subduction. *Solid Earth*, *9*, 267–294. https://doi.org/10.5194/se-9-267-2018

Göğüş, O. H., & Pysklywec, R. N. (2008). Near-surface diagnostics of dripping or delaminating lithosphere. *Journal of Geophysical Research: Solid Earth*, *113*(11), 1–11. https://doi.org/10.1029/2007JB005123

Göğüş, O. H., Pysklywec, R. N., şengör, A. M. C., & Gün, E. (2017). Drip tectonics and the enigmatic uplift of the Central Anatolian Plateau. *Nature Communications*, *8*(1), 1538. https://doi.org/10.1038/s41467-017-01611-3

Gouiza, M., & Naliboff, J. (2021). Rheological inheritance controls the formation of segmented rifted margins in cratonic lithosphere. *Nature Communications*, *12*(1), 1–9. https://doi.org/10.1038/s41467-021-24945-5

Haag, M. B., Baez, W. A., Sommer, C. A., Arnosio, J. M., & Filipovich, R. E. (2019). Geomorphology and spatial distribution of monogenetic volcanoes in the southern Puna Plateau (NW Argentina). *Geomorphology*, *342*, 196–209. https://doi.org/10.1016/j.geomorph.2019.06.008

Hacker, B. R., Abers, G. A., & Peacock, S. M. (2003). Subduction factory 1. Theoretical mineralogy, densities, seismic wave speeds, and H2O contents. *Journal of Geophysical Research: Solid Earth*, *108*(B1), 1–26. https://doi.org/10.1029/2001jb001127

Hacker, B. R., Kelemen, P. B., & Behn, M. D. (2015). Continental lower crust. *Annual Review of Earth and Planetary Sciences*, *43*, 167–205. https://doi.org/10.1146/annurev-earth-050212-124117

Hales, T. C., Abt, D. L., Humphreys, E. D., & Roering, J. J. (2005). A lithospheric instability origin for Columbia River flood basalts and Wallowa Mountains uplift in northeast Oregon. *Nature*, *438*(7069), 842–845. https://doi.org/10.1038/nature04313

He, Y., Puckett, E. G., & Billen, M. I. (2017). A discontinuous Galerkin method with a bound preserving limiter for the advection of non-diffusive fields in solid Earth geodynamics. *Physics of the Earth and Planetary Interiors*, *263*, 23–37. https://doi.org/10.1016/j.pepi.2016.12.001

Heister, T., Dannberg, J., Gassmöller, R., & Bangerth, W. (2017). High accuracy mantle convection simulation through modern numerical methods - II: Realistic models and problems. *Geophysical Journal International*, *210*(2), 833–851. https://doi.org/10.1093/gji/ggx195

Henriquez, S., DeCelles, P. G., Carrapa, B., Hughes, A., Davis, G. H., & Alvarado, P. (2020). Deformation history of the Puna plateau, Central Andes of northwestern Argentina. *Journal of Structural Geology*, 104133. https://doi.org/10.1016/j.jsg.2020.104133

Hirth, G., & Kohlstedt, D. (2003). Rheology of the upper mantle and the mantle wedge: A view from the experimentalists. In *Geophysical monograph series* (pp. 83–105). https://doi.org/10.1029/138GM06

Horton, B. K. (2018). Tectonic Regimes of the Central and Southern Andes: Responses to Variations in Plate Coupling During Subduction. *Tectonics*, *37*(2), 402–429. https://doi.org/10.1002/2017TC004624

Houseman, G. A., & Molnar, P. (1997). Gravitational (Rayleigh-Taylor) instability of a layer with non-linear viscosity and convective thinning of continental lithosphere. *Geophysical Journal International*, *128*(1), 125–150. https://doi.org/10.1111/j.1365-246X.1997.tb04075.x

Ibarra, F., Liu, S., Meeßen, C., Prezzi, C. B., Bott, J., Scheck-Wenderoth, M., Sobolev, S., & Strecker, M. R. (2019). 3D data-derived lithospheric structure of the Central Andes and its implications for deformation: Insights from gravity and geodynamic modelling. *Tectonophysics*, *766*(February), 453–468. https://doi.org/10.1016/j.tecto.2019.06.025

Isacks, B. L. (1988). Uplift of the central Andean Plateau and bending of the Bolivian Orocline. *Journal of Geophysical Research*, *93*(B4), 3211–3231. https://doi.org/10.1029/JB093iB04p03211

Jull, M., & Kelemen, P. B. (2001). On the conditions for lower crustal convective instability. *Journal of Geophysical Research: Solid Earth*, *106*(B4), 6423–6446. https://doi.org/10.1029/2000JB900357

Kapp, P., & DeCelles, P. G. (2019). Mesozoic–Cenozoic geological evolution of the Himalayan-Tibetan orogen and working tectonic hypotheses. *American Journal of Science*, *319*(3), 159–254. https://doi.org/10.2475/03.2019.01

Katsura, T., Yoneda, A., Yamazaki, D., Yoshino, T., Ito, E., Suetsugu, D., Bina, C., Inoue, T., Wiens, D., & Jellinek, M. (2010). Adiabatic temperature profile in the mantle. *Physics of the Earth and Planetary Interiors*, *183*(1-2), 212–218. https://doi.org/10.1016/j.pepi.2010.07.001

Kay, R. W., & Kay, S. M. (1993). Delamination and delamination magmatism. *Tectonophysics*, *219*(1-3), 177–189. https://doi.org/10.1016/0040-1951(93)90295-U

Kay, S. M., & Coira, B. L. (2009). Shallowing and steepening subduction zones, continental lithospheric loss, magmatism, and crustal fl ow under the Central Andean Altiplano-Puna Plateau. *Geological Society of America Memoir*, *204*, 229–259. https://doi.org/10.1130/2009.1204(11)

Kay, S. M., Coira, B., & Viramonte, J. (1994). Young mafic back arc volcanic rocks as indicators of continental lithospheric delamination beneath the Argentine Puna Plateau, central Andes. *Journal of Geophysical Research: Solid Earth*, *99*(B12), 24323–24339. https://doi.org/10.1029/94JB00896

Kay, S. M., & Mpodozis, C. (2002). Magmatism as a probe to the Neogene shallowing of the Nazca plate beneath the modern Chilean flat-slabs. *Journal of South American Earth Sciences*, *15*(1), 39–57. https://doi.org/10.1016/S0895-9811(02)00005-6

Kley, J., & Monaldi, C. R. (1998). Tectonic shortening and crustal thickness in the Central Andes: How good is the correlation-? *Geology*, *26*(8), 723–726. https://doi.org/10.1130/0091-7613(1998)026<0723:TSACTI>2.3.CO;2

Koptev, A., Burov, E., Gerya, T., Le Pourhiet, L., Leroy, S., Calais, E., & Jolivet, L. (2018). Plume-induced continental rifting and break-up in ultra-slow extension context: Insights from 3D numerical modeling. *Tectonophysics*, *746*, 121–137. https://doi.org/10.1016/j.tecto.2017.03.025

Kraemer, B., Adelmann, D., Alten, M., Schnurr, W., Erpenstein, K., Kiefer, E., Van Den Bogaard, P., & Görler, K. (1999). Incorporation of the Paleogene foreland into the Neogene Puna plateau: The Salar de Antofalla area, NW Argentina. *Journal of South American Earth Sciences*, *12*(2), 157–182. https://doi.org/10.1016/S0895-9811(99)00012-7

Kronbichler, M., Heister, T., & Bangerth, W. (2012). High accuracy mantle convection simulation through modern numerical methods. *Geophysical Journal International*, *191*(1), 12–29. https://doi.org/10.1111/j.1365-246X.2012.05609.x

Krystopowicz, N. J., & Currie, C. A. (2013). Crustal eclogitization and lithosphere delamination in orogens. *Earth and Planetary Science Letters*, *361*, 195–207. https://doi.org/10.1016/j.epsl.2012.09.056

Kusky, T. M., Windley, B. F., Wang, L., Wang, Z., Li, X., & Zhu, P. (2014). Flat slab subduction, trench suction, and craton destruction: Comparison of the North China, Wyoming, and Brazilian cratons. *Tectonophysics*, *630*(100), 208–221. https://doi.org/10.1016/j.tecto.2014.05.028

Levander, A., Schmandt, B., Miller, M. S., Liu, K., Karlstrom, K. E., Crow, R. S., Lee, C.-T. A., & Humphreys, E. D. (2011). Continuing Colorado plateau uplift by delamination-style convective lithospheric downwelling. *Nature*, *472*(7344), 461–465. https://doi.org/10.1038/nature10001

Lorinczi, P., & Houseman, G. A. (2009). Lithospheric gravitational instability beneath the South-east Carpathians. *Tectonophysics*, *474*(1-2), 322–336. https://doi.org/10.1016/j.tecto.2008.05.024

Lucassen, F., Becchio, R., Wilke, H. G., Franz, G., Thirlwall, M. F., Viramonte, J., & Wemmer, K. (2000). *Proterozoic-Paleozoic development of the basement of the Central Andes (18-26° S): A mobile belt of the South American craton* (tech. rep.).

Lucassen, F., Becchio, R., Harmon, R., Kasemann, S., Franz, G., Trumbull, R., Wilke, H. G., Romer, R. L., & Dulski, P. (2001). Composition and density model of the continental crust at an active continental margin - The Central Andes between 21° and 27°S. *Tectonophysics*, *341*(1-4), 195–223. https://doi.org/10.1016/S0040-1951(01)00188-3

Lucassen, F., Lewerenz, S., Franz, G., Viramonte, J., & Mezger, K. (1999). Metamorphism, isotopic ages and composition of lower crustal granulite xenoliths from the Cretaceous Salta Rift, Argentina. *Contributions to Mineralogy and Petrology*, *134*(4), 325–341. https://doi.org/10.1007/s004100050488

Marrett, R. A., Allmendinger, R. W., Alonso, R. N., & Drake, R. E. (1994). Late Cenozoic tectonic evolution of the Puna Plateau and adjacent foreland, northwestern Argentine Andes. *Journal of South American Earth Sciences*, *7*(2), 179–207. https://doi.org/10.1016/0895-9811(94)90007-8

Marrett, R., & Emerman, S. H. (1992). The relations between faulting and mafic magmatism in the Altiplano-Puna plateau (central Andes). *Earth and Planetary Science Letters*, *112*(1-4), 53–59. https://doi.org/10.1016/0012-821X(92)90006-H

McFarland, P. K., Bennett, R. A., Alvarado, P., & DeCelles, P. G. (2017). Rapid Geodetic Shortening Across the Eastern Cordillera of NW Argentina Observed by the Puna-Andes GPS Array. *Journal of Geophysical Research: Solid Earth*, *122*(10), 8600–8623. https://doi.org/10.1002/2017JB014739

McMillan, M., & Schoenbohm, L. M. (2020). Large-scale Cenozoic wind erosion in the Puna Plateau: The Salina del Fraile Depression. *Journal of Geophysical Research: Earth Surface*. https://doi.org/10.1029/2020JF005682

McMillan, M., Tye, A. R., & Schoenbohm, L. M. (in prep.). Geodynamics of continental back-arcs: Lithospheric foundering under a weak crust in the Central Andes. *Geosphere*.

Molnar, P. (2015). Gravitational instability of mantle lithosphere and core complexes. *Tectonics*, *34*(3), 478–487. https://doi.org/10.1002/2014TC003808

Molnar, P., & Bendick, R. (2019). Seismic Moments of Intermediate-Depth Earthquakes Beneath the Hindu Kush: Active Stretching of a Blob of Sinking Thickened Mantle Lithosphere? *Tectonics*, *38*(5), 1651–1665. https://doi.org/10.1029/2018TC005336

Molnar, P., & Garzione, C. N. (2007). Bounds on the viscosity coefficient of continental lithosphere from removal of mantle lithosphere beneath the Altiplano and Eastern Cordillera. *Tectonics*, *26*(2). https://doi.org/10.1029/2006TC001964

Molnar, P., & Houseman, G. A. (2004). The effects of buoyant crust on the gravitational instability of thickened mantle lithosphere at zones of intracontinental convergence. *Geophysical Journal International*, *158*(3), 1134–1150. https://doi.org/10.1111/j.1365-246X.2004.02312.x

Molnar, P., & Houseman, G. A. (2013). Rayleigh-Taylor instability, lithospheric dynamics, surface topography at convergent mountain belts, and gravity anomalies. *Journal of Geophysical Research: Solid Earth*, *118*(5), 2544–2557. https://doi.org/10.1002/jgrb.50203

Morfulis, M., Báez, W., Retamoso, S., Bardelli, L., Filipovich, R., & Sommer, C. A. (2020). Quantitative spatial distribution analysis of mafic monogenic volcanism in the southern Puna, Argentina: Implications for magma production rates and structural control during its ascent. *Journal of South American Earth Sciences*, *104*(September). https://doi.org/10.1016/j.jsames.2020.102852

Mulcahy, P., Chen, C., Kay, S. M., Brown, L. D., Isacks, B. L., Sandvol, E., Heit, B., Yuan, X., & Coira, B. L. (2014). Central Andean mantle and crustal seismicity beneath the Southern Puna plateau and the northern margin of the Chilean-Pampean flat slab. *Tectonics*, *33*(8), 1636–1658. https://doi.org/10.1002/2013TC003393

Murray, K. E., Ducea, M. N., & Schoenbohm, L. M. (2015). Foundering-driven lithospheric melting: The source of central Andean mafic lavas on the Puna Plateau (22°S–27°S). In *Geological Society of America Memoirs* (pp. 139–166). https://doi.org/10.1130/2015.1212(08)

Niemeyer, H., Götze, J., Sanhueza, M., & Portilla, C. (2018). The Ordovician magmatic arc in the northern Chile-Argentina Andes between 21° and 26° south latitude. *Journal of South American Earth Sciences*, *81*, 202–214. https://doi.org/10.1016/j.jsames.2017.11.016

Palma, M. A., Brisson, I., & Vujovich, G. (1990). Geológia del bloque de la Quebrada Honda , Puna Cartamarqueña. *Asociacion Geologica Aregentina, Revista*, *45*(1-2), 145–158.

Pardo-Casas, F., & Molnar, P. (1987). Relative motion of the Nazca (Farallon) and South American plates since Late Cretaceous time. *Tectonics*, *6*(3), 233–248. https://doi.org/10.1029/TC006i003p00233

Paterson, S. R., & Ducea, M. N. (2015). Arc magmatic tempos: Gathering the evidence. *Elements*, *11*(2), 91–98. https://doi.org/10.2113/gselements.11.2.91

Porter, R., Gilbert, H., Zandt, G., Beck, S. L., Warren, L., Calkins, J., Alvarado, P., & Anderson, M. (2012). Shear wave velocities in the Pampean flat-slab region from Rayleigh wave tomography: Implications for slab and upper mantle hydration. *Journal of Geophysical Research B: Solid Earth*, *117*(11), 1–21. https://doi.org/10.1029/2012JB009350

Pysklywec, R. N., & Cruden, A. R. (2004). Coupled crust-mantle dynamics and intraplate tectonics: Two-dimensional numerical and three-dimensional analogue modeling. *Geochemistry, Geophysics, Geosystems*, *5*, Q10003. https://doi.org/10.1029/2004GC000748

Quade, J., Dettinger, M. P., Carrapa, B., DeCelles, P. G., Murray, K. E., Huntington, K. W., Cartwright, A., Canavan, R. R., Gehrels, G. E., & Clementz, M. (2015). The growth of the central Andes, 22° S-26° S. In *Geological Society of America Memoirs* (pp. 277–308).

Ramos, V. A., & Folguera, A. (2009). Andean flat-slab subduction through time. *Geological Society, London, Special Publications*, *327*(1), 31–54. https://doi.org/10.1144/SP327.3

Ranalli, G., & Murphy, D. C. (1987). Rheological stratification of the lithosphere. *Tectonophysics*, *132*(4), 281–295. https://doi.org/10.1016/0040-1951(87)90348-9

Richards, J. P., Ullrich, T., & Kerrich, R. (2006). The Late Miocene-Quaternary Antofalla volcanic complex, southern Puna, NW Argentina: Protracted history, diverse petrology, and economic potential. *Journal of Volcanology and Geothermal Research*, *152*(3-4), 197–239. https://doi.org/10.1016/j.jvolgeores.2005.10.006

Riller, U., & Oncken, O. (2003). Growth of the central Andean plateau by tectonic segmentation is controlled by the gradient in crustal shortening. *Journal of Geology*, *111*(3), 367–384. https://doi.org/10.1086/373974

Risse, A., Trumbull, R. B., Coira, B., Kay, S. M., & van den Bogaard, P. (2008). 40Ar/39Ar geochronology of mafic volcanism in the back-arc region of the southern Puna plateau, Argentina. *Journal of South American Earth Sciences*, *26*(1), 1–15. https://doi.org/10.1016/j.jsames.2008.03.002

Rose, I., Buffett, B., & Heister, T. (2017). Stability and accuracy of free surface time integration in viscous flows. *Physics of the Earth and Planetary Interiors*, *262*, 90–100. https://doi.org/10.1016/j.pepi.2016.11.007

Rutter, E. H., & Brodie, K. H. (2004). Experimental grain size-sensitive flow of hot-pressed Brazilian quartz aggregates. *Journal of Structural Geology*, *26*(11), 2011–2023. https://doi.org/10.1016/j.jsg.2004.04.006

Saleeby, J. B., & Foster, Z. (2004). Topographic response to mantle lithosphere removal in the southern Sierra Nevada region, California. *Geology*, *32*(3), 245–248. https://doi.org/10.1130/G19958.1

Schnurr, W. B. W., Risse, A., Trumbull, R. B., & Munier, K. (2006). Digital Geological Map of the Southern and Central Puna Plateau, NW Argentina. In *The andes* (pp. 563–564). https://doi.org/10.1007/978-3-540-48684-8_29

Schoenbohm, L. M., & Carrapa, B. (2015). Miocene-Pliocene shortening, extension, and mafic magmatism support small-scale lithospheric foundering in the central Andes, NW Ar-

gentina. *Geological Society of America Memoirs*, *212*(09), 167–180. https://doi.org/10.1130/2015.1212(09)

Schoenbohm, L. M., & Strecker, M. R. (2009). Normal faulting along the southern margin of the Puna Plateau, northwest Argentina. *Tectonics*, *28*(5). https://doi.org/10.1029/2008TC002341

Scire, A., Biryol, C. B., Zandt, G., & Beck, S. L. (2015). Imaging the Nazca slab and surrounding mantle to 700 km depth beneath the central Andes (18°S to 28°S). *Memoir of the Geological Society of America*, *212*(02), 23–41. https://doi.org/10.1130/2015.1212(02)

Seggiaro, R., Becchio, R., Pereyra, F., & Martínez, L. (2007). *Hoja Geológica 2569-IV, Antofalla*. Servicio Geológico Minero Argentino.

Smith, M. E., Cassel, E. J., Jicha, B. R., Singer, B. S., & Canada, A. S. (2017). Hinterland drainage closure and lake formation in response to middle Eocene Farallon slab removal, Nevada, U.S.A. *Earth and Planetary Science Letters*, *479*, 156–169. https://doi.org/10.1016/j.epsl.2017.09.023

Stalder, N. F., Herman, F., Fellin, M. G., Coutand, I., Aguilar, G., Reiners, P. W., & Fox, M. (2020). The relationships between tectonics, climate and exhumation in the Central Andes (18–36°S): Evidence from low-temperature thermochronology. *Earth-Science Reviews*, *210*(October 2019), 103276. https://doi.org/10.1016/j.earscirev.2020.103276

Steinberger, B., & Calderwood, A. R. (2006). Models of large-scale viscous flow in the Earth's mantle with constraints from mineral physics and surface observations. *Geophysical Journal International*, *167*(3), 1461–1481. https://doi.org/10.1111/j.1365-246X.2006.03131.x

Strecker, M. R., Alonso, R. N., Bookhagen, B., Carrapa, B., Coutand, I., Hain, M. P., Hilley, G. E., Mortimer, E., Schoenbohm, L. M., & Sobel, E. R. (2009). Does the topographic distribution of the central Andean Puna Plateau result from climatic or geodynamic processes? *Geology*, *37*(7), 643–646. https://doi.org/10.1130/G25545A.1

Sundell, K. E., Saylor, J. E., Lapen, T. J., & Horton, B. K. (2019). Implications of variable late Cenozoic surface uplift across the Peruvian central Andes. *Scientific Reports*, *9*(1), 1–12. https://doi.org/10.1038/s41598-019-41257-3

Tassara, A., & Echaurren, A. (2012). Anatomy of the Andean subduction zone: Three-dimensional density model upgraded and compared against global-scale models. *Geophysical Journal International*, *189*(1), 161–168. https://doi.org/10.1111/j.1365-246X.2012.05397.x

Tassara, A., Götze, H. J., Schmidt, S., & Hackney, R. (2006). Three-dimensional density model of the Nazca plate and the Andean continental margin. *Journal of Geophysical Research: Solid Earth*, *111*(9), 1–26. https://doi.org/10.1029/2005JB003976

Trumbull, R. B., Riller, U., Oncken, O., Scheuber, E., Munier, K., & Hongn, F. D. (2006). The time-space distribution of Cenozoic volcanism in the South-Central Andes: A new data compilation and some tectonic implications. In *The andes* (pp. 29–43). https://doi.org/10.1023/A:1020794814975

Tye, A. R., McMillan, M., Schoenbohm, L. M., & Zhou, R. (2022). Late Cenozoic extensional formation of the Antofalla depression, southern Puna plateau, Argentina: An effect of lithospheric foundering? *Tectonics*.

Voss, R. (2002). Cenozoic stratigraphy of the southern Salar de Antofalla region, northwestern Argentina. *Andean Geology*, *29*(2), 167189. https://doi.org/10.4067/S0716-02082002000200002

Wang, H., & Currie, C. A. (2017). Crustal deformation induced by mantle dynamics: Insights from models of gravitational lithosphere removal. *Geophysical Journal International*, *210*(2), 1070–1091. https://doi.org/10.1093/gji/ggx209

Wang, H., Currie, C. A., & DeCelles, P. G. (2015). Hinterland basin formation and gravitational instabilities in the central Andes: Constraints from gravity data and geodynamic models. In *Geological Society of America Memoirs* (pp. 387–406). https://doi.org/10.1130/2015.1212(19)

Wang, H., Currie, C. A., & DeCelles, P. G. (2021). Coupling between lithosphere removal and mantle flow in the central Andes. *Geophysical Research Letters*, (Figure 1), 1–11. https://doi.org/10.1029/2021gl095075

Ward, K. M., Porter, R. C., Zandt, G., Beck, S. L., Wagner, L. S., Minaya, E., & Tavera, H. (2013). Ambient noise tomography across the Central Andes. *Geophysical Journal International*, *194*(3), 1559–1573. https://doi.org/10.1093/gji/ggt166

West, J. D., Fouch, M. J., Roth, J. B., & Elkins-Tanton, L. T. (2009). Vertical mantle flow associated with a lithospheric drip beneath the Great Basin. *Nature Geoscience*, *2*(6), 439–444. https://doi.org/10.1038/ngeo526

Wilks, K. R., & Carter, N. L. (1990). Rheology of some continental lower crustal rocks. *Tectonophysics*, *182*(1-2), 57–77. https://doi.org/10.1016/0040-1951(90)90342-6

Zandt, G., Gilbert, H., Owens, T. J., Ducea, M. N., Saleeby, J. B., & Jones, C. H. (2004). Active foundering of a continental arc root beneath the southern Sierra Nevada in California. *Nature*, *431*(7004), 41–46. https://doi.org/10.1038/nature02847

Zhou, R. (2015). *Regional Deformation and Dynamic Processes of the Southern Puna Plateau, Central Andes* (Doctoral dissertation). University of Toronto.

Zhou, R., & Schoenbohm, L. M. (2015). Late Miocene upper-crustal deformation within the interior of the southern Puna Plateau, central Andes. *Lithosphere*, *7*(3), 336–352. https://doi.org/10.1130/L396.1

Zhou, R., Schoenbohm, L. M., Sobel, E. R., Carrapa, B., & Davis, D. W. (2016). Sedimentary record of regional deformation and dynamics of the thick-skinned southern Puna Plateau, central Andes (26-27°S). *Earth and Planetary Science Letters*, *433*, 317–325. https://doi.org/10.1016/j.epsl.2015.11.012

Zhou, R., Schoenbohm, L. M., Sobel, E. R., Davis, D. W., & Glodny, J. (2017). New constraints on orogenic models of the southern Central Andean Plateau: Cenozoic basin evolution and bedrock exhumation. *Bulletin of the Geological Society of America*, *129*(1-2), 152–170. https://doi.org/10.1130/B31384.1

6 Conclusions

This thesis the geomorphology and geodynamics of orogenic plateaus through the lens one of the largest active orogenic plateaus, the Puna Plateau of NW Argentina. In doing so, it contributes to our understanding of the uplift of the Puna Plateau during the Paleogene, extensional deformation of the plateau during the Miocene–Pliocene, and it investigates the geodynamic drivers of these processes.

The major findings of the thesis are as follows:

- The Southern Puna Plateau was a broken foreland basin during the Eocene to Oligocene when the Sierra de Calalaste and Sierra de la Quebrada Honda were uplifted.
- The Antofalla region was incorporated into a retrovergent wedge, which included the Sierra de Calalaste and the Salina del Fraile, during the Late Oligocene to Middle Miocene.
- Late Miocene to Quaternary strata were deposited in a hanging-wall basin that developed due to a major episode of transient extension in the Antofalla region.
- This episode of transient extension is responsible for the formation of topographic depression now occupied by the Salar de Antofalla.
- The Salina del Fraile depression is erosional, and was eroded by wind over the last 8.2 Ma.
- Streamlined landforms around the Salina del Fraile are analogous to those observed on Mars.
- The response of a weak crust during lithospheric dripping is less well-known than that of a strong crust, but synthesis of existing studies suggests that it is a viable explanation for many geological phenomena.
- Weak-crust dripping results in surface uplift and upper-crustal extension, rather than subsidence and compression, and is predicted in regions with a weak (felsic) crust overlying a strong lithosphere.
- Observations of Southern Puna upper-crustal shortening followed by a transient episode of extension are consistent with the kinematics predicted by lithospheric dripping under a weak crust.

In summary, this thesis shows that lithospheric dripping can produce transient extension of a weak, granitic crust, even in convergent tectonic settings, which may explain much of the Cenozoic deformation and sedimentation of the Southern Puna Plateau. Combined with the literature cited throughout this thesis, this work suggests that the buildup and dripping of dense eclogitic roots may influence the deformation, uplift, and overall morphology of orogenic plateaus (DeCelles et al., 2009).

6.1 Remaining questions and research opportunities

First, although this thesis presents evidence (mountain range exhumation ages) for deformation of the Southern Puna as a broken foreland during the Paleogene, this is not a widely accepted conclusion. Some studies infer that the region was a contiguous foreland basin generated by lithospheric flexure (Zhou et al., 2016; Zhou et al., 2017). Flexural foreland basins tend to sit at relatively low elevations of 0 to 1 km above sea level. Other studies argue that the region had already obtained >3 km elevations by the Late Eocene (Canavan et al., 2014; Quade et al., 2015). The key to understanding the tectonic setting during this time is the Paleogene Quiñoas Formation (and its lateral equivalents deposited during the Eocene–Early Oligocene): the Quiñoas Formation is the sedimentary unit identified as a foreland basin deposit (Kraemer et al., 1999; Zhou et al., 2017), but it is also the same unit for which paleoelevation data indicate >3 km elevation (Canavan et al., 2014; Quade et al., 2015). Lacking any modern foreland basins sitting at such high elevations, these two interpretations seem to be mutually exclusive. The argument presented in Chapter 3 that the region was a broken foreland basin offers one potential solution to this problem. Broken foreland or intermontane basins can sit at relatively high elevations, but their semi-contiguous sediments cover a large area, similar to that of a flexural foreland basin. Future work should study this sedimentary unit in more detail where exposure is good (e.g., Cerro Campo Negro, Salina del Fraile, Antofagasta de la Sierra), and in more locations throughout the Southern Puna region, because better depositional age control is also needed for these hypotheses. The depositional age of the fine-grained fluvio-lacustrine member near the base of the Quiñoas Formation is particularly poorly constrained.

The observation that apatite fission track ages are predominantly Paleogene, even from major mountain ranges, suggests that exhumation of the Southern Puna was relatively slow. The arid climate that prevailed for much of the Cenozoic (e.g., Quade et al., 2015) also supports the notion that erosion rates were relatively low during deformation of the plateau. Thermochronometers with lower closure temperatures, such as apatite (U-Th)/He (AHe), may therefore be useful for documenting Neogene or later exhumation of major mountain ranges. Such data may also be useful for testing the hypothesis that the Antofalla Fault, a reverse fault, was reactivated as a normal or oblique normal fault, as footwall exhumation may be recorded in the AHe system. AHe may also record erosional exhumation of the Salina del Fraile, inferred based on geologic relationships to have occurred since at least 8.2 Ma.

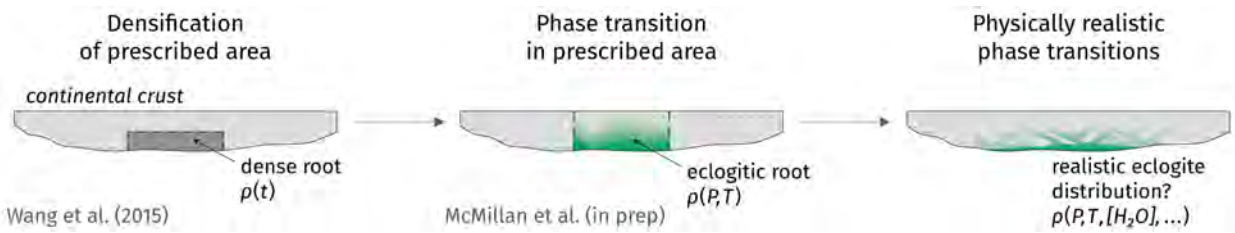

Figure 6.1: Eclogitization in geodynamic models. Illustration of how current geodynamic models simplify the increase in density (ρ) due to eclogitization as a function of time, pressure, and temperature. An acceptable model would consider the concentrations of reactants and products, especially water [H_2O], but models currently lack fluid migration.

The geodynamic models of this thesis suggest that eclogite production and lithospheric dripping can play a role in the uplift of an orogenic plateau. However, eclogite was only allowed to occur in the center of a weakened region of crust in the models, all but dictating that a plateau would form there. This simplification is due to a lack of realistic eclogitization schemes. Field observations of eclogite suggest that it is prone to occur in fluid-rich settings such as shear zones, fracture zones, and other damage zones (Austrheim, 1987, 1990), but geodynamic models rarely incorporate fluidization. Future research should aim to parameterize fluid circulation and more realistic phase transitions in the lower crust (Figure 6.1). Additionally, the fate of slab fluids, especially during episodes of flat slab subduction should be thoroughly investigated by numerical models as potential drivers of eclogite production and dripping.

The arid climate of orogenic plateaus suggests intriguing hypotheses for climate-tectonics interactions. As shown here, aridity reduces the efficiency fluvial and glacial erosion, limiting the rate at which crustal mass can be removed from an orogen. It is plausible that the accumulation of crustal mass due to tectonic thickening and aridity-limited erosion also plays a role in the production and foundering of eclogite (Pelletier et al., 2010). Lithospheric dripping beneath the Puna Plateau may partially be a result of the wide broken foreland region that existed prior to the Andean orogeny (as argued in Chapter 3) in the following sense. Intra-foreland uplifts in the Central Andes produce orographic rain shadows to the west. The interior of the plateau is hyperarid in part because of multiple tall mountain ranges flanking it to the east, blocking moisture from the Atlantic (Strecker et al., 2007). If the region experienced aridity as early as 35 Ma (Quade et al., 2015), this may have contributed to reduced erosion rates and preferential crustal thickening in the Puna region throughout the Cenozoic compared to more humid regions to the east. This could have led to eclogitization of the lower crust beneath the Puna region, while mass was more effectively removed from regions further east. Geodynamic models similar to those of Chapter 5, but incorporating surface processes or spatially variable erosion rates, could be used to explore this hypothesis.

Questions also remain concerning the weak-crust dripping hypothesis and its applicability to other locations. The literature synthesis and geodynamic models presented here suggest that lithospheric dripping beneath a weak crust produces predictable patterns of upper-crustal

deformation. Specifically, it predicts that a transient pulse of extension is associated with drip growth, and it predicts that coeval extension and contraction can occur in the same region. These heterogeneities arise due to the dynamic stresses and crustal flow associated with dripping. The concept may thus be applicable to regions where syn-convergent extension is observed, and where lithospheric dripping is a viable hypothesis. One such region is the Central Anatolian Plateau (Göğüş et al., 2017), and the applicability of this concept to other regions should be explored. To do so, it would be beneficial to explore the full range of parameters (crustal compositions, temperature, radiogenic heating) that yield a weak-crust drip using geodynamic models. Models should also investigate different boundary stresses (e.g., horizontal extension) so that the concept can be applied to regions such as the Great Basin, where a similar style of dripping has been hypothesized (West et al., 2009).

References

Austrheim, H. (1987). Eclogitization of lower crustal granulites by fluid migration through shear zones. *Earth and Planetary Science Letters*, 221–232.

Austrheim, H. (1990). The granulite-eclogite facies transition: A comparison of experimental work and a natural occurrence in the Bergen Arcs, western Norway. *Lithos*, *25*(1-3), 163–169. https://doi.org/10.1016/0024-4937(90)90012-P

Canavan, R. R., Carrapa, B., Clementz, M. T., Quade, J., DeCelles, P. G., & Schoenbohm, L. M. (2014). Early cenozoic uplift of the Puna plateau, central andes, based on stable isotope paleoaltimetry of hydrated volcanic glass. *Geology*, *42*(5), 447–450. https://doi.org/10.1130/G35239.1

DeCelles, P. G., Ducea, M. N., Kapp, P., & Zandt, G. (2009). Cyclicity in Cordilleran orogenic systems. *Nature Geoscience*, *2*(4), 251–257. https://doi.org/10.1038/ngeo469

Göğüş, O. H., Pysklywec, R. N., şengör, A. M. C., & Gün, E. (2017). Drip tectonics and the enigmatic uplift of the Central Anatolian Plateau. *Nature Communications*, *8*(1), 1538. https://doi.org/10.1038/s41467-017-01611-3

Kraemer, B., Adelmann, D., Alten, M., Schnurr, W., Erpenstein, K., Kiefer, E., Van Den Bogaard, P., & Görler, K. (1999). Incorporation of the Paleogene foreland into the Neogene Puna plateau: The Salar de Antofalla area, NW Argentina. *Journal of South American Earth Sciences*, *12*(2), 157–182. https://doi.org/10.1016/S0895-9811(99)00012-7

Pelletier, J. D., DeCelles, P. G., & Zandt, G. (2010). Relationships among climate, erosion, topography, and delamination in the Andes: A numerical modeling investigation. *Geology*, *38*(3), 259–262. https://doi.org/10.1130/G30755.1

Quade, J., Dettinger, M. P., Carrapa, B., DeCelles, P. G., Murray, K. E., Huntington, K. W., Cartwright, A., Canavan, R. R., Gehrels, G. E., & Clementz, M. (2015). The growth of the central Andes, 22° S-26° S. In *Geological Society of America Memoirs* (pp. 277–308).

Strecker, M. R., Alonso, R. N., Bookhagen, B., Carrapa, B., Hilley, G., Sobel, E. R., & Trauth, M. (2007). Tectonics and Climate of the Southern Central Andes. *Annual Review of Earth and Planetary Sciences*, *35*(1), 747–787. https://doi.org/10.1146/annurev.earth.35.031306.140158

West, J. D., Fouch, M. J., Roth, J. B., & Elkins-Tanton, L. T. (2009). Vertical mantle flow associated with a lithospheric drip beneath the Great Basin. *Nature Geoscience*, *2*(6), 439–444. https://doi.org/10.1038/ngeo526

Zhou, R., Schoenbohm, L. M., Sobel, E. R., Carrapa, B., & Davis, D. W. (2016). Sedimentary record of regional deformation and dynamics of the thick-skinned southern Puna Plateau, central Andes (26-27°S). *Earth and Planetary Science Letters*, *433*, 317–325. https://doi.org/10.1016/j.epsl.2015.11.012

Zhou, R., Schoenbohm, L. M., Sobel, E. R., Davis, D. W., & Glodny, J. (2017). New constraints on orogenic models of the southern Central Andean Plateau: Cenozoic basin evolution and bedrock exhumation. *Bulletin of the Geological Society of America*, *129*(1-2), 152–170. https://doi.org/10.1130/B31384.1

A Supporting information for Chapter 3

Tables S1 to S4 are not printed due to length. They are available online at the Scholars Portal Dataverse (https://doi.org/10.5683/SP3/XTFUJP).

Tectonics

Supporting Information for

Eocene to Quaternary deformation of the southern Puna Plateau: Thermochronology, geochronology, and structural geology of an Andean hinterland basin (NW Argentina)

M. McMillan[1], L. M. Schoenbohm[1,2], A. R. Tye[3], M. F. McMillan[4], R. Zhou[5]

[1]University of Toronto, Department of Earth Sciences, Toronto, Ontario, M5S 3B1, Canada.
[2]University of Toronto Mississauga, Department of Chemical and Physical Sciences, Mississauga, Ontario, L5L 1C6, Canada.
[3]Dixie State University, Department of Earth and Environmental Sciences, St. George, Utah, 84770, USA.
[4]University of Melbourne, School of Earth Sciences, Parkville, Victoria 3010, Australia.
[5]University of Queensland, School of Earth and Environmental Sciences, Brisbane, Queensland 4072, Australia.

Contents of this file

Figures S1 to S8
Table S5 to S6

Additional Supporting Information (Files uploaded separately)

Captions for Tables S1 to S4

Introduction

Figures include maps, photographs, and plots of data supporting the manuscript. Figure S1 is a large format geologic map and cross-section. Figures S2 and S3 depict annotated aerial imagery of sample locations and geologic interpretations. Figure S4 is a photograph of fault traces.

Table S1 gives the full results of maximum depositional age determination using zircon U-Pb ages and "detritalPy" software, following the methods described in the text. Table S2 contains all of the structural measurements collected during field work in the Antofalla region, primarily bedding plane orientations. Table S3 gives a summary of the results of apatite fission track analysis using the methods described in the text and in Table S3. Table S4 details the single-grain apatite data for each sample. Table S5 summarizes the parameters and results of HeFTy models as described in the text. Table S6 summarizes stratal thicknesses of geologic formations in the Antofalla region, which were used in construction of the cross-section.

All data generated in creating this manuscript is available in the attached spreadsheet files and online (https://doi.org/10.5683/SP3/XTFUJP).

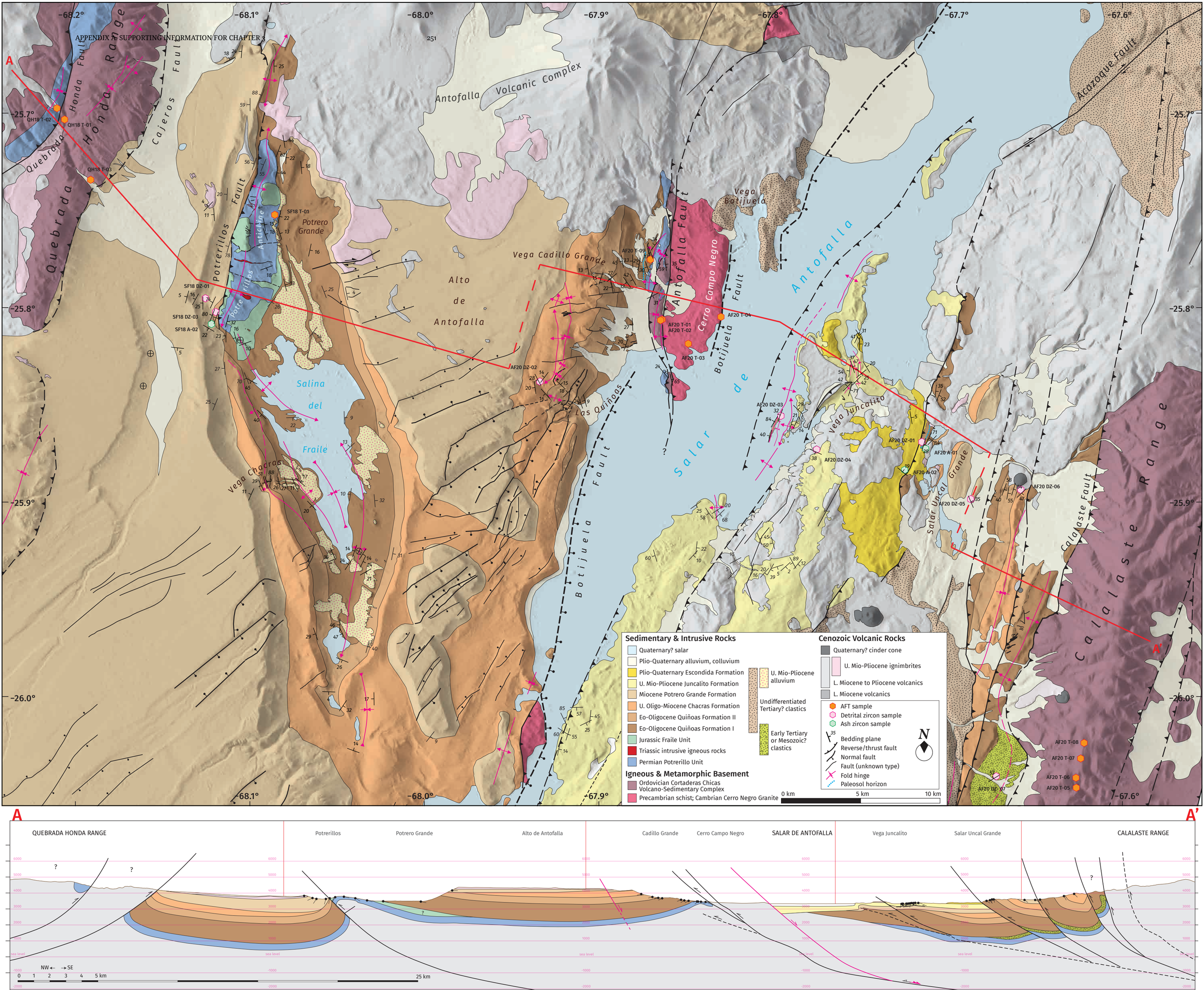
Quebrada Honda Range
Quebrada Honda Fault
Cajeros Fault
Potrerillos Fault
Potrerillos Anticline
Potrero Grande
Antofalla Volcanic Complex
Alto de Antofalla
Vega Cadillo Grande
Antofalla Fault
Cerro Campo Negro
Vega Botijuela
Botijuela Fault
Salar de Antofalla
Salina del Fraile
Las Quiñoas
Vega Chacras
Vega Juncalito
Salar Uncal Grande
Calalaste Fault
Calalaste Range
Acazoque Fault
QH18 T-01
QH18 T-02
QH18 T-03
SF18 T-01
SF18 DZ-01
SF18 DZ-03
SF18 A-02
AF20 T-01
AF20 T-02
AF20 T-03
AF20 T-04
AF20 T-05
AF20 T-06
AF20 T-07
AF20 T-08
AF20 T-09
AF20 DZ-01
AF20 DZ-02
AF20 DZ-03
AF20 DZ-04
AF20 DZ-05
AF20 DZ-06
AF20 DZ-07
AF20 A-01
AF20 A-02
A
A'
Sedimentary & Intrusive Rocks
Quaternary? salar
Plio-Quaternary alluvium, colluvium
Plio-Quaternary Escondida Formation
U. Mio-Pliocene Juncalito Formation
Miocene Potrero Grande Formation
U. Oligo-Miocene Chacras Formation
Eo-Oligocene Quiñoas Formation II
Eo-Oligocene Quiñoas Formation I
Jurassic Fraile Unit
Triassic intrusive igneous rocks
Permian Potrerillo Unit
U. Mio-Pliocene alluvium
Undifferentiated Tertiary? clastics
Early Tertiary or Mesozoic? clastics
Igneous & Metamorphic Basement
Ordovician Cortaderas Chicas Volcano-Sedimentary Complex
Precambrian schist; Cambrian Cerro Negro Granite
Cenozoic Volcanic Rocks
Quaternary? cinder cone
U. Mio-Pliocene ignimbrites
L. Miocene to Pliocene volcanics
L. Miocene volcanics
AFT sample
Detrital zircon sample
Ash zircon sample
Bedding plane
Reverse/thrust fault
Normal fault
Fault (unknown type)
Fold hinge
Paleosol horizon
N
0 km
5 km
10 km
QUEBRADA HONDA RANGE
Potrerillos
Potrero Grande
Alto de Antofalla
Cadillo Grande
Cerro Campo Negro
SALAR DE ANTOFALLA
Vega Juncalito
Salar Uncal Grande
CALALASTE RANGE
NW
SE
0 1 2 3 4 5 km
25 km
sea level

Figure S1. Large format geologic map and cross-section of the Antofalla region, reproduced in less detail as Figure 4 in the text.

Figure S2. Aerial image (provided by Google Earth) and topographic contour map showing location of apatite fission track samples in the Calalaste Range. Inset photo shows slickenfibre on a minor fault plane, likely due to flexural slip during pre-Cenozoic folding and shortening.

Figure S3. Aerial photographs illustrating folds, interpreted to be west-vergent fault propagation folds, in interbedded halite and sandstone strata on the eastern margin of the Salar de Antofalla. Main photo shows mapped folds and inferred blind thrust fault. Bottom-right inset shows detail of interbedded sandstone and halite deposits. Sandstone beds can be traced around the limbs of the fold, defining structural markers. Arrows point to individual sandstone beds (orangish-tan when exposed at the surface) that connect to linear features in the salt pan. Top-right inset shows where these folds suggest a ~14 km long blind thrust fault (area of main photograph boxed).

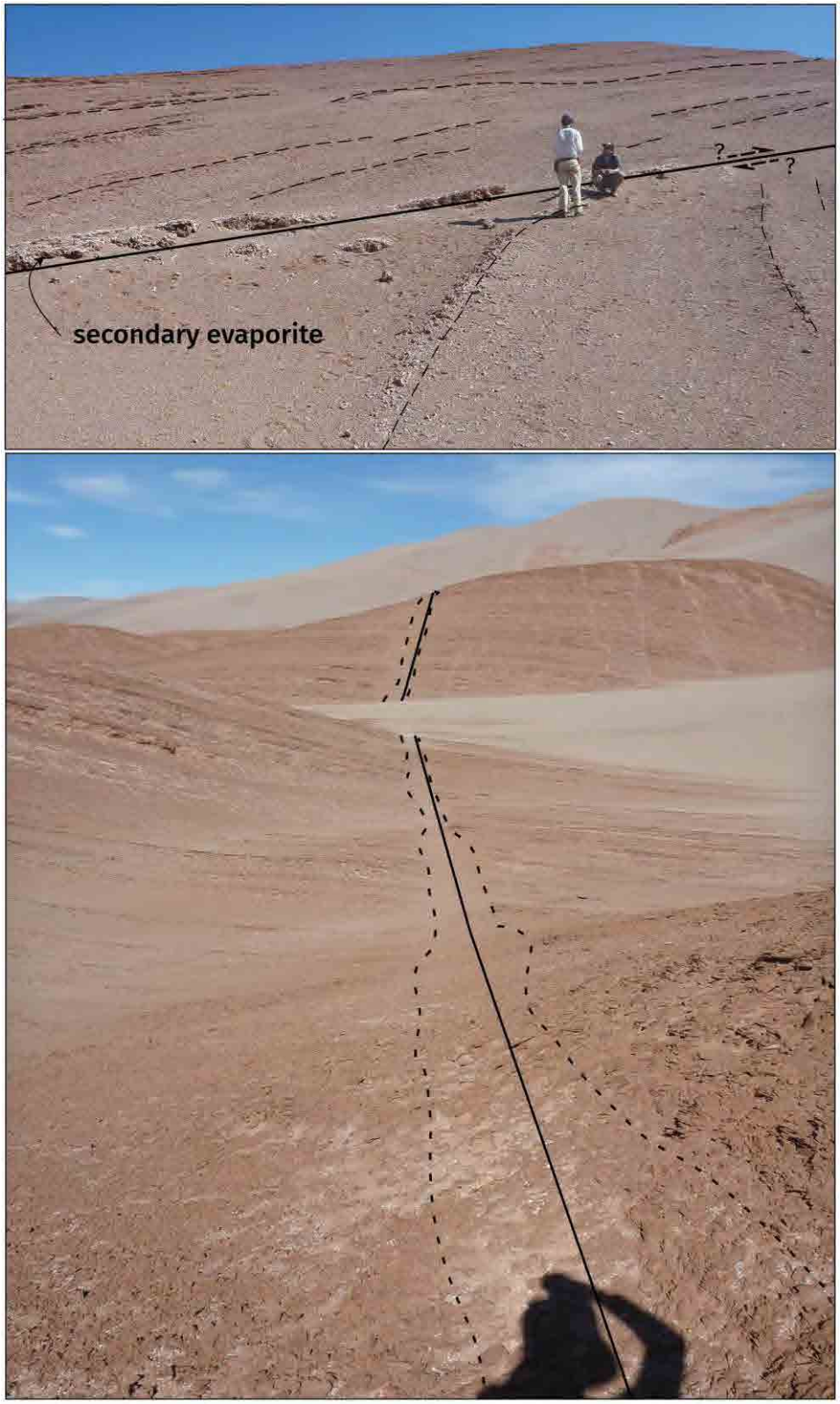

Figure S4. Photographs showing small faults in the fine-grained, thinly bedded sand-siltstone facies of the Lower Quiñoas Formation. Evaporitic soil development (commonly gypsisols) is

often observed on fault planes and unconformities. Fault plane traces annotated as solid lines. Dashed lines in the top photograph trace bedding contacts, showing change in dips across fault. Dashed lines in the lower photograph trace a damage zone where original bedding is destroyed and the rock is preferentially weathered, allowing the poorly exposed fault to be traced across the landscape.

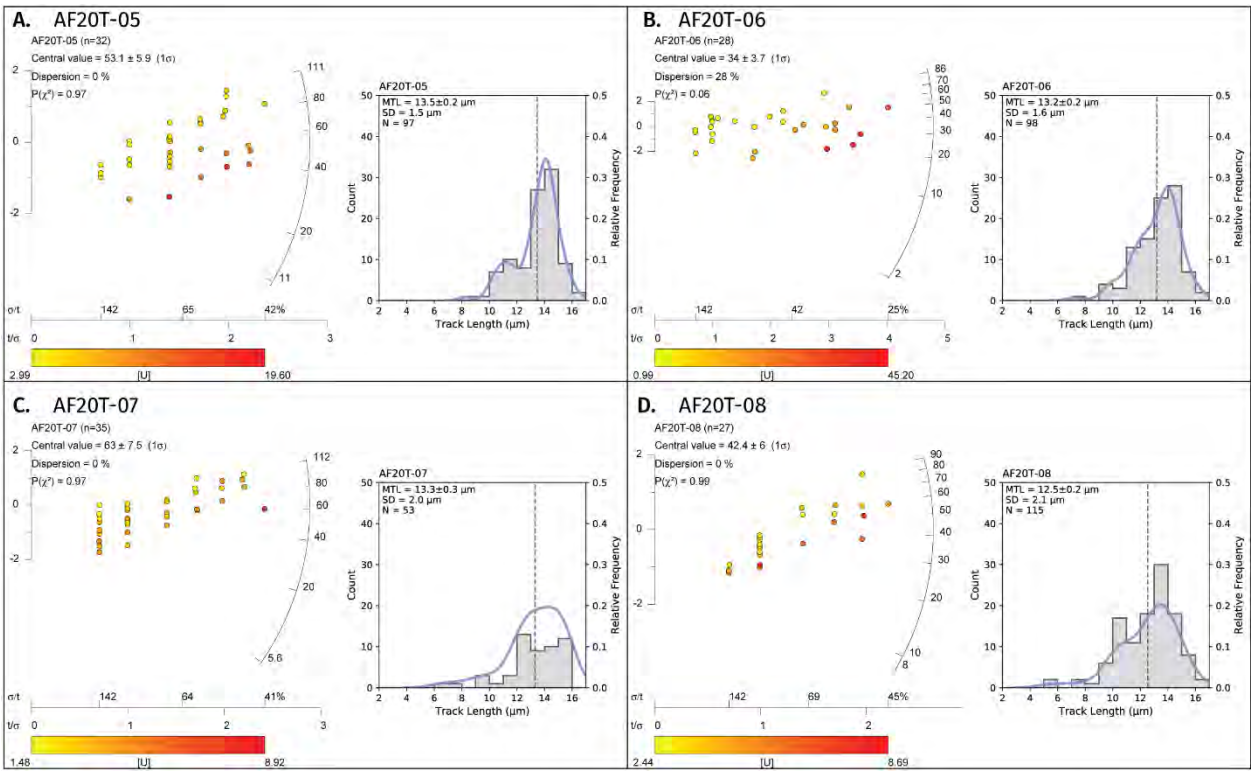

Figure S5. Radial plots and track length histograms for apatite fission track samples collected from the Calalaste Range. Radial plots are colored by uranium concentration ([U]).

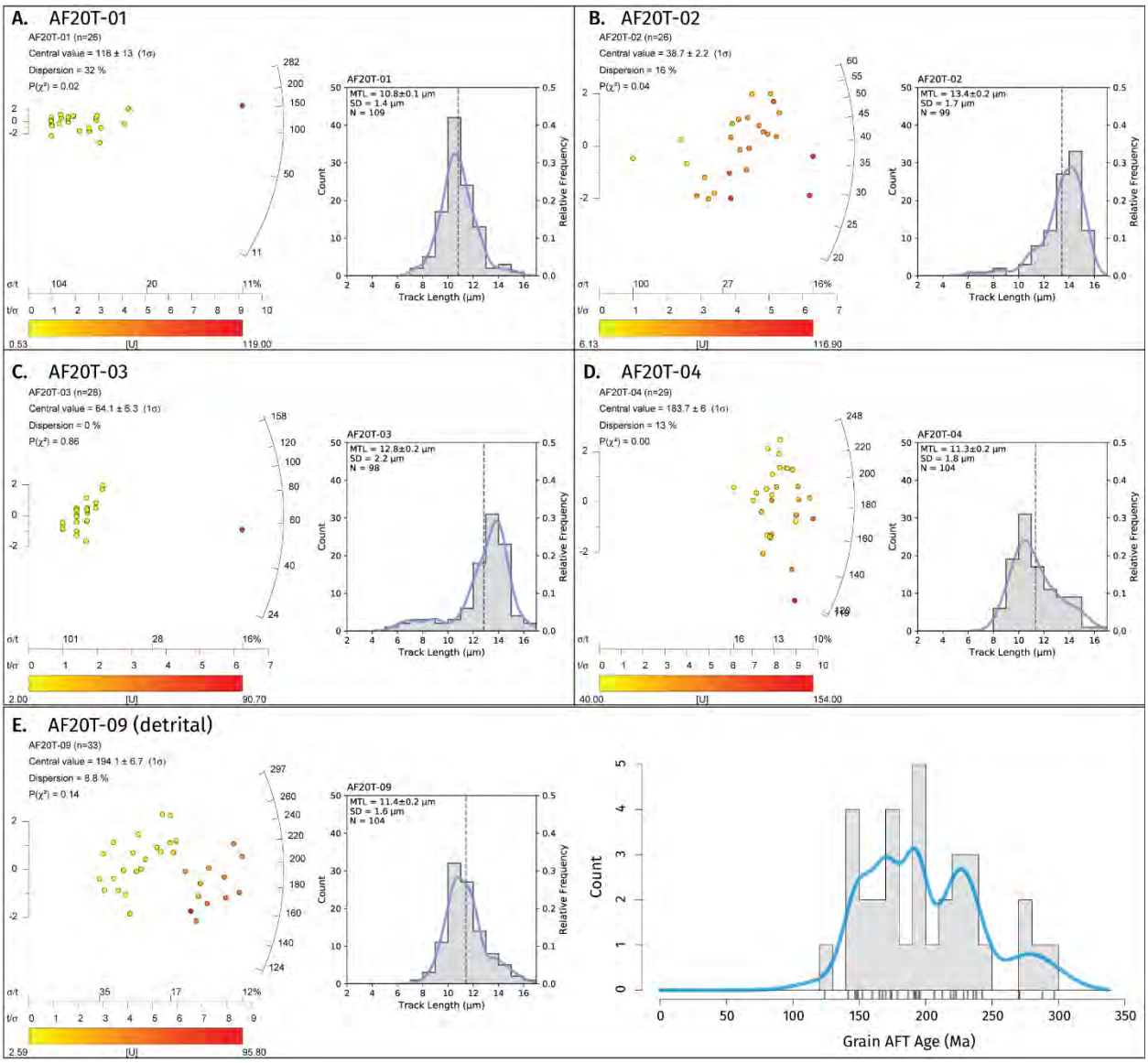

Figure S6. Radial plots and track length histograms for apatite fission track samples collected from Cerro Camp Negro and the Antofalla Fault system. Radial plots are colored by uranium concentration ([U]). Panel E depicts the detrital sample AF20T-09, including a histogram of grain ages on the right.

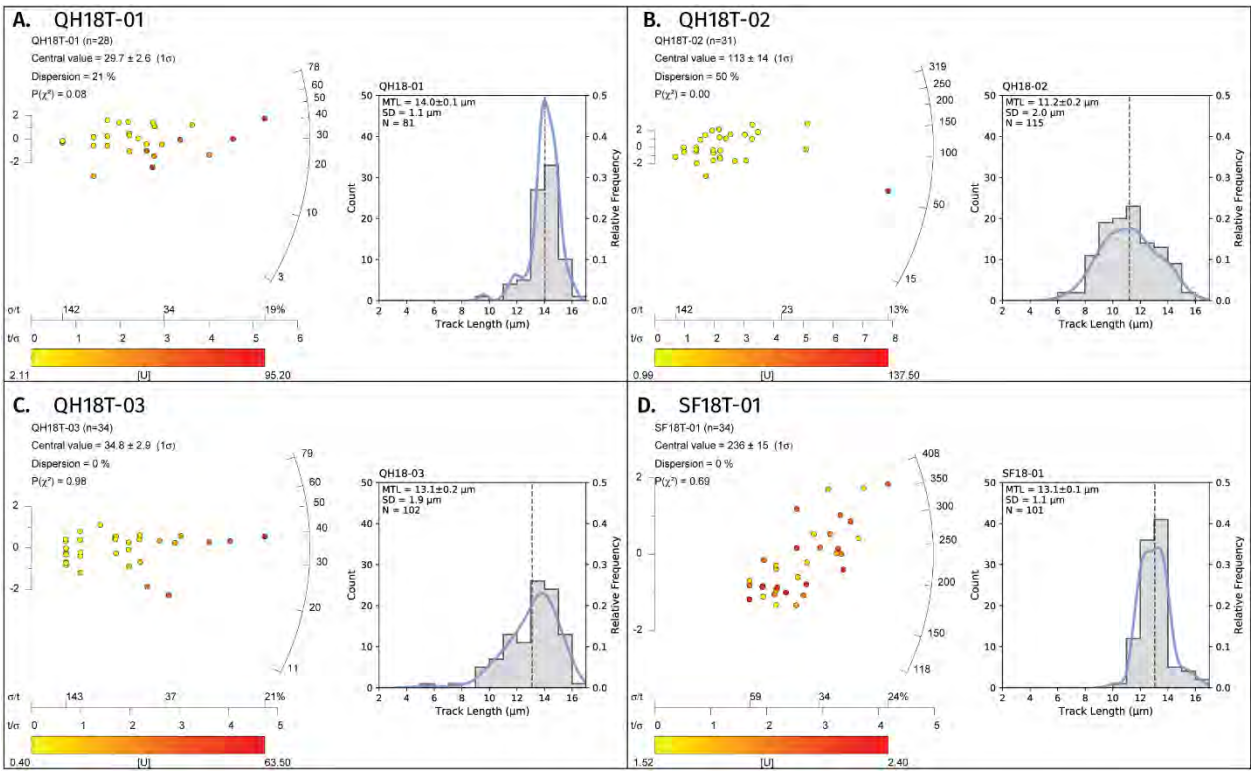

Figure S7. Radial plots and track length histograms for apatite fission track samples collected from the Quebrada Honda Range (A through C) and Salina del Fraile (D). Radial plots are colored by uranium concentration ([U]).

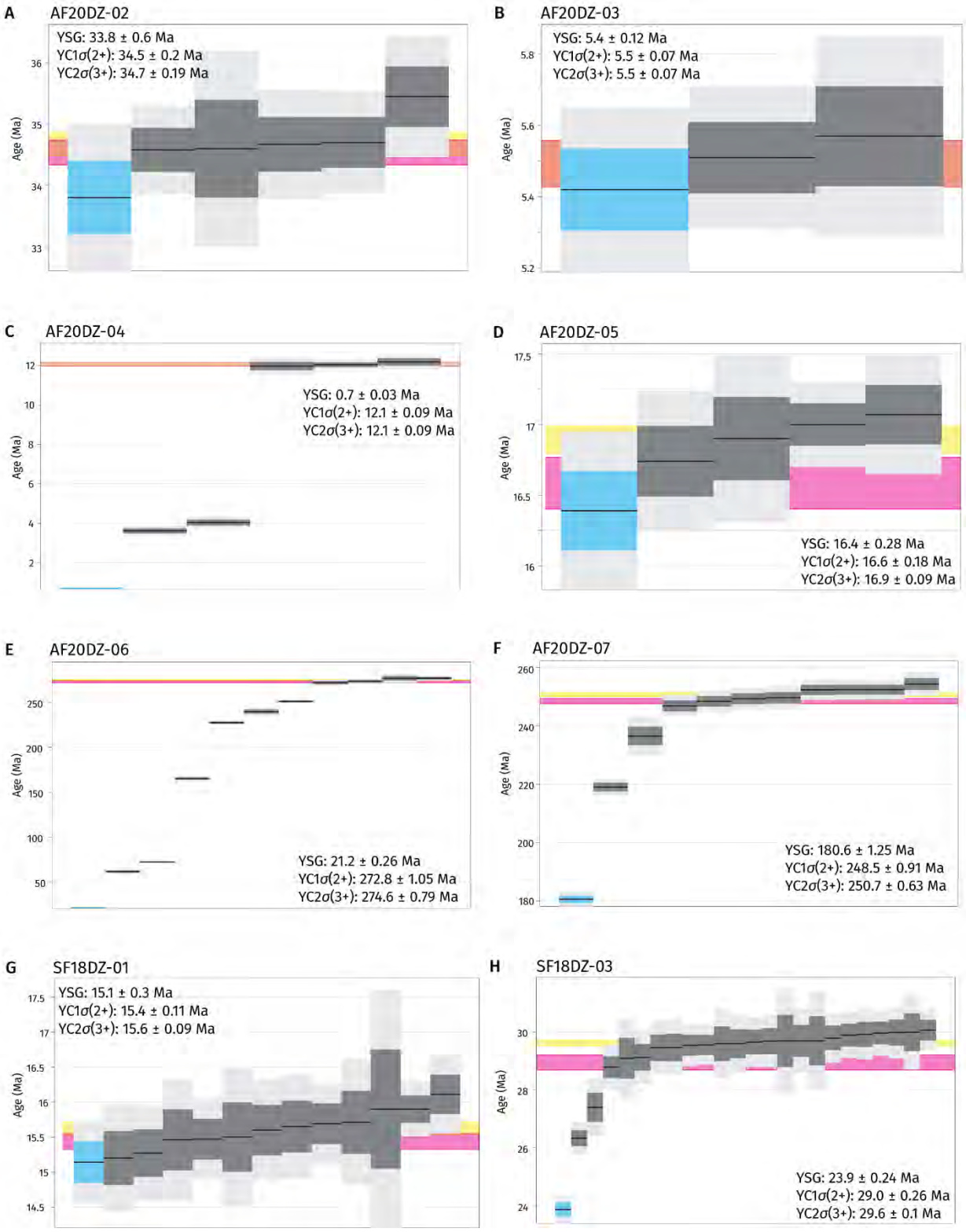

Figure S8. Plots of detrital zircon maximum depositional age determination, generated by the detritalPy software package. For each sample (A through H), the plots show individual grain

ages ranked from youngest to oldest by mean age. Ages plotted as mean (black line), ±1σ (dark gray rectangle), and ±2σ (light gray rectangle). Youngest single grain (YSG) is denoted by a blue rectangle. The age of the Youngest Cluster of 2 or more grains that overlap at the 1σ level (YC1σ[2+]) is denoted by the magenta region. The age of the Youngest Cluster of 3 or more grains that overlap at the 2σ level (YC2σ[3+]) is denoted by the yellow region. Where these last two regions overlap, the region appears orange. Annotated uncertainties are given at the 1σ level.

Table S1. Results of maximum depositional age determination for detrital and volcanic ash zircon samples.

Table S2. Structural measurements collected throughout the study area.

Table S3. Summary of apatite fission track analysis and methods used.

Table S4. Detailed data on single-grain apatite fission track ages and track length measurements.

Table S5. HeFTy thermal history modelling parameters and goodness-of-fit (GoF) statistics.

Sample	Paths	Acc.	Good	Pooled Age	Pred. Age	GoF	Length	Pred. Length	GoF
SF18T01	108599	7945	1000	223 +29/-26	223	1	14.15 ± 0.76	14.27 ± 0.71	0.89
QH18T01	637301	3780	1000	26.5 +4.2/-3.6	26.4	0.96	14.73 ± 0.89	14.97 ± 0.83	0.97
QH18T02	2439109	3920	500	85.1 +12/-10.5	85	0.99	12.79 ± 1.33	13.09 ± 1.40	0.99
QH18T03	251592	4689	1000	31.75 +5.9/-4.9	31.6	0.98	14.12 ± 1.42	14.24 ± 1.39	0.96
AF20T01	1775186	3202	500	118 +17/-15	118	0.96	12.43 ± 0.91	12.40 ± 0.80	0.93
AF20T02	192091	4131	1000	37.2 +3.7/-3.4	37.2	1	13.42 ± 1.73	13.75 ± 1.68	0.99
AF20T03	842702	44518	1000	58.5 +12.6/-10.4	58.3	0.98	12.84 ± 2.18	13.51 ± 1.58	0.62
AF20T04	375252	467	100	183 +11/-10	183	1	12.74 ± 1.24	12.87 ± 1.31	0.99
AF20T05	165777	4579	1000	46.5 +11.4/-9.2	46.5	0.99	14.40 ± 1.16	14.62 ± 1.15	0.95
AF20T06	265261	5006	1000	29.2 +5.3/-4.5	29.1	0.97	14.21 ± 1.13	14.35 ± 1.25	0.83
AF20T07	195209	8482	1000	49.0 +13.6/-10.6	49.1	0.98	14.20 ± 1.39	14.21 ± 1.55	0.95
AF20T08	241360	5071	1000	36.1 +12.0/-9.0	36	0.99	13.73 ± 1.38	13.81 ± 1.46	0.96

Table S6. Constraints on stratal thicknesses. Thicknesses are compiled from existing studies (Kraemer et al., 1999; Adelmann, 2001; Voss, 2002) and supplemented with field observations. FW and HW denote footwall and hanging wall, respectively.

	Potrerillos, FW	Potrerillos, HW	Potrero Grande	Cerro Campo Negro	Vega Juncalito	Calalaste Range
Escondida					varies	varies
Juncalito					240-420 m	
Potrero Grande	910 m		170 m	< 100 m		
Chacras	pinched out		pinched out	350 m		390-480 m
Quinoas (Upper)	<100 m		< 100 m	400 m		> 390 m
Quinoas (Lower)	pinched out		1100 m	750 m		> 840 m
Jurassic Fraile		150 m		missing		
Permian Potrerillos		>200 m		> 325 m		

B Supporting information for Chapter 4

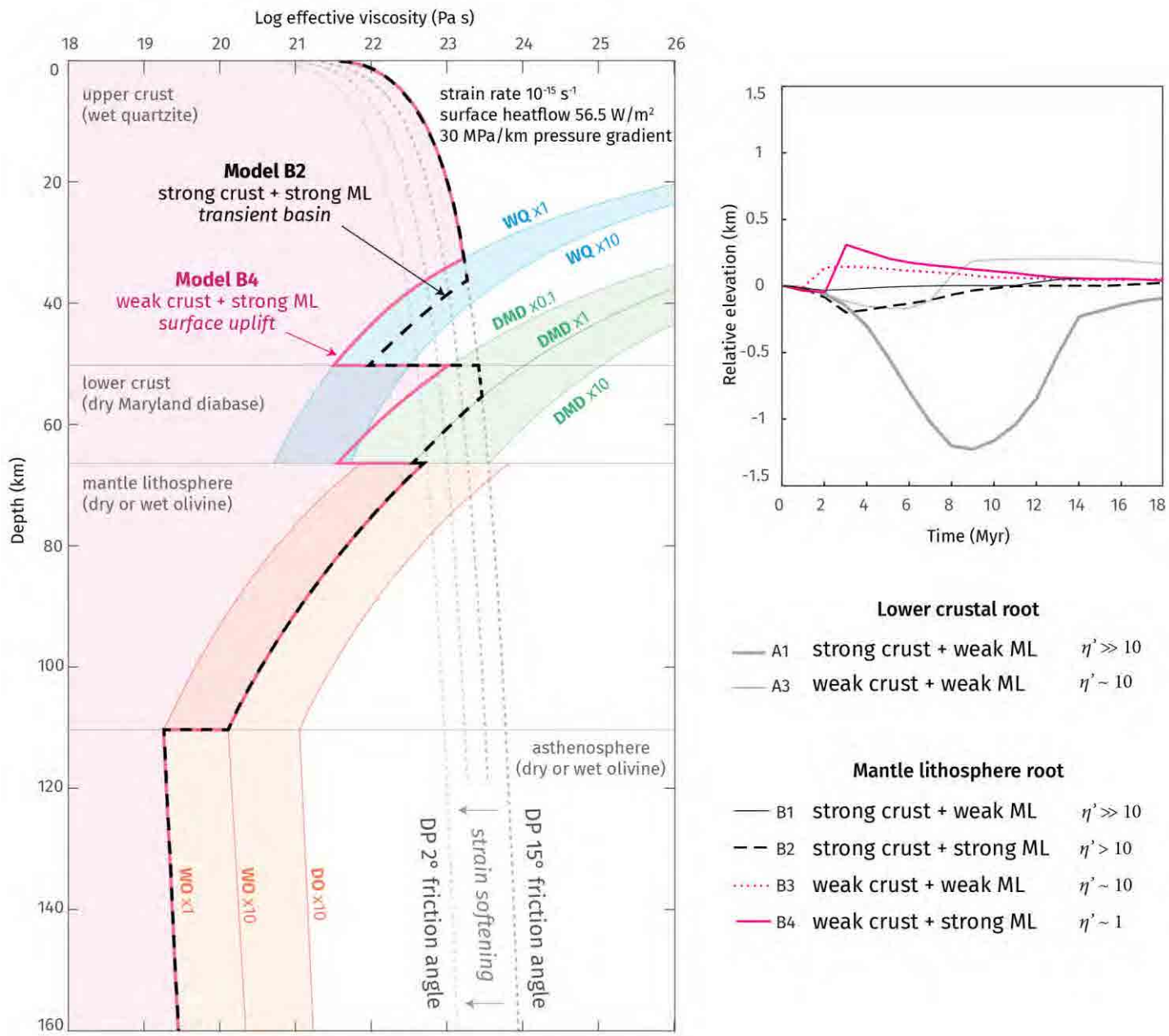

Supplementary Figure 1: Drip models from Wang et al. (2015) demonstrating how syn-drip subsidence (black lines) and uplift (magenta lines) both result from laboratory-derived rheologies with a Drucker-Prager yield criterion. Left panel plots effective viscosity vs. depth profiles of two illustrative models composed of various lithologies: wet quartzite (WQ), dry Maryland diabase (DMD), wet olivine (WO), and dry olivine (DO), along with Drucker-Prager yield envelopes (DP). These rheologies are weakened or strengthened by applying various strength factors between 0.1 and 10 (denoted, e.g. "×10"). Right panel plots surface elevation over the center of the drip through time, distinguishing weak-crust (surface uplift) from strong-crust (surface subsidence) styles of dripping. As discussed in the main paper, uplift vs. subsidence is controlled by relative crustal strength (η').

Supplementary Table 1: Summary of linear stability analyses (LSA) and numerical models (num.) of the characteristic wavelength of lithospheric dripping for an unstable layer of thickness h. Here, the unstable layer represents the mantle lithosphere, and the top boundary of the domain represents the Moho. While a characteristic wavelength $\lambda_c \sim 3h$ is common, when viscosity decays within the layer (with an e-folding length given by h/L), large wavelengths can occur if the overlying crust is decoupled from the lithosphere (large h/L).

Reference	Top boundary (Moho)	Density structure	Stress exponent (n)	Viscosity	substratum	h/L	λ_c	λ_c for h=40-80 km	method
Turcotte & Schubert (2002)	rigid	layered	1	uniform	Viscous layer		$2.568h$	100-200 km	LSA
Conrad & Molnar (1997)	rigid	layered	1	uniform	Viscous half-space		$3.7h$	150–300 km	LSA
Conrad & Molnar (1997)	rigid	layered	∞	uniform	Viscous half-space		$2.8h$	110–220 km	LSA
Conrad & Molnar (1997)	rigid	layered	1	layered	Inviscid half-space		$3h$	120–240 km	LSA
Conrad & Molnar (1997)	rigid	layered	∞	layered	Inviscid half-space		$3h$	120–240 km	LSA
Conrad & Molnar (1997)	rigid	linear decay	3.5	exp. decay	Viscous half-space	<0.5	$2.6h$	100–200 km	num.
Conrad & Molnar (1997)	rigid	linear decay	3.5	exp. decay	Viscous half-space	>6	$7.8L$	<50–100 km	num.
Harig et al. (2008)	stress-free	linear decay	1	exp. decay	Viscous half-space	4	$12.6h$	500–1000 km	num.
Harig et al. (2008)	stress-free	linear decay	1	exp. decay	Viscous half-space	1	$3.1h$	120–240 km	num.
Harig et al. (2008)	stress-free	linear decay	3	exp. decay	Inviscid half-space	4	$4.2h$	170–340 km	num.
Harig et al. (2008)	stress-free	linear decay	3	exp. decay	Inviscid half-space	1	$> 31h$	>1000 km	num.

References

Conrad, C. P., & Molnar, P. (1997). The growth of Rayleigh-Taylor-type instabilities in the lithosphere for various rheological and density structures. Geophysical Journal International, 129(1), 95–112. https://doi.org/10.1111/j.1365-246X.1997.tb00939.x

Harig, C., Molnar, P., & Houseman, G. A. (2008). Rayleigh-Taylor instability under a shear stress free top boundary condition and its relevance to removal of mantle lithosphere from beneath the Sierra Nevada. Tectonics, 27(6), 1–15. https://doi.org/10.1029/2007TC002241

Turcotte, D. L., & Schubert, G. (2002). Geodynamics, 472 pp. https://doi.org/10.1017/CBO9780511807442

Wang, H., Currie, C. A., & DeCelles, P. G. (2015). Hinterland basin formation and gravitational instabilities in the central Andes: Constraints from gravity data and geodynamic models. *Geological Society of America Memoirs*, *212*, 387–406. https://doi.org/10.1130/2015.1212(19)